climate

Assessment of Climate Change Impacts on Water Quantity and Quality at Small Scale Watersheds

Edited by

Ying Ouyang, Sudhanshu Sekhar Panda and Gary Feng

MDPI

Assessment of Climate Change Impacts on Water Quantity and Quality at Small Scale Watersheds

Assessment of Climate Change Impacts on Water Quantity and Quality at Small Scale Watersheds

Editors

Ying Ouyang
Sudhanshu Sekhar Panda
Gary Feng

MDPI

Editors

Ying Ouyang
USDA Forest Service
Southern Research Station
Mississippi State
United States

Sudhanshu Sekhar Panda
Institute of Environmental
Spatial Analysis
University of North Georgia
Oakwood
United States

Gary Feng
USDA
Agricultural Research Service
in Starkville
Mississippi State
United States

This is a reprint of articles from the Special Issue published online in the open access journal *Climate* (ISSN 2225-1154) (available at: www.mdpi.com/journal/climate/special_issues/climate_watersheds).

For citation purposes, cite each article independently as indicated on the article page online and as indicated below:

LastName, A.A.; LastName, B.B.; LastName, C.C. Article Title. *Journal Name* **Year**, *Volume Number*, Page Range.

Contents

About the Editors

Ying Ouyang

Ying Ouyang, Ph.D. in soil physics, registered Professional Hydrologist, and Fellow of Soil Science Society of American (SSSA). He is research hydrologist at the United States Department of Agriculture, Forest Service, Southern Research Station. Main field of interests and activities: (1) pilot- and basin-scale modeling of surface-ground water hydrological processes and water quality under changing climate; (2) multivariate (e.g., copula and wavelet) statistical analysis of temporospatial variability and trend of hydrological processes and water quality; (3) real-time monitoring of hydrological cycles in the soil–surface water–tree–atmosphere continuum; and (4) develop STELLA models for simulating couple transport of water and solute in vadose zone soil, biomass production and CO_2 emission in woody crop plantation, and wastewater treatment in constructed wetland.

Sudhanshu Sekhar Panda

Sudhanshu Sekhar Panda, Ph.D. is a professional Agricultural Engineer, specializes in soil and water engineering, precision agriculture, site-specific crop management (SSCM), and geospatial technology and its application in sustainable environmental management through decision support system development. He is a Professor at Institute for Environmental Spatial Analysis of University of North Georgia. His interest in research and teaching involves: 1) developing automated geospatial models for proactive management decision support in case of environmental geohazards in present climate change scenario; 2) developing artificial intelligence based real-time small ruminant health management system through animal movement tracking with RFIDs and providing instant suggestion to farmers on site-specific fodder production; 3) developing geospatial models to determine road crossings vulnerability through geo-morphological models; 4) studying the soil subsidence, groundwater contamination vulnerability, and sinkhole probability through geospatial modeling; 5) developing SSCM for row-crop agriculture, pasture/fodder/forage, horticulture, and forest production optimization; and 6) assisting in bioenergy research through precision agriculture, hydrologic analyses, and geospatial technology application.

Gary Feng

Gary Feng, Ph.D. in soil and water sciences, the Fellow of SSSA and American Society of Agronomy. Research Soil Scientist at United States Department of Agriculture, Agricultural Research Service. Areas of interests and activities: 1) surface–vadose–ground water hydrological processes under changing climate; 2) soil nutrients cycling, fate and transport; 3) agroecosystem modeling; (4) soil health measurement and assessment; and (5) soil and water management and conservation.

Editorial

Linking Climate-Change Impacts on Hydrological Processes and Water Quality to Local Watersheds

Ying Ouyang [1],*, Sudhanshu Sekhar Panda [2] and Gary Feng [3]

1   USDA, Forest Service, Southern Research Station, Center for Bottomland Hardwoods Research, Starkville, MS 39762, USA
2   Institute for Environmental Spatial Analysis, University of North Georgia, Oakwood, GA 30566, USA; sudhanshu.panda@ung.edu
3   Genetics and Sustainable Agriculture Research Unit, Crop Science Research Laboratory, USDA-Agricultural Research Service, P.O. Box 5367, 810 Highway 12 East, Starkville, MS 39762, USA; gary.feng@ars.usda.gov
*   Correspondence: ying.ouyang@usda.gov

1. Introduction

Estimation of hydrological processes and water quality is central to water resource management, clean water supply, environmental protection, and ecological services [1,2]. Climate change is a natural phenomenon, but anthropogenic activities such as fossil fuel burning, industrial pollution, land use change, and population growth have accelerated greenhouse gas emissions, which have, in turn, resulted in abnormal climate patterns [3]. These patterns exacerbate hydrologic and water quality uncertainties in predicting droughts, floods, water resource availability, environmental pollution, and ecosystem services. To mitigate such climate-change impacts, water resource managers and decision makers should be able to assess potential threats and develop strategies to adapt for future climatic conditions. Currently, projection of future climate impacts on hydrologic cycles and water quality are generally accomplished through process-based watershed models in conjunction with future climate-change scenarios that are created by the general circulation models (GCMs), regional climate models (RCMs), and coupled model inter comparison project phase (CMIP5). While these scenarios provide invaluable insights into the direction to project the future hydrologic and water quality trends, the limitations on using these scenarios are [4]: (1) They have low spatial resolution and are somewhat difficult to downscale for local watersheds (i.e., smaller than HUC12 level watersheds); (2) They have low temporal resolution (e.g., weekly or monthly time intervals) and are difficult to disaggregate into daily or hourly intervals required by some watershed models; and (3) They are not flexible to answer the "what-if" questions for local watersheds such as: What will happen to streamflow, water quality, and water availability in a small watershed if the abnormal and localized rainfall (cloudburst) events (e.g., very dry in July and very wet in November) occur in the next five years? In order to take those challenges and meet the needs, this Special Issue "Assessment of Climate Change Impacts on Water Quantity and Quality at Small Scale Watersheds", inspired by the Hydrology–H030 Session of the 2019 America Geophysical Union Fall Meeting, was initiated to circumvent the limitations.

2. Aims and Scope

The Special Issue is aimed to link climate-change impacts on hydrological processes and water quality for local watersheds or basins. Emphases are on climate-induced water resource vulnerabilities (e.g., flood, drought, groundwater, evapotranspiration, and water pollution) and methodologies (e.g., computer modeling, field measurement, and management practice) employed to mitigate and adapt climate-change impacts on water resources. In addition, application implications to water resource management were discussed in this Special Issue.

3. Presentation of the Published Papers

This Special Issue solicits 11 studies covering (1) various geographical locations around the world, including Indian subcontinent (northern Himalayan Terai, southern Indian River, and Cauvery and Godavari River basins), sub-Saharan Africa (Ethiopian Rift valley and Nile River Basin), western and southeastern United States (California Central Valley, Alabama, and Mississippi River Basin), and western and southern China (Xinjiang basin and Lijiang River basin); (2) hydrological processes such as springs, streamflow, surface runoff, evapotranspiration, and tree sapflow; (3) climate-change patterns such as drought, warming, and water-energy nexus; (4) surface and ground water quality such as nutrients, organic matter, salinity, and sediment; and (5) water resource management to improve economic, health, and other quality of lives. All eleven papers deal with local scale (or smaller than regional scale) watersheds or basins under the effects of climate change. Eight publications reported watershed modeling results, whereas three publications more or less reported results on experimental measurements. They are categorized into (i) Climate impacts on hydrology, (ii) Climate impacts on water quality, and (iii) Climate implications and adaptation in water resources management.

3.1. Climate Impacts on Hydrology

Hydrological processes at local watersheds are essential to water resource management, water supply planning, and ecosystem restoration and service under changing climate. In this collection, two studies were conducted in India; one analyzed the vulnerability of more than three million springs at the Indian Himalayan basin while the another analyzed the drought vulnerability in the southern Indian River basin. Daniel et al. [5] attempted to conceptualize vulnerability of Himalayan springs and identify the biophysical and socio-economic stressors affected on the springs. The conceptual framework is a useful theoretical construct for enabling policymakers and project managers to follow a structured process for arriving at decisions concerning judicious use of springs resources under changing climate. However, the study did not include specific hydrological processes. Kumar et al. [6] investigated monthly and seasonal drought in four major river basins in south Indian using GRACE-Based Groundwater Drought Index. Their study provided some robust quantitative results of GRACE water storage variations and a new approach to link surface and subsurface conditions when investigating droughts.

Another two studies center on China: one study investigated the spatiotemporal patterns of asymmetric warming in Xinjiang basin of western China using normalized difference vegetation index (NDVI) data, while the other study analyzed the effects of climate change scenarios on hydrological variables (i.e., evapotranspiration and runoff) in Lijiang River Basin by linking the outputs from the GCM with the Soil and Water Assessment Tool (SWAT). Heng et al. [7] analyzed spatiotemporal patterns of climate asymmetric warming and vegetation activities in an arid and semiarid region of Xinjiang basin, China, using the climate and NDVI data. They reported that the warming rates in this region are higher than the world average. Tan et al. [8] assessed the effects of climate change scenarios on evapotranspiration and surface runoff by linking the outputs from the GCM scenarios with the SWAT hydrologic model for a case study in the Lijiang River basin, China. These authors found that precipitation, temperature, and evapotranspiration will increase with uneven distributions under future climate conditions.

Studies in US cover drought and streamflow. He et al. [9] projected changes in water year types and hydrological drought in California's Central Valley in the 21st century using water year index classification approach. They found that hydrological droughts in the snowmelt season and wet season exhibit upward and downward trends, respectively. Quansah et al. [10] assessed streamflow due to future climate change in the Alabama River basin for the mid- and late-21st century by using climate-change scenarios in conjunction with SWAT model. They argued that while the simulation results are prone to inherent uncertainties, they could provide some critical information for stakeholders on sustainable water resource management under the changing climate. Both studies are warranted to

circumvent the limitations of climate-change scenarios as stated in the Introduction of this editorial summary.

Many water-energy models are not able to be applied in developing countries due to the lack of measured data, computational capacity, and skill requirement. However, Yimere and Assefa [11] developed a model to assess the Water-Energy relationship in the Nile River basin, Africa under future climate change scenario. Nonetheless, their study has limitations due to incomplete and inadequate data usage for model calibration and verification. Few studies have been devoted to investigating hydrological processes under changing climate through experimental measurements in this Special Issue. Using their field measured tree sapflow and weather data, Ouyang et al. [12] developed Structural Thinking and Experiential Learning Laboratory with Animation (STELLA) model to assess eastern cottonwood water flow using adjusted vapor pressure deficit under the changing climate conditions.

3.2. Climate Impact on Water Quality

Three studies in this collection dealt with water quality. Godebo et al. [13] assess water quality for irrigated agriculture, alongside perceptions and adaptations of farmers to climate change in the main Ethiopian Rift valley. Using data from 147 farmers and 162 surface and ground water quality samples, they reported that most groundwaters were unsuitable for long-term agricultural use due to their high salinity and sodium adsorption ratio. This is one of the major consequences of global warming/climate change that agriculture stakeholders including irrigation researchers are not being seriously considered yet. Pérez-Gutiérrez [14] investigated nutrient and sediment loads at a tailwater recovery ditch in Mississippi, US by using the annualized agricultural non-point source (AnnAGNPS) model. However, climate-change impacts on water quality have not been fully addressed in their study. Dewey et al. [15] performed field measurement to estimate the sources of sediment and organic matter fluxes in intermittent rivers and ephemeral streams (IRES) of a subtropical watershed in Mississippi, USA. They stated that climate-induced changes in precipitation and discharge may impact organic carbon fluxes from IRES.

3.3. Implications and Adaption

All papers except one [14] in this collection linked the research findings to climate-change implications and adaptions. Some of the climate implications and adaptions are very general, while others are specific and concrete. For example, the study on springs in the Indian Himalayas [5] synthesized climate stressors, indicators, and the conceptualization of vulnerability that provide a general evidence-based decision support system for better management of Himalayan springs under the changing climate, whereas the study on field measurement and STELLA modeling of tree sapflow using vapor pressure deficit [12] would provide a specific and new paradigm for researchers to predict tree sapflow under the changing climate by using the commonly available vapor pressure deficit data. Furthermore, the study on water quality threats due to climate change in the Ethiopian Rift valley [13] highlighted the complex nexus between high groundwater salinity and climate change, which provides a concrete direction for climate adaption to farmers.

4. Conclusions

The papers collected in this Special Issue tackle multiple aspects on how hydrological processes and water quality at local watersheds could be affected by climate change through hydrological modeling, statistical analysis, and field measurement. In addition, climate-change implications and adaptions based on research findings are discussed and are highly beneficial to local water resources managers and stakeholders. In addition, the studies in this collection provide a variety of research methods and approaches to tackle challenging questions faced by local watersheds under various climate change scenarios. Many of the studies emphasized the advantages of geospatial engineering and technology, i.e., geographic information systems (GIS), remote sensing, global navigation satellite system

(GNSS) application in solving water resources management issues that occurred in consequence of climate change. As water resources management decision support is essentially of spatio-temporal nature, GIS and GNSS helps in localized analyses and remote sensing data helps analyzing temporal changing scenario. STELLA, AnnAGNPS, SWAT, GRACE, and especially, GCM models used in the research papers in this special issue for water resources management decision support are all of spatio-temporal analytics models. As seen with wide-range of articles published in the Special Issue, climate-centric researchers engaged in the said topics will be highly benefitted. Readers of the Special Issue articles will get insight on geospatial engineering and technology and other advanced models usage in their future research on climate change affected hydrologic DSS development.

Today, most climate change studies focus on large regional and global scales or using climate change scenarios that have low flexibility with inaccurate data for local scale watersheds. The topics in this Special Issue provide a new research direction in dealing with local watersheds under changing climate and will receive a global interest for years to come. As the research articles in the Special Issue encompass various spatially (geographically) differentiated watersheds, covers developed, developing, and even poor countries with different watershed management conditions available to them due to funding availability, the research results, especially the decision supports developed through the studies, will be very beneficial in furthering watershed hydrologic research under changing climate. Studies in the Special Issue included heterogeneous environmental features, such as land use, soils, topography, climate/weather pattern, and above all hydrological scenarios, can help future studies that glean research methods from them.

Conflicts of Interest: The authors declare no conflict of interest.

References

1. Ouyang, Y.; Leininger, T.D.; Moran, M. Estimating effects of reforestation on nitrogen and phosphorus load reductions in the Lower Yazoo River Watershed, Mississippi. *Ecol. Eng.* **2015**, *75*, 449–456. [CrossRef]
2. Parajuli, P.B.; Jayakody, P.; Sassenrath, G.F.; Ouyang, Y. Assessing the impacts of climate change and tillage practices on stream flow, crop and sediment yields from the Mississippi River Basin. *Agric. Water Manag.* **2016**, *168*, 112–124. [CrossRef]
3. Ouyang, Y.; Wan, Y.; Jin, W.; Leininger, T.D.; Feng, G.; Han, Y. Impact of climate change on groundwater resource in a region with a fast depletion rate: The Mississippi Embayment. *J. Water Clim. Chang.* **2021**, *12*, 2245–2255. [CrossRef]
4. Ouyang, Y.; Parajuli, P.B.; Feng, G.; Leininger, T.D.; Wan, Y.; Dash, P. Application of Climate Assessment Tool (CAT) to estimate climate variability impacts on nutrient loading from local watersheds. *J. Hydrol.* **2018**, *563*, 363–371. [CrossRef] [PubMed]
5. Daniel, D.; Anandhi, A.; Sen, S. Conceptual Model for the Vulnerability Assessment of Springs in the Indian Himalayas. *Climate* **2021**, *9*, 121. [CrossRef]
6. Satish Kumar, K.; AnandRaj, P.; Sreelatha, K.; Bisht, D.S.; Sridhar, V. Monthly and Seasonal Drought Characterization Using GRACE-Based Groundwater Drought Index and Its Link to Teleconnections across South Indian River Basins. *Climate* **2021**, *9*, 56. [CrossRef]
7. Heng, T.; Feng, G.; Ouyang, Y.; He, X. The Spatiotemporal Patterns of Climate Asymmetric Warming and Vegetation Activities in an Arid and Semiarid Region. *Climate* **2020**, *8*, 145. [CrossRef]
8. Tan, Y.; Guzman, S.M.; Dong, Z.; Tan, L. Selection of Effective GCM Bias Correction Methods and Evaluation of Hydrological Response under Future Climate Scenarios. *Climate* **2020**, *8*, 108. [CrossRef]
9. He, M.; Anderson, J.; Lynn, E.; Arnold, W. Projected Changes in Water Year Types and Hydrological Drought in California's Central Valley in the 21st Century. *Climate* **2021**, *9*, 26. [CrossRef]
10. Quansah, J.E.; Naliaka, A.B.; Fall, S.; Ankumah, R.; Afandi, G.E. Assessing Future Impacts of Climate Change on Streamflow within the Alabama River Basin. *Climate* **2021**, *9*, 55. [CrossRef]
11. Yimere, A.; Assefa, E. Assessment of the Water-Energy Nexus under Future Climate Change in the Nile River Basin. *Climate* **2021**, *9*, 84. [CrossRef]
12. Ouyang, Y.; Leininger, T.D.; Renninger, H.; Gardiner, E.S.; Samuelson, L. A Model to Assess Eastern Cottonwood Water Flow Using Adjusted Vapor Pressure Deficit Associated with a Climate Change Impact Application. *Climate* **2021**, *9*, 22. [CrossRef]
13. Godebo, T.R.; Jeuland, M.A.; Paul, C.J.; Belachew, D.L.; McCornick, P.G. Water Quality Threats, Perceptions of Climate Change and Behavioral Responses among Farmers in the Ethiopian Rift Valley. *Climate* **2021**, *9*, 92. [CrossRef]

14. Pérez-Gutiérrez, J.D.; Paz, J.O.; Tagert, M.L.M.; Yasarer, L.M.W.; Bingner, R.L. Using AnnAGNPS to Simulate Runoff, Nutrient, and Sediment Loads in an Agricultural Catchment with an On-Farm Water Storage System. *Climate* **2020**, *8*, 133. [CrossRef]

15. Dewey, J.; Hatten, J.; Choi, B.; Mangum, C.; Ouyang, Y. Climate Drivers and Sources of Sediment and Organic Matter Fluxes in Intermittent Rivers and Ephemeral Streams (IRES) of a Subtropical Watershed, USA. *Climate* **2020**, *8*, 117. [CrossRef]

Conceptual Model for the Vulnerability Assessment of Springs in the Indian Himalayas

Denzil Daniel [1], Aavudai Anandhi [2] and Sumit Sen [1,3,*]

1   Centre of Excellence in Disaster Mitigation and Management, Indian Institute of Technology Roorkee, Roorkee 247667, India; denzil.dm@sric.iitr.ac.in
2   Biological Systems Engineering Program, College of Agriculture and Food Sciences, Florida A&M University, Tallahassee, FL 32307, USA; anandhi.swamy@famu.edu
3   Department of Hydrology, Indian Institute of Technology Roorkee, Roorkee 247667, India
*   Correspondence: sumit.sen@hy.iitr.ac.in; Tel.: +91-1332-284754

Abstract: The Indian Himalayan Region is home to nearly 50 million people, more than 50% of whom are dependent on springs for their sustenance. Sustainable management of the nearly 3 million springs in the region requires a framework to identify the springs most vulnerable to change agents which can be biophysical or socio-economic, internal or external. In this study, we conceptualize vulnerability in the Indian Himalayan springs. By way of a systematic review of the published literature and synthesis of research findings, a scheme of identifying and quantifying these change agents (stressors) is presented. The stressors are then causally linked to the characteristics of the springs using indicators, and the resulting impact and responses are discussed. These components, viz., stressors, state, impact, and response, and the linkages are used in the conceptual framework to assess the vulnerability of springs. A case study adopting the proposed conceptual model is discussed for Mathamali spring in the Western Himalayas. The conceptual model encourages quantification of stressors and promotes a convergence to an evidence-based decision support system for the management of springs and the dependent ecosystems from the threat due to human development and climate change.

Keywords: vulnerability assessment; Indian Himalayas; springs; springshed management; water security

1. Introduction

Springs in the mid-hills of the Hindu Kush Himalayas (HKH), crucially important for the survival of the 240 million hill and mountain people residing in the region [1], are drying [2–7]. The mid-hills are located at a lower elevation compared to the largest reserves of snow and ice outside the North and South Poles (the HKH sometimes referred to as the 'Third Pole'). Though the 10 rivers that originate in the glaciers of these 'water towers' benefit the nearly 2 billion people living in their hydrological downstream, this rich supply of freshwater reserves is out of reach for the mid-hill communities. These communities are dependent primarily on water stored underground and naturally drained through springs for their domestic and irrigation needs.

The paradoxical role of the humble springs, in contrast to the vast glaciers and rich rivers of the HKH, is not unusual considering the distribution of water on the surface of the 'Blue Planet'. Most of the water covering the Earth's surface, as seen from outer space, nearly 71% (hence the sobriquet 'Blue Planet'), is practically useless, with the actual reserves of freshwater accounting for only close to 2.5% of the total water of the world and the remaining reserves of water trapped in the world's oceans, saline lakes, and deep underground reservoirs [8]. Usable groundwater accounts for about 30% of these freshwater reserves, while flow in rivers, water in swamps, and freshwater lakes, together, make up a little over 0.03% [8]. Most of the entire groundwater reserves drain

into springs and streams at different time scales, ranging from less than a year to more than 100,000 years [9]. Going by these broad estimates, natural springs, which are freshwater resources at the interface of surface water and groundwater, where underground water emerges on to the Earth's surface, forming streams, ponds, and swamps [10], account for even less than 0.03% of the freshwater resources of the world at any given time.

Though seemingly small in terms of absolute volume of reserves of freshwater, springs have been a vital source of water for drinking and sanitation since ancient times (for example, Roman, Mesopotamian, Egyptian, and Chinese civilizations developed systems to tap and transport spring water) [11]. Even by recent estimates, water from karst springs, which are some of the largest springs of the world, provides drinking water to 678 million people, or 9.28% of the world's population [12]. The World Health Organization estimated in 2017 that 435 million people still draw water directly from unprotected wells and springs [13]. Though the share of springs in the global freshwater reserves is small, the dependence for water primarily on springs poses a water security threat in many parts of the world, especially the HKH. In this paper, we draw attention to the Indian Himalayas, a smaller geographical extent within the HKH, but the lessons learnt apply to the larger HKH region as well.

In the Indian Himalayan Region (IHR), springs are the main source of water for rural communities [14–16]. Both rural and urban settlements, with a combined population of nearly 50 million, depend on water sourced from springs for use in drinking, domestic, livestock, and agricultural water needs [14,17–19]. There are 60,000 villages, 500 growing townships, and 8–10 cities in the IHR, and 23.9% of all surface water schemes in IHR states are sourced from springs, with more than 20% of villages in IHR states reporting having a spring [14]. Even by conservative estimates, more than 50% of the population in the IHR, thus, are dependent on spring water for their sustenance [14]. Additionally, out of the 12.5% of cultivated area in the IHR, only 11% is irrigated, of which 65% is sourced from springs [14]. Though these numbers are a gross underestimation and are based on secondary data, these numbers represent the dependence of a large proportion of the population in the IHR on water sourced from springs [14]. IHR springs are also the source of the revered Himalayan rivers, such as headwater tributaries of the River Ganga and River Yamuna River [14]. Though a lack of studies that estimate the exact contribution of the Himalayan springs to the rivers originating in the Himalayas exists, there is some evidence to suggest that flow in these rivers during lean seasons is maintained, to a large extent, by contributions from springs and groundwater flow [2,6,14,20]. In several regions, springs are considered sacred, holding cultural and religious significance to communities dependent on them [3,21]. However, in recent decades, nearly 50% of perennial springs and 60% of low-discharge springs have shown a decline in discharge, if not being fully dried up [14].

In recent decades, a reduction in spring discharge and declining water quality have been observed in separate studies across the IHR (for example, Central Himalaya [2], Western Himalaya [4]). Isolated studies in different parts of the IHR report population growth [7,15], development activities (road construction) [4,15,22] and rapid urbanization [7], climate change and variability [6,21,23], and land use land cover changes [4,7] as reasons for the decline in spring discharge, and unplanned urban development for the poor water quality [24,25]. The author of [17] presents a synthesis of the effect of anthropogenic activities and climate change on springs and suggests measures to mitigate them. The impact of the drying of springs on the water security of the region is further aggravated by demand-side pressures on water resources. The Himalayas have seen an increase in the number of urban centers, an increase in the urban population due to migration of people from rural and semi-urban regions to these urban centers, and an increase in the seasonal floating population consisting of recreational and religious tourists [19]. The growth in the urban population has led to exploitation of water resources in the region, with urban centers dependent on water from springs and rivers through piped networks [26]. The

increasing demand and decreasing supply of freshwater from springs are a water security threat in the Himalayan region.

Led by an urgent need to unify efforts across the IHR at the national level, the National Institution for Transforming India [14] (NITI Aayog), a policy 'Think Tank' of the Government of India, constituted a working group in 2017 to assess the magnitude of the problem and synthesize policies, initiatives, and best practices from across the IHR [14]. With an estimated 3 million springs in the IHR alone [14], there exists a need for a framework to identify springs and regions in the IHR that are most vulnerable and thus need urgent attention for rejuvenation, restoration, and better management. This study aims at providing a conceptual framework to assess the vulnerability of the Himalayan springs. In the following sections, after defining the study region, we begin conceptualizing vulnerability (concept) to stressors in springs in the Indian Himalayas. This is followed by a systematic review of previously published research on each component of vulnerability assessment (operational procedures). The conceptual model is discussed through a case study of Mathamali spring in the Western Himalayas.

Vulnerability in the context of management of springs and other natural resources is not entirely novel in India. The National Rainfed Area Authority (NRAA) of the Ministry of Agriculture and Farmer Welfare, Government of India, developed a composite index for the prioritization of districts for development planning [27]. The 670 districts of the country, representing more than 90% of the population and geographical area, are ranked based on a composite index computed as a weighted aggregate of two rescaled indices (natural resource index and livelihood index), which are themselves weighted aggregates of 12 and 18 parameters, respectively. Similarly, a village-level assessment of climate-related vulnerability has been undertaken in Sikkim [21] using an exposure, sensitivity, and adaptive capacity framework. The drying up of springs is reported as an impact of climate change on the water resources of villages [15,21], and hence intensive studies on reviving dying springs were subsequently taken up in the drought-prone west and south districts identified based on vulnerability analysis at the village level. Both these studies prioritize development activities within administrative boundaries using an index-based approach. In the present study, we look at springs and clusters of springs as the unit of study. Inventorying of springs has been taken up in recent years in many states by governments (e.g., the Sikkim spring atlas developed by the Rural Development Department, Government of Sikkim, https://sikkim-springs.gov.in/spring_atlas, accessed on 9 June 2021) and non-governmental agencies (e.g., the spring atlas of Uttarakhand developed by CHIRAG, an NGO in Uttarakhand, http://chirag.org/wp-content/uploads/2019/07/SPRING-ATLAS-CHIRAG.pdf, accessed on 9 June 2021). Therefore, a quantitative measure of the vulnerability of springs will augment the inventory exercise to enable targeting of springs and clusters of springs requiring immediate attention for rejuvenation.

2. Study Region

The IHR comprises ten (10) states and four (4) hill districts of India stretching in an East–West orientation for 2500 km along the northern border of India. This region covers three (3) biogeographic zones—the Himalayas, the Trans Himalayas, and the northeast hills. A biogeographic zone is a large distinctive land unit of similar ecology, biome representation, community, and species [28] (the biogeographic classification of India was first published as a draft in 1988 by the Wildlife Institute of India (WII) and further refined and published in the review of the protected areas network for India). In developing a framework for vulnerability assessment, this paper focuses on the Himalayas biogeographic zone spread across five Indian states (Jammu and Kashmir, Himachal Pradesh, Uttarakhand, Sikkim, Arunachal Pradesh) and two hill districts of West Bengal (namely, Darjeeling and Kalimpong). The Himalayas further consist of four biotic provinces (North-West, West, Central, and East Himalayas). The North-West and West Himalayas are in the states of Jammu and Kashmir, Himachal Pradesh, and Uttarakhand. The central province comprises Sikkim and the hill districts of West Bengal, while Arunachal Pradesh is in East Himalaya.

In this paper, regions west of Nepal are considered the western region and the states east of Sikkim as the eastern region. Only Sikkim and the hill districts of West Bengal are in the central region of the Himalayas. The Kumaon region of Uttarakhand is sometimes considered as the Central Himalayas (e.g., [4]), but in this paper, the whole of Uttarakhand will be considered part of the western region of the Indian Himalayas.

3. Conceptualizing Vulnerability in Springs in the Indian Himalayas

In this study, we developed a conceptual model to represent vulnerabilities in the Indian Himalayan springs by adapting the triple complexity for adaptive management systems proposed in [29] and the WR-VISTA framework proposed in [30]. For this purpose, vulnerabilities in the Himalayan springs to stressors are considered a connected system consisting of the (1) complexity in water management and planning systems, (2) complexity of spring systems, and (3) complexity of stressor systems (Figure 1a,b). To represent this triple complexity, we need to translate stressors to impacts in the Himalayan springs. Top-down, bottom-up, and hybrid approaches can be useful for this (Figure 1a). Then, we represent the degree of stressors and springs using measured and/or surveyed information (variables and/or indicators; e.g., temperature, rainfall, water yield, farmer choice), and water management is represented using concepts (vulnerability). Finally, we translate the variables and/or indicators to concepts (Figure 1b) using four pathways (Figure 1c). Traditional studies use Path 1 (variable-model-vulnerability) and/or Path 2 (variable-vulnerability).
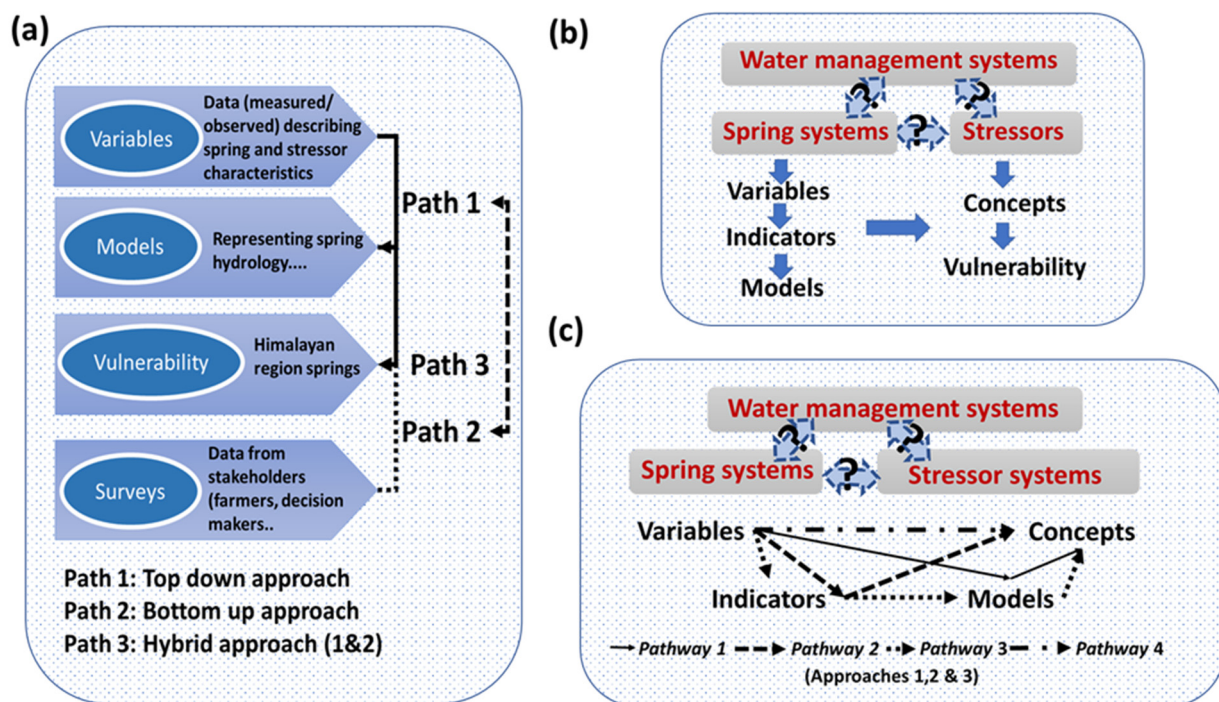
Figure 1. Vulnerability of Himalayan springs to variable and changing stressors. (**a**) Three approaches (based on starting points) that can be used in vulnerability assessments. (**b**) Systems approach to represent the triple complexity. (**c**) Approaches and pathways to representing the complexity in IHR. In (**b**) and (**c**), the inter-connectedness between the three systems is represented using dashed-bordered arrows. The solid-bordered arrows in (**b**) represent the general information flow while translating variables to the vulnerability concept. The first column of solid-bordered arrows (left-hand side) in (**b**) represents the water management systems and stressor systems, while the second column of solid-bordered arrows (right-hand side) in (**b**) represents the vulnerability of the water management system. The information flow through solid-bordered arrows in (**b**) is divided into four pathways using 4 arrow types in (**c**).

In our attempt to develop quantitative vulnerabilities of the Himalayan springs to stressors using indicators and the system's approach, we introduce two other potential pathways (Pathways 2 and 3, Figure 1c). For this, first, we developed a conceptual model

incorporating the systems approach which is based on systems theory, for vulnerability assessment. The systems theory [31] states that complex, nonlinear systems function differently in vivo than the separate scrutiny of their parts might indicate. The advantage of this study is derived from the systems approach's ability to extract information about the functioning of complex systems, which cannot be garnered from a sequence of isolated subsystem-scale studies [29].

The triple complexity we propose to be incorporated into the conceptual modeling framework process requires a holistic perspective rather than a reductionist perspective. Our problem has the common challenges of complex systems and data-scarce regions, including (1) multi-scale processes and multi-scale interactions; (2) emergent self-organization properties that reveal new behaviors; (3) multiple stressors and their interconnections; (4) limited understanding of processes; (5) theoretical concepts that cannot be measured directly; and (6) limited datasets to represent the processes and interactions. Quantifying issues enmeshed in multi-scaled connectivity is a fundamental characteristic of complex systems, and the process of the quantifying function within this complexity is the fundamental objective of the systems approach [32].

The developed conceptual framework identifies the stressors (internal/external), characterizes the processes in the springs in the Indian Himalayas, and synthesizes the impacts and responses from the literature and expert knowledge about the study region.

The top-down, bottom-up, and hybrid approaches are useful analytical starting points. Top-down approaches most frequently use measured/observed data (variables), which are then input to models that mathematically represent the system and take action, while in the bottom-up approach, information is collected using surveys, questionnaires, etc., from key stakeholders (e.g., producers, managers, planners) [29]. They can provide an appropriate starting point from an implementation perspective. Hybrid approaches also exist. These approaches utilize the stakeholder information from bottom-up models with the top-down models.

3.1. Typologies of Indian Himalayan Springs

A review of published research on springs in the Indian Himalayas reveals a diversity of springs in the region, and, consequently, these have been classified in numerous ways based on geology, hydrology, water chemistry, water temperature, human use, and the landscape of the recharge area (Table 1).

Table 1. Synthesis of typologies of Himalayan springs.

| Classification Type	Categories (Examples)	Region	Sources
Geology			
Bedrock	Triassic limestone, alluvium (flood plains), Karewas (lacustrine deposits), Panjal traps (volcanic rocks)	Western (Kashmir)	[23]
Geological structure (genesis and nature of water-bearing formation)	Fracture/joint-related springs, fault lineament-related springs, colluvial springs, springs originating in fluvial deposits, bedding plane-related springs, sill or dyke-related springs, karst springs, underwater springs	Western (Kumaon division, Uttarakhand)	[4]
Geo-structural controls	Thrust (lineament)-controlled, fault-controlled, bedding plane-controlled, fracture-controlled, joint-controlled, shear zone-controlled, fluvial deposit-related	Western (Nainital district, Kumaon division, Uttarakhand)	[6]
Based on the underlying geology	Depression, contact, fracture, karst, and fault springs	Western (Uttarakhand), Central (Sikkim), and Eastern (Arunachal Pradesh)	[2,15,33,34]
Hydrology			
Variation or persistence of flow	Springs with continuous flow, springs with interrupted flow, dead springs or springs that dried up very frequently	Western (Tehri-Garhwal district, Garhwal division, Uttarakhand)	[22]
Seasonality	Perennial springs (flow throughout the year), non-perennial springs (flow during some months), dry springs	Western (Nainital district, Kumaon division, Uttarakhand)	[6]
Based on spring hydrograph	Low discharge and highly seasonalWidely ranging discharge and seasonalHigh and perennial dischargeModerate and fairly constant and perennial discharge	Central (Sikkim)	[2]

Table 1. *Cont.*

Classification Type	Categories (Examples)	Region	Sources
Water Chemistry			
Water type (hydrochemical facies)	Ca–Mg–HCO3 water with low to moderate EC Ca–Mg–HCO3–SO4 water with moderate EC	Western (Himachal Pradesh)	[35]
Water Temperature			
Temperature (with indirect reference to mean annual air temperature)	Cold springs (8–14 °C) Warm springs (14–19°C) (MAAT is 12 °C)	Western (Kashmir)	[36]
Absolute temperature	Warm spring (25–37 °C) Scalding spring (temperature >50 °C)	Eastern (Arunachal Pradesh)	[37]
Human use			
Based on suitability for irrigation	Classification based on salinity, sodium hazard (sodium absorption ratio (SAR)), soluble sodium percentage (SSP), residual sodium carbonate (RSC), magnesium index, permeability index, Wilcox diagram	Western (Almora, Kumaon division, Uttarakhand)	[18]
Recharge area properties			
Nature of the landscape comprising the catchment of the spring	Reserve forest (mixed), reserve pine forest, open pine forest, rainfed agriculture, irrigated land, population <5000, population 5000–10,000, population >10,000	Western (Almora, Kumaon division, Uttarakhand)	[25]

Classification of springs based on vulnerability to stressors will further spring the rejuvenation, restoration, and sustainable management agenda in the Indian Himalayas. In the next section, stressors are identified based on a synthesis of findings from peer-reviewed published studies.

3.2. Systematic Review of Stressors of Himalayan Springs

As per the 2011 Census of India, 46.96 million people live in the IHR (except Kalimpong in West Bengal which was demarcated as a separate district only in 2017) which is a decadal increase of 18.42% as compared to the 2001 census. The average annual exponential growth rate for IHR has decreased from 2.25 to 1.71 for the decades 1991–2001 and 2001–2011, respectively, but is still higher than the pan-India annual growth rate of 1.64. These figures are indicative of population pressure on the mountain ecosystems of the Himalayas. However, a closer look at studies on Himalayan springs indicates at least two broad categories of stressors: biophysical and socio-economic, each of which can be both external and internal (Figure 2). These drivers present a lens to map recent changes observed in the Himalayan springs that are affecting their sustainable use.

The stressor categories are defined based on the predominant effect of the stressor on the spring system. The biophysical drivers are the inter-related effects of land use and land cover change, climate change, and tectonic movements within the Earth's crust. These changes alter the recharge of springs and also affect storage and flow paths from the water source to the springs. The socio-economic drivers are the effects of a growing population and rapid human and economic development in the Himalayas. These drivers result in demand-side pressures while, at the same time, stifling supply side processes in the spring systems. Rapid development has also resulted in a deteriorating water quality in some springs due to the transport of anthropogenic pollutants to water sources that feed the springs. Table 2 presents a synthesis of drivers of change in Himalayan springs from published research articles. There exists a dearth of research on springs in the eastern region, with existing research (for example, [34,37]) only characterizing the springs in select locations in this region.
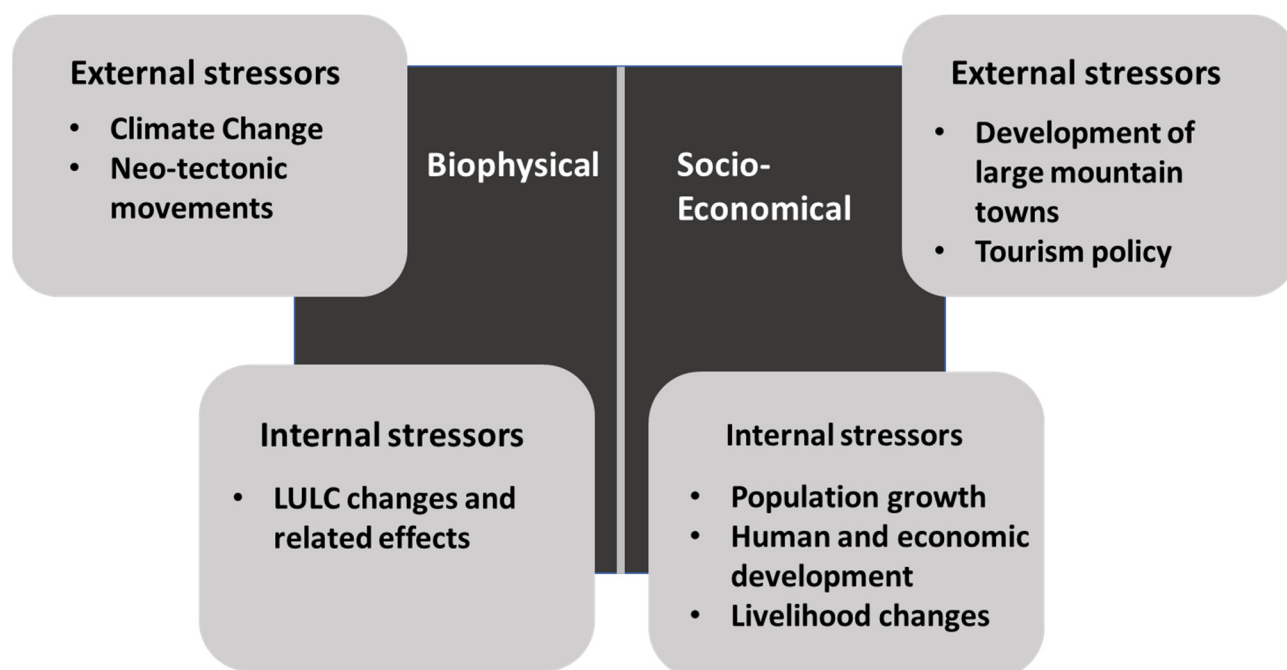
Figure 2. A conceptual representation of the challenges faced by the Himalayan springs: internal and external pressures and drivers impacting them.

Table 2. Synthesis of drivers of change in the Indian Himalayas.

	Drivers	**Sources**	**Region**
A	**Biophysical drivers**		
A.1	Internal		
A.1.1	Deforestation—forested land converted to barren land	[6]	Kumaon division, Uttarakhand, Western
A.1.2	Replacement of multi-storied oaks with single-storied pine forests	[4,38]	Kumaon division, Uttarakhand, Western
A.1.3	Change in the landscape in the recharge area—encroachment by invasive species (cacti and other xerophytes, Lantana camara, etc.)	[4]	Kumaon division, Uttarakhand, Western
A.1.4	Slope failures and landslides	[6]	Kumaon division, Uttarakhand, Western
A.1.5	Declining precipitation (particularly recycled precipitation recharging precipitation-fed springs)	[4]	Kumaon division, Uttarakhand, Western
A.1.6	Forest fires	[15]	Sikkim, Central
A.1.7	The decreasing trend of precipitation in the period of snow accumulation, i.e., November to February, resulting in rapid glacier retreat due to negative mass balance, affects glacier-fed springs	[23,39]	Kashmir, Western
A.1.8	Geomorphological features of the recharge area (upslope area) of the spring	[16]	Garhwal division, Uttarakhand, Western
A.2	External		
A.2.1	Precipitation decline due to climate change	[6]	Kumaon division, Uttarakhand, Western
A.2.2	Reduction in the temporal spread of rainfall due to climate change, particularly decrease in winter rainfall	[15,21]	Sikkim, Central
A.2.3	Increase in intensity of rainfall	[15,21]	Sikkim, Central
A.2.4	Shifting of climate zones to higher altitudes resulting in reduction in oak forests and consequent replacement by pine and mixed forests	[6]	Kumaon division, Uttarakhand, Western
A.2.5	Glacier retreat due to global warming and resulting negative mass balance	[23]	Kashmir, Western
A.2.6	Neo-tectonic movements, active movements of tectonic plates resulting in changing thrusts, faults, and lineaments that affect groundwater flow	[6]	Kumaon division, Uttarakhand, Western
B	**Socio-economic drivers**		
B.1	Internal		
B.1.1	Livelihood practices—uncontrolled grazing, frequent plowing for multiple cropping, and higher constructional activity in the recharge area affect the water holding capacity of the soil	[25]	Kumaon division, Uttarakhand, Western
B.1.2	Increasing fragmentation of landholdings. Therefore, springshed management requires greater coordination among more individuals who hold land in the recharge area.	[15]	Sikkim, Eastern

Table 2. *Cont.*

	Drivers	Sources	Region
B.1.3	Development in the vicinity of the spring	[22]	Garhwal division, Uttarakhand, Western
B.1.4	Road widening, excavation for roads	[4,6,22]	Garhwal and Kumaon division, Uttarakhand, Western
B.1.5	Expansion of canal network	[4]	Kumaon division, Uttarakhand, Western
B.1.6	Upslope cutting for settlement and big buildings	[6,22]	Garhwal and Kumaon division, Uttarakhand, Western
B.1.7	Encroachment into forest land for horticulture and agriculture	[4,6]	Kumaon division, Uttarakhand, Western
B.1.8	Industrialization, urbanization	[4]	Kumaon division, Uttarakhand, Western
B.1.9	Increasing population density in urban settlements, unplanned expansion, improper disposal of domestic sewage results in contamination of springs	[24,25,40]	Kumaon division, Uttarakhand, Western
B.1.10	Out-migration and urban migration of men resulting in the feminization of springs management that is challenging local institutions	[41]	IHR
B.2	External		
B.2.1	Development of densely populated settlements and large mountain towns in the same catchment as the springs under consideration, resulting in increasing demand for water	[5]	Kumaon division, Uttarakhand, Western
B.2.2	Adoption of tourism models in the IHR that are not appropriate for mountain ecosystems.	[41]	IHR

3.3. Characterizing the Stressors and the Springs in the Indian Himalayas

Stressors and springs have various characteristics such as properties, behaviors, internal processes, and position in the environment. For example, we can synthesize the typologies or classifications that use similarities of form and function to impose an order on springs. Basically, they are intellectual constructs in which objects with similar relevant attributes are grouped to represent the stressors and the springs. As evident from the schema of typologies of springs, a wide variety of information is collected related to springs which is then used in characterizing the springs. In an attempt to present a unified list, in this section, we follow a protocol for springshed management used successfully in the inventorying, rejuvenation, and management of springs in India. The authors of [33] presented, as an outcome of a consultative process with key stakeholders, a six-step protocol for the revival of springs in the Hindu Kush Himalayas drawing from previous experience in the implementation of spring and springshed management in Sikkim State of India under the Dhara Vikas program of the Rural Management and Development Department (RM&DD) of the Government of Sikkim. Steps 1 through 4 focus on knowledge generation and steps 5 and 6 on implementation. Table 3 summarizes the nature of data that are needed to identify the type of spring and manage it effectively. As it can be seen, some characteristics are measurable or quantifiable, while some other characteristics are qualitative.

The stressors are then identified by drawing a causal relationship between stressor variables and the state of the spring system. These stressors are characterized by measuring the change in the stressor variable while simultaneously quantifying the change in the 'state' of the spring. As classified earlier, we look at stressors as falling broadly into two categories, biophysical and socio-economical, though the effects are mostly combined, and sometimes the effect of one stressor in one category is on another stressor in the opposing category which finally impacts the 'state' variable of the spring. This interconnected nature of stressors should be kept in mind even while attempting to categorize the stressors. Characterization is conducted by identifying measurable properties (Table 4). For example, biophysical stressors are characterized by quantifying the change in climate variables such as precipitation and temperature at different temporal aggregations and scales, and by estimating the change in visible land cover year on year to quantify, for example, the decline in forest area, maximum areal extent of glacier fields and snowpacks, and canopy loss due to forest fires. Population increase, increase in the road and canal networks (reported as kilometers of roads constructed or canals excavated), increase in per capita demand of water to support upward economic and social mobility, etc., are some examples of properties of socio-economic stressors that can be quantified. Many of the stressors can be

characterized at a coarse spatial resolution from reports, data, and satellite imagery that are readily available. However, owing to the high spatially heterogeneous nature of the Himalayan landscapes, information at the local scale needs to be generated by (1) instrumentation within the springshed to measure, for example, rainfall and temperature, and by (2) adopting participatory methods at individual (key informant interview), household (household surveys), and community levels (village workshops, focused group discussions, transect surveys with community participants) to collect, for example, information on the use of natural resources (resource mapping, cropping calendars).

Table 3. Data requirements for identifying the type of springs.

Sl. No.	Spring and Springshed Characteristic/Property	Data Required/Method Used	
		Measurable	Qualitative
1.	Geographic location	Latitude, longitude, elevation	
2.	Administrative identifier	The village name, Gram Panchayat (lowest level of Panchayati Raj Institutions (PRIs) which form a part of the local self-governance system in India), district (an administrative division of an Indian state)	
3.	Springshed boundary, area of interest	Toposheets, GIS, transect walk—all water sources inventoried with GPS	
4.	Hydrology	Discharge, rainfall, flow duration curves, perennial or seasonal	
5.	Hydrogeological mapping	Classification into spring type—depression, contact, fracture, fault, or karst types; identification of bedrock (regional aquifers)	Geological map of the area, observations during transect walk, conceptual hydrogeological layout (cross-section and 3D) of the springshed demarcating recharge areas
6.	Water chemistry	pH, hardness, TDS, major constituents—HCO_3, SO_4, Na, Cl, Ca, Mg, Si; minor constituents—B, Ni, Co, K, F, Fe, strontium; trace constituents—heavy metals, nutrient concentrations (nitrates, phosphates ions), oxygen levels (DO, BOD)	
7.	Human use—potable or not		FGD, KII
8.	Water uses		FGD, KII, questionnaire survey—household survey; no. of households (from government records); no. of livestock (from livestock census); commercial uses; irrigated area
9.	Importance of the spring		KII—alternative sources of water, religious/cultural significance, perception of drying trends of the spring
10.	Land use in the springshed	LULC maps—historical (baseline) and current	Transect walk, KII—cropping patterns, seasons, change in LULC
11.	Management of the spring		KII—conflicts and conflict resolution, existing institutions, equity aspects: women, marginalized sections, power dynamics
12.	Access to the spring		KII, questionnaire—private, few households, common, women only, marginalized sections

Abbreviations: KII—key informant interview; FDG—focused group discussion; LULC—land use land cover.

Table 4. Measurable properties for characterization of stressors.

	Drivers	Sources	How Is This Measured?(or) What Is the Variable That Needs to Be Measured?
A	**Biophysical drivers**		
A.1	Internal		
A.1.1	Deforestation—forested land converted to barren land	[6]	LULC map for at least two years (baseline/historical and current) and calculating change in the area of each LULC class.
A.1.2	Replacement of multi-storied oaks with single-storied pine forests	[4,38]	Change in springshed aggregated evaporation losses from each LULC class.
A.1.3	Change in the landscape in the recharge area—encroachment by invasive species (cacti and other xerophytes, Lantana camara, etc.)	[4]	Indicator for depletion in soil moisture. Percentage of area covered by oak forests replaced by pines or cacti and other xerophytes.
A.1.4	Slope failures and landslides	[6]	Spatial distribution mapand density (landslides/km^2) of landslides developed after delineating existing landslides during fieldwork.

Table 4. *Cont.*

	Drivers	Sources	How Is This Measured?(or) What Is the Variable That Needs to Be Measured?
A.1.5	Declining precipitation (particularly recycled precipitation recharging precipitation-fed springs)	[4]	Can be determined by a multivariate regression model with evapotranspiration and land use (categorical variable) as dependent variables and precipitation as independent variables.
A.1.6	Forest fires	[15]	Thematic map of incidents of forest fires in the period under consideration (similar to landslide thematic map).
A.1.7	The decreasing trend of precipitation in the period of snow accumulation, i.e., November to February, resulting in rapid glacier retreat due to negative mass balance, affects glacier-fed springs	[23,39]	Trend (or variation) in total precipitation received during November to February.
A.1.8	Geomorphological features (aspect and slope) of the recharge area (upslope area) of the spring	[42]	Determined using Brunton compass during field survey. It can also be determined reliably from high-resolution DEM.
A.2	External		
A.2.1	Precipitation decline due to climate change	[6]	The trend in annual precipitation.
A.2.2	Reduction in the temporal spread of rainfall due to climate change, particularly decrease in winter rainfall	[15,21]	Trends in seasonal totals of rainfall.
A.2.3	Increase in intensity of rainfall	[15,21]	Trends in the number of rainy days in a year.
A.2.4	Shifting of climate zones to higher altitudes resulting in change reduction in oak forests and consequent replacement by pine and mixed forests	[6]	An indicator for shifting climate zones is % area covered by oak forests replaced by pines and mixed forest. Alternatively, change in mean elevation of oak forests, pine forests, and mixed forests. If the change is significant, then we can say that the climate zones have shifted.
A.2.5	Glacier retreat due to global warming	[23]	Glacier retreat due to climate change is established using long records of glacier length (average record length used is 94 years) [43].
A.2.6	Neo-tectonic movements, active movements of tectonic plates resulting in changing thrusts, faults, and lineaments that affect groundwater flow	[6]	The proximity of spring location to seismo-tectonically active thrust planes, for example, the main boundary thrust.
B	**Socio-economic drivers**		
B.1	Internal		
B.1.1	Livelihood practices—uncontrolled grazing, frequent plowing for multiple cropping, and higher constructional activity in the recharge area affect the water holding capacity of the soil	[25]	The number of livestock per 1000 households (normalized by the number of households and area of the district) can be used as an indicator for pressure on land due to grazing. District-wise data of the livestock census are available for the 19th livestock census (2012).An increase in the built-up area, increase in abandoned agricultural plots, and increase in % of agricultural plots can be seen as indicators for livelihood practices that affect the sustainability of springs.
B.1.2	Increasing fragmentation of landholdings. Therefore, springshed management requires greater coordination among more individuals who hold land in the recharge area.	[15]	Thematic map indicating the number of landholders per square kilometer similar to landslide map can be developed from household surveys.
B.1.3	Development in the vicinity of the spring	[22]	The proximity of each spring to the nearest census town. The greater the proximity, the lesser the impact of the town on the spring.
B.1.4	Road widening, excavation for roads	[4,6,22]	Key informant interview corroborated with village-level records.
B.1.5	Expansion of canal network	[4]	Key informant interview corroborated with village-level records.
B.1.6	Upslope cutting for settlement and big buildings	[6,22]	Village workshops and transect surveys to identify big construction projects and quantify area extent of upslope cutting.
B.1.7	Encroachment into forest land for horticulture and agriculture	[4,6]	% pixel area of forest land replaced by cultivated land from LULC change analysis.
B.1.8	Industrialization, urbanization	[4]	Increase in the built-up area from LULC change analysis
B.1.9	Increasing population density in urban settlements, unplanned expansion, improper disposal of domestic sewage results in contamination of springs	[24,25,40]	Thematic maps of percentage increase in population between last two censuses.
B.1.10	Out-migration and urban migration of men resulting in the feminization of springs management that is challenging local institutions	[41]	Household surveys and focused group discussions needed.
B.2	External		
B.2.1	Development of densely populated settlements and large mountain towns in the same catchment as the springs under consideration, resulting in increasing demand for water	[5]	The proximity of each spring to the nearest census town. The greater the proximity, the lesser the impact of the town on the spring.
B.2.2	Adoption of tourism models that are appropriate for plains in the IHR	[41]	Inventorying of villages with tourism as an alternative or primary source of livelihood.

3.4. Impact of 'Stressors' on the 'State' of Indian Himalayan Springs

For the vulnerability assessment of Indian Himalayan springs, this section discusses the selection of critical 'states' based on 'stressors' identified in different regions of the Himalayas. The impacts can follow more than one pathway and are linked to a change in state. Table 5 summarizes the findings from the literature reviewed.

Table 5. Impact of 'stressors' on the 'state' of Indian Himalayan springs.

Region	Stressor	Impact	State	Change in State
Sikkim, Central Himalayas	Climate Change • Change in the temporal spread of rainfall • Decrease in winter rainfall • Increase in intensity	• Forest fires and resulting drying up of springs • Poor accumulation and recharge during rainfall events resulting in the drying up of springs • The decline in production of winter crops • Women required to travel long distances to collect water	• Lean period discharge • No. of months of flow	• Decrease in lean period discharge • Change of perennial springs to seasonal or dried-up springs
Kashmir, Western Himalayas	• Winter precipitation—decreased rainfall in the period of snow accumulation • Global warming	• Glacier retreat	• The maximum discharge of the spring in a year	• Attenuation of maximum discharge • Karst springs are affected more than alluvial springs
Uttarakhand, Western Himalayas	• Climate change → The decline in precipitation from oceanic sources → → Shifting climate zones → Replacement of oak with pine → Conversion of forest land to barren land accelerated by clearing of forest for development and consequent erosion → Encroachment of alien species → The decline in recycled precipitation • Economic and human development → Excavation for roads and canals → Construction activity → Reduction in the extent of forest cover due to overgrazing, encroachment into forest land for agriculture and horticulture, excavation for roads and canals, etc. → Unsustainable practices such as overgrazing and bi-monthly plowing resulting in loss of topsoil → Development of large towns and consequent pressure on water sources → Unmanaged drains and improper sewage disposal	• Decreased infiltration, increased surface runoff • Decreased average seasonal discharge (in liters per day) in springs; the discharge measured periodically before the rainy season (June), immediately after the rainy season (October), and during winter (February) • Diminished discharge in streams; annual average in cumec per day • Springs in densely populated areas have high EC, low DO, high NO3-, and presence of coliform due to improper disposal of sewage	• Magnitude of discharge • Seasonality • Suitability of water for drinking	• Decrease in average discharge • Decrease in the number of perennial springs and consequent increase in the number of seasonal and dried-up springs • The presence of nitrates indicates contamination of the water

3.5. Responses in Springs Due to Impacts and Stressors

Many spring revival programs have been successfully undertaken in the many Himalayan states during recent decades. The NITI Aayog report on Inventory and Revival of Springs in the Himalayas for Water Security [14] (pp. 23–24) lists appropriate responses to deterioration of springs based on a synthesis of best practices in spring revival in India. Recharge area protection or spring source protection has been adopted in many

locations by limiting grazing, encroachment, and development activities in the recharge area of the springs. An emphasis on the 'springshed' approach in policy and action has furthered the effectiveness of source protection by adopting hydro-geological methods to recharge area identification rather than a ridge-to-valley approach with just protection of the ridge or upslope area, as conducted in traditional watershed management. The effectiveness of the recharge of springs is improved by implementing engineering measures (staggered and contour trenching, building check dams across small streams, construction of gabions/retaining walls/spurs, diversion drains) and vegetative measures (fuelwood, fodder and fruit tree plantations, grassland management, and hedgerow treatment) [14]. Locations experiencing glacier retreats can adopt measures to improve snow retention and collection of snow meltwater for spring recharge. These measures have been seen to be successful when implemented through local-level management and adoption of traditional knowledge. Demand management is another response where communities dependent on springs calibrate their water consumption to ensure the sustainability of the springs. This involves improvement in water distribution, implementation of water conservation practices, and organized management of springs. A return to community ownership of the resource and strengthening of village-level institutions for water management has been observed in the success stories of spring revival. This ensures the implementation of interventions for spring revival that are linked to the livelihoods of the communities involved, thus further ensuring the long-term sustainability of the interventions. The dearth of long-term data on spring discharge and quality has hampered early identification and implementation of spring revival. There is a need for setting up systems for regular monitoring of springs, with at least one each from distinct typologies within an administrative unit (say, a district) for assessing the impacts and effectiveness of responses on the springs.

3.6. Framework Developed

The conceptual framework developed in this study aims to represent the vulnerability of springs in general (Figure 3) using novel systems thinking approaches. In the following figure, the target system comprises internal elements (Himalayan springs), and these elements are defined by characteristics (dotted circles within the system). Some examples of the spring characteristics are discharge, flow duration curve, and households dependent on a spring. Representation of springs can include multiple elements, including biophysical (BP), economic (E), and social (S) elements, or their combinations (BPES).

Stressors are external to the target system and are classified as internal and external stressors. They are defined by characteristics (dotted circles within the star). When the target system is exposed to the stressors, impacts are represented as changes in the characteristics of the target system elements (disfigured circles, color changes), representing changes to BP, E, S, and BPES. Note that each element responds differently (or not at all) to a stressor. On the other hand, the stressor characteristics are assumed to have no changes during impact. The small, medium, and large changes in spring characteristics are represented as changes in only color, only shape, and both color and shape, respectively. For example, a large increase in the number of heavy-rainfall days (stressor) may have a larger impact on discharge when compared to no change in discharge for a small increase in the number of rainy days in any year. Similarly, a large increase in the proportion of barren land in the recharge area may have a larger impact on the seasonality of the spring when compared to encroachment into forest lands for agriculture and consequent withdrawal of recharge water to the spring for consumptive water for farm produce. Accordingly, vulnerability assessments will be carried out to assess the degree of stress on the target systems. The efforts will be targeted to utilize the benefits of change and reduce the harmful effects of change. The thick arrows represent the overall flow direction of processes in the conceptual framework as well as the direction of the movement of time. Stressors and target system characteristics, the impacts of stressors, responses, and restora-

tion efforts can be identified by literature reviews, expertise in the region, and available observed/measured/survey data.
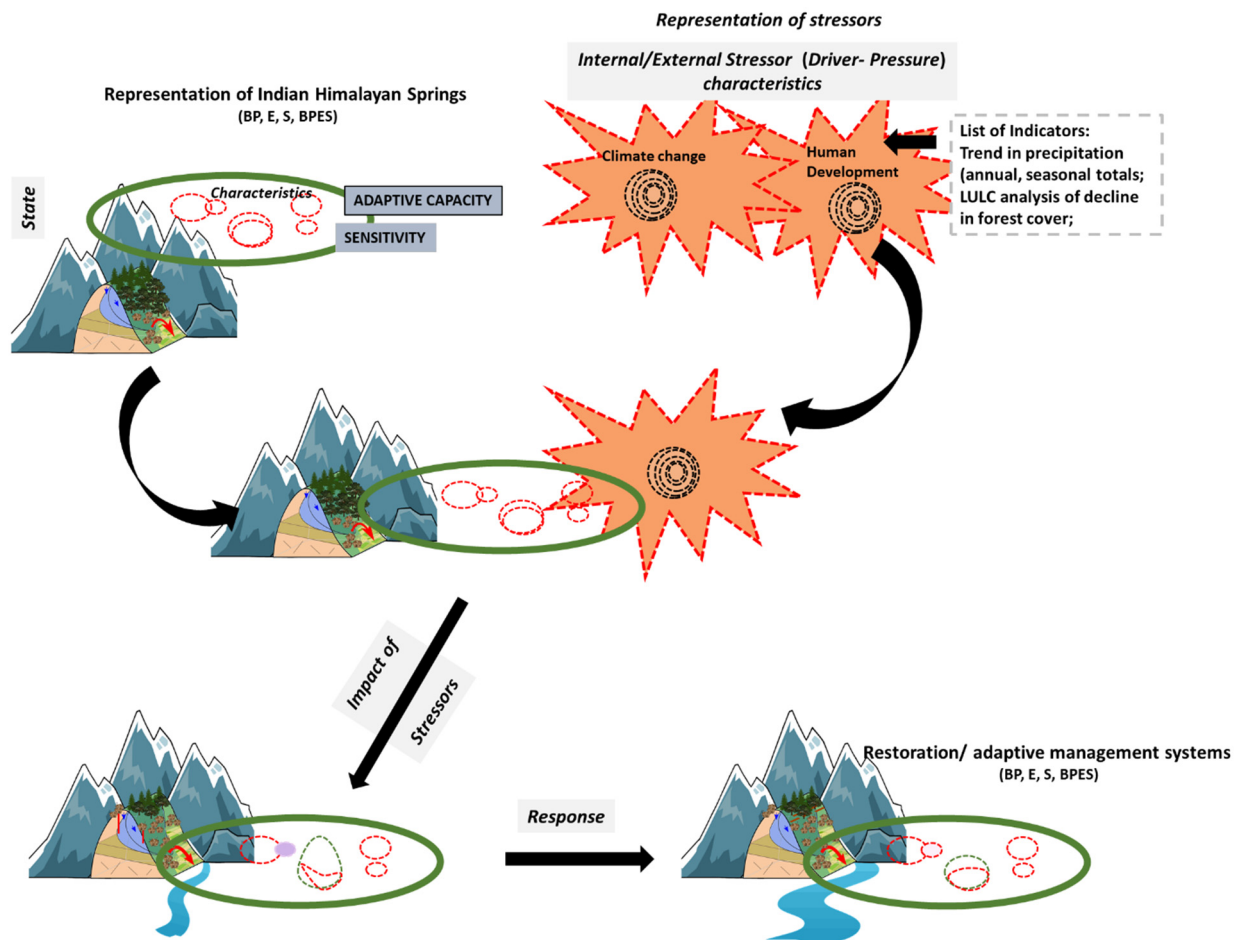
Figure 3. Conceptual framework.

4. Case Study

We present a limited stressor causal chain (Figure 4) using readily available data from previously published research for Mathamali spring in Dhanaulti Tehsil (administrative unit in India), Tehri-Garhwal district, Uttarakhand State of India. First, we look at the effect of biophysical stressors on springs. Analysis of annual and monsoon seasonal precipitation over a 60-year window (1955–2015) in the Tehri-Garhwal district shows a significant decreasing trend with the Theil-Sen slope reported as 8.22 mm/year and 6.80 mm/year, respectively [44]. It is important to note that this significant decreasing trend is higher than the annual and seasonal decreasing trend for the Uttarakhand meteorological sub-division (1.28 mm/year and 1.20 mm/year, respectively) based on an analysis of precipitation series for the years 1901–2019 [45]. A similar analysis of the most recent 30 years (1989–2018) of rainfall observations has also shown a decreasing trend, consistent with previous studies, in the annual and seasonal (southwest monsoon) totals of precipitation in Tehri-Garhwal district, but the reported trend is not statistically significant [46]. However, what was further reported in the 30-year analysis was a significant increasing trend in the number of heavy-rainfall days (daily rainfall >=6.5 mm) over the entire year, with no significant increase in the number of rainy days (daily rainfall >=2.5 mm) [46]. This implies that, on average in the most recent 30 years, over Tehri-Garhwal district and the springshed of Mathamali spring, there is an observed increase in the frequency of heavy-rainfall days, but the same (or slightly decreasing) annual and seasonal totals of precipitation deposited

over a water year. This is likely to result in less time for infiltration, increasing surface runoff, and, consequentially, less recharge for the same totals of precipitation. The increase in frequency in recent decades combined with the gradual decrease in precipitation over a great part of the previous century is a likely cause for the perceived decline in Mathamali spring's discharge.
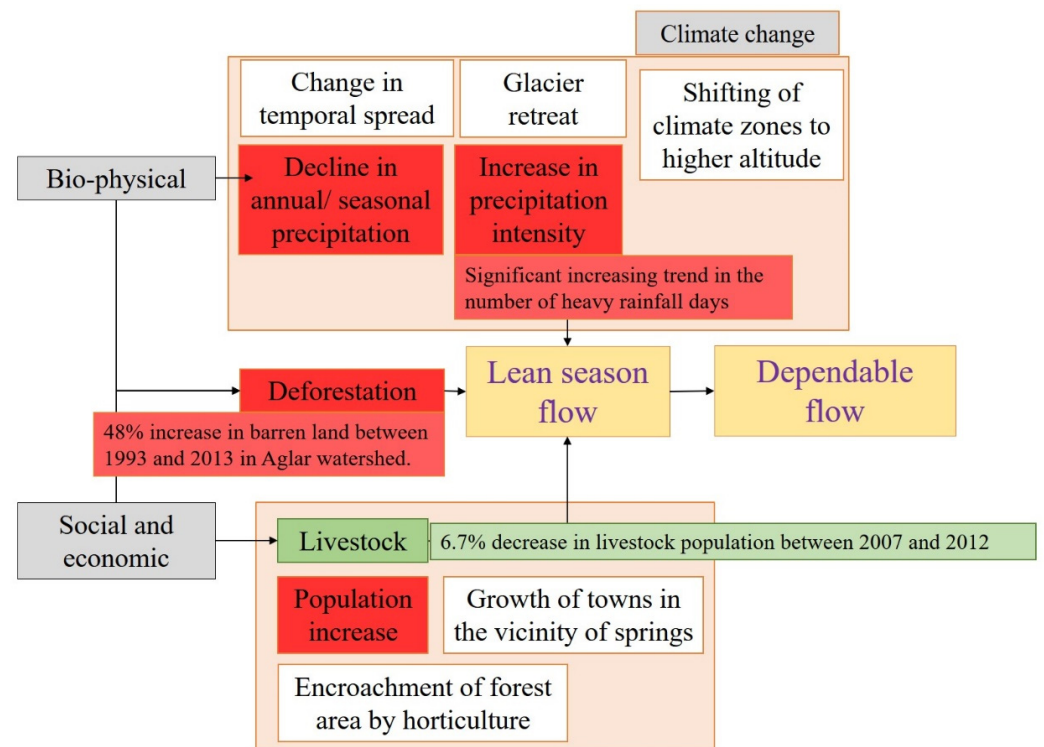
Figure 4. Characterization of stressors in Mathamali spring, Uttarakhand, India.

Furthermore, LULC analysis of the Aglar watershed [47], of which Mathamali spring forms a part, has shown a 48% increase in barren land between 1993 and 2017 and 19.8% between 1999 and 2017. Though the increase in barren land is very large in the early years of the time period, a conservative estimate of the decadal increase can be considered as closer to 10%. This is lower than the 28% increase in the fallow land in Uttarakhand State between 2007 and 2017, which increased from 108 thousand hectares in 2007–2008 to 150 thousand hectares in 2016–2017 (land use statistics, at a glance, for 2007–2008 to 2016–2017 published by the Ministry of Agriculture and Farmers Welfare, Government of India, November 2020, and accessed on https://eands.dacnet.nic.in/LUS_1999_2004.htm, accessed on 9 June 2021). An increase in barren land is likely to result in erosion and poorer retention of soil moisture, leading to a lower recharge of the spring.

Human and livestock populations exert pressure on the limited natural resources. We now look at the characteristics of human population and livestock population growth in Uttarakhand State vis à vis all-India growth numbers to identify and quantify the socio-economic stressors on the vulnerability of Mathamali spring. The average annual exponential growth rate of the human population in Uttarakhand for the decade 2001–2011 is 1.77, which is higher than the corresponding statistics of the IHR and pan-India, which are 1.71 and 1.64, respectively (2011 Census of India). The population growth rate being higher than other regions in the IHR indicates that the freshwater resources, including springs in Uttarakhand, are increasingly at risk of exploitation and consequent degradation (drying up of springs and contamination). Grazing practices exert pressure on the land, resulting in denudement of slopes in the recharge area. Between 2007 and 2012, the total livestock population in India decreased by 3.3% (18th and 19th livestock censuses of India). The corresponding decrease in the livestock population in Uttarakhand State is 6.7% (a decrease

from 51.41 lakh in 2007 to 47.95 lakh in 2012, as reported in 18th and 19th livestock censuses of India). This decrease in the livestock population in the 5-year period (2007–2012) must be seen in the context of a 5.6% decadal increase in India's total livestock population between 2003 and 2012 (17th and 19th livestock censuses). The recent decrease in the livestock population indicates that grazing pressure on land resources is not a significant stressor in the recent drying up of springs in Uttarakhand, yet the perceived drying up of Mathamali spring and the decadal increase in livestock indicate that the livestock population remains a socio-economic stressor on springs in general. The abandonment of agriculture (indicated by an increase in barren land) coupled with a growing livestock population and grazing practices (as a lucrative livelihood alternative to agriculture) puts further pressure on the denudement of slopes due to the combined effect of fallow ground in some locations and excessive grazing in other locations, thus affecting the recharge of springs and the decline in lean season flows. Therefore, in this case study of Mathamali spring, the biophysical stressors considered are the decline in annual and seasonal precipitation and the increase in barren land, while the socio-economic stressors are population and grazing pressures on land and water resources (Figure 4). The vulnerability index (*VI*) is estimated as a normalized aggregation of individual vulnerability indices (*VI$_i$*) due to each stressor, which is estimated using Equation (1). The equation is a modification of the similar equation suggested in [30] by trading time for space. Normalization is conducted by averaging the aggregated vulnerability index, aggregated using equal weights, but weights can be modified based on a detailed study of the impact of each stressor variable on the state of the spring. *VI* = 1 indicates a lower vulnerability of the spring to the stressors. The greater the *VI* deviates from 1 (*VI* < 1 and *VI* > 1), the greater the vulnerability of the spring of interest to the stressors compared to the springs located within the larger geographical extent. Here, by this definition of vulnerability, the effect of the stressors can be both detrimental (drying up of springs) and advantageous (increase in spring flow). The calculation of *VI* for Mathamali spring is demonstrated in Table 6.

$$VI_i = \frac{\text{Average value for the stressor variable in spring of interest}}{\text{Average value of the variable in the region (or country)}} \tag{1}$$

Table 6. Calculation of vulnerability index of Mathamali spring in Uttarakhand, India.

Stressor Variable	Measured Quantity of Stressor Variable and Units	Average Value of the Stressor Variable in the Spring of Interest	Average Value of the Variable in the Region	Vulnerability Index
Precipitation	Decline in annual precipitation, mm/year	8.22	1.28	6.4
	Decline in seasonal precipitation, mm/year	6.804	1.20	5.7
LULC	Decadal increase in barren (fallow) area, percentage	10	28	0.4
Human population	Average annual exponential growth rate, % per year	1.77	1.71	1.0
Livestock population	Increase in livestock population between two censuses, percentage	−6.70	−3.30	−2.0
		Aggregated vulnerability index		11.5
		Normalized aggregated vulnerability index		2.3

The negative sign indicates that the effect of the stressor is in the opposite direction compared to other stressors. For example, a decrease in the livestock population moves the *VI* further to less than 1 (in the negative direction).

The vulnerability index of 2.3 in the limited case study indicates that the combined effect of the stressors is to decrease the water availability and deteriorate the water quality of freshwater from Mathamali spring in Uttarakhand. The effect of the decrease in precipitation is the dominant stressor (*VI$_i$* >> 1) affecting the decline in discharge of Mathamali spring, which, to a small degree, is mitigated by the decrease in the livestock population (*VI$_i$* < 0 and absolute value of *VI$_i$* > 1), both in the region and locally. The increase in barren land in the vicinity of Mathamali spring lowers the vulnerability of Mathamali spring (*VI$_i$* < 1) when compared to springs in the larger geographical extent of Uttarakhand State but still affects the decline in discharge, but to a lesser extent compared to other springs in the larger geographical extent. The estimation of a single quantity (*VI*) for vulnerability

is a useful metric for comparing springs and clusters of springs within a region to help prioritize spring rejuvenation efforts in a region.

The impact of the stressors on Mathamali spring is a possible decrease in lean season flow, reported as dependable flow. Discharge at Mathamali spring has been recorded at hourly time intervals and aggregated to daily averages from February 2014 to February 2018 [48]. Similar to other Himalayan springs, there was a general perception in the community that the spring discharge at Mathamali spring was declining. The spring was instrumented for continuous discharge monitoring to quantify the state of the spring and the impact of engineering measures and vegetative measures implemented to capture the limited precipitation in the soil matrix and improve the recharge to the spring. The 75% dependable flow showed a gradual increase from 5.7 in 2014 to 13.44 and 19.45 LPM in the water years of 2015 and 2016, respectively. The increase in dependable flows can be attributed to recharge interventions, both engineering measures, such as construction of a gabion check dam, multiple contour trenches, and a few artificial ponds (khals), and vegetative measures of tree, shrub, and grass planting, implemented since 2010–2011 by Garhwal Vikas Kendra in the recharge area of Mathamali spring (as reported in the Himmothan Society annual report 2010-11, accessed on http://www.himmotthan.org/, accessed on 9 June 2021).

This limited causal chain can be improved by including more stressors as information is made available, resulting in a more complex analysis of the vulnerability of Mathamali spring (Figure 5). The responses to changes in the 'state' of the spring are indicated in the causal chain by arrows leading away from the 'state' of the spring. For example, the response to declining flows is structural and vegetative measures in the springshed recharge area. The effectiveness of this response may be affected by the fragmentation of landholdings. Smaller landholdings will require the mobilization of a larger number of persons to adopt land management practices in their land parcels to help improve discharge in the springs. Declining water quality in springs is largely due to development activities in the vicinity of the spring, and the appropriate response will be better waste management and proper planning for future development in the region.
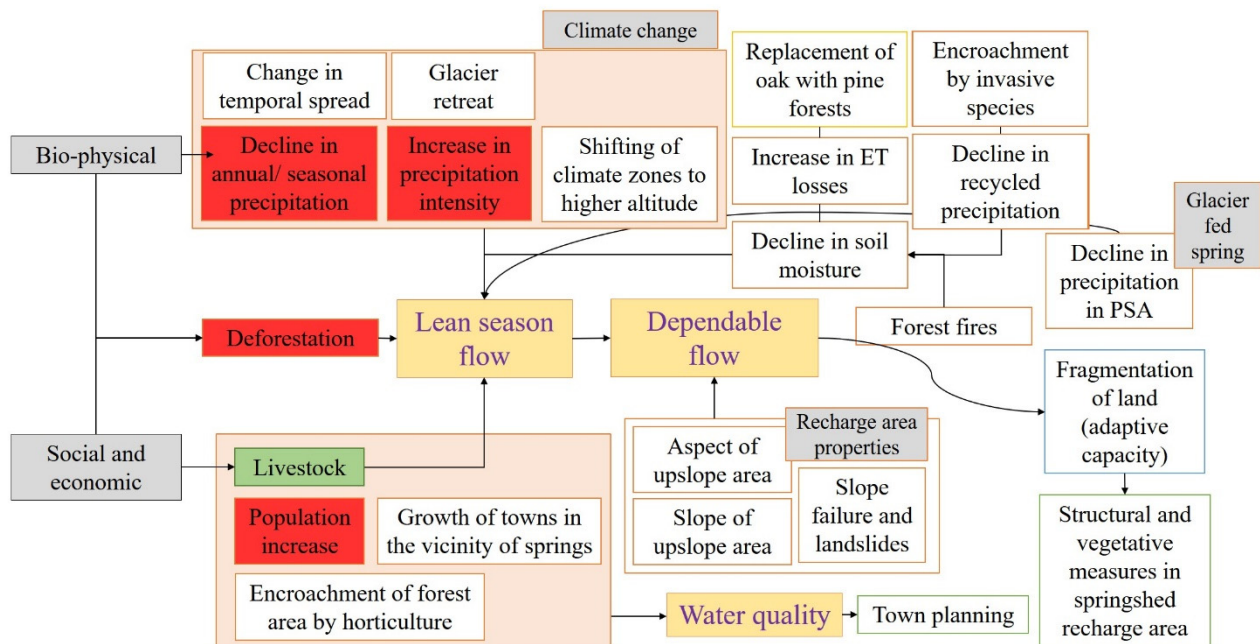

Figure 5. Vulnerability analysis of Mathamali spring, India.

5. Limitations in the Proposed Methodology

The main aim of this study was to propose a conceptual framework to represent the vulnerability of springs. The methodology enables the translation of theoretical constructs into actionable steps (operational procedure) and provides a take-off point for creativity in the use of indicators for quantifying vulnerability. Some immediate sources of error in the operational procedure for vulnerability analysis are presented in this section. First, the choice of stressors was conducted by deductive reasoning and constrained by the availability of easily accessible data. A suggested approach would be the use of regression models to establish the relationship between the state and stressors [49]. Second, constant weights were used in the normalization and aggregation of individual vulnerability indices. A correct choice of weights that reflects the correct interrelationship between the vulnerability stressors and the state of the spring is essential [30]. The weights can be improved through a consultative process of subject matter experts and stakeholders [27]. Thirdly, the present study demonstrated the use of readily available data (in a data-scarce region such as the HKH) for rapid assessment of vulnerability. In doing so, uniform time periods for analysis were not considered and could be a potential source of uncertainty. All datasets, as far as possible, should be suitably transformed to conduct the comparison of vulnerability stressors for the same time period (implying the same state of the system at the beginning of the time period). Fourthly, recent recharge interventions in the springshed comprising the spring may mitigate the effect of the stressors. This needs to be accounted for in the estimation of vulnerability to identify the springs which need further attention for springshed development and management. Finally, this study demonstrated an operational procedure for vulnerability analysis, the usefulness of which needs to be demonstrated in future work by using the procedure for prioritization of springshed development over a larger geographical region by enabling a ranking of all springs and clusters of springs within the region based on vulnerability to the stressors.

6. Conclusions

In this study, an attempt at conceptualizing vulnerability in Himalayan springs was carried out. First, the stressors (internal/external) affecting the springs were identified based on a systematic review of previously published research. Then, characteristics of the springs were identified, and causal links to the stressors were established by way of measurable quantities. By adopting a systems approach, a framework was then developed for representing the vulnerability of springs. This framework was demonstrated in the case study of Mathamali spring in the Western Himalayas. The case study was used to illustrate the operational procedure for vulnerability analysis. In the case study, vulnerability indices were computed for individual stressors, which were then aggregated and normalized to quantify the vulnerability of Mathamali spring. In the limited analysis, the dominant stressor affecting the vulnerability of Mathamali spring was identified as the decline in both the southwest monsoon (seasonal) and annual precipitation totals. The impacts and responses were synthesized from both the literature and expert knowledge.

The conceptual framework is a useful theoretical construct for enabling policymakers and project managers to follow a structured process for arriving at decisions concerning judicious use of resources towards a targeted springshed management of springs that are most vulnerable to biophysical and socio-economic stressors. This framework further addresses the pressing need for the synthesis of existing research findings related to Himalayan springs to extract information useful for decision-makers by capturing, visualizing, and organizing connections of a complex system through the conceptual framework. This study hopes to bridge the gap between the supply and demand of such useful information. With the impacts of stressors on springs becoming increasingly visible, identification of springs and clusters of springs requiring immediate attention has become necessary for efficient utilization of resources. The synthesis of stressors, identification of measurable indicators, and the conceptualization of vulnerability promote convergence towards

an evidence-based decision support system for rejuvenation and better management of Himalayan springs.

References

1. Scott, C.A.; Zhang, F.; Mukherji, A.; Immerzeel, W.; Mustafa, D.; Bharati, L. Water in the Hindu Kush Himalaya. In *The Hindu Kush Himalaya Assessment*; Springer Nature Switzerland AG: Cham, Switzerland, 2019; pp. 257–299.
2. Mahamuni, K.; Kulkarni, H. Groundwater Resources and Spring Hydrogeology in South Sikkim with Special Reference to Climate Change. In *Climate Change in Sikkim-Patterns, Impacts and Initiatives*; Arrawatia, M.L., Tambe, S., Eds.; Government of Sikkim: Gangtok, India, 2012; pp. 261–274. ISBN 978-81-920437-0-9.
3. Chapagain, P.S.; Ghimire, M.; Shrestha, S. Status of natural springs in the Melamchi region of the Nepal Himalayas in the context of climate change. *Environ. Dev. Sustain.* **2017**, *21*, 263–280. [CrossRef]
4. Valdiya, K.S.; Bartarya, S.K. Hydrogeological Studies of Springs in the Catchment of the Gaula River, Kumaun Lesser Himalaya, India. *Mt. Res. Dev.* **1991**, *11*, 239–258. [CrossRef]
5. Tiwari, P.C.; Joshi, B. Environmental Changes and Sustainable Development of Water Resources in the Himalayan Headwaters of India. *Water Resour. Manag.* **2011**, *26*, 883–907. [CrossRef]
6. Pant, C.C.; Rawat, P.K. Declining Changes in Spring Hydrology of Non-glacial River Basins in Himalaya: A Case Study of Dabka Catchment. In *Dynamics of Climate Change and Water Resources of Northwestern Himalaya*; Joshi, R., Kumar, K., Palni, L.M.S., Eds.; Springer International Publishing: Cham, Switzerland, 2015; pp. 151–179.
7. Tiwari, P. Land use changes in Himalaya and their impacts on environment, society and economy: A study of the Lake Region in Kumaon Himalaya, India. *Adv. Atmos. Sci.* **2008**, *25*, 1029–1042. [CrossRef]
8. Shiklomanov, I.A. World fresh water resources. In *Water in Crisis: A Guide to the World's Fresh Water Resources*; Gleick, P.H., Ed.; Oxford University Press: New York, NY, USA, 1993; pp. 13–24. ISBN 9780195076288.
9. Margat, J.; van der Gun, J. *Groundwater around the World*; CRC Press: Boca Raton, FL, USA, 2013.
10. Glazier, D.S. Springs. In *Reference Module in Earth Systems and Environmental Sciences*; Elsevier: Amsterdam, The Netherlands, 2014. [CrossRef]
11. Stevanović, Z. Utilization and regulation of springs. In *Groundwater Hydrology of Springs*; Butterworth-Heinemann: Burlington, MA, USA, 2010; pp. 339–388.
12. Stevanović, Z. Karst waters in potable water supply: A global scale overview. *Environ. Earth Sci.* **2019**, *78*. [CrossRef]
13. WHO. Factsheet on Drinking Water. Available online: https://www.who.int/news-room/fact-sheets/detail/drinking-water (accessed on 2 June 2021).
14. NITI Aayog. *Report of Working Group I Inventory and Revival of Springs in the Himalayas for Water Security*; NITI Aayog: New Delhi, India, 2018.
15. Tambe, S.; Kharel, G.; Arrawatia, M.L.; Kulkarni, H.; Mahamuni, K.; Ganeriwala, A.K. Reviving Dying Springs: Climate Change Adaptation Experiments From the Sikkim Himalaya. *Mt. Res. Dev.* **2012**, *32*, 62–72. [CrossRef]
16. Negi, G.C.S.; Joshi, V. Rainfall and Spring Discharge Patterns in Two Small Drainage Catchments in the Western Himalayan Mountains, India. *Environmentalist* **2004**, *24*, 19–28. [CrossRef]

17. Panwar, S. Vulnerability of Himalayan springs to climate change and anthropogenic impact: A review. *J. Mt. Sci.* **2020**, *17*, 117–132. [CrossRef]

18. Bhandari, N.S.; Joshi, H.K. Quality of spring water used for irrigation in the Almora District of Uttarakhand, India. *Chin. J. Geochem.* **2013**, *32*, 130–136. [CrossRef]

19. Bharti, N.; Khandekar, N.; Sengupta, P.; Bhadwal, S.; Kochhar, I. Dynamics of urban water supply management of two Himalayan towns in India. *Water Policy* **2020**, *22*, 65–89. [CrossRef]

20. Andermann, C.; Longuevergne, L.; Bonnet, S.; Crave, A.; Davy, P.; Gloaguen, R. Impact of transient groundwater storage on the discharge of Himalayan rivers. *Nat. Geosci.* **2012**, *5*, 127–132. [CrossRef]

21. Tambe, S.; Arrawatia, M.L.; Bhutia, N.T.; Swaroop, B. Rapid, cost-effective and high resolution assessment of climate-related vulnerability of rural communities of Sikkim Himalaya, India. *Curr. Sci.* **2011**, *101*, 165–173.

22. Agarwal, A.; Bhatnaga, N.K.; Nema, R.K.; Agrawal, N.K. Rainfall Dependence of Springs in the Midwestern Himalayan Hills of Uttarakhand. *Mt. Res. Dev.* **2012**, *32*, 446–455. [CrossRef]

23. Jeelani, G. Aquifer response to regional climate variability in a part of Kashmir Himalaya in India. *Hydrogeol. J.* **2008**, *16*, 1625–1633. [CrossRef]

24. Kumar, K.; Rawat, D.S.; Joshi, R. Chemistry of springwater in Almora, Central Himalaya, India. *Environ. Geol.* **1997**, *31*, 150–156. [CrossRef]

25. Joshi, B.K. Hydrology and nutrient dynamics of spring of Almora-Binsar area, Indian Central Himalaya: Landscapes, practices, and management. *Water Resour.* **2006**, *33*, 87–96. [CrossRef]

26. Singh, S.; Tanvir Hassan, S.M.; Hassan, M.; Bharti, N. Urbanisation and water insecurity in the Hindu Kush Himalaya: Insights from Bangladesh, India, Nepal and Pakistan. *Water Policy* **2020**, *22*, 9–32. [CrossRef]

27. NRAA. *Prioritization of Districts for Development Planning in India a Composite Index Approach*; National Rainfed Area Authority: Delhi, India, 2020.

28. Rodgers, W.A.; Panwar, H.S.; Mathur, V.B. *Wildlife Protected Area Network in Inda: A Review (Executive Summary)*; Wildlife Institute of India: Dehradun, India, 2000.

29. Anandhi, A. CISTA-A: Conceptual model using indicators selected by systems thinking for adaptation strategies in a changing climate: Case study in agro-ecosystems. *Ecol. Modell.* **2017**, *345*, 41–55. [CrossRef]

30. Anandhi, A.; Kannan, N. Vulnerability assessment of water resources-Translating a theoretical concept to an operational framework using systems thinking approach in a changing climate: Case study in Ogallala Aquifer. *J. Hydrol.* **2018**, *557*, 460–474. [CrossRef]

31. Von Bertalanffy, L. *General System Theory; Foundations, Development, Applications*; G. Braziller: New York, NY, USA, 1968.

32. Hopkins, T.S.; Bailly, D.; Støttrup, J.G. A Systems Approach Framework for Coastal Zones. *Ecol. Soc.* **2011**, *16*, 25. [CrossRef]

33. Shrestha, R.B.; Desia, J.; Mukherji, A.; Dhakal, M.; Kulkarni, H.; Mahamuni, K.; Bhuchar, S.; Bajracharya, S. *Protocol for Reviving Springs in the Hindu Kush Himalaya: A Practitioner's Manual 2018/4*; ICIMOD: Kathmandu, Nepal, 2018; ISBN 9789291156078.

34. Rajkonwar, M.; Gogoi, V.; Goswami, U.; Bezbaruah, D. A hydrogeological study of springs occurring along the Himalayan foothills of Mirem area, East Siang district, Arunachal Pradesh, India. *South East. Asian J. Sediment. Basin Res.* **2016**, *2*, 23–28.

35. Ansari, M.A.; Deodhar, A.; Kumar, U.S.; Khatti, V.S. Water quality of few springs in outer Himalayas-A study on the groundwater-bedrock interactions and hydrochemical evolution. *Groundw. Sustain. Dev.* **2015**, *1*, 59–67. [CrossRef]

36. Jeelani, G.; Kumar, U.S.; Bhat, N.A.; Sharma, S.; Kumar, B. Variation of $\delta 18O$, δD and 3H in karst springs of south Kashmir, western Himalayas (India). *Hydrol. Process.* **2014**, *29*, 522–530. [CrossRef]

37. Taye, C.D.; Chutia, A. Physical and Chemical characteristics of a few hot springs of Tawang and West Kameng District, Arunachal Pradesh, Northeast India. *J. Assam Sci. Soc.* **2016**, *57*, 47–55.

38. Singh, A.K.; Pande, R.K. Changes in spring activity: Experiences of Kumaun Himalaya, India. *Environmentalist* **1989**, *9*, 25–29. [CrossRef]

39. Jeelani, G.; Shah, R.A.; Fryar, A.E.; Deshpande, R.D.; Mukherjee, A.; Perrin, J. Hydrological processes in glacierized high-altitude basins of the western Himalayas. *Hydrogeol. J.* **2017**, *26*, 615–628. [CrossRef]

40. Jain, C.K.; Bandyopadhyay, A.; Bhadra, A. Assessment of ground water quality for drinking purpose, District Nainital, Uttarakhand, India. *Environ. Monit. Assess.* **2009**, *166*, 663–676. [CrossRef] [PubMed]

41. NITI Aayog. *Report of Working Group II Sustainable Tourism in the Indian Himalayan Region*; NITI Aayog: New Delhi, India, 2018.

42. Negi, G.C.S.; Joshi, V. Geohydrology of springs in mountain watershed: The need for problem solving research. *Curr. Sci.* **1996**, *71*, 772–776.

43. Oerlemans, J. Quantifying Global Warming from the Retreat of Glaciers. *Science* **1994**, *264*, 243–245. [CrossRef] [PubMed]

44. Malik, A.; Kumar, A. Spatio-temporal trend analysis of rainfall using parametric and non-parametric tests: Case study in Uttarakhand, India. *Theor. Appl. Climatol.* **2020**, *140*, 183–207. [CrossRef]

45. Singh, R.; Sah, S.; Das, B.; Potekar, S.; Chaudhary, A.; Pathak, H. Innovative trend analysis of spatio-temporal variations of rainfall in India during 1901–2019. *Theor. Appl. Climatol.* **2021**. [CrossRef]

46. Guhathakurtha, P.; Bandgar, A.; Menon, P.; Prasad, A.K.; Sable, S.T.; Sangwan, N. *Observed Rainfall Variability and Changes over Uttarakhand State, Met. Monograph No.: ESSO/IMD/HS/Rainfall Variability/28(2020)/52*; Indian Meteorological Department: Pune, India, 2020.

47. Shah, A.; Sen, S.; Dar, M.; Kumar, V. Land-Use/Land-Cover Change Detection and Analysis in Aglar Watershed, Uttarakhand. *Curr. J. Appl. Sci. Technol.* **2017**, *24*, 1–11. [CrossRef]
48. Kumar, V.; Sen, S. Evaluation of spring discharge dynamics using recession curve analysis: A case study in data-scarce region, Lesser Himalayas, India. *Sustain. Water Resour. Manag.* **2018**, *4*, 539–557. [CrossRef]
49. Mencló, A.; Boy, M.; Mas-Pla, J. Analysis of vulnerability factors that control nitrate occurrence in natural springs (Osona Region, NE Spain). *Sci. Total Environ.* **2011**, *409*, 3049–3058. [CrossRef] [PubMed]

Assessment of the Water-Energy Nexus under Future Climate Change in the Nile River Basin

Abay Yimere [1,2,*] and Engdawork Assefa [1]

[1] College of Development Studies, Center for Environment and Development, Addis Ababa University, Addis Ababa P.O. Box 9086, Ethiopia; engdawork.assefa@aau.edu.et

[2] Research Affiliate, Fletcher School of International Law and Diplomacy, Tufts University, 160 Packard Ave, Medford, MA 02155, USA

[*] Correspondence: abay.ezra@aau.edu.et; Tel.: +251-9441324445

Abstract: This study investigated the Water-Energy relationship in the Nile River Basin under changing climate conditions using an energy and water model. Climate change will likely affect both water and energy resources, which will create challenges for future planning and decision making, particularly considering the uncertainty surrounding the direction and magnitude of such effects. According to the assessment model, when countries depend heavily on hydropower for energy, power generation is determined by climate variability. For example, Ethiopia, Egypt, and Sudan are more hydropower-dependent than Burundi or Rwanda. As a result, the trading relationships and economic gains of these countries shift according to climate variability. Among 18 climate scenarios, four demonstrate a change in climate and runoff. Under these scenarios, trading partnerships and economic gains will favor Ethiopia and Egypt instead of Sudan and Egypt. This study examines the extent of potential climate challenges, their effects on the Nile River Basin, and recommends several solutions for environmental planners and decision makers. Although the proposed model has the novel ability of conducting scientific analyses with limited data, this research is still limited by data accessibility. Finally, the study will contribute to the literature on the climate chamber effects on regional and international trade.

Keywords: water model; energy model; climate scenario; Nile River Basin

1. Introduction

Water-Energy models are regularly updated to incorporate new developments; thus, they often vary in their technological requirements, data specifications, and computing capabilities. Many Water-Energy models cannot be applied to developing countries because data, high-computational demands, and skill requirements cannot be used to their full extent. This is because most models are developed in industrial countries and designed to match their technological development. Moreover, most energy models are not appropriate for developing countries because of the models' requirements, functions, and objectives [1,2]. For example, Nakata [1] examined models related to the energy environment, and Pandey [2] highlighted the importance of integrating the unique features of developing countries into the design and development of Water-Energy models. Furthermore, the data gap is a critical challenge for developing countries because it limits scenario discovery, hinders technological advances, and derails the impacts of policy analysis [3].

In light of these challenges, we developed a model to assess the Water-Energy relationship in the Nile River Basin that captures its unique riparian characteristics and conditions, including the informal energy sector, income and consumption, centralized market and supply options, and changing temporal patterns. As well as an integrative approach, the proposed accounting framework also emphasizes scenario discovery with limited data and fosters a data exchange between models until convergence is reached. Thus, the aim of this

study is to apply this tailored Water-Energy model to the Nile River Basin to investigate the regional effect of climate change on water and energy resources.

Literature Review

Strong links have long been recognized between water-resource and energy systems because water is essential to energy production. As of 2016, the energy sector accounted for approximately 15% of all fresh water use worldwide [4]. For the majority of developing nations in Africa, where hydropower is the principal source of energy, water and energy cannot be viewed separately. However, decision makers and policy makers had, until recently, overlooked the strong interdependence of these sectors, which has often led to situations where resources were either underused or exploited in a non-sustainable manner [5]. Thus, with growing demands for water in the food and industry sectors, as well as ever-increasing energy demands, an integrated assessment of the Water-Energy nexus has become even more relevant when evaluating alternatives for better decision making and management.

Climate change will likely affect both water and energy resources, which will create challenges for future planning, particularly considering the uncertainty surrounding the direction and magnitude of such effects. Rising temperatures will likely lead to an increased demand for irrigation due to increased evapotranspiration [6]. This additional need to meet the potential evapotranspiration (PET) demand or address additional evaporation losses will affect water allocation, with hydropower particularly vulnerable to a drier future [7]. Thus, a more inclusive analysis is required to evaluate future water and energy risks under a changing climate and assess the resiliency of a given Water-Energy system to resource variability and other competing demands.

Energy system models are important tools for analyzing future energy supply and demand at the national, state, and regional level under certain assumptions, such as developmental scenarios, electricity prices, availability, and energy-generation capacity [8]. Historically, energy accounting has been one of the key pillars of energy system studies, as it provides insight into the overall balance of an energy system [9]. Accordingly, Hoffman and Wood [10] recommended the energy-accounting approach as an essential framework for energy system research. Long-range Energy Alternative Planning (LEAP) is an extension of this approach, which addresses the recommendations of subsequent studies. However, the reference energy system (RES) is a natural outcome of the energy balance system [11]. RES audits all existing events across an energy supply chain by considering its technological level, scope, and features. The method developed by Hoffman and Wood [10] helps incorporate current and future technological options to enable the system to perform analyses. Following RES development and calibration, linear programming was developed to expand further and integrate the model. Subsequently, a model known as Brookhaven Energy System Optimization (BESOM) was developed for the purpose of resource allocation [12]. After linear programming and the development of BESOM, various models were developed and human abilities were increased, enabling the analysis of economic linkages through input–output analysis at national and regional levels. Historically, BESOM has served as a basis for many other model developments and derivatives [13].

Energy models have been categorized into three types based on the model approach: top-down, bottom-up, and hybrid [14–19]. Each type of model has a different aim. The bottom-up approach begins by describing the technologies for supply and demand; top-down models start by explaining the relationship among several components at the macroeconomic level; and hybrid approaches attempt to combine features of these two models. Various efforts have been made to integrate the bottom-up and top-down approaches into a hybrid model [16,17]. Typically, the top-down approach is more applicable to econometric, input–output, and general equilibrium features. The programing techniques (linear, nonlinear, mixed-integer, and neural theories) also describe the top-down approach. Conversely, bottom-up models are more applicable to optimization and simulation. Previous studies have also attempted to categorize models based on functionality [16,17].

Energy models have also been reviewed and evaluated based on their scope: from individual projects to multifaceted and global systems and from long-term to standalone projects [20–22]. Long-term models also pursue either a top-down, bottom-up, or hybrid approach. However, long-term models must adapt to long-term changes and have their parameters updated accordingly [17,23–25]. To that end, the long-term model embraces a system-wide approach. Major long-term bottom-up models include the Energy Flow Optimization Model (EFOM) and MARKAL [26]. EFOM, which was developed under the authorization of the European Commission, is a bottom-up engineering-oriented model designed to support regional energy strategies and policies [27]. MARKAL is, along with TIMES, a successful derivative of BESOM used by the European Commission to simulate the energy–environment system at the global, European, national, and community levels. The input data can easily tailor the model, which can capture energy supply-and-demand evolution for up to 100 years [28,29]. MESSAGE, which was later enhanced into MESSAGE I and MESSAGE II, is also considered to be an early generation of an optimization model. Previously, the World Energy Council and the Intergovernmental Panel on Climate Change used MESSAGE to develop energy transition pathways and greenhouse gas emission scenarios, respectively [30,31]. The Open-Source Energy Modeling System (OSeMOSYS) also belongs to the class of early bottom-up models [32].

In the 1990s, bottom-up models flourished, particularly with development of the Prospective Outlook on Long-term Energy Systems (POLES), World Energy Model (WEM), PRIMES, and LEAP. PRIMES can be modular [33] and is strongly linked to the generation of the PROMETHEUS mode. LEAP is essentially a simulation-model framework with minor input data requirements, and combines a top-down demand with a bottom-up supply [22,34]. AURORAxmp [35], EPI [36], CYME EATON [37], DER-CAM Distributed Energy Resources Customer Adoption Model [38], EMPS [39], Enertile [40], ENTIGRIS (Energy System Models at Fraunhofer ISE0 [41], ETSAP-TIAM [26], and PLEXOS (Energy Exemplar) [42] are all categorized as bottom-up models. PLEXOS, which was later extended to MOSEK and Xpress-MP, was developed as a linear and mixed-integer model. PLEXOS develops scenarios to capture regional markers and prices to perform market design and analysis with hydrological, thermal, and transmission features. AURORAxmp was designed to examine hydropower generation and load volatility under uncertain conditions. Likewise, in the 1980s, an expanded version of a top-down model was developed, called Phoenix, an extension of the general equilibrium model (GEM). Following its development, top-down models became prevalent, including the General Equilibrium Environmental Model (GREEN), MARKAL, GEM-E3, and EPPA [43–49]. Under the approval of the Secretariat of the Organization for Economic Cooperation and Development (OECD), GREEN has become a global model to evaluate the impact of economic activities on abating CO_2 emissions [50]. MARKAL was adapted to a top-down model to create both MARKAL–MACRO [51] and MARKAL–EPPA [45]. Hybrid energy models also include RETScreen [52], Natural Resources Canada [53], POLES [54], MESSAGE [55], LEAP [56], GCAM (Joint Global Change Research Institute) [57], and ETM [58].

In dealing with uncertainties, a stochastic approach is more desirable compared to a deterministic approach, which must be calibrated several times by changing input similar to that of Monte Carlo. This approach works like MARKAL's version of stochastic [59] and MESSAGE's stochastic [60]. Rigorous stochastic models for Water-Energy nexus systems have recently been developed, and they are considered vital for their meticulous results [61]. Concerning deterministic model studies, the supply side of the water nexus gets less attention given its optimization uncertainties [62]. One model was employed in a study of a transboundary water nexus (Albrecht et al., 2018) and more recently one was used in an analysis of the nexus in the Mekong river basin [63].

Some previous energy models have been developed and refined from case studies and experiments. For example, Welsch [20] further refined the open-source OSeMOSYS toolkit and TIMES—PLEXOS model to investigate the Irish energy system; Poncelet [64] employed TIMES to investigate the Belgium energy system; Haydt [65] also employed

LEAP, MARKAL/TIMES, and EnergyPLAN to investigate the Atlantic Ocean energy system in the Atlantic Ocean for the Azores; and Jaehnert and Doorman [66] combined EMPS and IRIE to understand the energy balance between input-out energy systems.

Furthermore, numerous tools have been suggested to improve decision making related to water resource management. For example, Mysiak et al. [67] proposed the integration of hydrological tools, and Rees et al. [68] developed a water balance model that calculates the balance between water supply and demand. Moreover, Li et al. [69] proposed a water resource management model that, under uncertain conditions, is expected to help decision makers identify and develop a response system for uncertain resource challenges. Another model developed by Van Cauwenbergh et al. [70] prioritizes water resource planning and management according to the requirements of environment and socioeconomic development. A fuzzy-set mathematical theory has also been proposed and recommended by researchers to address water resource management challenges through a robust decision-making process [71,72]. The Water Evaluation and Planning (WEAP) model developed by the Stockholm Environmental Institute (SEI) has been used to evaluate various water resource planning and management alternatives [73,74]. WEAP allocates water according to user-developed criteria, and the primary use of this model is for scenario development, through which it answers various "what if" questions pertaining to the demand and supply of water [75,76].

Most importantly, the stochastic models have shown superiority in providing long-term analysis of uncertainty and in helping grasp natural behaviors [77]. Harold Edwin Hurst, who studied the Nile River for about 60 years, observed that the time series of the river's annual flow displays statistical behaviors that do not fit into a series of simply random variation; instead, their tendency to occur in natural events are higher, of which these characteristics are known as Hurst Phenomena or Long–term Persistence (LTP) [78,79]. Scientists have used these extended time horizon research methods to study ensembles of synthetic hydrologic conditions that take annual, seasonal and decadal variability into consideration, including studies of the Boeoticos Kephisos Basin in Greece [80], the Nile River Basin in Africa [81], and documented the presence of LTP in precipitation [82], runoff [83], temperature [84] and in the hydrological cycle [85].

In conclusion, different energy models are applied according to their approach and techniques. Among the bottom-up energy models, OSeMOSYS [20,86] the Integrated MARKAL–EFOM System (TIMES) [26,27], and LEAP [21,74] have all been widely applied. Equally, water planners commonly employ the WEAP system [48,51,75], and RiverWare [87,88] as water system analysis modeling tools. In most cases, these two categories of models are applied separately using the energy model's output as the input to the water model and vice versa. Presently, the development of comprehensive models that consider both energy and water and model their systemic interactions is very limited. Of the few studies that have demonstrated this interaction, one describes an integrated approach using a water system in WEAP and an energy model in LEAP in Sacramento, California, [89] and one that took a climate, land use, energy, and water systems (CLEWs) approach, which involved a more comprehensive module-based approach where data were exchanged between the sectoral models in an iterative fashion [90].

Most existing energy system models are in an early stage of integrating energy and water, and lack temporal representation. Therefore, this study presents an integrated water and energy system model that captures the links between these sectors. A regional power integration energy model and a basin-wide water resource system model are coupled and simulated together to investigate how future climate change might impact the generating capacity of existing and future planned hydropower plants in the Nile River Basin, as well as the dynamics of trade between plants in the region. The main feature of this framework is the use of an iterative approach to exchange data between the models until convergence is established in the linked components. The model is applied to regional trade in the countries of the Nile River Basin under the Eastern Africa Power Pool (EAPP) and the future development scenario of the Program for Infrastructure Development in Africa

(PIDA) [91]. The impact of climate change is categorized and evaluated for scenarios of an unconstrained scenario, with unrestricted emissions of greenhouse gases and a future scenario, in which a restriction policy is imposed to limit emissions to a certain level, referred to as level one stabilization. These two scenarios reveal the possible advantages that could be achieved under a policy of adaptation.

2. Methods

A key element of the coupled Water-Energy modeling approach presented in this study involves simulating both the water system (to estimate hydropower generation constrained by water availability) and the energy system, applying feedback loops between the two models until equilibrium is achieved between hydropower generated from the water model and hydroelectric energy used in the energy model on a national level. To analyze the impact of climate change, the hydrologic model was simulated to estimate runoff corresponding to different climate scenarios (characterized by different changes in temperature and precipitation) to establish water availability for the water system model. Then, the coupled Water-Energy system was simulated for each climate change scenario. This configuration considers energy demands according to both water availability and energy cost after the energy mix is identified.

2.1. Energy and Water System Models

2.1.1. Energy Model

The energy system was modeled using the Regional Integration and Planning Assessment (RIPA) tool [8,24], configured in the General Algebraic Modeling System (GAMS) mathematical programming language [92,93]. RIPA is a bottom-up, dynamic, multiyear optimization program that makes use of mixed-integer programming (MIP) techniques to solve the optimal mix of generation and transmission by minimizing all discounted investment and operating costs while meeting the demands for different specified energy sources over the planning period. One of the inputs of RIPA is the generation technology and corresponding monthly available capacity over the simulation period. Monthly hydropower generation is one of the renewable energy inputs to the model that serves as the upper boundary of the maximum available resource from hydropower when solving for the country-level energy balance. After the optimal mix of generation is solved, the amount of energy not utilized in any of the technologies is reported as a "spill", together with the shadow prices obtained for the bounding constraints in the MIP optimization.

2.1.2. Water Model

The water resource system model simulates water allocation and hydropower generation from available resources by solving different Linear Programming (LP) problems that are defined iteratively at each time step in monthly intervals [94,95]. These problems are determined based on the priorities and nature of water and power demand and stream flow requirements. Hydropower generation is calculated from the flow passing through the turbine having a maximum capacity to fulfill the specified monthly energy demand. Hydropower generation is constrained by the available water in the system and the priority assigned to the demand. The model reports the total energy generation from each plant and the power deficit, i.e., the difference between the specified monthly energy demand and generation.

2.2. Formulation of Model Coupling

Although water and energy production/use can be interlinked in several ways, this study explored only hydropower generation and demand. The primary objective was to minimize spillage from the energy model and shift excess energy to other months in the same year by storing water. Initially, hydropower estimation was based on estimates of the country-level target demand. For storage hydropower plants, the initial estimates were taken from the average generation, whereas for existing hydropower plants, a rough

approximation was calculated as a percentage of the planned installed capacity for future infrastructure. For run-of-river hydropower plants, the maximum generating capacity was taken as the power target for each month. As their storage capacity is small or nonexistent, they are configured for maximum potential generation based on the available water in the system. However, the generation capacity for storage reservoirs can be constrained by water availability, priority demands for water that are higher than the level of energy generation, and reservoir rule curves used in addition to the specified demand. The information exchange between the water and energy system models and an example of model interaction are shown in Figure 1.
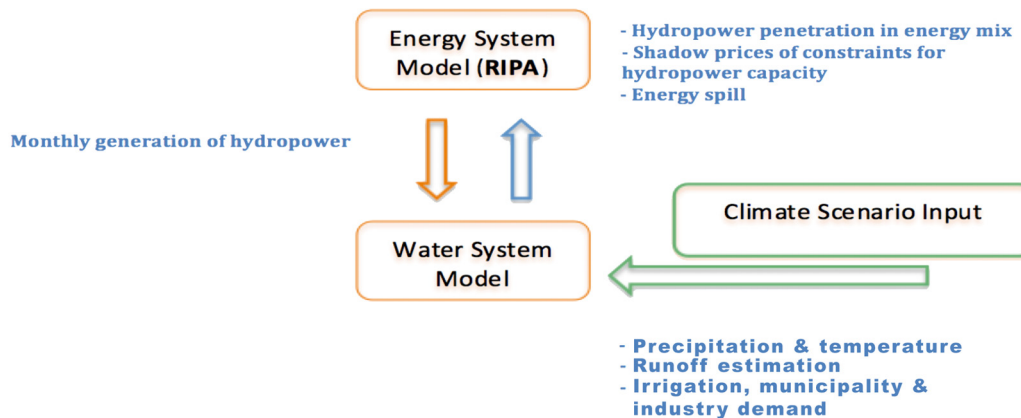
Figure 1. Schematic showing the Water-Energy interaction and climate modules. RIPA = Regional Integration and Planning Assessment tool.

An initial simulation of the water system was conducted to estimate the monthly energy demand at the plant level, which produces a time series of the monthly generated power. This power generation is then aggregated by country and used as an input in the energy system model to determine the optimum mix of energy for each sector and the unused energy "spill". From the energy mix, the hydropower outputs are then disaggregated back to the plant-level generation based on the ratio of the total generated energy determined from the water model to the energy demand determined for each plant, which is used for the next iteration, given in Equation (1). This ensures that the amount of generation from the water model is fully used in the energy mix.

$$Energy\ Demand_{plant,year} = HydroShare_{country} * \frac{Hydro\ Generation_{plant}}{\sum_{country} Hydropower\ Share\ in\ Energy\ mix} \tag{1}$$

The spills represent an extra level of generation capacity in the water system but which cannot be used in the energy mix at a particular time step due to other constraints and costs in the energy system. This excess capacity is distributed back to the hydropower plants and annually added to the existing required demand from plants based on the proportion of the deficit, given in Equation (2). This is a simplification that assumes a linear relationship between total country-level generation and generation from each hydropower plant in all time steps. In an actual case, where hydropower is highly nonlinear, this assumption in particular might be less efficient for a cascading hydropower system sharing the same river system. Then, this annual capacity is disaggregated to the monthly level based on the shadow prices. The idea behind this assumption is to give priority to months based on the relative value they will add to minimizing the cost while determining the energy mix. The shadow prices corresponding to maximum hydropower constraints in the energy model

are given by Equation (3). The reason for distributing the excess demand on an annual basis is the assumption that the reservoir storage exhibits annual cycles.

$$Demand\ Additional_{Annual,plant} = Spill_{Annual,country} * \frac{1 - deficit_{plant}}{\sum_c Annual\ Deficit_{Plant}} \qquad (2)$$

$$\sum_l vProduction_{hsc,c,y,m,l,h} * pYearSplit_{l,m} \leq pHydroUpperLimit_{c,h,hsc,m} \qquad (3)$$

The newly identified energy demands present a different water allocation scenario, which changes the water distribution and energy generation in the water system model and in extreme cases may affect generation in all plants. Therefore, the above step is executed iteratively to achieve equilibrium until either the total spill is zero or the amount of hydroelectricity utilized in the energy model converges to hydropower generation in the water system model.

The new established equilibrium does not necessarily represent an optimal configuration of hydropower generation for the water resource model. The distribution of spill based on shadow prices assures the optimal allocation of the spilled portion of demand; however, as the water model only explores the optimal allocation of resources for a time step, this does not guarantee optimal allocation over an entire year. However, given the limitation of the water model, a partial optimal point can be achieved that considers both the water availability and energy cost.

2.3. Climate Scenarios

The projections of changes in precipitation and temperature were derived from the hybrid frequency distributions (HFDs) of Schlosser et al. [96]. These are regionally downscaled model scenarios in the form of numerical hybridizations of 400 policy ensembles from the Massachusetts Institute of Technology (MIT) Integrated Global System Model (IGSM) [97,98] that correspond to 17 IPCC AR4 climate model results. The result is a meta-ensemble of climate change projections containing 6800 distinct members for possible adaptation. The MIT IGSM framework uses emission predictions and economic outputs from the MIT emission prediction and policy analysis model and earth system modeling predictions from the IGSM to drive a land system component, a crop model (CliCrop), and a water resource system model.

The HFD datasets characterize possible future climate outcomes, incorporating uncertainties in the structural differences of climate models, downscaling, and possible emission scenarios, as represented by different adopted policies. The two adopted policy scenarios corresponding to a restriction of global emissions of greenhouse gases to a concentration of 560 ppm CO_2 equivalent are referred to as level 1 stabilization (L1S) and unconstrained emissions. The scenario where no policy is adopted to constrain greenhouse gas emissions was considered in this assessment to compare the reduced level of impact as a result of policy adoption. The climate shocks were superimposed over historical reference case precipitation and temperature data obtained from the Climatic Research Unit (CRU) [99–102] to form climate scenarios.

Catchment runoff was simulated and hydrologic responses were characterized corresponding to the precipitation and temperature changes in each scenario using a conceptual hydrologic model called NAM (from the Danish Nedbør-Afstrømnings model). NAM is a deterministic, lumped, and conceptual rainfall–runoff model originally developed by the Institute of Hydrodynamics and Hydraulic Engineering at the Technical University of Denmark [103]. Climate change also affects irrigation water demand; thus, changes in the irrigation demand as a result of rising temperature were estimated for the scenarios.

3. Application of the Model to the Nile River Basin

We applied the integrated Water-Energy model to study the interactions between water and energy in the Nile River Basin, to assess the potential impact of climate change on the existing and future energy supply of countries within the basin, and to determine

how the electricity trade between countries might be affected by these changes over the period of 2010–2035, in monthly time intervals.

Hydropower is one of the principal sources of renewable energy in the Nile River Basin, where there is enormous opportunity for future development due to its highly underdeveloped nature. Climate-induced changes in the hydropower generating capacity will affect the existing and future dynamics of power trade among countries in the Nile River Basin. Although there is currently very limited cross-border electricity trading, several projects are in the pipeline, such as the Ethiopia Power Trade Project, the Nile Equatorial Lakes Interconnector Project, and the Regional Rusumo Falls Hydroelectric and Multipurpose Project (Figure 2); thus, hydropower generation will soon represent the dominant energy share in the basin, with increased levels of regional trade [104,105].
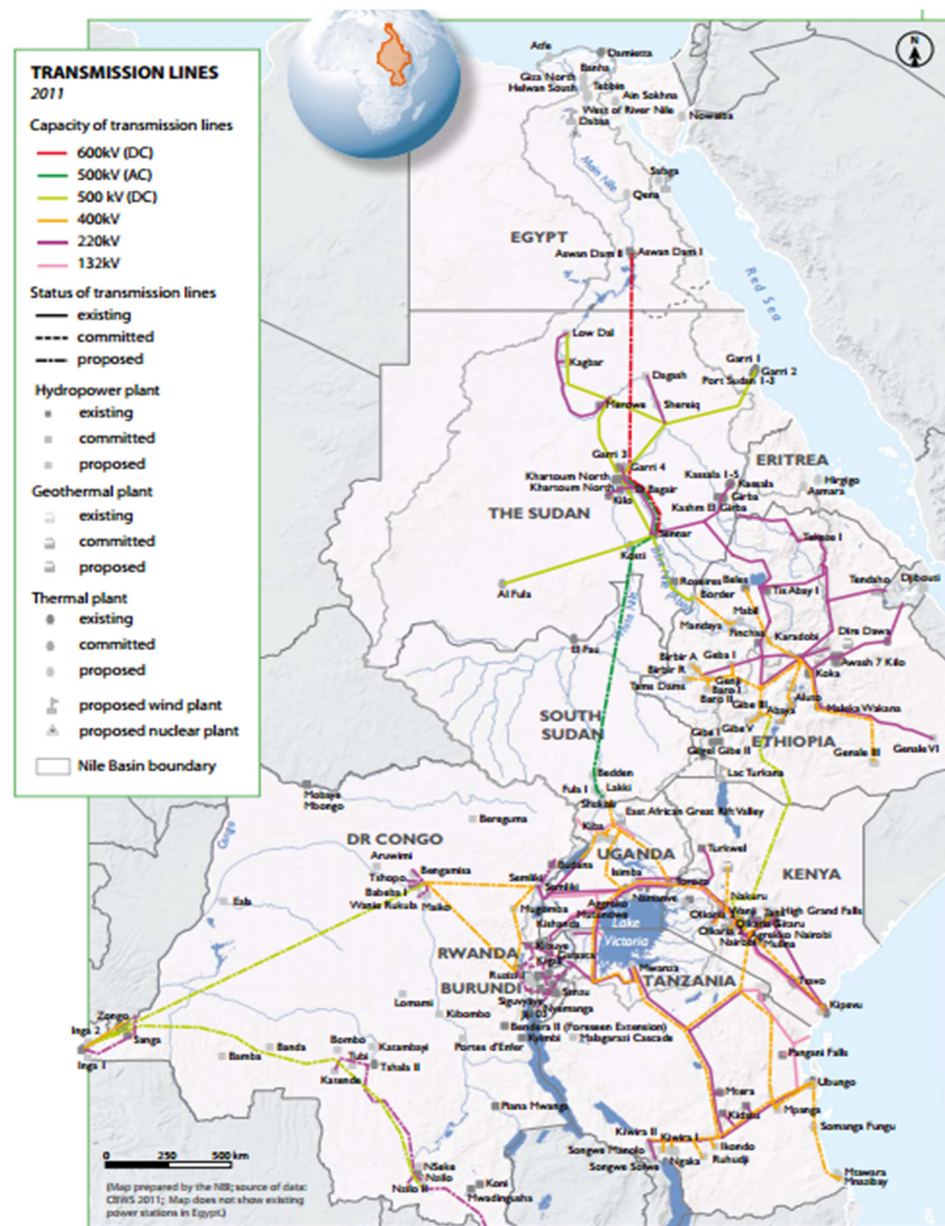

Figure 2. Planned and existing hydropower plants and regional interconnection links in the Nile River Basin (source: State of the Nile River Basin 2012, Nile Basin Initiative).

Hydropower generation was modeled on a monthly time step for existing and future hydropower facilities in the basin for a given level of initial estimates of the country-level

target demand. The energy demand for future plans was estimated as rough approximations obtained from either the project document or a percentage of the planned installed capacity of the plant. For run-of-river hydropower plants, the maximum generating capacity was taken as the power target for each month.

Hydropower plants that are located outside the Nile River Basin but contribute to country generation were considered to have a fixed generating capacity that did not vary with climate change. Although this was only an approximation used to simplify our analysis by limiting the hydrologic and water resource system analysis within the basin, the contribution from outside basins was proportionally small; thus, this simplification is unlikely to incur considerable error.

The existing capacity expansions and additional infrastructure expected to be built in the Nile River system were adopted from the PIDA development plan [91]. The level of capacity for all countries at five-year intervals is summarized [106,107] in Table 1. Djibouti is not within the Nile River system but it will be in the power grid; therefore, it was included in the energy model. The total installed capacity for the water model by the end of 2035 is approximately 24 TW, and the distribution is shown in Table 1. A study conducted by the Nile Basin Initiative (NBI) [108] indicated basin-wide power development options and trade opportunities. According to that study, the total energy demand in the Nile River Basin countries is expected to increase from 184 TWh in 2010 to 1170 TWh by 2035, representing an increase of 300% or more from current demand.

Table 1. Hydropower installed capacity for Nile River Basin countries (both within and outside the geographical extent of the Nile River Basin).

Year	Burundi	Djibouti	Egypt	Ethiopia	Kenya	Rwanda	Sudan	Tanzania	Uganda
2010–2015	37	0	2250	1070	733	77	1727	561	830
2015–2020	103	0	2275	6182	733	148	1841	598	1660
2021–2025	103	0	2282	9677	733	225	2665	623	2444
2025–2030	103	0	2282	13,862	733	278	3301	623	2501
2030–2035	97	0	2282	13,862	733	278	3597	623	2501

4. Results

The results of hydropower contributions over the simulation period are shown for each country in Figure 3. We can see significant changes in hydropower penetration across different climate scenarios for Ethiopia, Egypt, and Sudan. For Burundi and Rwanda, hydropower generation comes from outside the basin; therefore, it is assumed to be fixed across climate scenarios. For the remaining countries, hydropower comes from run-of-river plants and generally increases as a result of the higher runoff expected in the majority of climate scenarios; however, the slight fluctuations caused by climate change are smoothed out in the energy model, indicating that all generated power will be used to the highest potential. The mix of energy results indicates that hydropower will continue to dominate the system power supply; examples for three selected countries are shown in Figure 4. The differences between observed and simulated value from 2015 to 2020 are negligible; the observed hydropower generation for each country resembled the corresponding simulated pattern as demonstrated in Figure 3.
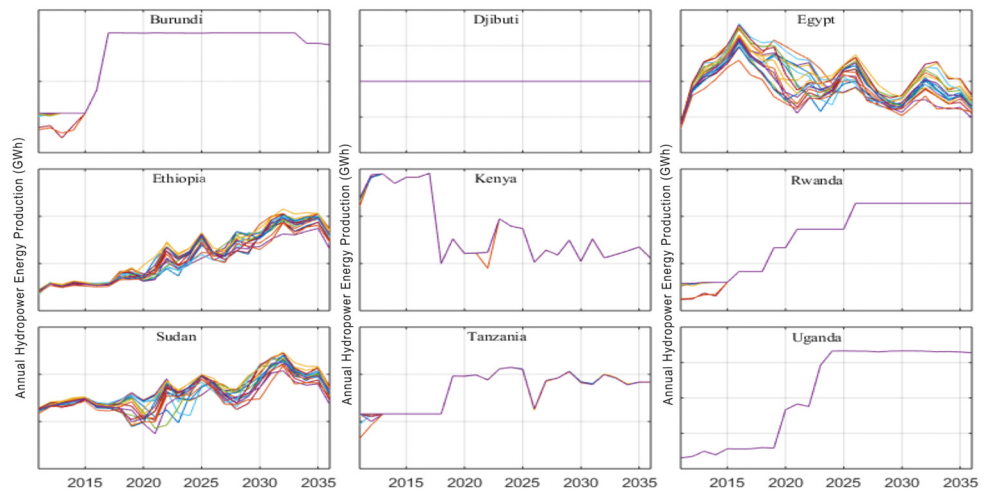
Figure 3. Annual hydropower energy production results Gigawatt hours (GWh) by country over the simulation period for selected climate change scenarios.

(a)

(b)

(c)
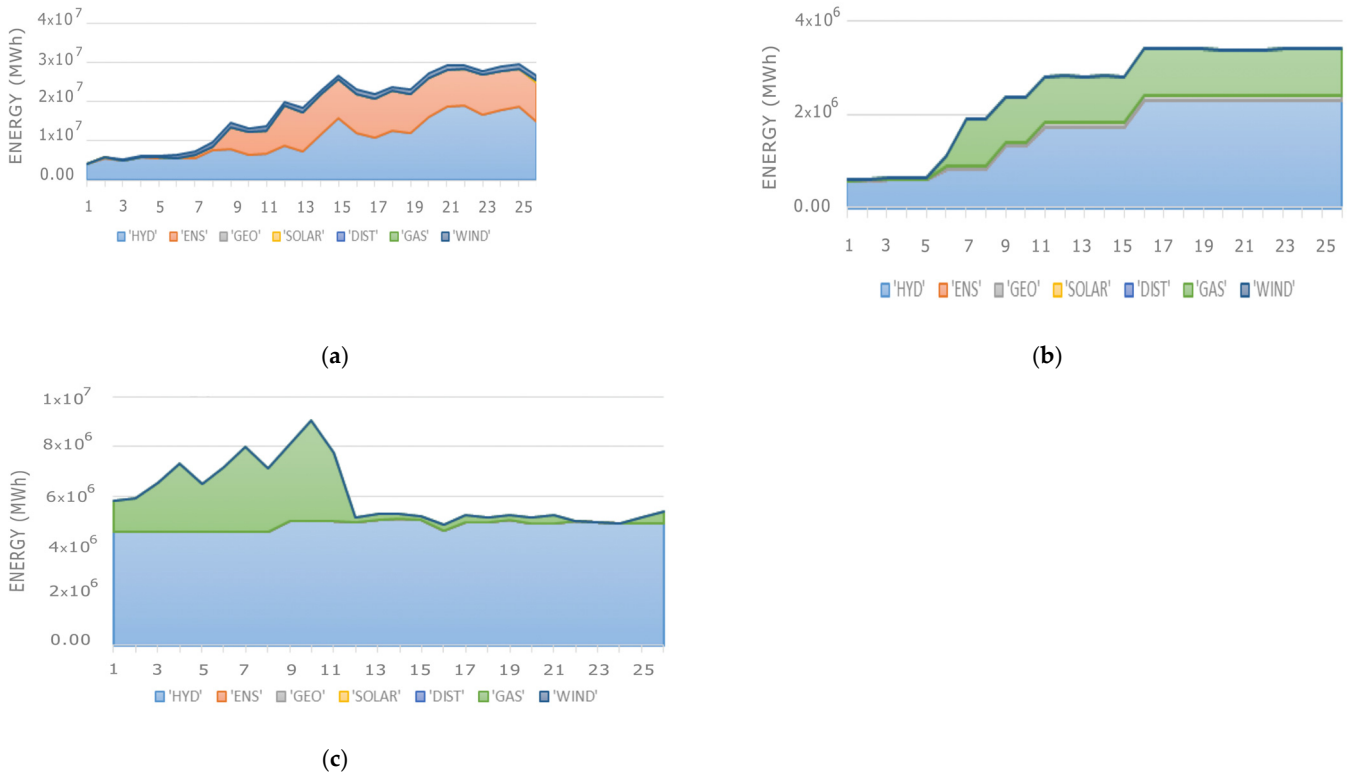
Figure 4. Energy mix trends over the simulation period for (**a**) Egypt, (**b**) Sudan, and (**c**) Tanzania.

The electricity trade results for the reference scenarios of the current (average for 2010–2014) and future (average for 2031–2035) conditions are shown in Figure 5. The results indicate that regional trade will grow stronger. Given the scenario assumption in the model, the highest degree of hydropower trade under conditions of no climate change is expected between Sudan and Egypt, and additional dams planned for the lower part of the Nile in Sudan will help meet Egypt's electricity demand and take preference over upstream dams (also see Figure 3).

	RWA	SUD	UGA	ETH	KEN	EGY	TAN	BUR
BUR	0.53							
EGY		27.95						
KEN			2.80	0.86	0.86			
RWA			1.79	2.30				
SUD			4.31		7.19		5.82	
TAN	0.02		0.08			1.98		
UGA	0.83	4.36		8.48		3.92		
ETH		7.25				8.56		
DJI					0.25			

	RWA	SUD	UGA	ETH	KEN	EGY	TAN	BUR
BUR	0.15							
EGY		1.97						
KEN			0.98					
RWA				0.45				0.01
SUD			1.00		2.46		1.98	
TAN	0.00		1.78					
UGA		1.43		0.09		0.44		
ETH		1.56						
DJI					0.02			

(**a**)   (**b**)
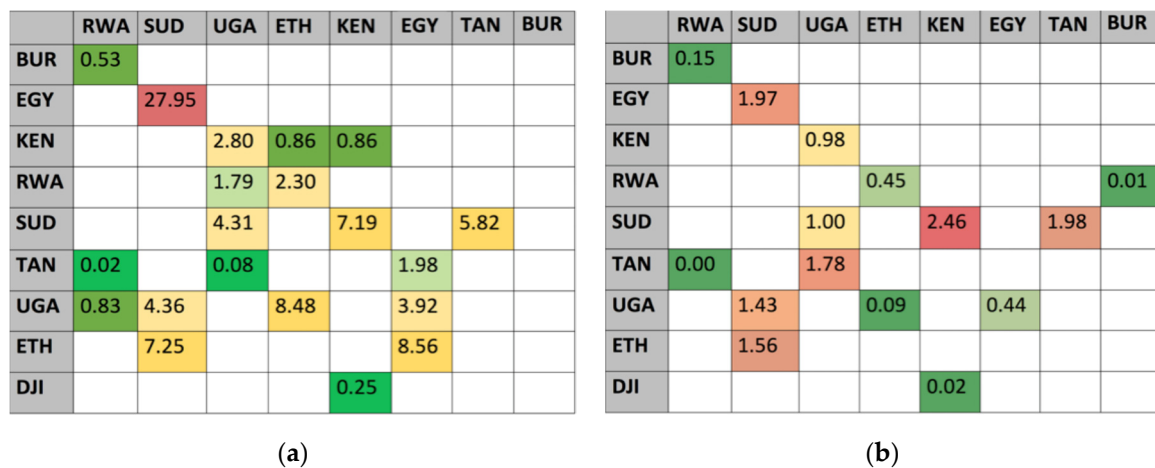
Figure 5. Total energy trade in Terawatt hours (TWh) among countries for the (**a**) current (2010–2014) and (**b**) future (2031–2035) reference case scenarios with no climate change.

One notable result of this study is that climate change is predicted to alter trade relationships. In some climate change scenarios, trade dynamics exhibit a complete shift, whereas other scenarios lead to either a reduced or increased level of trade. The manner in which trade evolves under the selected 18 climate change scenarios is shown in Figure 6 for the five major regional trade relationships. Four of the 18 scenarios exhibit a change from the reference case with the highest level of trade shifting from Egypt–Sudan to Egypt–Ethiopia. Furthermore, in five of the 18 scenarios, trade between Ethiopia and Sudan will no longer have an economic advantage. Four of the 18 scenarios represent a stringent change in climate, which translates into a change in runoff. Under these conditions, Sudan may not build the planned dam adjacent to Egypt; instead, the Ethiopian highland may be preferable for large storage and dam construction due to its high altitude and low evaporation [109]. As a result, the electricity/energy-trading partnership is predicted to shift from Egypt–Sudan to Egypt–Ethiopia. In summary, trading relationships and economic gains will change under climate variability, and these must be considered to ensure an integrated and comprehensive regional response to mitigating the risk of future climate impacts.
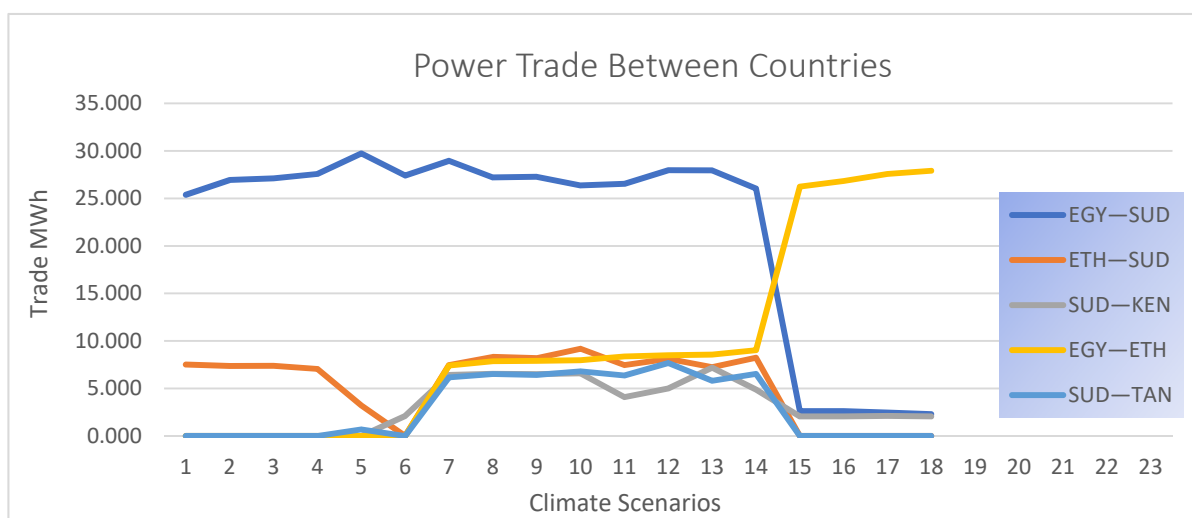
Figure 6. Average energy trade between countries for 2031–2035 under selected climate change scenarios (scenarios are sorted for better visualization).

5. Conclusions

This study proposed a framework for the integrated assessment of energy and water that captures the links among these sectors. This framework was applied to countries in the Nile River Basin to evaluate how energy will evolve under various climate change scenarios. The results indicated that, for selected scenarios, both the generating capacity and energy trade among countries could be significantly altered. Moreover, due to rapid economic growth in these countries, the demand for energy and water will continue to rise, stressing the shared river basin even more. Hydropower will continue to represent a major proportion of the energy supply in the Nile River Basin region; therefore, the integrated assessment of the energy and water nexus will be an essential component of planning for future development interventions and policy formulation.

The effects of climate change on the river system are critical and far-reaching. Countries where power generation depends heavily on hydroelectricity are highly vulnerable to climate variability. For example, the power generation capabilities of Egypt, Ethiopia, and Sudan fluctuate under climate variability; hence, their development is less sustainable. Moreover, energy trading plays a critical role in fostering cooperation and partnerships among the Nile basin countries. A change in climate could hamper trading relationships unless the countries develop a common framework to mitigate the adverse effects of climate change. A shift in trading partners and economic advantages from one country to another caused by climate change on shared water resources could also derail cooperation and lead to conflict and violence.

Water-Energy resources are an integrated part of sustainable development worldwide; however, growing climate variability on interannual to longer timescales will have an enormous effect on socioeconomic development, requiring adaptation on an individual, community, and national scale [110]. Energy is a crucial driving force for economic development as it fosters growth and transformation. Due to climate change uncertainties, governance of the Water-Energy system for greater economic benefits and regional cooperation becomes complicated and is compound by data limitations, which can impede robust analysis and assessment. The simple tailored model presented in this study provides a novel explanation for the Water-Energy governance strategy for a situation with limited data, thereby assisting policymakers and water resource planners in making decisions for the benefit of society and the economy. The proposed model is applicable to cases where the availability of complete and comprehensive data is inadequate.

A Water-Energy governance system that addresses climate variability and improved climate resilience are essential steps for reducing and managing future climate impacts. The proposed framework, which uses limited data through a tailored approach, can be used to undertake comprehensive and scientific analysis to inform policymakers about the dynamics of the Water-Energy governance system, including hydropower generation and allocation and future climate conditions to help water resource planners design and implement the necessary adaptations. Incorporating the findings of this assessment framework into both national and regional strategies can enhance the sustainable development of water and energy resources and foster trading partners and economic advantages. The Water-Energy analysis employed in this study can serve as a governance system for climate variability and risk management in cases with limited data to foster regional socioeconomic growth, increase resilience to climate vulnerability and variability, and enhance economic growth and cooperation at the policy and technical level.

Limitations were attributed to incomplete and inadequate data for verification and calibrations of the model to satisfy its minimum data requirements. The challenges were addressed through proxies and approximation techniques. The mode's flexibility is its core chrematistics of strength, and in terms of testing the model for a wide range of alternative scenarios is its limitation.

This analysis is carried out on foresight hydrological conditions. However, to account for different scales of variability, future studies should consider a wide range of synthetic hydrologic conditions that examine scenarios of annual, seasonal and decadal variability

over a more extended time to project the future climate of the Nile River basin and elucidate variations in water resources.

Author Contributions: Both authors contributed equally to the development of this article. A.Y. conceptualized methodological and theoretical formalism and performed the analysis. E.A. supervised the study. Both authors discussed the results and contributed to the final version of the manuscript. Both authors have read and agreed to the published version of the manuscript.

Conflicts of Interest: The authors declare no conflict of interest.

References

1. Nakata, T. Energy-economic models and the environment. *Prog. Energy Combust. Sci.* **2004**, *30*, 417–478. [CrossRef]
2. Pandey, R. Energy policy modelling: Agenda for developing countries. *Energy Policy* **2002**, *30*, 97–106. [CrossRef]
3. Worrel, E.; Ramesohl, S.; Boyd, G. Advances in energy forecasting models based on engineering economic. *Annu. Rev. Environ. Resour.* **2004**, *29*, 345–381. [CrossRef]
4. World Energy Outlook 2012 Home Page. Available online: https://www.iea.org/reports/world-energy-outlook-2012 (accessed on 2 February 2019).
5. Degefu, D.M.; He, W.; Zhao, J.H. Hydropower for sustainable water and energy development in Ethiopia. *Sustain. Water Resour. Manag.* **2015**, *1*, 305–314. [CrossRef]
6. Woznicki, S.A.; Nejadhashemi, A.P.; Parsinejad, M. Climate change and irrigation demand: Uncertainty and adaptation. *J. Hydrol. Reg. Stud.* **2015**, *3*, 247–264. [CrossRef]
7. Zeng, R.; Cai, X.; Ringker, C.; Zhu, T. Hydropower versus irrigation—An analysis of global patterns. *Environ. Res. Lett.* **2017**, *12*, 034006. [CrossRef]
8. Fattahi, A.; Sijm, J.; Faaij, A. *A Systemic Approach to Analyze Integrated Energy System Modeling Tools: A Review of National Models*; Elsevier: Amsterdam, The Netherlands, 2020; Volume 133, p. 110195.
9. Amaral, L.P.; Martins, N.; Gouveia, J.B. A review of energy theory, its application and latest developments. *Renew. Sustain. Energy Rev.* **2016**, *54*, 882–888. [CrossRef]
10. Hoffman, K.; Wood, D.O. Energy system modelling and forecasting. *Annu. Rev. Energy* **1976**, *1*, 423–453. [CrossRef]
11. Masoumzadeh, A.; Rasekhi, H.; Fathi, H.A. A comprehensive energy supply model in an office building based on the reference energy system. *Int. J. Sustain. Energy* **2016**, *35*, 88–102. [CrossRef]
12. Munasinghe, M.; Meier, P. *Energy Policy Analyis and Modelling*; Cambridge Books; Cambridge University: Cambridge, UK, 1993.
13. Hoffman, K.; Jorgenson, D.W. Economic and technological models for evaluation of energy policy. *Bell J. Econ.* **1977**, *8*, 444–466. [CrossRef]
14. Bouffaron, P.; Avrin, A.P. Prospective_Energ_Etique: L'exemple de SWITCH, un mod_ele de Planification du Syst_eme _Electrique Made in UC Berkeley. Bulletins Electroniques Etats-Unis. 2012. Available online: http://www.bulletins-electroniques.com/actualites/71765.htm (accessed on 2 May 2015).
15. Herbst, A.; Felipe, T.; Felix, R.; Eberhard, J. Introduction to energy systems modelling. *Swiss J. Econ. Stat.* **2012**, *148*, 111–135. [CrossRef]
16. Hourcade, J.C.; Jaccard, M.; Bataille, C.; Ghersi, F. Hybrid modeling: New answers to old challenges. *Energy J.* **2006**, *21*, 12.
17. Jebaraj, S.; Iniyan, S. A review of energy models. *Renew. Sustain. Energy Rev.* **2006**. [CrossRef]
18. Van Beeck, N. *Classification of Energy Models*; Citeseer; School of Economics and Management, Tilburg University: Tilburg, The Netherlands, 1999.
19. Subhes, C.; Govinda, B.; Timilsina, R. A review of energy system models. *Int. J. Energy Sect. Manag.* **2010**, *4*, 494–518.
20. Welsch, M.; Deane, P.; Howells, M.O.; Gallachóir, B.; Rogan, F.; Bazilian, M.; Rogner, H.H. Incorporating flexibility requirements into long-term energy system models—A case study on high levels of renewable electricity penetration in Ireland. *Appl. Energy* **2014**, *135*, 600–615. [CrossRef]
21. Despres, J. *Development of a Dispatch Model of the European Power System for Coupling with a Long-Term Foresight Energy Model*; Working Papers hal-01245554; HAL Archive: Lyon, France, 2015.
22. Després, J.; Hadjsaid, N.; Criqui, P.; Noirot, I. Modelling the impacts of variable renewable sources on the power sector: Reconsidering the typology of energy modeling tools. *Energy* **2015**, *80*, 486–495. [CrossRef]
23. Connolly, D.; Lund, H.; Mathiesen, B.V.; Leahy, M. A review of computer tools for analyzing the integration of renewable energy into various energy systems. *Appl. Energy* **2010**, *87*, 1059–1082. [CrossRef]

24. Pfenninger, S.; Hawkes, A.; Keirstead, J. Energy systems modeling for twenty-first century energy challenges. *Renew. Sustain. Energy Rev.* **2014**, *33*, 74–86. [CrossRef]
25. Sinha, S.; Chandel, S. Review of recent trends in optimization techniques for solar photovoltaic—Wind based hybrid energy systems. *Renew. Sustain. Energy Rev.* **2015**, *50*, 755–769. [CrossRef]
26. Loulou, R.; Labriet, M. ETSAP-TIAM: The TIMES integrated assessment model part I: Model structure. *Comput. Manag. Sci.* **2008**, *5*, 7–40. [CrossRef]
27. Cormio, C.; Dicorato, M.; Minoia, A.; Trovato, M. A regional energy planning methodology including renewable energy sources and environmental constraints. *Sustain. Energy Rev.* **2003**, *7*, 99–130. [CrossRef]
28. Centre for Renewable Energy Sources. Available online: http://www.cres.gr/kape/index_eng.htm (accessed on 21 March 2021).
29. ETSAP. MARKAL. IEA ETSAP 2014. Available online: http://www.iea-etsap.org/web/Markal.asp (accessed on 4 February 2021).
30. Nakicenovic, N.; Gruebler, A.; McDonald, A. (Eds.) *Global Energy Perspectives*; Cambridge University Press: Cambridge, UK, 1998.
31. Rao, S.; Riahi, K. The role of non-CO_2 greenhouse gases in climate change mitigation: Long-term scenarios for the 21st century. *Energy J.* **2006**, *27*, 177–200. [CrossRef]
32. Welsch, M. Enhancing the Treatment of Systems Integration in Long-Term Energy Models. Ph.D. Thesis, KTH Royal Institute of Technology, Stockholm, Sweden, 2013.
33. E3Mlab of ICCS/NTUA. PRIMES Model. 2008. Available online: http://www.e3mlab.ntua.gr/manuals/The_PRIMES_MODEL_2008.pdf (accessed on 5 January 2021).
34. Heaps, C.G. Long-Range Energy Alternatives Planning (LEAP) System. 2016. Available online: https://www.energycommunity.org (accessed on 12 March 2021).
35. AURORAxmp. Available online: http://epis.com/aurora_xmp/ (accessed on 8 February 2021).
36. EPIS. AURORAxmp. Available online: http://epis.com/powermarketinsights/index.php/tag/power-market-modeling// (accessed on 8 February 2021).
37. EATON. CYME Power Engineering Software. Available online: http://www.cyme.com/ (accessed on 3 January 2021).
38. Stadler, M.; Groissböck, M.; Cardoso, G.; Marnay, C. Optimizing Distributed Energy Resources and building retrofits with the strategic DER-CAModel. *Appl. Energy* **2014**, *132*, 557–567. [CrossRef]
39. EMPS: Multi Area Power-Market Simulator. Available online: https://www.sintef.no/en/software/emps-multi-area-power-market-simulator/ (accessed on 14 February 2021).
40. Entertile. Available online: http://www.enertile.eu (accessed on 1 February 2021).
41. Energy System Models at Fraunhofer ISE. Available online: http://www.entigris.org (accessed on 17 February 2021).
42. PLEXOS Integrated Energy Model. Available online: http://energyexemplar.com/software/plexos-desktop-edition/ (accessed on 9 February 2020).
43. Capros, P.; Regemorter, V.D.; Paroussos, L.; Karkatsoulis, P.; Fragkiadakis, C.; Tsani, S.; Charalampidis, I.; Revesz, T. *GEM-E3 Model Documentation*; JRC Working Papers JRC83177; Joint Research Centre (Seville site): Sevilla, Spain, 2013.
44. GreenNet. Guiding a Least Cost Grid Integration of RES-Electricity in an Extended Europe. GreenNet-EU 27 n.d. Available online: http://www.greennet-europe.org/ (accessed on 23 December 2020).
45. Schafer, A.; Jacoby, H.D. Experiments with a hybrid CGE-MARKAL model. *Energy J.* **2006**, *27*, 171–178. [CrossRef]
46. E3Mlab. GEM-E3 Model Manual 2010. Available online: http://147.102.23.135/e3mlab/GEM%20-%20E3%20Manual/Manual%20of%20GEM-E3.pdf (accessed on 16 October 2020).
47. Yang, Z.; Eckaus, R.S.; Ellerman, A.D.; Jacoby, H.D. *The MIT Emissions Prediction and Policy Analysis (EPPA) Model*; MIT: Cambridge, UK, 1996.
48. Yates, D.; Purkey, D.; Sieber, J.; Hubber-Lee, A.; Galbraith, H. WEAP21—A Demand-, Priority-, and Preference-Driven Water Planning Model. *Water Int.* **2005**, *30*, 487–500. [CrossRef]
49. Paltsev, S.; Reilly, J.M.; Jacoby, H.D.; Eckaus, R.S.; McFarland, J.R.; Sarofim, M.C.; Asadoorian, M.O.; Babiker, M.H.M. The MIT emissions prediction and policy analysis (EPPA) model: Version 4. In *MIT Joint Program on the Science and Policy of Global Change*; MIT Joint Program on the Science and Policy of Global Change: Cambridge, MA, USA, 2005.
50. Lee, H.; Oliveira-Martins, J.; Van der Mensbrugghe, D. *The OECD Green Model: An Updated Overview*; Organization for Economic Co-Operation and Development: Paris, France, 1994.
51. Manne, A.S.; Wene, C.O. *Markal-Macro: A Linked Model for Energy-Economy Analysis*; Brookhaven National Lab.: Upton, NY, USA, 1992.
52. Lee, K.H.; Lee, D.W.; Baek, N.C.; Kwon, H.M.; Lee, C.J. Preliminary determination of optimal size for renewable energy resources in buildings using RETScreen. *Energy* **2012**, *47*, 83–96. [CrossRef]
53. National Resources Canada. RETScreen International. Available online: http://www.retscreen.net/ (accessed on 19 November 2020).
54. POLES: Prospective Outlook on Long-Term Energy Systems. 2017. Available online: https://www.enerdata.net/solutions/poles-model.html (accessed on 12 December 2020).
55. Sullivan, P.; Krey, V.; Riahi, K. Impacts of considering electric sector variability and reliability in the MESSAGE model. *Energy Strategy Rev.* **2013**, *1*, 157–163. [CrossRef]
56. McPherson, M.; Karney, B. Long-term scenario alternatives and their implications: LEAP model application of Panama's electricity sector. *Energy Policy* **2014**, *68*, 146–157. [CrossRef]

57. Global Change Assessment Model—Joint Global Change Research. 2017. Available online: http://www.globalchange.umd.edu/gcam/ (accessed on 10 January 2021).

58. ETM Model. Available online: https://www.euro-fusion.org/collaborators/socio-economics/economics/model/ (accessed on 12 February 2021).

59. Kanudia, A.; Loulou, R. Robust responses to climate change via stochastic MARKAL: The case of québec. *Eur. J. Oper. Res.* **1998**, *106*, 15–30. [CrossRef]

60. Messner, S.; Golodnikov, A.; Gritsevskii, A. A stochastic version of the dynamic linear programming model MESSAGEIII. *Energy* **1996**, *21*, 775–784. [CrossRef]

61. Panciatici, P.; Campi, M.C.; Garatti, S.; Low, S.H.; Molzahn, D.K.; Sun, A.X.; Wehenkel, L. Advanced optimization methods for power systems. In Proceedings of the 2014 Power Systems Computation Conference, Wroclaw, Poland, 18–22 August 2014. [CrossRef]

62. Vakilifard, N.; Anda, M.; Bahri, A.P.; Ho, H. The role of water-energy nexus in optimising water supply systems–Review of techniques and approaches. *Renew. Sustain. Energy Rev.* **2018**, *82*, 1424–1432. [CrossRef]

63. Smajgl, A.; Ward, J.; Pluschke, L. Water–food–energy nexus–realising a new paradigm. *J. Hydrol.* **2016**, *533*, 533–540. [CrossRef]

64. Poncelet, K. *The Importance of Including Short Term Dynamics in Planning Models for Electricity Systems with High Shares of Intermittent Renewables*; IEA-ETSAP Workshop: Beijing, China, 2014.

65. Haydt, G.; Leal, V.; Pina, A.; Silva, C.A. The relevance of the energy resource dynamics in the mid/long-term energy planning models. *Renew. Energy* **2011**, *36*, 3068–3074. [CrossRef]

66. Jaehnert, S.; Doorman, G. Modelling an Integrated Northern European Regulating Power Market Based on a Common Day-Ahead Market. In Proceedings of the 33rd IAAE's International Conference, Rio de-Janeiro, Brazil, 6 June 2010.

67. Mysiak, J.; Giupponi, C.; Rosato, P. Towards the development of a decision support system for water resource management. Environ. *Model. Softw.* **2005**, *20*, 203–214. [CrossRef]

68. Rees, H.G.; Holmes, M.G.R.; Fry, M.J.; Young, A.R.; Pitson, D.G.; Kansakar, S.R. An integrated water resource management tool for the Himalayan region. *Environ. Model. Softw.* **2006**, *21*, 1001–1012. [CrossRef]

69. Li, W.; Abel, A.; Todtermuschke, K.; Zhang, T. Hybrid vehicle power transmission modeling and simulation with simulationX. In Proceedings of the 2007 International Conference on Mechatronics and Automation, Beijing, China, 2–5 August 2007.

70. Van Cauwenbergh, N.; Pinte, D.; Tilmant, A.; Frances, I.; Pulido-Bosch, A.; Vanclooster, M. Multi-objective, multiple participant decision support for water management in the Andarax catchment, Almeria. *Environ. Geol.* **2008**, *54*, 479–489. [CrossRef]

71. Coelho, A.C.; Labadie, J.W.; Fontane, D.G. Multicriteria decision support system for regionalization of integrated water resources management. *Water Resour. Manag.* **2012**, *26*, 1325–1346. [CrossRef]

72. Gaivoronski, A.A.; Sechi, G.M.; Zuddas, P. Balancing cost-risk in management optimization of water resource systems under uncertainty. *Phys. Chem. Earth* **2011**. [CrossRef]

73. Al-Omari, A. A methodology for the breakdown of NRW into physical and administrative losses. *Water Resour. Manag.* **2015**, *27*, 1913–1930. [CrossRef]

74. Stockholm Environment Institute, SEI. WEAP (Water Evaluation and Planning): User's Guide. 2015. Available online: https://www.weap21.org/downloads/WEAP_User_Guide.pdf (accessed on 21 June 2020).

75. Marcinek, J. Hydrological cycle and water balance. In *Global Change: Enough Water for All*; Lozán, J.L., Ed.; Wissenschaftliche Auswertungen: Hamburg, Germany, 2007.

76. Shumet, A.G.; Mengistu, K.T. Assessing the impact of existing and future water demand on economic and environmental aspects (Case study from Rift Valley Lake Basin: Meki-Ziway Sub Basin), Ethiopia. *Int. J. Waste Resour.* **2016**, *6*, 223. [CrossRef]

77. Koutsoyiannis, D. Hurst-Kolmogorov dynamics and uncertainty. *J. Am. Water Resourc. Assoc.* **2011**, *47*, 481–495. [CrossRef]

78. Hurst, H.E. Long term storage capacities of reservoirs. *Trans. Am. Soc. Civ. Eng.* **1951**, *116*, 776–808.

79. Tyralis, H.; Koutsoyiannis, D. Simultaneous estimation of the parameters of the Hurst- Kolmogorov stochastic process. *Stoch. Environ. Res. Risk Assess.* **2010**. [CrossRef]

80. Koutsoyiannis, D.; Efstratiadis, A.; Georgakakos, K.P. A stochastic methodological framework for uncertainty assessment of hydroclimatic predictions. *Geophys. Res. Abstr. Eur. Geosci. Union* **2007**, *9*, 06026.

81. Fraedrich, K. Fickian diffusion and Newtonian cooling: A concept for noise induced climate variability with long-term memory? *Stoch. Dyn.* **2002**, *2*, 403–412. [CrossRef]

82. Iliopoulou, T.; Papalexiou, S.M.; Markonis, Y.; Koutsoyiannis, D. Revisiting long-range dependence in annual precipita-tion. *J. Hydrol.* **2018**, *556*, 891–900. [CrossRef]

83. Tsoukalas, I.; Makropoulos, C.; Koutsoyiannis, D. Simulation of Stochastic Processes Exhibiting Any-Range Dependence and Arbitrary Marginal Distributions. *Water Resour. Res.* **2018**, *54*, 9484–9513. [CrossRef]

84. Markonisa, Y.; Moustakisb, Y.; Nasikab, C.; Sychovaa, P.; Dimitriadisb, P.; Hanela, M.; Mácaa, P.; Papalexiouc, S.M. Global estima-tion of long-term persistence in annual river runoff. *Adv. Water Resour.* **2018**, *113*, 1–12. [CrossRef]

85. Dimitriadis, P.; Koutsoyiannis, D.; Iliopoulou, T.; Papanicolaou, P. A global-scale investigation of stochastic similarities in marginal distribution and dependence structure of key hydrological-cycle processes. *Hydrology* **2021**, *8*, 59. [CrossRef]

86. Howells, M.; Rogner, H.; Strachan, N.; Heaps, C.; Huntington, H.; Kypreos, S.; Hughes, A.; Silvereira, S.; Carolis, J.; Bazillian, M.; et al. OSeMOSYS: The Open Source Energy Modeling System An introduction to its ethos, structure and development. *Energy Policy* **2011**, *39*, 5858–5870. [CrossRef]

87. Frevert, D.; Fulp, T.; Zagona, E.; Leavesley, G.; Lins, H. Watershed and River Systems Management Program: Overview of Capabilities. *J. Irrig. Drain. Eng.* **2006**, *132*, 92–97. [CrossRef]

88. Zagona, E.; Nowak, K.; Balaji, R.; Jerla, C.; Prairie, J. Riverware's Integrated Modeling and Analysis Tools for Long-Term Planning under Uncertainty. Available online: https://acwi.gov/sos/pubs/2ndJFIC/Contents/10F_ZagonaNowak_03_01_10.pdf (accessed on 24 January 2021).

89. Dale, L.L.; Karali, N.; Millstein, D.; Carnail, M.; Vicuña, S.; Borchers, N.; Bustos, E.; O'Hagan, J.; Purkey, D.; Heaps, C.; et al. An integrated assessment of water-energy and climate change in Sacramento, California: How strong is the nexus? *Clim. Chang.* **2015**, *132*, 223–235. [CrossRef]

90. Howells, M.; Hermann, S.; Welsch, M.; Bazilian, M.; Segerström, R.; Alfstad, T.; Gielen, D.; Rogner, H.; Fischer, G.; van Velthuizen, H.; et al. Integrated analysis of climate change, land-use, energy and water strategies. *Nat. Clim. Chang.* **2013**, *3*, 621–626. [CrossRef]

91. Programme for Infrastructure Development in Africa (PIDA). African Development Bank Home Page. Available online: https://www.afdb.org/en/topics-and-sectors/initiatives-partnerships/programme-for-infrastructure-development-in-africa-pida (accessed on 26 February 2021).

92. Bussieck, M.R.; Meeraus, A. Modeling Languages in Mathematical Optimization. In *The General Algebraic Modeling System (GAMS)*; Kallrath, J., Ed.; Springer: Boston, MA, USA, 2004; Volume 88, pp. 137–157.

93. Bussieck, R.M.; Drud, S.A.; Meeraus, A.A. MINLPLib—A collection of test models for mixed-integer nonlinear programming. *Inf. J. Comput.* **2003**, *15*, 114–119. [CrossRef]

94. Lin, F.T. A genetic algorithm for linear programming with fuzzy constraints. *J. Inf. Sci. Eng.* **2008**, *24*, 801–817.

95. Li, Y.P.; Huang, G.H.; Guo, P.; Nie, S.L. Interval-fuzzy possibilistic mixed integer linear programming for environmental management under uncertainty. *Int. J. Environ. Pollut* **2010**, *42*, 93–102. [CrossRef]

96. Schlosser, C.A.; Strzepek, K.; Fant, C.; Blanc, J.; Paltsev, S.; Jacoby, H.; Reilly, J.; Gueneau, A. The future of global water stress: An integrated assessment. *Earth's Future* **2014**, *2*, 341–361. [CrossRef]

97. Sokolove, A.P.; Stone, P.H.; Forest, C.E.; Prinn, R.; Sarofim, M.C.; Webster, M.; Paltsev, S.; Schlosser, C.A.; Kickighter, D.; Dutkiewkz, D.; et al. Probabilistic Forecast for Twenty-First-Century Climate Based on Uncertainties in Emissions (without Policy) and Climate Parameters. *J. Clim.* **2009**, *22*, 5175–5204. [CrossRef]

98. Webster, M.; Sokolov, P.A.; Reilly, M.J.; Forest, E.C.; Paltsev, S.; Schlosser, A.; Wang, C.; Kicklighter, D.; Sarofim, M.; Melillo, J.; et al. Analysis of climate policy targets under uncertainty. *Clim. Chang.* **2012**, *112*, 569–583. [CrossRef]

99. Hulme, M. Rainfall Changes in Africa: 1931–1960 to 1961–1990. *Int. J. Clim.* **1992**, *12*, 685–699. [CrossRef]

100. Hulme, M. Global warming. *Sage J.* **1994**, *18*, 401–410. [CrossRef]

101. Hulme, M.; Osborn, T.J.; Johns, T.C. Precipitation Sensitivity to Global Warming: Comparison of Observations with HADMCM2 Simulations. *Geophys. Res. Lett.* **1998**, *25*, 3379–3382. [CrossRef]

102. Michel, D.T.; Carter, R.T.; Jones, D.P.; Hulme, M.; New, M. A comprehensive set of high-resolution grids of monthly climate for Europe and the globe: The observed record (1901–2000) and 16 scenarios (2001–2100). In *Tydall Center for Climate Change Research Working Paper*; University of East Anglia: Norwich, UK, 2004; Volume 55.

103. Hielsen, S.S.; Hanse, E. Numerical simulation of rainfall–runoff process on daily basis. *Nord. Hydrol.* **1973**, *4*, 171–190. [CrossRef]

104. Economic Consulting Associates (ECA). *The potential of Regional Power Sector Integration: Nile Basin Initiative (NBI) Transmission and Trading Case Study*; ECA: London, UK, 2009.

105. Sridharan, V.; Broad, O.; Shivakumar, A.; Howells, M.; Boehlert, B.; Groves, D.G.; Rogner, H.H.; Taliotis, C.; Neumann, J.E.; Strzepek, K.M.; et al. Resilience of the Eastern African electricity sector to climate driven changes in hydropower generation. *Nat. Commun.* **2019**, *10*, 302. [CrossRef] [PubMed]

106. Nile Basin Initiative (NBI) Hydropower Potential and The Region's Rising Energy Demand. Available online: http://sob.nilebasin.org/pdf/Chapter%206%20Hydropower.pdf (accessed on 12 March 2021).

107. Nile Basin Initiative (NBI) Hydropower Generation Potential. Available online: https://atlas.nilebasin.org/treatise/hydropower-generation-potential/ (accessed on 12 March 2021).

108. Nile Basin Initiative (NBI). *State of the Nile River Basin Report*; NBI: Entebbe, Uganda, 2012; pp. 1–18.

109. Siam, M.S.; Eltahir, E.A.B. Climate Change enhances interannual variability of the Nile River flow. *Nat. Clim. Chang.* **2017**, *7*, 350–354.

110. Fischer, G.; Shah, M.; Van Velthuizen, H. *Climate Change and Agricultural Vulnerability*; IIASA: Laxenburg, Austria, 2012.

Monthly and Seasonal Drought Characterization Using GRACE-Based Groundwater Drought Index and Its Link to Teleconnections across South Indian River Basins

Kuruva Satish Kumar [1], Pallakury AnandRaj [1], Koppala Sreelatha [1], Deepak Singh Bisht [2]
and Venkataramana Sridhar [3],*

[1] Department of Civil Engineering, National Institute of Technology, Warangal 506002, India;
    satish005@student.nitw.ac.in (K.S.K.); anand@nitw.ac.in (P.A.); koppalasreelatha@student.nitw.ac.in (K.S.)
[2] National Institute of Hydrology, Roorkee 247667, India; dsbisht.ae@gmail.com
[3] Department of Biological Systems Engineering, Virginia Polytechnic Institute and State University,
    Blacksburg, VA 24061, USA
[*] Correspondence: vsri@vt.edu

Abstract: Traditional drought monitoring is based on observed data from both meteorological and hydrological stations. Due to the scarcity of station observation data, it is difficult to obtain accurate drought distribution characteristics, and also tedious to replicate the large-scale information of drought. Thus, Gravity Recovery and Climate Experiment (GRACE) data are utilized in monitoring and characterizing regional droughts where ground station data is limited. In this study, we analyzed and assessed the drought characteristics utilizing the GRACE Groundwater Drought Index (GGDI) over four major river basins in India during the period of 2003–2016. The spatial distribution, temporal evolution of drought, and trend characteristics were analyzed using GGDI. Then, the relationship between GGDI and climate factors were evaluated by the method of wavelet coherence. The results indicate the following points: GRACE's quantitative results were consistent and robust for drought assessment; out of the four basins, severe drought was noticed in the Cauvery river basin between 2012 and 2015, with severity of -27 and duration of 42 months; other than Godavari river basin, the remaining three basins displayed significant negative trends at monthly and seasonal scales; the wavelet coherence method revealed that climate factors had a substantial effect on GGDI, and the impact of Southern Oscillation Index (SOI) on drought was significantly high, followed by Sea Surface Temperature (SST) Index (namely, NINO3.4) and Multivariate El Niño–Southern Oscillation Index (MEI) in all the basins. This study provides reliable and robust quantitative result of GRACE water storage variations that shares new insights for further drought investigation.

Keywords: GRACE; GGDI; drought; wavelet coherence; teleconnections

1. Introduction

Drought is a dynamic natural phenomenon with high frequency and long duration characteristics that impact ecosystems and society in many ways [1–3]. Drought is a common natural disaster that has serious influence on water resources, agriculture, and socio-economic development due to its long-term persistence and frequent occurrence [4–6]. Thus, effective evaluation and monitoring of droughts are extremely necessary. Monitoring of traditional drought depends on ground data from meteorological and hydrological stations. Due to the scarcity of station observation data and the spatial heterogeneity of the regional environment, it is difficult to obtain accurate drought distribution characteristics, and also tough to replicate the large-scale information of drought [7].

To precisely monitor and assess drought characteristics, researchers have developed various drought indices such as the Palmer Drought Severity Index (PDSI) [8], Standardized Precipitation Index (SPI) [9], Standardized Precipitation Evapotranspiration Index

(SPEI) [10], and Effective Drought Index (EDI) [11], which can be applied to explore drought characteristics. PDSI, SPI, and SPEI have been the most widely used drought indices in recent decades [12,13]. Despite their broad applicability, these indices have their drawbacks and may not reproduce the conditions of drought accurately [14,15].

The aforementioned drought indices are related to land surface conditions and only a few indices are interrelated with remote sensing methods. Over the past years, the capabilities of remote sensing products amplified many folds, assessing the spatial and temporal variations at local and global scales. Gravity Recovery and Climate Experiment (GRACE) satellite measures the earth's gravity field to evaluate water storage changes globally [16,17]. The GRACE terrestrial water storage (TWS) dataset comprises all forms of water stored above and below the land surface that constitutes groundwater, surface water, soil moisture, and snow water equivalent [18,19]. GRACE-based TWS variations are commonly used in the evaluation of different hydrological assessments such as groundwater storage changes [20–26], terrestrial water storage variations [27–30], and hydrologic drought characterization [17,18,31–33].

Recently, many studies have been focused on monitoring and characterizing regional droughts using GRACE TWS [34–36]. Thomas et al. [32] developed a framework for assessing drought characterization, focusing on the total water storage deficits using GRACE TWS. Cao et al. [37] utilized GRACE TWS to develop a total storage deficit index for China. The Hydrological Drought Index was introduced by Yi and Wen [38] using GRACE data on the continental United States. The water storage deficit index for drought quantification was developed by Sinha et al. [18]. Zhao et al. [36] proposed a GRACE-based global gridded drought severity index named GRACE-DSI. Thomas et al. [39] evaluated the GRACE Groundwater Drought Index (GGDI) over the central valley of California, a regional aquifer subjected to significant drought periods and intensive human activities. Sinha et al. [17], with GRACE TWS and rainfall, developed the combined climatologic deviation index over India.

Due to large-scale climate variations in India, the spatio-temporal availability of surface and groundwater is very diverse and affects the agricultural and industrial productivity of the country [40]. A 2016 drought in India affected 330 million people with a more than USD 100 billion loss in the economy [41]. From this perspective, for the conservation of water resources, it is crucial to understand the variations of surface water and groundwater and its association with the teleconnection in India.

Utilizing the GRACE data, many studies have investigated drought characteristics throughout the globe. These studies only verified the capabilities of drought using GRACE data but not the associations between GRACE-based droughts and teleconnection factors. It is clear from earlier studies that telecommunication factors have a major effect on drought [42,43]. Many worldwide attempts have been made over past years to establish the relationship between climate variability and GRACE TWS changes, with most studies focused on El Niño–Southern Oscillation (ENSO). To evaluate the associations between the Multivariate ENSO Index (MEI) and GRACE mass anomalies, Phillips et al. [44] utilized the monthly GRACE TWS. Huang et al. [45] concluded that hydrological drought over the Columbia River basin was greatly influenced by ENSO and Arctic Oscillation (AO). Over the entire globe, Ni et al. [46] examined the links between ENSO and GRACE TWS. Vissa et al. [47] evaluated the relationship between ENSO-induced groundwater changes derived from GRACE and GLDAS over India. Liu et al. [48] explored the role of teleconnections over TWS variations within the Asian and eastern European regions. In the same way, few studies related to linkages between GRACE and teleconnections include Ni et al. [46], Chen et al. [49], Zhang et al. [50], Ndehedehe et al. [51], Anyah et al. [52], Han et al. [53], and Wang et al. [54]. Thus, climate variables influence the drought directly or indirectly that results in detailed investigation between them.

It is worth mentioning that, in India, approximately 50% of the population depends on agriculture that relies on surface and groundwater resources. As the availability of surface water is not uniform through space and time, groundwater resources have emerged as the

primary source for agriculture, domestic application, and industry. Increased water demand contributes to the overexploitation of surface water and groundwater during drought times. Successful river basin scale drought monitoring is important for water resource management and drought mitigation plans. Several studies have shown that anthropogenic activities and climate change have exacerbated drought-related calamities [13,55,56].

To the best of our knowledge, previous studies have focused on the relationship of several atmospheric variables such as precipitation, temperature, vapor pressure, and humidity with teleconnections in India [57–60]. Nonetheless, a comprehensive and systematic analysis between GRACE and teleconnections is vague, particularly for India. Therefore, this novel study addresses this research gap by exploring the drought situation over south Indian river basins with GGDI and identifying the linkages between drought and large-scale climate oscillations during 2003–2016. In the present study, we assessed the effect of four major climate oscillations, namely, Multivariate ENSO Index (MEI), Southern Oscillation Index (SOI), Dipole Mode Index (DMI), and NINO3.4 Sea Surface Temperature (SST) on GGDI over Indian river basins using the GRACE TWS dataset for the period of 2003–2016. The detailed analysis was accomplished over Godavari (GRB), Krishna (KRB), Pennar and east flowing rivers between Pennar and Cauvery (PCRB), and Cauvery (CRB) river basins in order to illustrate the linkages between GGDI and climate oscillations. Moreover, gridded monthly and seasonal drought trends were evaluated using the modified Mann–Kendall (MMK) trend test over four river basins (combined). Seasonal trends were evaluated for four seasons of India, namely, (i) post-monsoon rabi (PMon-R -January to March), (ii) pre-monsoon (PMon-April to June), (iii) monsoon (Mon-July to September), and (iv) post-monsoon kharif (PMon-K-October to December).

The objectives of this study were (1) to determine the changing characteristics of terrestrial water storage anomaly (TWSA) over South Indian river basins at monthly, seasonal, and annual timescales; (2) to analyze the spatial distribution and temporal evolution of drought using GGDI; (3) to evaluate the trend characteristics of GGDI over South Indian river basins during 2003–2015 with the MMK trend test; and (4) apply wavelet coherence method to evaluate the relationships between GGDI and climate oscillations.

2. Materials and Methods

2.1. Study Area

India is the seventh largest country in the world, covering 22 major river basins of which there are 4 river basins, namely, (i) Godavari river basin (GRB), (ii) Krishna river basin (KRB), (iii) Pennar and east flowing rivers between Pennar and Cauvery (PCRB), and (iv) Cauvery river basin (CRB), which were all considered for this study (India-WRIS, 2012). In Figure 1, the study area map is presented; further details regarding the study area can be found in Kumar et al. [33].

2.2. Data

2.2.1. Gravity Recovery and Climate Experiment (GRACE)

GRACE monthly products are mainly generated by the Jet Propulsion Laboratory (JPL), Center for Space Research at the University of Texas (CSR), and the German Research Center for Geosciences (GFZ). In the present study, GRACE monthly mass grids (RL06 mascon solutions) processed at Jet Propulsion Laboratory (JPL) with a spatial resolution of $0.5° \times 0.5°$ between 2003 and 2016 were used to estimate the terrestrial water storage anomalies (TWSA) (https://grace.jpl.nasa.gov (accessed on 20 March 2021)). The mascon solutions are associated with the baseline period from January 2004 to December 2009 [33,61]. Moreover, glacial isostatic adjustment (GIA) correction was removed, with no need for smoothing filter and north-south striping [61]. To fill the missing monthly GRACE datasets, we adopted the linear interpolation method, which is effective and is extensively used in handling the missing data [33,62].
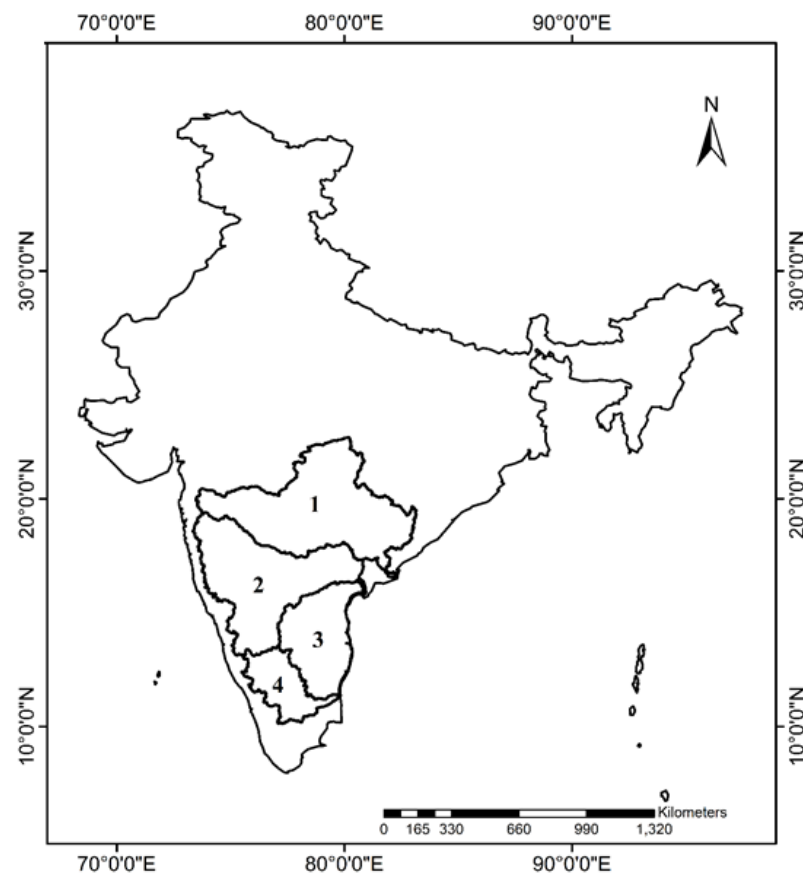
Figure 1. Study region map showing the river basins considered for the study ((1) Godavari river basin (GRB), (2) Krishna river basin (KRB), (3) Pennar and East flowing rivers between Pennar and Cauvery (PCRB), and (4) Cauvery river basin (CRB)).

2.2.2. Global Land Data Assimilation System (GLDAS)

In the present study, the latest release of GLDAS Noah model, i.e., NOAH10_M 2.1 products with the spatial resolution of $1° \times 1°$ consistent with GRACE product was adopted for the period of 2003–2016 and used for the analysis (https://disc.gsfc.nasa.gov/ (accessed on 20 March 2021)). All the datasets were resampled to $1° \times 1°$ using the bilinear interpolation method, and further analysis was performed in this study.

2.2.3. Meteorological Data

In the present study, gridded precipitation data from the India Meteorological Department (IMD) was considered from 2003 to 2016 with a spatial resolution of $0.25° \times 0.25°$ for the study region [63,64].

2.2.4. Climate Data

Monthly climate oscillations, namely, NINO 3.4, Multivariate ENSO Index (MEI), Southern Oscillation Index (SOI), and Dipole Mode Index (DMI) for the period of 2003–2016 were utilized in the study. Monthly SST anomaly data (NINO3.4) were obtained from http://www.esrl.noaa.gov/psd/gcos_wgsp/Timeseries/Data/nino34.long.anom.data (accessed on 20 March 2021). For ENSO, the MEI was selected and obtained from https://www.esrl.noaa.gov/psd/enso/mei (accessed on 20 March 2021). The SOI data were obtained from the NOAA Earth System Research Laboratory (https://psl.noaa.gov/gcos_wgsp/Timeseries/SOI/ (accessed on 20 March 2021)). The Indian Ocean Dipole (IOD) is measured as DMI due to the dipole mode in the tropical Indian Ocean, and the DMI data were obtained from http://www.jamstec.go.jp/frcgc/research/d1/iod/DATA/dmi (accessed on 20 March 2021).

2.3. Method

2.3.1. Retrieval of Groundwater Storage Change

Terrestrial water storage anomalies (TWSA) were derived from GRACE satellite observations. The groundwater storage anomalies (GWSA) at any time t are calculated by subtracting soil moisture storage anomalies (SMSA) and canopy water storage anomalies (CWSA) from the GRACE-based TWSA.

The soil moisture storage anomaly (SMSA) was calculated for NOAH land surface model using the following equation:

$$SMSA_t = SMS_t - \overline{SMS_{2004-2009}} \qquad (1)$$

wre $SMSA_t$ = soil moisture anomaly with respect to time t; SMS_t = soil moisture at time t; and $\overline{SMS_{2004-2009}}$ = average soil moisture w.r.t at the baseline period from January 2004 to December 2009, the same as that of GRACE terrestrial water storage.

Similarly, the canopy water storage anomaly (CWSA) was calculated for NOAH land surface model using the following equation:

$$CWSA_t = CWS_t - \overline{CWS_{2004-2009}} \qquad (2)$$

wre $CWSA_t$ = canopy water storage anomaly w.r.t time t; CWS_t = canopy water storage at time t; and $\overline{CWS_{2004-2009}}$ = average canopy water storage w.r.t the base line period from January 2004 to December 2009, same as that of GRACE terrestrial water storage.

The GWSA is calculated as

$$GWSA_t = TWSA_t - SMSA_t - CWSA_t \qquad (3)$$

2.3.2. GRACE Groundwater Drought Index (GGDI)

In the present study, dimensionless GGDI was implemented to examine the drought characteristics related to groundwater. Firstly, monthly climatology, C_i (climatology for month i, ($i = 1, 2, \ldots 12$)), was calculated as follows:

$$C_i = \frac{1}{n_i} \sum_{1}^{n_i} GWSA_i \qquad (4)$$

where i represents month (i = 1, 2, ... 12) and n represents number of years. In the present study, GRACE TWS was considered from 2003 to 2016 with $n = 14$. The monthly climatology C_i was calculated for each month individually using groundwater storage anomalies (GWSA). The effect of seasonality in groundwater storage changes is removed by using the monthly climatology [39].

Secondly, the monthly climatology was subtracted from GWSA to obtain groundwater storage deviation (GWSD), which signifies the net deviation in the volume of groundwater storage on the basis of seasonal variability. Finally, the GWSD was normalized by removing the mean and divided by standard deviation as follows:

$$GGDI = \frac{GWSD_t - \overline{x}_{GWSD}}{S_{GWSD}} \qquad (5)$$

where $\overline{x}_{GWSD}$ and S_{GWSD} are the mean and standard deviation of GWSD, respectively. GGDI is the normalized net deviation in groundwater storage volume; the GGDI classification is given in Table 1. For detailed information regarding GGDI, refer to Thomas et al. [39].

Table 1. Classification of the Gravity Recovery and Climate Experiment (GRACE) Groundwater Drought Index (GGDI) used in the study (Wang et al., 2020).

Grade	Classification	GGDI
I	No drought	$-0.5 < \text{GGDI}$
II	Mild drought	$-1.0 < \text{GGDI} \leq -0.5$
III	Moderate drought	$-1.5 < \text{GGDI} \leq -1.0$
IV	Severe drought	$-2.0 < \text{GGDI} \leq -1.5$
V	Extreme drought	$\text{GGDI} \leq -2.0$

The run theory approach is used to determine the characteristics of drought, such as severity and duration using GGDI. Drought duration (D) is the period of time where the GGDI remains below the fixed threshold value (threshold value of -0.8). The minimum duration of drought is considered as 1 month, as the drought event is defined at aggregation of monthly time scale. Drought severity (S) is the cumulative values of GGDI within the drought duration.

2.3.3. Standardized Precipitation Evapotranspiration Index (SPEI)

Standardized Precipitation Evapotranspiration Index (SPEI) considers potential evapotranspiration (PET) along with precipitation, utilizing all the advantages of SPI. In this study, SPEI was estimated on a 12-month timescale using the IMD precipitation and temperature datasets from 2003 to 2016. The positive SPEI indicates a wet condition and negative SPEI indicates a dry condition. The index is reliable and flexible with respect to space and time in reproducing water deficiencies; therefore, drought characteristics are well assessed with SPEI at different timescales. The detailed procedure regarding SPEI is provided in the Supplementary Materials section.

2.3.4. Modified Mann–Kendall (MMK) Trend Test

The traditional nonparametric Mann–Kendall test is the most widely applied trend test all over the world. However, the persistence of hydrometeorological dataset will affect the Mann–Kendall test results. Therefore, Hamed and Rao [65] estimated the MMK test where it can remove the autocorrelation, which is consistent and robust in finding the trend of a time series [66]. This study implemented the MMK trend test to evaluate the spatial drought trend characteristics over 4 river basins of south India from 2003 to 2016. The detailed procedure regarding MMK test is provided in the Supplementary Materials section.

2.3.5. Wavelet Coherence

Within the time-frequency space, wavelet coherence can be used to determine the relationship between the 2 time series data by estimating the correlation between them that varies between 0 and 1. In accordance with Torrence and Webster [67] and Grinsted et al. [68], coefficient of wavelet coherence between the 2 sets of time series data can be denoted as follows:

$$R^2(s,\tau) = \frac{\left|S\left(s^{-1}W_{xy}(s,\tau)\right)\right|^2}{S\left(s^{-1}|W_x(s,\tau)|^2\right).S\left(s^{-1}|W_y(s,\tau)|^2\right)} \tag{6}$$

where $R^2(s,\tau)$ = coherence coefficient minimum and maximum coherence at 0 and 1, and $W_{xy}(s,\tau)$ = cross wavelet transforms between two series. Equation (6) resembles the coefficient of determination equation, and thus the wavelet coherence varies between 0 and 1 [69]. S = smoothing operator represented as given below [70]:

$$S(W) = S_{scale}(S_{time}(W(s,\tau))) \tag{7}$$

The smoothing along wavelet axis is represented as S_{scale} and S_{time}. In the present study, the wavelet coherence was examined at 5% significance level or at the confidence interval > 95%.

3. Results

3.1. Changing Characteristics of TWSA over River Basins

Seasonal and annual scale GRACE TWSA analysis was performed over four basins. The results showed distinct seasonal and annual TWSA characteristics over these river basins. In the Mon and PMon-K seasons, the GRB showed positive TWSA values, while negative TWSA values were detected in the PMon season. The positive and negative TWSA values were shown by the PMon-R season. On annual basis, TWSA displayed a significant upward trend with the highest values observed in 2013 and 2014. The TWSA in the GRB tended to decrease from 2003 to 2005, leading to a significant drought between 2003 and 2005, as shown in Figure 2. As seen in Figure 2, except for the year of 2015, the KRB showed positive TWSA values in the Mon and PMon-K seasons. Except for the PMon-R season in 2011, the PMon and PMon-R seasons displayed negative TWSA values. Annual TWSA values showed a significant upward and a downward trend of TWSA values and most of the negative trends were observed between 2003 and 2005, and between 2012 and 2016, leading to severe droughts.
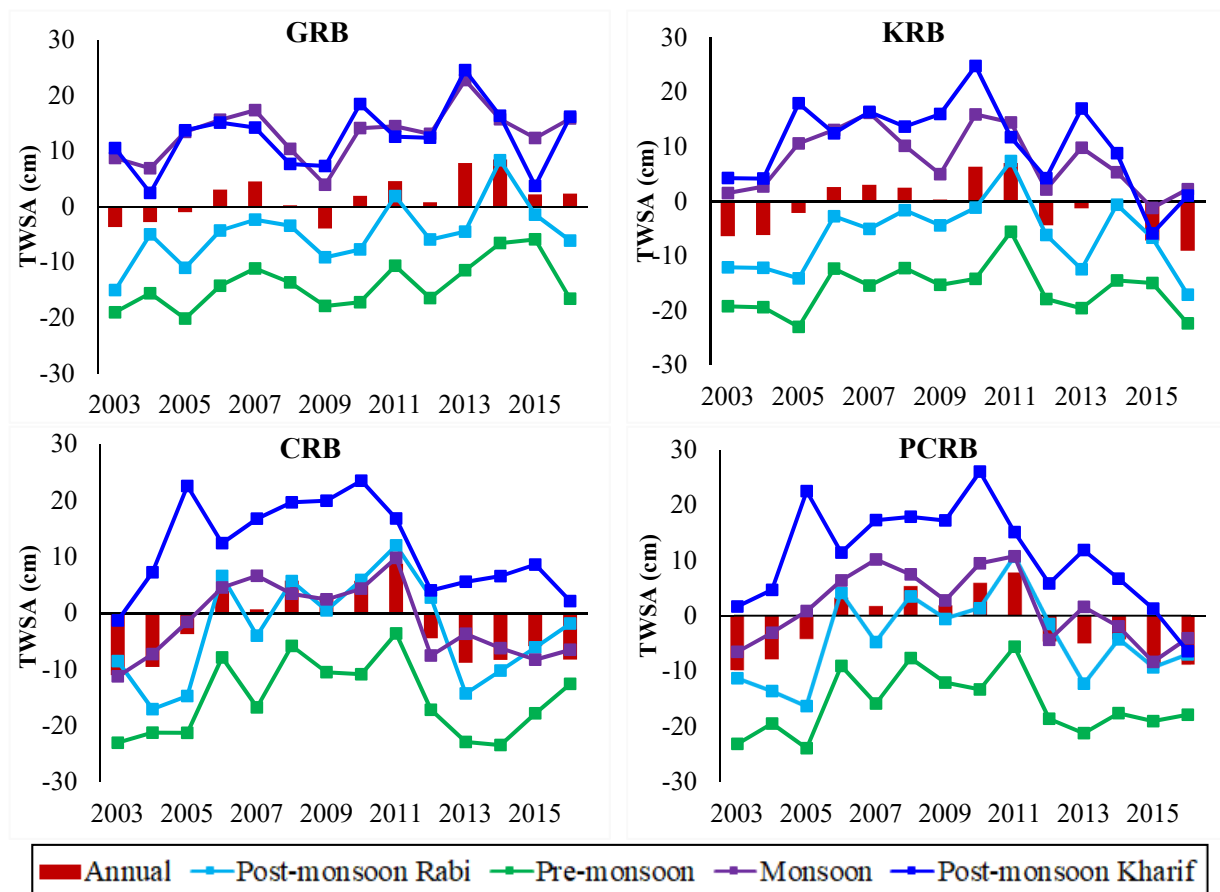
Figure 2. Multiscale (seasonal and annual) terrestrial water storage anomaly (TWSA) variations over GRB, KRB, CRB, and PCRB from 2003 to 2016 (Godavari river basin (GRB), Krishna river basin (KRB), Pennar and east flowing rivers between Pennar and Cauvery (PCRB), and Cauvery river basin (CRB)).

From Figure 2, the CRB and PCRB exhibited positive and negative TWSA for PMon-K and PMon seasons, respectively. Positive and negative TWSA values were observed in the Mon and PMon-R seasons, with most of the negative values between 2003 and 2005, and

between 2012 and 2016. Annual TWSA values exhibited a downward trend between 2012 and 2016, leading to severe drought, followed by the 2003–2005 event. Overall, from the beginning of the 21st century, TWSA showed a downward trend over the four river basins on seasonal and annual scales.

3.2. Basin-Wise GGDI-Identified Drought Event Analysis

Figure 3 represents GGDI-based temporal evolution characteristics of drought and major drought events for the four river basins from 2003 to 2016. The solid red line represents the GGDI, and the green shaded region indicates the period of drought events. The GGDI exhibited upward and downward trends over each river basin with different change characteristics, demonstrating that the droughts reported using GGDI were increasing in these river basins during the period of 2003–2016. For all the four basins, major decreasing trends were observed between 2003 and 2005, 2011 and 2013, and 2014 and 2016. We can see from the GGDI time series that droughts have become more frequent across these river basins in recent years. For the drought characterization, dry spells of more than three months were considered for drought event analysis in this study [32]. The identified drought events were denoted as "DE", followed by event order for that particular basin.

As shown in Figure 3a, with reference to GGDI, four major drought events were detected in GRB, i.e., during (i) DE1—January to December 2003, (ii) DE2—March 2004 to July 2005, (iii) DE3—June 2008 to July 2010, and (iv) DE4—August 2015 to February 2016. The longest drought event over GRB extended for 26 months between 2008 and 2010 (DE3). Among four drought events, DE1, 2, and 4 were characterized as moderate drought, and DE3 as severe drought.

As shown in Figure 3b, five major drought events were observed in KRB: (i) DE1—January 2003 to May 2004, (ii) DE2—July 2004 to July 2005, (iii) DE3—June 2012 to May 2013, (iv) DE4—June to November 2014, and (v) DE5—July 2015 to June 2016. Among these drought events, DE1, 3, and 4 were characterized as mild drought; DE2 as moderate drought; and DE5 as extreme drought. For KRB, the longest drought was observed for 17 months between 2003 and 2004 (DE1).

As shown in Figure 3c, four major drought events were identified over CRB: (i) DE1—January 2003 to May 2004, (ii) DE2—July 2004 to August 2005, (iii) DE3—June 2012 to November 2015, and (iv) DE4—August to December 2016. DE1, 3, and 4 were characterized as severe drought, and DE2 as moderate drought, with the longest drought extended for 42 months between 2012 and 2015 (DE3).

As shown in Figure 3d, five major drought events were observed in PCRB: (i) DE1—January 2003 to May 2004, (ii) DE2—July 2004 to August 2005, (iii) DE3—June 2012 to July 2013, (iv) DE4—June 2014 to February 2016, and (v) DE5—August to December 2016. DE1 and 3 were characterized as moderate drought, and DE2, 4, and 5 were characterized as severe drought, with the longest drought extended for 21 months between 2014 and 2016 (DE4). Overall, for the four river basins of South India, GGDI can be considered a strong indicator of drought.

3.3. SPEI-Based Drought Event Analysis

Figure 4 represents SPEI-12 timeseries with major drought events represented in red bands for the four river basins from 2003 to 2016. The SPEI-12 exhibited upward and downward trends over each river basin during the period of 2003–2016. For all the four basins, major decreasing trends were observed between 2003 and 2004, 2012 and 2013, and 2014 and 2016. From the SPEI-12 time series, it is evident that droughts have become more recurrent and prolonged across four river basins in recent years. The identified drought events were denoted as "DE", followed by event order for that particular basin.
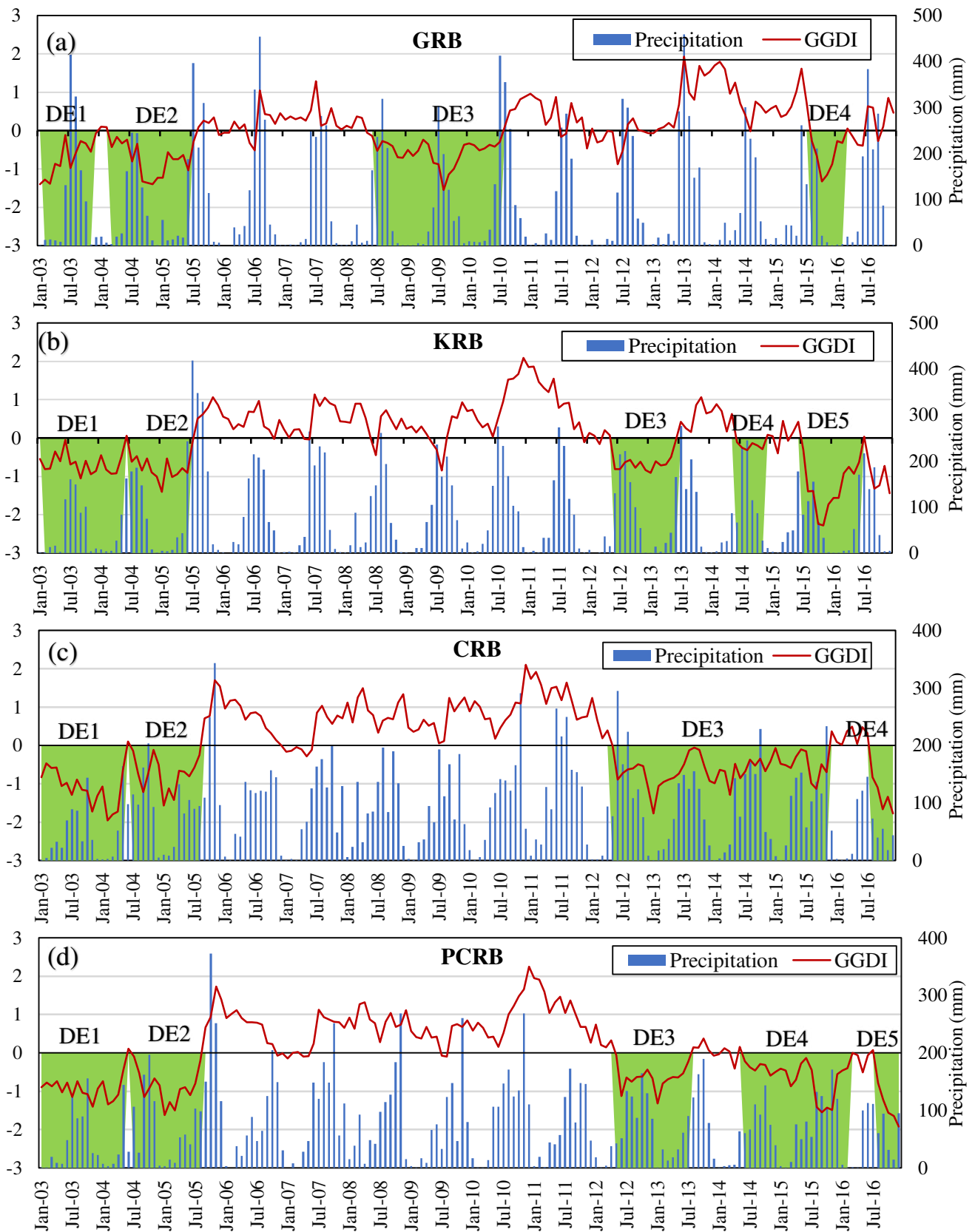
Figure 3. Monthly GRACE Groundwater Drought Index (GGDI) and precipitation timeseries with major drought events represented with green bands for (**a**) GRB, (**b**) KRB, (**c**) CRB, and (**d**) PCRB. "DE" represents drought event (Godavari river basin (GRB), Krishna river basin (KRB), Pennar and east flowing rivers between Pennar and Cauvery (PCRB), and Cauvery river basin (CRB)).
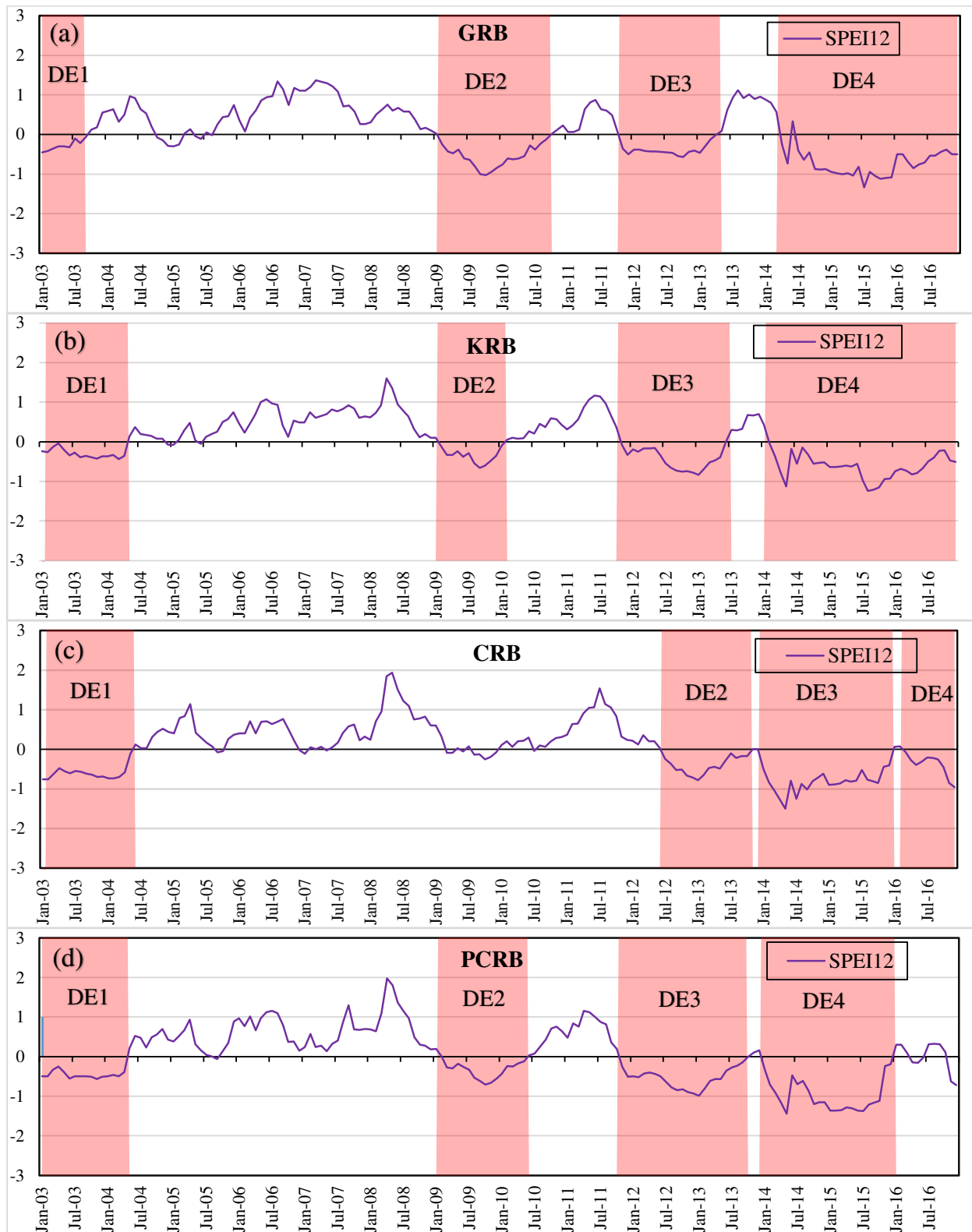
Figure 4. Monthly Standardized Precipitation Evapotranspiration Index (SPEI)-12 timeseries with major drought events represented with red bands for (**a**) GRB, (**b**) KRB, (**c**) CRB, and (**d**) PCRB. "DE" represents drought event (Godavari river basin (GRB), Krishna river basin (KRB), Pennar and East flowing rivers between Pennar and Cauvery (PCRB), and Cauvery river basin (CRB)).

As seen in Figure 4a, four major drought events were evident in GRB: (i) DE1—January 2003 to August 2003, (ii) DE2—February 2009 to September 2010, (iii) DE3—November 2011 to April 2013, and (iv) DE4—April 2014 to December 2016. DE1 and 3 were characterized as moderate drought, and DE2 and 4 were characterized as severe drought, with the longest drought extended for 33 months between 2014 to 2016 (DE4).

As seen in Figure 4b, four major drought events were observed in KRB: (i) DE1— January 2003 to April 2004, (ii) DE2—February 2009 to January 2010, (iii) DE3—November 2011 to June 2013, and (iv) DE4—February 2014 to December 2016. DE1, 2, and 3 were characterized as moderate drought, and DE4 was characterized as severe drought, with the longest drought extended for 35 months between 2014 to 2016 (DE4).

As seen in Figure 4c, four major drought events were observed in CRB: (i) DE1— January 2003 to May 2004, (ii) DE2—June 2012 to October 2013, (iii) DE3—January 2014 to December 2015, and (iv) DE4—May 2016 to December 2016. DE1, 2, and 4 were characterized as moderate drought, and DE3 was characterized as severe drought, with the longest drought extended for 24 months between 2014 to 2015 (DE3).

As seen in Figure 4d, four major drought events were observed in PCRB: (i) DE1— January 2003 to April 2004, (ii) DE2—February 2009 to May 2010, (iii) DE3—November 2011 to September 2013, and (iv) DE4—January 2014 to December 2015. DE1, 2, and 3 were characterized as moderate drought, and DE4 was characterized as severe drought, with the longest drought extended for 24 months between 2014 to 2015 (DE4).

Comparisons of GRACE-based drought with SPEI from Figures 3 and 4 were analyzed. In GRB, drought events were commonly observed during 2008–2010 and 2015–2016 for GGDI as well as SPEI. In KRB, three major drought events were observed between 2003 and 2004, 2012 and 2013, and 2015 and 2016 for both SPEI and GGDI. In CRB, for both SPEI and GGDI, two major drought events were observed during 2003–2005 and 2012–2015. IN PCRB, 2003–2004 and 2012–2016 were two major drought events that were noticed (SPEI and GGDI). Variations in the drought duration were observed between GGDI- and SPEI-based droughts. More drought events were observed using GGDI when compared with the SPEI. As each drought index is different in terms of construct and variables involved, differences in characterizing drought events are expected among the indices. Thus, variations in the drought events were observed between GGDI and SPEI. Therefore, GGDI-based drought analysis is important and may offer additional insights in identifying the extreme droughts over the river basins in which 50% of the population depends on agriculture.

3.4. Basin-Wise Drought Characteristics Using GGDI

Table 2 represents the drought characteristics (severity and duration) calculated from GGDI over four river basins. For GRB, the highest severity of −14.64 was observed for a duration of 26 months between June 2008 and July 2010. In KRB, the highest severity of −15.72 was observed for a duration of 12 months (July 2015 to June 2016), followed by −11.56 severity with a duration of 17 months (January 2003 to May 2004). The CRB experienced the height drought period among all the four basins, with severity of −27.02 observed for 42 months from June 2012 to November 2015. PCRB observed the highest severity of −16.33 for a duration of 17 months (January 2003 to May 2004), followed by severity of −13.38 with the highest duration of 21 months (June 2014 to February 2016) in this basin. All the four basins experienced droughts during 2003–2005 and 2015–2016.

Table 2. Drought characteristics (severity and duration) calculated from GGDI for the drought events identified for GRB, KRB, CRB, and PCRB.

| Time Period	Severity	Duration (No. of Months)
Godavari (GRB)		
Jan 2003 to Dec 2003	−8.72	12
Mar 2004 to Jul 2005	−12.91	17
Jun 2008 to Jul 2010	−14.64	26
Aug 2015 to Feb 2016	−4.87	7
Krishna (KRB)		
Jan 2003 to May 2004	−11.56	17
Jul 2004 to Jul 2005	−10.08	13
Jun 2012 to May 2013	−8.47	12
Jun to Nov 2014	−1.56	6
Jul 2015 to Jun 2016	−15.72	12
Aug to Dec 2016	−5.41	5
Cauvery (CRB)		
Jan 2003 to May 2004	−19.27	17
Jul 2004 to Aug 2005	−10.56	14
Jun 2012 to Nov 2015	−27.02	42
Aug to Dec 2016	−6.71	5
Pennar and east flowing rivers between Pennar and Cauvery (PCRB)		
Jan 2003 to May 2004	−16.33	17
Jul 2004 to Aug 2005	−12.52	14
Jun 2012 to Jul 2013	−9.71	14
Jun 2014 to Feb 2016	−13.38	21
Aug to Dec 2016	−7.14	5

3.5. Gridded Monthly and Seasonal GGDI-Based Drought Trend Characteristics

Gridded monthly and seasonal drought trends were evaluated using MMK trend test over four river basins (combined) during 2003–2016, which are presented in Figure 5. Figure 6a represents the Z_s values of GGDI over four river basins during 2003–2016. "⊗", "△", and "⊠" denote significant (positive and negative) values at 0.1, 0.05, and 0.01 levels, respectively. Figure 6b represents the Kendall tau values.

3.5.1. Monthly Trends

As shown in Figure 5, GRB exhibited monthly significant positive and negative trends from January to December. From January to July, GRB exhibited positive trends at different significant levels (0.01, 0.05, and 0.1 percentiles). The highest significant positive trends were observed in the month of May at the upper part of the basin, whereas the bottom part of the basin showed a downward trend from January to July. From August to December, significant negative trends at 1, 5, and 10% were observed in the downward region of the basin. The highest significant negative trends were seen during August and September. Highly fluctuating positive and negative trends were observed in GRB compared to the other three basins. As shown in Figure 6a, most of the significant positive Z_s values of GGDI were observed in GRB compared to other basins. Out of 12, 4 months (January, March, June, and July) exhibited significant positive values at 0.1 and 0.05 levels. In terms of Figure 6b, strong positive trends were observed in the months of March, June, and July.

As seen in Figure 5, KRB displayed monthly positive and negative (non-significant) trends from January to July. From August to December, significant negative trends were observed at 0.01, 0.05, and 0.1 levels. Most of the negative trends were observed in the month of September followed by August. No significant positive trends were observed in the Krishna basin. As shown in Figure 6a, significant negative Z_s values of GGDI were observed during August, September, and October months at 0.1 level. The remaining months showed positive and negative Z_s values (no significant). Figure 6b shows that strong negative trends were observed from August to October over KRB.
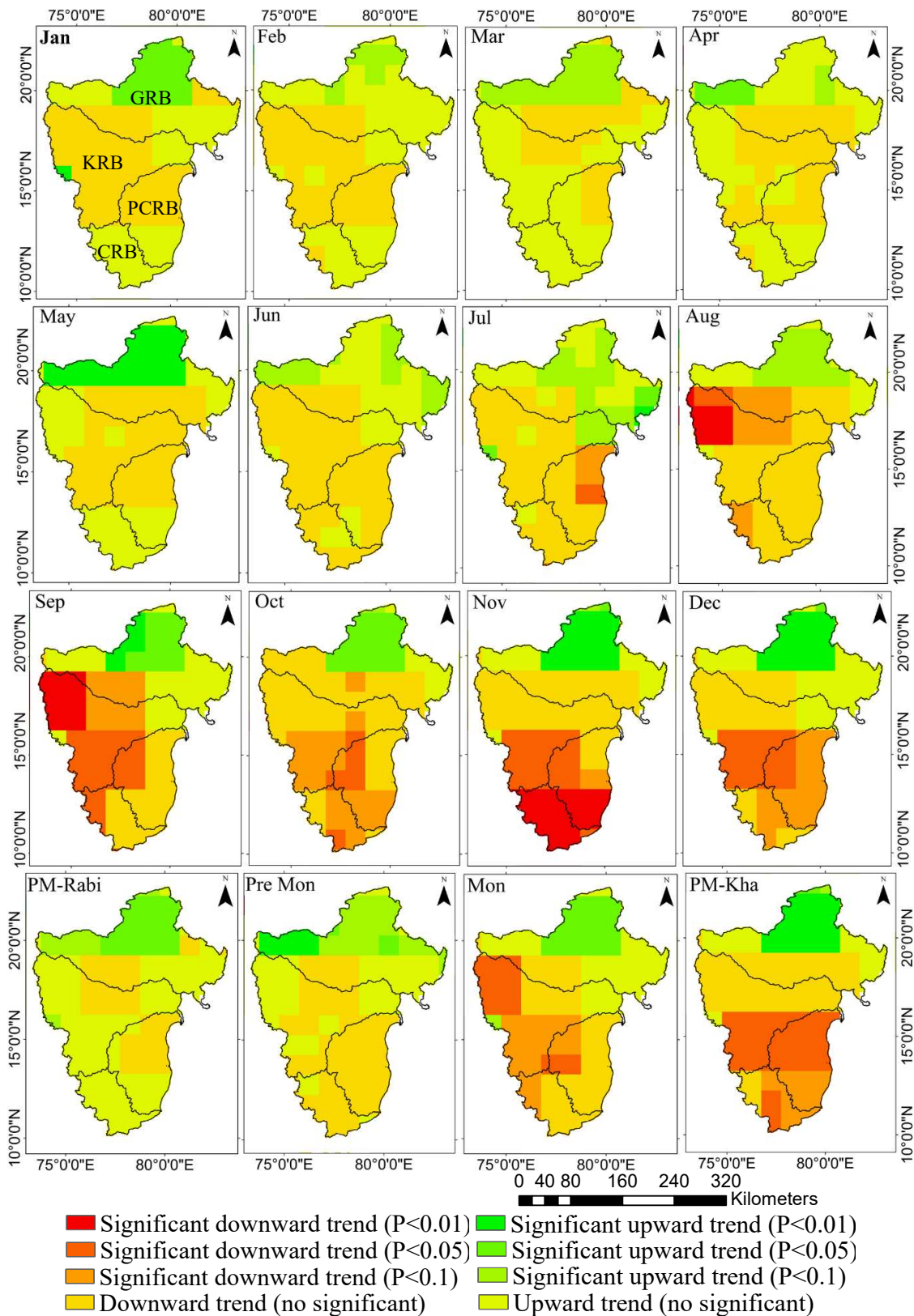
Figure 5. Monthly and seasonal trends of GRACE Groundwater Drought Index (GGDI) using the modified Mann–Kendall (MMK) trend test over the four river basins (combined) during 2003–2016. The post-monsoon rabi, pre-monsoon, monsoon, and post-monsoon kharif seasons are denoted as PM-Rabi, Pre Mon, Mon, and PM-Kha, respectively. GRB, KRB, PCRB, and CRB represents the river basins (Godavari river basin (GRB), Krishna river basin (KRB), Pennar and east flowing rivers between Pennar and Cauvery (PCRB), and Cauvery river basin (CRB)).
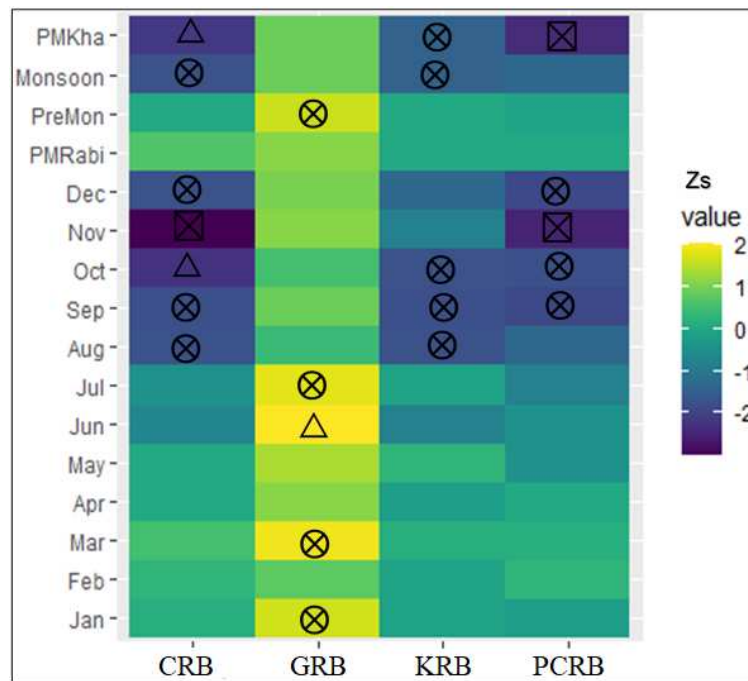
(a)
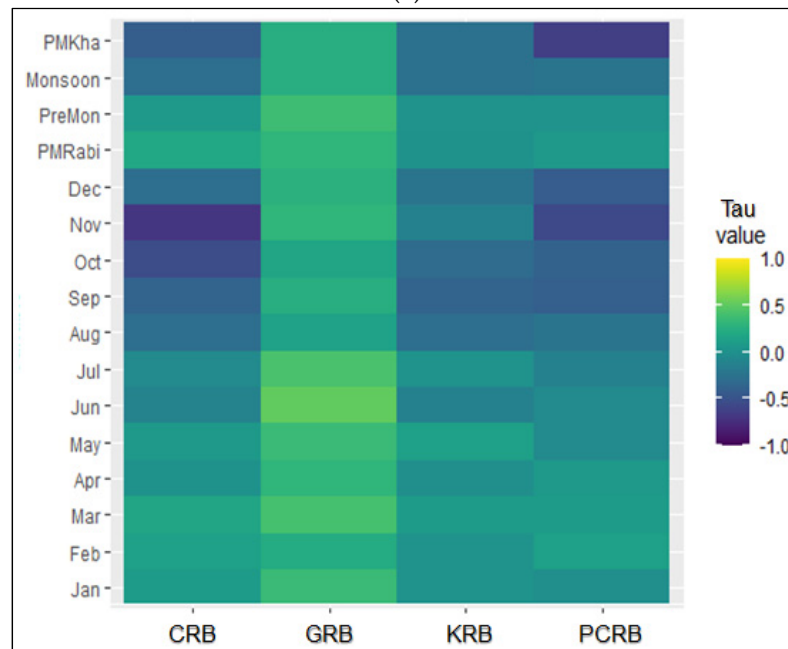
(b)

Figure 6. (**a**) Z_s values of GRACE Groundwater Drought Index (GGDI) over the four river basins during 2003–2016. "⊗", "△", and "⊠" denote significant (positive and negative) values at 0.1, 0.05, and 0.01 levels, respectively (Godavari river basin (GRB), Krishna river basin (KRB), Pennar and east flowing rivers between Pennar and Cauvery (PCRB), and Cauvery river basin (CRB)). (**b**) Monthly and seasonal Kendall tau values over the four river basins during 2003–2016 (Godavari river basin (GRB), Krishna river basin (KRB), Pennar and east flowing rivers between Pennar and Cauvery (PCRB), and Cauvery river basin (CRB)).

As we can see from Figure 5, PCRB and CRB demonstrated monthly positive and negative (non-significant) trends from January to July. From August to December, significant negative trends were observed at 0.01, 0.05, and 0.1 levels. A complete downward trend was observed over CRB (PCRB) in the month of November (December). In terms of

Figure 6a, we can see that significant negative Z_s values of GGDI were observed during August to December months at 0.01, 0.05, and 0.1 levels. The highest significant negative Z_s values were observed for the month of November for both PCRB and CRB. Overall, KRB and CRB displayed most of the significant negative trends and Z_s values compared to GRB and PCRB, and significant positive trends were observed only in GRB. As seen in Figure 6b, strong negative trends were observed in the month of November, followed by October and December in both CRB and PCRB.

3.5.2. Seasonal Trends

The four seasons considered for the study, namely, PMon-R, PMon, Mon, and PMon-K exhibited significant positive trends over GRB. In KRB, CRB, and PCRB, PMon-R and PMon seasons showed upward and downward (non-significant) trends. In comparison, KRB, CRB, and PCRB showed significant negative trends in the Mon and PMon-K seasons. As shown in Figure 5, most of the significant negative trends were observed in the PMon-K, followed by the Mon season. Overall, from season to season, significant positive trends were converted to significant negative trends, with highest significant negative trends shown in the PMon-K season. As seen in Figure 6a, GRB exhibited positive Z_s values in all the seasons, with all remaining basins having positive and negative Z_s values (significant and insignificant). PMon-K season displayed the highest significant negative Z_s values in all the basins, followed by Mon season. In terms of Figure 6b, we see that PMon-R and PMon exhibited strong positive trends in GRB followed by CRB. On the other hand, in PMon-K season, strong negative trends were observed in PCRB and CRB. Decrease in precipitation was observed during 2002–2016, which led to nearly four major drought events.

3.6. Gridded Monthly and Seasonal Trend Characteristics in Terms of Precipitation

3.6.1. Monthly Trends

Figure 7 represents the monthly and seasonal precipitation trends using the MMK trend test over the four river basins (combined) during the period of 2003–2016. From Figure 7, we can see that GRB exhibited monthly significant downward trends in the lower and middle parts of the basin during January to December, except in March and June. However, the upper part of the basin showed a significant upward trend, except in May and August. In January, and from August to December, GRB exhibited significant downward trends (0.05, and 0.1 percentiles, respectively). The highest significant positive trends were observed in the months of June and July at 0.01 and 0.05 percentiles, respectively, whereas downward trends were observed during November, December, and January at 1, 5, and 10 %, respectively. The highest significant negative trends were shown during August and September. Highly fluctuating positive and negative trends were observed in GRB compared to other three basins. From Figure 6a, we can see that most of the significant positive Z_s values of GGDI were observed in GRB in comparison to other basins. Out of the 12 months, 3 months (March, April, and June) exhibited significant positive values at 0.01 and 0.05 levels.

From Figure 7, we see that during February to April and December, KRB displayed monthly significant positive trends at 0.01, 0.05, and 0.1 levels in the upper part of the basin, whereas the other portion of the basin showed significant negative trends at the 0.05 level. The basin was covered with significant negative trends in the months of May, September, October, and November at the 0.1 level. No significant positive trends were observed in KRB. As shown in Figure 6a, significant negative Z_s values of GGDI were observed during the months of August, September, and October at the 0.1 level. Both insignificant negative and positive trends were negotiable in KRB.
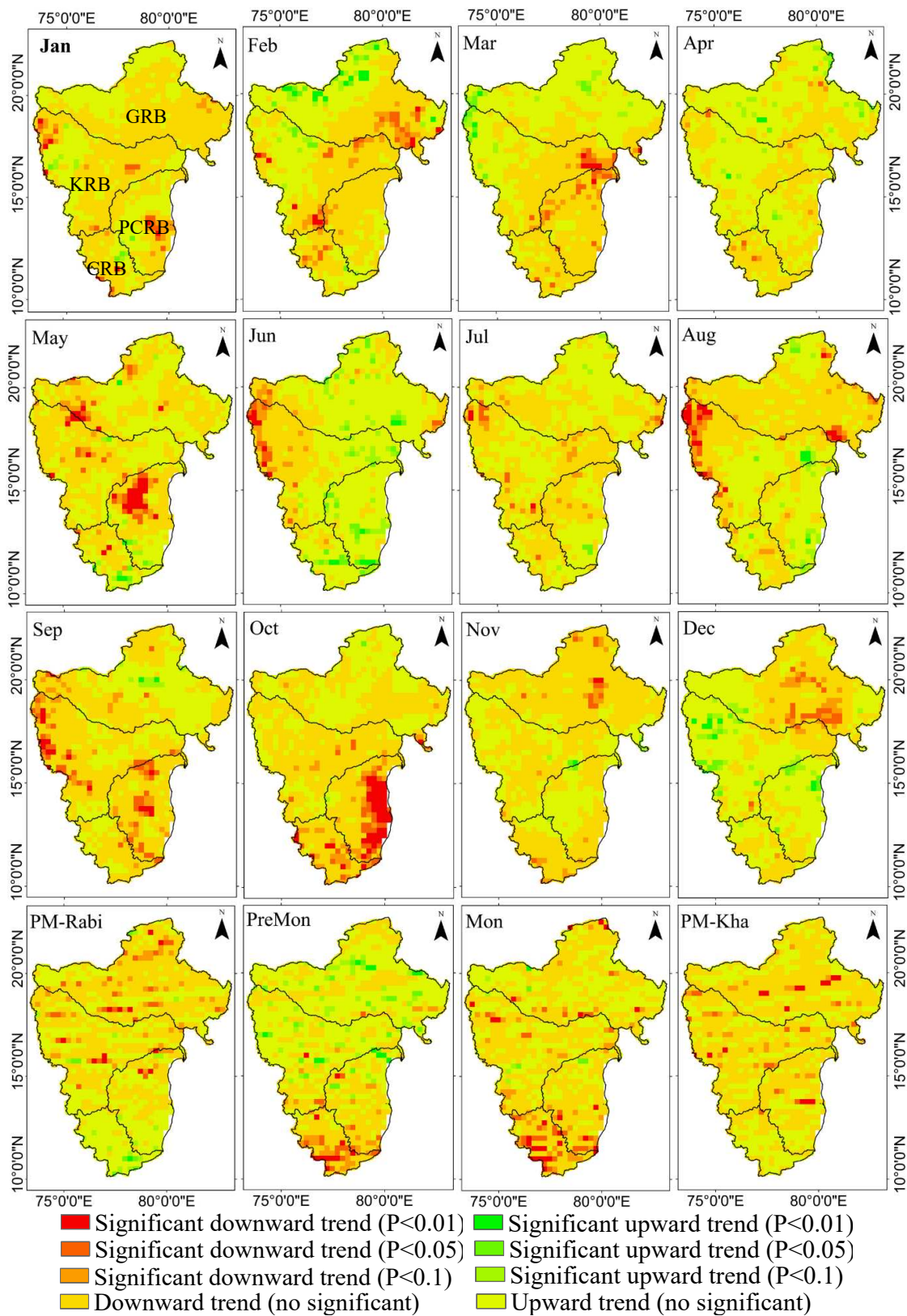
Figure 7. Monthly and seasonal precipitation trends using the MMK trend test over the four river basins (combined) during 2003–2016. The post-monsoon rabi, pre-monsoon, monsoon, and post-monsoon kharif seasons are denoted as PM-Rabi, Pre Mon, Mon, and PM-Kha, respectively. GRB, KRB, PCRB, and CRB represent the river basins (Godavari river basin (GRB), Krishna river basin (KRB), Pennar and east flowing rivers between Pennar and Cauvery (PCRB), and Cauvery river basin (CRB)).

From Figure 7, we see that monthly significant positive trends were observed in June, August, and December over PCRB and in the months of June and December over CRB at 0.01 and 0.05 levels, respectively. Highly significant negative trends were observed during October in PCRB and CRB at 0.01 and 0.05 levels. Significant positive and negative trends were observed during January to May and September to November in PCRB and CRB at 0.01, 0.05, and 0.1 levels.

3.6.2. Seasonal Trends

Seasonally (Figure 7), significant positive trends were observed during the PMon and Mon seasons at 0.01 and 0.05 levels in GRB and KRB. Significant negative and positive trends were observed during PMon-R and PMon-K over GRB, KRB, CRB, and PCRB at 0.01, 0.05, and 0.1 levels. However, in case of PMon and Mon seasons, PCRB and CRB exhibited the most significant negative trends compared to positive trends at 0.05 and 0.01 levels. Highly significant positive trends were observed in CRB compared to all other basins.

Overall, from the analysis, GGDI was found to be strongly influenced by variability of precipitation in the study region. Results stated that study region experienced significant decreasing trend in precipitation and GGDI. Assessment of GGDI and precipitation variability showed a significant linear trend both monthly and seasonally.

3.7. The Correlation between GGDI and Climate Factors

Previous studies have shown that droughts were closely related to climate variables [47,48,55,60]. In the present study, MEI, NINO3.4, SOI, and DMI were chosen to describe the influences of teleconnections over droughts. Moreover, wavelet coherence was employed to evaluate the link between GGDI and climate factors over South Indian river basins during 2003–2016.
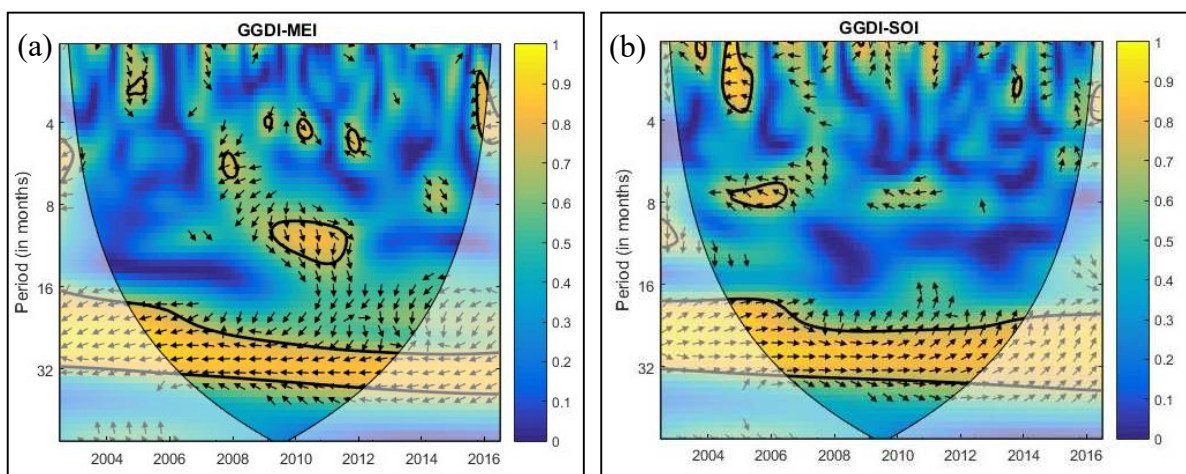
The wavelet coherence between monthly GGDI and climate factors were presented in Figure 8 over GRB. From Figure 8, the coherence at interannual variability was observed continuously between 2007 and 2016 on time scales of 20–36 months, and intermittency was observed between 4 and 12 months at different years for MEI. In the case of SOI, coherence at interannual variability was observed between 2002 and 2005, and 2007 and 2016 periods on time scales varying from 16 to 40 months. For NINO3.4, intermittency was reduced between the 2002 and 2007 period for time scales of 10–34 months, and intermittency was observed at different years between 4 and 10 months. Compared to other teleconnections at different scales during different years, the effect of DMI was weak.

For KRB, the wavelet coherence between GGDI and climate factors are provided in Figure 9. It can be noted from the figure that high wavelet coherence is noticed at an annual scale, characterizing the dominant effect of groundwater for MEI, SOI, NINO 3.4, and DMI. Interannual variability was detected at time scales of 2 to 14 months for MEI, 4–10 months for SOI, and 2–10 months for NINO3.4. However, for DMI, interannual variability highly varied in the overall period.

For CRB, the wavelet coherence between monthly GGDI and climate factors are presented in Figure 10. From Figure 10, we can see that the influence of MEI is observable over the time scales of 10–30 months for the period 2002–2011. Interannual variability of SOI was observed within the 10 to 12-month time scale, whereas annual variability was observed for the time scale of 16–32 months over the period of 2002–2012. Annual variability of NINO3.4 was observed between 2002 and 2011 for an 18–32-month time scale, and interannual variability was observed for the time scale of 6–16 months. Influence of DMI was highly significant for the time scale of 14–40 months; for the period 2002–2009, the annual variability was significantly high compared to NINO3.4, SOI, and MEI.
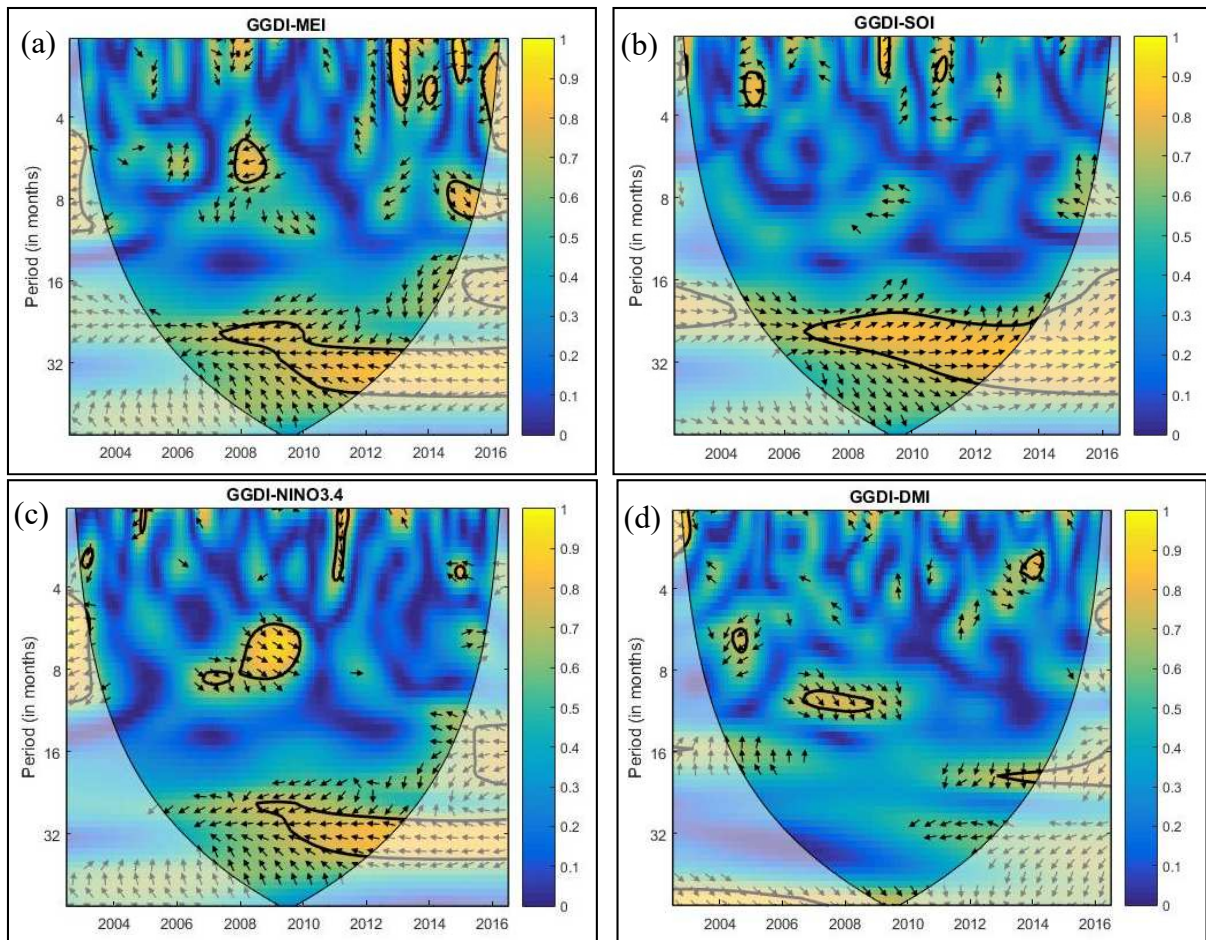
Figure 8. Wavelet coherence between monthly GRACE Groundwater Drought Index (GGDI) and (**a**) Multivariate El Niño–Southern Oscillation Index (MEI), (**b**) Southern Oscillation Index (SOI), (**c**) NINO 3.4, and (**d**) Dipole Mode Index (DMI) over Godavari river basin (GRB). The 95% confidence level is presented as thick contour and the relative phase relationship is represented by arrows with anti-phase pointing left and in-phase pointing right.

Figure 9. *Cont.*
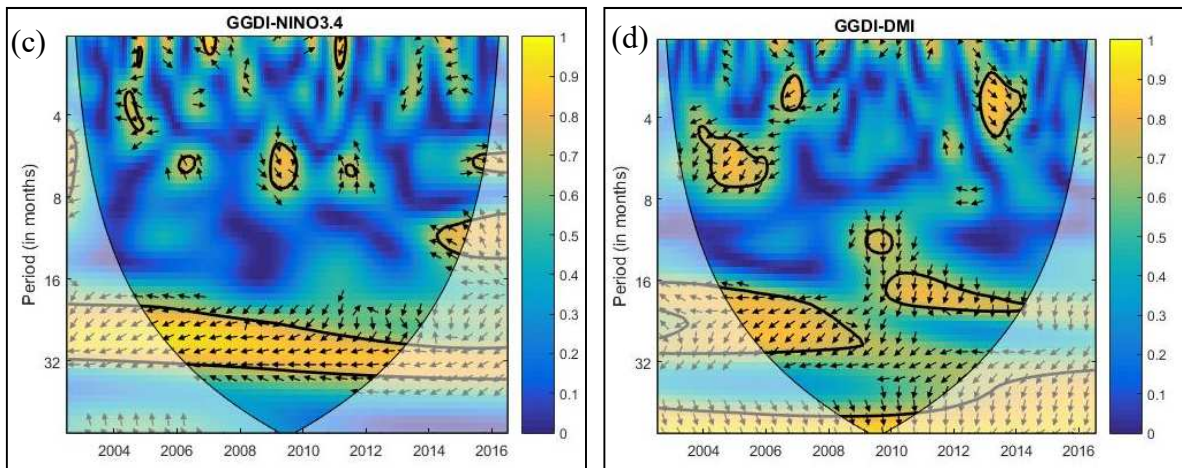
Figure 9. Wavelet coherence between monthly GRACE Groundwater Drought Index (GGDI) and (**a**) MEI, (**b**) SOI, (**c**) NINO 3.4, and (**d**) DMI over Krishna river basin (KRB). The 95% confidence level is presented as thick contour and the relative phase relationship is represented by arrows with anti-phase pointing left and in-phase pointing right.
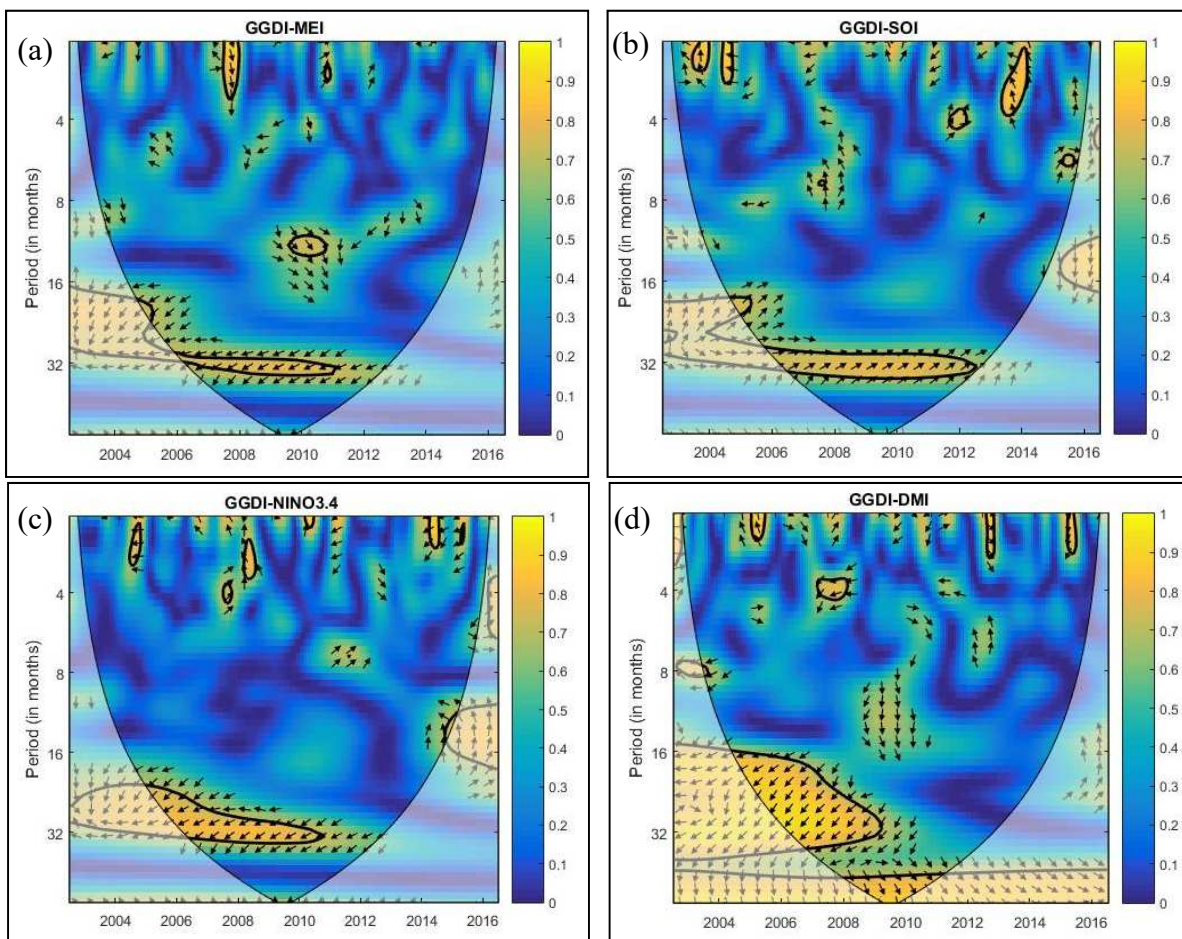
Figure 10. Wavelet coherence between monthly GRACE Groundwater Drought Index (GGDI) and (**a**) MEI, (**b**) SOI, (**c**) NINO 3.4, and (**d**) DMI over Cauvery river basin (CRB). The 95% confidence level is presented as thick contour and the relative phase relationship is represented by arrows with anti-phase pointing left and in-phase pointing right.

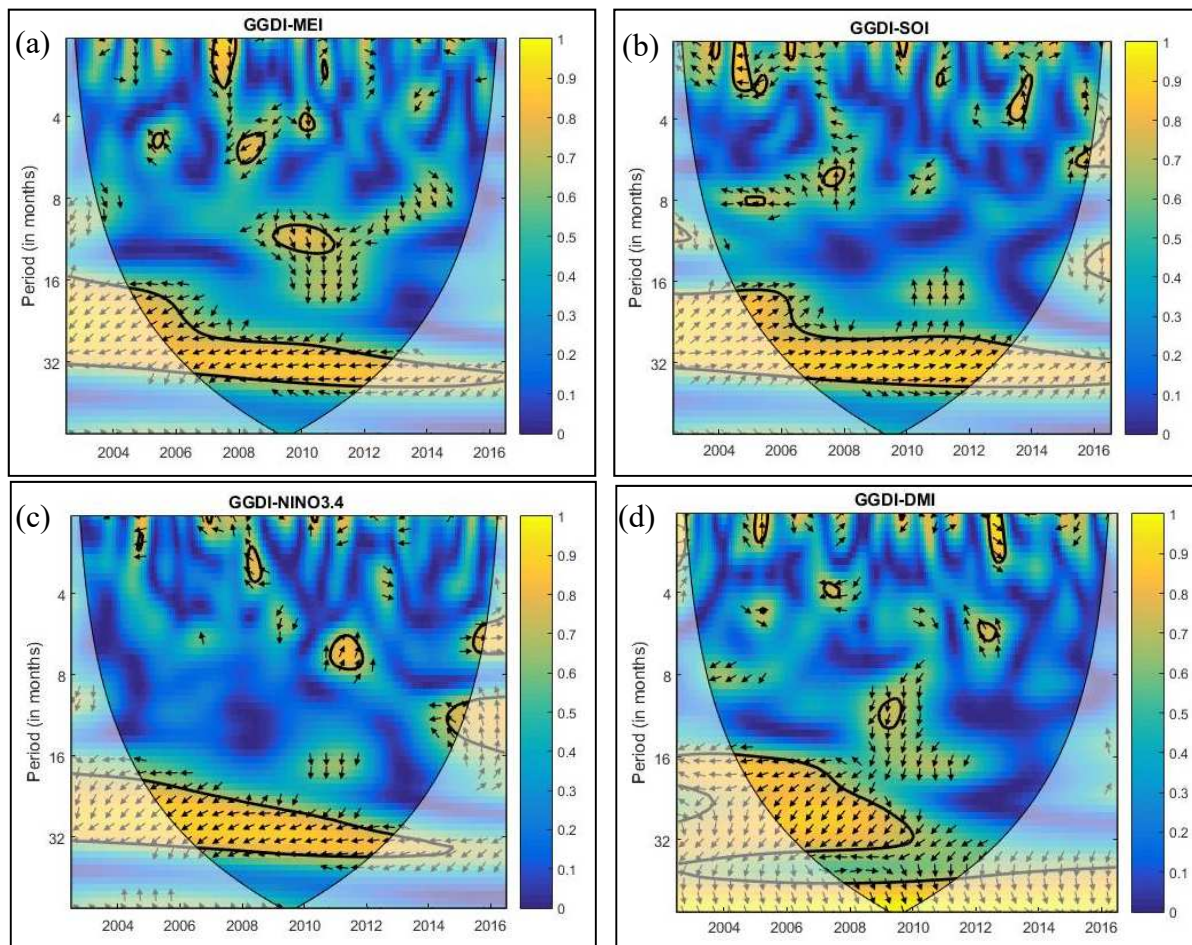For PCRB, the wavelet coherence between monthly GGDI and climate factors were presented in Figure 11. As seen in Figure 11, the annual variability of MEI was significantly dominant for all the years between the time scale of 16–32 months. Interannual

variability was also observed between the time scale of 4–10 months at different years. The influence of interannual variability was observed at different years between the time scale of 2–14 months. However, annual variability was seen for all the years between 16 and 32 months. Annual variability was comparatively less in NINO3.4 when compared with MEI, SOI, and DMI. Interannual variability was observed between the time scales of 4–14 months over the years of 2009–2016. Annual variability of DMI was highly significant for 16–32-month time scales between the years 2002 and 2010, continuing for 33–40-month time scales for all the years. Moreover, interannual variability was observed between the time scale of 4–14 months for different years.


Figure 11. Wavelet coherence between monthly GRACE Groundwater Drought Index (GGDI) and (**a**) MEI, (**b**) SOI, (**c**) NINO 3.4, and (**d**) DMI over Pennar and east flowing rivers between Pennar and Cauvery (PCRB). The 95% confidence level is presented as thick contour and the relative phase relationship is represented by arrows with anti-phase pointing left and in-phase pointing right.

3.8. Spatial Distribution of Drought

Generally, most of the drought events were seen during 2003–2005, 2008–2010, 2012–2013, and 2014–2016. Spatial distribution of the yearly average GGDI timeseries was plotted (Figure 12) to depict the spatial variation of drought throughout the basins. From Figure 12, we can see that 2003, 2015, and 2016 were the most drought-affected years in all the river basins. KRB exhibited the severe drought throughout the basin in 2016 followed by PCRB and CRB. For GRB, the GGDI varied between −0.5 and −2 during 2003–2005, 2009, 2012, 2015, and 2016. For KRB, it varied between −0.5 and −2 for the years 2003–2005, 2009, and 2012–2016. For CRB and PCRB, a range from −0.5 to −2 for the years 2003–2005 and 2012–2016 were noticed. KRB was the severely affected basin during the past decade

compared to the other basins. Drought had been considerably relieved during 2006, 2007, and 2011. Therefore, appropriate drought-resistant measures should be implemented in these river basins to reduce the impact of drought disaster and improve the capability of drought resistance.
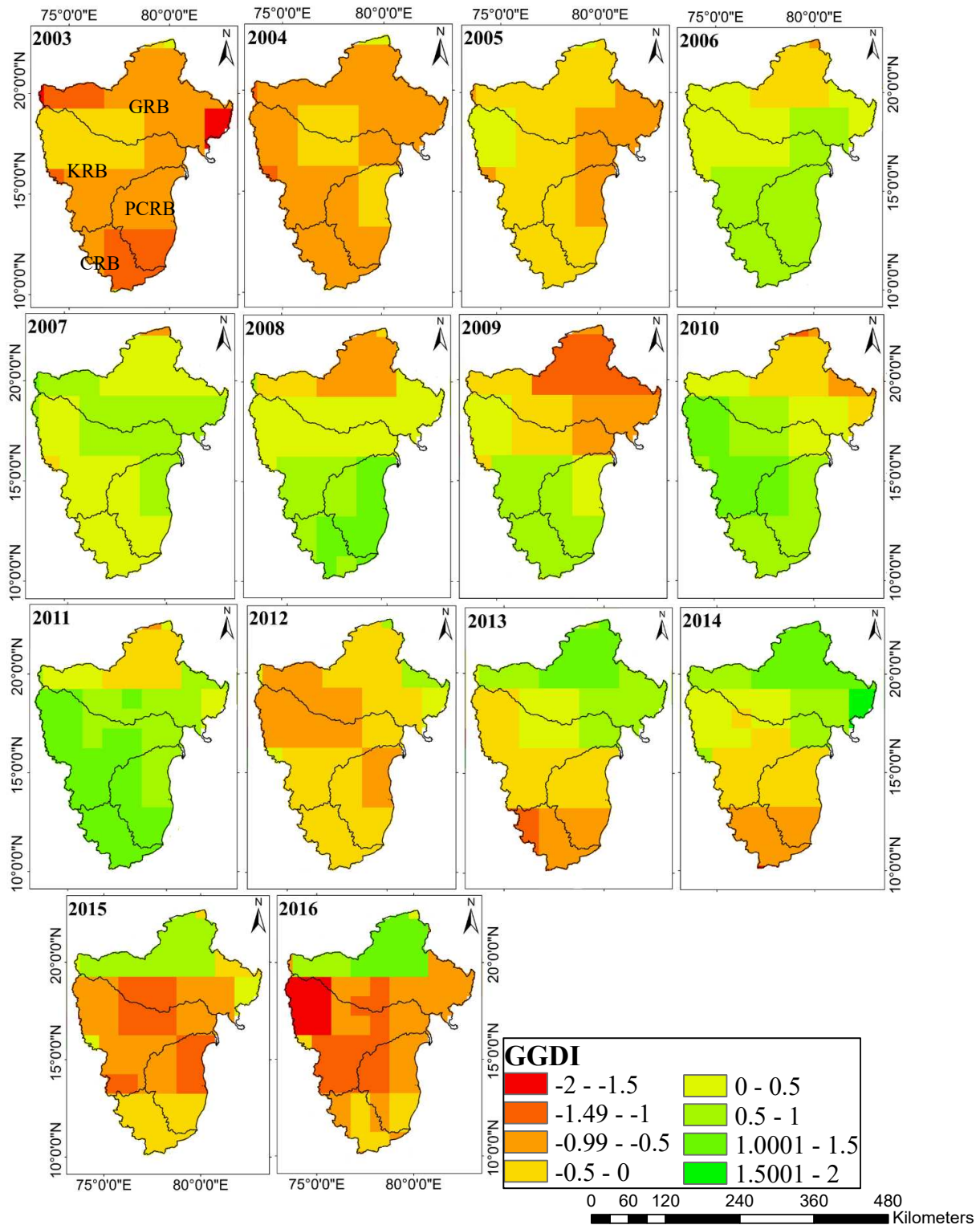
Figure 12. Spatial distribution of yearly averaged GRACE Groundwater Drought Index (GGDI) timeseries for GRB, KRB, CRB, and PRB (combined) (Godavari river basin (GRB), Krishna river basin (KRB), Pennar and east flowing rivers between Pennar and Cauvery (PCRB), and Cauvery river basin (CRB)).

4. Discussion

4.1. Influence Factors of Drought

Droughts in India pose extraordinary challenges to the food production, socio-economic aspects, livelihood, and gross domestic product. India has a long history of droughts with lasting effects on crops, surface, and subsurface water resources, and rural livelihoods [55,71]. Water availability and crop production were affected by the recent drought of 2015–2016 over large parts of southern India with lower reservoir storage. Additionally, the 2015–2016 drought affected around 330 million people and caused groundwater depletion in the South Indian states [72,73]. Failure of monsoon rainfall or its receipt in smaller quantities may often result in drought over major parts of India. The effect of anthropogenic factors on drought, along with natural factors, cannot be overlooked. Due to the uneven distribution of rainfall, spatially and temporally, surface and subsurface water resources are scarce over India [33]. Mishra [73] stated that the 2015–2018 drought affected groundwater and surface water availability in the southern part of India and was linked to climate indices. Farmers disproportionately use electricity and fossil fuels to pump groundwater to compensate for the lack of rainfall. In particular, cultivation costs for rice and other rainy season (kharif) crops are also rising due to increased use of energy and diesel for the collection of groundwater [74]. Excessive withdrawal of groundwater to save crops in drought conditions has drained groundwater in most parts of the world, therefore ultimately triggering a drought crisis.

Researchers have established that climate factors play a major role in the process of drought formation [42,75]. Additionally, the wavelet coherence results from Section 3.5 have shown that climate factors (MEI, SOI, DMI, and NINO3.4) have had an extreme influence on drought evolution. In particular, in the Indian regions, MEI, SOI, and NINO3.4 had the greatest influence on drought (Figures 8–11). There are several teleconnections that influence the variability of TWS along with its components over India. Although earlier studies primarily focused on the effect of ENSO over TWS [46,47], it is unlikely to be able find a single indicator to represent all climatic variability features over large regions [76]. In the current study, four widely used climate factors were considered, and their links with GGDI were evaluated; the results show that for each river basin, the teleconnections differed considerably with GGDI. Therefore, TWS attributions and predictions or indices calculated using TWS (GGDI) centered on a single teleconnection should be treated with caution, and multiple teleconnections are suggested for the assessment of TWS changes and their components.

As shown in Figures 8–11, the coherence of GGDI with teleconnections (MEI, SOI, DMI, and NINO3.4) at ≈32 months period may be due to the correlation between climate indices (correlation o MEI with SOI/DMI/NINO3.4). Therefore, analyzing the standalone effect of teleconnection factors on the GGDI series may provide better correlation between GGDI and teleconnection after removing the effect of other influential time series [77,78].

4.2. Uncertainty Analysis

Numerous areas of uncertainty were encountered in the present study. First, to avoid the uncertainty induced by observational and data processing errors, we considered modern mascon solution data instead of the spherical harmonic coefficients data [79]. Still, the mascon solutions developed by various organizations still have ambiguities due to diverse background models as well as data processing approaches. In addition, the JPL mascon solutions considered different hydrological models to adjust the scale factors, which eventually contributes to the presence of uncertainty. Second, to minimize the GLDAS uncertainty, the ensemble mean of several hydrological models (Noah, VIC, CLM, Mosaic) was suggested [37]. However, similar to GRACE data, the Noah model has the same spatial resolution. Thus, we adopted the GLDAS Noah model outputs in the present study to reduce the uncertainty related to spatial resolution in evaluating water storage calculations. Finally, using linear interpolation techniques, the missing GRACE data were filled out, which may have triggered some uncertainties. However, since the approach is

prevalent, easy, and extensively used in the handling of missing data, we followed similar techniques in filling the GRACE dataset gaps [33,80], and the results suggest that the linear interpolation approach was appropriate.

4.3. Advantages and Limitations

GRACE satellite gravimetry plays an important role in the identification of drought in regions where data related to water storage variations is inadequate [81]. To reduce the influence of various errors in the GRACE spherical harmonic coefficients, one can apply various filtering processes, yet results suggest the possibility of weak signals in the derived product. Therefore, scale factors are applied to recover the signal leakage caused by the filtering processes [82]. In order to resolve these data processing errors, we adopted GRACE mascon solutions, which are equal to or superior to traditional GRACE spherical harmonic coefficients, in the current research [65]. Therefore, using GRACE mascon solutions, changing characteristics of TWS, in identifying the teleconnections with GGDI, and hence the drought situation over river basins in southern India were explored. In regions where hydrometeorological data are minimal, GRACE data are an important means of estimating and managing the drought. The GGDI drought index was evaluated in this analysis to identify drought events. The GGDI is a normalized index that can be used to objectively compare spatio-temporal drought, providing a strong evidence for evaluating surplus and deficit groundwater availability [39]. This study positively established the drought events between 2003 and 2005, 2008 and 2010, and 2013 and 2015, which were consistent with the results of Sinha et al. [17] and Kumar et al. [33]. Severe drought events between 2008 and 2010 for GRB, 2015 and 2016 for KRB, and 2003 and 2004 for PCRB were also reported by Kumar et al. [33], which are consistent with the drought events obtained using GGDI in this study (Figure 3, Table 2). Moreover, the interaction of GGDI with climate indices exhibited the fact that teleconnections had a substantial effect on drought across southern India's river basins.

Although GGDI based on GRACE dataset can be used to categorize drought characteristics effectively and expediently, there are still some limitations. GRACE datasets have only been available since 2002, covering only a few years of data; with longer temporal datasets, the results will therefore be more accurate [32]. Although GRACE data resolution is relatively low, it considers the changes in water storage (including soil water and surface snow) that comes from rainfall, evapotranspiration, river transportation, and deep underground infiltration. GRACE is the key technology in gravity satellite sensors to improve accuracy and monitoring gravity field in terrestrial hydrology. GRACE provides realistic spatiotemporal variations of vertically integrated measurement of water storage at precision of tens of millimeters of equivalent thickness. The new GRACE Follow On (GRACE FO) satellite datasets will provide a valuable solution for the long-term evaluation of TWS variations and their associated studies, resulting in significant improvements in our knowledge of GRACE-related studies. Moreover, the effect of anthropogenic activities (groundwater extraction, regional water division, mining) over mass changes of the earth surface cannot be overlooked [83]. These effects (influence of human activities) are generally ignored due to the lack of observed datasets, as well as difficulties in the collection and measurement of relevant information. Therefore, analyzing the influence of anthropogenic activities on variations in water storage may provide a fresh insight into the future of science.

5. Conclusions

In the present study, during 2003–2016, the drought characteristics were examined and evaluated using the GRACE-based groundwater storage as a metric over four major river basins in India. The spatial distribution, temporal evolution of drought, and trend characteristics were analyzed using GGDI during 2003–2016 over KRB, CRB, GRB, and PCRB. Then, using the wavelet coherence method, we evaluated the relationship between GGDI and climate factors. GRACE datasets provide significant benefits in detecting droughts and revealing information about large-scale groundwater depletion, where hydrometeorologi-

cal data are limited and data related to water storage variations are insufficient. This study has provided reliable and robust quantitative results of GRACE water storage variations that provide a new approach to link surface and subsurface condition while investigating droughts, and the methodology can be applied to any other region. The key findings from this research are as follows:

- The distinct seasonal and annual variations of TWSA were observed in four river basins. The PMon and PMon-R seasons exhibited negative TWSA values, while Mon and PMon-K seasons showed positive TWSA variations in all the river basins. Annually, TWSA values showed significant upward and downward trends, with most of the negative trends observed between 2003 and 2005, and 2012 and 2016, indicating severe droughts.
- The GGDI-identified drought events exhibited different temporal change characteristics in all the river basins. The most severe drought event was observed in CRB between 2012 and 2016, followed by GRB between 2008 and 2010. All the four basins exhibited drought events between 2003 and 2005, and KRB, CRB, and PCRB experienced droughts between 2012 and 2016.
- Drought severity and duration were evaluated using GGDI for four river basins. The CRB experienced the longest drought period among all the four basins, with a severity of -27.02 observed for 42 months during June 2012 to November 2015.
- The monthly and seasonal trends were evaluated using the MMK test. Significant monthly negative trends were observed during August to December in KRB, CRB, and PCRB. Seasonal negative trends were also significant in Mon and PMon-K in CRB, KRB, and PCRB.
- The wavelet coherence analysis effectively demonstrated the teleconnections between climate indices and drought events. The influence of SOI on drought was significantly high, followed by NINO3.4 and MEI in all the basins. SOI has the strongest impact in detecting the progression of drought compared to other climate indices in these river basins.

References

1. Mishra, A.K.; Singh, V.P. Drought modeling—A review. *J. Hydrol.* **2011**, *403*, 157–175. [CrossRef]
2. Kang, H.; Sridhar, V. Combined statistical and spatially distributed hydrological model for evaluating future drought indices in Virginia. *J. Hydrol. Reg. Stud.* **2017**, *12*, 253–272. [CrossRef]
3. Kang, H.; Sridhar, V. Assessment of future drought conditions in the Chesapeake Bay watershed. J. Am. *Water Resour. Assoc.* **2017**, *54*, 160–183. [CrossRef]
4. Sahoo, A.K.; Sheffield, J.; Pan, M.; Wood, E.F. Evaluation of the Tropical Rainfall Measuring Mission Multi-Satellite Precipitation Analysis (TMPA) for assessment of large-scale meteorological drought. *Remote Sens. Environ.* **2015**, *159*, 181–193. [CrossRef]
5. Cammalleri, C.; Vogt, J.; Salamon, P. Development of an operational low-flow index for hydrological drought monitoring over Europe. *Hydrol. Sci. J.* **2017**, *62*, 346–358. [CrossRef]
6. Kang, H.; Sridhar, V. Improved drought prediction using near real-time climate forecasts and simulated hydrologic conditions. *Sustainability* **2018**, *10*, 1799. [CrossRef]
7. Long, D.; Shen, Y.J.; Sun, A.; Hong, Y.; Longuevergne, L.; Yang, Y.T.; Li, B.; Chen, L. Drought and flood monitoring for a large karst plateau in Southwest China using extended GRACE data. *Remote Sens. Environ.* **2014**, *155*, 145–160. [CrossRef]
8. Palmer, W.C. *Meteorological Drought*; Weather Bureau US Department of Commerce: Washington, DC, USA, 1965; Volume 30.
9. Mckee, T.B.; Doesken, N.J.; Kleist, J. The relationship of drought frequency and duration to time scales. *Am. Meteorol. Soc.* **1993**, *58*, 174–184.
10. Vicente-Serrano, S.; Beguería, M.S.; López-Moreno, J.I. A multiscalar drought index sensitive to global warming: The standardized precipitation evapotranspiration index. *J. Clim.* **2010**, *23*, 1696–1718. [CrossRef]
11. Park, J.H.; Kim, K.B.; Chang, H.Y. Statistical properties of effective drought index (EDI) for Seoul, Busan, Daegu, Mokpo in South Korea. *Asia-Pac. J. Atmos. Sci.* **2014**, *50*, 453–458. [CrossRef]
12. Sehgal, V.; Sridhar, V.; Juran, L.; Ogejo, J. Integrating Climate Forecasts with the Soil and Water Assessment Tool (SWAT) for High-Resolution Hydrologic Simulation and Forecasts in the Southeastern U.S. *Sustainability* **2018**, *10*, 3079. [CrossRef]
13. Bisht, D.S.; Sridhar, V.; Mishra, A.; Chatterjee, C.; Raghuwanshi, N.S. Drought characterization over India under projected climate scenario. *Int. J. Climatol.* **2019**, *39*, 1889–1911. [CrossRef]
14. Ma, S.Y.; Wu, Q.X.; Wang, J.; Zhang, S.Q. Temporal evolution of regional drought detected from GRACE TWSA and CCI SM in Yunnan Province, China. *Remote Sens.* **2017**, *9*, 1124. [CrossRef]
15. Sehgal, V.; Sridhar, V.; Tyagi, A. Stratified drought analysis using a stochastic ensemble of simulated and in-situ soil moisture observations. *J. Hydrol.* **2017**, *545*, 226–250. [CrossRef]
16. Scanlon, B.R.; Zhang, Z.; Save, H.; Sun, A.Y.; Müller Schmied, H.; van Beek, L.P.H.; Wiese, D.N.; Wada, Y.; Long, D.; Reedy, R.C.; et al. Global models underestimate large decadal declining and rising water storage trends relative to GRACE satellite data. *Proc. Natl. Acad. Sci. USA* **2018**, *115*, E1080–E1089. [CrossRef]
17. Sinha, D.; Syed, T.H.; Reager, J.T. Utilizing combined deviations of precipitation and GRACE-based terrestrial water storage as a metric for drought characterization: A case study over major Indian river basins. *J. Hydrol.* **2019**, *572*, 294–307. [CrossRef]
18. Sinha, D.; Syed, T.H.; Famiglietti, J.S.; Reager, J.T.; Thomas, R.C. Characterizing drought in India using GRACE observations of terrestrial water storage deficit. *J. Hydrometeorol.* **2017**, *18*, 381–396. [CrossRef]
19. Zhang, Y.F.; He, B.; Guo, L.L.; Liu, D.C. Differences in response of terrestrial water storage components to precipitation over 168 global river basins. *J. Hydrometeorol.* **2019**, *20*, 1981–1999. [CrossRef]
20. Rodell, M.; Velicogna, I.; Famiglietti, J.S. Satellite-based estimates of groundwater depletion in India. *Nature* **2009**, *460*, 999–1002. [CrossRef]
21. Famiglietti, J.S.; Lo, M.; Ho, S.L.; Bethune, J.; Anderson, K.J.; Syed, T.H.; Swenson, S.C.; De Linage, C.R.; Rodell, M. Satellites measure recent rates of groundwater depletion in California's Central Valley. *Geophys. Res. Lett.* **2011**, *38*, L03403. [CrossRef]
22. Castle, S.L.; Thomas, B.F.; Reager, J.T.; Rodell, M.; Swenson, S.C.; Famiglietti, J.S. Groundwater depletion during drought threatens future water security of the Colorado River basin. *Geophys. Res. Lett.* **2014**, *41*, 5904–5911. [CrossRef] [PubMed]
23. Bhanja, S.N.; Mukherjee, A.; Saha, D.; Velicogna, I.; Famiglietti, J.S. Validation of GRACE based groundwater storage anomaly using in-situ groundwater level measurements in India. *J. Hydrol.* **2016**, *543*, 729–738. [CrossRef]
24. Katpatal, Y.B.; Rishma, C.; Singh, C.K. Sensitivity of the Gravity Recovery and Climate Experiment (GRACE) to the complexity of aquifer systems for monitoring of groundwater. *Hydrogeol. J.* **2018**, *26*, 933–943. [CrossRef]
25. Sridhar, V.; Ali, S.A.; Lakshmi, V. Assessment and validation of total water storage in the Chesapeake Bay watershed using GRACE. *J. Hydrol. Reg. Stud.* **2019**, *24*, 100607. [CrossRef]
26. Verma, K.; Katpatal, Y.B. Groundwater monitoring using GRACE and GLDAS data after downscaling within basaltic aquifer system. *Groundwater* **2019**, *58*, 143–151. [CrossRef] [PubMed]
27. Syed, T.H.; Famiglietti, J.S.; Rodell, M.; Chen, J.; Wilson, C.R. Analysis of terrestrial water storage changes from GRACE and GLDAS. *Water Resour. Res.* **2008**, *44*, W02433. [CrossRef]
28. Soni, A.; Syed, T.H. Diagnosing land water storage variations in major Indian river basins using GRACE observations. *Glob. Planet. Chang.* **2015**, *133*, 263–271. [CrossRef]
29. Panda, D.K.; Wahr, J. Spatiotemporal evolution of water storage changes in India from the updated GRACE-derived gravity records. *Water Resour. Res.* **2016**, *52*, 135–149. [CrossRef]

30. Singh, A.K.; Jasrotia, A.S.; Taloor, A.K.; Kotlia, B.S.; Kumar, V.; Roy, S.; Ray, P.K.C.; Singh, K.K.; Singh, A.K.; Sharma, A.K. Estimation of quantitative measures of total water storage variation from GRACE and GLDAS-NOAH satellites using geospatial technology. *Quat. Int.* **2017**, *444*, 191–200. [CrossRef]

31. Frappart, F.; Papa, F.; da Silva, J.S.; Ramillien, G.; Prigent, C.; Seyler, F.; Calmant, S. Surface freshwater storage and dynamics in the Amazon basin during the 2005 exceptional drought. *Environ. Res. Lett.* **2012**, *7*, 044010. [CrossRef]

32. Thomas, A.C.; Reager, J.T.; Famiglietti, J.S.; Rodell, M. A GRACE-based water storage deficit approach for hydrological drought characterization. *Geophys. Res. Lett.* **2014**, *41*, 1537–1545. [CrossRef]

33. Kumar, K.S.; Rathnam, E.V.; Sridhar, V. Tracking seasonal and monthly drought with GRACE-based terrestrial water storage assessments over major river basins in South India. *Sci. Total Environ.* **2020**, *763*, 142994. [CrossRef] [PubMed]

34. Ma, M.; Ren, L.; Singh, V.P.; Yang, X.; Yuan, F.; Jiang, S. New variants of the Palmer drought scheme capable of integrated utility. *J. Hydrol.* **2014**, *519*, 1108–1119. [CrossRef]

35. Zhao, M.; Velicogna, I.; Kimball, J.S. Satellite observations of regional drought severity in the continental United States using GRACE-based terrestrial water storage changes. *J. Clim.* **2017**, *30*, 6297–6308. [CrossRef]

36. Zhao, M.; Velicogna, I.; Kimball, J.S. A global gridded dataset of grace drought severity index for 2002–14: Comparison with PDSI and SPEI and a case study of the Australia millennium drought. *J. Hydrometeorol.* **2017**, *18*, 2117–2129. [CrossRef]

37. Cao, Y.P.; Nan, Z.T.; Cheng, G.D. GRACE gravity satellite observations of terrestrial water storage changes for drought characterization in the arid land of Northwestern China. *Remote Sens.* **2015**, *7*, 1021–1047. [CrossRef]

38. Yi, H.; Wen, L. Satellite gravity measurement monitoring terrestrial water storage change and drought in the continental United States. *Sci. Rep.* **2016**, *6*, 19909. [CrossRef]

39. Thomas, B.F.; Famiglietti, J.S.; Landerer, F.W.; Wiese, D.N.; Molotch, N.P.; Argus, D.F. GRACE groundwater drought index: Evaluation of California central Valley groundwater drought. *Remote Sens. Environ.* **2017**, *198*, 384–392. [CrossRef]

40. Bhuvaneswari, K.; Geethalakshmi, V.; Lakshmanan, A.; Srinivasan, R.; Sekhar, N.U. The Impact of El Niño/Southern Oscillation on Hydrology and Rice Productivity in the Cauvery Basin, India: Application of the Soil and Water Assessment Tool. *Weather Clim. Extrem.* **2013**, *2*, 39–47. [CrossRef]

41. Drought Situation to Cost Rs 6.5 Lakh Crore to Economy. Available online: https://www.assocham.org/newsdetail.php?id=5678 (accessed on 20 March 2021).

42. Dai, A. Drought under global warming: A review. *Wires Clim. Chang.* **2011**, *2*, 45–65. [CrossRef]

43. Wang, H.J.; Chen, Y.N.; Pan, Y.P.; Li, W.H. Spatial and temporal variability of drought in the arid region of China and its relationships to teleconnection indices. *J. Hydrol.* **2015**, *523*, 283–296. [CrossRef]

44. Phillips, T.; Nerem, R.S.; Fox-Kemper, B.; Famiglietti, J.S.; Rajagopalan, B. The influence of ENSO on global terrestrial water storage using GRACE. *Geophys. Res. Lett.* **2012**, *39*, L16705. [CrossRef]

45. Huang, S.Z.; Huang, Q.; Chang, J.X.; Leng, G.Y. Linkages between hydrological drought, climate indices and human activities: A case study in the Columbia River Basin. *Int. J. Climatol.* **2016**, *36*, 280–290. [CrossRef]

46. Ni, S.N.; Chen, J.L.; Wilson, C.R. Global Terrestrial Water Storage Changes and Connections to ENSO Events. *Surv. Geophys.* **2018**, *39*, 1–22. [CrossRef]

47. Vissa, N.K.; Anandh, P.C.; Behera, M.M.; Mishra, S. ENSO-induced groundwater changes in India derived from GRACE and GLDAS. *J. Earth Syst. Sci.* **2019**, *128*, 115. [CrossRef]

48. Liu, X.; Feng, X.; Ciais, P.; Fu, B. Widespread decline in terrestrial water storage and its link to teleconnections across Asia and eastern Europe. *Hydrol. Earth Syst. Sci.* **2020**, *24*, 3663–3676. [CrossRef]

49. Chen, J.L.; Wilson, C.R.; Tapley, B.D. The 2009 exceptional Amazon flood and interannual terrestrial water storage change observed by GRACE. *Water Resour. Res.* **2010**, *46*, W12526. [CrossRef]

50. Zhang, Z.; Chao, B.; Chen, J.; Wilson, C. Terrestrial water storage anomalies of Yangtze River basin droughts observed by GRACE and connections with ENSO. *Glob. Planet. Chang.* **2015**, *126*, 35–45. [CrossRef]

51. Ndehedehe, C.E.; Awange, J.L.; Kuhn, M.; Agutu, N.O.; Fukuda, Y. Climate teleconnections influence on West Africa's terrestrial water storage. *Hydrol. Process.* **2017**, *31*, 3206–3224. [CrossRef]

52. Anyah, R.O.; Forootan, E.; Awange, J.; Khaki, M. Understanding linkages between global climate indices and terrestrial water storage changes over Africa using GRACE products. *Sci. Total Environ.* **2018**, *635*, 1405–1416. [CrossRef]

53. Han, Z.; Huang, S.; Huang, Q.; Leng, G.; Wang, H.; He, L.; Fang, W.; Li, P. Assessing GRACE-based terrestrial water storage anomalies dynamics at multi-timescales and their correlations with teleconnection factors in Yunnan Province, China. *J Hydrol.* **2019**, *574*, 836–850. [CrossRef]

54. Wang, F.; Wang, Z.; Yang, H.; Di, D.; Zhao, Y.; Liang, Q. Utilizing GRACE-based groundwater drought index for drought characterization and teleconnection factors analysis in the North China Plain. *J. Hydrol.* **2020**, *585*, 124849. [CrossRef]

55. Mishra, A.K.; Singh, V.P. A review of drought concepts. *J. Hydrol.* **2010**, *391*, 202–216. [CrossRef]

56. Thilakarathne, M.; Sridhar, V. Characterization of future drought conditions in the Lower Mekong Basin. *Weather. Clim. Extremes.* **2017**, *17*, 47–58. [CrossRef]

57. Sharma, P.J.; Patel, P.L.; Jothiprakash, V. Hydroclimatic teleconnections of large-scale oceanic-atmospheric circulations on hydrometeorological extremes of Tapi Basin, India. *Atmos. Res.* **2020**, *235*, 104791. [CrossRef]

58. Gupta, V.; Jain, M.K. Impact of ENSO, Global Warming, and Land Surface Elevation on Extreme Precipitation in India. *J. Hydrol. Eng.* **2020**, *25*, 05019032. [CrossRef]

59. Gehlot, L.K.; Jibhakate, S.M.; Sharma, P.J.; Patel, P.L.; Timbadiya, P.V. Spatio-Temporal Variability of Rainfall Indices and their Teleconnections with El Niño-Southern Oscillation for Tapi Basin, India. *Asia-Pac. J Atmos. Sci.* **2020**, *57*, 99–118. [CrossRef]

60. Gupta, V.; Jain, M.K. Unravelling the teleconnections between ENSO and dry/wet conditions over India using nonlinear Granger causality. *Atmos. Res.* **2021**, *247*, 105168. [CrossRef]

61. Scanlon, B.R.; Zhang, Z.Z.; Save, H.; Wiese, D.N.; Landerer, F.W.; Long, D.; Longuevergne, L.; Chen, J.L. Global evaluation of new GRACE mascon products for hydrologic applications. *Water Resour. Res.* **2016**, *52*, 9412–9429. [CrossRef]

62. Wu, Q.F.; Si, B.C.; He, H.L.; Wu, P.T. Determining regional-scale groundwater recharge with GRACE and GLDAS. *Remote Sens.* **2019**, *11*, 154. [CrossRef]

63. Rajeevan, M.; Bhate, J.; Jaswal, A.K. Analysis of variability and trends of extreme rainfall events over India using 104 years of gridded daily rainfall data. *Geophys. Res. Lett.* **2008**, *35*, L18707. [CrossRef]

64. Srivastava, A.K.; Rajeevan, M.; Kshirsagar, S.R. Development of high resolution daily gridded temperature data set (1969–2005) for the Indian Region. *Atmos. Sci. Lett.* **2009**, *10*, 249–254. [CrossRef]

65. Hamed, K.H.; Rao, A.R. A modified Mann–Kendall trend test for autocorrelated data. *J. Hydrol.* **1998**, *204*, 219–246. [CrossRef]

66. SatishKumar, K.; Rathnam, E.V. Comparison of six trend detection methods and forecasting for monthly groundwater levels—A case study. *ISH J. Hydraul. Eng.* **2020**. [CrossRef]

67. Torrence, C.; Webster, P.J. Interdecadal changes in the ENSO–Monsoon System. *J. Clim.* **1999**, *12*, 2679–2690. [CrossRef]

68. Grinsted, A.; Moore, J.C.; Jevrejeva, S. Application of the cross wavelet transform and wavelet coherence to geophysical time series. *Nonlinear Process. Geophys.* **2004**, *11*, 561–566. [CrossRef]

69. Liu, P.C. Wavelet spectrum analysis and ocean wind waves. In *Wavelets in Geophysics*; Foufoula-Georgiou, E., Kumar, P., Eds.; Academic Press: New York, NY, USA, 1994; pp. 151–166.

70. Chang, X.; Wang, B.; Yan, Y.; Hao, Y.; Zhang, M. Characterizing effects of monsoons and climate teleconnections on precipitation in China using wavelet coherence and global coherence. *Clim. Dyn.* **2019**, *52*, 5213–5228. [CrossRef]

71. Mooley, D.A.; Parthasarathy, B. Droughts and Floods over India in Summer Monsoon Seasons 1871–1980. In *Variations in the Global Water Budget*; Springer: Dordrecht, The Netherlands, 1983; pp. 239–252.

72. UNICEF. Drought in India 2015–16: When Coping Crumples—A Rapid Assessment of the Impact of Drought on Children and Women in India. 2016. Available online: https://reliefweb.int/report/india/drought-india-2015-16-when-coping-crumbles-rapid-assessment-impact-drought-children-and (accessed on 20 March 2021).

73. Mishra, V. Long-term (1870–2018) drought reconstruction in context of surface water security in India. *J. Hydrol.* **2019**, *580*, 124228. [CrossRef]

74. Gautam, R.C. Impacts of drought on crops and ways to mitigate it. *Indian Farming* **2012**, *62*, 13–19.

75. Sehgal, V.; Sridhar, V. Effect of hydroclimatological teleconnections on watershed-scale drought predictability in Southeastern U.S. *Int. J. Climatol.* **2018**, *38* (Suppl. 1), e1139–e1157. [CrossRef]

76. Zhu, Z.C.; Piao, S.L.; Xu, Y.Y. The effects of teleconnections on carbon fluxes of global terrestrial ecosystems. *Geophys. Res. Lett.* **2017**, *44*, 3209–3218. [CrossRef]

77. Tan, X.; Gan, T.Y.; Shao, D. Wavelet analysis of precipitation extremes over Canadian ecoregions and teleconnections to large-scale climate anomalies. *J. Geophys. Res. Atmos.* **2016**, *121*, 14469–14486. [CrossRef]

78. Aryal, Y.; Zhu, J. Multimodel ensemble projection of meteorological drought scenarios and connection with climate based on spectral analysis. *Int. J. Climatol.* **2020**, *40*, 3360–3379. [CrossRef]

79. Swenson, S.; Wahr, J. Post-processing removal of correlated errors in GRACE data. *Geophys. Res. Lett.* **2006**, *33*, L08402. [CrossRef]

80. Sun, Z.L.; Zhu, X.F.; Pan, Y.Z.; Zhang, J.S.; Liu, X.F. Drought evaluation using the GRACE terrestrial water storage deficit over the Yangtze River Basin, China. *Sci. Total Environ.* **2018**, *634*, 727–738. [CrossRef]

81. Yirdaw, S.Z.; Snelgrove, K.R.; Agboma, C.O. GRACE satellite observations of terrestrial moisture changes for drought characterization in the Canadian Prairie. *J. Hydrol.* **2008**, *356*, 84–92. [CrossRef]

82. Landerer, F.W.; Swenson, S.C. Accuracy of scaled GRACE terrestrial water storage estimates. *Water Resour. Res.* **2012**, *48*, W04531. [CrossRef]

83. Tang, Q.H.; Zhang, X.J.; Tang, Y. Anthropogenic impacts on mass change in North China. *Geophys. Res. Lett.* **2013**, *40*, 3924–3928. [CrossRef]

Article

Assessing Future Impacts of Climate Change on Streamflow within the Alabama River Basin

Joseph E. Quansah [1,*]**, Amina B. Naliaka** [2]**, Souleymane Fall** [1]**, Ramble Ankumah** [1] **and Gamal El Afandi** [1]

1   Department of Agricultural and Environmental Sciences, Tuskegee University, Tuskegee, AL 36088, USA; sfall@tuskegee.edu (S.F.); rankumah@tuskegee.edu (R.A.); gelafandi@tuskegee.edu (G.E.A.)
2   School of Earth Systems and Sustainability, Southern Illinois University, Carbondale, IL 62901, USA; amina.naliaka@siu.edu
*   Correspondence: jquansah@tuskegee.edu; Tel.: +1-3347278419

Abstract: Global climate change is expected to impact future precipitation and surface temperature trends and could alter local hydrologic systems. This study assessed the likely hydrologic responses and changes in streamflow due to future climate change within the Alabama River Basin (ARB) for the mid-21st century 2045 ("2030–2060") and end-21st century 2075 ("2060–2090"). Using an integrated modeling approach, General Circulation Model (GCM) datasets; the Centre National de Recherches Météorologiques Climate Model 5 (CNRM-CM5), the Community Earth System Model, version 1–Biogeochemistry (CESM1- BGC.1), and the Hadley Centre Global Environment Model version 2 (HADGEM2-AO.1), under medium Representative Concentration Pathway (RCP) 4.5, and based on World Climate Research Program (WCRP)'s Couple Model Intercomparison Phase 5 (CMIP5), were assimilated into calibrated Soil and Water Assessment Tool (SWAT). Mann–Kendall and Theil Sen's slope were used to assess the trends and magnitude of variability of the historical climate data used for setting up the model. The model calibration showed goodness of fit with minimum Nash–Sutcliffe Efficiency (NSE) coefficient values of 0.83 and Coefficient of Determination (R^2) of 0.88 for the three gages within the ARB. Next, the research assessed changes in streamflow for the years 2045 and 2075 against that of the reference baseline year of 1980. The results indicate situations of likely increase and decrease in mean monthly streamflow discharge and increase in the frequency and variability in peak flows during the periods from the mid to end of the 21st century. Seasonally, monthly streamflow increases between 50% and 250% were found for spring and autumn months with decreases in summer months for 2045. Spring and summer months for 2075 resulted in increased monthly streamflow between 50% and 300%, while autumn and spring months experienced decreased streamflow. While the results are prone to inherent uncertainties in the downscaled GCM data used, the simulated dynamics in streamflow and water availability provide critical information for stakeholders to develop sustainable water management and climate change adaptation options for the ARB.

Keywords: climate change; streamflow; SWAT model; GCM; CNRM-CM5; CESM1-BGC.1; HADGEM2-AO.1; Alabama River Basin

1. Introduction

According to the United Nations Framework Convention on Climate Change [1], climate change could be defined as "a change of climate which is attributed directly or indirectly to human activity that alters the composition of the global atmosphere and which is in addition to natural climate variability observed over comparable time periods" [1]. Climate change may be due to natural internal processes or external forcings, such as modulations of the solar cycles, volcanic eruptions, and persistent anthropogenic changes in the composition of the atmosphere or inland use [2]. The latest Intergovernmental Panel on Climate Change (IPCC) assessment reports show global climate change as a scientific

reality and one of the most significant challenges facing humanity today [3]. Climate change is mainly manifested by the change in global mean surface temperatures.

Temperature data from several scientists and organizations show that global climate warming trends have been increasing rapidly in the past few decades [4]. Globally, nineteen of the twenty warmest years all have occurred since 2001, except for 1998, with 2016 being the warmest on record since 1880 [5]. The 10 warmest years in the 140-year record all have occurred since 2005, with the six warmest years being the six most recent years [4]. The ten warmest Augusts have all occurred since 1998, and the five warmest have occurred since 2015 [4]. Averaged as a whole, the August 2020 global land and ocean surface temperature was 0.94 °C (1.69 °F) above average, and the second highest August temperature since 1880 [3]. According to National Oceanic and Atmospheric Administration (NOAA) (2020), both August 2020 global land-only and 2016 ocean-only surface temperatures were among the highest ever recorded, at 1.26 °C (2.27 °F) and 0.82 °C (1.48 °F) above average, respectively [4]. Human-induced global warming reached approximately 1 °C above pre-historic levels in 2017 and is projected to reach to 1.5 °C above pre-industrial levels by 2040 [6]. Rising sea surface temperatures have resulted in increases in tropical storms and hurricanes [7]. Additionally, global average sea levels are projected to continue to rise (approximately 7.2 to 23.6 inches/18–59 cm/0.18–0.59 m) by the end of the century [8]. All these facts add credence to the IPCC's conclusion that climate change is real, will continue to increase in severity, and requires human and governmental actions to control the current trends.

Historically, increases in surface temperature have resulted in changes in the intensity spatial distribution, and temporal trends in precipitation, and have subsequently impacted different regional and local hydrologic systems around the world [7,9]. Climate change is expected to modify the hydrologic cycle and has significant implications for water resources. These include observed increased evaporation rates, a higher proportion of precipitation received as rain rather than snow, earlier and shorter runoff seasons, changes in water budget and streamflows, increased water body temperatures, such as the warming of lakes and rivers, and decreased water quality in both inland and coastal areas [10–12]. Impacts of climate change on freshwater ecosystems also include observed changes in species composition, organism abundance, productivity, and phenological shifts [13]. Aquatic habitats, as well as water quality, have been negatively affected, resulting in lower levels of dissolved oxygen, increases in pollutants, pathogens, nutrients, and invasive species as well as algal blooms [10,11,14]. Additionally, there have been losses and changes in the distribution of aquatic species with higher rates of evapotranspiration resulting in some water bodies shrinking [12].

Variability in precipitation relative to evaporation and increasing surface temperatures cause changes in residence time, water budget, and water temperature dynamics of lakes, streams, rivers, and other water bodies [15]. Temporal and spatial variabilities in precipitation intensity have the potential to cause shifts in the connectivity of water bodies as well as in erosion rates that could affect the inflow and outflow dynamics of various water bodies for different regions [15]. For instance, according to the United States Environmental Protection Agency (U.S. EPA) during the past 75 years, seven-day low flow has generally increased in the Northeast and Midwest regions of the United States while parts of the Southeast and the Pacific Northwest regions have generally had decreases in low flows [16,17]. Moreover, three-day high-flow trends have varied from region to region across the U.S., with high flows observed to have generally increased or changed little in the Northeast since 1940, while high flows have also increased in some West Coast streams and decreased in others [16,17]. Annual average streamflow has increased at many sites in the Northeast and Midwest, while other regions have seen few substantial changes [16,17]. Net water supplies have increased in areas with sufficient rainfall while certain areas have experienced long droughts and decreases in net water supply [17,18]. This decrease is partly due to the temperature rise and associated increase in evaporation rates in most areas [17,18]. Parametric and nonparametric-based assessment of historical long-term trends and seasonal variability in streamflow have shown increasing and decreasing flow

trends for different hydrologic regions [19,20]. Regions experiencing a decline in the water supply are likely to experience an increase in water demand because of the increasing population. The decrease in water supply could be particularly significant for agriculture, energy production, municipal, industrial, and other uses [21]. Changes in the timing, intensity, and duration of precipitation negatively affect water quality. As a result of increased rainfall and intense rainstorms, flooding and surface runoff transport large volumes of water and contaminants into water bodies. Intense flooding events can also overwhelm water infrastructures including storm, combined sewer, and wastewater systems, causing untreated pollutants to directly enter and contaminate source water supply systems. In regions with increased rainfall frequency and intensity, more pollution and sedimentation might result from runoff. On the other hand, reduced rainfall and increased temperatures will result in drier soils and lead to increasing incidences of wildfires making land more vulnerable to soil erosion [22]. Increasing occurrences of tropical storms will result in increased flooding which may consequently damage infrastructure and lead to coastal erosion [23]. Climate change has adversely impacted food security and terrestrial ecosystems as well as contributed to desertification and land degradation in many regions [3]. Sustainable land management, including sustainable forest management, can prevent and reduce land degradation, maintain land productivity, and sometimes reverse the adverse impacts of climate change on land degradation, while contributing to mitigation and adaptation solutions [3].

To effectively assess future hydrologic responses to climate change, scientists utilize hydrologic modeling integrated with future projected climate dataset derived from the World Climate Research Program (WCRP) and IPCC's General Circulation Models (GCMs). The GCMs are the most advanced tools for simulating the response of the global climate system to increasing greenhouse gas concentrations [23]. GCMs provide geographically and physically consistent estimates of future regional climate conditions and changes throughout the planet based on physical processes involving the atmosphere, ocean, and land surface [23,24]. The latest GCM dataset is the WCRP's Coupled Model Intercomparison Project Phase 6 (CMIP6). These new generation climate models have resulted in significant improvements in the knowledge and understanding of future climate variability and change. Greenhouse gas emission scenarios are the primary radiative forcing that drive the GCMs. There are a standard set of scenarios for future global greenhouse gas emissions based on land use, population growth, technology, industrialization, and other factors that are employed by climate modelers [23]. These are the Representative Concentration Pathways (RCPs), and are expressed as the amount, by the year 2100, of the earth's radiative imbalance in watts per square meter of earth's surface. RCPs were introduced in the Fifth IPCC Assessment and are used to prescribe radiative forcing inputs to climate models [23,25–27]. The four standard RCPs are RCP2.6, RCP4.5, RCP6.5, and RCP8.5, which represent increases of +2.6, +4.5, +6.5, and +8.5 watts per square meter (W/m^2), respectively. The RCP 2.6 scenario is a relatively low greenhouse-gas emission scenario, while RCP 4.5, RCP 6.5, and RCP 8.5 appear as reasonable choices to represent medium to high stabilization radiative forcing emission scenarios [23]. As an integral part of assessing impacts of climate change on hydrologic systems, downscaled GCM data under various RCP scenarios are assimilated into hydrologic models to simulate past, current, and future hydrologic processes, and responses to different climate conditions [28–31]. Due to spatial scales and inherent uncertainties in downscaled GCM datasets integrated into hydrologic models, there could be substantial variability in simulated hydrologic outputs and responses to climate change [32].

The State of Alabama, in the southern U.S., has experienced over the years periods of flooding and low flows as a result of changing climate. For instance, in 1990, the Alabama River flooded homes in Selma and Montgomery, while in 2007 and 2016 severe drought hit the region. Reduced runoff and lower groundwater levels in the summer could impact water availability to satisfy Alabama's growing and competing needs for municipal, industrial, agricultural irrigation, and recreational uses of water [33]. Large groundwater

withdrawals in the coastal zones of Baldwin and Mobile counties, which include the Mobile Bay and Gulf Shores regions, have increased salinity in wells due to saltwater intrusion into the aquifers [34]. An increase in sinkhole formation has also been associated with growing groundwater withdrawals [35]. Warmer and drier conditions, particularly if accompanied by rising sea levels, could compound these types of problems due to higher demand and lower flows. Lower flows and higher temperatures could also degrade water quality by concentrating pollutants and reducing the assimilation of wastes [33]. One of the largest off-stream uses of water in Alabama is thermoelectric power generation. Higher water temperatures could reduce the efficiency of industrial and power plant cooling systems and might make it increasingly difficult to meet regulatory standards for acceptable downstream water temperatures, particularly during extremely warm periods. Increases in precipitation would alleviate these impacts. However, higher rainfall, particularly during the traditional winter-spring flood season, could contribute to localized flooding and increased levels of pesticides and fertilizers in runoff from agricultural areas [33]. Historically, Alabama experienced the hottest temperatures in the 1920s and 1930s, followed by a substantial cooling of almost 2 °F into the 1960s and 1970s. Since that cool period, temperatures have risen by about 1.5 °F, such that the most recent decades have experienced records above the long-term average, but slightly cooler than the 1920s/1930s [36]. Because of the large cooling that occurred in the middle of the 20th century, the southeastern United States is one of the few regions globally that has not experienced overall warming since 1900, while the United States as a whole has warmed by about 1.5 °F. In the summer, daytime high temperatures have typically ranged between 85 °F and 95 °F, with temperatures regularly exceeding 95°F across the state [36].

Under a higher emissions pathway, historically unprecedented warming is projected by the end of the 21st century. Even under a lower pathway of greenhouse gas concentrations, temperatures are projected to exceed historical record levels by the middle of the 21st century. However, there is a large range of temperature increases projected under both pathways, and under the lower pathway, a few projections are slightly warmer than historical records [36]. Warming is projected despite the lack of a long-term temperature trend in Alabama because the increased warming influence of greenhouse gases is expected to become greater than the natural variations that have dominated Alabama's temperatures [36]. Future changes in average annual precipitation are uncertain. However, any increase in temperature will cause a more rapid rate of loss of soil moisture during dry periods. This will likely increase the intensity of naturally occurring droughts in the future. Increases in extreme precipitation are projected for Alabama because it is virtually certain that atmospheric water vapor will increase in a warmer world [36,37]. Therefore, both droughts and wetter episodes are expected to occur, and this increase in various types of extreme climatic events is one of climate change hallmarks [38].

Because of the above observations, it is critical to assess future climate change impacts on hydrologic systems and water resources. The objective of the study was to assess the likely hydrologic responses and changes in mean monthly streamflow discharge due to future climate change within the Alabama River Basin (ARB), for the mid (2030–2060) and end (2060–2090) of the 21st century. The integrated modeling approach used involved the assimilation of the three best performing downscaled CMIP5 GCM data, namely the Centre National de Recherches Météorologiques Climate Model 5 (CNRM-CM5), the Community Earth System Model, version 1–Biogeochemistry (CESM1- BGC.1), and the Hadley Centre Global Environment Model version 2 (HADGEM2-AO.1), under medium emission scenario (RCP 4.5) into the Soil and Water Assessment Tool (SWAT) to simulate monthly streamflow variability and magnitude for the years 2045, representing the mid-21st century ("2030–2060"), and 2075, representing the end-21st century ("2060–2090"). The results from this study together with the relevant knowledge about the Alabama River Basin, and other related research studies would provide critical information for the development of climate change adaptation solutions to ensure sustainable management of water resources within the Alabama River Basin and the southeastern USA in general.

2. Materials and Methods

2.1. Study Area

The study area is the Alabama River Basin (ARB), which consists of Alabama, Coosa, Tallapoosa, and Cahaba River Basins (Figure 1). The ARB covers the northwestern part of Georgia and enters through northeastern Alabama, covering a region which includes the central and southeastern Alabama and covers a total drainage area of approximately 59,051 km^2 [39]. The headwater streams of the ARB river basin rise in the Blue Ridge Mountains of Georgia and Tennessee and flow southwest, combining at Rome, Georgia, to form the Coosa River [39]. The confluence of the Coosa and Tallapoosa Rivers in central Alabama forms the Alabama River, which flows through Montgomery and Selma. The Alabama River then joins with the Tombigbee River at the bottom of the ARB about 45 miles north of Mobile to form the Mobile River, which flows into Mobile Bay at an estuary of the Gulf of Mexico [39] The ARB contributes 33,600 ft^3/s (951.5 m^3/s) of streamflow to the Mobile River [39].
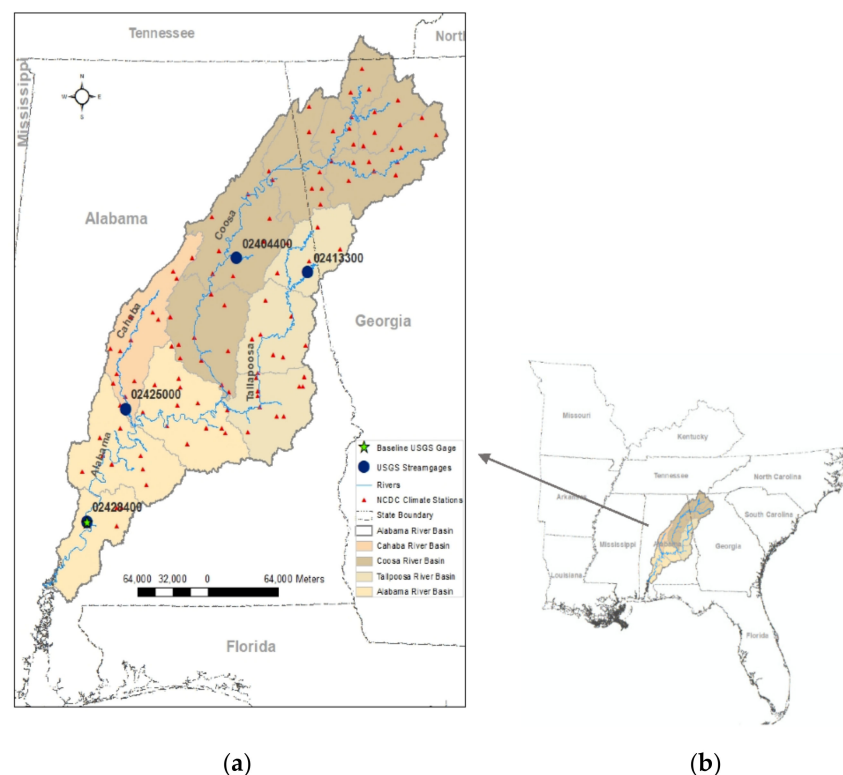
Figure 1. The study area: (**a**) the major basins, climate stations, and U.S. Geological Survey (USGS) gages; (**b**) location of the basin within Alabama and southeastern U.S.

The state of Alabama has a humid, subtropical climate, with mild winters and hot summers. Extreme temperatures range from near 110 °F in the summer to values below zero in the winter [39]. In the southern end of the basin, the average maximum January temperature is 60 °F, and the average minimum January temperature is 37 °F [39]. The maximum average July temperature is 91 °F; in the southern end of the basin, the corresponding minimum value is 69 °F [39]. The frost-free season varies in length from about 200 days in the northern valleys to about 250 days in the southern part of the basin [39]. The ARB has elevation that ranges from sea level to 1278 m and has soil type consisting mainly of sandy loam and silty loam [40]. The average annual precipitation for the ARB is 1379 mm, mainly from rainfall and limited contributions from snowfall [40]. The dominant land use types for the ARB are forestry (about 73%) and agriculture (about 17%), consisting mainly of hay/pasture, corn, cotton, peanuts, and soybean. The large forest land cover results in

high evapotranspiration ranging from 762 to 1067 mm (56–78% of annual precipitation), generally increasing from north to south [40].

2.2. Soil and Water Assessment Tool

The Soil and Water Assessment Tool (SWAT) is an ecohydrological model developed by the United States Department of Agriculture (USDA)–Agricultural Research Service (ARS) [41]. SWAT is a continuous-time, semi-distributed, dynamic, and spatially distributed model, based on mathematical descriptions of physical, biogeochemical, and hydrochemical processes in simulating hydrologic processes, streamflow, impacts of land use and agricultural management practices on water quality, the fate and transport of pollutants, sediment, and agricultural chemical yields, at various watershed scales [41,42]. The major model components are weather conditions, hydrology, soil properties, plant growth, and land management, as well as loads and flows of nutrients, pesticides, bacteria, and pathogens. SWAT can simulate major hydrologic processes including evapotranspiration (ET), surface runoff, infiltration, percolation, shallow aquifer, and deep aquifer flow, and channel routing [41]. Moreover, [43] provide details and the theoretical background of the SWAT model. The SWAT model is one of the most widely used hydrologic and water quality models worldwide and can be applied across a range of watershed scales, climatic zones, environmental conditions, and management systems extensively for a broad range of hydrologic and/or environmental studies and decision making [42]. The international use of SWAT has mostly been attributed to its flexibility in addressing water resource problems.

2.3. General Circulation Models and Uncertainties

Although CMIP5 GCMs have been widely applied in the assessment of hydrologic responses to climate change, there are uncertainties associated with outputs of GCMs. According to [44], the greatest source of uncertainty is the large spatial and temporal scale of GCMs. This gives rise to another source of uncertainty: the downscaling techniques that are necessary to convert GCM model outputs to scales that are useful for most hydrological modeling applications [23]. Another critical source of uncertainty in GCM is the accuracy in the projections of drought conditions. According to [45], uncertainties in projected drought scenarios could contribute as high as 97% to total uncertainty in climate models. Research work by [46] projected that, while precipitation is likely to increase in the 21 century, frequencies in droughts are expected to increase by between 10% and 50% over most land areas.

Therefore, there are different levels of uncertainties depending on the accuracy of the downscaled GCM data and the RCP greenhouse gas emission scenarios being used. Several researchers have been able to assess climate change impact across a range of spatial and temporal scales using GCM data that most accurately simulate historical climate conditions of their study areas [24,29,31]. RCP 4.5 and 8.5 are identified as conservative and severe, respectively in CMIP5 projections to demonstrate the sensitivity of Midwestern U.S. watersheds to future climatic changes [31].

In this study, we considered the top three CMIP5 GCMs climate data recommended for southeastern United States (U.S.) by U.S. Geological Survey (USGS). USGS evaluated CMIP5 GCMs concerning how well they reproduced the observed climate of the Southeastern U.S. Monthly data (temperature and precipitation) from 41 GCMs of the CMIP5 were compared to observations for the 20th century for the Southeastern United States and surrounding areas. They utilized a suite of statistics/metrics that characterize various aspects of the regional climate. Each GCM's performance was then assessed and ranked, based on its ability to reproduce the observed climatic variables [47]. Overall, the highest-ranked models included the CNRM-CM5/CNRM-CM5-2 pair of models, the CESM1/CCSM4 family of models (except for CESM1-WACCM), and the CMCC-CM/CMCC-CMS pair of models. Other high scoring models are MPI-ESM-LR, the "CC" versions of the GISS family of models, and HadGEM2-ES. For this study CNRM-CM5 [48], CESM1-BGC.1 [49], and

HADGEM2-AO.1 [50] model data, under medium stabilization radiative forcing emission scenario (RCP4.5), were selected based on their performance as compared to observation data for the research watershed for the years between 1980 and 2010.

2.4. Historical and Future Climate Scenario Data

This study utilized historical climate and streamflow data (1980–2010) and statistically downscaled GCM CMIP5 climate data (daily precipitation, minimum and maximum temperatures) for the years 2045 (representing the mid-21st century (2030–2060) and 2075 (representing the end-21st century (2060–2090), under medium stabilization radiative forcing emission scenario (RCP4.5). The historical data were used together with other watershed and geospatial data to set up, calibrate, and validate the SWAT model. The downscaled future climate data were assimilated into calibrated SWAT models to simulate and analyze the dynamics of future streamflow for selected GCMs under RCP4.5 scenario. A detailed description of the scenario is provided by [51]. Data from CNRM-CM5 [48], CESM1-BGC.1 [49], and HADGEM2-AO.1 [50] models were used in this study. The data (1/16° resolution) were obtained from http://gdo-dcp.ucllnl.org/downscaled_cmip_projections/ (accessed on 2 July 2018) [52]. The different GCM simulations were run and assessed on monthly time steps, from January 1 to December 31 for the years 2045 and 2075, to evaluate future changes in streamflow dynamics and water availability. Streamflow projections from the different models were then compared to those for the baseline year of 1980 to assess climate change impacts.

2.5. Hydrologic Modeling Data

The data used as input for the SWAT model included the USDA National Elevation Data (NED), historical climate, streamflow, water quality, USDA National Agricultural Statistics Service (NASS) cropland, State Soil Geographic (STATSGO), and downscaled GCM data. The data used, sources, and description are as shown in Table 1.

Table 1. Table showing geospatial and climate data and sources.

Data	Data Source	Data Description
Elevation (30 m)	United States Department of Agriculture Geospatial Data Gateway http://datagateway.nrcs.usda.gov	National Elevation Dataset
State Soil Geographic data	United Stated Department of Agriculture Geospatial Data Gateway http://datagateway.nrcs.usda.gov	Soil classification and properties
Land Use (30 m)	United Stated Department of Agriculture Geospatial Data Gateway http://datagateway.nrcs.usda.gov	National Land Cover Dataset Land
Historical Climate	National Climatic Data Center http://www.ncdc.noaa.gov/cdo-web	Daily rainfall, maximum and minimum temperature
Streamflow	United States Geological Survey Water Data https://waterdata.usgs.gov/nwis	Monthly streamflow
Future Climate	http://gdo-dcp.ucllnl.org/downscaled_cmip_projections/	Downscaled General Circulation Model data for 2045 and 2075

2.6. SWAT Model Setup, Calibration, and Validation Analysis

The geospatial data were processed and assimilated into the SWAT model. An initial cold/default simulation was run to obtain the initial performance of the model, which then served as the basis for the calibration of long-term water balance [53]. The model was then calibrated, validated, and assessed for performance accuracy and efficiency.

According to [54], calibration is the process that involves the effort to parameterize a model to a given set of local conditions, thereby reducing the prediction uncertainty. Nash–Sutcliffe Efficiency (NSE) coefficient [55] (Equation (1) and the Coefficient of Determination (R^2) (Equation (2) statistics were used to assess the performance of the SWAT model. The

NSE is commonly used to assess the predictive performance of hydrologic models and has values ranging from $-\infty$ to 1. A hydrologic model is considered as having optimal performance if NSE values are above 0.5, with a 1 indicating a perfect match of model simulation with measured data [56]. R^2 represents the correlation between the simulated and measured data, with values ranging between 0 and 1, where 0 corresponds to no correlation and 1 indicates a perfect correlation [56]. A high R^2 value may not necessarily be an indication of an acceptable model performance or efficiency [57,58]. A good assessment of the acceptability of R^2 value, is to make graphical comparison of the series scatter plots to ensure their closeness to the 1:1 ratio line and also observe the good-of-fit of the resulting hydrographs of simulated and measured data. Generally, R^2 values are higher than corresponding NSE values.

Measured data from three USGS gages (02404400, 02413300, and 02425000) were used for monthly calibration for the period 1995–2005, and monthly validation was performed for the period 1985–1995. The hydrologic parameters that were systematically changed in the calibration included initial SCS runoff curve number for moisture condition II (CN2), soil evaporation compensation factor (ESCO), available water capacity of first soil layer (mm/mm) (SOL_AWC), baseflow alpha factor (days)(ALPHA_BF), threshold depth of water in the shallow aquifer for return flow to occur (mm H2O) (GWQMIN) and groundwater "revap" coefficient (GW_REVAP).

$$NSE = 1 - \frac{\sum_{i=1}^{n}(O_i - P_i)^2}{\sum_{i=1}^{n}(O_i - O_{avg})^2} \tag{1}$$

$$R^2 = \left[\frac{\sum_{i=1}^{n}(O_i - O_{avg})(P_i - P_{avg})}{\sqrt{\sum_{i=1}^{n}(O_i - O_{avg})^2 \sum_{i=1}^{n}(P_i - P_{avg})^2}} \right]^2 \tag{2}$$

where, n is the total number of observations or simulation; i is number of values, O is measured values; P is predicted or simulated output values.

2.7. Climate Trend Analysis

The time series of the historical climate data for the period between 1980 and 2010 was analyzed for temporal variability trends using the non-parametric Mann–Kendall method [59] and the magnitude of the trends was determined using Theil Sen's slope estimator [60,61]. Trend analysis was performed to quantify the rate of change, the magnitude of trend, the sign (increase or decrease) in change and whether the change in the annual rainfall and temperature was statistically significant. The trend test was positive (increasing) for precipitation and minimum temperature and non-null for maximum temperature (Table 2). All three climate variables showed little to no observable long-term variation over the historical period between 1980 and 2010.

Table 2. Mann–Kendall Trend Test Results.

Variable	Number of Years	Mann–Kendall	Trend
Precipitation	30	+	1
Maximum Temperature	30	+	0
Minimum Temperature	30	+	1

2.8. Analysis of Simulated Baseline versus Future Streamflow Discharge

To study streamflow changes resulting from projected climate change, streamflow discharge and hydrographs for the historical baseline year of 1980 were analyzed against those under future climate conditions for the mid (2045) and end (2075) of the 21st century. The time series of total streamflow discharge for projected climate conditions under the

selected climate scenario were analyzed for changes against that for baseline periods. To achieve this, measured streamflow from the USGS gage closest to the watershed outlet (USGS gage 02428400 in Figure 1) was utilized because there was no USGS gage at the main watershed outlet. The simulated average streamflow based on historical climate data for the baseline periods were compared to the simulated streamflow for future climate conditions, mainly to determine the changes in streamflow discharge values and trends in peak flow variabilities that could occur within the study area for the years 2045 and 2075.

3. Results and Discussion

3.1. Comparison of GCM Climate Variables with Observed Baseline Values

The selected GCMs predicted changes in average daily maximum temperature ranging between 24.29 °C and 27.42 °C, average daily minimum temperatures between 11.33 °C and 14.75 °C, and average daily precipitation between 3.62 and 3.99 mm for 2045. Predictions for 2075 showed changes ranging between 3.63 and 4.48 mm for average daily precipitation, 24.30 °C–27.98 °C for average daily maximum temperature, and 11.32 °C–14.62 °C for average minimum daily temperature. CESM1-BGC.1 predicted an increase in average daily precipitation, while HADGEM2-AO and CNRM-CM5 predicted decreases in average daily precipitation for 2045 compared to the 1980 baseline values. For 2075, both CESM1-BGC.1 and HadGEM2-AO.1 had predictions above the 1980 baseline value while CNRM-CM5 prediction was below the 1980 baseline value. CESM1-BGC.1 and HadGEM2-AO.1 predicted a rise in average daily minimum and maximum temperatures above the baseline temperatures years for both 2045 and 2075. CNRM-CM5 predicted a decrease in average daily maximum temperature for both 2045 and 2075 compared to 1980 baseline values and an increase in average minimum temperatures for both 2045 and 2075. The CNRM-CM5 model projected the lowest change in both temperature and precipitation while HADGEM2-AO projected the largest increase change for both climate variables. The summary of the daily average values and change statistics for historical baseline and projected climatic variables are shown in Table 3.

Table 3. GCM projected average daily climatic variables and percentage change to 1980 baseline values.

Climate Data Type	Precipitation (mm/day)	Precipitation Change (%)	Maximum Temperature (°C)	Maximum Temperature Change (%)	Minimum Temperature (°C)	Minimum Temperature Change (%)
Baseline_1980	3.93		24.42		10.69	
CNRM-CM5_2045	3.62	−7.89	24.29	−0.53	11.33	5.99
CESM1-BGC.1_2045	3.99	1.53	27.42	12.29	14.75	37.98
HADGEM2-AO.1_2045	3.91	−0.509	26.89	10.11	13.46	25.91
CNRM-CM5_2075	3.63	−7.63	24.3	−0.49	11.32	5.89
CESM1-BGC.1_2075	3.99	1.53	26.47	8.39	13.25	23.95
HADGEM2-AO.1_2075	4.48	13.99	27.98	14.58	14.62	36.76

3.2. SWAT Model Calibration, Validation Results and Performance

Calibration and validation processes were performed to ensure acceptable performance efficiency for the SWAT model. Measured streamflow data for USGS gage stations 02404400, 02413300, and 02425000 were used to calibrate (1995–2005) and validate (1985–1995) the SWAT model. Six sensitive parameters were modified to calibrate total streamflow, surface runoff, and baseflow. The calibrated parameters included CN2, ESCO, SOL_AWC, ALPHA BF, GWQMN, and GW_REVAP (Table 4). The calibrated model was further validated for the period 1985–1995. Statistical results for the monthly simulation

calibration and validation processes for the different gage stations within the watershed are listed in Table 5. For the calibration period, the SWAT simulated flow fitted well with the observed data. The resulting NSE values ranged between 0.83 and 0.89, R^2 values ranged between 0.88 and 0.90 for the calibration period; NSE for the validation period ranged from 0.78 to 0.94, and the R^2 ranged from 0.85 to 0.94. Figures 2 and 3 show the scatter plots and results of the objective functions for all three gages used for the calibration and validation.

Table 4. Default and calibrated Soil and Water Assessment Tool (SWAT) variables values used in the study.

Streamflow Calibration	Component Variables	Description of Variables	Default Value	Calibrated Value	Input File
Surface	CN2	SCS runoff curve number for moisture condition II	27–94	Reduced by 4 for all sub-basins	.mgt
	ESCO	Soil evaporation compensation factor	0.95	0.90	.bsn
	SOL_AWC	Soil available water capacity	0–0.35	Increased by 0.2	.sol
Baseflow	ALPHA_BF	Groundwater recession factor	0.048d	replaced with 0.3	.gw
	GW_REVAP	Groundwater revap coefficient	0.02	increased by 0.1	.gw
	GWQMIN	Threshold depth of water in the shallow aquifer required for return flow to occur	1000	800	.gw

**Table 5.** Model performance statistics for streamflow calibration and validation.

Station Location	USGS Gage No.	Drainage Area (km²)	Calibration		Validation	
			R^2	NSE	R^2	NSE
Choccolocco Creek at Jackson Shoal near Lincoln	2404400	1245	0.88	0.87	0.92	0.92
Little Tallapoosa River near Newell	2413300	1050	0.90	0.82	0.85	0.78
Cahaba River near Marion Junction	2425000	4567	0.90	0.89	0.94	0.94
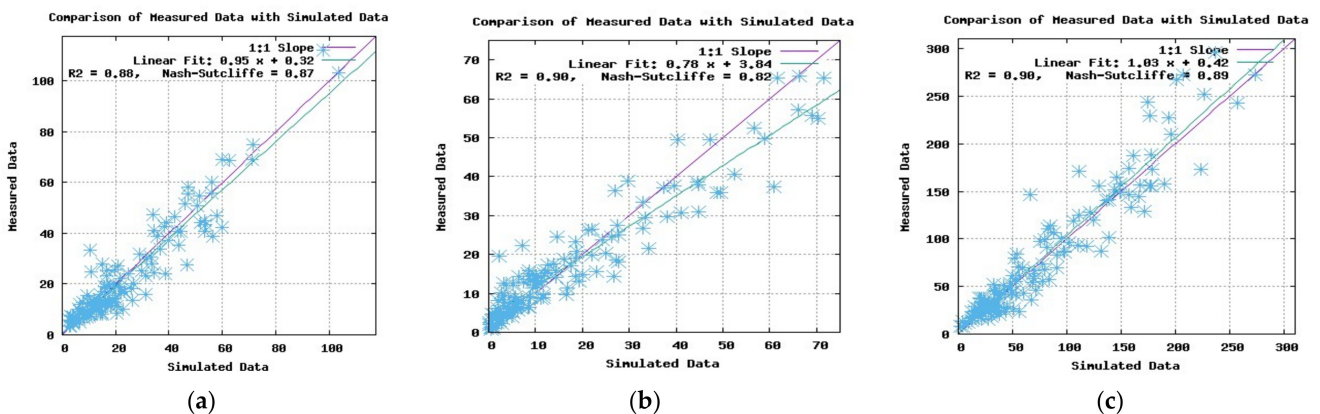
Figure 2. Scatter plot and objective functions for calibration period for (**a**) Choccolocco Creek at Jackson Shoal near Lincoln at USGS Gage 02404400, (**b**) Little Tallapoosa River near Newell near Newell at USGS Gage 24133000, and (**c**) Cahaba River near Marion Junction at USGS Gage 02425000.

While the model efficiency was good, SWAT produces poor simulation performance in dry seasons and for low flow situations. The research analyzed the lowest 10 percentile of flow for all three of the USGS gages used for the calibration (Figure 4). The scatter plots and objective functions showed that the model under-predicted streamflow discharge during

drought conditions or low flow situations. Low streamflow modeling and calibrations are better assessed specific models [62], over long calibration periods, and with a targeted multi-objective functions approach [63]. The ARB is a large basin, which has limited data for low flows, considering monthly simulation over the calibration period. Moreover, the research focused more on general streamflow changes, and SWAT model performance efficiency from the objective functions and goodness of fits of the hydrographs were high enough and appropriate for the climate change studies.
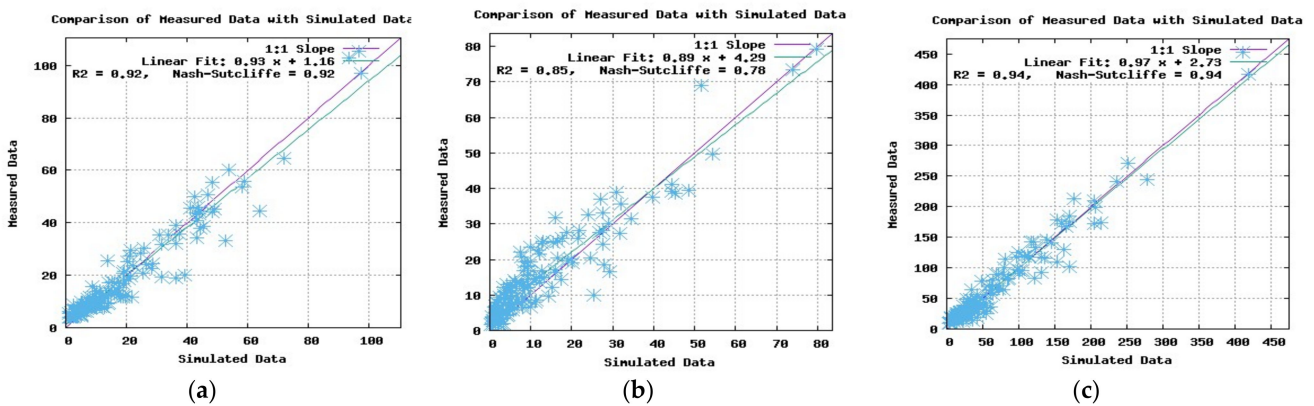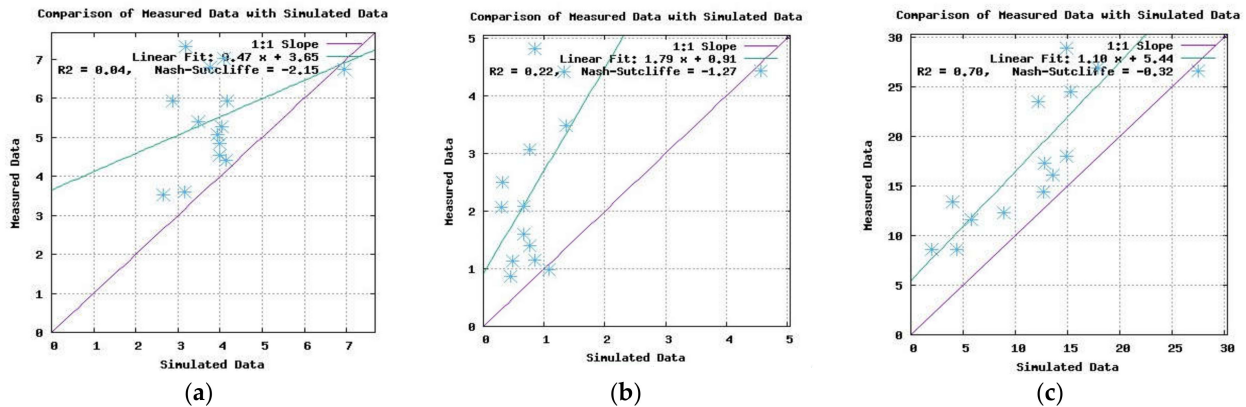

Figure 3. Scatter plot and objective functions for validation period for (**a**) Choccolocco Creek at Jackson Shoal near Lincoln at USGS Gage 02404400, (**b**) Little Tallapoosa River near Newell near Newell at USGS Gage 24133000, and (**c**) Cahaba River near Marion Junction at USGS Gage 02425000.

Figure 4. Scatter plot and objective functions for calibration of low flows (lower 10% percentile) for USGS gages (**a**) 02404400, (**b**) 24133000, and (**c**) 02425000.

The hydrographs (Figures 5–7) of the measured and simulated streamflow data for the calibration (1995–2005) and validation (1985–1995) periods show high goodness of fit and a reliable measure of the performance of the SWAT model.
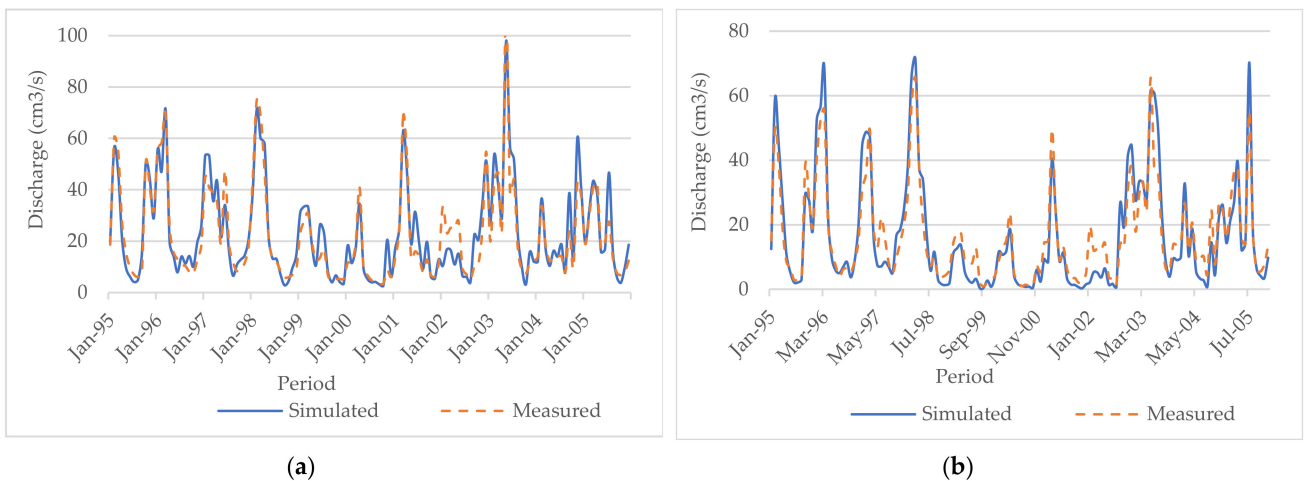
Figure 5. Monthly streamflow hydrographs for (**a**) calibration and (**b**) validation periods at USGS gage 02404400, on the Choccolocco Creek at Jackson Shoal near Lincoln.
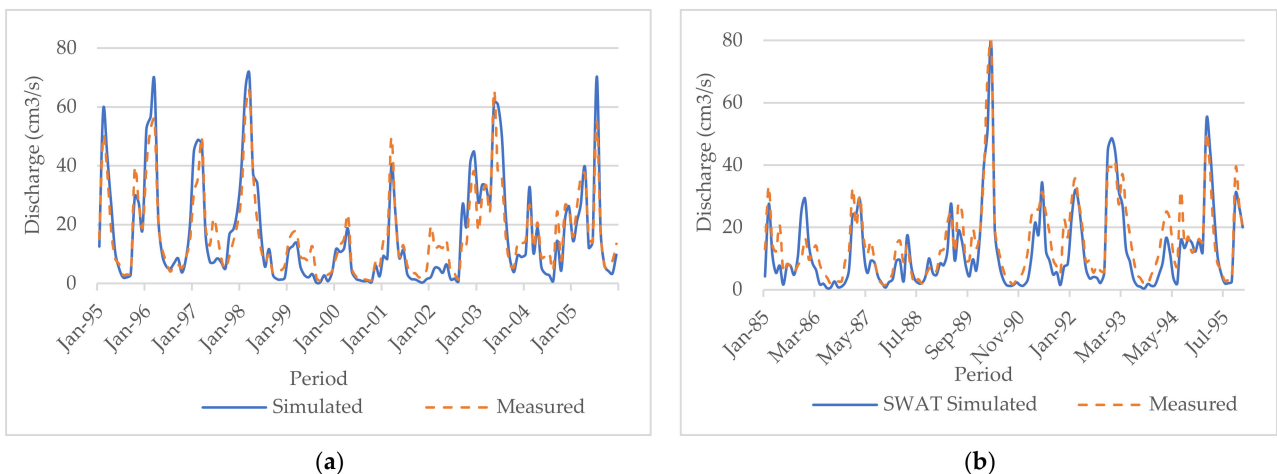
Figure 6. Monthly streamflow hydrographs for (**a**) calibration and (**b**) validation periods at USGS gage 02413300, on the Little Tallapoosa River near Newell.
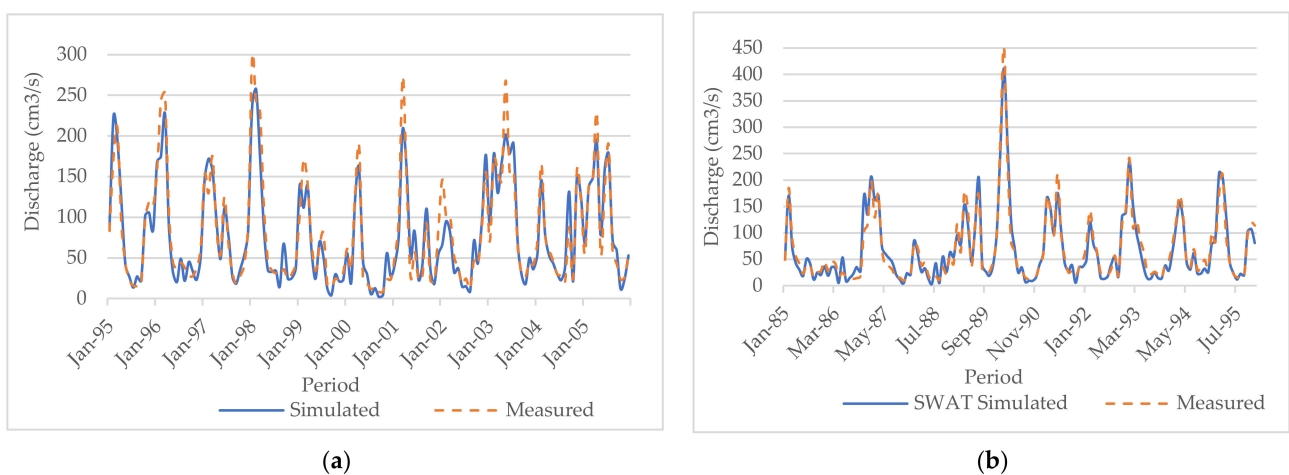
Figure 7. Monthly streamflow hydrographs for (**a**) calibration and (**b**) validation periods at USGS gage 02425000, on the Cahaba River near Marion Junction.

3.3. Analysis of Simulated Baseline against Future Streamflow

Figure 8a,b show the relative change in monthly streamflow discharge between 1980 baseline against 2045 and 2075 simulated streamflow discharge values, respectively. The majority of the relative changes ranged between −100% and 292% for 2045 and 2075, with only HADGEM for June 2075 showing a higher change above 421%. There were decreased changes up to 100% in streamflow for winter months for almost all scenarios and years, and general increases for spring, summer, and fall seasons.

(a)   (b)

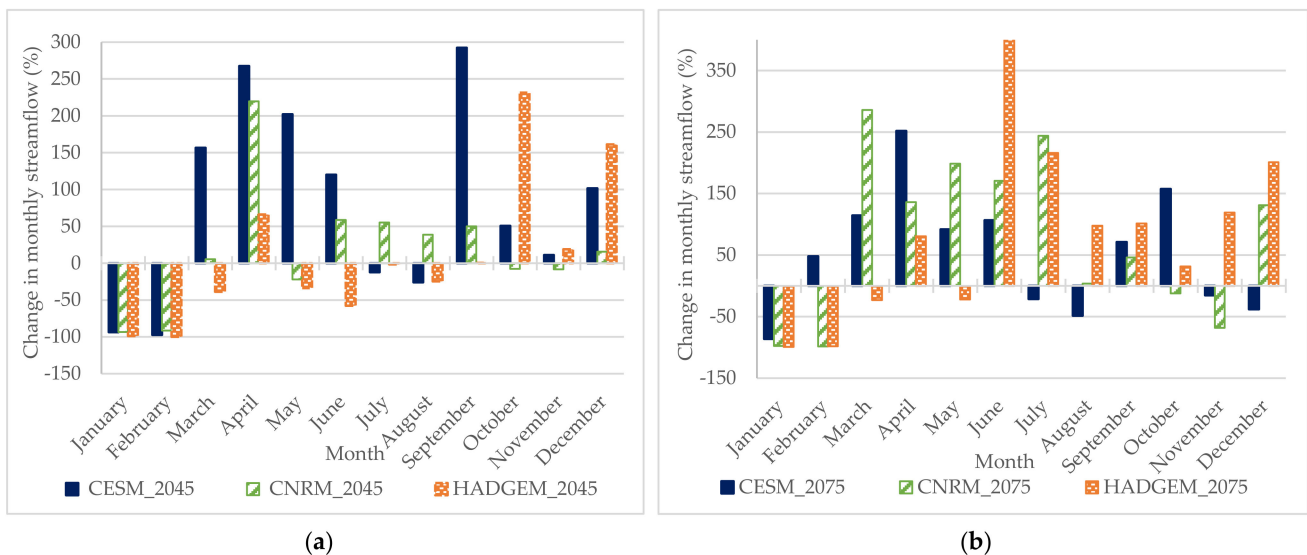**Figure 8.** Percentage changes in monthly streamflow for 2045 (**a**) and 2075 (**b**) relative to 1980 baseline values.

Figures 9 and 10 show the simulated average monthly streamflow hydrographs and Tables 6 and 7 show the average monthly streamflow discharge for the years 2045 and 2075, for the three GCMs against that for 1980 (baseline). For the year 2045, average streamflow discharge based on CNRM-CM5 and HADGEM2-AO.1 GCMs showed decreased values compared to 1980 baseline values, while CESM1-BGC.1 simulated the highest increase in streamflow discharge. For the year 2075, streamflow simulations based on all three GCMs had higher/increased average annual streamflow discharge compared to 1980 baseline value. However, the different GCMs streamflow hydrographs for both 2045 and 2075 had higher monthly variabilities and peak flows compared to 1980 baseline values, especially in winter, spring, and fall months Figures 9 and 10).

Seasonally, monthly streamflow increases between 50 and 250% were simulated for spring and autumn months with decreases in summer months for 2045. Spring and summer months for 2075 resulted in increased monthly streamflow between 50 and 300%, while autumn and spring months had decreased streamflow. The year 2075 is expected to have higher increased streamflow discharges with higher frequencies of variable peak flows. This result is unique to the research area and southern USA region, yet similar to other research findings that predicted future increases in temperature and moderate increases in precipitation will result in increases in future streamflow discharge and variability in average daily and monthly streamflow discharge [32]. While the results are prone to inherent uncertainties associated with the downscaling of the GCMs used, the hydrographs indicate that the ARB is likely to experience generally slight increase in streamflow discharge for 2045 and a relatively higher increase in 2075, especially during the winter and spring months, with higher frequencies in monthly peak flows.
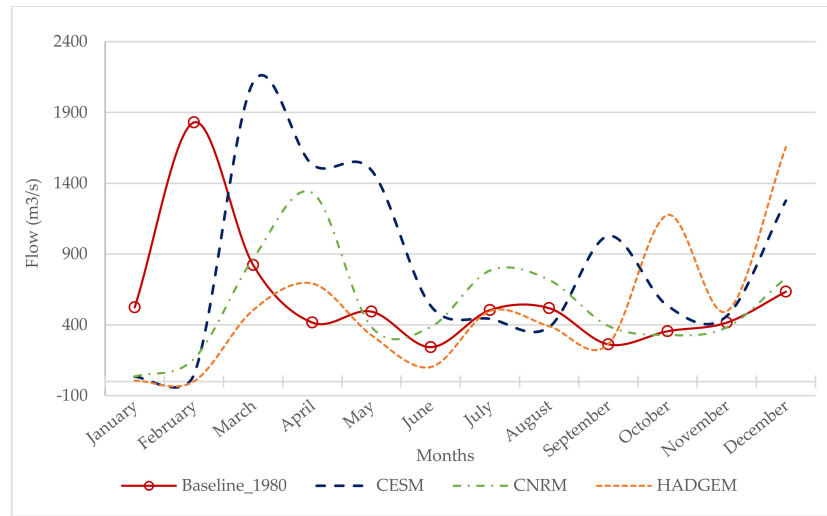
Figure 9. Simulated streamflow for1980 baseline and 2045 climate conditions.
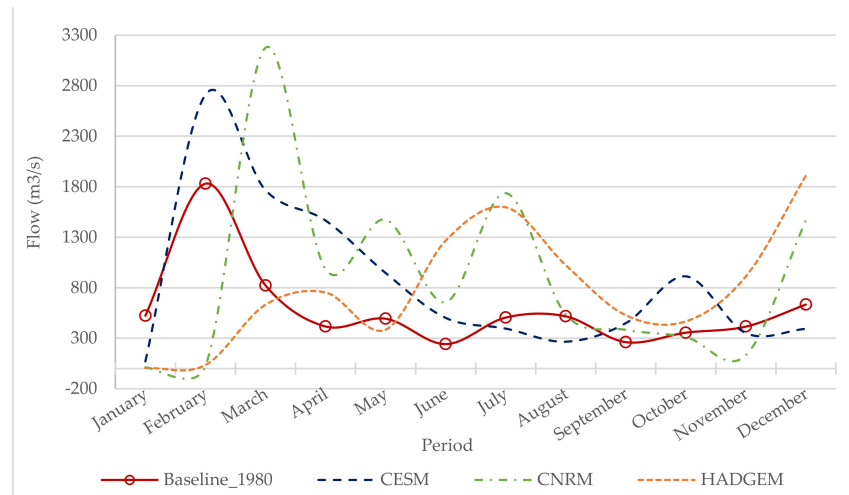
Figure 10. Simulated streamflow for1980 baseline and 2075 climate conditions.

Table 6. Comparison of simulated 1980 baseline monthly streamflow (m^3/s) to 2045 streamflow from the different General Circulation Models (GCMs).

Months	Baseline	CESM (m^3/s)	CNRM (m^3/s)	HADGEM (m^3/s)
January	523.58	33.61	35.15	6.19
February	1829.83	48.65	160.30	1.39
March	823.17	2112.00	867.90	504.60
April	416.82	1532.00	1333.00	692.00
May	493.85	1491.00	385.10	327.20
June	242.73	534.40	385.40	102.40
July	504.61	443.00	783.30	497.20
August	517.92	384.50	717.70	390.80
September	261.99	1028.00	392.90	262.90
October	354.82	534.90	328.10	1176.00
November	415.98	461.90	381.40	495.20
December	634.01	1277.00	731.80	1656.00
Average	584.94	823.41	541.84	509.32
Percentage change to 1980 baseline		40.77	−7.37	−12.93
Correlation between baseline and GCMs		−0.18	−0.20	−0.22

Table 7. Comparison of simulated 1980 baseline monthly streamflow (m^3/s) to 2075 streamflow from the different GCMs.

Months	1980 Baseline	CESM (m^3/s)	CNRM (m^3/s)	HADGEM (m^3/s)
January	523.58	71.79	11.42	4.73
February	1829.83	2710.00	25.84	35.61
March	823.17	1765.00	3176.00	632.00
April	416.82	1466.00	983.60	753.20
May	493.85	946.00	1474.00	384.80
June	242.73	501.70	657.00	1266.00
July	504.61	396.40	1736.00	1596.00
August	517.92	266.40	536.40	1024.00
September	261.99	448.30	382.80	528.40
October	354.81	913.10	311.50	466.80
November	415.98	351.40	132.10	911.20
December	634.01	392.50	1466.00	1908.00
Average	584.94	852.38	907.72	792.56
Percentage change to 1980 Baseline		45.72	55.18	35.49
Correlation between baseline and GCMs		0.79	−0.01	−0.35

4. Conclusions

The goal of the study was to use an integrated modeling approach that assimilated downscaled climate data into the SWAT model to estimate hydrologic responses to future climatic variability and change within the ARB. The approach utilized data from three CMIP5 GCMs under the IPCC medium emission scenario (RCP 4.5). After calibration and validation, the SWAT model performed well in simulating historical streamflow within the ARB, although the model under-predicted streamflow during dry season and low flow conditions.

The projected climate conditions based on downscaled GCMs were compared to 1980 baseline conditions at a USGS gage within the watershed. This comparison indicated that HADGEM and CESM projected increases in average minimum and maximum temperature for the future climate conditions. Conversely, the CNRM model indicated that the climatic variables would exhibit lower values, specifically temperature and precipitation when compared to variables for the baseline year. In general, the research results indicate situations of likely periods of increase and decrease in streamflow and water availability during the periods from mid to end of the 21st century. It was projected that changes in future climate conditions within the ARB could result in positive and negative changes in monthly streamflow compared to the baseline years. It is expected that there would be a slight increase in annual streamflow in 2045 and a considerable increase in 2075, under medium emission scenario. The results indicate situations of likely increase and decrease in mean monthly streamflow discharge and increase in the frequency and variability in peak flows during the periods from mid to end of the 21st century. Seasonally, monthly streamflow increases between 50 and 250% were simulated for spring and autumn months with decreases in summer months for 2045. Spring and summer months for 2075 resulted in increased monthly streamflow between 50 and 300%, while autumn and spring months had decreased streamflow. As discussed earlier, the result is prone to inherent uncertainties associated with the downscaling techniques used to convert GCM model outputs to scales that are useful for hydrological modeling applications. Moreover, since SWAT under-estimates low flows, this could have some level of uncertainty in the predicted changes in future streamflow variabilities.

Nevertheless, the findings indicate potential periods of both increased and decreased streamflow and resulting water availability impacts for the future mid and end of the century. Changing water budgets and availability including droughts and flooding situations could have adverse impacts on many sectors including agriculture, forestry, industries, and hydroelectric power systems. These potential impacts raise questions about the need for climate change adaptation to ensure efficient and sustainable management of water and

water-related disasters within the research watershed, Alabama, and the U.S. in general. The ARB is typical of many watersheds in the region; therefore, this study and results provide information on how similar watersheds might respond to future climate changes. Moreover, the study helps fill some of the research gaps and need for more information on how projected climate changes could impact water quantity in southeastern USA watersheds, specifically Alabama, which currently lacks studies related to climate changes.

Author Contributions: Conceptualization, J.E.Q., A.B.N., and S.F.; methodology, J.E.Q., S.F., and A.B.N.; software, A.B.N.; validation, J.E.Q. and A.B.N.; formal analysis, A.B.N., J.E.Q., and S.F.; investigation, J.E.Q. and A.B.N.; resources, A.B.N.; data curation, A.B.N.; writing—original draft preparation, A.B.N.; writing—review and editing, J.E.Q., A.B.N., S.F., R.A., and G.E.A.; visualization, J.E.Q. and S.F; supervision, J.E.Q.; project administration, J.E.Q.; funding acquisition, J.E.Q. All authors have read and agreed to the published version of the manuscript.

References

1. UN General Assembly. United Nations Framework Convention on Climate Change (UNFCCC) (1992): Resolution Adopted by the General Assembly, 20 January 1994, A/RES/48/189. Available online: https://www.refworld.org/docid/3b00f2770.html (accessed on 12 June 2018).
2. IPCC. *Climate Change 2001: Synthesis Report. A Contribution of Working Groups I, II, and III to the Third Assessment Report of the Integovernmental Panel on Climate Change*; Watson, R.T., the Core Writing Team, Eds.; Cambridge University Press: Cambridge, UK; New York, NY, USA, 2001; p. 398.
3. IPCC. *IPCC Special Report on Climate Change, Desertification, Land Degradation, Sustainable Land Management, Food Security, and Greenhouse Gas Fluxes in Terrestrial Ecosystems: Summary for Policymakers*. 2019. Available online: https://www.ipcc.ch/site/assets/uploads/2019/08/4.-SPM_Approved_Microsite_FINAL.pdf (accessed on 5 April 2019).
4. NASA. Scientific Consensus: Earth's Climate is Warming. Available online: https://climate.nasa.gov/scientific-consensus/ (accessed on 19 November 2020).
5. NASA Goddard Institute for Space Studies (GISS): Facts. 2020. Available online: https://climate.nasa.gov/vital-signs/global-temperature/ (accessed on 1 November 2020).
6. Allen, M.R.; Dube, O.P.; Solecki, W.; Aragón-Durand, F.; Cramer, W.; Humphreys, S.; Kainuma, M.; Kala, J.; Mahowald, N.; Mulugetta, Y.; et al. *Framing and Context. In Global Warming of 1.5 °C. An IPCC Special Report on the Impacts of Global Warming of 1.5 °C above Pre-Industrial Levels and Related Global Greenhouse Gas Emission pathways, in the Context of Strengthening the Global Response to the Threat of Climate Change, Sustainable Development, and Efforts to Eradicate Poverty*; Masson-Delmotte, V., Zhai, P., Pörtner, H.-O., Roberts, D., Skea, J., Shukla, P.R., Pirani, A., Moufouma-Okia, W., Péan, C., Pidcock, R., et al., Eds.; The Intergovernmental Panel on Climate Change: Geneva, Switzerland, 2018.
7. Seneviratne, S.I.; Nicholls, N.; Easterling, D.; Goodess, C.M.; Kanae, S.; Kossin, J.; Luo, Y.; Marengo, J.; McInnes, K.; Rahimi, M.; et al. Changes in climate extremes and their impacts on the natural physical environment. In *Managing the Risks of Extreme Events and Disasters to Advance Climate Change Adaptation*; Field, C.B.V., Barros, T.F., Stocker, D., Qin, D.J., Dokken, K.L., Ebi, M.D., Mastrandrea, K.J., Mach, G.-K., Plattner, S.K., Allen, M., Eds.; A Special Report of Working Groups I and II of the Intergovernmental Panel on Climate Change (IPCC); Cambridge University Press: Cambridge, UK; New York, NY, USA, 2012; pp. 109–230.
8. IPCC. *Climate Change Synthesis Report Summary Chapter for Policymakers*; IPCC: Geneva, Switzerland, 2014.
9. UNESCO. *The impact of global change on water resources: The Response of UNESCO's International Hydrologic Programme*; Division of Water Sciences: Paris, France, 2011. Available online: https://unesdoc.unesco.org/ark:/48223/pf0000192216 (accessed on 5 December 2020).
10. Bates, B.C.; Kundzewicz, Z.W.; Wu, S.; Palutikof, J.P. (Eds.) *Climate Change and Water. Technical Paper of the Intergovernmental Panel on Climate Change*; IPCC Secretariat: Geneva, Switzerland, 2008.
11. Gleick, P.H. Water- The potential consequences of climate variability and change for the water resources of the United States. In *The Report of the Water Sector Assessment Team of the National Assessment of the Potential Consequences of Climate Variability and Change for the U.S. Global Change Research Program*; Peter, H.G., Ed.; Pacific Institute for Studies in Development, Environment, and Security: Oakland, CA, USA, 2000; pp. 126–151. ISBN 1-893790-04-5.

12. U.S. Environmental Protection Agency (EPA). *Climate Change Indicators in the United States*, 4th ed.; EPA 430-R-16-004; 2016. Available online: www.epa.gov/climate-indicators (accessed on 20 May 2020).

13. Weiskopf, S.R.; Rubenstein, M.A.; Crozier, L.G.; Gaichas, S.; Griffis, R.; Halofsky, J.E.; Hyde, K.J.W.; Morelli, T.L.; Morisette, J.T.; Muñoz, R.C.; et al. Climate change effects on biodiversity, ecosystems, ecosystem services, and natural resource management in the United States. *Sci. Total Environ.* **2000**, *733*. [CrossRef] [PubMed]

14. Pitz, C.F. Predicted Impacts of Climate Change on Groundwater Resources of Washington State. Department of Ecology, The State of Washington. Report No. 16-03-006; 2016. Available online: https://fortress.wa.gov/ecy/publications/documents/1603006.pdf (accessed on 7 April 2019).

15. Vincent, W.F. *Effects of Climate Change on Lakes*; Elsevier Inc.: Quebec City, QC, Canada, 2009; pp. 55–60.

16. Lins, H.F. *USGS Hydro-Climatic Data Network 2009 (HCDN-2009)*; U.S. Geological Survey Fact Sheet 2012-3047; U.S. Geological Survey: Reston, VA, USA, 2009. Available online: https://pubs.usgs.gov/fs/2012/3047/pdf/fs2012-3047.pdf (accessed on 8 June 2020).

17. U.S. Geological Survey (USGS). *Analysis of Data from the National Water Information System*; U.S. Geological Survey (USGS): Reston, VA, USA, 2006.

18. Hoegh-Guldberg, O.; Jacob, D.; Taylor, M.M.; Bindi, M.; Brown, S.; Camilloni, I.; Diedhiou, A.; Djalante, R.; Ebi, K.L.; Engelbrecht, F.; et al. Impacts of 1.5 °C global warming on natural and human systems. In *Global Warming of 1.5 °C. An IPCC Special Report on the Impacts of Global Warming of 1.5 °C above Pre-Industrial Levels and Related Global Greenhouse Gas Emission Pathways, in the Context of Strengthening the Global Response to the Threat of Climate Change, Sustainable Development, and Efforts to Eradicate Poverty*; Masson-Delmotte, V., Zhai, P., Pörtner, H.-O., Roberts, D., Skea, J., Shukla, P.R., Pirani, A., Moufouma-Okia, W., Péan, C., Pidcock, R., et al., Eds.; 2018; In Press.

19. Ali, R.; Kuriqi, A.; Abubaker, S.; Kisi, O. Long-Term Trends and Seasonality Detection of the Observed Flow in Yangtze River Using Mann-Kendall and Sen's Innovative Trend Method. *Water* **2019**, *11*, 1855. [CrossRef]

20. Kuriqi, A.; Ali, R.; Pham, Q.B.; Gambini, J.M.; Gupta, V.; Malik, A.; Linh, N.T.T.; Joshi, Y.; Anh, D.T.; Dong, X.; et al. Seasonality shift and streamflow flow variability trends in central India. *Acta Geophys.* **2020**, *68*, 1461–1475. [CrossRef]

21. Pathak, T.; Maskey, M.; Dahlberg, J.; Kearns, F.; Bali, K.; Zaccaria, D. Climate change trends and impacts on California agriculture: A detailed review. *Agronomy* **2018**, *8*, 25. [CrossRef]

22. Mirzabaev, A.; Wu, J.; Evans, J.; García-Oliva, F.; Hussein, I.A.G.; Iqbal, M.H.; Kimutai, J.; Knowles, T.; Meza, F.; Nedjraoui, D.; et al. Desertification. In *Climate Change and Land: An IPCC Special Report on Climate Change, Desertification, Land Degradation, Sustainable Land Management, Food Security, and Greenhouse Gas Fluxes in Terrestrial Ecosystems*; Shukla, P.R., Skea, J., Calvo Buendia, E., Masson-Delmotte, V., Pörtner, H.-O., Roberts, D.C., Zhai, P., Slade, R., Connors, S., van Diemen, R., et al., Eds.; IPCC: Geneva, Switzerland, 2019.

23. IPCC. *Climate Change 2014: Synthesis Report Summary for Policymakers.* Contribution of Working Groups I, II and III to the Fifth Assessment Report of the Intergovernmental Panel on Climate Change. Available online: https://www.ipcc.ch/site/assets/uploads/2018/02/AR5_SYR_FINAL_SPM.pdf (accessed on 12 August 2020).

24. Randall, D.A.; Wood, R.A.; Bony, S.; Colman, R.; Fichefet, T.; Fyfe, J.; Kattsov, V.; Pitman, A.; Shukla, J.; Srinivasan, J.; et al. *Climate Models and Their Evaluation*; Cambridge University Press: Cambridge, UK, 2007.

25. Alexander, L.V.; Arblaster, J.M. Historical and projected trends in temperature and precipitation extremes in Australia in observations and CMIP5. *Weather Clim. Extremes* **2017**, 34–56. [CrossRef]

26. Li, Z.; Jin, J. Evaluating climate change impacts on streamflow variability based on a multisite multivariate GCM downscaling method. *Hydrol. Earth Syst. Sci. Discuss.* **2017**, 1–22. [CrossRef]

27. Miao, C.; Duan, Q.; Sun, Q.; Huang, Y.; Kong, D.; Yang, T.; Gong, W. Assessment of CMIP5 climate models and projected temperature changes over Northern Eurasia. *Environ. Res. Lett.* **2004**, *9*. [CrossRef]

28. Koch, J.; Cornelissen, T.; Fang, Z.; Bogena, H.; Diekkrüger, B.; Kollet, S.; Stisen, S. Inter-comparison of three distributed hydrological models with respect to seasonal variability of soil moisture patterns at a small forested catchment. *J. Hydrol.* **2016**, *533*, 234–249. [CrossRef]

29. Leta, O.T.; El-Kadi, A.I.; Dulai, H.; Ghazal, K.A. Assessment of climate change impacts on water balance components of Heeia watershed in Hawaii. *J. Hydrol. Reg. Stud.* **2016**, *8*, 182–197. [CrossRef]

30. Mohammed, I.N.; Bomblies, A.; Wemple, B.C. The use of CMIP5 data to simulate climate change impacts on flow regime within the Lake Champlain Basin. *J. Hydrol. Reg. Stud.* **2016**, *3*, 160–186. [CrossRef]

31. Sunde, M.G.; He, H.S.; Hubbart, J.A.; Urban, M.A. Integrating downscaled CMIP5 data with a physically based hydrologic model to estimate potential climate change impacts on streamflow processes in a mixed-use watershed. *Hydrol. Proc.* **2017**, *31*, 1790–1803. [CrossRef]

32. Su, B.; Huang, J.; Zeng, X.; Gao, C.; Jiang, T. Impacts of climate change on streamflow in the upper Yangtze River basin. *Clim. Change* **2017**, *141*, 533–546. [CrossRef]

33. Kleinschmidt, E. Alabama River Basin Management Plan. 2005. Available online: http://www.adem.state.al.us/programs/water/nps/files/AlabamaBMP.pdf (accessed on 4 July 2020).

34. Murgulet, D.G.; Tick, G. The extent of saltwater intrusion in southern Baldwin County, Alabama. *Environ. Geol.* **2008**, *55*, 1235–1245. [CrossRef]

35. Sinclair, W.C. Sinkhole development resulting from ground water withdrawal in the Tampa Area, Florida. In *USGS Water-Resources Investigations Report 81-50*; 1982. Available online: https://pubs.usgs.gov/wri/1981/0050/report.pdf (accessed on 14 June 2020).

36. Runkle, J.; Kunkel, K.; Stevens, L.; Frankson, R. Alabama State climate summary. In *NOAA Technical Report NESDIS 149-AL*; March 2019 Revision; Auburn University: Auburn, AL, USA, 2017; 4 pp.

37. Karl, T.R.; Melillo, J.M.; Peterson, T.C. Global Climate Change Impacts in the United States. 2009; Volume 54. Available online: www.globalchange.gov/usimpacts (accessed on 12 August 2018).

38. IPCC. *Summary for Policymakersin: Managing the Risks of Extreme Events and Disasters to Advance Climate Change Adaptation*; Field, C.B.V., Barros, T.F., Stocker, D., Qin, D.J., Dokken, K.L., Ebi, M.D., Mastrandrea, K.J., Mach, G.-K., Plattner, S.K., Allen, M., Eds.; A Special Report of Working Groups I and II of the Intergovernmental Panel on Climate Change; Cambridge University Press: Cambridge, UK; New York, NY, USA, 2012; pp. 14–15.

39. U.S. Army Corps of Engineers (USACE). *Environmental Data Inventory, State of Alabama: Mobile, Alabama*; USACE: Washington, DC, USA, 1998.

40. Gangrade, S.; Kao, S.-C.; McManamay, R.A. Multi-model Hydroclimate Projections for the Alabama-Coosa-Tallapoosa River Basin in the Southeastern United States. *Nat. Res. Sci. Rep.* **2020**, *10*. [CrossRef] [PubMed]

41. Arnold, J.G.; Srinivasan, R.; Muttiah, R.S.; Williams, J.R. Large area hydrologic modeling and assessment part I: Model development. *J. Am. Water Resour. Assoc.* **1998**, *34*, 73–89. [CrossRef]

42. Krysanova, V.; White, M. Advances in water resources assessment with SWAT—An overview. *Hydrol. Sci. J.* **2015**, *60*, 771–783. [CrossRef]

43. Neitsch, S.L.; Arnold, J.G.; Kiniry, J.R.; Srinivasan, R.; Williams., J.R. *Soil and Water Assessment Tool, User Manual, Version 2000*; Grassland, Soil and Water Research Laboratory-Agricultural Research Service: Temple, TX, USA. Available online: https://swat.tamu.edu/media/1294/swatuserman.pdf (accessed on 8 January 2019).

44. Bennett, J.C.; Grose, M.R.; Corney, S.P.; White, C.J.; Holz, G.K.; Katzfey, J.J.; Post, D.A.; Bindoff, N.L. Performance of an empirical bias-correction of a high-resolution climate dataset. *Int. J. Climatol.* **2014**, *34*, 2189–2204. [CrossRef]

45. Aryal, Y.; Zhu, J. Multimodel ensemble projection of meteorological drought scenarios and connection with climate based on spectral analysis. *Int. J. Climatol.* **2020**, *40*, 3360–3379. [CrossRef]

46. Zhao, T.; Dai, A. The magnitude and causes of global drought changes in the twenty-first century under a low–moderate emissions scenario. *J. Clim.* **2015**, *28*, 4490–4512. [CrossRef]

47. Rupp, D.E. An evaluation of 20th century climate for the Southeastern United States as simulated by Coupled Model Intercomparison Project Phase 5 (CMIP5) global climate models. U.S. Geological Survey Open-File Report; U.S. Geological Survey: Reston, VA, USA, 2016; 32 p. [CrossRef]

48. Voldoire, A.; Sanchez-Gomez, E.; Salas, D.; Mélia, Y.; Decharme, B.; Cassou, C.; Sénési, S.; Valcke, S.; Beau, I.; Alias, A.; et al. The CNRM-CM5.1 global climate model: Description and basic evaluation. *Clim. Dyn.* **2011**, *40*, 2091–2121. [CrossRef]

49. Long, M.C.; Lindsay, K.S.; Peacock, S.; Moore, J.K.; Doney, S.C. Twentieth-Century Oceanic Carbon Uptake and Storage in CESM1(BGC). *J. Clim.* **2013**, *26*, 6775–6800. [CrossRef]

50. Bellouin, N.; Collins, W.J.; Culverwell, I.D.; Halloran, P.R.; Hardiman, S.C.; Hinton, T.J.; Jones, C.D.; McDonald, R.E.; McLaren, A.J.; O'Connor, F.M.; et al. The HadGEM2 family of Met Office Unified Model climate configurations. *Geosci. Model Devel.* **2011**, *4*, 723–757.

51. Thomson, A.M.; Calvin, K.V.; Smith, S.J.; Kyle, G.P.; Volke, A.; Patel, P.; Delgado-Arias, S.; Bond-Lamberty, B.; Wise, M.A.; Clarke, L.E.; et al. RCP4.5: A pathway for stabilization of radiative forcing by 2100. *Clim. Chang.* **2011**, *109*, 77. [CrossRef]

52. Maurer, E.P. Uncertainty in hydrologic impacts of climate change in the Sierra Nevada, California under two emissions scenarios. *Clim. Chang.* **2007**, *82*, 309–325. [CrossRef]

53. Quansah, J.E.; Engel, B.A.; Chaubey, I. Tillage Practices Usage in Early Warning Prediction of Atrazine Pollution. *Transac. ASABE* **2008**, *51*, 1311–1321. [CrossRef]

54. Arnold, J.G.; Moriasi, D.N.; Gassman, P.W.; Abbaspour, K.C.; White, M.J.; Srinivasan, R.; Santhi, C.; Harmel, R.D.; van Griensven, A.; Van Liew, N.W.; et al. SWAT: Model use, calibration, and validation. *Trans. ASABE* **2012**, *55*, 1491–1508. [CrossRef]

55. Nash, J.E.; Sutcliffe, J.V. River flow forecasting through conceptual models: Part 1. A discussion of principles. *J. Hydrol.* **1970**, *10*, 282–290. [CrossRef]

56. Moriasi, D.N.; Arnold, J.G.; Van Liew, M.W.; Bingner, R.L.; Harmel, R.D.; Veith, T.L. Model evaluation guidelines for systematic quantification of accuracy in watershed simulations. *Trans. ASABE* **2007**, *50*, 885–900. [CrossRef]

57. Krause, P.; Boyle, D.P.; Base, F. Comparison of different efficiency criteria for hydrological model assessment. *Adv. Geosci.* **2005**, *5*, 89–97. [CrossRef]

58. McCuen, R.H. Assessment of Hydrological and statistical significance. *J. Hydrol. Eng. ASCE* **2016**, *21*. [CrossRef]

59. Mann, H.B. Nonparametric tests against trend. *Econometrica* **1945**, *13*, 245–259. [CrossRef]

60. Sen, P. Estimated of the regression coefficient based on Kendall's Tau. *J. Am. Stat. Assoc.* **1968**, *39*, 1379–1389. [CrossRef]

61. Theil, H. A rank-invariant method of linear and polynomial regression analysis, I, II, III. In *Henri Theil's Contributions to Economics and Econometrics*; Volume 23, Springer: Dordrecht, The Netherlands, 1992. [CrossRef]

62. Parra, V.; Arumí, J.L.; Muñoz, E. Identifying a Suitable Model for Low-Flow Simulation in Watersheds of South-Central Chile: A Study Based on a Sensitivity Analysis. *Water* **2019**, *11*, 1506. [CrossRef]

63. Garcia, F.; Folton, N.; Oudin, L. Which objective function to calibrate rainfall–runoff models for low-flow index simulations? *Hydrol. Sci. J.* **2017**. [CrossRef]

Article

Projected Changes in Water Year Types and Hydrological Drought in California's Central Valley in the 21st Century

Minxue He *, Jamie Anderson, Elissa Lynn and Wyatt Arnold

California Department of Water Resources, 1416 9th Street, Sacramento, CA 95814, USA;
Jamie.Anderson@water.ca.gov (J.A.); Elissa.Lynn@water.ca.gov (E.L.); Wyatt.Arnold@water.ca.gov (W.A.)
* Correspondence: kevin.he@water.ca.gov; Tel.: +1-916-651-9634

Abstract: The study explores the potential changes in water year types and hydrological droughts as well as runoff, based on which the former two metrics are calculated in the Central Valley of California, United States, in the 21st century. The latest operative projections from four representative climate models under two greenhouse-gas emission scenarios are employed for this purpose. The study shows that the temporal distribution of annual runoff is expected to change in terms of shifting more volume to the wet season (October–March) from the snowmelt season (April–July). Increases in wet season runoff volume are more noticeable under the higher (versus lower) emission scenario, while decreases in snowmelt season runoff are generally more significant under the lower (versus higher) emission scenario. In comparison, changes in the water year types are more influenced by climate models rather than emission scenarios. When comparing two regions in the Central Valley, the rain-dominated Sacramento River region is projected to experience more wet years and less critical years than the snow-dominated San Joaquin River region due to their hydroclimatic and geographic differences. Hydrological droughts in the snowmelt season and wet season mostly exhibit upward and downward trends, respectively. However, the uncertainty in the direction of the trend on annual and multi-year scales tends to be climate-model dependent. Overall, this study highlights non-stationarity and long-term uncertainty in these study metrics. They need to be considered when developing adaptive water resources management strategies, some of which are discussed in the study.

Keywords: water year type; hydrological drought; climate change; adaptive strategies; Central Valley

1. Introduction

There is growing evidence that global warming is changing the water cycle in terms of altering the spatial and temporal distributions of water availability worldwide. Specifically, changes in the magnitude, timing, frequency, and form of precipitation (rainfall/snowfall) and runoff (rainfed runoff/snow melt/glacier melt) have been widely observed [1–9]. The changes are projected to intensify through the end of this century [10–15]. These changes have profound impacts on water resources management, particularly in water-limited arid or semi-arid environments, including the State of California, United States (U.S.).

As a globally important economy, California is the most populous State and one of the most productive agriculture areas in the United States [16]. The State has built a vast and complex water storage and transfer system to redistribute water from the wetter northern half of the State to the drier southern half, which has a higher population and water demand and, from the wet season to the dry season, when the demand is the highest but precipitation is minimal, to support its population/agriculture and sustain its economy. The system contains hundreds of dams, reservoirs, pumping and hydropower plants, and thousands of kilometers of delivery aqueducts, canals, conduits, and tunnels [17,18]. Operations of the system are regulated by state and federal rules and decisions to ensure that the flow and water quality standards are met for municipal, agricultural, and environmental usage. These include the Water Right Decision 1641 (D1641) of the California State Water Resources Control Board [19] and the more recent Biological Opinion (BO) of

U.S. Fish and Wildlife Service [20], among others. The flow and water quality objectives prescribed in D1641 and BO vary across different water year types (WYTs). WYTs are classifications that designate the wetness or dryness (and thus water availability) of the interested regions [21]. In California, five different types of water years are defined (wet, above normal, below normal, dry, and critical) based on the wet season (October–March) runoff and snowmelt season (April–July) runoff, together with preset runoff thresholds. During the wet season, flood management is typically one of the highest priorities for water managers; during the snowmelt season, water supply is normally a bigger concern. Before snowmelt season starts or during the snowmelt season when the full April–July runoff is not observable, the forecasted April–July runoff is applied instead. In operations, a set of regression equations is used to forecast a range of April–July runoff volumes with different occurrence probabilities (specifically a low, a most likely, and a high forecast with 90%, 50%, and 10% exceedance probabilities, respectively) to account for hydroclimatic uncertainty in the period from the forecast time to the end of July [22–25]. In addition to WYTs and flow volumes (e.g., with different exceedance probabilities), drought indices have also been explored or applied to inform water operations, particularly drought response and planning practices in California. These indices include the Palmer Drought Severity Index [26], deciles [27], Standard Precipitation Index [28], Aggregate Drought Index [29], Standardized Runoff Index [30], Standardized Precipitation-Evapotranspiration Index [31], Multivariate Standardized Drought Index [32], and Groundwater Drought Index [33].

The determination and application of the water year classification, runoff quantiles, and drought indices are based on the stationarity assumption that the future hydroclimate in California would mimic the historical conditions. However, existing research has reported non-stationary changes in hydroclimatic variables across the State. The changes include warming [34,35], more rain versus snow in precipitation partition [36], declining snowpack [3,37], earlier streamflow timing [38–40], among others. There is a strong consensus that these changes are expected to manifest themselves in the future [41–43], while there is much less certainty on the changing magnitudes that largely depend on future greenhouse gas emissions [44,45]. A worldwide collaborative framework, titled Coupled Model Intercomparison Project (CMIP), was designed to better understand future climate uncertainty in a multi-model and multi-emission scenario context [46]. The CMIP is developed in phases and it provides multi-model projected climate dataset (representing the start-or-the-art climate science at the time when a specific phase is developed) to support regional, national, and international assessment of climate change. The project is currently in its sixth phase (CMIP6) [47]. However, phase five (CMIP5) is the most recent completed and operative phase [48]. Based on downscaled CMIP5 climate projections through the end the current century, California developed its latest (the fourth) climate assessment (CCCA4) to guide statewide climate adaptive planning activities.

A number of studies have applied the CCCA4 dataset in assessing the potential changes in California's future hydroclimate and their impacts on the State's water operations. Refs. [49,50] examined changes in precipitation and temperature. They reported consistent warming across all of the climate models with large uncertainties in precipitation changes on seasonal and annual scales. Refs. [51,52] investigated changes in future streamflow. They projected wetter wet season and drier dry seasons in the future. Refs. [53,54] assessed the impacts of projected hydroclimatic changes on the State's water system. They concluded that, under the current system and operating rules, water deliveries would become less reliable. Ref. [50] explored trends in the Standardized Precipitation-Evapotranspiration Index and noted increasing meteorological drought risks across the State particularly in dry regions. Nevertheless, no studies have analyzed the potential changes in hydrological droughts, runoff quantiles, as well as water year type distributions in California based on the latest operative CCCA4 dataset. Ref. [21] evaluated how climate change affects water year classification in the State. However, an older generation of climate projections (from the third phase of CMIP, CMIP3) was utilized in that study. CMIP5 has advances over CMIP3 in terms of model spatial resolution, concept of future

radiative forcing, available variables, among others [55]. When compared to CMIP3 climate projections, the CIMP5 projections have significant improvements on key Pacific climate patterns and they show different climatic characteristics (wetter and warmer) in the Sierra Nevada region of California [56,57].

The current study aims to fill this gap. Specifically, the study examines the potential changes in water year type distribution, as well as hydrological drought and different ranges of runoff (at temporal scales that are meaningful to practical water resources management operations in California) through the 21st century with non-stationary, but highly uncertain, climatic conditions. The uncertainty in future climate is represented by a set of climate models from the latest operative CMIP5 under two different greenhouse gas emission scenarios. The rest of the paper is structured, as follows. Section 2 describes the study area, variables, dataset, and metrics in detail. Section 3 presents the results and findings of the study. Section 4 discusses the potential causes and implications of these findings as well as future work. Section 5 summarizes the study.

2. Materials and Methods

2.1. Study Area

The Central Valley of California is a major water supply source for the State. It contains the largest two river systems in the State, including the Sacramento River region on the north and San Joaquin River region on the south (Figure 1). There is a large variation in elevation in the Valley, which ranges from near sea level to about 3800 m. The Valley has a Mediterranean-like climate, with hot/dry summers and cool/wet winters. The majority of annual precipitation in the Valley occurs in the wet season (October–March). The high elevations of the Valley typically receive more (than lower elevations) precipitation, due to orographic effects during storms. The storm characteristics dictate the freezing elevation above (below) which precipitation falls as snowfall (rainfall). Rainfall fuels winter runoff, while the accumulated snow in high elevations melts out in the spring and early summer. Rain runoff and snowmelt both drain to major reservoirs that serve multiple purposes, including flood management (during the wet season) and water supply management (rest of the year). In water planning and management practices, the California Department of Water Resources (DWR) tracks the runoff of four major watersheds in the Sacramento River region: Sacramento River above Bend Bridge (SBB), Feather River at Oroville (FTO), Yuba River at Smartville (YRS), and American River at Folsom (AMF) as well as and four important watersheds in the San Joaquin River region: Stanislaus River at New Melones (SNS), Tuolumne River at Don Pedro (TLG), Merced River at Lake McClure (MRC), and San Joaquin River at Millerton Lake (SJF). The sum of runoff from these four watersheds in each region is used to represent the overall wetness of each region in practice.

Sacramento watersheds have lower elevations as compared to the San Joaquin watersheds, and, thus, are warmer in general [52]. Among four Sacramento watersheds, the median elevation varies from about 1357 m (SBB) to 1611 m (FTO). In contrast, the median elevation ranges from around 1549 m (MRC) to 2345 m (SJF) in San Joaquin watersheds. Overall, Sacramento watersheds receive more precipitation and are geographically larger in size. Therefore, the average total average annual runoff of Sacramento four rivers (21.6 billion m^3) is much larger when compared to that of the San Joaquin four rivers (7.1 billion m^3). However, runoff from the San Joaquin watersheds is dominated by snowmelts, due to the relatively higher watershed elevations. Snowmelt runoff, which is typically represented by runoff of the snowmelt season from April–July, accounts for two-thirds of the annual total runoff for San Joaquin four rivers (versus about one-third for Sacramento four rivers).

2.2. Study Variables and Dataset

This study focuses on Sacramento four rivers' total runoff (SAC4) and San Joaquin four rivers' total runoff (SJQ4) at three temporal scales that are important to water operations in California. These include the annual scale, wet season (October–March) scale, and snowmelt season (April–July) scale. Runoff volumes at these three scales are applied in

calculating operational water supply indices for Sacramento River region and San Joaquin River region, which will be detailed in Section 2.3. When looking at projected trends in hydrological drought (Section 3.3), the study also explores multi-year scales that range from two to five years, since droughts historically occur at these multi-year scales in California.
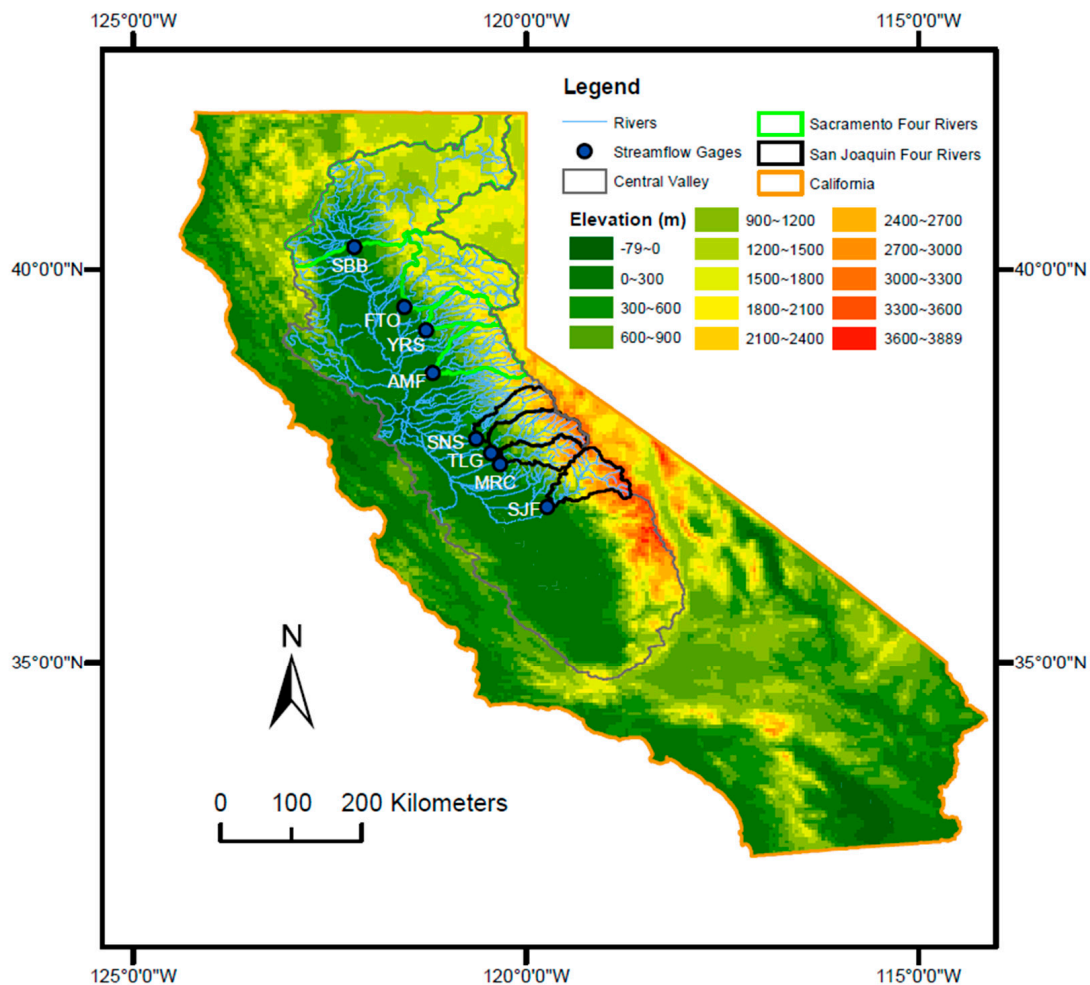
Figure 1. Location map showing four rivers in the Sacramento River region and four rivers in the San Joaquin River region in the Central Valley of California.

Historical SAC4 and SJQ4 runoff data are derived from the monthly full natural flow record for each study watershed. Those are operational data that are quality-controlled and generally available since the 1900s (data sources provided in Appendix A). The projected SAC4 and SJQ4 runoff are obtained from the recently released California's Fourth Climate Change Assessment (CCCA4; http://cal-adapt.org/). CCCA4 provides "the scientific foundation for understanding climate-related vulnerability at the local scale and informing resilience actions" across California [58]. CCCA4 produced a set of datasets for that purpose. The datasets, including statewide daily downscaled (to 1/16th degree) precipitation and temperature projections from 2006–2099 [59], as well as corresponding daily runoff projections at each study watershed derived via the Variable Infiltration Capacity (VIC) hydrologic model (that is driven by those precipitation/temperature projections) [60]. Those precipitation and temperature projections were generated via an ensemble of 32 general circulation models (GCMs) that participated in the Coupled Model Intercomparison Project Phase 5 (CMIP5) under two emission scenarios, named Representative Concentration Pathways (RCP) 4.5 (lower emission scenario) and RCP 8.5 (high emission scenario). The DWR Climate Change Technical Advisory Group (CCTAG) rigorously evaluated available GCMs and identified a subset of 10 GCMs for use in California water resources planning. These

10 GCMs can "produce reasonably realistic simulations of global, regional, and California-specific climate features" and they are deemed as "currently the most suitable for California climate and water resource assessment and planning purposes" [52]. Out of those CCTAG-selected 10 GCMs, CCCA4 further identified four representative priority GCMs spanning the precipitation and temperature changes in all GCMs that closely simulate California's climate [61]. Those four GCMs include (1) a "cool/wet" model CNRM-CM5; (2) an "average" model CanESM2; (3) a "warm/dry" model HadGEM2-ES; and, (4) a "complement" model MIROC5 that "is most unlike the first three models for the best coverage of different possibilities" (referring to Table A1 in Appendix A for more information on the GCMs). Seven metrics covering different seasonal and annual precipitation and temperature measures were utilized in selecting these four models out of 32 available models. Each model was ranked for each of the seven metrics. A weighted rank was determined for each model based on which selection was made. For a detailed explanation on the selection criteria and procedure, the readers are referred to [61]. It is worth noting that, in climate change studies, it is not uncommon to examine the mean of projections from an ensemble of climate models. In the current study, since an "average" model (CanESM2) has already been included as one of the study models, which was deemed to be representative of the average conditions of all GCMs [61], no additional model-averaging was applied to avoid repetition.

To summarize, the study variables are derived via the following procedure:

(1) Daily precipitation and temperature projections under RCP4.5 and RCP 8.5 from an 80-year period (2020–2099) at each study watershed from these four GCMs are used in order to drive the VIC model to generate corresponding runoff projections in the same period.

(2) The runoff projections are bias-corrected to historical data. The bias-correction method is detailed in [61]. Appendix A provides the sources of the bias-corrected runoff projections.

(3) For each watershed, the bias-corrected daily runoff projection is aggregated to April–July total runoff volume, October–March total volume, and annual total volume.

(4) For the Sacramento River region (San Joaquin River region), the corresponding total runoff volumes from four rivers in the region are summed together to yield SAC4 (SJQ4) April–July total volume, October–March total volume, and annual total volume. The resultant variables are utilized to determine the water year types as well as the standardized streamflow index (explained in detail in the following Section 2.3).

(5) Changes are obtained by comparing those bias-corrected SAC4 and SJQ4 runoff projections against the corresponding SAC4 and SJQ4 runoff observations during an equal length of historical period from 1920–1999. Appendix A also provides the sources of historical runoff data.

2.3. Study Metrics

This study investigates changes in the exceedance probabilities of seasonal (wet and snowmelt seasons) and annual runoff, water year types, and a standard streamflow drought index.

The California Department of Water Resources (DWR) adopts five water year types in planning and management operations [21]. There are five different types, including wet year (W), above normal year (AN), below normal year (BN), dry year (D), and critical year (C). The classification is based on a water year index that is derived from full natural flow measurements. For the Sacramento River region, the water year index (WYI) is calculated as:

$$\text{WYI}_{\text{SAC}} = 40\% \times \text{AJ}_{\text{SAC4}} + 30\% \times \text{OM}_{\text{SAC4}} + 30\% * \text{WYI}_{\text{SACPre}} \qquad (1)$$

where AJ_{SAC4} and OM_{SAC4} represent the April–July runoff and October–March runoff of Sacramento four rivers in the current water year (in the unit of million acre-feet, MAF); $\text{WYI}_{\text{SACPre}}$ is the water year index of the previous water year. If $\text{WYI}_{\text{SACPre}}$ exceeds 10 MAF, then 10 MAF is be applied instead. A water year with WYI_{SAC} above 9.2 MAF

(below 5.4 MAF) is classified as a wet year (critical year). Otherwise, when WYI_{SAC} exceeds 7.8 MAF (less than 6.5 MAF), a water year is defined as an above normal year (dry year). Finally, a year with WYI_{SAC} ranging from 6.5 to 7.8 MAF is designated as a below normal year.

Similarly, the WYI for San Joaquin River region is determined as:

$$WYI_{SJQ} = 60\% \times AJ_{SJQ4} + 20\% \times OM_{SJQ4} + 20\% \times WYI_{SJQPre} \tag{2}$$

When compared with WYI_{SAC}, calculation of the WYI_{SJQ} applies 20% greater weight to snowmelt period runoff and reduces the wet period runoff and the influence of the previous year's index by 10%. The WYI_{SJQPre} is capped at 4.5 MAF (rather than 10 MAF for WYI_{SACPre}) [21]. The smaller cap in the previous year's index and higher coefficient for April–July runoff (mostly from snowmelt) reflect the relatively smaller annual runoff received in more snow dominated San Joaquin River region (versus Sacramento River region). Accordingly, the thresholds utilized in classifying water year types in San Joaquin River regions are also different. A water year is designated as a wet (critical) year when the calculated WYI_{SJQ} is over 3.8 MAF (below 2.1 MAF). Otherwise, when WYI_{SJQ} exceeds 3.1 MAF (less than 2.5 MAF), a water year is classified as an above normal year (dry year). When WYI_{SJQ} ranges from 2.5 MAF to 3.1 MAF, the year is defined as a below normal year.

In addition to water year types, the runoff volumes with different exceedance probabilities that guide water operations in California are further examined here. One operational example is that in DWR's official water supply forecasts [22], in addition to the most probable (median) forecast, a low forecast (with 90% exceedance probability) and a high forecast (10% exceedance) are also issued. In light of that, this study further looks at changes in runoff at seasonal (October–March and April–July) and annual scales that are represented by different exceedance probabilities.

Finally, effective drought management is imperative in securing reliable water supply and sustaining economic development in California. Standardized drought indices are typically applied in supporting drought management practices in the State [62]. This study examines the projected changes in a nonparametric drought index, titled Standardized Streamflow Index (SSI), for SAC4 and SJQ4 at designated time scales. This index is calculated via the Standardized Drought Analysis Toolbox (SDAT) of [63]. The SDAT uses the empirical Gringorten plotting position for deriving the marginal distribution of the target historical or projected runoff variable. The empirical probability of the variable is then transformed into a standardized value. This method requires no assumption on a parametric distribution function and, thus, no parameter estimation. Typically, a value of SSI over 2 (less than −2) indicates extremely wet conditions (extreme droughts). Otherwise, a value larger than 1 (smaller than −1) designates wet conditions (dry conditions). SSI ranging from −1 to 1 indicates a neutral condition. This study further assesses the trends in projected SSIs. For this purpose, the widely used non-parametric Mann–Kendall test [64,65] is employed to assess the significance of a trend with a significance level of 0.05. The non-parametric Theil–Sen approach [66,67] is utilized for determining the trend slope.

3. Results

3.1. Exceedance Probability

Figure 2 depicts the exceedance probability curves of the observed and projected Sacramento four rivers' (SAC4) total runoff volume on three temporal scales (water year, October–March, and April–July). The sample size for each probability curve is 80, covering 1920–1999 for the observations and 2020–2099 for the projections, respectively. The "complement" (MIROC5) and "warm/dry" (HadGEM2-ES) models project generally similar annual (water year total) runoff as the historical baseline. Meanwhile, the "cool/wet" (CNRM-CM5) and "average" (CanESM2) models both project higher annual runoff across all of the exceedance probabilities under both emission scenarios (Figure 2a). However, for October–March runoff, all of the models tend to project higher volumes than the historical baseline under both emission scenarios (Figure 2b). This is particularly the case for the

"cool/wet" model. Conversely, for April–July runoff, all models project lower than the baseline volumes (Figure 2c). For a specific model, declines in the April–July runoff are more pronounced under the higher emission scenario when compared to the lower emission scenario. In Sacramento River region, historical October–March runoff accounts for a majority of the annual total runoff (red curves in Figure 2a,b). Projected decreases in April–July runoff are outweighed by projected increases in October–March runoff (Figure 2b,c, note the scale difference between these two panels), leading to overall increases in total annual runoff projections. Comparing two emission scenarios, the "cool/wet" model and the "average" model generally predict higher October–March runoff and lower April–July runoff under the higher emission scenario. The "warm/dry" model projects more annual and October–March runoff and less April–July runoff under the higher emission scenario, while the results are mixed for the "complement" model across three time scales.
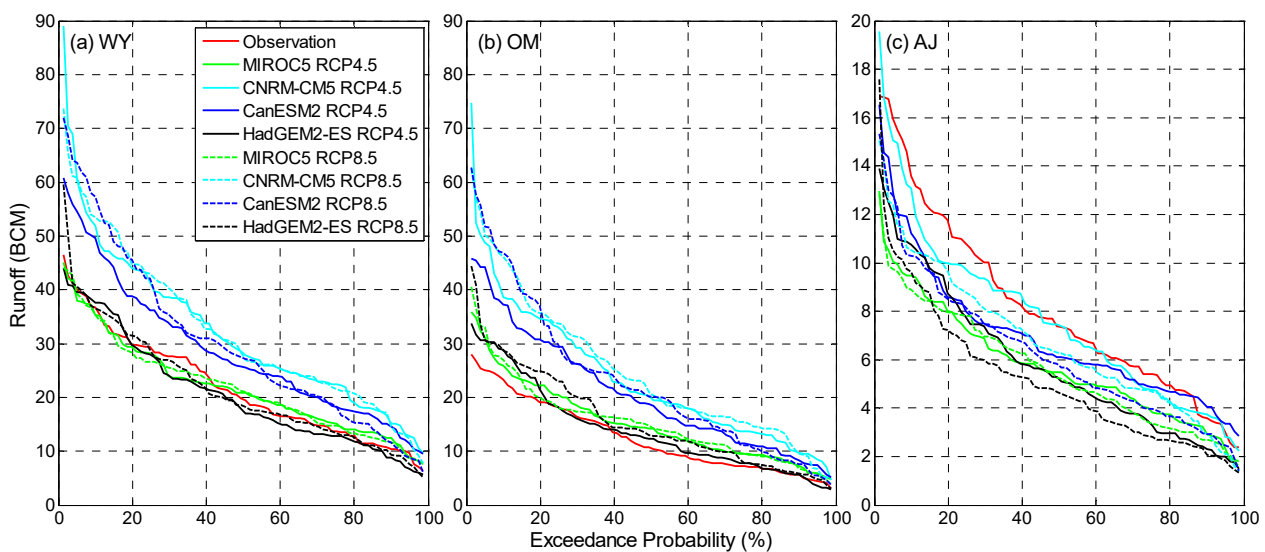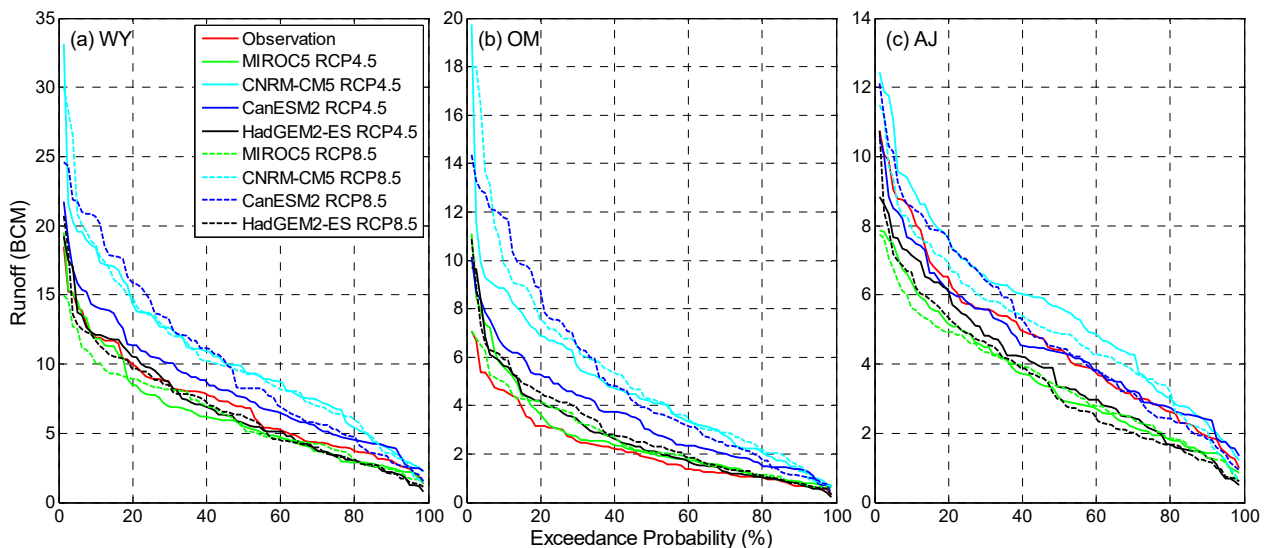

Figure 2. Exceedance probability curves for observed and projected (**a**) water year; (**b**) October–March; and, (**c**) April–July total SAC4 runoff volume. Note the scale difference in *Y*-axis across three panels.

Similarly, San Joaquin four rivers' (SJQ4) total annual runoff is projected to increase across nearly all of the exceedance probabilities via the "cool/wet" model (CNRM-CM5) and the "average" model (CanESM2) (Figure 3a). The increases are generally larger for higher flows with lower exceedance probabilities. Meanwhile, the "complement" model (MIROC5) and "warm/dry" model (HadGEM2-ES) project similar annual runoff to the the historical baseline. One difference from the Sacramento rivers (SAC4) is that the "complement" projection on SJQ4 tends to be slightly drier than the corresponding baseline. Similar to the Sacramento River region, the San Joaquin River region is expected to experience larger volumes of October–March runoff than the baseline in all of the projections (Figure 3b). The increases are larger for runoff volumes with lower exceedance probability. Different from the Sacramento River region, not all four models project decreases in the April–July runoff (Figure 3). The "cool/wet" model projects increases under both of the emission scenarios for the San Joaquin River region. The "average" model also projects increases under the higher emission scenario. This difference highlights the geographic differences between these two regions, which will be discussed in Section 4. Finally, under the higher emission scenario, the "cool/wet" model projects higher October–March runoff and lower April–July runoff, while the "average" model predicts higher runoff across all three time scales, a result that is consistent with the Sacramento River region.

In brief, projections for both of the regions share some common features. The "cool/wet" model and "average" model project increases in annual runoff and all four models project increases in the October–March runoff for both regions under both emission scenarios. In addition, under the higher emission scenario, the "cool/wet" model projects more (than

historical baseline) October–March runoff and less April–July runoff, while the "average" model projects increased runoff across all three time scales for both of the regions. There are also some differences, a significant one of which is that while all models project decreases in April–July runoff in the Sacramento River region in most cases, the "cool/wet" model projects increases in April–July runoff in the San Joaquin River region across most exceedance probabilities, particularly under the lower emission scenario.

Figure 3. Exceedance probability curves for observed and projected (**a**) water year; (**b**) October–March; and, (**c**) April–July total SJQ4 runoff volume. Note scale difference in *Y*-axis across three panels.

3.2. Water Year Type

Historically (1920–1999), wet years, near-normal years (including above normal and below normal years), and dry conditions (containing both dry and critical years) are almost evenly distributed in the Sacramento River (Figure 4a; Figure A1 in Appendix A). When compared to wet years (33%), dry conditions occur slightly more frequently (36%), while near-normal years are marginally less (31%). During the historical period (1920–1999), critical years account for about one-sixth (16%) of years. Under the "complement" (MIROC5) lower emission projection (Figure 4b), both wet years and dry conditions are expected to decrease by 7% and 8%, respectively, when compared to the historical baseline. Meanwhile, near-normal years are projected to increase, particularly for below normal years (12% increase). For the same climate model under the higher emission scenario (Figure 4f), slightly more wet years and dry conditions are projected. Like the "complement" model, the "warm/dry" (HadGEM2-ES) model projects are fewer (than historical baseline) wet years under both emission scenarios. However, more critical years are expected in the "warm/dry" projections when compared to the historical baseline.

The "cool/wet" (CNRM-CM5) projection and "average" (CanESM2) projection are strikingly different from that of the "complement" projection and "warm/dry" projection. Under the lower emission scenario (Figure 4c,d), the wet years are expected to markedly increase, while the dry conditions are projected to decline distinctly compared to the historical baseline. When compared to the "average" model, the "cool/wet" model projects even more wet years (62% versus 49%) and less critical years (4% versus 5%). The "average" model projects more near-normal years (44%) than both the "cool/wet" model (29%) and the corresponding historical baseline (31%). Under the higher emission scenario, the "cool/wet" model projects fewer wet years and more near-normal years, while the changes in dry conditions are minimal when compared to that of the lower emission scenario (Figure 4g versus Figure 4c). The "average" model projects more wet years, more dry conditions, and less near-normal years (Figure 4h versus Figure 4d).
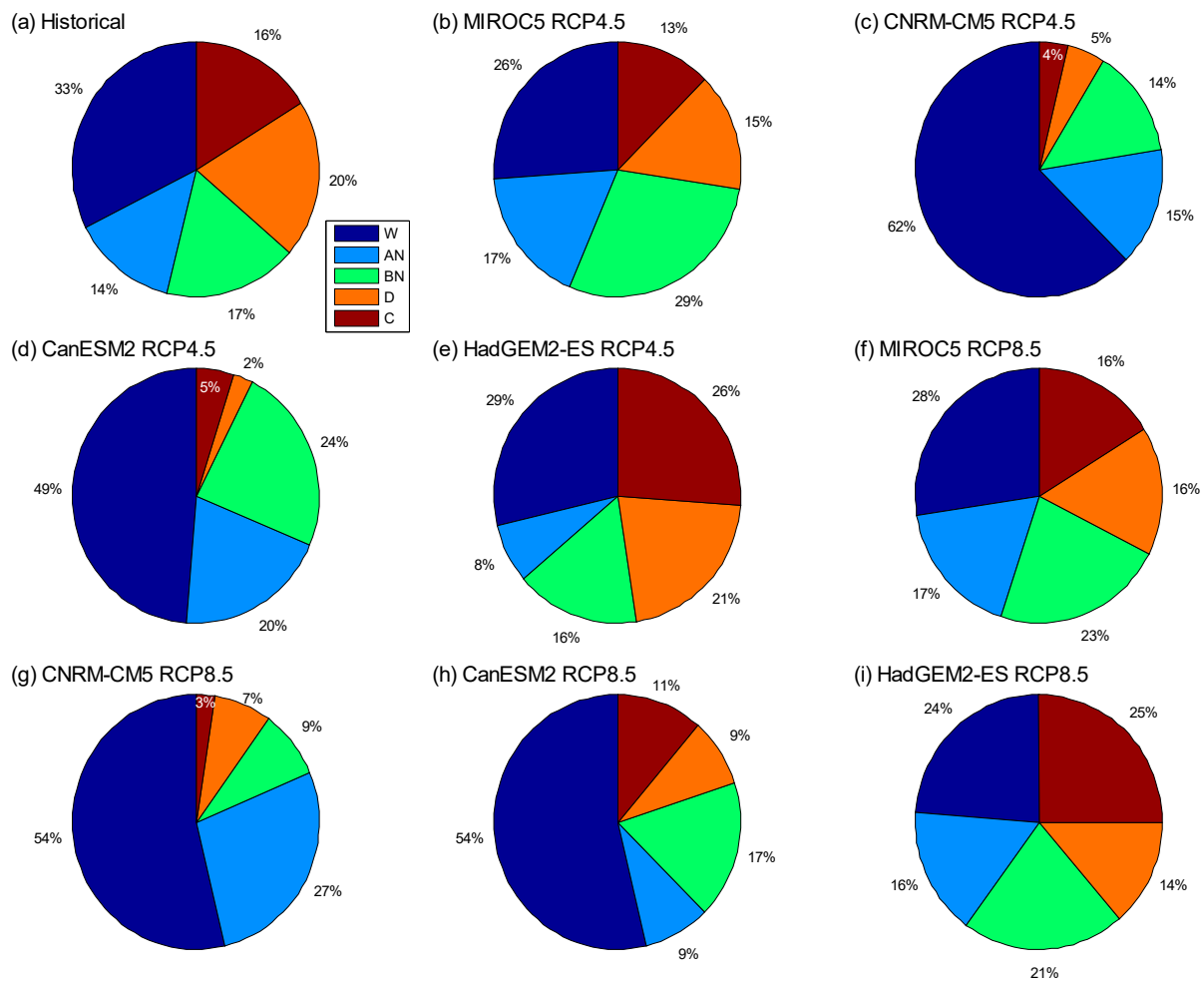
Figure 4. Historical and projected water year type distribution of SAC4.

Like the Sacramento River region, the San Joaquin River region observes nearly evenly distributed wet, near-normal, and dry/critical years in the historical period (Figure 5a; Figure A2 in Appendix A). However, it experiences slightly fewer wet years (3% less) and more critical years (4% more). When compared to the historical baseline, both the "complement" model (MIROC5) and the "warm/dry" model (HadGEM2-ES) project fewer wet years and significantly more critical years under both emission scenarios (Figure 5b,e,f,i). Even fewer wet years are expected under the higher emission scenario and for the "complement" model. Both of the models project that approximately 50% of years are expected to be in dry or critical years (versus 34% in the historical baseline). Contrariwise, the "cool/wet" model (CNRM-CM5) projects remarkably more wet years and fewer critical years (Figure 5c,g). Particularly under the lower emission scenario, the wet years are projected to nearly double, while the critical years and the overall dry conditions are expected to roughly decrease by half. The "average" model (CanESM2) also projects an increase in wet years (Figure 5d,h). However, the increase is relatively milder when compared to that of the "cool/wet" model, particularly under the lower emission scenario. In addition, the declines in critical years and the overall dry conditions in "average" projections are also smaller.

In summary, the near uniform historical distribution of wet years, near-normal years, and dry (including critical) years in both Sacramento River and San Joaquin River regions is projected to significantly change in almost all of the models and emission scenarios analyzed here. In general, the "cool/wet" and "average" models project more frequent wet years and less critical and dry years. Conversely, the "warm/dry" model project fewer wet years and more critical years. The "complement" model projects fewer wet years overall.

When comparing two regions, more critical years are consistently projected in the San Joaquin Region across all the climate models under both emission scenarios.
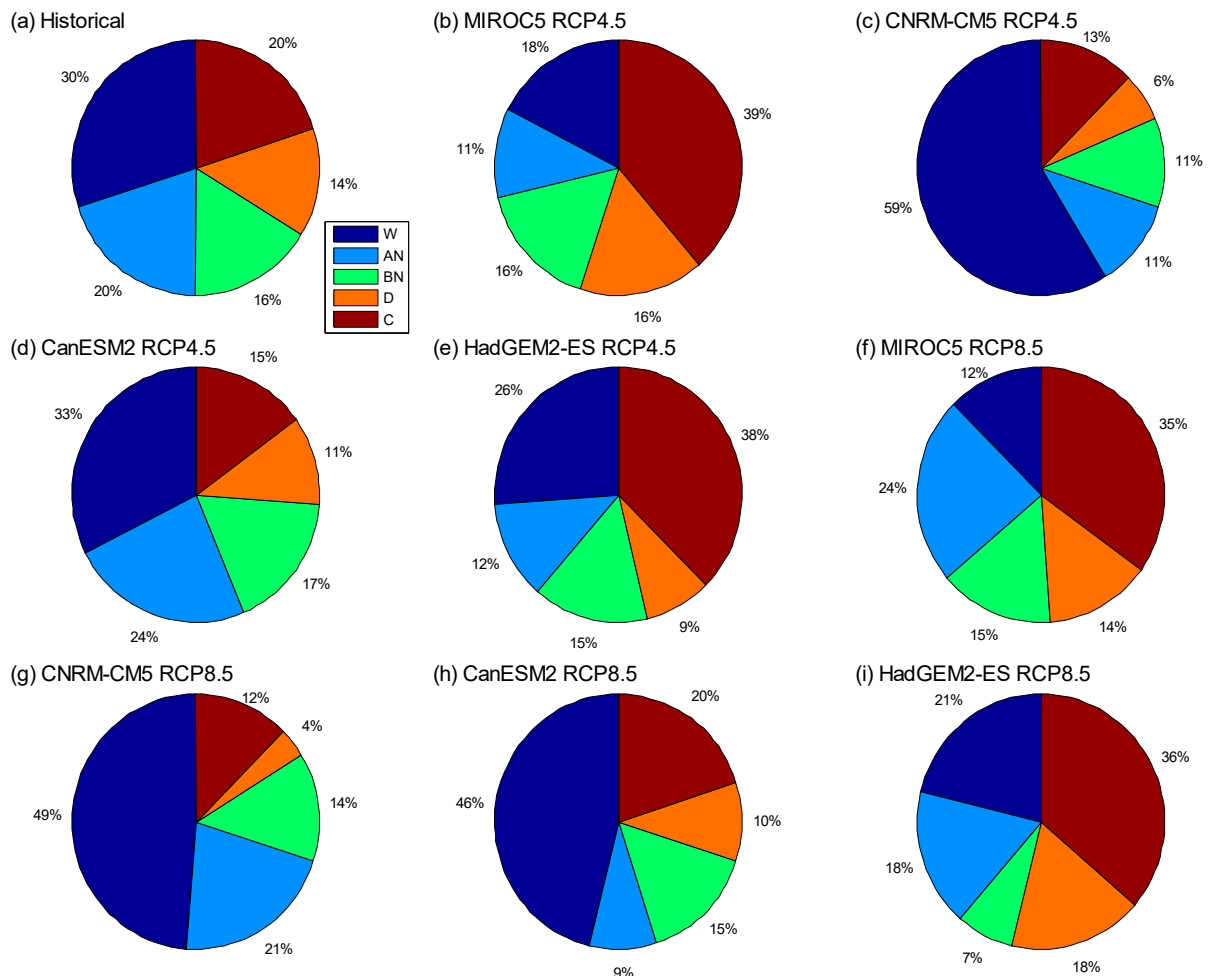

Figure 5. Historical and projected water year type distribution of SJQ4.

3.3. Standardized Streamflow Index

During the historical period (water year 1920–1999), there are slightly more dry conditions (AJ SSI < 0 for 56% of the time) than wet conditions (AJ SSI > 0 for 44% of the time) in the Sacramento River region (Figure 6a) in terms of the April–July Standard Streamflow Index. There are two extremely wet cases (1952 and 1983) and two extremely dry cases (1924 and 1977), respectively. The mean and variance of the index are −0.1 and 1.0, respectively (Table A2 in Appendix B). Except for the "cool/wet" model (CNRM-CM5) under the lower emission scenario, dry conditions are projected to increase, ranging from 3% ("cool/wet" model under RCP 8.5) to 13% ("average" (CanESM2) and "warm/dry" (HadGEM2-ES) models under RCP 8.5) in all other cases as compared to the historical baseline. Extremely wet conditions are expected to consistently decrease across all models under both emission scenarios. Both the "complement" and "cool/wet" models project increases in the number of extreme dry conditions under both emission scenarios, so does the "warm/dry" model under RCP 4.5. However, the increases (from 2 to 3) are moderate. The mean index values generally become smaller. In general, under both of the emission scenarios, the "warm/dry" ("cool/wet") projections have the smallest (largest) mean values. Only the "cool/wet" and the "warm/dry" projections under RCP 4.5 exhibit higher than the baseline variability, as they have higher variance values.
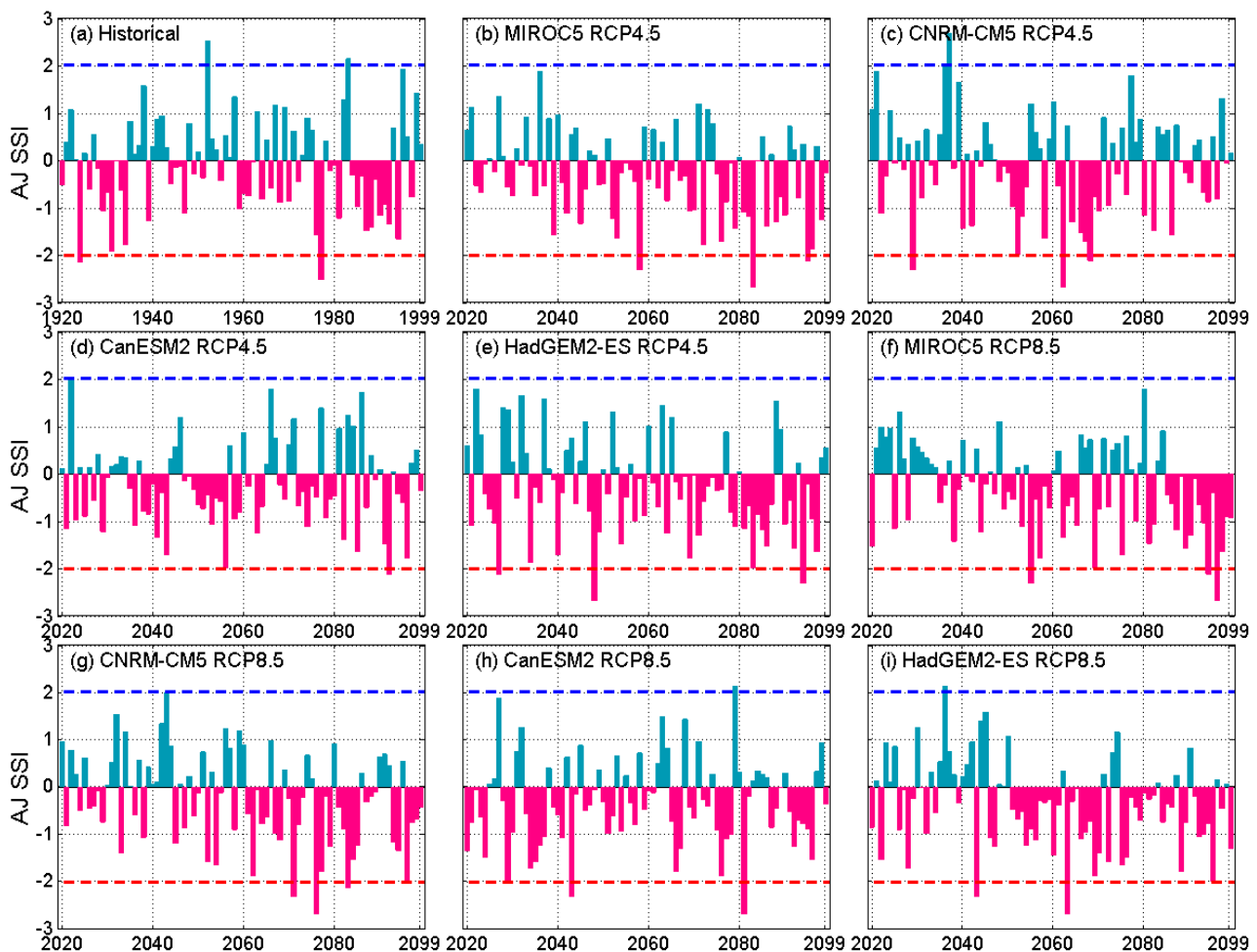
Figure 6. Historical and projected April–July Standardized Streamflow Index (SSI) for SAC4. Values that are above the blue dash line represent extremely wet conditions while values below the red dash line indicate extremely dry conditions.

Historically, when measured by April–July SSI (Figure 7), the distribution of wet (48%) and dry conditions (52%) over the San Joaquin River region is similar to that of the Sacramento River region. The former has the same number of extremely dry conditions (in 1924 and 1977) as the latter, but with one less extremely wet condition. The mean (-0.09) and variance (0.94) of the index of the former are also similar to their counterparts of the latter (Table A2 in Appendix B). Differently, "cool/wet" (CNRM-CM5) and "average" (CanESM2) models both project more (than the baseline) or similar wet conditions under both emission scenarios. The corresponding mean April–July SSI values are also larger than the historical mean. These two models also project more extremely wet conditions. Conversely, the other two models ("complement" (MIROC5) and "warm/dry" (HadGEM2-ES) project more extremely dry conditions. However, the magnitudes of projected increases or decreases in extreme conditions are generally small (e.g., up to two more extremely wet years and up to one more extremely dry year). In terms of variability, both "cool/wet" and "warm/dry" projections have higher than the baseline variance under both emission scenarios. The SSI indices on the annual and October–March time scales (Figures A1–A4 in the Appendices A and B) share some similarities with April–July SSI for both regions. Specifically, projected changes in extremely wet and dry conditions are not expected to be dramatic. Nevertheless, there are also some noticeable differences. One major difference is that more wet conditions are expected based on annual SSI and October–March SSI. This is particularly the case for October–March SSI, where nearly all four models project wetter than baseline conditions over both regions under both emission scenarios.

These observations are generally in line with what the runoff exceedance probabilities in Figures 4 and 5 have shown.
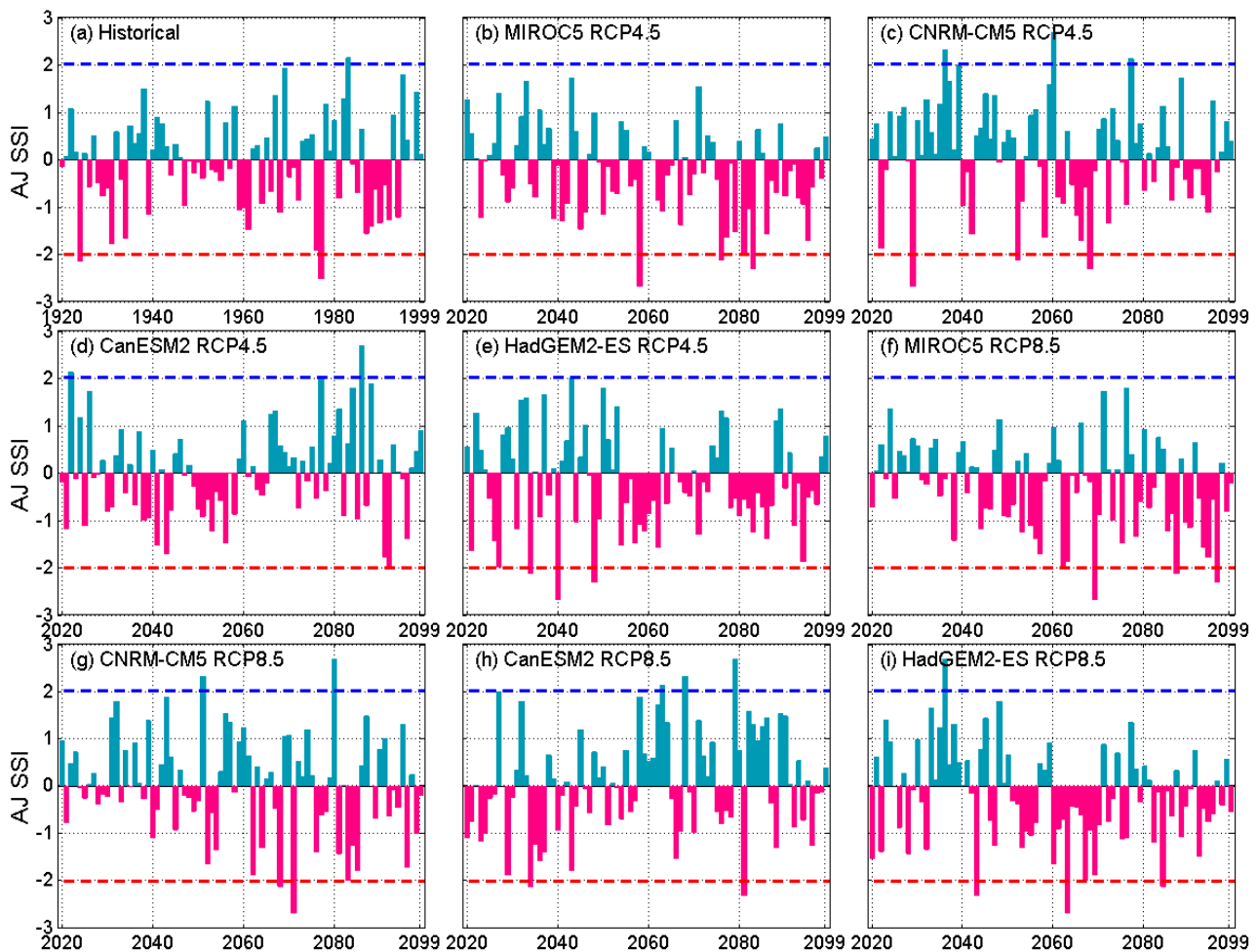
Figure 7. Historical and projected April–July SSI for SJQ4. Values above the blue dash line represent extremely wet conditions, while values below the red dash line indicate extremely dry conditions.

In addition to the SSI time series that are depicted in Figures 6 and 7, the study further examines the overall trend of historical and projected SSI indices. For projected SSI, temporal scales that are longer than one year are also explored, as multi-year droughts are not uncommon in California. Table 1 presents the corresponding trend slope information. Table A3 of Appendix B provides the corresponding *p*-values. In the historical period (1920–1999), SAC4 and SJQ4 SSIs have increasing trends on October–March and multi-year (two to five years) scales, while the annual and April–July indices have decreasing trends. The magnitude of the trend slope is the highest for both regions for April–July SSI. However, all of the historical SSI trends are not shown to be statistically significant.

For the Sacramento River region, all of the models project downward trends in April–July SSI, indicating that April–July is projected to become drier. The slopes that are associated with the "complement" model (MIROC5) and the "warm/dry" model (HadGEM2-ES) under both emission scenarios are statistically significant. On annual and multi-year scales, the "complement" model projections and "warm/dry" projections also exhibit downward trends. In contrast, the "cool/wet" (CNRM-CM5) and "average" (CanESM2) models project increasing trends. The increasing trends that are associated with the "average" model are all statistically significant, along with the trends of the "cool/wet" projections under the higher emission scenarios on multi-year scales. Regarding October–March SSIs,

except for the "average" model and "warm/dry" model under the lower emission scenario, increasing trends are projected in other cases.

Table 1. Trend slope of SSI indices (numbers in **bold** indicate statistically significant slopes).

Scenarios		OM	AJ	WY	Two-Year	Three-Year	Four-Year	Five-Year
SAC4	Historical	0.005	−0.008	−0.001	0.003	0.004	0.004	0.005
MIROC5 (complement)	RCP 4.5	−0.002	**−0.011**	−0.005	**−0.011**	**−0.016**	**−0.019**	**−0.022**
	RCP 8.5	0.004	**−0.013**	−0.002	−0.002	−0.004	−0.002	−0.004
CNRM-CM5 (cool/wet)	RCP 4.5	0.005	−0.001	0.004	0.005	0.007	0.008	0.007
	RCP 8.5	0.007	**−0.008**	0.005	**0.009**	**0.008**	**0.009**	**0.009**
CanESM2 (average)	RCP 4.5	**0.009**	−0.003	0.008	**0.010**	**0.009**	**0.001**	**0.011**
	RCP 8.5	**0.011**	−0.002	**0.010**	**0.013**	**0.015**	**0.018**	**0.020**
HadGEM2-ES (warm/dry)	RCP 4.5	−0.004	**−0.012**	−0.007	−0.008	**−0.011**	**−0.014**	**−0.016**
	RCP 8.5	0.001	**−0.011**	−0.004	−0.003	−0.007	**−0.009**	**−0.010**
SJQ4	Historical	0.004	−0.005	−0.002	0.002	0.002	0.002	0.000
MIROC5 (complement)	RCP 4.5	−0.003	**−0.010**	**−0.008**	**−0.013**	**−0.019**	**−0.023**	**−0.027**
	RCP 8.5	0.002	**−0.011**	−0.006	**−0.009**	**−0.009**	**−0.012**	**−0.015**
CNRM-CM5 (cool/wet)	RCP 4.5	0.004	−0.002	0.002	0.000	0.001	0.000	0.000
	RCP 8.5	**0.008**	−0.005	0.004	0.004	0.005	0.006	0.007
CanESM2 (average)	RCP 4.5	**0.008**	0.006	0.007	0.006	0.006	0.005	0.006
	RCP 8.5	**0.018**	0.008	**0.015**	**0.018**	**0.021**	**0.024**	**0.025**
HadGEM2-ES (warm/dry)	RCP 4.5	0.001	−0.008	−0.005	**−0.008**	**−0.011**	**−0.014**	**−0.016**
	RCP 8.5	0.007	−0.008	−0.002	−0.004	−0.006	−0.007	−0.008

For San Joaquin River region, except for the "average" model (CanESM2), all of the models project decreasing trends in April–July SSIs under both emission scenarios. However, only the "complement" (MIROC5) projections are statistically significant. On annual and multi-year scales, similar to those of the Sacramento River region, the "complement" model and "warm/dry" model (HadGEM2-ES) project decreasing trends in SSIs while it is the opposite for the "cool/wet" model (CNRM-CM5) and "average" model. Only trends of the "complement" model are mostly statistically significant, along with trends of the "average" model under the higher emission scenario and most trends of the "warm/dry" model under the lower emission scenario. For October–March SSIs, increasing trends (wetter) are projected, with the exception of the "complement" model under the lower emission scenario. In terms of magnitude, the trend slope values of the "average" ("complement") model are generally larger than that of the "cool/wet" ("warm/dry") model. Projections under the higher emission generally have larger (smaller) slope values than their lower emission scenario counterparts for the "cool/wet" model and "average" model (the "complement" model and the "warm/dry" model).

In summary, the projected changes in SSI vary across different climate models and emission scenarios, as well as across different temporal scales. Overall, April–July SSIs and October–March SSIs tend to decline and increase throughout the projection period, respectively, highlighting the non-stationarity in these projections. The "complement" model and "warm/dry" model generally project negative (i.e., drier) trends in SSIs on annual and multi-year scales, while it is the opposite for the other two models. Despite these differences, projected changes in the number of extremely wet conditions and extreme drought are not substantial according to all four models under both of the scenarios in both study regions.

4. Discussion

4.1. Attribution of Potential Changes

This study indicates that water year types, annual and seasonal runoff volumes, and hydrological droughts through the end of this century are expected to change from the corresponding historical baselines. The changes vary across different projection models under different emission scenarios. Some of the changes are common to both the Sacramento River region and San Joaquin River region, while the others are region-specific. These changes stem from projected changes in the precipitation and temperature, which are the basis of runoff projections, as well as the geographic differences between two regions.

All four GCMs suggest non-stationary increases in the October–March temperature over both of the regions. The increases are more noticeable under the higher emission scenarios than in the lower emission scenarios (Table 2; Figures A7 and A8, and Table A4 in Appendix B). Previous studies have reported that future warming is expected to elevate the freezing elevation, leading to more precipitation falling as rainfall rather than snowfall [8], earlier snowmelt [68], and more winter runoff [38,39]. October–March precipitation is also projected to increase in most models, with greater increases expected under the higher (versus lower) emission scenario. The compound effect of warming and increases in precipitation is to increase runoff during October–March, particularly under the higher emission scenario, which confirms what Figures 2b and 3b show.

Table 2. The mean of historical (1920–1999) and projected (2020–2099) precipitation and temperature data at annual and seasonal scales.

Scenarios		Precipitation (mm)			Temperature (°C)		
		OM	**AJ**	**WY**	**OM**	**AJ**	**WY**
SAC4	Historical	820	169	1018	4.5	13.8	9.8
MIROC5 (complement)	RCP 4.5	858	135	1027	5.4	15.5	11.1
	RCP 8.5	864	142	1039	6.1	16.0	11.8
CNRM-CM5 (cool/wet)	RCP 4.5	1064	166	1275	5.9	15.7	11.4
	RCP 8.5	1090	165	1294	6.9	16.7	12.5
CanESM2 (average)	RCP 4.5	996	162	1219	6.1	16.1	11.8
	RCP 8.5	1045	159	1287	7.1	17.3	13.0
HadGEM2-ES (warm/dry)	RCP 4.5	807	147	991	6.0	16.2	11.8
	RCP 8.5	848	146	1029	7.2	17.4	13.1
SJQ4	Historical	869	166	1060	3.5	11.7	8.3
MIROC5 (complement)	RCP 4.5	838	130	998	4.7	14.0	10.1
	RCP 8.5	839	126	990	5.4	14.7	10.8
CNRM-CM5 (cool/wet)	RCP 4.5	1127	151	1317	4.9	14.0	10.1
	RCP 8.5	1138	149	1325	6.0	15.0	11.2
CanESM2 (average)	RCP 4.5	1016	145	1211	5.2	14.0	10.4
	RCP 8.5	1157	142	1364	6.3	15.3	11.6
HadGEM2-ES (warm/dry)	RCP 4.5	876	137	1048	5.0	14.5	10.4
	RCP 8.5	879	142	1054	6.3	15.5	11.7

April–July runoff largely comes from snowmelt, as 1 April is typically deemed as the date when snowpack peaks in the mountainous areas of California [69]. The projected non-stationary warming in the wet season likely leads to earlier snowpack peak and melting [70], resulting in a smaller-than-usual snowpack on 1 April and, thus, less April–July runoff. This is particularly the case under the higher (versus lower) emission scenario where higher

warming is projected. April–July precipitation also contributes to runoff during this period. On average, all four GCMs project non-stationary decreases in the April–July precipitation under both emission scenarios for both regions (Table 2). This confirms the decline in April–July runoff across nearly all of the exceedance probabilities in Sacramento River region, as shown in Figure 2c. However, in the San Joaquin River region, the "cool/wet" model suggests mostly increases in April–July runoff (Figure 3c). The apparent difference is most likely attributable to differences in the regions' elevations. Because Sacramento River watersheds are generally lower, a increasing freezing elevation that is caused by warming likely caps most parts of these watersheds, depending on the magnitude of warming, and leads to significantly reduced snowpack accumulation. In contrast, the higher elevation of San Joaquin River watersheds makes them more resilient to a rising freezing elevation. Figure 8 depicts the trends in historical and projected 1 April snow water equivalent (SWE) for both of the regions. Historically, the Sacramento River region has a downward trend, while the San Joaquin River region has a slightly upward trend, although both trends are not statistically significant. During the projection period (2020–2099), all four GCMs project significant decreasing trends in 1 April SWE in the Sacramento River region, particularly under the higher emission scenarios where greater warming is expected (versus the lower emission scenario). In comparison, for the San Joaquin River region, only one model ("complement") projects a significant negative trend under the lower emission scenario and three models (all but the "average" model) suggest a significant negative trend under the higher emissions scenario. This result suggests that the San Joaquin River region is less hydrologically sensitive in a warming climate as compared with the Sacramento River region, a finding that is replicated in previous studies [52,71,72].
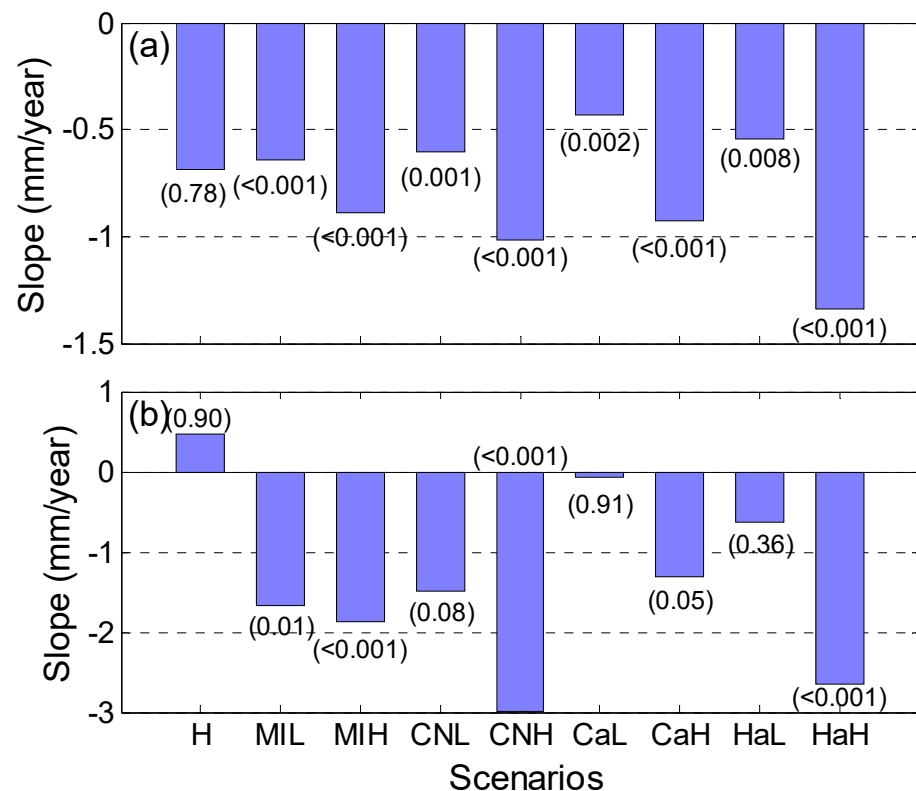
Figure 8. Trend Slope of 1 April Snow Water Equivalent for (**a**) SAC4 and (**b**) SJQ4 during historical (1930–1999) and projected periods (2020–2099) under different scenarios. Value in the bracket represents the corresponding *p*-value. H: historical; MIL: MIROC5 RCP 4.5; MIH: MIROC5 RCP 8.5; CNL: CNRM-CM5 RCP 4.5; CNH: CNRM-CM5 RCP 8.5; CaL: CanESM2 RCP 4.5; CaH: CanESM2 RCP 8.5; HaL: HadGEM2-ES RCP 4.5; HaH: HadGEM2-ES RCP 8.5. Appendix A provides the corresponding data source.

Any changes in October–March and April–July runoff will drive changes in annual runoff, water year types, and hydrological droughts. Collectively, they account for over 95% of total annual runoff for both regions during the historical period. Their values dominate the hydrological drought index calculation and water year type classification. With regard to hydrological droughts, the projected decreases in April–July runoff and increases in October–March runoff explain the overall negative trends in April–July SSIs and positive trends in October–March SSIs in both regions under both emission scenarios (Figures 6 and 7; Table 1). However, on the annual scale and multi-year scale, the projected changes in SSIs vary with different climate models.

Regarding water year types, the water year index (based on which water year type is determined) for Sacramento River region consists of 40% of April–July runoff and 30% of October–March runoff (Equation (1)). In comparison, for the San Joaquin River region, these ratios are 60% and 20%, respectively (Equation (2)). The study indicates that the October–March runoff is projected to increase for both regions, particularly for the "cool/wet" model and the "average" model. The study also shows that April–July runoff is expected to decrease (with a few exceptions for the San Joaquin River region). Historically, the October–March runoff and April–July runoff account for about tw-thirds of annual runoff in Sacramento River region and San Joaquin River region, respectively. As such, increases in October–March and decreases in the April–July runoff have different implications for the two regions. For the Sacramento River region, increases in October–March runoff are expected to outweigh projected decreases in April–July runoff, although the weight that is assigned to the latter in water year index calculation (Equation (1)) is 10% higher (versus nearly one-third lower in its contribution to annual runoff), leading to generally higher water year indices. For San Joaquin River region, however, decreases in April–July runoff are expected to largely dominate increases in October–March runoff, since (1) the contribution to annual runoff from the former is almost twice of that from the latter; and (2) the weight of the former (Equation (2)) is three times of that for the latter. Thus, the resulting water year indices for the San Joaquin River region are expected to decline, when compared to the historical baseline. These observations explain what has been illustrated in Figures 4 and 5 that, in comparison with the San Joaquin River region, under any emission scenario via any climate model, the Sacramento River region is projected to have (1) more wet years; (2) more near-normal years (including above normal and below normal years); and, (3) less critical years. Despite these differences, there are some similarities between two regions that are climate model specific as different models project considerably different future climate conditions (Table 2; Figures A7 and A8). Specifically, under "cool/wet" and "average" projections, both of the regions are projected to experience more (than historical baseline) wet years and less critical and dry years; under "warm/dry" projections, it is the opposite (Figures 2 and 3). These uncertainties in future water year typing that are rooted in climate models are somehow different from the findings reported in a previous study [21], which projected (1) more (than the historical baseline) dry and critical years while less normal and wet years in the Sacramento River region; and, (2) consistently more (than the historical baseline) critical years in the San Joaquin River region throughout the current century. In comparison, the current study suggests that there is less certainty among different climate models on future changes in water year types. However, it is worth noting that these two studies are not directly comparable in terms of that (1) the current study uses climate projections from the latest operative climate models in the CMIP5 project (versus CMIP3 projections in the [21] study) that are specifically selected for planning studies in California (CCCA4); and, (2) the current study uses the observed (versus simulated in the [21] study) water year types as the historical baseline in comparison; and, (3) the current study examines the changes in a 80-year period (versus 50-year in the [21] study), which provides more samples for each of five categories of water year types.

4.2. Implications and Future Work

From a scientific point of view, the findings of the study highlight that (1) uncertainties in climate change science (as represented by different climate models) have considerable implications on changes in water year classification and hydrological droughts; and, (2) when and where changes in runoff volumes and hydrological droughts (represented by trends) manifest themselves in major water supply regions in California as a result of a changing climate. The first point above underlines the importance of selecting climate models that represent the start-of-the-art climate science in this type of analysis. The current study utilizes four priority climate models that were recommended in California's Fourth Climate Change Assessment, which was based on CMIP5 projections. In fact, the newer CMIP6 projections are available at a considerably coarse spatial scale, although their use has been largely limited to the research community at this point [47]. California's next (fifth) climate assessment is in the scoping phase, and it is expected to downscale and tailor CMIP6 projections for planning and management practices in the State. We will update the analysis based on newer climate projections once they become available. The second point underscores that stationarity will most likely not hold valid in a changing climate. Indices that are calculated under the stationarity assumption will become less informative further into the future when higher warming and larger changes (i.e., stronger non-stationarity) in precipitation are projected. As discussed in [21], weights that are assigned to different predictors in calculating water year indices (Equations (1) and (2)) or the threshold values applied in classifying water year types may need to be updated in order to reflect a changing climate. California Department of Water Resources is conducting a comprehensive study to develop "adaptative" water year indices for both Sacramento River and San Joaquin River regions by exploring a wide range of future possible and plausible climate conditions. This work will be presented in a follow-up study.

From a practical standpoint, the findings of this study can inform decision-makers in long-term water resources planning. For instance, this study indicates that wet season runoff is projected to increase in both the Sacramento River and San Joaquin River regions in the four representative models used. This indicates greater (than the historical) flooding risks in both of the regions. In light of this, it is imperative to increase the resilience of the current system to big floods. Another option is to divert flood water to recharge groundwater. The potential benefits include flood risk reduction, land subsidence mitigation, ecosystem enhancement, drought preparedness, among others. California Department of Water Resources recently proposed an integrated water resource management strategy that uses flood water for managed aquifer recharge on agricultural lands [73]. The State is in the early phase of implementing this strategy. As another example, this study shows that the April–July runoff is projected to increase in most cases, particularly for less snow-dominated Sacramento River region. This implies increased drought risk and less reliable water supply in spring and summer. In the most recent 2012–2015 statewide drought, the State successfully explored various drought responses, including water conservation and water transfer, using alternative water supply resources [74].

5. Conclusions

This study highlights the non-stationarity and long-term uncertainty in key variables typically applied in guiding water resources planning and management in the State of California, United States. These variables include water year types as well as runoff volumes and hydrological droughts at temporal scales that are meaningful to water operations. Specifically, the study indicates that the temporal distribution of annual runoff is expected to change in terms of shifting more volume to wet season from snowmelt season for both major water supply regions in California. Increases in wet season runoff volume are more noticeable under the higher (versus lower) emission scenario, while decreases in the snowmelt season runoff are generally more significant under the lower (versus higher) emission scenario. In comparison, changes in water year types are more influenced by climate models, rather than emission scenarios. "Cool/wet" and "average" models

both project more wet years and less critical years for both regions throughout the end of this century, while the "warm/dry" model projects more critical years and less wet years. When comparing two regions, generally speaking, the Sacramento River region is expected to experience more wet years and less critical years than the San Joaquin River region, due to their hydroclimatic and geographic differences. Hydrological droughts in future snowmelt season and wet season exhibit upward and downward trends in most scenarios, respectively. However, changing directions in hydrological droughts on annual and multi-year scales tend to be climate-model and scenario dependent.

These findings suggest that adaptive water resources management strategies need to take considerable uncertainty in future climate and the more certain hydro-climatic non-stationarity into account. In light of these findings, California Department of Water Resources (DWR) is exploring climate-adaptive water year typing methods and assessing their potential impacts on the current water classification system and water operations in the State. DWR is also developing plans to reduce flood risks and increase water supply reliability. These efforts will be reported in our following-up studies.

Appendix A. Historical Data and GCM Information

Data Sources:

(a) Historical full natural flow record
SBB: http://cdec.water.ca.gov/dynamicapp/staMeta?station_id=SBB
FTO: http://cdec.water.ca.gov/dynamicapp/staMeta?station_id=FTO
YRS: http://cdec.water.ca.gov/dynamicapp/staMeta?station_id=YRS
AMF: http://cdec.water.ca.gov/dynamicapp/staMeta?station_id=AMF
SNS: http://cdec.water.ca.gov/dynamicapp/staMeta?station_id=SNS
TLG: http://cdec.water.ca.gov/dynamicapp/staMeta?station_id=TLG
MRC: http://cdec.water.ca.gov/dynamicapp/staMeta?station_id=MRC
SJF: http://cdec.water.ca.gov/dynamicapp/staMeta?station_id=SJF
(b) Historical precipitation and temperature https://www.esrl.noaa.gov/psd/data/gridded/data.livneh.html
(c) Historical snow water equivalent https://cdec.water.ca.gov/reportapp/javareports?name=PAGE6
(d) California Fourth Climate Change Assessment streamflow projections https://cal-adapt.org/tools/streamflow/
(e) California Fourth Climate Change Assessment precipitation and temperature projections https://cal-adapt.org/data/loca/
(f) California Fourth Climate Change Assessment snow water equivalent projections https://cal-adapt.org/tools/snowpack
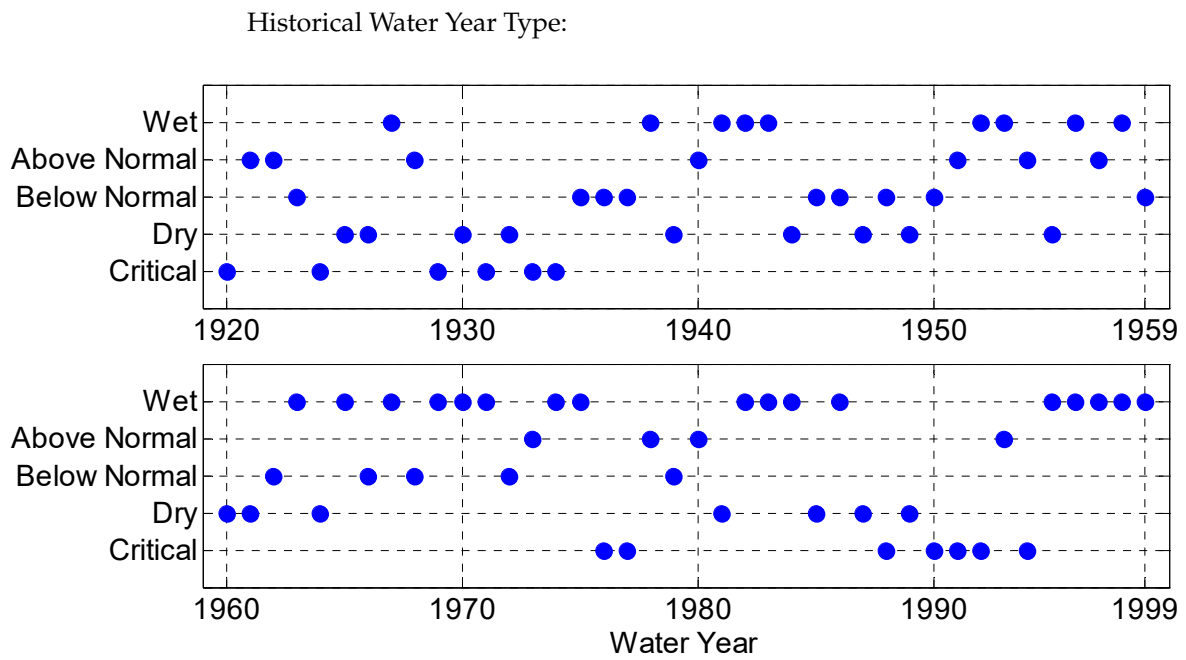
Historical Water Year Type:

Figure A1. Historical water year type classification in the Sacramento River region.
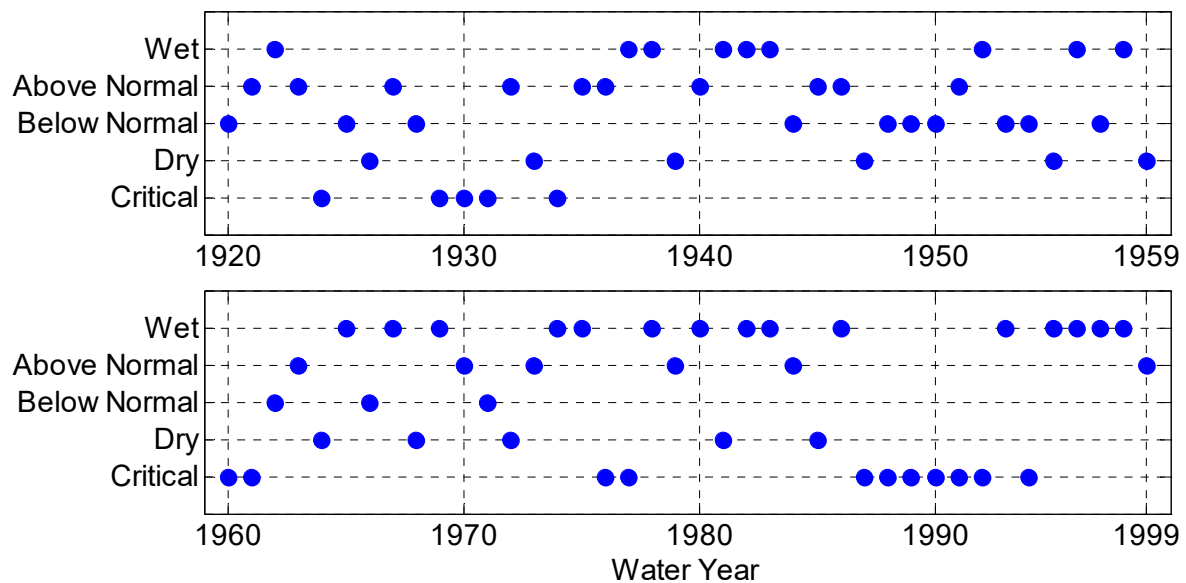
Figure A2. Historical water year type classification in the San Joaquin River region.

Table A1. GCMs selected for this study [1].

Model ID	Model Name	Model Institution
Cool/wet	CNRM-CM5	Centre National de Recherches Météorologiques/Centre Européen de Recherche et de Formation Avancée en Calcul Scientifique
Average	CanESM2	Canadian Centre for Climate Modeling and Analysis
Warm/dry	HadGEM2-ES	Met Office Hadley Centre/Instituto Nacional de Pesquisas Espaciais
Complement	MIROC5	Atmosphere and Ocean Research Institute (The University of Tokyo), National Institute for Environmental Studies, and Japan Agency for Marine-Earth Science and Technology

[1] Adapted from [61].

Appendix B. Additional Results
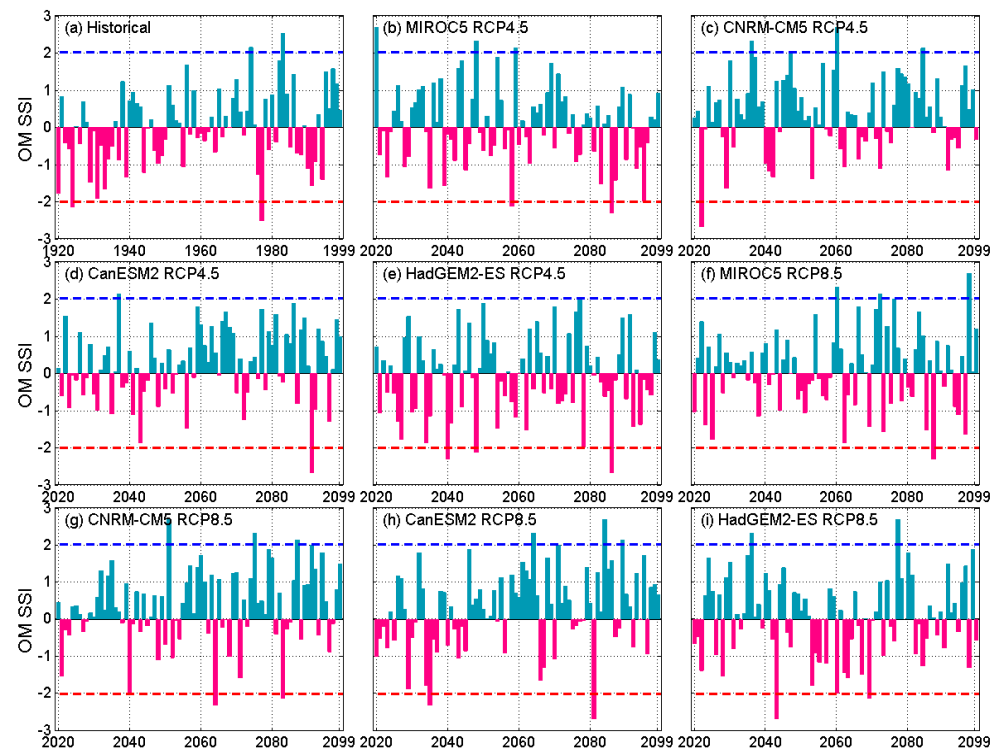
Figure A3. Historical and projected October–March SSI for SAC4. Values above the blue dash line represent extremely wet conditions while values below the red dash line indicate extremely dry conditions.
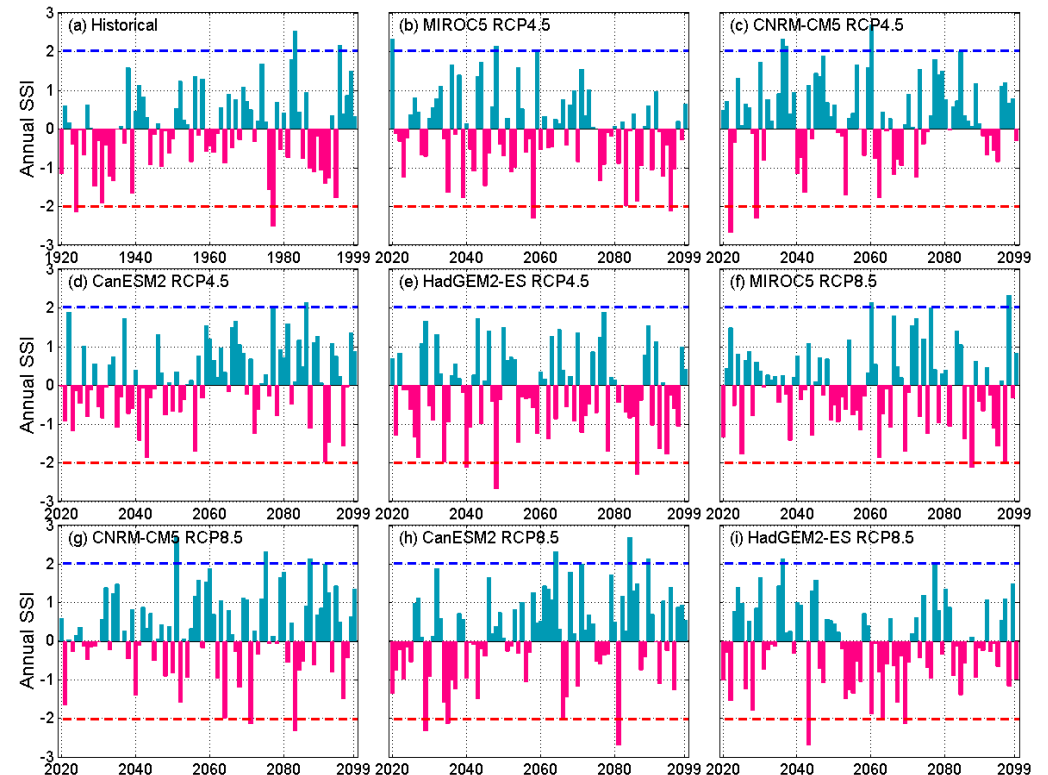
Figure A4. Historical and projected annual SSI for SAC4. Values above the blue dash line represent extremely wet conditions while values below the red dash line indicate extremely dry conditions.
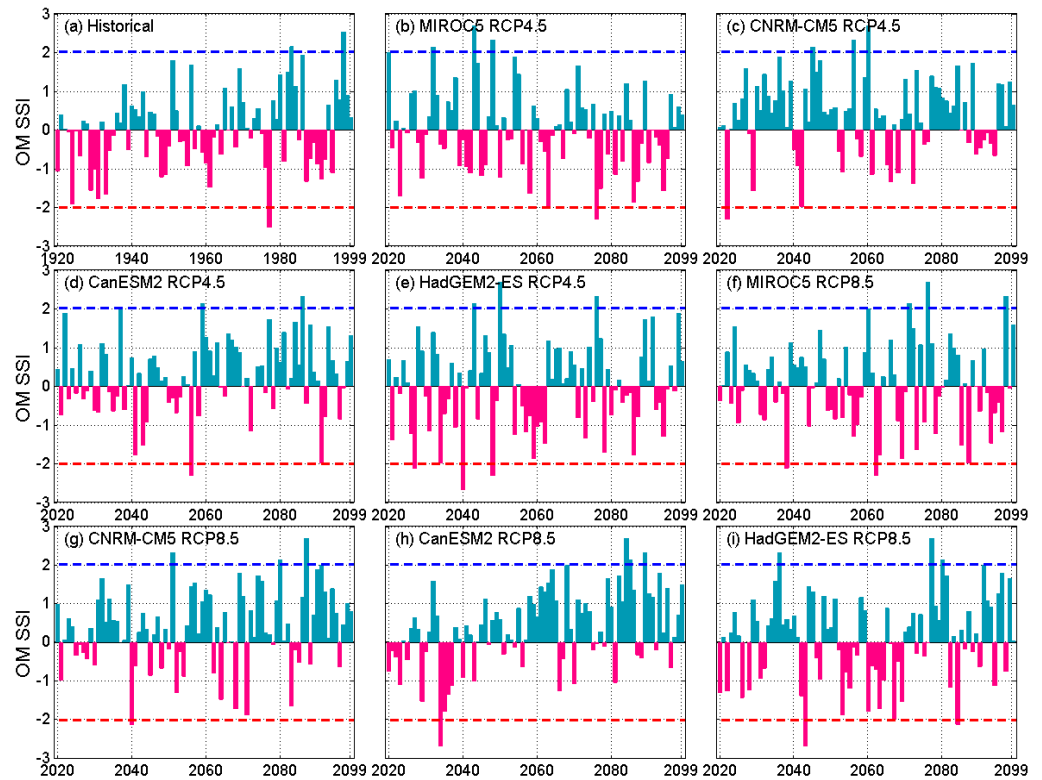
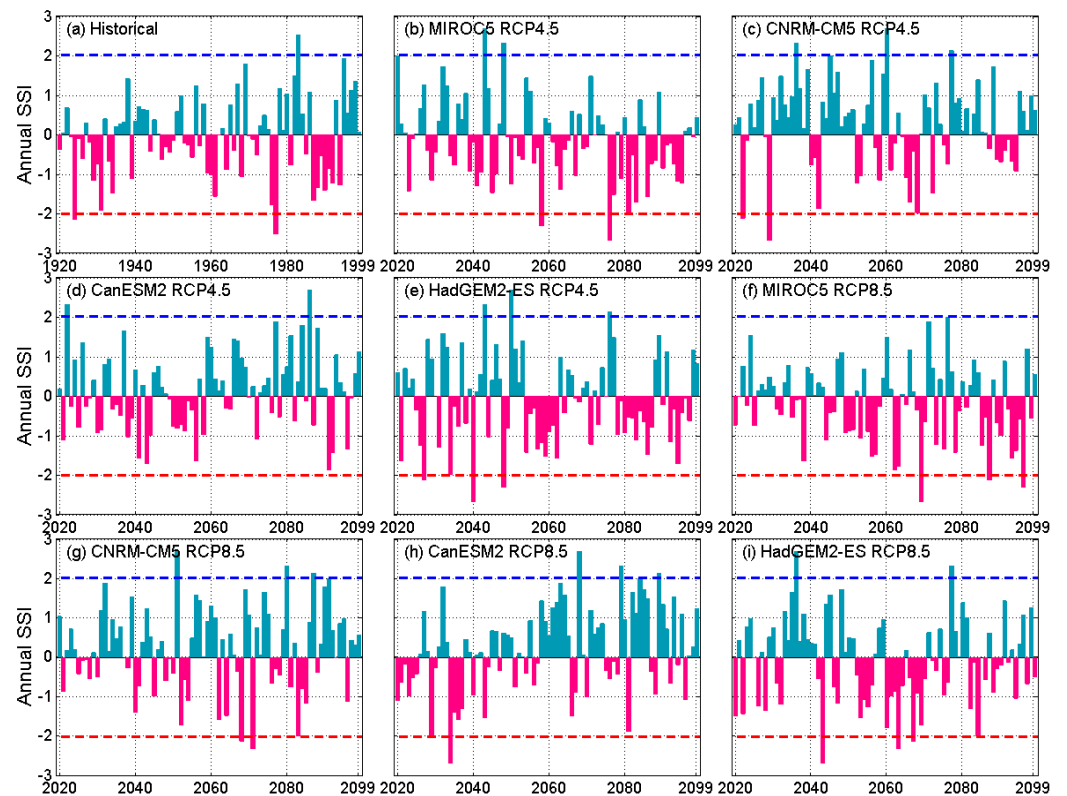**Figure A5.** Historical and projected October–March SSI for SJQ4. Values above the blue dash line represent extremely wet conditions while values below the red dash line indicate extremely dry conditions.

Figure A6. Historical and projected annual SSI for SJQ4. Values above the blue dash line represent extremely wet conditions while values below the red dash line indicate extremely dry conditions.

**Table A2.** Mean and variance of seasonal and annual SSI indices.

Scenarios		AJ		OM		WY	
		Mean	Variance	Mean	Variance	Mean	Variance
SAC4	Historical	−0.10	1.00	−0.04	1.03	−0.07	1.01
MIROC5 (complement)	RCP 4.5	−0.32	0.83	0.05	1.06	−0.07	1.01
	RCP 8.5	−0.10	1.08	0.37	0.97	0.27	1.10
CNRM-CM5 (cool/wet)	RCP 4.5	−0.24	0.75	0.23	0.89	0.12	0.92
	RCP 8.5	−0.30	1.02	−0.10	1.12	−0.18	1.10
CanESM2 (average)	RCP 4.5	−0.32	0.85	0.09	1.05	−0.06	1.01
	RCP 8.5	−0.24	0.93	0.35	1.00	0.24	1.09
HadGEM2-ES (warm/dry)	RCP 4.5	−0.32	0.85	0.26	1.13	0.13	1.25
	RCP 8.5	−0.36	0.85	0.04	1.16	−0.10	1.06
SJQ4	Historical	−0.09	0.94	−0.02	0.98	−0.08	0.97
MIROC5 (complement)	RCP 4.5	−0.28	0.86	0.00	1.07	−0.16	1.04
	RCP 8.5	0.12	1.15	0.36	0.96	0.24	1.11
CNRM-CM5 (cool/wet)	RCP 4.5	0.00	0.89	0.24	0.86	0.11	0.93
	RCP 8.5	−0.21	1.07	−0.02	1.27	−0.12	1.24
CanESM2 (average)	RCP 4.5	−0.31	0.86	0.02	1.11	−0.20	0.93
	RCP 8.5	0.02	1.11	0.36	0.98	0.22	1.11
HadGEM2-ES (warm/dry)	RCP 4.5	0.05	1.19	0.34	1.02	0.20	1.19
	RCP 8.5	−0.23	1.03	0.07	1.24	−0.10	1.17

Table A3. *p*-values of trends in SSI indices presented in Table 1.

Scenarios		OM	AJ	WY	Two-Year	Three-Year	Four-Year	Five-Year
SCA4	Historical	0.256	0.057	0.896	0.654	0.519	0.443	0.333
MIROC5 (complement)	RCP 4.5	0.764	0.004	0.275	0.011	<0.001	<0.001	<0.001
	RCP 8.5	0.337	<0.001	0.749	0.738	0.535	0.663	0.479
CNRM-CM5 (cool/wet)	RCP 4.5	0.196	0.906	0.250	0.191	0.070	0.059	0.121
	RCP 8.5	0.095	0.035	0.264	0.033	0.024	0.021	0.009
CanESM2 (average)	RCP 4.5	0.036	0.526	0.057	0.037	0.050	0.035	0.021
	RCP 8.5	0.006	0.522	0.024	0.004	0.002	<0.001	<0.001
HadGEM2-ES (warm/dry)	RCP 4.5	0.389	0.003	0.131	0.055	0.012	0.002	0.002
	RCP 8.5	0.948	0.006	0.381	0.409	0.092	0.036	0.023
SJQ4	Historical	0.399	0.261	0.719	0.783	0.790	0.810	0.994
MIROC5 (complement)	RCP 4.5	0.522	0.006	0.046	0.001	<0.001	<0.001	<0.001
	RCP 8.5	0.759	0.001	0.118	0.035	0.026	0.003	<0.001
CNRM-CM5 (cool/wet)	RCP 4.5	0.287	0.724	0.729	0.954	0.906	0.963	0.970
	RCP 8.5	0.044	0.227	0.381	0.361	0.171	0.082	0.057
CanESM2 (average)	RCP 4.5	0.041	0.168	0.125	0.133	0.200	0.244	0.290
	RCP 8.5	<0.001	0.057	<0.001	<0.001	<0.001	<0.001	<0.001
HadGEM2-ES (warm/dry)	RCP 4.5	0.875	0.069	0.272	0.043	0.013	0.003	0.001
	RCP 8.5	0.145	0.056	0.724	0.354	0.112	0.098	0.092

Table A4. Slopes of trends in precipitation and temperature (bold number indicates that trend is statistically significant).

Scenarios		Precipitation (mm/Year)			Temperature (Deg. C/Decade)		
		OM	**AJ**	**WY**	**OM**	**AJ**	**WY**
SCA4	Historical	2.52	0.00	2.52	0.06	0.00	0.05
MIROC5 (complement)	RCP 4.5	−1.02	−0.40	−1.46	**0.17**	**0.29**	**0.25**
	RCP 8.5	−0.54	−0.21	−0.28	**0.41**	**0.46**	**0.45**
CNRM-CM5 (cool/wet)	RCP 4.5	−0.30	0.28	0.33	**0.30**	**0.28**	**0.30**
	RCP 8.5	3.39	−0.39	3.39	**0.59**	**0.64**	**0.63**
CanESM2 (average)	RCP 4.5	3.51	0.05	3.62	**0.18**	**0.22**	**0.22**
	RCP 8.5	**5.98**	0.00	**6.62**	**0.53**	**0.66**	**0.64**
HadGEM2-ES (warm/dry)	RCP 4.5	0.09	−0.18	−0.23	**0.34**	**0.33**	**0.36**
	RCP 8.5	−0.12	**−0.85**	−0.47	**0.57**	**0.74**	**0.69**
SJQ4	Historical	1.33	−0.10	1.27	0.03	−0.05	−0.01
MIROC5 (complement)	RCP 4.5	−1.26	−0.26	−2.22	**0.20**	**0.32**	**0.27**
	RCP 8.5	−1.34	−0.49	−1.64	**0.44**	**0.49**	**0.48**
CNRM-CM5 (cool/wet)	RCP 4.5	−2.19	0.33	−1.18	**0.31**	**0.28**	**0.30**
	RCP 8.5	1.80	−0.50	1.52	**0.59**	**0.70**	**0.63**
CanESM2 (average)	RCP 4.5	2.38	0.03	2.31	**0.19**	**0.16**	**0.20**
	RCP 8.5	**7.65**	0.03	**8.60**	**0.55**	**0.59**	**0.59**
HadGEM2-ES (warm/dry)	RCP 4.5	0.16	−0.06	−0.37	**0.35**	**0.32**	**0.36**
	RCP 8.5	0.61	**−0.86**	0.24	**0.57**	**0.72**	**0.67**
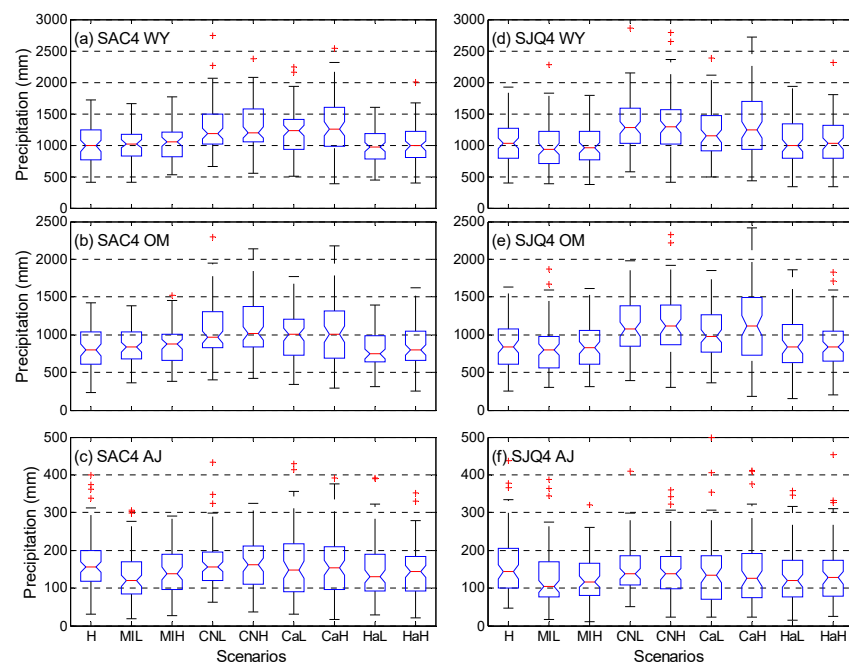
Figure A7. Historical (water year 1920–1999) and projected (water year 2020–2099) annual precipitation (first row), October–March precipitation (second row), and April–July precipitation (Third Row) for SAC4 (first column) and SJQ4 (second column). H: historical; MIL: MIROC5 RCP 4.5; MIH: MIROC5 RCP 8.5; CNL: CNRM-CM5 RCP 4.5; CNH: CNRM-CM5 RCP 8.5; CaL: CanESM2 RCP 4.5; CaH: CanESM2 RCP 8.5; HaL: HadGEM2-ES RCP 4.5; HaH: HadGEM2-ES RCP 8.5. The corresponding data source provided in Appendix A.
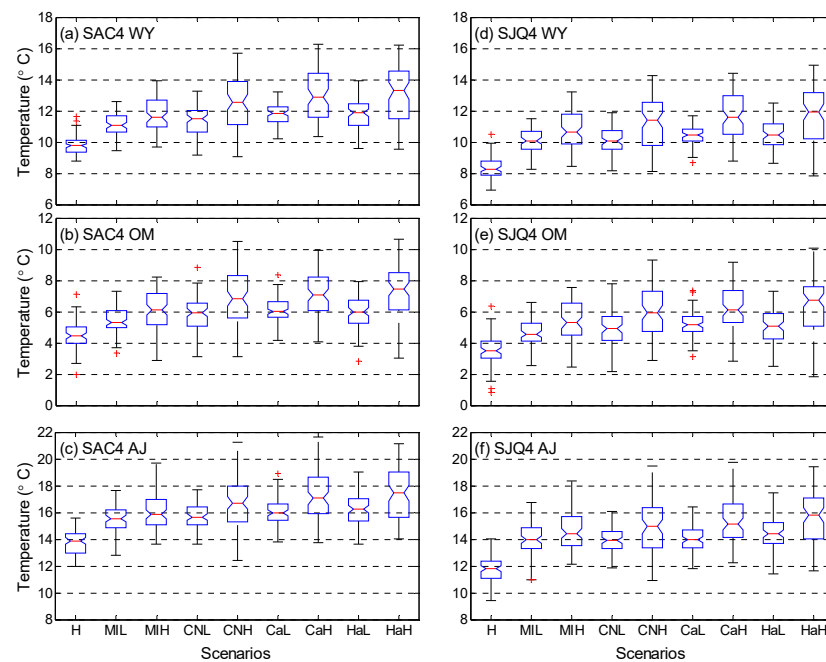
Figure A8. Historical (water year 1920–1999) and projected (water year 2020–2099) annual temperature (first row), October–March temperature (second row), and April–July temperature (Third Row) for SAC4 (first column) and SJQ4 (second column). H: historical; MIL: MIROC5 RCP 4.5; MIH: MIROC5 RCP 8.5; CNL: CNRM-CM5 RCP 4.5; CNH: CNRM-CM5 RCP 8.5; CaL: CanESM2 RCP 4.5; CaH: CanESM2 RCP 8.5; HaL: HadGEM2-ES RCP 4.5; HaH: HadGEM2-ES RCP 8.5. The corresponding data source provided in Appendix A.

Acronyms and Abbreviations

AJ	April–July
AMF	American River at Folsom
AN	Above Normal Years
BN	Below Normal Years
BO	Biological Opinion
CCCA4	California's Fourth Climate Change Assessment
CMIP	Coupled Model Intercomparison Project
D1641	Water Right Decision 1641
DWR	California Department of Water Resources
FTO	Feather River at Oroville
GCM	General Circulation Model
MAF	Million Acre-feet
MRC	Merced River at Lake McClure
OM	October–March
RCP	Representative Concentration Pathways
SAC	Sacramento Four Rivers
SBB	Sacramento River above Bend Bridge
SDAT	Standardized Drought Analysis Toolbox
SJF	San Joaquin River at Millerton Lake
SJQ4	San Joaquin Four Rivers
SNS	Stanislaus River at New Melones
SSI	Standardized Streamflow Index
SWE	Snow Water Equivalent
TLG	Tuolumne River at Don Pedro
VIC	Variable Infiltration Capacity Model
WYI	Water Year Index
WYT	Water Year Type
YRS	Yuba River at Smartville

References

1. Dyurgerov, M.B.; Meier, M.F. Twentieth century climate change: Evidence from small glaciers. *Proc. Natl. Acad. Sci. USA* **2000**, *97*, 1406–1411. [CrossRef]
2. Easterling, D.R.; Evans, J.L.; Groisman, P.Y.; Karl, T.R.; Kunkel, K.E.; Ambenje, P. Observed variability and trends in extreme climate events: A brief review. *Bull. Am. Meteorol. Soc.* **2000**, *81*, 417–426. [CrossRef]
3. Mote, P.W.; Hamlet, A.F.; Clark, M.P.; Lettenmaier, D.P. Declining mountain snowpack in western North America. *Bull. Am. Meteorol. Soc.* **2005**, *86*, 39–50. [CrossRef]
4. Oerlemans, J. Extracting a climate signal from 169 glacier records. *Science* **2005**, *308*, 675–677. [CrossRef] [PubMed]
5. Huntington, T.G. Evidence for intensification of the global water cycle: Review and synthesis. *J. Hydrol.* **2006**, *319*, 83–95. [CrossRef]
6. Barnett, T.P.; Pierce, D.W.; Hidalgo, H.G.; Bonfils, C.; Santer, B.D.; Das, T.; Bala, G.; Wood, A.W.; Nozawa, T.; Mirin, A.A. Human-induced changes in the hydrology of the western United States. *Science* **2008**, *319*, 1080–1083. [CrossRef] [PubMed]
7. Milly, P.C.; Betancourt, J.; Falkenmark, M.; Hirsch, R.M.; Kundzewicz, Z.W.; Lettenmaier, D.P.; Stouffer, R.J. Stationarity is dead: Whither water management? *Science* **2008**, *319*, 573–574. [CrossRef]
8. Berghuijs, W.; Woods, R.; Hrachowitz, M. A precipitation shift from snow towards rain leads to a decrease in streamflow. *Nat. Clim. Chang.* **2014**, *4*, 583–586. [CrossRef]
9. Williams, A.P.; Cook, E.R.; Smerdon, J.E.; Cook, B.I.; Abatzoglou, J.T.; Bolles, K.; Baek, S.H.; Badger, A.M.; Livneh, B. Large contribution from anthropogenic warming to an emerging North American megadrought. *Science* **2020**, *368*, 314–318. [CrossRef]
10. Diffenbaugh, N.S.; Scherer, M.; Trapp, R.J. Robust increases in severe thunderstorm environments in response to greenhouse forcing. *Proc. Natl. Acad. Sci. USA* **2013**, *110*, 16361–16366. [CrossRef]
11. Yoon, J.-H.; Wang, S.S.; Gillies, R.R.; Kravitz, B.; Hipps, L.; Rasch, P.J. Increasing water cycle extremes in California and in relation to ENSO cycle under global warming. *Nat. Commun.* **2015**, *6*, 1–6. [CrossRef] [PubMed]
12. Chikamoto, Y.; Timmermann, A.; Widlansky, M.J.; Balmaseda, M.A.; Stott, L. Multi-year predictability of climate, drought, and wildfire in southwestern North America. *Sci. Rep.* **2017**, *7*, 1–12. [CrossRef] [PubMed]
13. Asadieh, B.; Krakauer, N.Y. Global change in streamflow extremes under climate change over the 21st century. *Hydrol. Earth Syst. Sci.* **2017**, *21*, 5863. [CrossRef]
14. Swain, D.L.; Langenbrunner, B.; Neelin, J.D.; Hall, A. Increasing precipitation volatility in twenty-first-century California. *Nat. Clim. Chang.* **2018**, *8*, 427–433. [CrossRef]
15. Shannon, S.; Smith, R.; Wiltshire, A.; Payne, T.; Huss, M.; Betts, R.; Caesar, J.; Koutroulis, A.; Jones, D.; Harrison, S. Global glacier volume projections under high-end climate change scenarios. *Cryosphere* **2019**, *13*, 325–350. [CrossRef]
16. USCB. *United States Census Bureau QuickFacts: United States*; U.S. Census Bureau: Washington, DC, USA, 2019.
17. Becker, L.; Yeh, W.; Fults, D.; Sparks, D. Operations models for central valley project. *J. Water Resour. Plann. Manag. Div. Am. Soc. Civ. Eng.* **1976**, *102*, 101–115.
18. Sabet, M.H.; Coe, J.Q. Models for water and power scheduling for the California State Water Project. *J. Am. Water Resour. Assoc.* **1986**, *22*, 587–596. [CrossRef]
19. CSWRCB. *Water Right Decision 1641*; CSWRCB: Sacramento, CA, USA, 1999; p. 225.
20. USFWS. *Formal Endangered Species Act Consultation on the Proposed Coordinated Operations of the Central Valley Project (CVP) and State Water Project (SWP)*; USFWS: Sacramento, CA, USA, 2008; p. 410.
21. Null, S.E.; Viers, J.H. In bad waters: Water year classification in nonstationary climates. *Water Resour. Res.* **2013**, *49*, 1137–1148. [CrossRef]
22. Rosenberg, E.A.; Wood, A.W.; Steinemann, A.C. Statistical applications of physically based hydrologic models to seasonal streamflow forecasts. *Water Resour. Res.* **2011**, *47*, 47. [CrossRef]
23. Harrison, B.; Bales, R. Skill assessment of water supply forecasts for western Sierra Nevada watersheds. *J. Hydrol. Eng.* **2016**, *21*, 04016002. [CrossRef]
24. He, M.; Whitin, B.; Hartman, R.; Henkel, A.; Fickenschers, P.; Staggs, S.; Morin, A.; Imgarten, M.; Haynes, A.; Russo, M. Verification of ensemble water supply forecasts for Sierra Nevada watersheds. *Hydrology* **2016**, *3*, 35. [CrossRef]
25. He, M.; Russo, M.; Anderson, M. Predictability of seasonal streamflow in a changing climate in the Sierra Nevada. *Climate* **2016**, *4*, 57. [CrossRef]
26. Palmer, W.C. *Meteorological Drought*; US Department of Commerce, Weather Bureau: Silver Spring, MD, USA, 1965; Volume 30.
27. Gibbs, W.; Maher, J. *Rainfall Deciles as Drought Indicators*; Commonwealth of Australia: Melbourne, Australia, 1967.
28. McKee, T.B.; Doesken, N.J.; Kleist, J. The relationship of drought frequency and duration to time scales. In Proceedings of the 8th Conference on Applied Climatology, Anaheim, CA, USA, 17–22 January 1993; pp. 179–183.
29. Keyantash, J.A.; Dracup, J.A. An aggregate drought index: Assessing drought severity based on fluctuations in the hydrologic cycle and surface water storage. *Water Resour. Res.* **2004**, *40*, 1–13. [CrossRef]
30. Shukla, S.; Wood, A.W. Use of a standardized runoff index for characterizing hydrologic drought. *Geophys. Res. Lett.* **2008**, *35*, L02405. [CrossRef]
31. Vicente-Serrano, S.M.; Beguería, S.; López-Moreno, J.I. A multiscalar drought index sensitive to global warming: The standardized precipitation evapotranspiration index. *J. Clim.* **2010**, *23*, 1696–1718. [CrossRef]

32. Hao, Z.; AghaKouchak, A. Multivariate standardized drought index: A parametric multi-index model. *Adv. Water Resour.* **2013**, *57*, 12–18. [CrossRef]

33. Thomas, B.F.; Famiglietti, J.S.; Landerer, F.W.; Wiese, D.N.; Molotch, N.P.; Argus, D.F. GRACE groundwater drought index: Evaluation of California Central Valley groundwater drought. *Remote Sens. Environ.* **2017**, *198*, 384–392. [CrossRef]

34. Bonfils, C.; Duffy, P.B.; Santer, B.D.; Wigley, T.M.; Lobell, D.B.; Phillips, T.J.; Doutriaux, C. Identification of external influences on temperatures in California. *Clim. Chang.* **2008**, *87*, 43–55. [CrossRef]

35. Das, T.; Hidalgo, H.; Pierce, D.; Barnett, T.; Dettinger, M.; Cayan, D.; Bonfils, C.; Bala, G.; Mirin, A. Structure and detectability of trends in hydrological measures over the western United States. *J. Hydrometeorol.* **2009**, *10*, 871–892. [CrossRef]

36. Knowles, N.; Dettinger, M.D.; Cayan, D.R. Trends in snowfall versus rainfall in the western United States. *J. Clim.* **2006**, *19*, 4545–4559. [CrossRef]

37. Kapnick, S.; Hall, A. Causes of recent changes in western North American snowpack. *Clim. Dyn.* **2012**, *38*, 1885–1899. [CrossRef]

38. Stewart, I.T.; Cayan, D.R.; Dettinger, M.D. Changes toward earlier streamflow timing across western North America. *J. Clim.* **2005**, *18*, 1136–1155. [CrossRef]

39. Regonda, S.K.; Rajagopalan, B.; Clark, M.; Pitlick, J. Seasonal cycle shifts in hydroclimatology over the western United States. *J. Clim.* **2005**, *18*, 372–384. [CrossRef]

40. Hidalgo, H.G.; Das, T.; Dettinger, M.D.; Cayan, D.R.; Pierce, D.W.; Barnett, T.P.; Bala, G.; Mirin, A.; Wood, A.W.; Bonfils, C. Detection and attribution of streamflow timing changes to climate change in the western United States. *J. Clim.* **2009**, *22*, 3838–3855. [CrossRef]

41. Das, T.; Dettinger, M.D.; Cayan, D.R.; Hidalgo, H.G. Potential increase in floods in California's Sierra Nevada under future climate projections. *Clim. Chang.* **2011**, *109*, 71–94. [CrossRef]

42. Das, T.; Maurer, E.P.; Pierce, D.W.; Dettinger, M.D.; Cayan, D.R. Increases in flood magnitudes in California under warming climates. *J. Hydrol.* **2013**, *501*, 101–110. [CrossRef]

43. Rhoades, A.M.; Ullrich, P.A.; Zarzycki, C.M. Projecting 21st century snowpack trends in western USA mountains using variable-resolution CESM. *Clim. Dyn.* **2018**, *50*, 261–288. [CrossRef]

44. Maurer, E.P. Uncertainty in hydrologic impacts of climate change in the Sierra Nevada, California, under two emissions scenarios. *Clim. Chang.* **2007**, *82*, 309–325. [CrossRef]

45. Cayan, D.R.; Luers, A.L.; Franco, G.; Hanemann, M.; Croes, B.; Vine, E. Overview of the California climate change scenarios project. *Clim. Chang.* **2008**, *87*, 1–6. [CrossRef]

46. Meehl, G.A.; Boer, G.J.; Covey, C.; Latif, M.; Stouffer, R.J. The coupled model intercomparison project (CMIP). *Bull. Am. Meteorol. Soc.* **2000**, *81*, 313–318. [CrossRef]

47. Eyring, V.; Bony, S.; Meehl, G.A.; Senior, C.A.; Stevens, B.; Stouffer, R.J.; Taylor, K.E. Overview of the Coupled Model Intercomparison Project Phase 6 (CMIP6) experimental design and organization. *Geosci. Model Dev.* **2016**, *9*, 1937–1958. [CrossRef]

48. Taylor, K.E.; Stouffer, R.J.; Meehl, G.A. An overview of CMIP5 and the experiment design. *Bull. Am. Meteorol. Soc.* **2012**, *93*, 485–498. [CrossRef]

49. Dettinger, M.; Anderson, J.; Anderson, M.; Brown, L.R.; Cayan, D.; Maurer, E. Climate change and the Delta. *San Fr. Estuary Watershed Sci.* **2016**, *14*, 14. [CrossRef]

50. He, M.; Schwarz, A.; Lynn, E.; Anderson, M. Projected changes in precipitation, temperature, and drought across California's hydrologic regions in the 21st century. *Climate* **2018**, *6*, 31. [CrossRef]

51. Mallakpour, I.; Sadegh, M.; AghaKouchak, A. A new normal for streamflow in California in a warming climate: Wetter wet seasons and drier dry seasons. *J. Hydrol.* **2018**, *567*, 203–211. [CrossRef]

52. He, M.; Anderson, M.; Schwarz, A.; Das, T.; Lynn, E.; Anderson, J.; Munévar, A.; Vasquez, J.; Arnold, W. Potential Changes in Runoff of California's Major Water Supply Watersheds in the 21st Century. *Water* **2019**, *11*, 1651. [CrossRef]

53. Wang, J.; Yin, H.; Reyes, E.; Smith, T.; Chung, F. *Mean and Extreme Climate Change Impacts on the State Water Project*; California's Fourth Climate Change Assessment, California Energy Commission: Sacramento, CA, USA, 2018.

54. Ray, P.; Wi, S.; Schwarz, A.; Correa, M.; He, M.; Brown, C. Vulnerability and risk: Climate change and water supply from California's Central Valley water system. *Clim. Chang.* **2020**, *161*, 177–199. [CrossRef]

55. Woldemeskel, F.; Sharma, A.; Sivakumar, B.; Mehrotra, R. Quantification of precipitation and temperature uncertainties simulated by CMIP3 and CMIP5 models. *J. Geophys. Res. Atmos.* **2016**, *121*, 3–17. [CrossRef]

56. Polade, S.D.; Gershunov, A.; Cayan, D.R.; Dettinger, M.D.; Pierce, D.W. Natural climate variability and teleconnections to precipitation over the Pacific-North American region in CMIP3 and CMIP5 models. *Geophys. Res. Lett.* **2013**, *40*, 2296–2301. [CrossRef]

57. Ficklin, D.L.; Letsinger, S.L.; Stewart, I.T.; Maurer, E.P. Assessing differences in snowmelt-dependent hydrologic projections using CMIP3 and CMIP5 climate forcing data for the western United States. *Hydrol. Res.* **2016**, *47*, 483–500. [CrossRef]

58. Bedsworth, L.; Cayan, D.; Franco, G.; Fisher, L.; Ziaja, S. *California's Fourth Climate Change Assessment Statewide Summary Report*; California's Fourth Climate Change Assessment, California Energy Commission: Sacramento, CA, USA, 2018; p. 133.

59. Pierce, D.W.; Cayan, D.R.; Thrasher, B.L. Statistical downscaling using localized constructed analogs (LOCA). *J. Hydrometeorol.* **2014**, *15*, 2558–2585. [CrossRef]

60. Liang, X.; Wood, E.F.; Lettenmaier, D.P. Surface soil moisture parameterization of the VIC-2L model: Evaluation and modification. *Glob. Planet. Chang.* **1996**, *13*, 195–206. [CrossRef]

61. Pierce, D.W.; Kalansky, J.F.; Cayan, D.R. *Climate, Drought, and Sea Level Rise Scenarios for California's Fourth Climate Change Assessment*; Technical Report CCCA4-CEC-2018-006; California Energy Commission: Sacramento, CA, USA, 2018.

62. He, M.; Gautam, M. Variability and trends in precipitation, temperature and drought indices in the State of California. *Hydrology* **2016**, *3*, 14. [CrossRef]

63. Farahmand, A.; AghaKouchak, A. A generalized framework for deriving nonparametric standardized drought indicators. *Adv. Water Resour.* **2015**, *76*, 140–145. [CrossRef]

64. Mann, H.B. Nonparametric tests against trend. *Econometrica* **1945**, *13*, 245–259. [CrossRef]

65. Kendall, M. *Rank Correlation Methods*; Charles Griffin: London, UK, 1975.

66. Thiel, H. A rank-invariant method of linear and polynomial regression analysis, Part 3. In Proceedings of the Koninalijke Nederlandse Akademie van Weinenschatpen A, Amsterdam, The Netherlands, 25 February 1950; pp. 1397–1412.

67. Sen, P.K. Estimates of the regression coefficient based on Kendall's tau. *J. Am. Stat. Assoc.* **1968**, *63*, 1379–1389. [CrossRef]

68. Dettinger, M.D.; Cayan, D.R. Large-scale atmospheric forcing of recent trends toward early snowmelt runoff in California. *J. Clim.* **1995**, *8*, 606–623. [CrossRef]

69. Serreze, M.C.; Clark, M.P.; Armstrong, R.L.; McGinnis, D.A.; Pulwarty, R.S. Characteristics of the western United States snowpack from snowpack telemetry (SNOTEL) data. *Water Resour. Res.* **1999**, *35*, 2145–2160. [CrossRef]

70. Margulis, S.A.; Cortés, G.; Girotto, M.; Durand, M. A Landsat-era Sierra Nevada snow reanalysis (1985–2015). *J. Hydrometeorol.* **2016**, *17*, 1203–1221. [CrossRef]

71. Huning, L.S.; AghaKouchak, A. Mountain snowpack response to different levels of warming. *Proc. Natl. Acad. Sci. USA* **2018**, *115*, 10932–10937. [CrossRef]

72. Lynn, E.; Cuthbertson, A.; He, M.; Vasquez, J.P.; Anderson, M.L.; Coombe, P.; Abatzoglou, J.T.; Hatchett, B.J. Precipitation-phase partitioning at landscape scales to regional scales. *Hydrol. Earth Syst. Sci.* **2020**, *24*, 5317–5328. [CrossRef]

73. DWR. *Flood-MAR White Paper*; California Department of Water Resources: Sacramento, CA, USA, 2018; p. 56.

74. Lund, J.R. California's agricultural and urban water supply reliability and the Sacramento–San Joaquin Delta. *San Franc. Estuary Watershed Sci.* **2016**, *14*, 6. [CrossRef]

Selection of Effective GCM Bias Correction Methods and Evaluation of Hydrological Response under Future Climate Scenarios

Yaogeng Tan [1] , **Sandra M. Guzman** [2,*] , **Zengchuan Dong** [1] **and Liang Tan** [3]

1   College of Hydrology and Water Resources, Hohai University, Nanjing 210098, China;
    170201010014@hhu.edu.cn (Y.T.); zcdong@hhu.edu.cn (Z.D.)
2   Agricultural and Biological Engineering Department, Indian River Research and Education Center,
    University of Florida, Fort Pierce, FL 34945, USA
3   Three Gorges Hydrology and Water Resources Survey, Bureau of Hydrology, Yangtze River Water
    Conservancy Commission, Yichang 443000, China; sxtanl@cjh.com.cn
*   Correspondence: sandra.guzmangut@ufl.edu

Abstract: Global climate change is presenting a variety of challenges to hydrology and water resources because it strongly affects the hydrologic cycle, runoff, and water supply and demand. In this study, we assessed the effects of climate change scenarios on hydrological variables (i.e., evapotranspiration and runoff) by linking the outputs from the global climate model (GCM) with the Soil and Water Assessment Tool (SWAT) for a case study in the Lijiang River Basin, China. We selected a variety of bias correction methods and their combinations to correct the lower resolution GCM outputs of both precipitation and temperature. Then, the SWAT model was calibrated and validated using the observed flow data and corrected historical GCM with the optimal correction method selected. Hydrological variables were simulated using the SWAT model under emission scenarios RCP2.6, RCP4.5, and RCP8.5. The results demonstrated that correcting methods have a positive effect on both daily precipitation and temperature, and a hybrid method of bias correction contributes to increased performance in most cases and scenarios. Based on the bias corrected scenarios, precipitation annual average, temperature, and evapotranspiration will increase. In the case of precipitation and runoff, projection scenarios show an increase compared with the historical trends, and the monthly distribution of precipitation, evapotranspiration, and runoff shows an uneven distribution compared with baseline. This study provides an insight on how to choose a proper GCM and bias correction method and a helpful guide for local water resources management.

Keywords: GCM; bias correction methods; hydrological simulation; climate change

1. Introduction

Global climate change and its impact on hydrology and water resources have received special attention due to its effects on land use and development [1]. The hydrologic cycle in watersheds is changing greatly under the influence of global climate change. According to the fifth assessment report of Intergovernmental Panel on Climate Change (IPCC5), the average global surface temperature has risen by 1.5 °C since the industrial revolution, confirming that climate change is happening all over the world [2,3] and brings out more obvious fluctuation of precipitation and evaporation at both annual and interannual scales. This changing climate will eventually influence hydro systems, including spatial and temporal runoff distribution as well as available water resources [4]. According to the 4th version of the *World Water Development Report* (WWDR), the availability of water resources will decrease as the human demand for water increases continuously. Under the dual effects of climate

change and social development, some river basins are facing problems such as the frequent occurrence of extreme hydrological events including drought and flood [5]. Climate is therefore becoming a crucial factor of vulnerable changes in global water circulation.

One of the ways to analyze climate effects on runoff, evapotranspiration, and water resources are Global Circulation Models (GCMs). GCMs provide insights of both historical and future climate scenarios. It can simulate the evolution of the earth's climate system and its state changes over time, including the atmosphere, land surface conditions, sea, and ice [6]. The Coupled Model Intercomparison Project 5 (CMIP5) developed new future climate scenarios called representative concentration pathways (RCPs) [7] and gives many possibilities for future climate scenarios. Many countries and institutions have made their own GCMs to provide convenience for climatic and hydrological researchers [8–10]. Several simulated GCMs have been used as an important input of Soil and Water Assessment Tool (SWAT) models to assess the hydrological responses to climate change in many watersheds [3,4,11,12]. However, the direct use of GCM outputs in studies of hydrological impacts still remains a challenge as the GCM output usually shows errors and uncertainties with observed data [1,13]. Thus, GCM output should be either downscaled to match with the basin scale [14] or corrected to decrease the systematic bias between simulated and observed data to increase model precision and accuracy before being used in any climate and hydrological analysis.

For bias correction methods, correction techniques can be mainly classified into two categories: simple scaling technique (mainly containing linear scaling (LS) and power transformation method (PT)) and sophisticated distribution mapping methods (with Empirical cumulation distribution function (ECDF) of the most typical) [15]. Many researchers have evaluated the performances of different bias correction methods. For example, Luo et al. [16] compared the effects of LS, DT (Daily Transition), LOCI (Local Intensity Scaling), PT, VARI (Variance Scaling), and ECDF methods of either precipitation or temperature in the Kaidu River Basin in Xinjiang, China, and found that ECDF performs better than other methods. Teutschbein et al. [17] also made the introduction and comparison of these different correction methods in Sweden, and also found that all the methods are effective, while distribution mapping is of relatively more success.

Beside GCMs, hydrological modeling is also a powerful tool in the analysis of climate change as it is responsible for providing information on the impacts of future scenarios in the availability of water resources based on land use. There are numerous hydrological models developed by many researchers [18–21]. In general terms, they can be classified into two categories: lumped and distributed. Lumped hydrological modeling, such as the SIMHYD model [22] and *Génie Rural à 4 paramètres Journalier* (GR4J) model [23], places emphasis on physical principles, aiming at reproducing the non-linear water balance occurring at a finite scale in the soil [24]. For example, Li et al. [3] simulated and predicted the future runoff of the Tibetan Plateau by using a combination of the SIMHYD and GR4J models. Distributed hydrological models, with Shertan and the variable infiltration capacity (VIC) model being relatively typical, considered the spatial uneven distribution of environmental variables, such as precipitation and different land uses, as compared with a lumped model [25]. It provides many simulation functions and can expand runoff simulation to water resources and environmental management [26]. Birkinshaw et al. [14] predicted the outflow of the Three Gorges Reservoir using the Shertan hydrological model under climate change. The semi-distributed hydrological model is another category that usually separates a large watershed into several sub-watersheds with simple structure and higher accuracy [27]. The Soil and Water Assessment Tool (SWAT), a basin-scale and physical-based hydrological model, is one of the most used semi-distributed models for hydrological applications. For example, Muhammad et al. [12] used global climate data to drive the SWAT model to analyze the future trends of temperature, rainfall, and runoff in different climate scenarios in northwestern Pakistan. Luo et al. [1] constructed a harmony control model based on the coupling of the SWAT hydrological model, water quality model, and ecological model based on the harmony theory. However, the simulation results of the hydrological models often contain uncertainties including parameter calibration and selection of hydrological models, but the main source is still from the bias

and low resolution of GCM outputs [28,29]. Although studies have focused on different methods of bias correction of GCM outputs, few studies have presented a combination method of bias correction that may reduce errors more efficiently.

Moreover, there is no doubt that climate changes influence hydrological regimes, especially evapotranspiration and runoff, but the changing hydrological variables would further simultaneously affect the socioeconomic water resources supply and demand system because the amount of water resources is mostly from precipitation. There are also a great number of studies that assess the responses of water resources under climate change. For example, Chattopadhyay et al. [28] evaluated evapotranspiration and hydrological droughts in the Kentucky River Basin by using SWAT. Fonseca et al. [11] also assessed the total runoff changes under future RCPs of the Tâmega River Basin in the north of Portugal by using the Hydrological Simulation Program FORTRAN (HSPF) model. Previous studies have obtained abundant results of hydrological changes under climate change in arid and semi-arid areas like northwest China. However, relatively fewer studies have put emphasis on monsoon and humid areas with the same problems. Although arid or semi-arid areas are more likely to encounter extreme hydrological events, especially droughts, monsoon and humid areas are no better than arid areas as they are more likely to encounter flood disasters, which cause numerous economic losses and a threat to human lives. For example, flood events almost happen every summer, especially in Southern China. Therefore, it is still necessary to further analyze the mutual relationship between the changing climate and hydrological processes, because future climate change is still giving greater challenges to regional water supply and demand balance in more areas, which is of practical significance to hydrology, water allocation, and scientific and sustainable water management.

In this paper, the links between climate and hydrology are studied to better understand the impacts of hydrological variables on climate change and their responses to the water resources system. The selection and analysis of GCM outputs are examined. The SWAT model is applied to simulate both the historical and future runoff based on changing climates. The main objectives of this study are to (1) analysis the historical and future GCMs outputs using several bias correction methods and their hybrid method; (2) to explore the runoff and evapotranspiration response to future climate projections; and (3) to give different strategies according to future scenarios to provide references for water management

2. Materials and Methods

2.1. Study area and data

The Lijiang River Basin is located in Guilin city, Guangxi, which is the branch basin of the Pearl River Basin. It is enclosed between the latitude of 24°40′ N–26°00′ N and the longitude of 110°00′ E –110°40′ E. It is a karstic area with elevation ranging from 17 to 2111 m, with an average elevation of 1061 m. The average temperature of this area is 18 °C and the annual average rainfall is about 1500–2000 mm, and has a total area of 6375 km^2 (Figure 1). The detailed observed data of each weather or hydrological station are shown in Figure 1, and the meteorological and hydrological data are from http://data.cma.cn/ and the local hydrological yearbook over years. Although the Lijiang River Basin is located in South China, where the total amount of runoff from rainfall is relatively abundant, hydrological extremes, including droughts and floods, are frequent. The uneven distribution of the precipitation and runoff at both time and spatial scales is one of the effects of climate change in this basin [5]. Climatic events, such as droughts and floods, are closely affecting people lives and local economic development. Therefore, assessing the hydrological response to complicated climate changes is of great necessity.
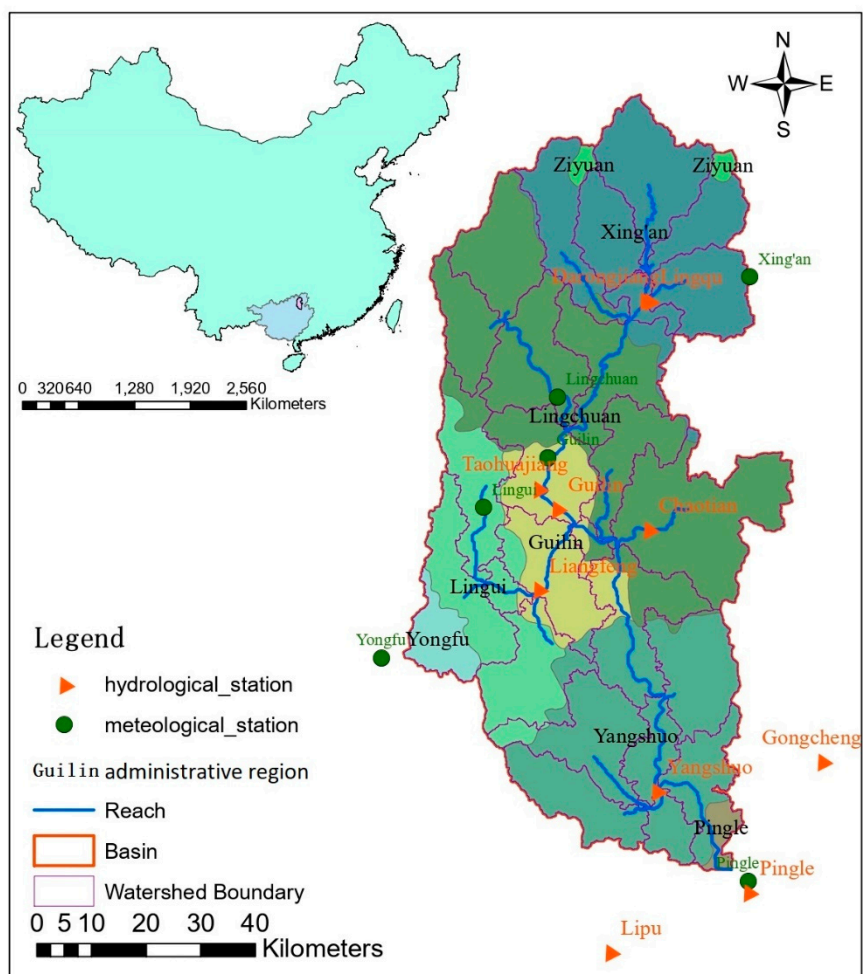
Figure 1. Location of Lijiang River Basin with digital elevation model DEM, and meteorological and hydrological stations.

The input data for SWAT modeling included the digital elevation model (DEM), hydrological, and meteorological data. The DEM data of the shuttle radar topography mission (SRTM) with resolution of 1×1 m were obtained from http://www.gscloud.cn. Hydrological data, including observed streamflow, land use, and soil data, were retrieved from the local hydrological yearbook and resource and environment data cloud platform (http://www.resdc.cn). Soil data were from the harmonized world soil database (HWSD) and their parameters were determined by the soil–plant–atmosphere–water (SPAW) tool. Climate data included both observed and GCM data, containing precipitation, maximum/minimum temperature, relative humidity, sunshine duration, and wind speed. Precipitation data were used to simulate the runoff, while others were used to simulate the potential evapotranspiration. The climate data of both observed and GCM were all at a daily scale. The observed data were from the meteorological stations presented in Figure 1, and GCMs were based on the fifth assessment report (AR5) of Intergovernmental Panel on Climate Change (IPCC) and developed several GCM data (http://www.ipcc-data.org/sim/gcm_monthly/AR5/index.html) of both historical and RCPs. Considering there are dozens of GCM outputs within IPCC and it is unrealistic to assess all of the GCM outputs, we used three GCMs (BNU-ESM, IPSL-CM5A-MR, and MIROC5) in this study, and three future RCPs (RCP2.6, RCP4.5, RCP8.5) were used. These three GCMs included all three RCPs and were presented just as an example to analyze the bias correction process and give a reference on how to correct the bias of other GCMs. The GCM outputs were corrected with observed data for the historical period of 1964–2005. Then, the corrected method was applied to the future period of 2016–2055.

2.2. Bias correction and Evaluation of GCM Outputs

2.2.1. Overview of Bias Correction Methods

Before setting up SWAT, the GCM outputs were preprocessed. GCMs often show significant biases including systematic model errors if compared with observed variables, especially precipitation and temperature [30]. To fully assess the future impacts of climate change on hydrological process, GCM is an effective tool to generate future climate patterns. In contrast to climate reanalysis, GCMs used for climate change impact assessment do not have the aim to fully represent observed daily values of meteorological variables. Instead, they try to represent climatological patterns, such as mean, trend, and seasonality. The reason is that GCM for reanalysis tries to meet initial conditions closely, but GCM for climate change assessment tries to follow boundary conditions. The SWAT model is forced by the original GCM simulations against the observed data. Bias correction is not required if there are small biases between simulated and observed data; otherwise, it is required as it is not suitable for hydrological modeling [18]. However, GCMs are usually based on climatological assumptions that usually emerge some non-ignorable errors compared with observed data. The original purpose of bias correction is, therefore, to make the GCM output close to the corresponding observed data as much as possible to decrease the errors of GCM outputs. Table 1 lists the equations of multiple bias correction methods and corresponding references used in this study. A detailed description of each bias correction can be found in Supplementary Materials.

Table 1. Equations of multiple bias correction methods and corresponding symbol definition.

Correction Methods	Mathematical Equations	Coverage	References
Linear Scaling (LS)	$P_{cor}^{LS}(t) = P_{GCM}(t) \times \frac{\mu_m(P_{obs}(t))}{\mu_m(P_{GCM}(t))}$ $T_{cor}^{LS}(t) = T_{GCM}(t) + [\mu_m(T_{obs}(t)) - \mu_m(T_{GCM}(t))]$	Precipitation and Temperature	[17]
Local Intensity Scaling (LOCI)	$s = \frac{\mu(P_{OBS}\|P_{OBS}\geq OBS,thres) - P_{OBS,thres}}{\mu(P_{GCM}\|P_{GCM}\geq GCM,thres) - P_{GCM,thres}}$ $P_{cor}^{LOCI}(t) = \max\left(0, P_{OBS,thres} + s\left(P_{GCM}(t) - P_{GCM,thres}\right)\right)$	Precipitation	[17,31]
Empirical Cumulative Distribution Function (ECDF)	$F(x) = \int_0^x f(t\|\alpha,\beta)dt = \frac{1}{\beta^\alpha \Gamma(\alpha)} \int_0^x t^{\alpha-1} e^{-\frac{t}{\beta}} dt \quad x \geq 0; \alpha, \beta > 0$ $G(x) = \int_{-\infty}^x g(t\|\mu,\sigma^2)dt = \int_{-\infty}^x \frac{1}{\sqrt{2\pi}\sigma} e^{-\frac{(t-\mu)^2}{2\sigma^2}} dt$ $P_{cor}^{ECDF}(t) = ecdf_{obs}^{-1}[ecdf_{GCM}(P(t))]$ $T_{cor}^{ECDF}(t) = ecdf_{obs}^{-1}[ecdf_{GCM}(T(t))]$	Precipitation and temperature	[15,32]
Variance Scaling (VARI)	$T_{cor}^{VARI}(t) =$ $[T_{LS}(t) - \mu_m(T_{LS}(t))] \cdot \frac{\sigma_m(T_{obs}(t))}{\sigma_m[T_{LS}(t) - \mu_m(T_{LS}(t))]} + \mu_m(T_{LS}(t))$	Temperature	[33,34]
	Symbols		
	P	Precipitation	
	μ()	Mean value	
	T	Temperature	
	s	Scaling factor	
	μ(A|B)	The mean value of A that satisfies the condition of B	
	$F(x)$, $f(t\|\alpha,\beta)$	Cumulative distribution function and probability density function of Gamma distribution with two parameters α and β. Precipitation variable obey this distribution	
	$G(x)$, $g(t\|\mu,\sigma^2)$	Cumulative distribution function and probability density function of normal distribution with two parameters μ and σ^2. Temperature variable obey this distribution	
	ecdf	Empirical cumulative distribution function	
	σ()	Standard deviation	
	Subscripts		
	cor	Corrected variables	
	obs	Observed variables	
	GCM	Original GCM variables	
	m	Monthly interval	
	thres	Threshold	

2.2.2. Hybrid Method

We also combined the bias correction methods to increase the correction precision, based on the assumption that the hybrid method may correct GCM output bias more efficiently compared with using only one method. We selected a combination of two of those methods in order to reduce computational cost. For each hybrid, the output of the initial correction becomes the input of the hybrid method. We use the hybrid of VARI&ECDF and LS&LOCI to correct temperature and precipitation, respectively, in this study, while LS&ECDF is used to correct both temperature and precipitation data. Thus, the developed hybrid bias correction is shown as follows:

$$T_{cor}^{VARI\&ECDF}(t) = ecdf_{OBS}^{-1}\left[ecdf\left(T_{cor}^{VARI}(t)\right)\right] \tag{1}$$

$$P_{cor}^{LS\&LOCI}(t) = \max\left(0, P_{obs,THRES} + s\left(P_{cor}^{LS}(t) - P_{LS,thres}\right)\right) \tag{2}$$

$$T_{cor}^{LS\&ECDF}(t) = ecdf_{OBS}^{-1}\left[ecdf\left(T_{cor}^{LS}(t)\right)\right] \tag{3}$$

$$P_{cor}^{LS\&ECDF}(t) = ecdf_{OBS}^{-1}\left[ecdf\left(P_{cor}^{LS}(t)\right)\right] \tag{4}$$

2.3. Description and Development of the SWAT Model

2.3.1. A brief Description of SWAT Model

The SWAT model is a typical semi-distributed model that has higher accuracy, which separates a large watershed into several sub-watersheds that consist of hydrological response units (HRUs) to increase its resolution. This includes a comprehensive coverage of basin behaviors and strong compatibility with a geographic information system (GIS) and diverse algorithms for hydrological processes [35]. For this study, we are evaluating the effects of climate change in runoff and evapotranspiration. SWAT calculates runoff based on the Soil Conservation Service [36] for estimating the amount of runoff under varying land use and soil types [37,38]:

$$Q_{surf} = \frac{(R_{day} - 0.2S)^2}{R_{day} + 0.8S} \tag{5}$$

$$S = 25.4\left(\frac{1000}{CN} - 10\right) \tag{6}$$

where Q_{surf}, R_{day}, S, and CN denote surface runoff (mm), rainfall depth (mm), retention parameter, and curve number. The curve number is determined by different types of land uses and soils that are classified by hydrological groups. For details on runoff calculations, see [38].

The groundwater runoff is presented as follows:

$$Q_{gw} = \frac{8000KH}{L^2} \tag{7}$$

where K, H, and L are the permeability coefficient (mm/d), depth of the diving surface (m), and the distance from the watershed of the sub-basin to the main channel (m), respectively.

Potential evapotranspiration (PET) was evaluated before calculating actual evapotranspiration using the Penman–Monteith equation:

$$ET_0 = \frac{0.408\Delta(H_{net} - G) + \gamma\frac{900}{T+273}u_2\left(e_z^0 - e_z\right)}{\Delta + \gamma(1 + 0.34u_2)} \tag{8}$$

where ET_0 is the potential evapotranspiration (mm/d), Δ is the slope vapor pressure curve (kPa/°C), H_{net} is the net radiation (MJ/m^2/d), G is the soil heat flux density (MJ/m^2/d), T is air temperature at 2 m height (°C), u_2 is wind speed at 2 m height (m/s), e_z^0 and e_z are the saturation and actual vapor pressure of air

at height z (kPa), and γ is the psychrometric constant (kPa/°C). Then, the actual evapotranspiration is calculated by evaporating the rainfall intercepted by the plant canopy and calculating the maximum amount of transpiration and sublimation/soil evaporation [38]. Therefore, evapotranspiration is determined by many environmental variables including temperature, solar radiation, humidity, etc.

2.3.2. SWAT Model Setup

The Soil and Water Assessment Tool (SWAT) was developed to simulate the runoff of the watershed in both historical and future periods under different scenarios of climate change. In this study, we used ArcSWAT2012, which is the extensional toolbar of ArcGIS 10.2 to setup the SWAT model. The simulated runoff of the historical period was used to calibrate and validate the performance of the SWAT model, while projected GCM outputs were used to predict the runoff in the future period. SWAT was developed based on the theory of the water balance equation [27,39]:

$$SW_t = SW_i + \sum_{i=1}^{t}\left(P_i - Q_{i,surf} - ET_i - f_i - Q_{i,gw}\right) \tag{9}$$

where SW_t and SW_0 (mm) are the soil water content at the tth and ith time interval, respectively. In this case, subscript i is the initial time. P_i (mm), $Q_{i,surf}$ (mm), ET_i (mm), f_i (mm), and $Q_{i,gw}$ (mm) are the precipitation, surface runoff, evapotranspiration, infiltration, and base flow at ith time interval. The SWAT model first divides the watershed into several small sub-basins according to the Digital Elevation Model (DEM) data and river system of the watershed. Then, the smallest unit of the watershed, HRU, is generated based on soil, land use, and slope. Each HRU contains these three elements. For this study, the watershed was divided in 29 sub-basins and 822 HRUs. Apart from DEM, land use, and soil data, SWAT also needs daily climate data including precipitation, maximum and minimum temperature, solar radiation, relative humidity, and wind speed to generate the hydrological process of a watershed. Additionally, SWAT also contains a weather generator model (WXGEN) that can generate water data or fill the gaps of observed climate data.

2.3.3. Model Performance Assessment

In this study, we used SWAT calibration and uncertainty program (SWAT-CUP) to evaluate the uncertainty and its performance of parameters by using the sequential uncertainty fitting (SUFI2) algorithm. We selected three years (1964–1966) for model warming up, while 1967–1975 and 1976–1984 were selected as calibration and validation periods, respectively. To evaluate the performance of the SWAT model, R^2, mean square error (MSE), and Nash–Sutcliffe Efficiency (NSE) were used. The value of R^2 and NSE range from −1 to 1 and from negative infinity to 1, respectively. In general, the closer the values of R^2 and NSE are to 1, the better the simulation effect is. If R^2 is greater than 0.6, while NSE is greater than 0.5, the simulation effect is satisfactory. If NSE is greater than 0.75, the simulation effect is efficient. The expressions of R^2 and NSE are shown below:

$$R^2 = \frac{\left[\sum_{i=1}^{n}\left(Q_{obs,i} - \overline{Q_{obs}}\right)\left(Q_{sim,i} - \overline{Q_{sim}}\right)\right]^2}{\sum_{i=1}^{n}\left(Q_{obs,i} - \overline{Q_{obs}}\right)^2 \sum_{i=1}^{n}\left(Q_{sim,i} - \overline{Q_{sim}}\right)^2} \tag{10}$$

$$MSE = \frac{\sum_{i=1}^{n}\left(Q_{obs,i} - Q_{sim,i}\right)^2}{\text{var}\left(Q_{obs,i}\right)} \tag{11}$$

$$NSE = 1 - \frac{\sum\limits_{i=1}^{n} \left(Q_{obs,i} - Q_{sim,i}\right)^2}{\sum\limits_{i=1}^{n} \left(Q_{obs,i} - \overline{Q_{obs}}\right)^2} \tag{12}$$

where $Q_{obs,i}$ and $Q_{sim,i}$ are the observed and simulated streamflow at ith time interval, respectively. $\overline{Q_{obs}}$ and $\overline{Q_{sim}}$ are the average observed and simulated streamflow, respectively, during the entire evaluating period.

3. Results

3.1. Assessment of the GCM Outputs Using Multiple Bias Correction Methods

Due to the various number of GCMs that are unrealistic to analyze the bias correction methods for a full scale as there are dozens of GCM outputs, we selected and compared three GCM outputs for this study as the examples to test which bias method is relatively better. Figure 2 shows the Taylor diagram for the GCM corrections for daily data of 1964~2005. Measurements of evaluation include standard deviation (STD), root mean square error (RMSE), and correlation coefficient (CC). The CC of each original GCM of maximum temperature ranged from 0.6 to 0.8, while the CC of minimum temperature ranged from 0.8 to 0.9. The standard RMSE of both maximum and minimum temperature ranged from 0.5 to 1. Even if there was a relatively good simulation of original GCM of temperature, there was still an improvement of all the correction methods compared with original GCMs. To quantify the effect of the improvement, we also compared each improved percentage, which is shown in Figure 2. It can be seen from Figure 2 that for all three GCMs of temperature, each correction method is closer to the corresponding original GCMs and the effect of the hybrid method is better than either of the single methods in both CC and RMSE indexes.

Precipitation is more uncertain than temperature in terms of how dynamic the variable is, missed data, and record errors. Many factors determine the amount of precipitation, which is the main source of uncertainty. Moreover, when the frequency of precipitation data is higher, the error also increases. That is why the daily simulation result of the original GCM is poor compared with temperature, which is reflected by the CC of the original GCM only in the range from 0.01 to 0.1, and RMSE is larger than 1 (Figure 2). In addition, for the same climate variables, the monthly simulation is better than daily simulation results. Although the CC of the original GCM is very low, there is enough room for improvement. All the correction methods perform well in terms of CC. The CC is around 0.2 compared with the value before correction (0.01 to 0.1), which is the reason why the percentages of increase in CC have exceeded 100% (Table 2). However, the acute changes happen in RMSE in the BNU-ESM and IPSL-CM5A-MR models, which is reflected by the minus value which means the increasing trend of RMSE. Fortunately, the RMSE of MIROC5 performs well and all ECDF-corrected methods in each model are effective. For this phenomenon, we can contribute it for the uncertainty of the GCM itself that is determined by many factors, and the determinants may be also numerous and extremely complicated. From Table 3, we can see that the ECDF-corrected method performs also better in terms of NSE, and when it is combined with LS, the effect is greatly improved compared with LOCI and its hybrid with LS. It can also be seen from Table 3 that the value of all other correcting methods has greatly improved compared with the original GCM, which demonstrated that all the correcting methods have a positive effect. The effect of the hybrid method of precipitation can also be superimposed, except in the MIROC5 model and LS&LOCI method in the IPSL-CM5A-MR model. Although the value of NSE is slightly less than 0, the NSE value of the hybrid method is greatly better than the original and corresponding single GCM. This means the simulation of the process may have errors due to the uncertainty and complicated determinants, but the overall simulation result is reliable.
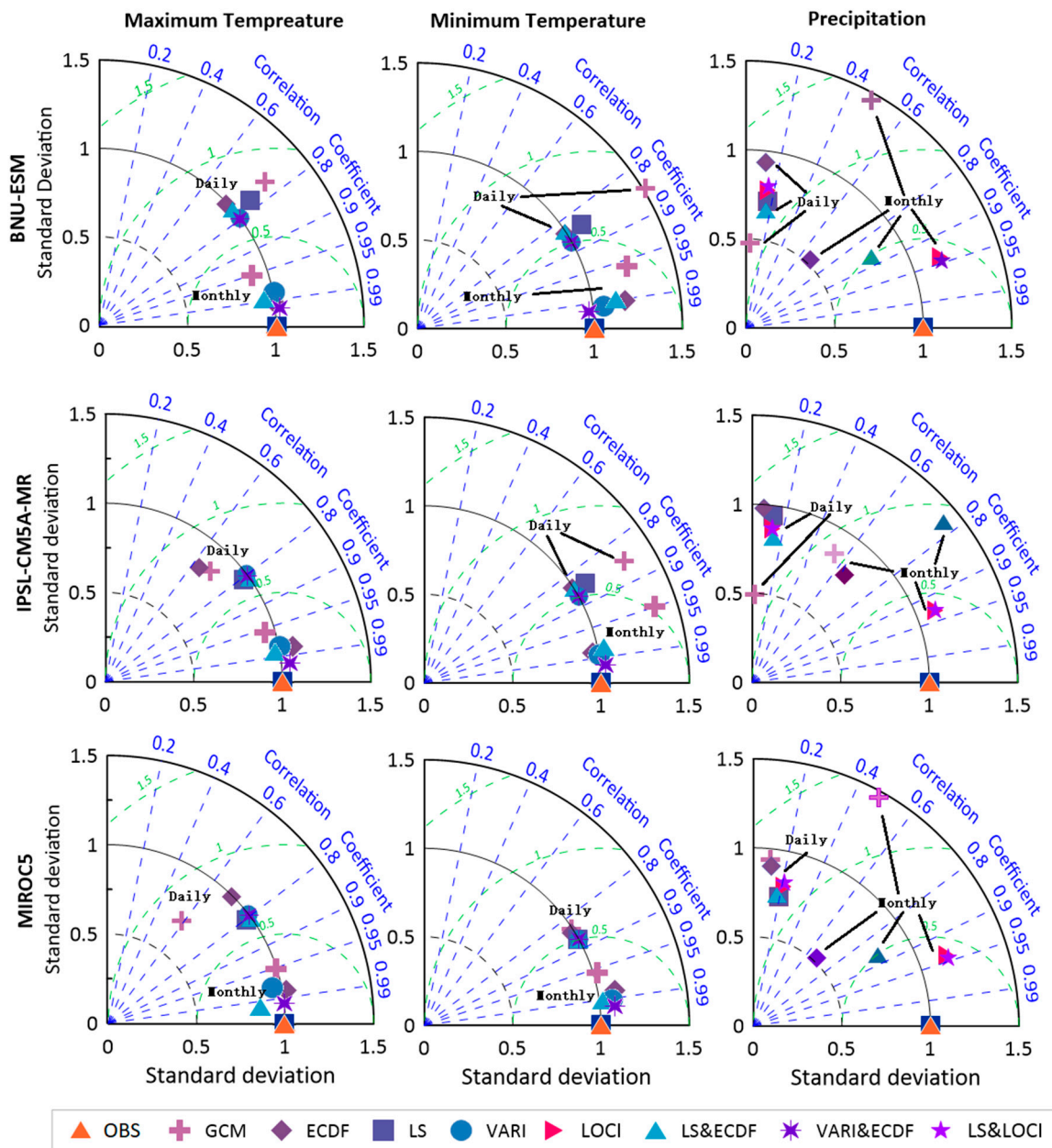
Figure 2. Taylor diagrams comparing the original and corrected GCMs of different methods of precipitation and minimum and maximum temperature of both daily (1960.1.1–2005.12.31) and monthly (1960.1–2005.12).

Table 2. The percentage of change of correlation coefficient CC and root mean square error in each corrected method relative to the original daily precipitation as well as temperature of GCMs (unit: %).

Predictions	Correcting Methods	CC			RMSE		
		BNU-ESM	IPSL-CM5A-MR	MIROC5	BNU-ESM	IPSL-CM5A-MR	MIROC5
Precipitation	LS	115.34	174.44	154.82	−6.70	−17.23	12.94
	ECDF	17.93	53.92	62.64	1.36	2.21	19.10
	LOCI	120.99	224.29	163.86	−9.47	−12.51	10.80
	LS&ECDF	154.53	351.29	87.03	−3.66	−8.17	21.19
	LS&LOCI	119.55	223.67	155.84	−10.66	−12.59	19.67
Maximum temperature	LS	10.31	22.55	38.93	12.32	14.09	16.69
	ECDF	2.90	4.65	5.20	11.36	6.39	4.08
	VARI	24.10	18.65	34.04	23.59	10.42	12.92
	LS&ECDF	12.09	24.20	40.46	16.61	14.65	17.01
	VARI&ECDF	24.88	20.03	35.54	24.13	15.51	18.91
Minimum temperature	LS	1.41	1.19	8.61	24.04	16.81	11.58
	ECDF	1.19	1.20	2.79	26.00	18.72	3.96
	VARI	8.50	8.56	8.81	35.94	26.77	11.77
	LS&ECDF	2.26	2.30	9.43	27.53	19.81	12.77
	VARI&ECDF	8.96	8.92	8.99	36.02	26.86	11.91

Notes: CC is the increase percentage and RMSE is the decrease percentage. For example, in BNU-ESM, the CC value of the maximum temperature of the LS method has increased by 10.31%, while RMSE value has decreased by 12.32%.

Table 3. Nash–Sutcliffe efficiency (NSE) coefficient for both original and corrected daily GCM in the historical period of daily precipitation as well as temperature.

Correcting Methods	Precipitation			Maximum Temperature			Minimum Temperature		
	BNU-ESM	IPSL-CM5A-MR	MIROC5	BNU-ESM	IPSL-CM5A-MR	MIROC5	BNU-ESM	IPSL-CM5A-MR	MIROC5
GCM	−0.64	−0.69	−0.67	0.31	0.50	0.45	0.38	0.53	0.68
LS	−0.30	−0.63	−0.27	0.47	0.63	0.62	0.72	0.75	0.81
ECDF	−0.15	−0.14	−0.10	0.45	0.43	0.41	0.69	0.69	0.70
LOCI	−0.36	−0.25	−0.33	/	/	/	/	/	/
VARI	/	/	/	0.59	0.60	0.59	0.80	0.80	0.81
LS&ECDF	−0.12	−0.09	−0.32	0.52	0.65	0.63	0.67	0.69	0.76
LS&LOCI	−0.27	−0.15	−0.37	/	/	/	/	/	/
VARI&ECDF	/	/	/	0.60	0.61	0.59	0.75	0.75	0.75

3.2. Calibration and Validation of the SWAT Model

Calibration and validation processes were performed using monthly streamflow data given by the Pingle, Yangshuo, Lingqu, and Guilin hydrological stations. The first three years (1964–1966) were used to warm up and were not adopted in the model evaluation. The periods 1967~1975 and 1976~1984 were selected as calibration and validation periods. Visual comparison of the continuous data of observed and simulated streamflow in both calibration and validation periods is shown in Figure 3 and the statistical evaluation result is demonstrated in Table 4. It can be seen that the R^2 values of four stations in both the two periods all exceeded 0.8 and NSE values also exceeded 0.7. Meanwhile, the MSE value in both periods was less than 0.3. It can also be indicated from Figure 3 that the monthly flow trends in the two periods for each hydrological station almost stayed the same, suggesting the simulation results have a relatively good performance.

Table 4. Simulation effect evaluation of monthly streamflow of four hydrological stations.

Hydrological Station	Calibration Period			Validation Period		
	R^2	MSE	NSE	R^2	MSE	NSE
Pingle	0.87	0.23	0.77	0.82	0.25	0.71
Yangshuo	0.89	0.16	0.85	0.86	0.16	0.81
Lingqu	0.87	0.15	0.76	0.85	0.26	0.77
Guilin	0.87	0.16	0.82	0.86	0.20	0.82
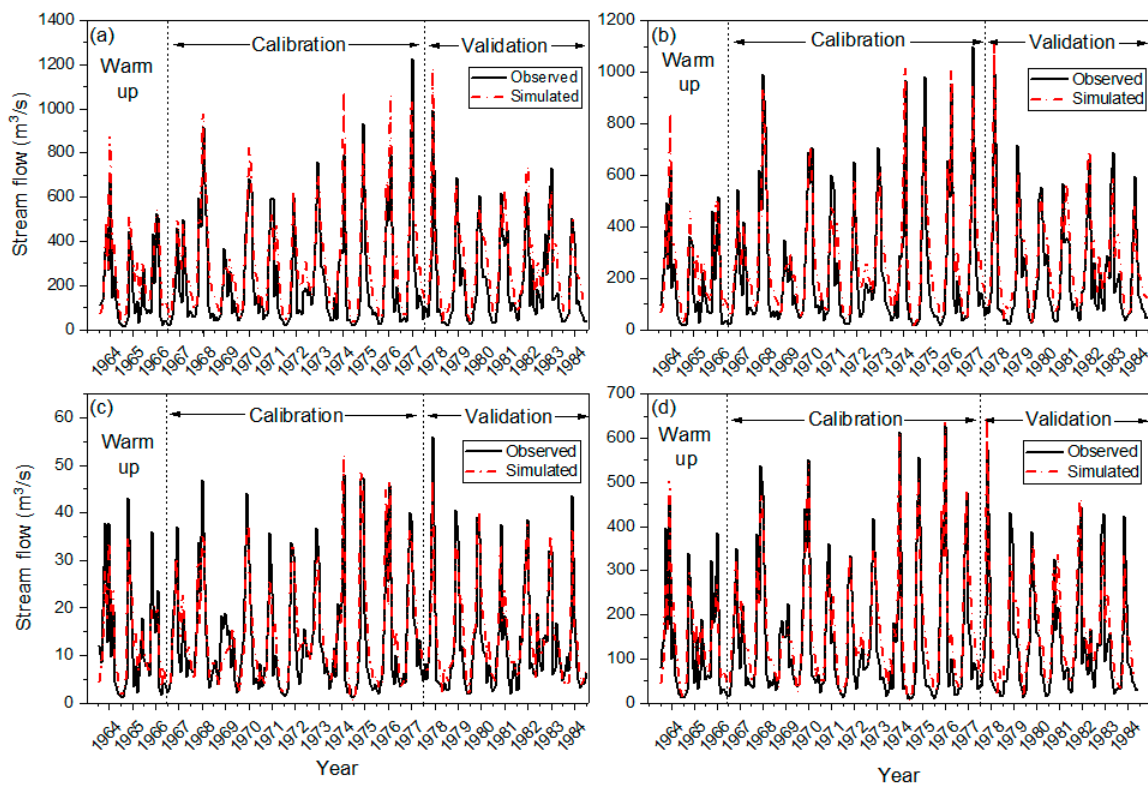
Figure 3. SWAT model calibration and validation results: comparison between simulated and observed monthly stream flows of four hydrological stations: (**a**) Pingle; (**b**) Yangshuo; (**c**) Lingqu; (**d**) Guilin.

3.3. Projected Climate Change Response to Hydrological Systems

3.3.1. Changes in Projected Precipitation and Temperature

Of all the single models, the performances of temperature seem to be similar, while those of precipitation vary from different similar models. For example, the ECDF method for monthly temperature performs poorer than other single methods (see Figure 2). This can be contributed to the statistical errors and the definition ambiguity of the drizzle rainfall, and less static errors of the observed temperature. However, the performance of the hybrid method of both monthly and daily scales of both precipitation and temperature is better compared with the single method in most cases. According to the correction results shown by Table 3, we found that precipitation correction performed the best in the LS&ECDF method in the IPSL-CM5A-MR method; the same GCM performed relatively better in temperature compared with the other two models. The LS&ECDF and VARI perform the best in maximum and minimum temperature, respectively. In this study, we used the abovementioned model and method to drive the SWAT model to simulate the hydrological variables.

The multiyear trends of all the historical and future scenarios and the changes in the total amount of precipitation and temperature are shown in Figure 4 and Table 5. In general, it presented increasing trends in all the scenarios in temperature and the increasing ratios of future scenarios (with the increase rate of 0.3, 0.25, and 0.53 °C per decade) are all greater than the historical periods (with the increase rate of 0.17 °C per decade). A greater ratio of temperature increase occurred in the RCP8.5 scenario compared with other RCP and historical scenarios. Similarly, the annual average temperature demonstrated the same change as the multiyear trend. Moreover, no matter from a multiyear trend or annual average perspective, the effect of RCP8.5 is the most obvious. Unlike the multiyear trend of temperature, the multiyear precipitation change reflects the increasing trend only in historical and RCP4.5 scenarios, with the increasing rate of 23.48 and 124.09 mm per decade. However, the descending trend in RCP8.5 (77.47 mm per decade) is less than that in RCP4.5 (35.87 mm per decade). Although

there is a descending trend in both RCP2.6 and RCP8.5 scenarios, the annual average precipitation in both scenarios is greater than that in the historical period. Besides, the increasing percentage change in RCP8.5 is greater than any of the other scenarios, which presents the same phenomenon as temperature in these two points.
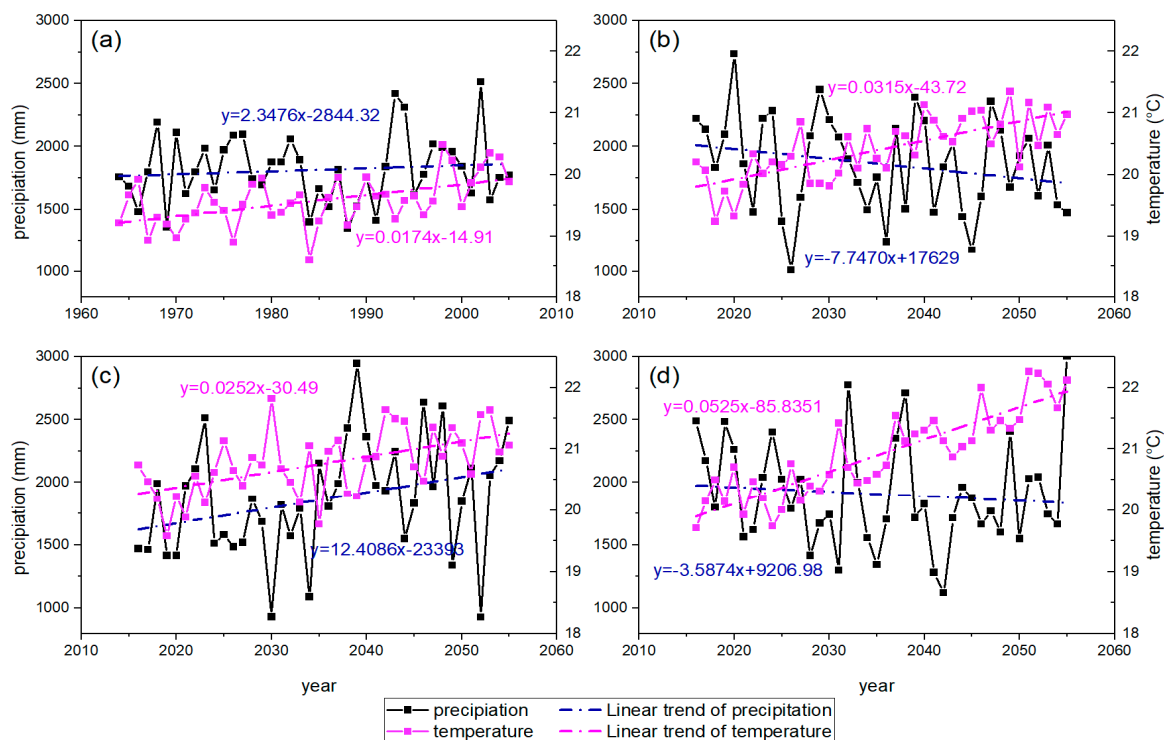

Figure 4. Yearly changing trend of precipitation and temperature of both historical and future period: (**a**) historical, (**b**) RCP2.6, (**c**) RCP4.5, and (**d**) RCP8.5.

Table 5. The amount of annual precipitation and temperature during the historical and future period.

Hydrological Variables	Scenarios			
	Historical	RCP2.6	RCP4.5	RCP8.5
Precipitation(mm)	1814.41	1860.18	1864.76	1904.89
Temperature(°C)	19.56	20.41	20.76	20.92

Figure 5 presents the monthly distribution of precipitation and temperature for each scenario, and it can be seen that the annual monthly temperature in future scenarios is always greater than the historical period except in November and December. The increasing rate presents a relatively obvious ratio from March to June compared with other months. When comparing with different future scenarios, the monthly temperature in RCP4.5 and RCP8.5 is always greater than RCP2.6. When it comes to precipitation, it is quite different from temperature. The precipitation in future scenarios increased in flood seasons, especially in July and August, and the rest of the months presented a decreasing trend. The temporal distribution of precipitation seems to be more uneven and the peak precipitation is increased and delayed. This means the peak precipitation happens in May with its value of about 350 mm in the historical period, while that in future scenarios has changed to about 550 mm and happened in July. This distribution change is likely to be manifestations of climate change.
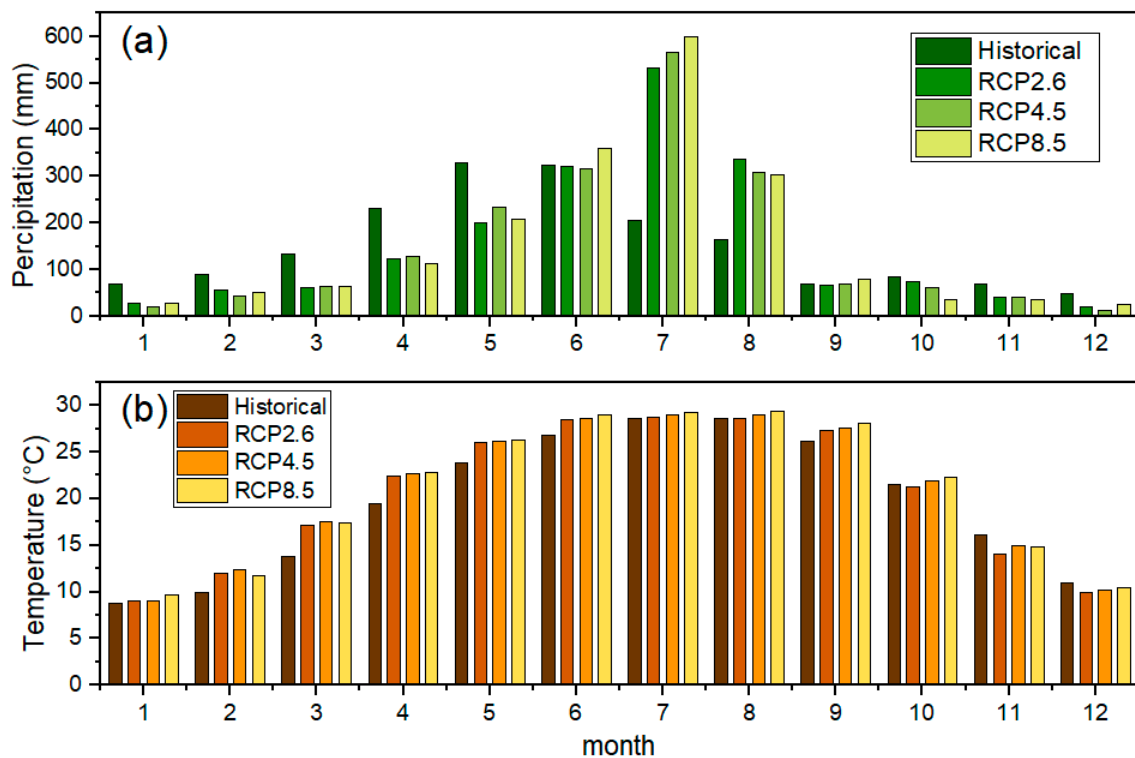
Figure 5. Monthly changes of hydrological variables in the whole study area in both historical (1964–2005) and future (2016–2055) period: (**a**) precipitation; (**b**) temperature.

3.3.2. Changes in Future Runoff and Evapotranspiration

Figure 6 shows the multiyear trend of runoff and evapotranspiration of both historical and future periods based on three scenarios. These results showed the comprehensive effects of climate change based on the different emission scenarios. It can be seen from Figure 6 that the multiyear trend of runoff presents the descending trend in RCP2.6 and RCP8.5, while it showed an increasing trend in RCP4.5 and the historical period. The descending rate in RCP2.6 is slightly greater (4.1×10^8 m^3 per decade) than in RCP8.5 (2.2×10^8 m^3 per decade), while the increasing rate in RCP4.5 is greater (7.2×10^8 m^3 per decade) than in the historical period (1.9×10^8 m^3 per decade). This happens because the precipitation in the corresponding RCP scenarios is the same trend. However, RCP itself in the future scenarios is not the real-time trend that is based on several assumptions; therefore, different RCPs as well as GCMs and trends of either increase or decrease are both possibilities. The total amount of runoff in future cases is also more than that in the historical case (Table 6). That means the total runoff in the future has also increased and the maximum amount of runoff occurs under RCP8.5. The changes are similar with that of precipitation (see Table 5, the annual average precipitation in future scenarios is more than that in historical scenarios). When focusing on the monthly distribution of runoff (Figure 7a), it showed a similar change as precipitation. The runoff will experience relatively positive changes in mid-period and later-period flood seasons (June to November) and negative changes in other periods, and the effect under RCP8.5 is more visible compared with other future scenarios in the mid-period flood season. Besides, the peak value is much greater and appears later compared with the historical period, suggesting the annual distribution of runoff is changed and becoming more uneven under the impacts of climate change.
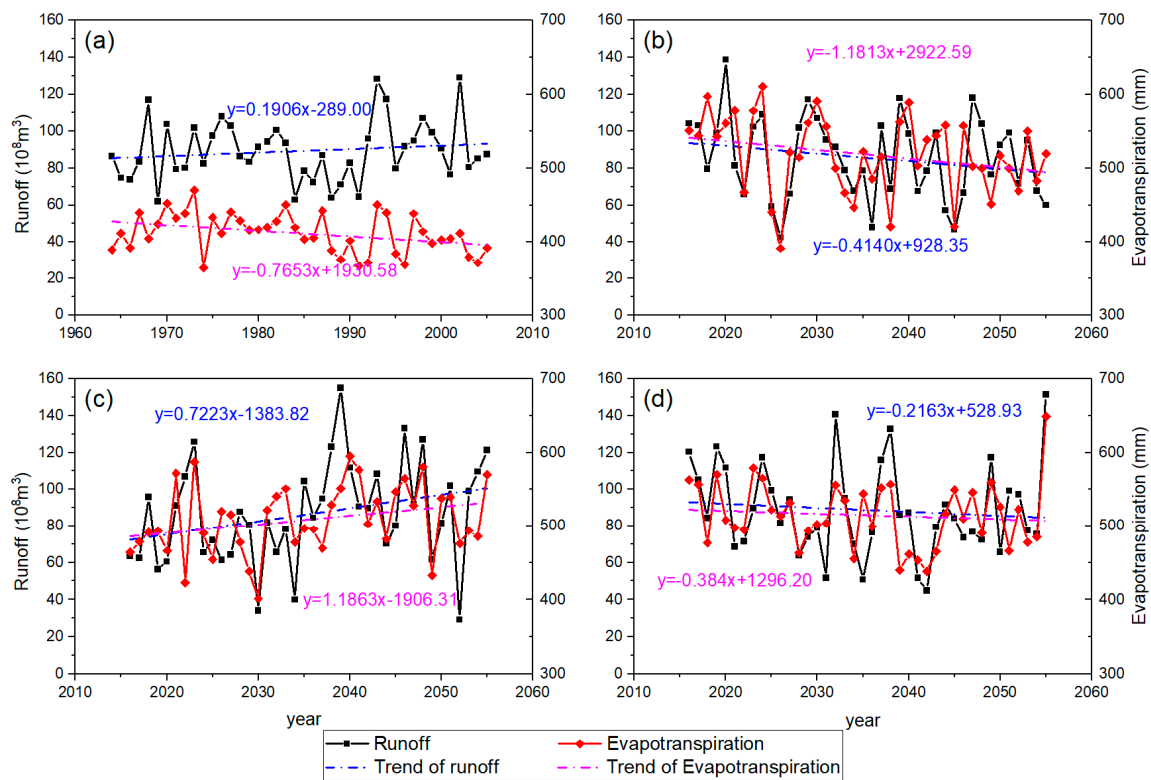
Figure 6. Yearly changing trend of runoff and evapotranspiration of both historical and future period: (**a**) historical, (**b**) RCP2.6, (**c**) RCP4.5, and (**d**) RCP8.5.

Table 6. The amount of annual runoff and evapotranspiration during the historical and future period.

Hydrological Variables	Scenarios			
	Historical	**RCP2.6**	**RCP4.5**	**RCP8.5**
Runoff (10^8 m^3)	85.26	90.61	92.48	94.64
Evapotranspiration (mm)	411.83	508.45	514.57	518.15

The multiyear trends of evapotranspiration are the same as runoff in future scenarios, and this is even reflected in the increasing or decreasing rates. That is, the trend of evapotranspiration under RCP2.6 and RCP8.5 is decreasing while that in RCP4.5 is increasing, which is the same as the corresponding scenarios of runoff. Additionally, the decreasing rate in RCP8.5 (3.8 mm per decade) is also slightly less than in RCP2.6 (11.8 mm per decade). The annual average evapotranspiration in the future period is much greater than in the historical period (Table 6). This happens because the temperature in future scenarios is increasing greatly due to climate change, and the evapotranspiration will increase as temperature increases according to the Penman–Monteith equation. When comparing different future scenarios, the highest and the lowest increase ratio occurs in RCP8.5 and RCP2.6, respectively. The monthly distribution of evapotranspiration is also changed under the impact of climate change. We can see from Figure 7b that the evapotranspiration in flood seasons in all future scenarios is more than that in the historical period. The effect is obvious, especially in flood seasons from May and August. For non-flood seasons, it is either less than or keeps pace with historical periods. It is observed that the distribution of evapotranspiration is also changed and becomes uneven under climate change in each scenario.
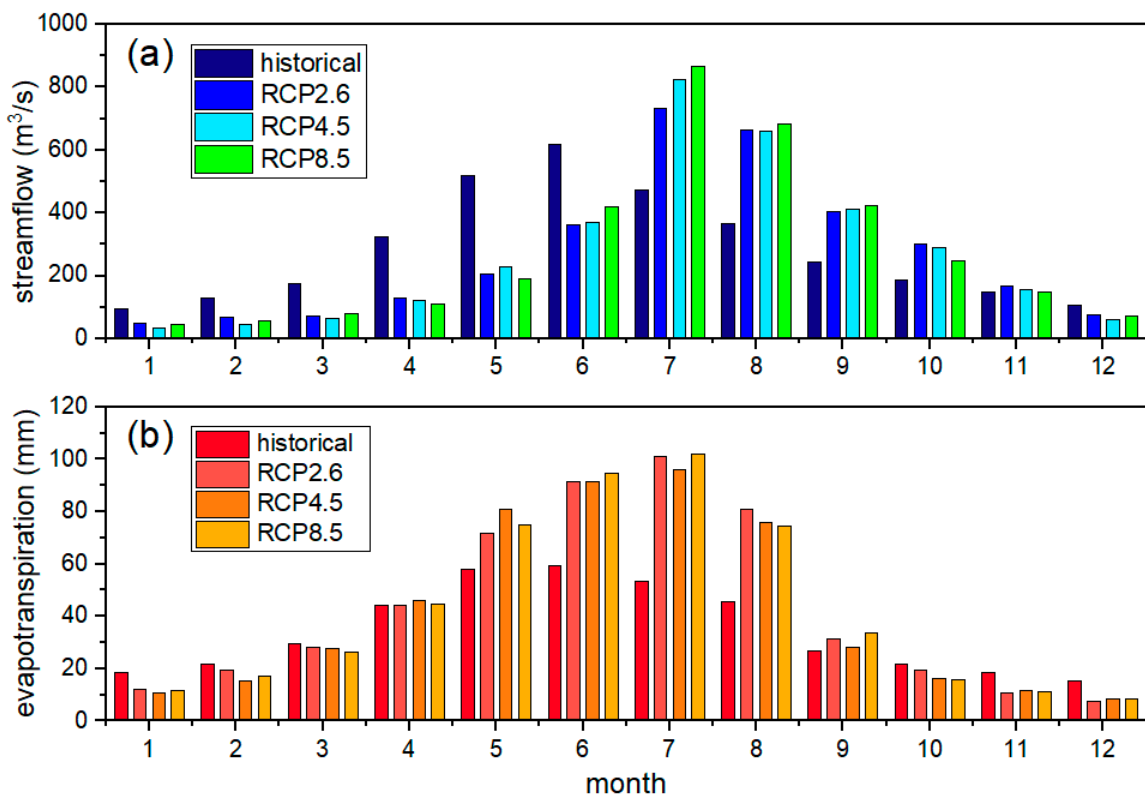
Figure 7. Monthly changes of hydrological variables in the whole study area in both historical (1964–2005) and future (2016–2055) period: (**a**) streamflow; (**b**) evapotranspiration.

4. Discussion

4.1. Comparison of Different Bias Correction Methods

Research on the impact of climate change has become popular in the last few decades. However, it is of great necessity to correct the GCM bias in that there will be systematic error in subsequent runoff simulating without bias correction. According to the previous studies in this field, the effect of GCM itself and the ECDF method of bias correction perform relatively well in higher latitudes and elevations where there is less precipitation, which brings about less uncertainty compared with humid and subtropical areas [1,16]. For low latitude and monsoon areas where there may be more precipitation with more uncertainties, the NSE value would be a little smaller but near zero so the model is still reliable. Additionally, the time interval also affects the NSE value, as monthly or average daily precipitation performs more perfectly than long-term daily data [16]. From this point of view, the results can also support the validity of the bias correction method used in this study.

According to the correction results (Table 3), the ECDF-corrected method performs better than the LOCI-corrected and LS-corrected method. This result is also validated in other research works, where the study area has similar climate conditions [15,32]. The change of precipitation is nonlinear and the LS method will not correct as perfectly as we expected. LOCI is independent of distribution compared with ECDF in that its scaling factors are calibrated on mean values of precipitation, and features instabilities in estimating the process of temporal variability. Therefore, it cannot correct the error adequately when the data are significantly curved and intensity-dependent [33]. ECDF is corrected based on the distribution of the long-term observed data, which is respectively representative and closer to the observed distribution data. That is also the reason why when LOCI is combined with LS, the simulation is poor compared with the hybrid method of LS&ECDF. Temperature simulating is much better than precipitation because of its lower uncertainty and determinants, and variance is smaller than precipitation. This is reflected by the greater value of NSE in temperature than

precipitation, which means the model is reliable from both the overall and process perspective. Moreover, there is no sudden change in temperature as it is relatively stable, whereas the rainfall occurs with a certain probability that is difficult to quantify. That is why the value of RMSE in precipitation has an acute change. However, there is a normal change in MIROC5 so GCM itself also has uncertainty. Therefore, choosing a proper correcting method and GCM is also a key point before hydrological modeling. Additionally, the VARI-corrected method performs better than the LS-corrected method because VARI is the extension of LS as it considered both mean and variance of the total sample, which can be comprehended as the combination of linear and variable scaling [34,35]. Meanwhile, other hybrid methods perform also greater than corresponding single methods in both precipitation and temperature other than some exceptions, which means the effect of hybrid methods performs better than single methods to some extent, although it may not work in all the scenarios absolutely. After all, the sample size of climate data is too large and uncertainty is more likely to emerge, and it also has regional specificities. Therefore, the results are still valuable and provides a good reference to similar studies.

4.2. Variations of Hydrological Variables Caused by the Impacts of Climate Change

In general, the impacts of climate change showed intense temporal heterogeneity of hydrological variables in this study. According to the theoretical basis provided by [38], the amount of runoff is determined by the precipitation and condition of the underlying surface and evapotranspiration is determined mainly by temperature, humidity, and solar radiation. The annual average changes of evapotranspiration in 2016–2055 have increased by about 20% in three future scenarios, which can be mainly contributed to the changes of temperature, because the annual temperature has also increased about 1 °C (Figure 8b,d). There is no doubt that global warming is in process and will last for decades [2,27], and it is also the same with Lijiang River Basin. Both the multiyear trend of temperature (Figure 4) and the absolute temperature are increasing, contributing to the relatively large increasing ratio of evapotranspiration. The increasing temperature also contributes to the increasing value of evapotranspiration (about 100 mm, see Figure 5). Previous studies also indicated that continuous global warming will experience the growth of evapotranspiration compared with the past (Luo et al., 2019; Bibi et al., 2016). However, the changes in monthly temperature and evapotranspiration do not completely match (Figure 8b,d); for example, the increasing change in evapotranspiration in July and August is greater than that of temperature in the same period. This is probably because evapotranspiration is not only determined by temperature, but also solar radiation and humidity, as the solar radiation in these two months is much larger than other months, which brings about uncertainty factors to some extent. The evapotranspiration also varies in different climate scenarios. For example, its value in RCP8.5 (518.15 mm) is higher than those in RCP2.6 (508.45 mm) and 4.5 (514.51 mm) (see Table 6). This is easy to understand because a higher concentration of CO_2 emission occurs in the RCP8.5 scenario, which is likely to accelerate the greenhouse effect, which accelerates the increase in temperature, which contributes to the increasing evapotranspiration. There is no doubt that in the study area located in South China, sunshine duration is longer than other areas, especially in summer, as it is close to the equator. Yet, one thing is certain: the total amount of evapotranspiration is increasing compared with the historical period under the impact of climate change.

Climate change is also reflected in the changes more in temperature, but also in precipitation. Our results showed that annual average precipitation has increased (Table 5 and Figure 8a), which is consistent with other studies with similar conditions of the study area [27]. Simultaneously, the distribution of the monthly precipitation has also changed, reflected by the sharp increase in rainfall in the flood season (May to September) and decrease in the non-flood season (October to next April) (Figure 8a) as well as the delay of the peak occurrence time (Figure 5a), which may consequently lead to greater floods in the future flood season and frequent drought events in the non-flood season. Consequently, similar changes will also occur in the distribution of runoff (Figure 8c). Therefore, the stakeholders of water resources management should take measures towards this issue

like floodwater utilization—gathering the water resources in flood seasons to meet the needs in dry seasons. With the increasing precipitation, runoff is also increasing compared with baseline. Although evapotranspiration increases in future scenarios, the study area is a monsoon and humid area where annual precipitation is larger than evapotranspiration and future precipitation is also increasing as we speculated. Moreover, the dual effect of increasing precipitation and temperature can accelerate streamflow. This is validated by its value under different climate scenarios. The runoff in RCP8.5 is 94.64×10^8 m^3, which is less than that under RCP2.6 (90.61×10^8 m^3) and RCP4.5 (92.48×10^8 m^3), in which the precipitation and temperature are also lower compared with RCP8.5. Thus, we can speculate that the increasing trend of the annual amount of runoff will happen during 2060–2100. Zhang et al. [27] also showed that the change in streamflow is influenced by the simultaneous changes of precipitation and temperature and showed similar results in the 2020s, 2050s, and 2080s; their study area is also a monsoon area that is similar to the area in this study. In contrast, other studies [1,35,40,41] with alpine and dry areas, where evapotranspiration is more than precipitation, show a decreasing trend in runoff.
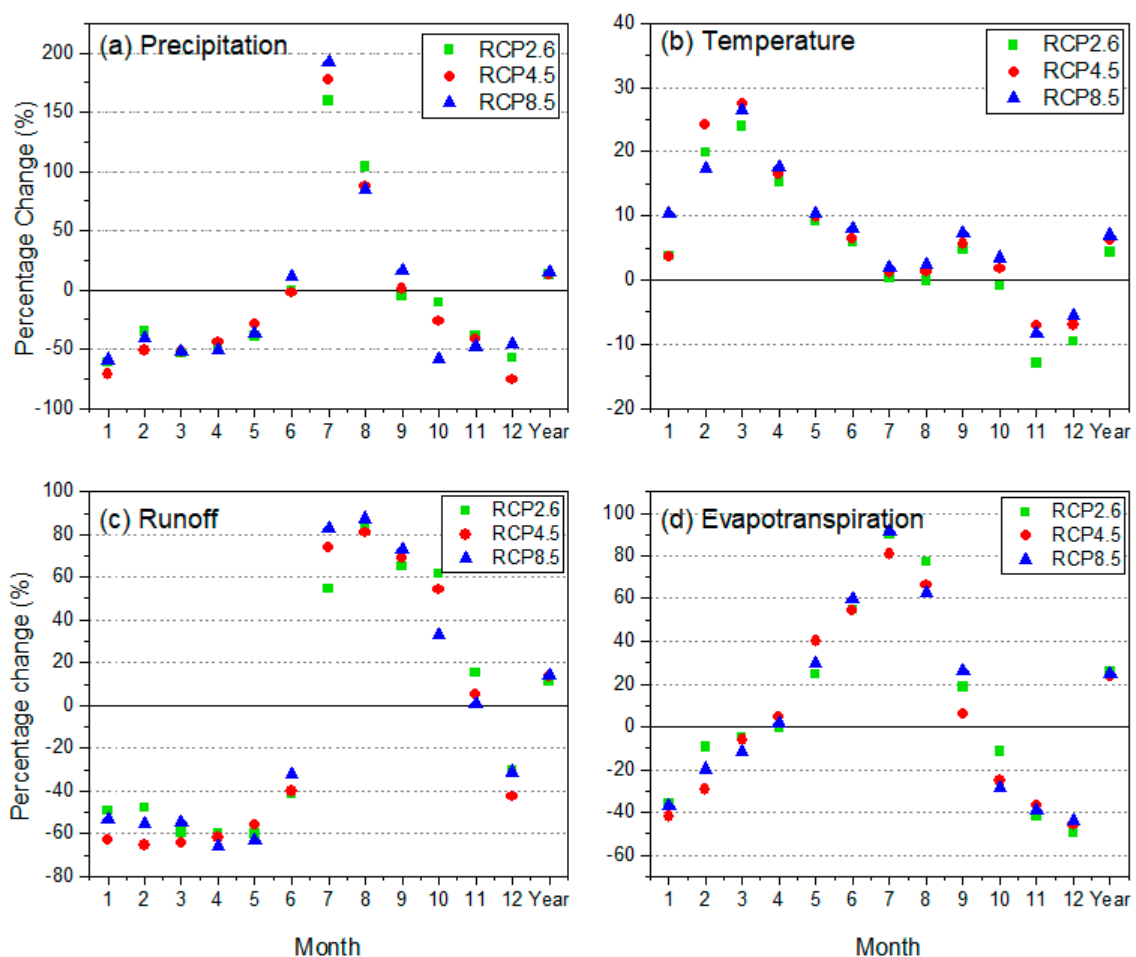
Figure 8. Percentage changes in all hydrological variables.

4.3. Changing Hydrological Variables Compared with Other Areas

We compared the hydrological response of climate change in the Lijiang River Basin with other related watersheds. As presented in this study, the annual average of temperature, evapotranspiration, and precipitation will increase in the future. The results are also validated in Piao et al. [42], which performed a similar study in Southern China. Although runoff has slightly decreased in the study area, it is affected by both increasing precipitation and evapotranspiration, and the theorical

runoff could either increase or decrease. Related research obtained similar findings. For example, Zhang et al. [27] assessed the hydrological response of climate change in the Xin River Basin, which is also a monsoon and humid area and is also located in Southern China. This study showed the increasing change of precipitation and temperature, and the result of runoff is close to baseline, which showed similar changes in this study. The monthly precipitation and runoff distribution are also similar to this study as the peak flow occurs in summer, although the peak value of the Xin River Basin is in early- and mid-summer, while in this study, it occurs in mid-summer. The annual average runoff in the 2080s is more than that in the 2050s, and runoff in the 2050s is also greater than in the 2020s. Stagge et al. [43] has also demonstrated the increasing trend of annual runoff in the Potomac River located in Mid-Atlantic US, with an average increasing percentage of only 2.7%, 4.0%, and 4.3% in short-, mid-, long-term future periods.

When comparing with the areas that are different from our study area, the results are different. In this case, different conditions are usually with higher altitude and drier climates, and their annual precipitation is usually less than most monsoon areas [44]. However, most arid areas have more runoff compared with humid and monsoon areas, in that there is more snow accumulation in winter and snow melt in spring as temperature rises [1,12]. Therefore, hydrological elements have heterogeneity in multiple areas of different conditions. In general, in humid and monsoon areas, especially in southern China, the precipitation and runoff usually demonstrate the seasonal characteristics and annual precipitation is usually greater than arid areas with higher altitude, such as the typical areas of Western China and Central Asia.

5. Conclusions

In this study, we analyzed several GCM outputs by using both single and combined bias correction methods and selected the most suitable corrected GCM as input for the SWAT model. The historical (1964–2005) and future scenarios (2016–2055) with three RCPs were used to simulate the precipitation, temperature, evapotranspiration, and runoff. The hydrological variables indicated great heterogeneity, especially in monthly distribution. The following conclusions can be drawn in this study:

(1) All the correction methods have a positive effect compared with the original GCM. For precipitation, the ECDF-corrected method performs better than LOCI and LS, and the effect of the hybrid method containing ECDF is also more obvious than that containing LOCI. The correcting method except ECDF is less obvious in the BNU-ESM and IPSL-CM5A-MR model in terms of RMSE, but it is better in the MIROC5 model, which demonstrates the GCM itself has uncertainty and complicated determinants. For temperature, the simulating result is better than precipitation as it has less uncertainty, and VARI performs the best among the single methods.

(2) The hybrid method of correcting precipitation and temperature has the superimposed effect in terms of NSE in most cases of the study area, which means the effect of the hybrid method is more obvious than either of the single methods to some extent. Therefore, choosing a proper GCM and correcting method is also a key procedure, and this paper can provide a reference for the method of bias correction.

(3) Both the trend of temperature changes in multiyear and its annual average value are increasing and the maximum rate occurs in the RCP8.5 scenario. The monthly distribution of temperature also increased in each month. The trend of precipitation changes in multiyear showed an increasing trend in RCP4.5, while other future scenarios showed a decreasing trend, but the annual average precipitation is increasing relative to baseline, and the maximum changing rate is under RCP8.5. The monthly distribution trend of precipitation is uneven, reflected by the increase in mid-flood season, decrease in other seasons, increase in peak flow, and delay of the peak occurrence time.

(4) The annual evapotranspiration increased in all three future scenarios, but the multiyear trend increase only occurred in RCP4.5. Its positive changes also occurred in flood seasons and kept pace with historical periods in non-flood seasons. The multiyear trend of runoff increased only in RCP4.5 and the annual average of runoff decreased slightly compared with baseline, but in future scenarios,

the multiyear average runoff has increased compared with baseline and the maximum runoff occurs under RCP8.5. The monthly distribution of runoff is similar to precipitation and also showed the uneven trend in the future. As the precipitation continues increasing compared with baseline and raising the temperature can accelerate the streamflow, the annual average runoff in the further future may increase.

Although this research determined the hydrological response to climate change for the Lijiang River Basin, there are some issues that require further discussion; for example, the uncertainty of GCM outputs analysis and the performance of several GCM outputs that best fit the study area. The standard should be various and comprehensive and not limited to R^2 or NSE. Another valuable endeavor would be using more samples of GCM outputs. The best bias correction methods may differ from multiple GCM outputs as GCM outputs are generated based on several assumptions that cause uncertainties, and the uncertainties analysis based on more samples can be conducted in our further studies.

References

1. Luo, M.; Liu, T.; Meng, F.; Duan, Y.; Bao, A.; Xing, W.; Feng, X.; de Maeyer, P.; Frankl, A. Identifying climate change impacts on water resources in Xinjiang, China. *Sci. Total Environ.* **2019**, *676*, 613–626. [CrossRef]

2. Intergovernmental Panel on Climate Change (IPCC). *AR5 Synthesis Report: Climate Change*; Cambridge University Press: Cambridge, UK, 2014.

3. Li, F.; Zhang, Y.; Xu, Z.; Teng, J.; Liu, C.; Liu, W.; Mpelasoka, F. The impact of climate change on runoff in the southeastern Tibetan Plateau. *J. Hydrol.* **2013**, *505*, 188–201. [CrossRef]

4. Ruelland, D.; Ardoin-Bardin, S.; Collet, L.; Roucou, P. Simulating future trends in hydrological regime of a large Sudano-Sahelian catchment under climate change. *J. Hydrol.* **2012**, *424*, 207–216. [CrossRef]

5. Lin, Q.X.; Wu, Z.Y.; Singh, V.P.; Sadeghi, S.H.R.; He, H.; Lu, G. Correlation between hydrological drought, climatic factors, reservoir operation, and vegetation cover in the Xijiang Basin, South China. *J. Hydrol.* **2017**, *549*, 512–524. [CrossRef]

6. Almazroui, M.; Islam, M.N.; Saeed, F.; Alkhalaf, A.K.; Dambul, R. Assessing the robustness and uncertainties of projected changes in temperature and precipitation in AR5 Global Climate Models over the Arabian Peninsula. *Atmos. Res.* **2017**, *194*, 202–213. [CrossRef]

7. Meinshausen, M.; Smith, S.J.; Calvin, K.; Daniel, J.S.; Kainuma, M.; Lamarque, J.; Matsumoto, K.; Montzka, S.; Raper, S.; Riahi, K. The RCP greenhouse gas concentrations and their extensions from 1765 to 2300. *Clim. Chang.* **2011**, *109*, 213–241. [CrossRef]

8. Xin, X.; Zhang, L.; Zhang, J.; Wu, T.; Fang, Y. Climate change projections over East Asia with BCC-CSM1.1 climate model under RCP scenarios. *J. Meteorol. Soc. Jpn.* **2013**, *91*, 413–429. [CrossRef]

9. Chen, J.; Frauenfeld, O.W. Surface air temperature changes over the twentieth and twenty-first centuries in China simulated by 20 CMIP5 models. *J. Clim.* **2014**, *27*, 3920–3937. [CrossRef]

10. Siew, J.H.; Tangang, F.T.; Juneng, L. Evaluation of CMIP5 coupled atmosphere-ocean general circulation models and projection of the Southeast Asian winter monsoon in the 21th century. *Int. J. Climatol.* **2014**, *34*, 2872–2884. [CrossRef]

11. Fonseca, A.R.; Santos, J.A. Predicting hydrological flows under climate change: The Tamega Basin as an analog for the Mediterranean region. *Sci. Total Environ.* **2019**, *668*, 1013–1024. [CrossRef]

12. Anjum, M.N.; Ding, Y.; Shangguan, D.; Ahmad, I.; Ijaz, M.W.; Farid, H.U.; Yagoub, Y.E.; Zaman, M.; Adnan, M. Performance evaluation of latest integrated multi-satellite retrievals for Global Precipitation Measurement (IMERG) over the northern highlands of Pakistan. *Atmos. Res.* **2018**, *205*, 134–146. [CrossRef]

13. Chu, J.T.; Xia, J.; Xu, C.Y.; Singh, V.P. Statistical downscaling of daily mean temperature, pan evaporation and precipitation for climate change scenarios in Haihe River of China. *Theor. Appl. Climatol.* **2010**, *99*, 149–161. [CrossRef]

14. Birkinshaw, S.J.; Guerreiro, S.B.; Nicholson, A.; Liang, Q.; Quinn, P.; Zhang, L.; He, B.; Yin, J.; Fowle, H.J. Climate change impacts on Yangtze River discharge at the Three Gorges Dam. *Hydrol. Earth Syst. Sci.* **2017**, *21*, 1911–1927. [CrossRef]

15. Piani, C.; Haerter, J.O.; Coppola, E. Statistical bias correction for daily precipitation in regional climate models over Europe. *Theor. Appl. Climatol.* **2010**, *99*, 187–192. [CrossRef]

16. Luo, M.; Liu, T.; Meng, F.; Duan, Y.; Frankl, A.; Bao, A.; De Maeyer, P. Comparing bias correction methods used in downscaling precipitation and temperature from regional climate models: A case study from the Kaidu river basin in Western China. *Water* **2018**, *10*, 1046. [CrossRef]

17. Teutschbein, C.; Seibert, J. Bias correction of regional climate model simulations for hydrological climate-change impact studies: Review and evaluation of different methods. *J. Hydrol.* **2012**, *456*, 12–29. [CrossRef]

18. Hashino, M.; Yao, H.; Yoshida, H. Studies and evaluations on interception processes during rainfall based on a tank model. *J. Hydrol.* **2002**, *255*, 1–11. [CrossRef]

19. Steele-Dunne, S.; Lynch, P.; McGrath, R.; Semmler, T.; Wang, S.; Hanafin, J.; Nolan, P. The impacts of climate change on hydrology in Ireland. *J. Hydrol.* **2008**, *356*, 28–45. [CrossRef]

20. Gao, C.; Liu, L.; Ma, D.; He, K.; Xu, Y.P. Assessing responses of hydrological processes to climate change over the southeastern Tibetan Plateau based on resampling of future climate scenarios. *Sci. Total Environ.* **2019**, *664*, 737–752. [CrossRef]

21. Gao, J.; Holden, J.; Kirkby, M. Modelling impacts of agricultural practice on flood peaks in upland catchments: An application of the distributed TOPMODEL. *Hydrol. Process.* **2017**, *31*, 4206–4216. [CrossRef]

22. Chiew, F.H.S.; Siriwardena, L. *Estimation of SIMHYD Parameter Values for Application in Ungauged Catchments 1*; University of Melbourne: Melbourne, Australia, 2005.

23. Harlan, D.; Wangsadipura, M.; Munajat, C.M. Rainfall-runoff modeling of Citarum Hulu River basin by using GR4J. *Proc. World Congr. Eng.* **2010**, *2*, 1–5.

24. Martina, M.L.V.; Todini, E.; Liu, Z. Preserving the dominant physical processes in a lumped hydrological model. *J. Hydrol.* **2011**, *399*, 121–131. [CrossRef]

25. Wi, S.; Ray, P.; Demaria, E.M.C.; Steinschneider, S.; Brown, C. A user-friendly software package for VIC hydrologic model development. *Environ. Model. Softw.* **2017**, *98*, 35–53. [CrossRef]

26. Wang, Z.G.; Liu, C.M.; Wu, X.F. A review of the studies on distributed hydrological model based on DEM. *J. Nat. Resour.* **2003**, *18*, 168–173.

27. Zhang, Y.; You, Q.; Che, C.; Ge, J. Impacts of climate change on streamflows under RCP scenarios: A case study in Xin River Basin, China. *Atmos. Res.* **2016**, *178–179*, 521–534. [CrossRef]

28. Chattopadhyay, S.; Edwards, D.R.; Yu, Y.; Hamidisepehr, A. An Assessment of Climate Change Impacts on Future Water Availability and Droughts in the Kentucky River Basin. *Environ. Process.* **2017**, *4*, 477–507. [CrossRef]

29. Xu, Y.-P.; Zhang, X.; Ran, Q.; Tian, Y. Impact of climate change on hydrology of upper reaches of Qiantang River basin, East China. *J. Hydrol.* **2013**, *483*, 51–60. [CrossRef]

30. Christensen, J.H.; Boberg, F.; Christensen, O.B.; Lucas-Picher, P. On the need for bias correction of regional climate change projections of temperature and precipitation. *Geophys. Res. Lett.* **2008**, *35*. [CrossRef]

31. Schmidli, J.; Frei, C.; Vidale, P.L. Downscaling from GCM precipitation: A benchmark for dynamical and statistical downscaling methods. *Int. J. Climatol. J. R. Meteorol. Soc.* **2006**, *26*, 679–689. [CrossRef]

32. Jakob Themeßl, M.; Gobiet, A.; Leuprecht, A. Empirical-statistical downscaling and error correction of daily precipitation from regional climate models. *Int. J. Climatol.* **2011**, *31*, 1530–1544. [CrossRef]

33. Chen, J.; Brissette, F.P.; Poulin, A.; Leconte, R. Overall uncertainty study of the hydrological impacts of climate change for a Canadian watershed. *Water Resour. Res.* **2011**, *47*. [CrossRef]

34. Chen, J.; Brissette, F.P.; Leconte, R. Uncertainty of downscaling method in quantifying the impact of climate change on hydrology. *J. Hydrol.* **2011**, *401*, 190–202. [CrossRef]

35. Zhang, H.; Huang, G.H.; Wang, D.; Zhang, X. Multi-period calibration of a semi-distributed hydrological model based on hydroclimatic clustering. *Adv. Water Resour.* **2011**, *34*, 1292–1303. [CrossRef]

36. Soil Conservation Service (SCS). *National Engineering Handbook, Hydrology, Section 4*; Soil Conservation Service; US Department of Agriculture: Washington, DC, USA, 1956.

37. Rallison, R.E.; Miller, N. Past, present, and future SCS runoff procedure. In *Rainfall-Runoff Relationship/ Proceedings, Proceedings of the International Symposium on Rainfall-Runoff Modeling, Starkville, MS, USA, 18–21 May 1981*; Singh, V.P., Ed.; Water Resources Publications: Littleton, CO, USA, 1982.

38. Neitsch, S.L.; Arnold, J.G.; Kiniry, J.R.; Williams, J.R. *Soil and Water Assessment Tool Theoretical Documentation Version 2009*; Texas Water Resources Institute, Texas A&M University: College Station, TX, USA, 2011.

39. Arnold, J.G.; Srinivasan, R.; Muttiah, R.S.; Williams, J.R. Large area hydrologic modeling and assessment part I: Model development. *J. Am. Water Resour. Assoc.* **1998**, *34*, 73–89. [CrossRef]

40. Naz, B.S.; Kao, S.C.; Ashfaq, M.; Rastogi, D.; Mei, R.; Bowling, L.C. Regional hydrologic response to climate change in the conterminous United States using high-resolution hydroclimate simulations. *Glob. Planet. Chang.* **2016**, *143*, 100–117. [CrossRef]

41. Fang, G.; Yang, J.; Chen, Y.; Zhang, S.; Deng, H.; Liu, H.; De Maeyer, P. Climate change impact on the hydrology of a typical watershed in the Tianshan Mountains. *Adv. Meteorol.* **2015**, *2015*. [CrossRef]

42. Piao, S.; Ciais, P.; Huang, Y.; Shen, Z.; Peng, S.; Li, J.; Zhou, L.; Liu, H.; Ma, Y.; Ding, Y.; et al. The impacts of climate change on water resources and agriculture in China. *Nature* **2010**, *467*, 43–51. [CrossRef]

43. Stagge, J.H.; Moglen, G.E. A nonparametric stochastic method for generating daily climate-adjusted streamflows. *Water Resour. Res.* **2013**, *49*, 6179–6193. [CrossRef]

44. Gao, G.; Chen, D.; Xu, C.Y.; Simelton, E. Trend of estimated actual evapotranspiration over China during 1960–2002. *J. Geophys. Res.* **2007**. [CrossRef]

The Spatiotemporal Patterns of Climate Asymmetric Warming and Vegetation Activities in an Arid and Semiarid Region

Tong Heng [1] [ID], **Gary Feng** [2,*] [ID], **Ying Ouyang** [3] [ID] **and Xinlin He** [1] [ID]

[1] College of Water and Architectural Engineering, Shihezi University, Shihezi 832021, China; htshz121@163.com (T.H.); hexinlin2002@163.com (X.H.)
[2] USDA-ARS, Genetic and Sustainable Agricultural Research Unit, 810 Hwy 12 East, Mississippi State University, Starkville, MS 39762, USA
[3] USDA Forest Service, Center for Bottomland Hardwoods Research, 775 Stone Blvd., Thompson Hall, Room 309, Mississippi State University, Starkville, MS 39762, USA; ying.ouyang@usda.gov
[*] Correspondence: gary.feng@usda.gov; Tel.: +1-1662-320-7449

Abstract: Asymmetric warming was bound to have a major impact on terrestrial ecosystems in arid regions during global warming. Further study was necessary to reveal the spatiotemporal patterns of asymmetric warming in Xinjiang; this study analyzed the climate and normalized difference vegetation index (NDVI) data (2000–2020). The change trends of the day and nighttime warming (DNW), seasonal warming, and the diurnal temperature range in northern Xinjiang (S1) and southern Xinjiang (S2) were determined. The findings indicated that the DNW rate showed a significant ($p < 0.05$) upward trend, especially in winter. The nighttime warming rate (0.65 °C $(decade)^{-1}$) was faster than the daytime warming rate (0.4 °C $(decade)^{-1}$), and the diurnal temperature range between daytime and nighttime exhibited a decreasing trend. The diurnal temperature range was the highest in spring and the lowest in winter. Extreme values of the diurnal temperature range appeared in autumn (48.6 °C) and winter (12.3 °C) and both in S1. The T_{min} in S1 had an abruption trend in 2006–2017, the T_{max} in S2 had an abruption trend in 2005–2011, and the probability of spatial abruption in S1 was higher than that in S2. The partial correlation between the NDVI and T_{min} was significantly higher than that between the NDVI and T_{max} in the area where the significance test passed; therefore, asymmetric nighttime warming had a greater impact on the NDVI than the asymmetric daytime warming.

Keywords: asymmetric warming; normalized difference vegetation index; second-order partial correlation analysis; day and nighttime warming; diurnal temperature range

1. Introduction

Since the 1950s, terrestrial ecosystems have experienced a continuous warming process [1–3]. With the increase in global average temperature, there is growing evidence suggesting that asymmetric patterns of day and nighttime warming (DNW) and seasonal warming are common in the warming process [4–7]. This phenomenon is called asymmetric warming [8]. The global average temperature has risen by 0.89 °C over the last 100 years [9], and the rate of temperature increase is 0.13 °C $(decade)^{-1}$ [10,11]. Average global temperatures are projected to increase by 0.91–2 °C throughout the mid-21st century [12,13]. Located in the eastern part of Eurasia, China is one of the most complex regions experiencing global climate change and is strongly influenced by the eastern continental monsoon climate and the northwest inland arid climate [14,15]. In the past 40 years, the average surface temperature in China has risen by 1.1 °C, which is higher than the global warming rate [16–20].

The persistent enhancement of asymmetric warming will have significant impacts on terrestrial vegetation and even on the whole structure, functions, and services of ecosystems.

The IPCC's (Intergovernmental Panel on Climate Change) fourth assessment reported that the global nighttime warming rate from 1957 to 2007 was 1.4 times the daytime warming rate [21,22]. Davy et al. [23] showed that the warming rate in summer was faster than that in spring and autumn in the high latitudes of the Northern Hemisphere. As an important part of terrestrial ecosystems, the growth and development of vegetation are bound to be affected by asymmetric warming. These generally relate differences in the temperature trends to regionalized cloud cover, precipitation, or soil moisture. Peng et al. [24] analyzed the interannual covariations of the satellite-derived normalized difference vegetation index (NDVI) with asymmetric warming over the Northern Hemisphere; their study showed that daily maximum temperatures were positively correlated with the NDVI in humid areas and had a significant negative correlation with the NDVI in arid areas. Xu et al. [25] investigated vegetated growth dynamics (annual productivity, seasonality, and the minimum amount of vegetated cover) in China and their relations with climatic factors during 1982–2011, and they believed that vegetation productivity was positively correlated with the nighttime warming rate. Nemani et al. [26] analyzed the climatic data and satellite observations of vegetation activity during 1982–1999 and found that vegetation growth representing the response cycle of asymmetric warming in high-latitude and high-altitude areas was shorter than that in low-latitude and low-altitude areas. Cong et al. [27] showed that asymmetric warming could accelerate respiration in plants and increase the decomposition rate of organic matter. However, little is known about the warming trends in the relationships between NDVI and asymmetric warming and precipitation, and understanding this is crucial for predicting how climate change would affect vegetation activity in the future.

Located in the arid and semiarid region of China, with a temperate continental climate, Xinjiang is a typical "mountain-oasis-desert" ecosystem [28]. As the area is affected by the sea-land distribution and the uplift of the Qinghai-Tibet Plateau, the differences in soil water-thermal status and geographical vegetation differentiation between S1 and S2 have been significant; these differences have led to different sensitivities of the vegetation types to climate factors in Xinjiang [29,30]. At present, research on the responses of vegetation activities to asymmetric warming mainly focuses on the differences in interannual average temperature and the geographic spatial and seasonal changes in vegetation types [31–33]. The changing trends of asymmetric warming, abruption characteristics, and the influence of precipitation on the NDVI over different time series have received little attention. Given this, in the context of global asymmetric warming, this paper was based on a global NDVI dataset, monthly minimum (T_{min}) and maximum temperature (T_{max}) data, and precipitation data in Xinjiang from 2000 to 2020. Least squares linear regression, Yamamoto and Mann–Kendall nonparametric randomization tests, and second-order partial correlation analysis were used to study the spatiotemporal patterns and abruption signatures of daytime and nighttime warming, seasonal warming, the diurnal temperature range, and the response of vegetation activities to asymmetric warming. The goal of this study was to provide a reference for the impacts of asymmetric warming on the vegetation ecosystems in Xinjiang.

2. Materials and Methods

2.1. Site Description

The geomorphological features of Xinjiang (73°40′–96°23′ E and 34°25′–49°10′ N) consist of 3 mountains and 2 basins, with a west-east width of approximately 1950 km, south-north length of approximately 1550 km, and a total area of 1.66×106 km^2. The mountain and basins, from north to south, are the Altai Mountains, the Junggar Basin, the Tianshan Mountains, the Tarim Basin, and the Karakoram Mountains. The Tianshan Mountains lie across the middle of the region [34]. On the basis of the meteorological definition and geomorphological characteristics of Xinjiang, the study area is further categorized into two regions: northern Xinjiang (S1) and southern Xinjiang (S2), with the Tianshan Mountain as the boundary (Figure 1). The mean annual temperatures in S1 and S2 are 13 and

19 °C, and the annual precipitation values are 180 and 95 mm, respectively; these precipitation values are only 15–28% of the average precipitation level of China (630 mm, 2000–2020).
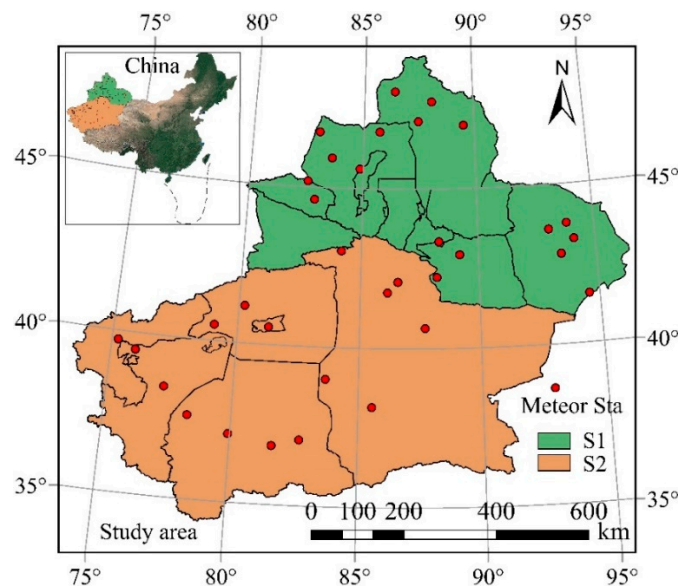

Figure 1. Distribution of meteorological stations in the studied region.

Meteorological data were obtained from the dataset of monthly surface climate data of the China Meteorological Science Data service network (http://cdc.cma.gov.cn). The weather data are the maximum daytime temperature (T_{max}), the minimum nighttime temperature (T_{min}), and precipitation. To ensure homogeneity and the longest continuous observation, data from 34 ground-based meteorological stations of the China Meteorological Administration (CMA) were used in the study. The Kriging interpolation method was chosen in ArcGIS 10.4 with the spatial analyst extension and raster images. According to the existing seasonal division method [35], the monthly dataset was further averaged to spring (March, April, and May), summer (June, July, and August), autumn (September, October, and November), winter (December, January, and February), the growing season (April to October), and the non-growing season (November to March of the subsequent year).

The NDVI dataset from 2000 to 2020 was acquired from the MOD13A3 product of Goddard Space Flight Center, LAADS, NASA (https://ladsweb.modaps.eosdis.nasa.gov/), and the spatiotemporal resolution is 1 km, 30 days, respectively. This dataset was synthesized by the maximum value synthesis method (MVS) and processed by cloud, aerosol, water vapor, etc.; it is the longest time series currently acquired by the TERRA satellite.

2.2. Research Methods

The least-square linear regression method was applied to analyze the trend of DNW at the regional and pixel scales [36,37], and the significance of regression coefficients was determined by the *t*-test (*p*-values). * indicated significant (*p* = 0.05). ** indicated extremely significant (*p* = 0.01). The diurnal warming rate was calculated element-by-element, and the spatiotemporal patterns of the DNW rates in different seasons were analyzed.

$$C_j = \frac{19 \times \sum_{i=1}^{19} i \cdot \varphi - \sum_{i=1}^{19} i \cdot \sum_{i=1}^{19} \varphi}{19 \sum_{i=1}^{19} i^2 - \left(\sum_{i=1}^{19} i\right)^2} \tag{1}$$

where *i* is the time series, ranging from 2000 to 2020; φ is the specified factor, including NDVI, T_{min}, and T_{max}; C_j is the change tendency rate of the φ pixel in 20 years, $C_j > 0$ indicates that the φ factor of

pixel *j* has an increasing trend in the past 20 years, $C_j < 0$ indicates a decreasing trend, and $C_j = 0$ indicates no change.

Mann–Kendall and Yamamoto methods were employed to test the abruption of temperature in each time series [38,39]. Mann–Kendall method is a non-parametric statistical test. It is suitable for both type variable and ordinal variable, with no specific requirements on the distribution of samples, and Pearson correlation results were not dominated by outliers. The major mathematical methods were as follows:

For the time series, a rank s series is constructed:

$$S_k = \sum_{i=1}^{k} r_i \, k = 2,3\ldots n \tag{2}$$

$$r_i = \begin{cases} 1 \ x_i > x_j \\ 0 \ x_i < x_j \end{cases} j = 1,2\ldots i \tag{3}$$

where rank series S_k is the cumulative number of the *i* time value greater than *j* time. The statistics was defined under the assumption that the time series were independent:

$$UF_k = \frac{\left| S_k - E(S_k) \right|}{\sqrt{var(S_k)}} k = 1,2\ldots n \tag{4}$$

$$UB_k = -UF_k \, k = n, n-1\ldots 1 \tag{5}$$

where $UF_1 = 0$, $E(S_k)$ and $var(S_k)$ are the mean and variance of S_k. When x_1, $x_2 \ldots x_n$ were independent of each other and had the same continuous distribution, they were calculated as follows:

$$\begin{cases} E(S_k) = \frac{k(x-1)}{4} \\ var(S_k) = \frac{k(x-1)(2k+5)}{72} \end{cases} k = 2,3\ldots n \tag{6}$$

Set UF_k and UB_k as standard normal distribution, given a significance value $\alpha = 0.05$, critical value $U_{0.05} = \pm1.96$, and two statistical sequence curves of UF_k and UB_k and the two critical lines (±1.96) were drawn in one graph.

Yamamoto method explores the abruption characteristics from two parts: climate information and climate noise. In this study, DPS 7.05 (http://www.chinadps.net/) was used to process the abruption data. The specific method was to define a signal-to-noise ratio:

$$\frac{S}{N} = \frac{\left| \overline{x_1} - \overline{x_2} \right|}{S_1 + S_2} \tag{7}$$

where *S* is the population sample variance, and *N* is the length of the population sample sequence; $\overline{x_1}$ and $\overline{x_2}$ are average values of 2 sub-sample sets; S_1 and S_2 are variance of sub-sample. Molecular was defined when $S/N > 1.0$.

To eliminate the interference of other variables except for temperature and precipitation, the second-order partial correlation analysis was used to investigate the influence of DNW on vegetation NDVI [39–41]. First, the second-order partial correlation between T_{max} and NDVI was analyzed through limiting the influence of T_{min} and precipitation; second, the second-order partial correlation between T_{min} and NDVI was analyzed through limiting the influence of T_{max} and precipitation. The second-order partial correlation coefficient was calculated based on the first-order partial correlation coefficient, and the first-order correlation coefficient needed to be calculated for

Pearson's correlation coefficient (zero-order). The partial correlation coefficients were calculated as follows:

$$r_{\alpha\delta} = \frac{\sum_{i=1}^{n}(\alpha_i - \overline{\alpha})(\varphi_i - \overline{\delta})}{\sqrt{\sum_{i=1}^{n}(\alpha_i - \overline{\alpha})^2 \sum_{i=1}^{n}(\delta_i - \overline{\delta})^2}} \quad (8)$$

$$r_{\alpha\delta.1} = \frac{r_{\alpha\delta} - r_{\alpha.1}r_{\delta.1}}{\sqrt{1-r_{\alpha.1}^2} \cdot \sqrt{1-r_{\delta.1}^2}} \quad (9)$$

$$r_{\alpha\delta.12} = \frac{r_{\alpha\delta.1} - r_{\alpha2.1}r_{\delta2.1}}{\sqrt{1-r_{a2.1}^2} \cdot \sqrt{1-r_{\delta2.1}^2}} \quad (10)$$

where α and φ are principal variables by partial correlation coefficients; 1 and 2 are control variables; $r_{\alpha\delta}$ is correlation coefficient; $r_{\alpha\delta.1}$ is the first-order partial correlation coefficient; $r_{\alpha\delta.12}$ is the second-order partial correlation coefficient. *t*-test was used to test the significance of the calculated second-order partial correlation coefficient. The formula is as follows:

$$t = \frac{r\sqrt{n-q-1}}{\sqrt{1-r^2}} \quad (11)$$

where *r* is correlation coefficient; *n* and *q* are the number of samples and degrees of freedom.

3. Results

3.1. Interpreting Trends in Asymmetric Warming over Time

The interannual variation trend of DNW was calculated by a linear regression equation (Figure 2). Over the past 20 years, T_{max} and T_{min} in Xinjiang showed different degrees of warming trends. DNW had a local response period, i.e., cooling down every 2–3 years. The warming rates of T_{max} in S1 and S2 were 0.5 and 0.3 °C (decade)$^{-1}$, respectively, but the overall T_{max} in S1 was 3–5 °C lower than that in S2 ($p < 0.01$). The warming rates of T_{min} in S1 and S2 were 0.8 and 0.5 °C (decade)$^{-1}$, respectively. From 2000–2020, the interannual T_{min} in S1 increased from −7.1 to −4.3 °C, and the T_{min} in S2 increased from −0.8 to 1.4 °C. Therefore, the interannual T_{max} and T_{min} in both S1 and S2 presented asymmetrical daytime and nighttime temperature warming, i.e., the nighttime warming rates (0.65 °C (decade)$^{-1}$) were faster than the daytime warming rates (0.40 °C (decade)$^{-1}$).
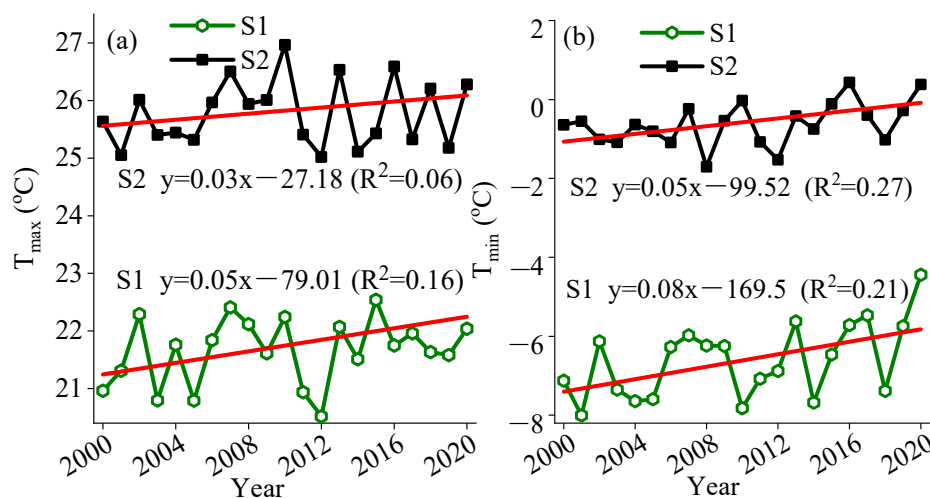
Figure 2. T_{max} (**a**) and T_{min} (**b**) trends in the S1 and S2 regions with arid and semiarid climate, 2000–2020.

There was considerable variation in the trends of seasonal T_{max} and T_{min} warming in S1 and S2 (Figure 3). The T_{max} in S1 showed a cooling downward trend in summer and significant warming in other seasons. The T_{max} in S2 showed a warming trend only in winter and a cooling down trend in other seasons. The T_{min} in S1 showed a cooling down trend in autumn and significant increases in other seasons. The T_{min} in S2 showed cooling downward trends in summer and autumn and significant warming trends in spring and winter. In addition, S1 and S2 had opposite temperature trends in spring T_{max}, summer T_{min}, and autumn T_{max}; in these three seasons, the T_{max} and T_{min} in S1 both showed a warming trend, while the temperatures in S2 showed a cooling trend. This phenomenon is mainly due to the latitude differences between S1 and S2, which further supports the significant warming trend in higher latitudes in the northern hemisphere.
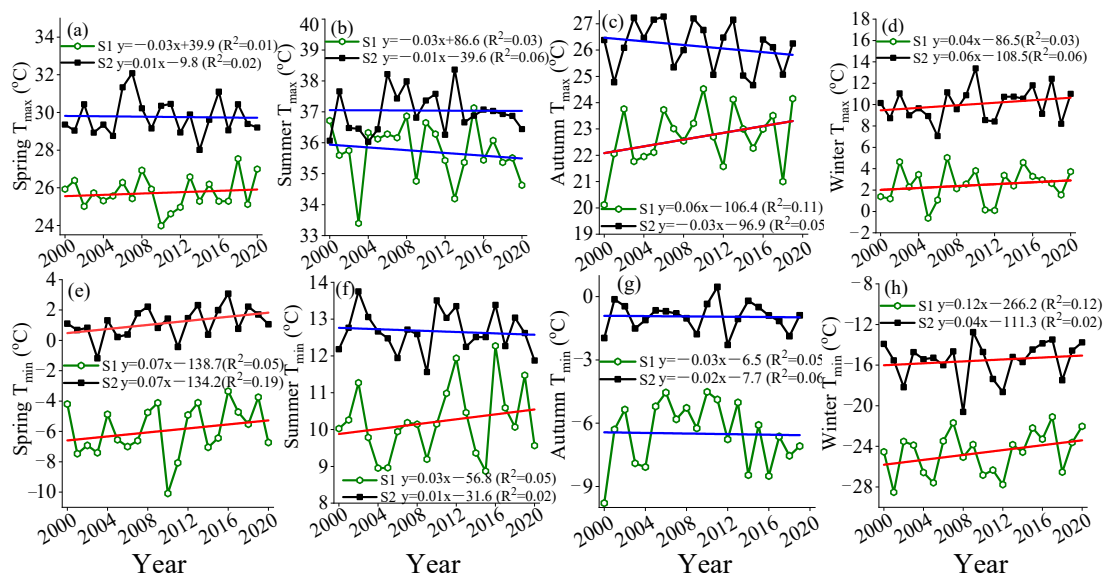
Figure 3. Seasonal T_{max} and T_{min} temperature trends in the studied regions S1 and S2, (**a**): spring T_{max}, (**b**): summer T_{max}, (**c**): autumn T_{max}, (**d**): winter T_{max}, (**e**): spring T_{min}, (**f**): summer T_{min}, (**g**): autumn T_{min}, (**h**): winter T_{min}. S1 and S2 represent two regions of the study area.

The DNW rates in S1 and S2 were asymmetrical in the four seasons. The warming rates of T_{min} in winter and spring in S1 were 3 and 3.5 times those of T_{max}, respectively; S1 had higher nighttime warming trends than daytime warming trends in spring, summer, and winter, while the opposite trend was seen for autumn. The warming rates of T_{min} in spring and autumn in S2 were higher than the T_{max} warming trend; inversely, for the daytime warming trend, the warming rate of T_{max} was higher than the T_{min} warming trend in winter, and the warming rate of T_{min} in winter in S2 was 0.6 times that of T_{max}. In addition, the warming rates of T_{min} and T_{max} were $-0.1\ ^{\circ}$C (decade)$^{-1}$ in summer, which failed to pass the significance test at the 0.05 level; thus, the cooling trend was not significant. Comparing the DNW rates of the two study areas, the warming rates of T_{max} in autumn in S1 and T_{max} in winter in S2 were the same (0.6 $^{\circ}$C (decade)$^{-1}$) and were significantly higher than those in other seasons ($p < 0.01$). The T_{min} warming rate in S1 was fastest in winter (1.2 $^{\circ}$C (decade)$^{-1}$), and the T_{min} warming rate in S2 was fastest in spring (0.7 $^{\circ}$C (decade)$^{-1}$).

There were regional differences in the diurnal temperature ranges in S1 and S2 in the four seasons (Figure 4). From 2000 to 2020, the diurnal temperature ranges in spring, summer, autumn, and winter in Xinjiang were 30.2, 25.3, 28.6, and 24.4 $^{\circ}$C, respectively. The interannual diurnal temperature range showed a trend of spring > autumn > summer > winter. The diurnal temperature range in S1 was significantly higher than that in S2 in the spring and summer seasons in the second part of the time series (2013–2020); the trends in other seasons were not significant. The maximum and minimum diurnal temperature ranges appeared in autumn (48.6 $^{\circ}$C) and winter (12.3 $^{\circ}$C) in Xinjiang, and both

appeared in S1 areas. The maximum diurnal temperature range in S2 appeared in the winter of 2008 (47.8 °C).
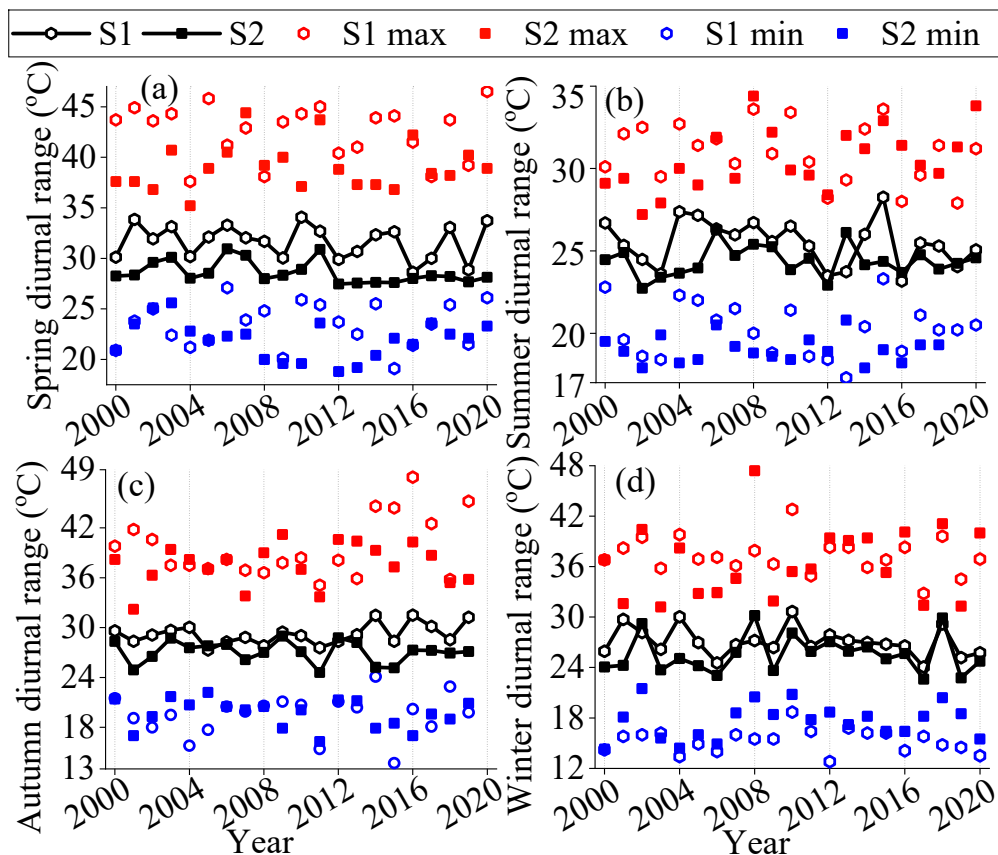
Figure 4. Seasonal variation trend of diurnal temperature range, (**a**): spring, (**b**): summer, (**c**): autumn, (**d**): winter. The red and blue scatter points represent the maximum and minimum of the daily range; S1 and S2 represent two regions of the study area.

### 3.2. Spatial Distribution Characteristics of Asymmetric Warming

The warming rates of T_{max} and T_{min} in Xinjiang from 2000 to 2020 were spatially inconsistent (Figure 5a,b). Specifically, the T_{max} warming rate was between −0.04 and 2.19 °C (decade)$^{-1}$, and the T_{min} warming rate was between −3.4 and 4.38 °C (decade)$^{-1}$. The DNW rates in S1 and S2 both showed asymmetric warming trends, and the DNW rate in S1 was significantly higher than that in S2. The T_{max} and T_{min} in S2 showed cooling trends in the southwest and central regions, and the proportions of cooling trends were 5.3% and 2.9%, respectively.

The warming rate of the diurnal temperature range in the growing season in Xinjiang showed asymmetric warming trends of −2.07 and 2.15 °C (decade)$^{-1}$ appeared in the western and eastern regions (Figure 5c), i.e., the trend was high in the eastern parts of the province, while in the western parts, the trend was low. The warming rate of the diurnal temperature range in the nongrowing season showed south- and north-low, middle-high trend (Figure 5d). In general, the diurnal temperature range in S2 showed a downtrend in the growing season, while that in S1 only showed a downtrend during the nongrowing season of vegetation.

3.3. Abruption Characteristics of DNW Warming

The abruption of DNW in Xinjiang was analyzed by the Yamamoto test (Figure 6). The changing point of T_{max} warming in S1 and S2 occurred in 2006. The warming of T_{min} in S1 had a strong abruption

in 2006 and a weak abruption in 2010, but the warming of T_{min} in S2 did not reach the detection standard of abruption. Therefore, the probability of S1 abruption was overall higher than that of S2.
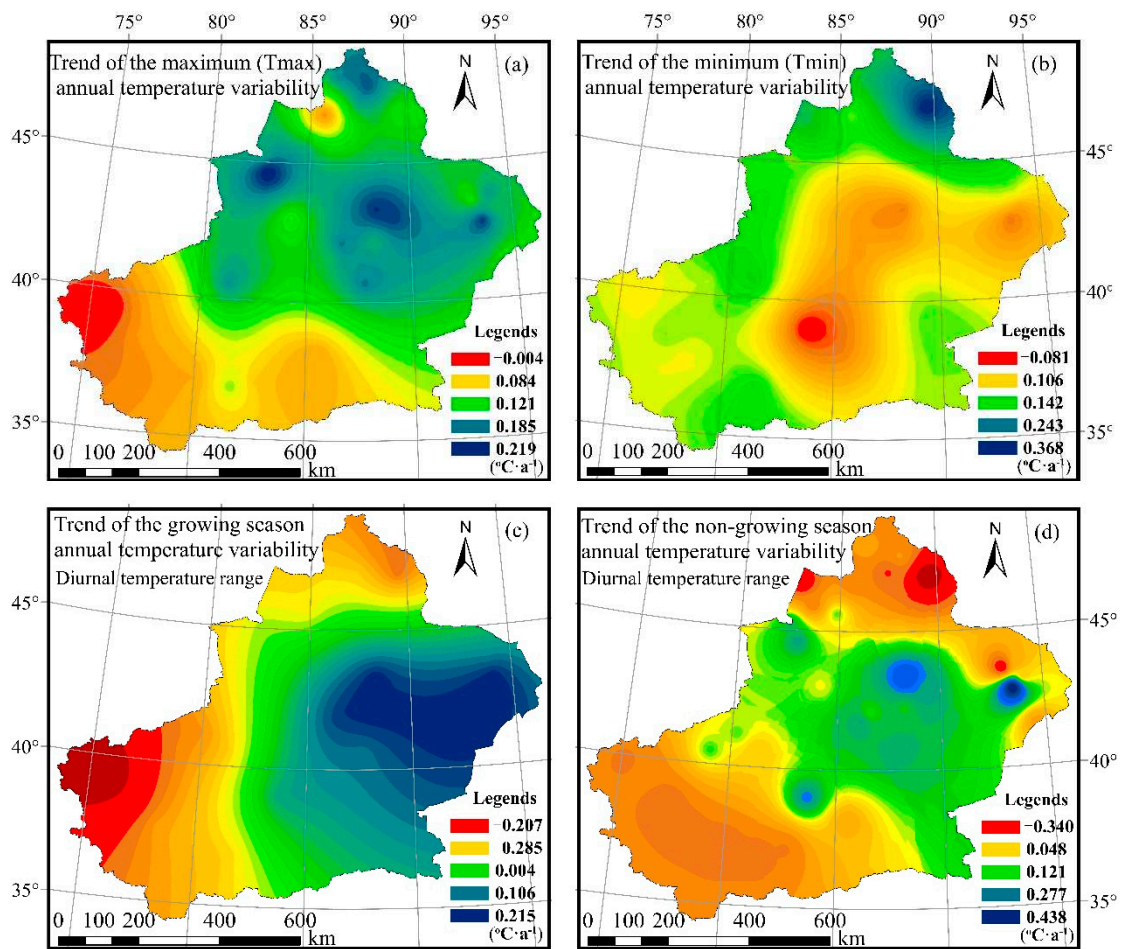

Figure 5. The spatial distribution of averaged T_{max} and T_{min} over 20 years in the arid and semiarid region, (**a**): the trend of T_{max}, (**b**): the trend of T_{min}, (**c**): diurnal range in the growing season of vegetations, (**d**): diurnal range in the non-growing season of vegetations. S1 and S2 represent two regions of the study area.
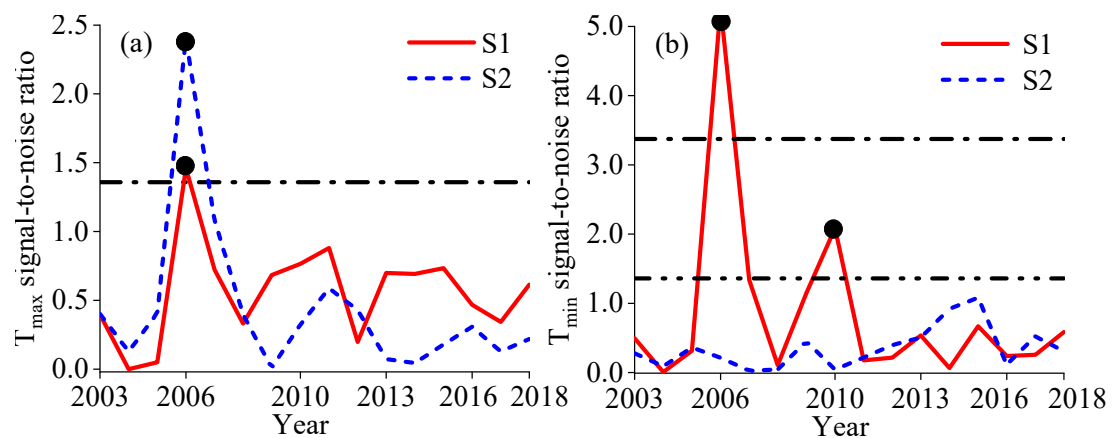
Figure 6. Abrupt change detection for (**a**): T_{max}, (**b**): T_{min}, Yamamoto test. S1 and S2 represent two regions of the study area.

The Mann–Kendall abruption test curve of DNW in Xinjiang was analyzed (Figure 7). Taking the critical value at the (±) 95% confidence level ($Z\alpha/2 = 1.96$) and a 5% degree of precision, it could be found from the UF and UB curves of the reverse time series, as well as their intersection point, that the warming trends of T_{min} in S1 and S2 showed upward trends since 2003. Among the abruption results, S1 only presented a point abruption in 2017 ($p < 0.01$); the first intersection point of the UF and UB curves appeared in 2006, and this intersection point was within the confidence interval. Therefore, it was determined that the first abruption year of T_{min} warming in S1 was 2006; the abruption then reached an extremely significant level in 2017. The warming trend of T_{max} in S1 was not significant (p for the trend = 0.103), while the warming trend of T_{max} in S2 showed an upward trend in 2005–2011. The S2 region presented a point abruption in 2011 ($p < 0.01$); the first intersection point of the UF and UB curves also appeared in 2006, and this intersection point was within the confidence interval. Similarly, the abruption of T_{max} warming in S2 started in 2005 and reached an extremely significant level in 2011.
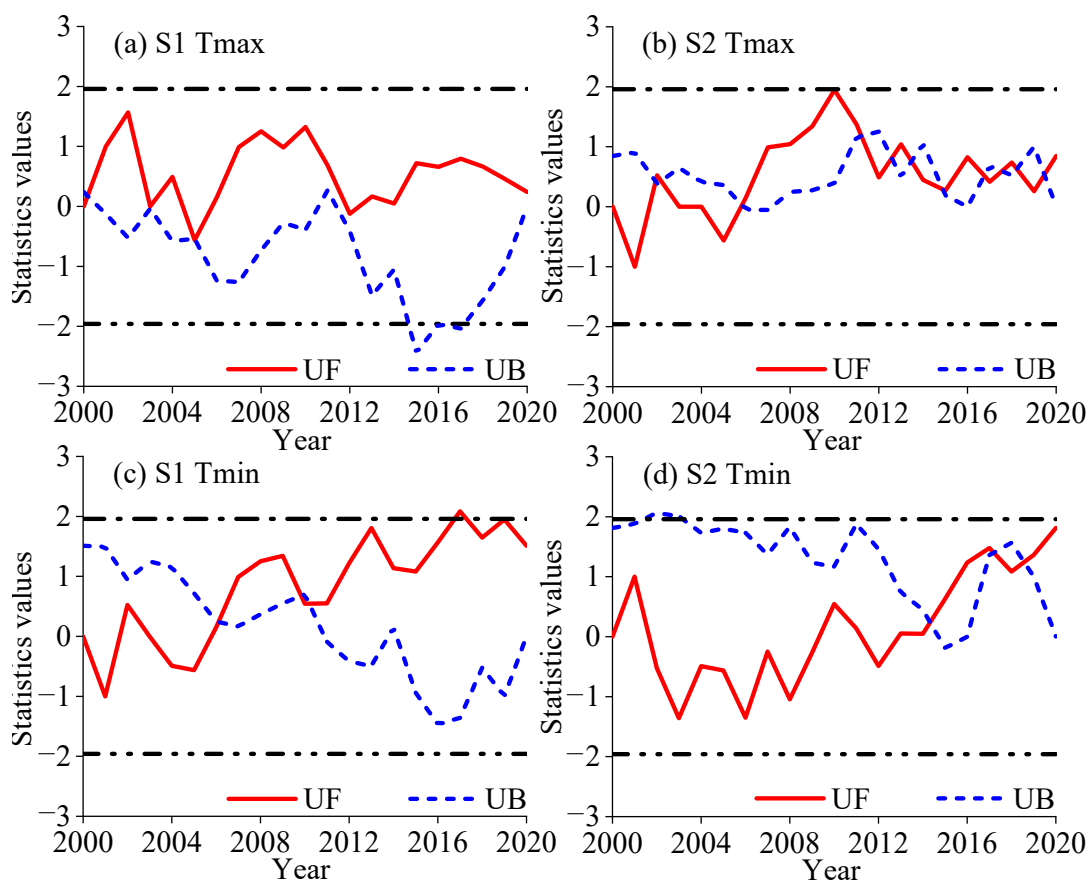
Figure 7. Mann–Kendall test for monotonic trend of (**a**) T_{max} over S1 region, (**b**) T_{max} over S1 region, (**c**) T_{min} over S1 region, and (**d**) T_{min} over S1 region. S1 and S2 represent two regions of the study area, UF and UB are statistics about temperature series, which obeys standard normal distribution. If UF and UB intersect, they represent the start time of an abrupt change.

3.4. Partial Correlation Analysis between Vegetation Activity and Asymmetric DNW in Xinjiang

Precipitation was included as a control variable, and partial correlation analysis of NDVI and DNW was carried out at 34 meteorological stations in Xinjiang (Figure 8). The area of a positive correlation between the NDVI and T_{max} accounted for approximately 32.8% of the total pixels, of which 7.7% showed a significant positive correlation ($p < 0.05$). Approximately 68.1% of the studied area and T_{max} were negatively correlated, and 4.7% of those pixels were significantly negatively correlated

($p < 0.05$). The negative correlation areas were mainly distributed in the central part of the S1 area (Junggar Basin).
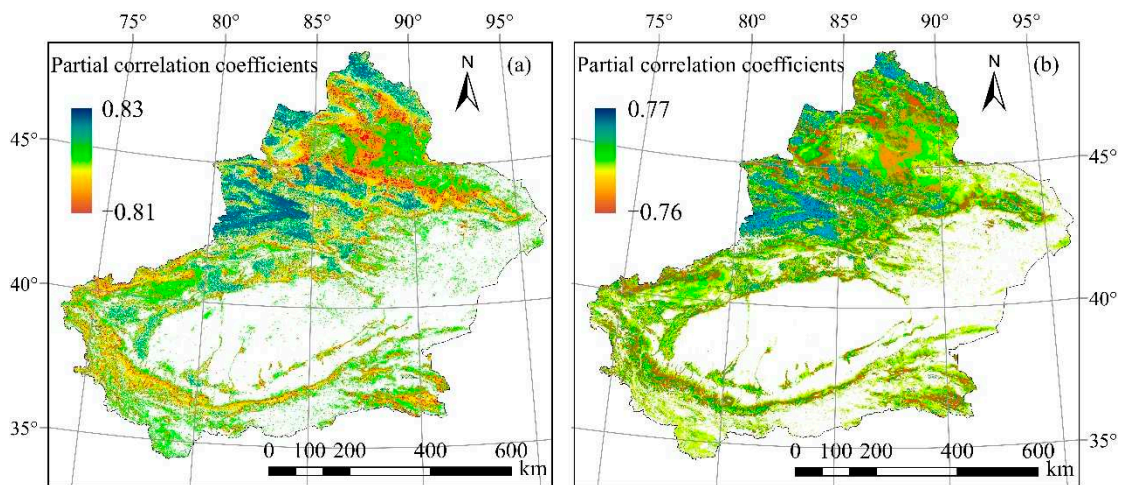
Figure 8. The partial correlation coefficient of vegetation NDVI (normalized difference vegetation index) with T_{max} (**a**) and T_{min} (**b**) in the arid and semiarid regions.

The distribution pattern of the correlation between NDVI and T_{min} was opposite to that of NDVI and T_{max}; approximately 60.7% of the studied area and T_{min} were positively correlated, of which 10.2% showed a significant positive correlation ($p < 0.05$). Approximately 39.1% of the studied area and T_{min} were negatively correlated, and 6.1% of those pixels were significantly negatively correlated ($p < 0.05$). The negative correlation areas were mainly distributed in the north-central part of the S1 area (Gurbantünggüt Desert plain). Thus, the effect of nighttime warming on vegetation in Xinjiang was more extensive than the effect of daytime warming. From the spatial distribution of DNW, the distribution trend of the partial correlation coefficient between NDVI and DNW was basically consistent in the S2 area.

4. Discussion

4.1. Causes of Asymmetric Warming

The warming rates of T_{max} and T_{min} in Xinjiang from 2000 to 2020 showed significant upward trends. The warming rate of T_{min} was 1.6 times (S1) to 1.67 times (S2) that of T_{max}. Li et al. [10] found that the summer T_{max} and T_{min} warming trends in Xinjiang from 1961 to 2005 were significant and that the interannual warming rate was 0.28 °C. The results of this study showed that the warming rates of T_{max} and T_{min} in the S2 area were 0.3 and 0.5 °C $(decade)^{-1}$, respectively, which were higher than those reported by Li et al. [10]. The warming rates of T_{max} and T_{min} further corroborated the research results. Tan et al. [5] showed that the global land surface temperature in the past 50 years increased significantly faster at nighttime than in the daytime and that the nighttime warming rate was 1.4 times that of the daytime. The DNW trends in S1 and S2 in this study had global coherence, and the warming rates in these areas were higher than the world average. However, the DNW was asymmetric; i.e., the nighttime warming rate (0.65 °C $(decade)^{-1}$) was faster than the daytime warming rate (0.4 °C $(decade)^{-1}$). The S1 study area has a temperate continental arid and semiarid climate with a large basin area, while S2 has a warm temperate continental arid climate and the world's second-largest mobile desert. The atmospheric inverse radiation in S2 is higher than that in S1, and the average annual precipitation in S1 is twice that in S2. These climate differences affect the atmospheric circulation of the two regions; thus, the difference in climate types was the main reason that the nighttime warming rate

was higher than the daytime warming rate [42,43]. Another possible explanation for this is the impact of human activities on DNW [44,45].

4.2. Abruption Trend Analysis of Asymmetric Warming

In Xinjiang, T_{max} and T_{min} experienced sudden warming in 2011 and 2017, respectively, and the warming trend of T_{min} after 2005 was significant. There were also asymmetric changes in the abruption times of T_{max} and T_{min}. The Yamamoto and Mann–Kendall tests indicated good consistency of the abruption test results over time; i.e., the abruption probability in S1 was higher than that in S2, and the abruptions occurred mainly in nighttime trends in S1 and daytime trends in S2. The S1 study area showed an abruption trend in T_{min} from 2006 to 2017, and S2 also showed an abruption trend in T_{max} from 2005 to 2011; both study areas experienced upward trends. This showed that the duration of warming abruption of the extreme T_{min} values in S1 was longer than that of the extreme T_{max} values in S2, and the duration of warming abruption in S1 was twice as long as that of S2 for extreme T_{max} values. At the same time, this result indicated that the temperature difference of DNW in Xinjiang would show a decreasing trend in the future.

4.3. Effects of Asymmetric Warming on Vegetation NDVI

The NDVI is an indicator of vegetation growth change, and the responses of NDVI to T_{max} and T_{min} reflect the effects of DNW asymmetric warming on terrestrial ecology. However, the DNW was asymmetric, i.e., the effect of nighttime (0.65 °C (decade)$^{-1}$) warming on vegetation activity was more significant than that of daytime warming. A possible reason for this result is that plants fix carbon (C) by photosynthesis during the day, while respiration takes place all the time (day- and nighttime). The imbalanced DNW rate leads to an increase in the respiration of plants at nighttime and prompts an increase in the soil organic matter decomposition rate [25]. The growth of vegetation must rely on environmental temperatures for energy to regulate internal biochemical processes and further regulate growth in the phenological period. Nemani et al. [26] found that the limiting factor for vegetation growth in high-latitude and high-altitude areas was temperature. High-altitude vegetation was more sensitive to the asymmetry of DNW; this result was in line with the results obtained in the current study. Xinjiang is located in an arid and semiarid area, and water shortage is the main limiting factor for vegetation growth. The NDVI values were positively correlated with T_{max} and T_{min} in S1 (Junggar Basin desert steppe) and S2 (Taklimakan Desert basin); this correlation is largely attributable to the physiological regulation mechanism of vegetation, which enhances the water absorption capacity of plant roots experiencing drought stress. Peng et al. [22] suggested that DNW both enhanced and inhibited vegetation growth through different disturbance mechanisms. The western area of S1 has sufficient precipitation compared with that of S2; T_{max} warming has a more significant positive effect on coniferous forests, broad-leaved forests, and meadow grasslands. When T_{max} warms continuously and exceeds the optimal temperature required for vegetation growth, vegetation growth will be inhibited; previously, vegetation growth was mainly limited by precipitation. In addition, continuous warming of T_{max} accelerates the evaporation of soil water in the daytime and aggravates the drought stress of the soil. In this situation, the vegetation cannot obtain the necessary moisture from the soil; therefore, the response of vegetation growth to increasing T_{max} in S1 was mostly negatively correlated, and the response of grassland vegetation to increasing T_{max} was significant. In contrast, S2 has scarce precipitation all year, a dry climate, and a high-altitude vegetation water supply that mostly comes from alpine meltwater. The NDVI was weakly correlated with T_{max} in S2. To better explain the response mechanisms of vegetation activity and vegetation growth stress to extreme climate events and climate change, human activities and vegetation physiological characteristics should be comprehensively considered in future research.

5. Conclusions

This study analyzed monthly T_{max}, T_{min}, precipitation, and NDVI datasets (2000–2020) and determined the change trends of DNW, seasonal warming, and the diurnal temperature range in S1 and S2. The conclusions are as follows.

During the study period between 2000 and 2020, the DNW in S1 and S2 of Xinjiang showed warming trends, and the warming rates were higher than the world average. However, DNW, seasonal warming, and the diurnal temperature range in S1 and S2 were asymmetrical, and the nighttime warming rate (0.65 °C (decade)$^{-1}$) was faster than the daytime warming rate (0.4 °C (decade)$^{-1}$). The S1 area had higher nighttime warming trends than daytime warming trends in spring, summer, and winter, while the opposite trend was identified in autumn. The nighttime warming trend in S2 in spring and autumn was higher than the daytime warming trend, and the opposite trend was observed in winter. The interannual diurnal temperature range showed a trend of spring > autumn > summer > winter. The positive partial correlation between NDVI and T_{min} was significantly higher than that between NDVI and T_{max} in the area where the significance test passed. The abruption probability in S1 was higher than that in S2, and the abruptions mainly occurred in nighttime warming in S1 and daytime warming in S2. The S1 area showed an abruption trend in T_{min} from 2006 to 2017, and S2 also showed an abruption trend in T_{max} from 2005 to 2011; both exhibited upward trends. The responses of vegetation activities to DNW in Xinjiang had significant spatial differences, especially between the Junggar Basin (S1) and Gurbantünggüt Desert plain (S2).

Conflicts of Interest: The authors declare no conflict of interest.

References

1. Sévellec, F.; Drijfhout, S.S. A novel probabilistic forecast system predicting anomalously warm 2018-2022 reinforcing the long-term global warming trend. *Nat. Commun.* **2018**, *9*, 1–12. [CrossRef]
2. Hui, C.; Zheng, X. Uncertainty in Indian Ocean Dipole response to global warming: The role of internal variability. *Clim. Dyn.* **2018**, *51*, 3597–3611. [CrossRef]
3. Wills, R.C.J.; Schneider, T.; Wallace, J.M.; Dbattisti, D.S.; Hartmann, D.L. Disentangling Global Warming, Multidecadal Variability, and El Niño in Pacific Temperatures. *Geophys. Res. Lett.* **2018**, *45*, 2487–2496. [CrossRef]
4. Donat, M.G.; Alexander, L.V. The shifting probability distribution of global daytime and night-time temperatures. *Geophys. Res. Lett.* **2012**, *39*. [CrossRef]
5. Tan, J.; Piao, S.; Chen, A.; Zeng, Z.; Ciais, P.; Janssens, I.A.; Mao, J.; Myneni, R.B.; Peng, S.; Peñuelas, J.; et al. Seasonally different response of photosynthetic activity to daytime and night-time warming in the Northern Hemisphere. *Glob. Chang. Biol.* **2014**, *21*, 377–387. [CrossRef] [PubMed]
6. Clark, J.S.; Melillo, J.; Mohan, J.; Salk, C. The seasonal timing of warming that controls onset of the growing season. *Glob. Chang. Biol.* **2013**, *20*, 1136–1145. [CrossRef]
7. Jansen, M.F.; Ferrari, R.; Mooring, T.A. Seasonal versus permanent thermocline warming by tropical cyclones. *Geophys. Res. Lett.* **2010**, *37*. [CrossRef]
8. Karl, T.R.; Jones, P.D.; Knight, R.W.; George, K.; Thomas, C.P. A New Perspective on Recent Global Warming: Asymmetric Trends of Daily Maximum and Minimum Temperature. *Bull. Am. Meteor. Soc.* **1993**, *74*, 1007–1024. [CrossRef]

9. Yan, T.; Song, H.; Zeng, H. Spring phenophases of larch are more sensitive to spring warming than to year-round warming: Results of a seasonally asymmetric warming experiment. *For. Ecol. Manag.* **2020**, *474*, 118368. [CrossRef]

10. Li, Q.; Chen, Y.; Shen, Y.; Li, X.; Xu, J. Spatial and temporal trends of climate change in Xinjiang, China. *J. Geogr. Sci.* **2011**, *21*, 1007–1018. [CrossRef]

11. Chou, C.; Neelin, J.D. Mechanisms of Global Warming Impacts on Regional Tropical Precipitation. *J. Clim.* **2004**, *17*, 2688–2701. [CrossRef]

12. Vicente-Serrano, S.M.; Beguería, S.; López-Moreno, J.I. A Multiscalar Drought Index Sensitive to Global Warming: The Standardized Precipitation Evapotranspiration Index. *J. Clim.* **2010**, *23*, 1696–1718. [CrossRef]

13. Xie, S.-P.; Deser, C.; Vecchi, G.A.; Ma, J.; Teng, H.; Wittenberg, A.T. Global Warming Pattern Formation: Sea Surface Temperature and Rainfall. *J. Clim.* **2010**, *23*, 966–986. [CrossRef]

14. Dong, W.; Jiang, Y.; Yang, S. Response of the starting dates and the lengths of seasons in Mainland China to global warming. *Clim. Chang.* **2009**, *99*, 81–91. [CrossRef]

15. Zhu, C.; Wang, B.; Qian, W. Why do dust storms decrease in northern China concurrently with the recent global warming? *Geophys. Res. Lett.* **2008**, *35*. [CrossRef]

16. He, W.P.; Feng, G.; Wang, L.; Wang, C.J.; Zhou, G.H.; Wan, S.Q. Potential impacts of global warming on extreme warm month events in China. *Acta Phys. Sin.* **2009**, *58*, 5083–5090.

17. Zhang, A.; Bian, R.; Hussain, Q.; Li, L.; Pan, G.; Zheng, J.; Zhang, X.; Zheng, J. Change in net global warming potential of a rice-wheat cropping system with biochar soil amendment in a rice paddy from China. *Agric. Ecosyst. Environ.* **2013**, *173*, 37–45. [CrossRef]

18. Sun, W.; Mu, X.; Song, X.; Wu, D.; Cheng, A.; Qiu, B. Changes in extreme temperature and precipitation events in the Loess Plateau (China) during 1960–2013 under global warming. *Atmos. Res.* **2016**, *168*, 33–48. [CrossRef]

19. Li, L.; Zha, Y. Satellite-based regional warming hiatus in China and its implication. *Sci. Total. Environ.* **2019**, *648*, 1394–1402. [CrossRef]

20. Zhou, M.; Zhou, G.; Lv, X.; Zhou, L.; Ji, Y. Global warming from 1.5 to 2 °C will lead to increase in precipitation intensity in China. *Int. J. Clim.* **2019**, *39*, 2351–2361. [CrossRef]

21. Li, H.; Chen, H.; Wang, H.; Yu, E. Future precipitation changes over China under 1.5 °C and 2.0 °C global warming targets by using CORDEX regional climate models. *Sci. Total. Environ.* **2018**, *641*, 543–554. [CrossRef] [PubMed]

22. Hans, M.F. An updated assessment of the risks from climate change based on research published since the IPCC Fourth Assessment Report. *Clim. Chang.* **2009**, *97*, 469–482. [CrossRef]

23. Davy, R.; Esau, I.; Chernokulsky, A.; Outten, S.; Zilitinkevich, S. Diurnal asymmetry to the observed global warming. *Int. J. Clim.* **2017**, *37*, 79–93. [CrossRef]

24. Peng, S.; Piao, S.; Ciais, P.; Myneni, R.B.; Chen, A.; Chevallier, F.; Dolman, A.J.; Janssens, I.A.; Peñuelas, J.; Zhang, G.; et al. Asymmetric effects of daytime and night-time warming on Northern Hemisphere vegetation. *Nat. Cell Biol.* **2013**, *501*, 88–92. [CrossRef]

25. Xu, G.; Zhang, H.; Chen, B.; Zhang, H.; Innes, J.L.; Wang, G.; Yan, J.; Zheng, Y.; Zhu, Z.; Myneni, R.B. Changes in Vegetation Growth Dynamics and Relations with Climate over China's Landmass from 1982 to 2011. *Remote. Sens.* **2014**, *6*, 3263–3283. [CrossRef]

26. Nemani, R.R.; Keeling, C.D.; Hashimoto, H. Climate-driven increases in global terrestrial net primary production from 1982 to 1999. *Science* **2003**, *300*, 1560–1563. [CrossRef]

27. Cong, N.; Shen, M.; Yang, W.; Yang, Z.; Zhang, G.; Piao, S. Varying responses of vegetation activity to climate changes on the Tibetan Plateau grassland. *Int. J. Biometeorol.* **2017**, *61*, 1433–1444. [CrossRef]

28. Xu, C.; Li, J.; Zhao, J.; Gao, S.; Chen, Y. Climate variations in northern Xinjiang of China over the past 50 years under global warming. *Quat. Int.* **2015**, *358*, 83–92. [CrossRef]

29. Shi, Y.; Shen, Y.; Kang, E.; Li, D.; Ding, Y.; Zhang, G.; Hu, R. Recent and Future Climate Change in Northwest China. *Clim. Chang.* **2007**, *80*, 379–393. [CrossRef]

30. Tao, H.; Fischer, T.; Su, B.; Mao, W.; Jiang, T.; Fraedrich, K. Observed changes in maximum and minimum temperatures in Xinjiang autonomous region, China. *Int. J. Clim.* **2017**, *37*, 5120–5128. [CrossRef]

31. Su, T.; Feng, G.; Zhou, J.; Ye, M. The response of actual evaporation to global warming in China based on six reanalysis datasets. *Int. J. Clim.* **2014**, *35*, 3238–3248. [CrossRef]

32. Zhang, L.; Yu, D.; Shi, X.; Weindorf, D.C.; Zhao, L.; Ding, W.; Wang, H.; Pan, J.; Li, C. Simulation of global warming potential (GWP) from rice fields in the Tai-Lake region, China by coupling 1:50,000 soil database with DNDC model. *Atmos. Environ.* **2009**, *43*, 2737–2746. [CrossRef]

33. Zhao, P.; Yang, S.; Yu, R. Long-Term Changes in Rainfall over Eastern China and Large-Scale Atmospheric Circulation Associated with Recent Global Warming. *J. Clim.* **2010**, *23*, 1544–1562. [CrossRef]

34. Feng, Y.; Coleman, R.G.; Tilton, G.; Xiao, X. Tectonic evolution of the West Junggar Region, Xinjiang, China. *Tectonics* **1989**, *8*, 729–752. [CrossRef]

35. Woods, P.R.; Bailey, K.R.; Wood, C.M.; Johnson, B.D. Submaximal exercise gas exchange is an important prognostic tool to predict adverse outcomes in heart failure. *Eur. J. Hear. Fail.* **2011**, *13*, 303–310. [CrossRef]

36. Decundo, J.; Susana, N.; Diéguez, G.M.; Agustina, R.; Alejandro, L.S. Impact of water hardness on oxytetracycline oral bioavailability in fed and fasted piglets. *Vet. Med. Sci.* **2019**, *5*. [CrossRef]

37. Liu, L.; Guo, Z.; Huang, G.; Wang, R. Water Productivity Evaluation under Multi-GCM Projections of Climate Change in Oases of the Heihe River Basin, Northwest China. *Int. J. Environ. Res. Public Heal.* **2019**, *16*, 1706. [CrossRef]

38. Liu, Z.; Wang, R.; Tian, X.; Zhong, X.; Gangopadhyay, J.; Cole, R.; Ikemoto, N.; Chen, S.R.W.; Wagenknecht, T. Dynamic, inter-subunit interactions between the N-terminal and central mutation regions of cardiac ryanodine receptor. *J. Cell Sci.* **2010**, *123*, 1775–1784. [CrossRef]

39. Suh, W.W.; Cho, S.H.; Yoo, J.Y.; Kim, H.S.; Song, H.R.; Kim, W.J.; Lee, S.M.; Hong, M. Relationship between Psychological Correlates and Empathy in Medical Students: A Cross-Sectional Study. *Psychiatry Investig.* **2019**, *16*, 766–772. [CrossRef]

40. Wj, J.; Chen, X.; Khaytin, I.; Bonds, A.B.; Casagrande, V.A. Relationship between spontaneous and evoked spike-time correlations in primate visual cortex. *J. Neurophysiol.* **2009**, *101*, 2279–2289. [CrossRef]

41. Buermann, W.; Forkel, M.; O'Sullivan, M.; Sitch, S.; Friedlingstein, P.; Haverd, V.; Jain, A.K.; Kato, E.; Kautz, M.; Lienert, S.; et al. Widespread seasonal compensation effects of spring warming on northern plant productivity. *Nature* **2018**, *562*, 110–114. [CrossRef]

42. Karl, T.R.; Kukla, G.; Razuvayev, V.N.; Changery, M.J.; Quayle, R.G.; Heim, R.R.; Easterling, D.R.; Bin Fu, C. Global warming: Evidence for asymmetric diurnal temperature change. *Geophys. Res. Lett.* **1991**, *18*, 2253–2256. [CrossRef]

43. Jiang, S.; Wang, K.; Mao, Y. Rapid Local Urbanization around Most Meteorological Stations Explain the Observed Daily Asymmetric Warming Rates across China from 1985 to 2017. *J. Clim.* **2020**, *33*, 1–57. [CrossRef]

44. Che, R.; Deng, Y.; Wang, W.; Rui, Y.; Cui, X.; Tahmasbian, I.; Tang, L.; Wang, S.; Wang, Y.; Xu, Z.; et al. Long-term warming rather than grazing significantly changed total and active soil procaryotic community structures. *Geoderma* **2018**, *316*, 1–10. [CrossRef]

45. Thakuri, S.; Dahal, S.; Shrestha, D.; Guyennon, N.; Romano, E.; Colombo, N.; Salerno, F. Elevation-dependent warming of maximum air temperature in Nepal during 1976–2015. *Atmos. Res.* **2019**, *228*, 261–269. [CrossRef]

Tewodros R. Godebo [1,*] , **Marc A. Jeuland** [2] , **Christopher J. Paul** [3] , **Dagnachew L. Belachew** [4] and **Peter G. McCornick** [5]

1   Department of Environmental Health Sciences, School of Public Health and Tropical Medicine, Tulane University, New Orleans, LA 70112, USA
2   Sanford School of Public Policy and Duke Global Health Institute, Duke University, P.O. Box 90239, Durham, NC 27708, USA; marc.jeuland@duke.edu
3   Department of Public Administration, North Carolina Central University, 1801 Fayetteville St, Durham, NC 27707, USA; cpaul5@nccu.edu
4   School of Earth Sciences, Addis Ababa University (AAU), Addis Ababa P.O. Box 1176, Ethiopia; dagnachew.legesse@aau.edu.et
5   Daugherty Water for Food Global Institute (DWFI), University of Nebraska, Lincoln, NE 68588, USA; pmccornick@nebraska.edu
*   Correspondence: tgodebo@tulane.edu

Abstract: This work aims to assess water quality for irrigated agriculture, alongside perceptions and adaptations of farmers to climate change in the Main Ethiopian Rift (MER). Climate change is expected to cause a rise in temperature and variability in rainfall in the region, reducing surface water availability and raising dependence on groundwater. The study data come from surveys with 147 farmers living in the Ziway–Shala basin and water quality assessments of 162 samples from groundwater wells and surface water. Most groundwater samples were found to be unsuitable for long term agricultural use due to their high salinity and sodium adsorption ratio, which has implications for soil permeability, as well as elevated bicarbonate, boron and residual sodium carbonate concentrations. The survey data indicate that water sufficiency is a major concern for farmers that leads to frequent crop failures, especially due to erratic and insufficient rainfall. An important adaptation mechanism for farmers is the use of improved crop varieties, but major barriers to adaptation include a lack of access to irrigation water, credit or savings, appropriate seeds, and knowledge or information on weather and climate conditions. Local (development) agents are identified as vital to enhancing farmers' knowledge of risks and solutions, and extension programs must therefore continue to promote resilience and adaptation in the area. Unfortunately, much of the MER groundwater that could be used to cope with declining viability of rainfed agriculture and surface water availability, is poor in quality. The use of saline groundwater could jeopardize the agricultural sector, and most notably commercial horticulture and floriculture activities. This study highlights the complex nexus of water quality and sufficiency challenges facing the agriculture sector in the region, and should help decision-makers to design feasible strategies for enhancing adaptation and food security.

Keywords: climate change; perception; adaptation; irrigation water quality; agriculture; smallholder farmers; Ethiopia Rift Valley

Highlights

- Most groundwater and lake waters in the Ethiopian Rift are unsuitable for agricultural use.
- Lack of and erratic rainfall are the main causes of crop failure in the region.

- Use of improved seeds constitutes the primary adaptation for dealing with water scarcity.
- Barriers to adaptation include limited access to water, credit/savings, improved seeds, and weather/climate information.
- Extension (development) agents are critical for enhancing farmers' knowledge and adaptability to climatic variability.

1. Introduction

Climate change impact assessment studies have shown that changes in quantities and variability of rainfall, as well as rising temperatures, are increasing stress in many agriculture and water systems, and affecting human and ecological health and well-being, with likely worsening effects in the future [1–5]. Although the specific magnitude of these changes and their consequences is subject to scientific uncertainty and regional heterogeneity, there is high confidence that the agricultural sector is particularly vulnerable, and that negative impacts will be concentrated in developing countries [1,6–11]. This may be particularly true for semi-arid regions of African countries, where local economies typically remain heavily reliant on climate-sensitive and low productivity rainfed agriculture [10–12]. Other major drivers, such as urbanization, population growth, competition for and degradation of water and natural resources, and other developments, are creating new challenges for local environments and communities [13–17]. Ethiopia is a prototypical example with a large and rapidly growing population of about 110 million [18], 80% of whose livelihoods are provided by agriculture [19]. The agriculture sector in Ethiopia is extremely important, as it contributes about one-third of the nation's GDP [19–21]. Additionally, while there has been notable progress in improving agricultural productivity in recent years, there is still considerable scope to intensify production and thereby increase food security at local and national levels [22,23]. Meanwhile, climate change threatens to undo this progress [24]. This study focuses on the Main Ethiopian Rift (MER), a semi-arid region where livelihoods are dominated by subsistence rainfed agriculture, and where water availability is highly seasonal and has high interannual variability [25–27].

Agriculture in the MER, as in many regions of Sub-Saharan African countries, is characterized by high labor inputs, low capitalization and mechanization, routine occurrence of water deficits relative to crop requirements, and resultant low productivity. Difficult cultivation conditions constrain farmers' net incomes and capacity for investing in strategies that advance productivity and improve resilience to existing variability, and inhibit modernization of the agricultural sector. Given the already delicate hydrological balance in such regions [15,24], and the need to increase agricultural production, additional reduction of precipitation or increased variability under climate change will add to existing pressure on local populations, and could compromise the livelihoods of millions of rural inhabitants. To build resilience and reduce vulnerability, proactive planning is vital for adaptation to climate change and coping with a wide set of agricultural and water sector stressors [28]. Farmers are aware of environmental change and use a variety of strategies to adapt [10,29,30].

In the agricultural sector, common adaptation methods include the promotion of crop varieties and livestock species that are better suited to dry and hot conditions, irrigation, crop diversification, adoption of mixed crop and livestock farming systems, and shifting of planting dates [31–35]. The provision or expansion of irrigated agriculture, whether small-scale/farmer-led, large scale public or commercial investment, or some combination thereof [36], could serve to relieve problems stemming from water variability and seasonal water scarcity. At the same time, however, irrigated agriculture, especially that supported by large-scale public systems, creates its own sustainability challenges, since such systems can be costly to develop, manage, and maintain [37]. In the MER, for example, where irrigated farms are currently expanding, water quality studies indicate that many water resources are highly saline (e.g., Na, Cl, and B) and unsuitable for irrigation over the long term [38,39]. The effects of low-quality irrigation water may not always be appar-

ent immediately, as these relate to soil characteristics such as permeability, and to crop choices, especially when soils are already saline and alkaline. Salinity and sodium hazard indicators—such as the sodium adsorption ratio (SAR) [40–42]—can be used to assess the suitability of irrigation water sources [43–45], as excessive Na^+ concentrations and salinity can affect both soil and crops. High Na^+ content in irrigation water can enhance cation-exchange replacement of Na^+ in water to Ca^{2+} and Mg^{2+} ions in the soil, thereby reducing soil permeability and water infiltration [46].

This study discusses results obtained from an agricultural survey conducted to understand farmers' sensitivity and perceptions of changing climate, and to explore the influence of these on crop production and other adaptation choices. The type and role of adaptation mechanisms to complex regional stressors were assessed across a range of agro-climatic microzones within the Ziway–Shala Basin of the MER. In addition to these surveys, the quality of surface and groundwater sources was assessed to determine the suitability of these for irrigation use in the region. Understanding these aspects is critical for enhancing policy responses in the region, and is of great importance for the sustainable development of its agricultural sector under future climate and environmental change.

2. Study Area and Regional Setting

The study area comprises two large basins; the Ziway–Shala and Abaya-Chamo, plus a small catchment (Awasa) located in the central portion of the Main Ethiopian Rift (MER) valley. The MER is characterized by a chain of lakes (Ziway–Langano–Abijata–Shala–Awasa–Abaya–Chamo) that lie at an average altitude of 1600 m above sea level (m.a.s.l). These lakes receive surface inflow from rivers and springs that drain the western and eastern highlands (elevation above 2500 m.a.s.l. on average) bordering the MER. The climatic conditions in the highlands, along the escarpment, and on the Rift valley floor differ dramatically. Mean annual rainfall in the highlands ranges from about 800 mm to over 2400 mm, while the Rift valley is semi-arid to arid, with rainfall varying from 300 mm to 800 mm [47,48]. The mean annual temperature in the highlands is less than 15 °C and evaporation does not exceed 1000 m per year; on the Rift floor, the mean temperature is greater than 20 °C, and evaporation exceeds 2500 mm [49]. Rainfall in the Rift is concentrated during the summer months from June to September, with additional modest rains coming from March to May. During the long, dry period between October and February, water is extremely scarce. Overall, because evapotranspiration significantly exceeds rainfall, the water quality in the Rift valley, particularly in its lakes, is highly degraded. Nonetheless, surface and groundwater resources are currently used by many of the region's small-scale agroindustries, commercial irrigators, and floriculture farms.

Indeed, one of the notable developments in past decades has been the introduction and rapid expansion of irrigated agricultural activity. A continuum of scales and business models from smallholder farmer irrigation schemes (i.e., farmer-led irrigated agriculture) to large scale private and state farms have been established over this period. Foreign and national investment and expertise has flowed in to support such enterprises and stimulate production in enclosed vegetable and flower cultivation areas.

3. Materials and Methods

This study combined water sampling and testing and smallholder surveys to obtain a comprehensive view of farming options for coping with climate change. Descriptions of each of these follow below.

3.1. Water Sampling and Analysis

Groundwater and surface water samples that are used for drinking and irrigation (specifically those surface waters surveyed around Lake Ziway and Arata), were collected in the Ziway–Shala and Abaya-Chamo basins in April–May 2010, March 2011 and November 2012. A total of 162 water samples were collected from 135 groundwater wells, 8 cold springs, 8 rivers and 11 lakes (Figure 1). The groundwater samples were most typically

collected from active pumping wells, after allowing the water to flow for a few minutes. Samples from springs and lakes were collected at the mouth of the source and 50–100 m away from the shore, respectively. First, in situ measurements of pH, temperature and electrical conductivity (EC) were conducted for all samples. Next, samples for major and trace element analysis were filtered in the field using 0.45 μm filters, directly into 60 mL polyethylene bottles. These bottles had been cleaned with trace metal grade ~1N HCl and ~1N HNO$_3$ and then rinsed with deionized water having resistivity >18 MΩ/cm. Major cation/trace metal samples were immediately acidified with high-purity HNO$_3$ (Fisher Optima). Unfiltered and unacidified samples were also collected into 60 mL and 30 mL polyethylene bottle to allow measurement of alkalinity.
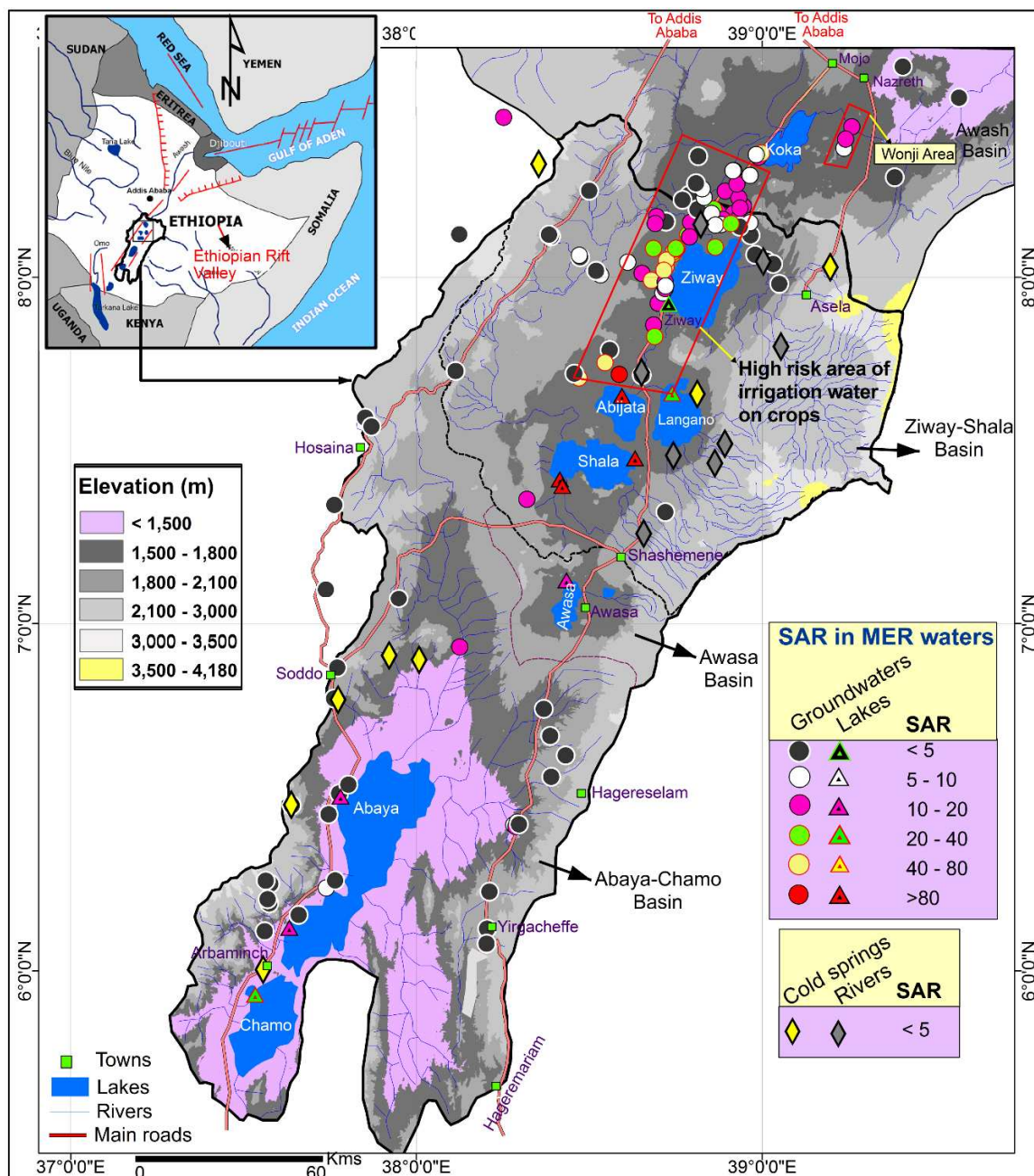
Figure 1. Distribution of water sampling sites in the MER according to type (groundwater, lakes, cold springs and rivers). SAR values are color-coded. Note that the red rectangle represents an area where use of poor quality water for irrigation purposes poses substantial risks.

Concentrations of major cations—calcium (Ca^{2+}), magnesium (Mg^{2+}), sodium (Na^+), and silica (SiO_2)—were measured using a direct-current plasma spectrometer (DCP) calibrated using solutions prepared from plasma-grade single-element standards. Major anions of chloride (Cl^-), sulfate (SO_4^{2-}), and nitrate (NO_3^-) were analyzed using an ion chromatograph (IC). Total alkalinity (as HCO_3^-) was measured using titration techniques to pH 4.5. Trace elements—boron (B) and other trace metals—were analyzed via a Perkin-Elmer Elan 5000 inductively coupled plasma–mass spectrometer (ICP-MS), calibrated to the National Institute of Standards and Technology (NIST) 1643e standard.

3.2. Water Quality Parameters for Agriculture

The most important constituents of concern for agriculture include several major ions (Na^+, Cl^-, HCO_3^-, Ca^{2+} and Mg^{2+}), and trace elements such as boron. Critical parameters that constrain soil permeability and crop yields are salinity (as electrical conductivity; EC), the sodium adsorption ratio (SAR; defined as $SAR = Na^+/\sqrt{(Ca^{2+} + Mg^{2+})/2})$) or percent sodium (defined as Percent $Na = Na^+/(Na^+ + K^+ + Ca^{2+} + Mg^{+2}) * 100$), and residual sodium carbonate (RSC; defined as $RSC = (CO_3^{2-} + HCO_3^-) - (Ca^{2+} + Mg^{+2})$).

3.3. Farmer Surveys

A cross-sectional transect survey was conducted across different agro-climatic zones spanning from the highlands to the escarpment and then to the Rift floor in the Ziway–Shala basin (Figure 2). In order to select for variation in growing conditions, clusters of communities conveniently accessible at each location were enrolled along the main road transect but situated at different elevations, or that were identified through prior discussions with local government (e.g., water) offices. A total of 147 farmers (143 male and 4 female subjects) aged between 19 and 77 years (mean: 43.7 years) were then interviewed in December–January 2012. Upon identifying a sample community at a given elevation, field workers approached households in a community and presented a formal letter from Addis Ababa University about the study and were asked if they consented to be interviewed. All respondents granted informed consent, and the anonymity of all investigated subjects has been preserved. Each farm surveyed was assigned a unique identifying code enabling it to be matched to spatially referenced data on weather and climate.
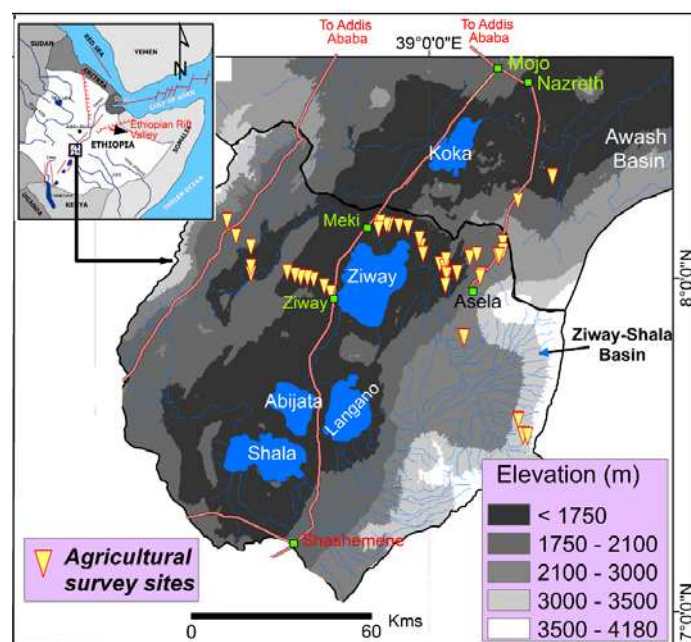

Figure 2. Location of agricultural survey sites.

During face-to-face interviews, data were collected on the farmer's household characteristics; land ownership; animal husbandry; cropping; input costs (e.g., for seeds, fertilizer and pesticides); factors affecting crop yield; source(s) of water for agriculture (rainfed or irrigation); recent history of crop failure; farm income; distance to the nearest market; and adaptive capacity. Regarding the latter, questions related to the use of improved seed varieties and fertilizer, adjustments in cropping patterns, crop marketing, soil and water conservation, and access to extension services. Farmers were also asked a set of questions on perceptions of recent trends in the timing of rainfall, its predictability and amount, trends in temperature change (comparing the past three years to ten years prior), and measures they had taken to adapt to those perceived changes. Finally, farmers were asked about constraints limiting their ability to adapt to any perceived changes. The coded survey data were subsequently entered using Microsoft Excel 2010 and SPSS spreadsheet-based statistical packages.

The survey data were analyzed in a regression framework using Stata software. The main outcome for this analysis was farmer adaptation behavior [31–33,50]. In order to measure adaptation behavior, a simple index was generated by counting the number of farming adaptation behaviors named in the survey. This index ranges from 0 to 10 in the sample, with a mean of 4.4, and is approximately normally distributed. The index variable was regressed using Ordinary Least Squares regression on explanatory variables of interest available from the full sample of 147 surveys. The key explanatory variables included climate awareness (information received from the Development "extension" Agent), literacy, number of neighbors, and if the farmer had experienced a crop failure in the past five years. Further, the economic status of the farmer was controlled for via inclusion of variables indicating farmer productivity (farm revenue per hectare), the number of cattle owned (a traditional form of wealth), and indicators for access to electricity and irrigation. Each of these variables was expected to have a positive relationship with the adaptation index, as they should enable a farmer to more readily engage in adaptation. Still, the relationships between them should not be interpreted as causal (given concerns about reverse causality), and our analysis is therefore primarily descriptive. Moreover, high levels of significance are not expected given the small sample size, the sensitivity of the available measurements, and the complexity of adaptation decision making. The regression model does include fixed effects by district, which best accounts for unobserved geographic characteristics that might help determine adaptation behaviors.

3.4. Focus Groups with Key Informants

Finally, focus group discussions (FGDs) were conducted during the field work mainly with community leaders and other farmers in 6 representative rural villages in the Ziway–Shala basin. These FGDs allowed for more in depth probing on questions related to knowledge of climate change, and to assess more qualitatively what it meant for both them and their broader communities.

4. Results and Discussions

This section describes the main results of the study, beginning with the water quality assessments, analysis of its irrigation suitability, and then presenting the survey results.

4.1. Water QUality and Suitability for Agriculture

Various hydrochemical constituents present in irrigation water can negatively affect crop productivity and soil fertility. This is especially true for sources that are subject to evaporative enrichment, such as the surface waters of the MER. Given that farmers are likely to face dwindling supplies of water under climate change [25], they may seek to increase the use of more reliable sources such as lake water or groundwater, in order to substitute for or supplement increasingly unreliable rainfall and seasonal supplies. The most important constituents of concern for agriculture include several major ions (Na^+, Cl^-, HCO_3^-, Ca^{2+} and Mg^{2+}), and trace elements such as boron. Critical parameters that

constrain soil permeability and crop yields are salinity (as electrical conductivity; EC), the sodium adsorption ratio (SAR), and residual sodium carbonate (RSC) [51–53]. The sample analysis indicated that most water sources have EC below 3000 μS/cm and SAR below 80. Rivers and cold springs have EC below 500 μS/cm and SAR below 3. The rift floor lakes range from fresh (e.g., Lake Ziway) to highly alkaline (e.g., Lake Chitu) (Figure 1). The EC levels of the highly alkaline lakes of Shala, Abijata, and Chitu were especially high, at 22,500, 40,800 and 45,800 μS/cm, respectively.

4.2. Effect of EC and SAR on Water Infiltration

Excessive Na^+ and salinity concentrations in irrigation water create hazards for both soil and crops. High Na^+ content in irrigation water can enhance cation-exchange replacement of Na^+ in water for Ca^{2+} and Mg^{2+} ions in soil, thereby reducing soil permeability and water infiltration [43]. The suitability of the various sampled waters for infiltration was evaluated using the Ayers and Westcot [45] classification that shows the relationships between salinity and sodicity (Figure S1). Most samples fall in the ranges corresponding to severe infiltration reduction (Table 1). Even at low EC, the high SAR can cause water infiltration problems. While infiltration may sometimes remain acceptable when both SAR and EC values are high, salinity beyond the safe threshold for a crop may still inhibit yields by restricting the amount of soil water that is available. Specifically, crop yields tend to decline linearly beyond this threshold, especially in arid and semi-arid regions [54,55]. Vegetable crops are often particularly sensitive [54].

Table 1. Water source types and their suitability for irrigation based on the Ayers and Westcot [45]. classification.

Irrigation Water Quality	Groundwater Wells	Rivers	Lakes	Cold Springs
Severe	76	6	5	6
Slight to moderate	54	2	1	2
No problem	5	0	0	0

Irrigation water quality was also evaluated using the USDA classification diagram (Richards, 1954) (Figure 3). The diagram classifies the suitability of water for agricultural purposes into four categories based on SAR and EC: SAR (S1, S2, S3 and S4), and salinity (C1, C2, C3 and C4) where 1, 2, 3, 4 represents low, medium, high and very high, respectively (Table 2). Eighteen of the groundwater samples and most of the cold spring and river samples from the study were found to lie in category C1-S1, with low salinity and low sodium, which indicates suitability for irrigation water in almost all soil types. Sixty groundwater samples including Lake Ziway fall in the category C2-S1 and C3-S1 (medium to high salinity and low sodium). Waters in these categories can be used for irrigation in almost all soil types with little danger of exchangeable sodium. Lake Ziway is indeed the only freshwater lake in the Rift that is intensively used for irrigation at this time. An additional four groundwater samples that fall into the medium salinity hazard class (C2) but have sodium levels ranging from S2 to S4 can still be used if accompanied by a moderate amount of leaching.
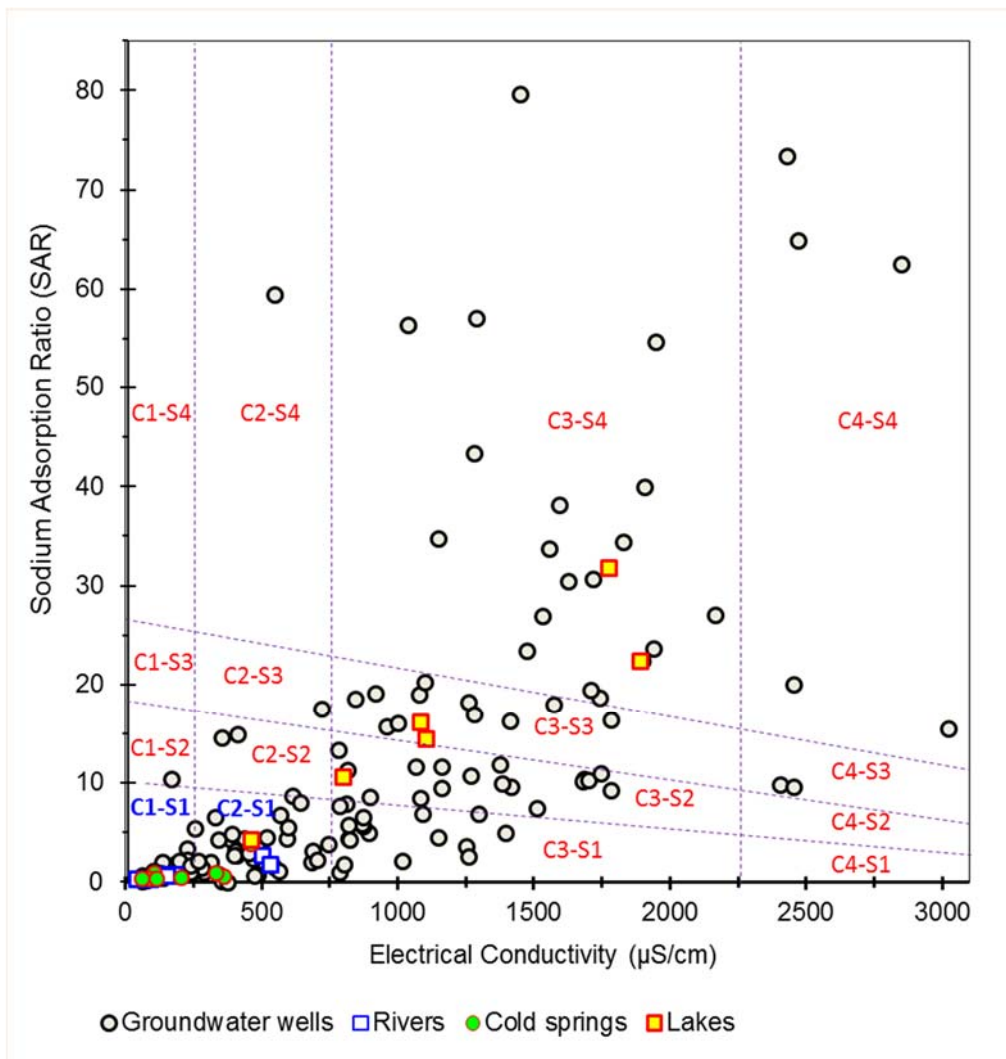
Figure 3. Suitability of water sources for irrigation, based on USDA classification (after Richards [46]).

**Table 2.** Water types and irrigation water classifications as shown in Figure 3.

	Groundwater Wells	Rivers	Lakes	Cold Springs
C1S1	18	6	-	6
C2S1	42	2	1	2
C3S1	18	-	-	-
C2S4	1	-	-	-
C3S4	19	-	2	-
C4S4	5	-	-	-
C2S3	1	-	-	-
C3S3	11	-	2	-
C4S3	2	-	-	-
C2S2	2	-	-	-
C3S2	16	-	1	-
C4S2	-	-	1	-

Most (71 groundwater samples and all lakes except Lake Ziway) samples, however, were categorized to be of high to very high salinity (C3 and C4), and medium to very high sodium (S2, S3 and S4). These samples cannot be used in soils with restricted drainage. Even with adequate drainage, special management for salinity control is typically required

and salt-tolerant crops should be selected. Analyzing the spatial distribution of suitability for irrigation, it becomes apparent that most groundwater wells and rivers emerging from or nearer the highlands (including Lake Ziway) are suitable for irrigation with little danger to the soil and crops. The other lake and groundwater samples, however, would require treatment before application if they are to be used for irrigation over the long term.

An additional limiting factor for irrigation water is the presence of HCO_3^- anions, which can trigger carbonate precipitation and cause scaling in irrigation pipes and pumps. Saturation of carbonate minerals may reduce the Ca^{2+} and Mg^{+2} content of the soil water, and consequently increase SAR values. As described above, the RSC is an alternative measure of the Na^+ content in water that also accounts for Ca^{2+} and Mg^{+2}. If RSC <1.25, the water is considered safe, while >2.5 indicates that the water is not appropriate for irrigation. In the groundwater samples, RSC varied from –1.3 to 33.4; while 20 of the samples were found safe, 60% were deemed unsuitable for irrigation, with the remainder falling in between.

Different plants have varying tolerance to salinity, but adverse effects on crop yields are typically apparent at EC exceeding 1000 μS/cm [42]. Similarly, concentrations of boron above 0.5 mg/L significantly reduce crop yields, particularly for boron-sensitive crops such as strawberries, beans, onion, and garlic [42]. Figure 4 shows that the salinity and boron in a large proportion of the groundwater wells exceeds these threshold values.
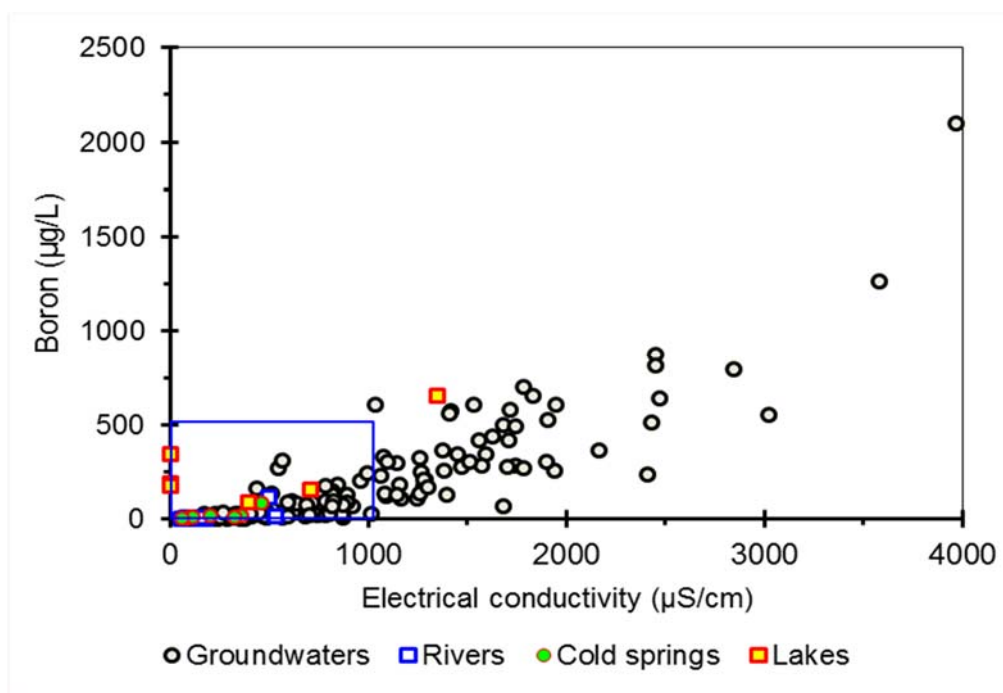
Figure 4. Variation of boron and electric conductivity (EC) in MER groundwater. The squared region indicates where values are acceptable for irrigation water, and values outside these areas suggest potential problems with sustained utilization.

All in all, these results indicate that sustained application of MER groundwater would likely not be possible due to water quality concerns. This limits the ability of irrigators to supplement irregular or insufficient surface water supplies with more dependable groundwater sources. Of course, for soils that have never been or are infrequently used, crop productivity is less likely to be harmed by high salinity water during the initial periods of use. Other factors such as climate, soil type, crop and plant species and management practices also need to be accounted for when identifying acceptable levels of irrigation water salinity and sodicity [54].

5. Results of the Farm Surveys

The 147 interviewed farmers are predominantly male (94.6%, n = 139) and heads of their households (98.4%). Males tend to be the primary agricultural decision-makers in Ethiopia [56]. More than 87% of the households are from the Oromo ethnic group. About 75% of the heads of household could read and write at the time of the survey, while 28% had had no formal education. The farming system of the study areas was dominated by mixed cropping and livestock husbandry (for 90% of the farmers), while a minority of farmers exclusively grew crops. Farm households depend on crops for both food and cash income. Below, we describe the main survey outcomes of the study, namely crop choice, use of irrigation, perceptions of climate stresses and change, factors determining good and bad crop yield, climate change impacts on agriculture, and adaptation practices and constraints.

5.1. Crop Choice

Across the different agro-climatic zones, at the time of the survey, farmers grew crops suitable to existing rainfall and temperature conditions. In the Rift floor areas (<1750 m), maize and teff were the predominant crops, but this area is also suitable for other cereals including wheat, haricot bean and sorghum. Farmers located at higher altitudes (1750–2100 m), meanwhile, grew mostly maize, wheat and teff, and highland (>2100 m) farmers predominantly produced wheat and barley. Other highland crops include fava bean, field pea and maize. These varying cropping patterns indicate that farmers are well-attuned to the historic climatic advantages in their specific locations. Still, farmers reported changes in the climate that are endangering their practices, especially in the lowlands. In the rift, farmers also use improved seed for crops such as of maize, wheat, barley and haricot bean as a primarily response to rainfall variability although access to these seeds is limited.

5.2. Farmers' Irrigation Use

Most farmers in the survey do not use irrigation, but rather rely on rainwater to cultivate cereal crops. Many farmers do view irrigation as an important opportunity to improve their agricultural system but lack the capacity or knowledge to access and utilized surface and groundwater sources. In the irrigated areas surveyed in the Rift Valley (at Arata and around Lake Ziway), farmers produce horticultural crops that include tomato, onion, pepper and cabbage. The farmers that use irrigation typically achieve better productivity and profits, although they also report occasionally losing their crops due to excessive rain, or lack of profit due to price reductions during productive periods. As demonstrated in the previous section on water quality and as shown in Figures 1 and 2, high quality water sources do exist in the region that could be or were already being used for irrigation. For instance, the existing and on-going development of the floriculture sector in the MER (such as Meki and Ziway towns in the MER) is mainly based on surface water (Lake Ziway and its rivers) resources. Most groundwater sources in the region are too poor in quality for agricultural use, however (e.g., Figure 1; red block area), and increased groundwater extraction may also threaten the sustainability of the aquifer, which is essential for many of the region's rural drinking water supplies. With regard to drinking water, these sources have also previously been shown to be contaminated with elevated levels of fluoride and arsenic [38,39,57]. Continued monitoring of the quantity and quality of the groundwater resources is essential to mitigate the associated negative impacts.

5.3. Perceptions of Climate Stresses and Climate Change

Most farmers reported in the survey that lack of rain is one of the main constraints to agricultural productivity. Many also indicated that they thought rainfall was becoming more erratic. Figure 5 shows farmers' perceptions of changes in the pattern of rainfall and temperature. More than 70% of the farmers stated that rain comes and stops later than expected, compared to ten years ago. Moreover, a majority perceives that the climate is

drier, hotter, less predictable and generally worse for farming than it used to be, especially in lowland areas. A few farmers (6%) report no changes in temperature and rain. Despite perceptions of more erratic precipitation, some farmers report that their farm output is improving due to their use of improved seeds and fertilizers.
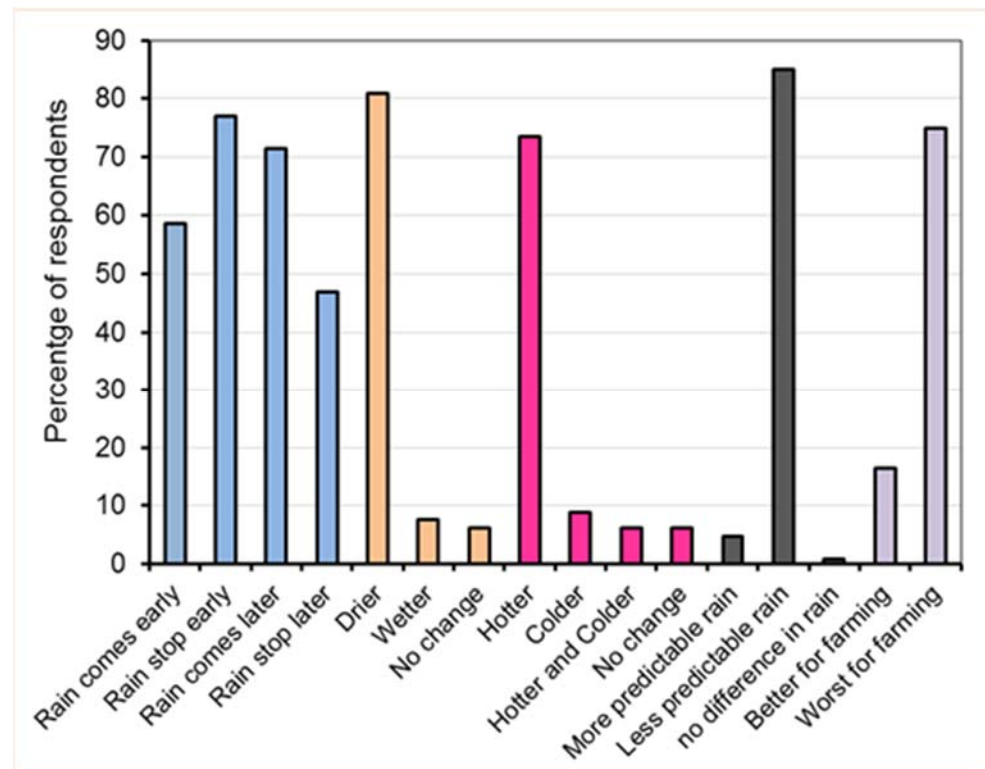

Figure 5. Farmer perceptions of climate change in the Ziway–Shala basin.

In focus groups, it was noted that farmers were generally aware that changes to the climate are becoming a serious problem. These changes are widely perceived as being related to rainfall variability (rain comes too early and stops too late, and is uneven in amount, whether too high or too low), and farmers in the Rift especially reported experiencing a significant reduction in overall rainfall, alongside extreme and unexpected, rare heavy rainfall episodes. In the highlands, complaints were primarily related to variability, rather than to the quantity of rainfall. Due to rainfall shortage in the Rift, farmers start planting drought-tolerant early maturing maize varieties, though there is limited supply of such seeds. In some cases when there has been no rainfall in April and May, farmers forgo planting entirely. Maize productivity is also decreasing from time to time; however, farmers are achieving enhanced returns by shifting to wheat, barley and teff cultivation.

5.4. Factors Determining Good and Bad Crop Yield

Farmers pointed out that uninterrupted and sufficient quantities of rain, availability of farming inputs (fertilizer and seeds), and personal efforts are the most important factors determining a good crop season and productivity (Figure 6). In contrast, lack of or excessive rain or unexpected rain, low crop price, lack of available and affordable inputs, and insufficient personal effort all contribute negatively to crop productivity and profit (Figure S2). Rainfall appears most important in these responses. The study revealed that insect pests and diseases are also major problems facing farmers in the region.
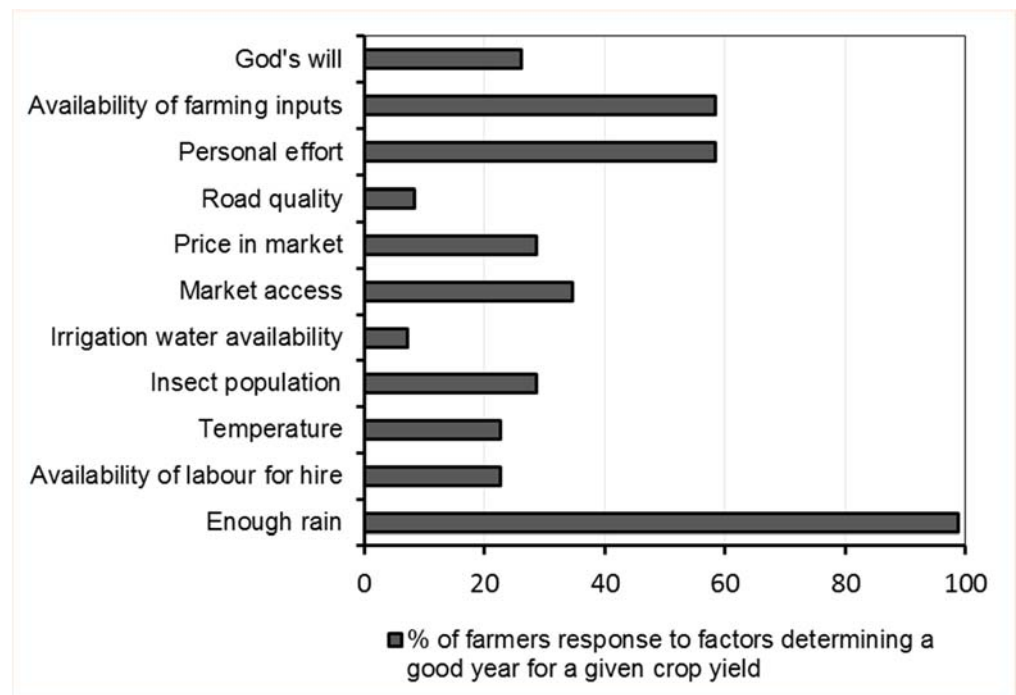
Figure 6. Relative importance of factors determining a good crop year.

*5.5. Climate Change Impacts on Agriculture, Adaptation Practices and Constraints*

In the 5 years prior to the survey, 66.7% of the farmers reported experiencing crop failure at least once. Crop failure occurred in the Rift floor (<1750 m) an average of 1.6 times in a 5-year period, in contrast to only 0.5 times in the highlands (>2100 m). The majority (80%) of farmers on the Rift floor and 22% in the highlands had experienced at least one crop failure in the 5 years preceding the survey. Table 3 shows the frequency of crop failure at different altitudes. Lack of rain (61% of respondents) and unexpected rain (27%) are the most important determinants of these frequent crop failures. Agriculture in the Rift faces about 76% more crop failures than in the highlands. Crop failures were stated as the cause of food shortages for some households, and a need for food assistance.

Table 3. Frequency of reported crop failures in the past 5-year at different elevations.

Crop Failure in the Past 5 Years	1640–3100 m (*n* = 147)	<1750 m (*n* = 76)	1750–2100 m (*n* = 35)	>2100 m, Elevation. (*n* = 36)
	Percentage of respondents			
0	33.3	19.7	17.1	77.8
1	24.5	23.7	48.6	2.8
2	25.2	34.2	20.0	11.1
3	16.3	22.4	11.4	8.3
4	0.68	0.0	2.9	0.0
Average crop failure	1.14	1.6	1.3	0.5

Practices that farmers are implementing to improve their farming, as reported in the survey, are summarized in Figure 7. About 70% of sample respondents stated that they use high yield crop varieties or early maturing seeds. A large proportion of farmers use fertilizer——mostly DAP (Diammonium Phosphate) and urea——and roughly half of them practice crop rotation to improve soil conditions and yield, and to minimize the buildup of weeds, insect pests and plant diseases. The most common crop rotations are between cereal crops. Among irrigators, vegetables and cereals are also commonly rotated. Farmers use terracing and afforestation, conserve seeds and other natural resources, and use irrigation

as key practices to improve productivity. A few wealthy farmers in the highlands use mechanized technology (e.g., renting tractors) to quickly collect crops during harvest.
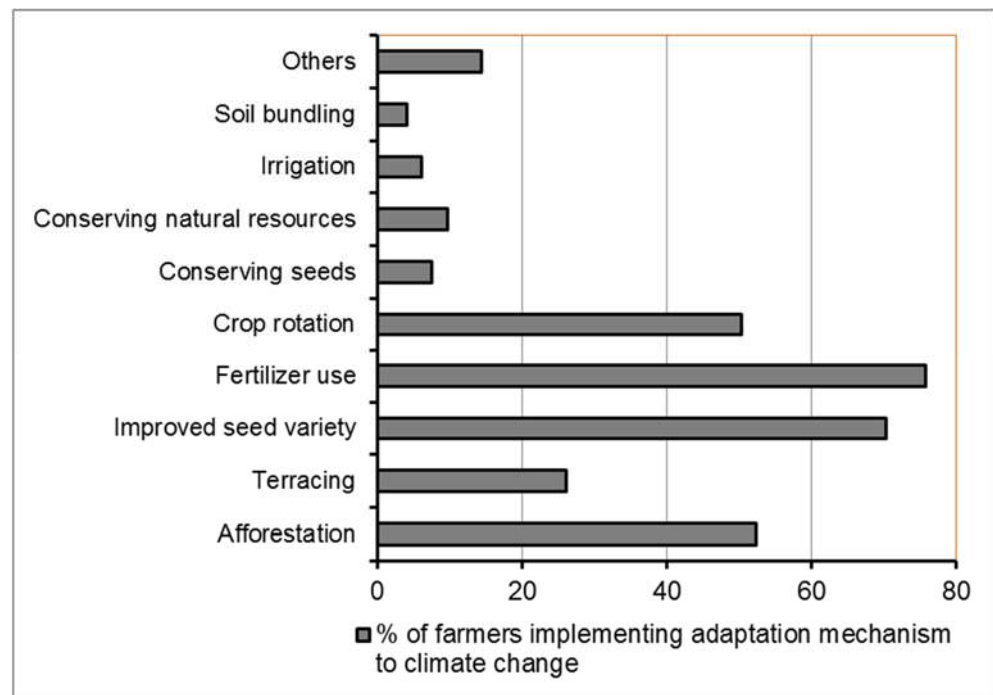
Figure 7. Different measures farmers use to improve productivity.

As a response to rainfall shortages, farmers in the Rift reported increasing planting of drought-resistant early maturing maize varieties (as well as wheat, haricot, and barley), though there is limited supply of such seeds. Farmers sometimes skip planting maize when the rains fail in April and May, and many were shifting away from maize in favor of wheat, barley and teff. In focus groups, many farmers argued that deforestation for firewood and charcoal production were major contributors to environmental or climate changes and expressed concern over the loss of pollinators from overuse of chemical pesticides in the area's floriculture farms. Farmers in several sites indicated they were involved in the protection and planting of new trees (i.e., area closure plans), as part of efforts organized by the regional government, while others mentioned projects to build ponds, enhance water conservation and flood protection, replace chemical fertilizer with manure/compost, and increase crop rotation and diversity to respond to climate stresses. Furthermore, farmers noted that over 350 million trees had been planted in one day (29 July 2019) across the country as part of Ethiopia's Green Legacy Initiative, setting a new record. This effort was conceived to help counter the effects of deforestation and climate change.

Lack of access to water, credit or savings, knowledge, information on weather and climate change were identified as major barriers to adaptation to climate and environmental change (Figure S3). Some farmers in the Rift Valley are also reluctant to take available loans when they get access to credit, due to the high uncertainty concerning rainfall, and the associated risk of crop failure and inability to pay back loans. Farmers unable to pay their loans are sometimes forced to sell to livestock or end up mired in bad debts. While market access or transportation was not identified as a major barrier to adaptation, many farmers noted that markets do not function in a way that allows them to maximize earnings. Specifically, more than 50% of farmers sell their crops within 3 months of harvest, which is also the period when prices are lowest. Farmers feel that they have limited bargaining power over prices, which are typically set by local traders. Farmers associations are nonetheless trying to organize to purchase crops from local farmers while the price is low, so as to sell them to the market when prices rise, and allow for increased revenues.

The regression analysis (Table 4) reveals relevant patterns in the determinants of farmer adaptation to climate change. While receipt of information on climate change does not significantly predict adaptation, it does have a positive relationship as would be predicted based on the role of Development Agents in transmitting information. Other studies have similarly found that extension services are positively associated with adaptation, presumably reflecting access to information and other resources that empower farm households to adjust to climate risks [32,50]. Farmer literacy is positive and significant at the $p < 0.10$ level, which is suggestive of a greater ability to receive and process information from external sources, or of correlation with higher socio-economic status and ability to adapt. Farmer productivity (farm revenue per hectare) also has a positive and statistically significant correlation with adaptation at the $p < 0.10$ level, even when controlling for other measures of wealth and economic well-being (though this may also indicate that adaptation leads to greater productivity). While not significant, several other variables have a positive relationship with adaptation, such as experience with crop failure and the number of neighbors. Farmers must take into account a large variety of factors and both individual and community characteristics in order to determine how and when to adapt [58].

Table 4. Regression of adaptation behaviors on farmer characteristics.

Variables	Adaptation Index
Climate Information from Development Agent	0.25 (0.517)
Literacy	0.72 * (0.428)
Number of Proximate Neighbors	0.05 (0.114)
Experienced Crop Failure in Prior 5 years	0.51 (0.461)
Log Productivity (Revenue/Ha)	0.33 * (0.171)
Cattle Owned	0.01 (0.031)
Access to Electricity	0.03 (0.572)
Access to Irrigation	−0.0 (0.564)
Constant	0.51 (1.786)
Observations	147
R-squared	0.135
District Fixed Effects	Yes

Standard errors in parentheses; * $p < 0.1$.

6. Conclusions, Policy Implications, and Future Work

Climate change impact assessment studies have shown changes in the quantity and variability of rainfall, as well as rising temperatures in Ethiopia—by an average of 1 °C since 1960, which is projected to increase by 1.81 °C in 2040–2059 [59]. Climate change is threatening rainfed agriculture and rural livelihoods in many parts of the world, especially in highly vulnerable regions and in low-income countries in Africa, such as Ethiopia. The location of this study, the Rift Valley of Ethiopia, is highly vulnerable to climate stressors [5,20,60]. Our study relied on the analysis of primary data on water quality, obtained to evaluate the suitability of different sources for irrigation, as well as survey data pertaining to farmers' perceptions, their adaptation behaviors, and general barriers that challenge adaptation in the MER.

The most salient climate-related shocks in the region are a lack of rainfall and the high variability of rainfall, and crop failures are common. The study also identified several adaptation mechanisms undertaken by households in response to climate-related shocks: the use of new high yield crop varieties, early maturing seeds, increased fertilizer application, and changing crop rotations. They also use terracing, afforestation, seed saving, the conservation of natural resources and irrigation to increase productivity, reduce risk, and control environmental degradation. Irrigation is a common adaptation response to reduced water availability globally, but our assessments of the suitability of irrigation water point to several threats in the MER. First, judging by measures of EC and SAR, most water sources are categorized as having severe or slight to moderate negative implications for

soil permeability and reduced water infiltration. In addition, high bicarbonate and boron concentrations pose water quality threats for cultivation.

It is observed that the role of Extension ("Development") Agents (DAs) is vital to enhancing farmers' knowledge of potential adaptation strategies. This service is currently available in the study basin and is critical for increasing farmers' adaptability in the face of continuing climatic variability. Meanwhile, the main barriers to adaptation include a lack of access to water, credit or savings, lack of appropriate seeds, knowledge and information on weather and climate. Improving access to credit, increased ability to arbitrage sales over seasons with high market prices for local agricultural products, enhancing access and distribution of sufficient seeds (in variety and amounts), early warning on weather during planting and harvesting seasons, and knowledge transfer on effective farming practices (e.g., the use of fertilizers that are suitable and proper amount for a given soil type) are some of the measures that should to be taken to improve farmers' productivity and adaptive capacity to climate change.

Based on the findings of this study, it would be unwise to further develop irrigated agriculture without establishing that water sources being exploited in specific sites are of sufficient quality. Nonetheless, the viability of rain-fed agriculture is clearly threatened by the changing climate, and crop failures are increasingly prevalent in communities, particularly those located in the Rift floor. This situation calls for careful planning of alternative livelihoods strategies for households, by decision-makers who understand these challenges and are willing to design new strategies for adaptation, food security, and enhanced rural well-being.

6.1. Water and Farmers' Survey Data Collection Time and Its Implication in the Study Area

While the data collection was carried out over a decade ago, it provides useful and rich reference information that can be used as a baseline for examining future changes pertaining to a very data limited region. We use these data to assess the dynamics inherent in farming practices, farmers' perceptions of and adaptation to changing climate and crop productivity, in a context where climatic changes were already being experienced in significant ways. Observing the livelihood of the communities in this region over time, we are confident that no major changes in practices have occurred currently and that agriculture remains unproductive, with the use of antiquated farming practices, very limited or no technology use, and low capacity and resources to invest in improved productivity. Given most groundwater sources in the Rift are not suitable for agriculture due to salinity, which is one of the reasons for the increased pressure on the use of the fresh water sources from Ziway lake and its tributaries. Subsistence agriculture continues to be the main source of income for most farmers in the region. While it may be necessary to monitor specific changes in farmers' behavior and practices over the recent period, we do not anticipate significant changes given that farmers have generally remained in similar conditions marked by a lack of capacity to respond to changing environmental conditions. This includes responses to climate variability and trends, which have increased vulnerability relative to conditions experienced ten years ago.

6.2. Implication of the Study to Current and Future Local Policies

Our findings on adaptation and barriers to adaptation suggest the need to intensify agricultural productivity by increasing irrigation and technology use in the farming practices in the region. This will improve farmers' food security and income. Considering the farmers' high reliance on unpredictable rainwater for agriculture, policy driven actions that support irrigation use, with particular attention not only to water availability but also to water quality, are critical. Enforcing the regulation of water quality is particularly important to avoid salinization of the soil, which may further exacerbate declining crop productivity in the face of ongoing climate warming. Since freshwater scarcity in the region is prevalent, water use is more determined by its availability or quantity than water quality in the region.

6.3. Future Work

Our study highlighted water quality issues that could threaten irrigation-based adaptation in the MER, while demonstrating that the region's farmers perceive changes in climate (temperature and rainfall variability) but are limited in their ability to adapt to them. These results can be useful as baseline information for additional in-depth studies on the impacts of surface and ground water irrigation use on soil salinity and agricultural productivity. Further work should be carried out to identify suitable water management strategies that address water scarcity while paying heed to water quality challenges (e.g., high salinity, SAR, and bicarbonate). In addition, the study showed the dependence of farmers on specific seed varieties (early maturing, drought-tolerant, and high yielding crops) whose supply is limited, and whose uptake may have other unintended long-term consequences. High-yield seed varieties that are suitable for saline soil or viable in arid and semi-arid conditions continue to be needed, and soil stability and recovery must be carefully considered in future work.

References

1. IPCC. *Climate Change 2014: Impacts, Adaptation, and Vulnerability*; Part A: Global and Sectoral Aspects; Field, C.B., Barros, V.R., Dokken, D.J., Mach, K.J., Mastrandrea, M.D., Bilir, T.E., Chatterjee, M., Ebi, K.L., Estrada, Y.O., Genova, R.C., et al., Eds.; Cambridge University Press: Cambridge, UK; New York, NY, USA, 2014.
2. IPCC. *Climate Change 2007: The Physical Science Basis*; Solomon, S., Qin, D., Manning, M., Chen, Z., Marquis, M., Averyt, K.B., Tignor, M., Miller, H.L., Eds.; Cambridge University Press: New York, NY, USA, 2007.
3. IPCC. *Climate Change 2001: Impacts, Adaptations and Vulnerability*; Cambridge University Press: Cambridge, UK, 2001.
4. Challinor, A.; Wheeler, T.; Garforth, C.; Craufurd, P.; Kassam, A. Assessing the vulnerability of food crop systems in Africa to climate change. *Clim. Chang.* **2007**, *83*, 381–399. [CrossRef]
5. Thornton, P.K.; Jones, P.G.; Owiyo, T.; Kruska, R.L.; Herrero, M.T.; Kristjanson, P.M.; Notenbaert, A.M.O.; Bekele, N.; Omolo, A. *Mapping Climate Vulnerability and Poverty in Africa*; Report to the Department for International Development; ILRI: Nairobi, Kenya, 2006; p. 200.

6. Cui, Z.; Zhang, H.; Chen, X.; Zhang, C.; Ma, W.; Huang, C.; Zhang, W.; Mi, G.; Miao, Y.; Li, X.; et al. Pursuing sustainable productivity with millions of smallholder farmers. *Nat. Cell Biol.* **2018**, *555*, 363–366. [CrossRef]

7. Lesk, C.; Rowhani, P.; Ramankutty, N. Influence of extreme weather disasters on global crop production. *Nat. Cell Biol.* **2016**, *529*, 84–87. [CrossRef]

8. He, Q.; Zhou, G. Climate-associated distribution of summer maize in China from 1961 to 2010. *Agric. Ecosyst. Environ.* **2016**, *232*, 326–335. [CrossRef]

9. Asseng, S.; Ewert, F.; Martre, P.; Rotter, R.P.; Lobell, D.B.; Cammarano, D.; Kimball, B.A.; Ottman, M.J.; Wall, G.W.; White, J.W.; et al. Rising temperatures reduce global wheat production. *Nat. Clim. Chang.* **2015**, *5*, 143–147. [CrossRef]

10. Conway, D.; Schipper, E.L.F. Adaptation to climate change in Africa: Challenges and opportunities identified from Ethiopia. *Glob. Environ. Chang.* **2011**, *21*, 227–237. [CrossRef]

11. Rosell, S. Regional perspective on rainfall change and variability in the central highlands of Ethiopia, 1978–2007. *Appl. Geogr.* **2011**, *31*, 329–338. [CrossRef]

12. Tilahun, H.; Teklu, E.; Michael, M.; Fitsum, H.; Awulachew, S.B. Comparative Performance of Irrigated and Rainfed Agriculture in Ethiopia. *World Appl. Sci. J.* **2011**, *14*, 235–244.

13. Von Grebmer, K.; Bernstein, J.; de Waal, A.; Prasai, N.; Yin, S.; Yohannes, Y. *2015 Global Hunger Index: Armed Conflict and the Challenge of Hunger*; International Food Policy Research Institute: Washington, DC, USA, 2015.

14. IFAD. Highlights Annual Report. 2012. Available online: https://www.ifad.org/en/web/knowledge/publication/asset/391848 43 (accessed on 5 March 2021).

15. Legesse, D.T.; Abiye, A.; Vallet-Coulomb, C.; Abate, H. Streamflow sensitivity to climate and land cover changes: Meki River, Ethiopia. *Hydrol. Earth Syst. Sci.* **2010**, *14*, 1–11. [CrossRef]

16. Legesse, D.; Vallet-Coulomb, C.; Gasse, F. Analysis of the hydrological response of a tropical terminal lake, Lake Abiyata (Main Ethiopian Rift Valley) to changes in climate and human activities. *Hydrol. Process.* **2004**, *18*, 487–504. [CrossRef]

17. Alemayehu, T.; Furi, W.; Legesse, D. Impact of water overexploitation on highland lakes of eastern Ethiopia. *Environ. Earth Sci.* **2007**, *52*, 147–154. [CrossRef]

18. World Bank. 2019. Available online: https://data.worldbank.org/country/ethiopia (accessed on 12 February 2021).

19. Byerlee, D.; Spielman, D.J.; Alemu, D.; Gautam, M. *Policies to Promote Cereal Intensification in Ethiopia: A Review of Evidence and Experience*; Discussion Paper 00707; International Food Policy Research Institute, Development Strategy and Governance Division: Washington, DC, USA, 2007.

20. World Bank. *Managing Water Resources to Maximise Sustainable Growth: A Country Water Resources Assistance Strategy for Ethiopia*; World Bank: Washington, DC, USA, 2006.

21. World Bank Country Profile. 2018. Available online: https://databank.worldbank.org/views/reports/reportwidget.aspx? Report_Name=CountryProfile&Id=b450fd57&tbar=y&dd=y&inf=n&zm=n&country=ETH (accessed on 20 February 2021).

22. Byerlee, D.; Stevenson, J.; Villoria, N. Does intensification slow crop land expansion or encourage deforestation? *Glob. Food Secur.* **2014**, *3*, 92–98. [CrossRef]

23. Taffesse, A.S.; Dorosh, P.; Gemessa, S.A. 3 Crop Production in Ethiopia: Regional Patterns and Trends. *Food Agric. Ethiop.* **2014**, *53*. [CrossRef]

24. Muluneh, A.; Bewket, W.; Keesstra, S.; Stroosnijder, L. Searching for evidence of changes in extreme rainfall indices in the Central Rift Valley of Ethiopia. *Theor. Appl. Clim.* **2017**, *128*, 795–809. [CrossRef]

25. Li, L.; Li, W.; Ballard, T.; Sun, G.; Jeuland, M. CMIP5 model simulations of Ethiopian Kiremt-season precipitation: Current climate and future changes. *Clim. Dyn.* **2016**, *46*, 2883–2895. [CrossRef]

26. Paul, C.J.; Jeuland, M.A.; Godebo, T.R.; Weinthal, E. Communities coping with risks: Household water choice and environmental health in the Ethiopian Rift Valley. *Environ. Sci. Policy* **2018**, *86*, 85–94. [CrossRef]

27. Kassie, B.T.; Rötter, R.P.; Hengsdijk, H.; Asseng, S.; Van Ittersum, M.K.; Kahiluoto, H.; Van Keulen, H. Climate variability and change in the Central Rift Valley of Ethiopia: Challenges for rainfed crop production. *J. Agric. Sci.* **2013**, *152*, 58–74. [CrossRef]

28. Calow, R.C.; Macdonald, A.M.; Nicol, A.L.; Robins, N.S. Ground Water Security and Drought in Africa: Linking Availability, Access, and Demand. *Ground Water* **2010**, *48*, 246–256. [CrossRef]

29. Adimassu, Z.; Kessler, A. Factors affecting farmers' coping and adaptation strategies to perceived trends of declining rainfall and crop productivity in the central Rift valley of Ethiopia. *Environ. Syst. Res.* **2016**, *5*, 255. [CrossRef]

30. Adimassu, Z.; Kessler, A.; Stroosnijder, L. Farmers' strategies to perceived trends of rainfall and crop productivity in the Central Rift Valley of Ethiopia. *Environ. Dev.* **2014**, *11*, 123–140. [CrossRef]

31. Sadiq, M.A.; Al-Hassan, R.M.; Kuwornu, J.K.M. Vulnerability of Smallholder Maize Farming Households to Climate Variability in the Eastern Region of Ghana. In *Climate Change and Sub-Saharan Africa: The Vulnerability and Adaptation of Food Supply Chain Actors*; Kuwornu, J.K.M., Ed.; Vernon Press: Wilmington, DE, USA, 2019; pp. 173–189.

32. Deressa, T.T.; Hassan, R.M.; Ringler, C.; Alemu, T.; Yesuf, M. Determinants of farmers' choice of adaptation methods to climate change in the Nile Basin of Ethiopia. *Glob. Environ. Chang.* **2009**, *19*, 248–255. [CrossRef]

33. Dinar, A.; Hassan, R.; Mendelsohn, R.; Benhin, J. *Climate Change and Agriculture in Africa. Impact Assessment and Adaptation Strategies*; Earthscan: London, UK; Centre for Environmental Economics and Policy in Africa (CEEPA): London, UK, 2008; p. 189. ISBN 9781844075478.

34. Mendelsohn, K. A Ricardian analysis of the impact of climate change on African cropland. *Afr. J. Agric. Resour. Econ.* **2008**, *2*, 1–23.

35. Hussain, S.S.; Mudasser, M. Prospects for wheat production under changing climate in mountain areas of Pakistan—An econometric analysis. *Agric. Syst.* **2007**, *94*, 494–501. [CrossRef]

36. Daugherty Water for Food Global Institute. *Pathways to Increasing Farmer-Led Investments in Sustainable Agricultural Water Management in Sub-Saharan Africa*; DWFI Working Paper; DWFI: Lincoln, NE, USA, 2018.

37. Lankford, B.A.; Makin, I.; Matthews, N.; Noble, A.; McCornick, P.G.; Shah, T. A compact to revitalise large-scale irrigation systems using a leadership-partnership-ownership 'Theory of change'. *Water Altern.* **2016**, *9*, 1–32.

38. Rango, T.; Vengosh, A.; Dwyer, G.; Bianchini, G. Mobilization of arsenic and other naturally occurring contaminants in ground-water of the Main Ethiopian Rift aquifers. *Water Res.* **2013**, *47*, 5801–5818. [CrossRef] [PubMed]

39. Rango, T.; Kravchenko, J.; Atlaw, B.; McCornick, P.G.; Jeuland, M.; Merola, B.; Vengosh, A. Groundwater quality and its health impact: An assessment of dental fluorosis in rural inhabitants of the Main Ethiopian Rift. *Environ. Int.* **2012**, *43*, 37–47. [CrossRef] [PubMed]

40. Al-Bassam, A.M.; Al-Rumikhani, Y.A. Integrated hydrochemical method of water quality assessment for irrigation in arid areas: Application to the Jilh aquifer, Saudi Arabia. *J. Afr. Earth Sci.* **2003**, *36*, 345–356. [CrossRef]

41. Ayers, R.S.; Westcot, D.W. *Water Quality for Agriculture*; Food and Agriculture Organization of the United Nations: Rome, Italy, 1985.

42. Richards, L.A. *Diagnosis Improvement Saline Alkali Soils*; US Department of Agriculture Handbook, No. 60; Soil and Water Conservative Research Branch, Agricultural Research Service, US Department of Agriculture: Morris, MN, USA, 1954.

43. Naseh, M.R.V.; Noori, R.; Berndtsson, R.; Adamowski, J.; Sadatipour, E. Groundwater Pollution Sources Apportionment in the Ghaen Plain, Iran. *Int. J. Environ. Res. Public Health* **2018**, *15*, 172. [CrossRef]

44. Nishanthiny, S.C.; Thushyanthy, M.; Barathithasan, T.; Saravanan, S. Irrigation water quality based on hydro chemical analysis, Jaffna, Sri Lanka. *Am. Eurasian J. Agric. Environ. Sci.* **2010**, *7*, 100–102.

45. Grattan, S. *Irrigation Water Salinity and Crop Production*; University of California Agriculture and Natural Resources: Davis, CA, USA, 2002.

46. Shaki, A.; Adeloye, A. Evaluation of quantity and quality of irrigation water at Gadowa irrigation project in Murzuq basin, southwest Libya. *Agric. Water Manag.* **2006**, *84*, 193–201. [CrossRef]

47. Vallet-Coulomb, C.; Legesse, D.; Gasse, F.; Travi, Y.; Chernet, T. Lake evaporation estimates in tropical Africa (Lake Ziway, Ethiopia). *J. Hydrol.* **2001**, *245*, 1–18. [CrossRef]

48. NRMRD-MOA. *Agro-Ecological Zones of Ethiopia*; Natural Resources Management and Regulation Department of MOA: Addis Ababa, Ethiopia, 1998.

49. Le Turdu, C.; Tiercelin, J.J.; Gibert, E.; Travi, Y.; Lezzar, K.E.; Richert, J.P.; Massault, M.; Gasse, F.; Bonnefille, R.; Decobert, M.; et al. The Ziway Shala lake basin system, Main Ethiopian Rift: Influence of volcanism, tectonics, and climatic forcing on basin formation and sedimentation. *Paleogeogr. Palaeoclimatol. Palaeoecol.* **1999**, *150*, 135–177. [CrossRef]

50. Abid, M.; Scheffran, J.; Schneider, U.; Ashfaq, M. Farmers' perceptions of and adaptation strategies to climate change and their determinants: The case of Punjab province, Pakistan. *Earth Syst. Dyn.* **2015**, *6*, 225–243. [CrossRef]

51. Sadashivaiah, C.; Ramakrishnaiah, C.R.; Ranganna, G. Hydrochemical analysis and evaluation of groundwater quality in Tumkur Taluk, Karnataka State, India. *Int. J. Environ. Res. Public Health* **2008**, *5*, 158–164. [CrossRef]

52. Fipps, G. *Irrigation Water Quality Standards and Salinity Management Strategies*; Texas Agricultural Extension Service, Texas A&M University System: College Station, TX, USA, 2003; pp. 1–19.

53. Zhang, H. Classification of Irrigation Water Quality. Oklahoma Cooperative Extension Service Id: PSS-2401. 2017. Available online: https://extension.okstate.edu/fact-sheets/classification-of-irrigation-water-quality.html (accessed on 3 June 2021).

54. Zörb, C.; Geilfus, C.; Dietz, K. Salinity and crop yield. *Plant Biol.* **2019**, *21*, 31–38. [CrossRef] [PubMed]

55. Maas, E.V.; Hoffman, G.J. Crop Salt Tolerance: Evaluation of Existing Data. In Proceedings of the International Salinity Conference, Lubbock, TX, USA, 16–20 August 1976; pp. 187–198.

56. Gebre, G.G.; Hiroshi, I.; Dil Bahadur, R.; Yuichiro, A.; Hisako, N. Gender Gaps in Market Participation Among Individual and Joint Decision-Making Farm Households: Evidence from Southern Ethiopia. *Eur. J. Dev. Res.* **2021**, *33*, 649–683. [CrossRef]

57. Rango, T.; Paul, C.J.; Jeuland, M.; Tekle-Haimanot, R. Biomonitoring of metals and trace elements in urine of central Ethiopian populations. *Int. J. Hyg. Environ. Health* **2019**, *222*, 410–418.

58. Paul, C.J.; Weinthal, E.S.; Bellemare, M.F.; Jeuland, M.A. Social capital, trust, and adaptation to climate change: Evidence from rural Ethiopia. *Glob. Environ. Chang.* **2016**, *36*, 124–138. [CrossRef]

59. WBG Climate Change Knowledge Portal (CCKP). Ethiopia Projected Future Climate. 2020. Available online: https://climateknowledgeportal.worldbank.org/country/ethiopia/climate-data-projections (accessed on 3 April 2021).

60. Boko, M.; Niang, I.; Nyong, A.; Vogel, C.; Githeko, A.; Medany, M.; Osman-Elasha, B.; Tabo, R.; Yanda, P. Africa. In *Climate Change 2007: Impacts, Adaptation and Vulnerability*; Parry, M.L., Canziani, O.F., Palutikof, J.P., van der Linden, P.J., Hanson, C.E., Eds.; Cambridge University Press: Cambridge, UK; New York, NY, USA, 2007; pp. 433–467.

A Model to Assess Eastern Cottonwood Water Flow Using Adjusted Vapor Pressure Deficit Associated with a Climate Change Impact Application

Ying Ouyang [1,*] **, Theodor D. Leininger** [2] **, Heidi Renninger** [3] **, Emile S. Gardiner** [2] **and Lisa Samuelson** [4]

[1] USDA Forest Service, Center for Bottomland Hardwoods Research, 775 Stone Blvd., Thompson Hall, Room 309, Mississippi State, MS 39762, USA

[2] USDA Forest Service, Center for Bottomland Hardwoods Research, 432 Stoneville Road, Stoneville, MS 38776, USA; ted.leininger@usda.gov (T.D.L.); emile.gardiner@usda.gov (E.S.G.)

[3] Department of Forestry, Mississippi State University, Hood Road, MS 39762, USA; hr427@msstate.edu

[4] School of Forestry and Wildlife Sciences, Auburn University, Auburn, AL 36849, USA; samuelj@auburn.edu

[*] Correspondence: ying.ouyang@usda.gov

Abstract: Short-rotation woody crops have maintained global prominence as biomass feedstocks for bioenergy, in part due to their fast growth and coppicing ability. However, the water usage efficiency of some woody biomass crops suggests potential adverse hydrological impacts. Monitoring tree water use in large-scale plantations would be very time-consuming and cost-prohibitive because it would typically require the installation and maintenance of sap flux sensors and dataloggers or other instruments. We developed a model to estimate the sap flux of eastern cottonwood (*Populus deltoides*. Bartr. ex Marsh.)) grown in bioenergy plantations. This model is based on adjusted vapor pressure deficit (VPD) using Structural Thinking and Experiential Learning Laboratory with Animation (STELLA) software (Architect Version 1.8.2), and is validated using the sap flux data collected from a 4-year-old eastern cottonwood biomass production plantation. With R^2 values greater than 0.79 and Nash Sutcliffe coefficients greater than 0.69 and p values < 0.001, a strong agreement was obtained between measured and predicted diurnal sap flux patterns and annual sap flux cycles. We further validated the model using eastern cottonwood sap flux data from Aiken, South Carolina, USA with a good agreement between method predictions and field measurements. The model was able to predict a typical diurnal pattern, with sap flux density increasing during the day and decreasing at night for a 5-year-old cottonwood plantation. We found that a 10% increase in VPD due to climate change increased the sap flux of eastern cottonwood by about 5%. Our model also forecasted annual sap flux characteristics of measured cycles that increased in the spring, reached a maximum in the summer, and decreased in the fall. The model developed here can be adapted to estimate sap flux of other trees species in a time- and cost-effective manner.

Keywords: cottonwood; climate change; sap flux; STELLA; vapor pressure deficit

1. Introduction

Fossil fuel consumption has been strongly tied to various sources of environmental degradation. Climate change, in particular, is attributed in part to CO_2 emissions, and this issue has motivated continuing efforts to identify sustainable alternatives to fossil fuels [1–4]. Various types of biomass have been identified as renewable bioenergy feedstocks of global significance [4–9]. Algae, agronomic crops, grasses, trees, municipal wastes, and other biological materials can be sourced for biomass, and biomass can be converted to solid, liquid, or gaseous fuels to yield energy for industrial, commercial, and domestic uses. The US Department of Energy is promoting an increased usage of biofuels in the United States by targeting the creation of a biomass supply of 1 billion dry tons per year by 2030 [4].

Tree and shrub cultivation in short-rotation (2–15 years) provides for high-yielding bioenergy feedstock production. Over the past several decades, researchers have refined improvements in short-rotation tree and shrub species such as eastern cottonwood (*Populus deltoides* Bartr. ex Marsh.), willow (*Salix spp.* L.), and eucalyptus (*E. globulus* Labill.) by selecting for rapid growth, pest tolerance, and site suitability [10,11]. Eastern cottonwood is a fast-growing poplar and one of the largest native North American broadleaf trees [12]. Eucalyptus is among the fastest growing hardwood plantation species utilized around the world. Its suitability to plantation culture is driving current research and development towards application to large-scale biomass production in the southern United States [11,13]. Shrub willows have been selected for short-rotation intensive culture in the northeastern, north–central, and mid-Atlantic regions of the United States [14].

There are, however, concerns about the water use of trees in short-rotation bioenergy systems, especially in regard to the potential adverse environmental impacts of excessive water use [15–19]. Scott and Lesch [20] reported a 90 to 100% reduction in stream flow for eucalyptus and a 40 to 60% reduction in stream flow for pines (*Pinus spp.* L.) in the first 8 years or so after planting. Morris et al. [21] studied water use in the eucalyptus plantations of southern China and noted that annual water use by these plantations is about 550 mm, but potential annual water use could reach 865 mm where soil water was not limiting. Flanagan et al. [19] used the eddy covariance measurement of evapotranspiration (ET) to estimate water use in a riparian cottonwood ecosystem in Alberta, Canada. They found a comparatively high water use driven by relatively warm summer temperatures and high vapor pressure deficit ((VPD) which is the difference between the amount of moisture in the air and the maximum (saturated) amount of moisture the air can hold) and supported by sufficient availability of alluvial groundwater. In regard to VPD, Weih [22] reported that fast-growing hybrid willows are generally more sensitive to water stress and have lower water use efficiency than slower-growing wild clones. Though the studies cited above provide valuable insights into water use by trees in short-rotation bioenergy systems, the long-term, continuous, and real-time monitoring of water use by trees in biomass production plantations has rarely been conducted.

Sap flux measurement is currently the most widely used method for assessing individual tree water use. Its advantages include a well-established technology, the ability to continuously monitor trees for lengthy time periods, and the fact that instrumentation does not modify the ambient environment [23,24]. However, for commercially sized biomass production plantations, it would be very time-consuming and costly to install and maintain a sufficient number of sensors and dataloggers to accurately and continuously assess tree water use with real-time resolution. Therefore, there is a need to develop practical and reliable methods for estimating tree water use in intensively managed short-rotation woody crop systems.

This problem may be addressed with an understanding of the relationships between sap flux and its driving environmental variables [24–29]. Hogg et al. [25] compared the sap flux and eddy flux of water vapor in a boreal deciduous forest and found that the sap flux response lagged behind eddy flux measurements by about 1 hour diurnally—presumably because of water storage within the trees. Nadezhdina [26], who studied sap flux in apple trees (*Malus domestica Borkh.*) over one growing season, found correlations to the diurnal patterns of leaf water potential, air temperature, relative humidity, and solar radiation. Wilson et al. [27] compared forest evapotranspiration with sap flux, VPD, soil water budget, and eddy covariance. Reasonably good agreement was observed between sap flux and VPD as well as sap flux and eddy covariance based on annual data. Liu et al. [29] studied the sap flux of sawtooth oak (*Quercus acutissima* Carruth) and china-fir (*Cunninghamia lanceolate* (LAMB) Hook.) relative to photosynthetically active radiation (PAR), air temperature, relative humidity, VPD, precipitation, and soil water content. Significant linear correlations were found between sap flux and PAR, air temperature, and VPD, but not soil water content. These studies establish mechanistic relationships between tree water flux and certain environmental variables based on the response of stomata to environmental drivers,

but most of the reported relationships were obtained using annual data that provided low correlation coefficients. Diurnal sap flux patterns are typically not distinctly parallel to the diurnal patterns of environmental variables. Therefore, it is difficult and inaccurate to simply predict diurnal sap flux directly from environmental variables.

Climate change is a natural phenomenon. However, anthropogenic activities such as fossil fuel burning, industrial pollution, deforestation, and population growth have greatly accelerated greenhouse gas emissions and resulted in extremely abnormal climate change patterns [30]. Climate change over the last several decades has been linked to atmospheric water vapor content increase, precipitation pattern shifts, snow cover reduction and ice melt, and surficial hydrological cycle changes [30]. Lasch et al. [31] investigated the impacts of short-rotation coppice plantation with aspen (*P. tremula* L.) in Eastern Germany under changing climate conditions. These authors found that the aspen plantations contributed to regional CO_2 mitigation and carbon sequestration, but had negative on the regional water budget due to climate change. Griffiths et al. [32] reviewed the environmental effects on short-rotation woody crop production. They cited long-term water use, C dynamics, and soil quality studies as being needed to evaluate the potential effects of climate change. Currently, our understanding of climate change effects upon the sap flux of eastern cottonwood in short-rotation plantations is basically unknown.

The goal of this study was to develop a novel model for estimating diurnal and annual sap flux of trees in short-rotation biomass production plantations associated with climate change impacts. To accomplish this goal, we based our model on adjusted VPD using Structural Thinking and Experiential Learning Laboratory with Animation (STELLA) software, and used eastern cottonwood as the plantation tree species. We investigated the relationship between adjusted VPD and eastern cottonwood sap flux to address the following objectives: (1) establish a model using diurnal patterns and annual cycles of adjusted VPD to predict those of measured eastern cottonwood sap flux; (2) validate the model using an independent sap flux dataset collected from sensor measurements; and (3) apply the model to predict eastern cottonwood sap flux in the absence of measured sap flux data under a changing climate. It should be noted that we approached the problem of predicting sap flux with the variable VPD because VPD data are easy to obtain from local weather stations, and sap flux tends to follow VPD more closely than other environmental variables such as air temperature and PAR. The model developed here provides a new paradigm for estimating the sap flux of trees in short-rotation bioenergy plantations in a time- and cost-effective manner.

1.1. Study Site

This work is based on sap flux measurements collected at a biomass production plantation located near Hollandale, Washington County, Mississippi, US (see Figure 1). The plantation was established in 2012 to study eastern cottonwood and black willow (*S. nigra* L.) biomass production under several planting densities and harvest regimens.

The plantation is situated on a site with Sharkey clay soil that is poorly drained, and the site was previously used for rice (*Oryza sativa*) production. For this study, we instrumented six representative eastern cottonwood trees (each 3 years old) with a planting density of 1 m × 1 m and a plot area of 1.01 hectare, with 2 cm long laboratory made heat dissipation type sensors [33] to collect sap flux measurements from September 2015 to September 2016. One constructed sensor pair consists of a reference and heated sensor, each containing thermocouples within hypodermic needles. Each sensor was installed radially in the xylem of each tree at a height of 120 cm, where the diameter at breast height (DBH) was measured. The sensors were about 10 cm apart vertically, and the immediate area of the stem was covered with insulated aluminum shielding that prevented solar radiation from impacting readings. All sensors were connected to a CR1000 datalogger and AM 16/32/B multiplexer (Campbell Scientific Inc., Logan UT, USA) and the instrumentation was powered by rechargeable marine deep cycle batteries connected to a solar panel (Figure 1b). The system was programmed to measure voltage differences between sensors

corresponding to thermocouple temperature differences every 30 s, and data were averaged every 30 min. As water flows through the xylem, it cools the heated sensor relative to the reference sensor and, therefore, temperature differences between sensors can be used to infer sap flux rates. Collected data were transmitted to an office computer through a wireless carrier (Verizon Inc.). This real-time system enabled periodic monitoring for malfunctions and quick troubleshooting. Meanwhile, time series VPD data with the same collection interval (i.e., every 30 min) were downloaded from an on-site weather station (https://www.hobolink.com). Missing data from the on-site station were replaced with data from the nearest weather station, which was located about 40 km north of the study site (https://www.wunderground.com/history /airport/KGLH/). The VPD data were calculated using the following formula [34]:

$$D_{vp} = \left[1 - \left(\frac{RH}{100}\right)\right] * 610.7 * 10^{\frac{7.5T_{air}}{237.3+T_{air}}} \tag{1}$$

where D_{vp} is the vapor pressure deficit (Pa), *RH* is the relative humidity (%), and T_{air} is the air temperature (°C). Differences in sap flux sensor temperature were converted to sap flux densities (g/m²/s) with the widely accepted empirical equation developed by Granier [33] using the software program Baseliner version 4. Data were scaled to the tree level (g/s) with DBH measurements on the assumption that the entire cross-sectional area was conductive sapwood.
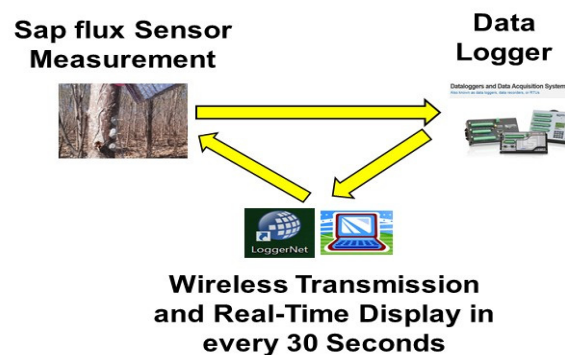

Figure 1. A short-rotation woody crop plantation used in this study near Hollandale, Mississippi, USA (**a**) and real-time monitoring of sap flux from eastern cottonwood using the sensor–datalogger system (**b**).

1.2. Adjusted VPD and its Correlation with Sap Flux

The measured hourly sap flux and VPD over the study period illustrated that the highest diurnal peaks for these two variables were not aligned (Figure 2a). That is, the highest peaks for hourly sap flux occurred mostly in the summer, whereas the highest peaks for hourly VPD were observed in the early fall. Analysis of hourly measured sap flux and VPD over the one-year study period (Figure 2b) revealed a very weak relationship between these variables (R^2 = 0.263). Further examination of measured sap flux and VPD at diurnal scales in spring, summer, and fall (there are no leaves in winter) revealed the following three distinct patterns (Figure 3): (1) sap flux peaked around 10:00 a.m. under normal conditions; (2) peak VPD typically lagged about 3 hours behind peak sap flux; and (3) sap flux maintained a constant value close to zero from 9:00 p.m. at night to 6:00 a.m. the next morning, while VPD remained above zero during the same period. Based on these observations, unadjusted diurnal VPD would be unsuitable for predicting diurnal sap flux. However, VPD could be adjusted to develop a stronger correlation with sap flux.
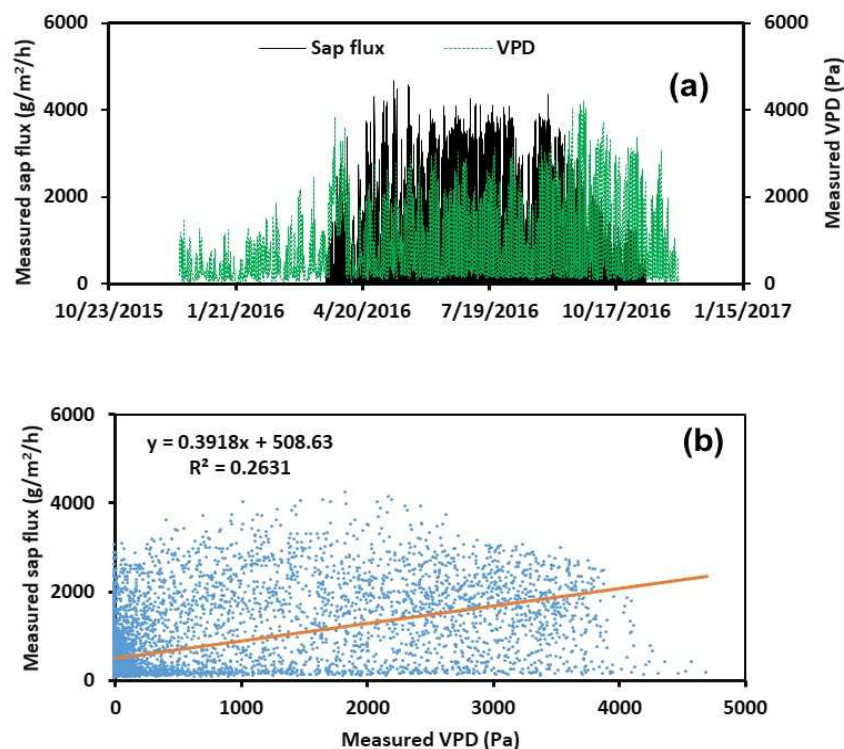

Figure 2. Time series plots of the measured sap flux and the measured vapor pressure deficit (VPD) (**a**) and their correlation (**b**) for eastern cottonwood in a biomass production plantation near Hollandale, MS, USA.

We employed the following eight steps (Figure 4) to adjust measured VPD and develop a mathematical relationship between sap flux and adjusted VPD.

1. Measured VPD was shifted about 3 hours ahead so that diurnal VPD peaks corresponded to diurnal sap flux peaks (Figure 5). Such adjustment is needed for a better prediction of sap flux behaviors using VPD. The 3-hour time shift ahead was only for this study site and could be varied with sites and tree species.
2. VPD was adjusted to a minimum value at night. This adjustment was necessary because eastern cottonwood sap flux was typically lowest from 9:00 p.m. at night to 6:00 a.m. the next morning.
3. Measured VPD was increased by a factor of 2.4 at 10:00 a.m. so that the adjusted VPD peak was coincident with measured sap flux. The adjustment factor "2.4" was

estimated from our experimental data, and this value can be changed for different tree species or sites.
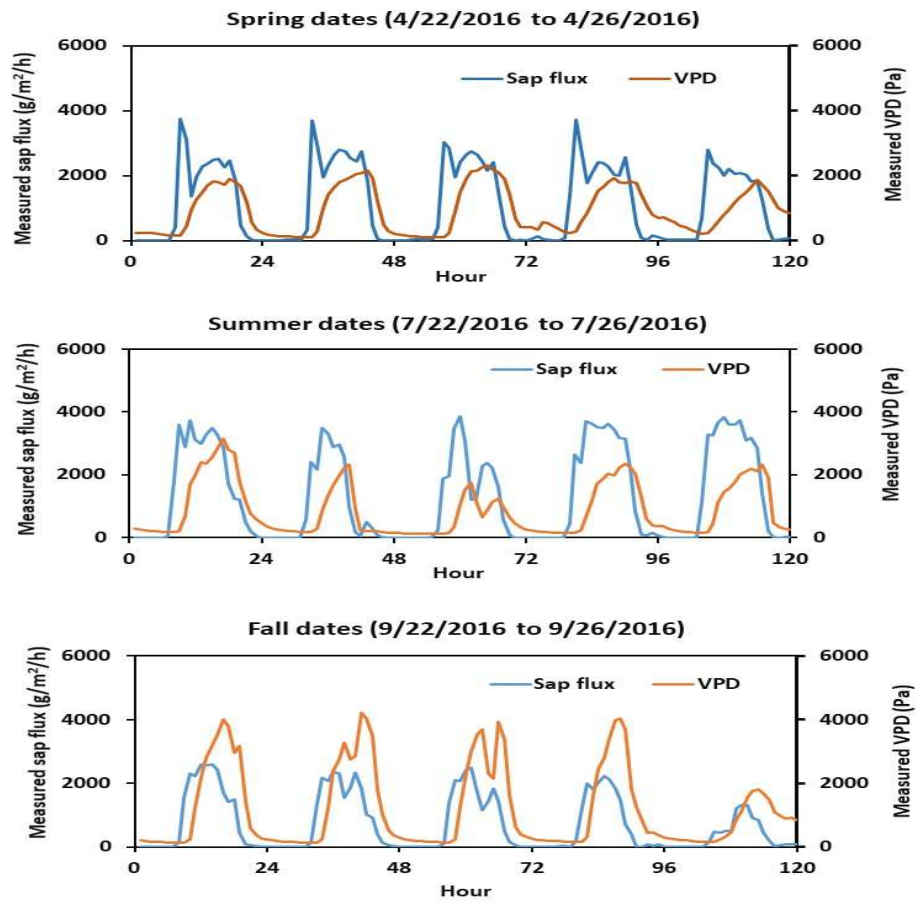
Figure 3. Diurnal sap flux and VPD as measured on selected spring, summer, and fall dates for eastern cottonwood in a biomass production plantation near Hollandale, Mississippi, USA.

4. A correction factor was imposed to adjust the annual cycle of VPD to match the annual sap flux cycle. This correction factor (*F*) was calculated with Equation (2) below.

$$F = 1.1 * EXP\left((-0.3) * \left(\frac{t - \beta}{\alpha}\right)^2\right) \tag{2}$$

where *t* is the hour of year, β is a time constant that specifies the hour of year when maximum sap flux occurs (5100 h in this example), and α is a constant characterizing the shape of the annual sap flux cycle (1500 in this example). This constant was obtained from measured annual eastern cottonwood sap flux.

5. VPD was adjusted to near zero for the dormant season. Our measurements confirmed no sap flux during the late fall, winter, and early spring months when the deciduous eastern cottonwood bores no leaves.

6. We assumed soil water availability did not limit sap flux based on our field observations during the study period.

7. Regression analysis was used to develop a function to predict measured sap flux from adjusted VPD. Equation (3) below was developed for this study.

$$Q_{sapflow} = \quad 5E - 08 * VPD^3_{adjusted} - 0.0006 * VPD^2_{adjusted}$$
$$+2.5167 * VPD_{adjusted} - 16.45 \tag{3}$$

where Q is the sap flux (g/m^2/h) and $VPD_{adjusted}$ is the adjusted VPD (Pa). A detailed discussion of Equation (3) is provided in the Results and Discussion Section.

8. Because eastern cottonwood sap flux is affected by age (which is correlated to DBH), we accounted for the age effect with Equation (4):

$$F_{age} = 0.038 e^{0.0431DBH} \tag{4}$$

where F_{age} is the age factor and DBH (cm) increases as time elapses. Equation (4) was developed from data reported by Schaeffer et al. [35], who measured the sap flux and DHB of eastern cottonwood growing in the San Pedro River system of southeastern Arizona. Combining Equations (3) and (4) yields the following equation:

$$Q_{sapflow}^{adjusted} = (1 + F_{age}) * Q_{sapflow} \tag{5}$$

where $Q_{sapflow}^{adjusted}$ is the age-adjusted sap flux (g/m^2/h). Equation (5) is used to predict age-adjusted eastern cottonwood sap flux in this study.
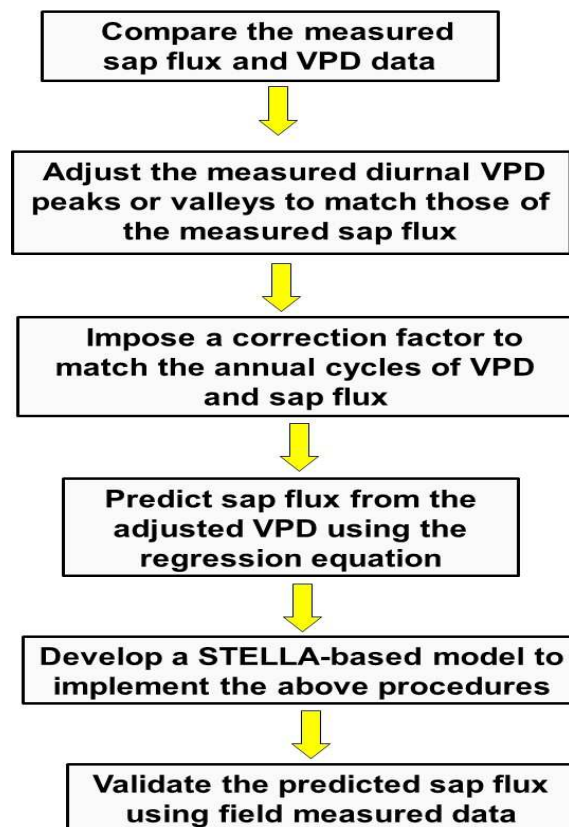

Figure 4. A flowchart showing the procedures used to develop a Structural Thinking and Experiential Learning Laboratory with Animation (STELLA)-based model for predicting sap flux using the adjusted VPD.
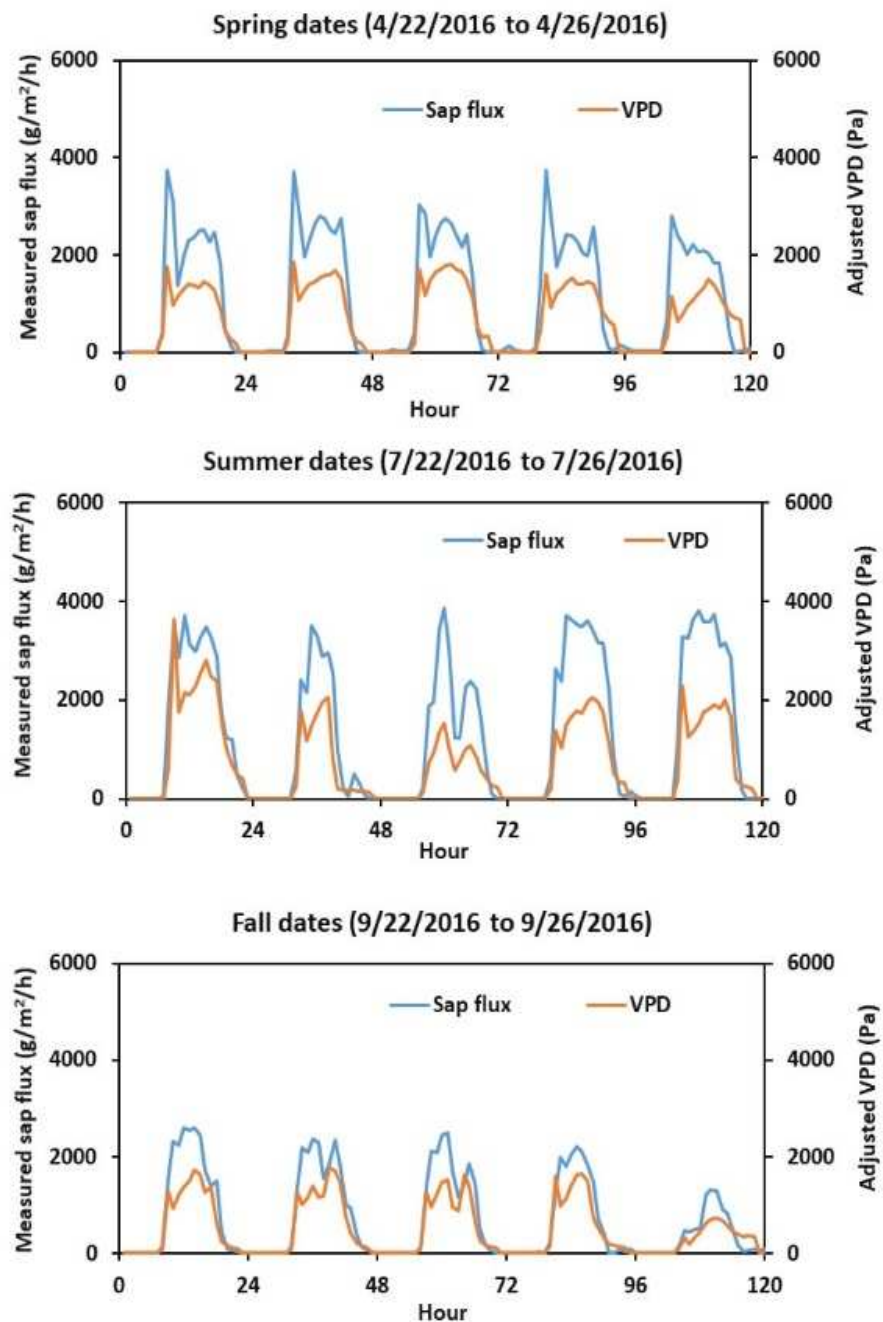
Figure 5. Measured sap flux and adjusted VPD for selected dates in spring, summer, and fall for eastern cottonwood in a biomass production plantation near Hollandale, MS, USA.

1.3. STELLA Model

The eight steps listed above were applied to the development of a STELLA model. STELLA is a software package used to develop system dynamic models by creating a pictorial diagram of a system and assigning appropriate values and functions to it (http://www.iseesystems.com). System dynamic models created with STELLA have been widely used [36–39]. Figure 6 provides the STELLA modeling map, which illustrates the conditions and equations (in the dashed boxes) established for this study. The STELLA model (with an hourly time step) we created is further described below. Referring to Figure 6, data for Step 1 is stored as input data in the converter (or a circle) labeled "Measured VPD with shifting 3 hours ahead." Steps 2, 3, and 5 are completed in the converter labeled "Adjusted VPD" according to the conditions in the dashed box.
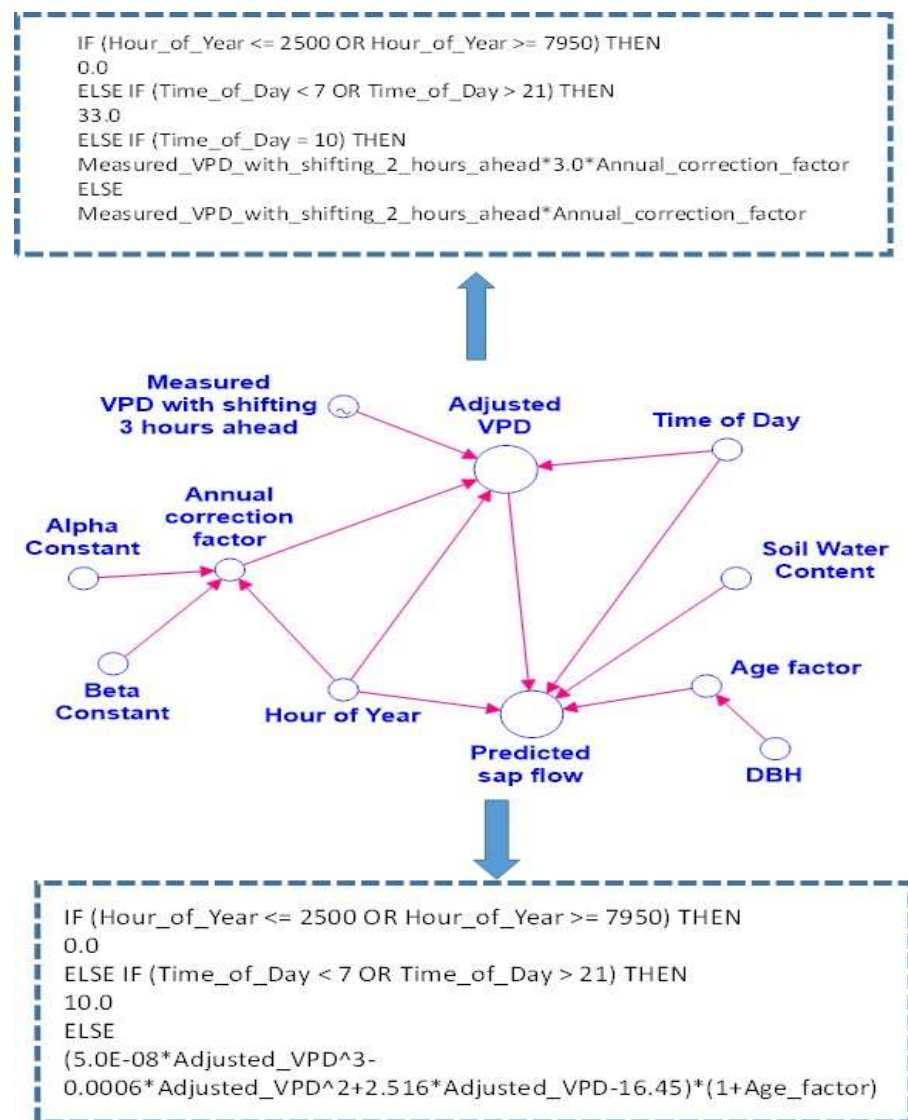
Figure 6. A STELLA modeling map for estimating the sap flux of eastern cottonwood from adjusted VPD.

The routine first determines if time of year (in hours) is less than 2500 h or greater than 7950 h (representing the winter period). If either condition is true, adjusted VPD is set to zero. Then, if time of a day is <7 h or >21 h (representing the nocturnal period), adjusted VPD is set to the minimum value for a site—the value for our study site is 33 Pa. If the time of day is 10 am, the VPD, after having been shifted 3 hours, was adjusted by multiplying it by 2.4 (as explained in Step 3). Step 4 and Equation (1) are processed in the converter labeled "Annual correction factor." It should be noted that we initiated simulation at the beginning of winter (i.e., 12 December 2015) and terminated simulation at the end of the following fall (i.e., 11 December 2016), but start and end times can be changed as appropriate. It should also be noted that our field experiment started in September 2015 and the collection of sap flux data began in December 2015. After adjusted VPD was calculated, predicted sap flux was estimated with Equation (5) in the converter labeled "Predicted sap flow."

2. Results and Discussion

2.1. Measured Sap Flux, Adjusted VPD, and Model Validation

The relationship between measured sap flux and adjusted VPD for the one-year study period is illustrated in Figure 7. The values of $R^2 = 0.823$ and $p < 0.001$ (Figure 7a) indicate

that sap flux can be reliably predicted from adjusted VPD. This was further confirmed in Figure 7b, which shows that the diurnal peaks of these two variables shared a relatively similar annual cycle. Though the results above show that measured sap flux correlated well with adjusted VPD, they do not confirm if sap flux predicted by the STELLA model accurately matches measured sap flux. Therefore, model validation is necessary prior to its application. It should be pointed out that sap flux measurements collected from three of the six eastern cottonwood trees instrumented in this study were used to develop Equation (3) and perform initial validation of the model, while sap flux data from the three remaining trees were used as an independent dataset for additional validation of the model. The initial validation of predicted sap flux against measured sap flux from the first three trees is provided in Figure 8. The validation was measured using statistical parameters such as R^2, the Nash Sutcliffe coefficient (NSE), and normalized root mean square error (nRMSE). The nRMSE is calculated as follows [40]:

$$\text{nRMSE} = \frac{1}{O_{ave}} \left(\sqrt{\frac{\sum_{i=1}^{n}(O_i - S_i)^2}{n}} \right) \tag{6}$$

where O_i is the field observation, S_i is the model prediction, O_{ave} is the average number of field observations, and n is the total number of field observations.
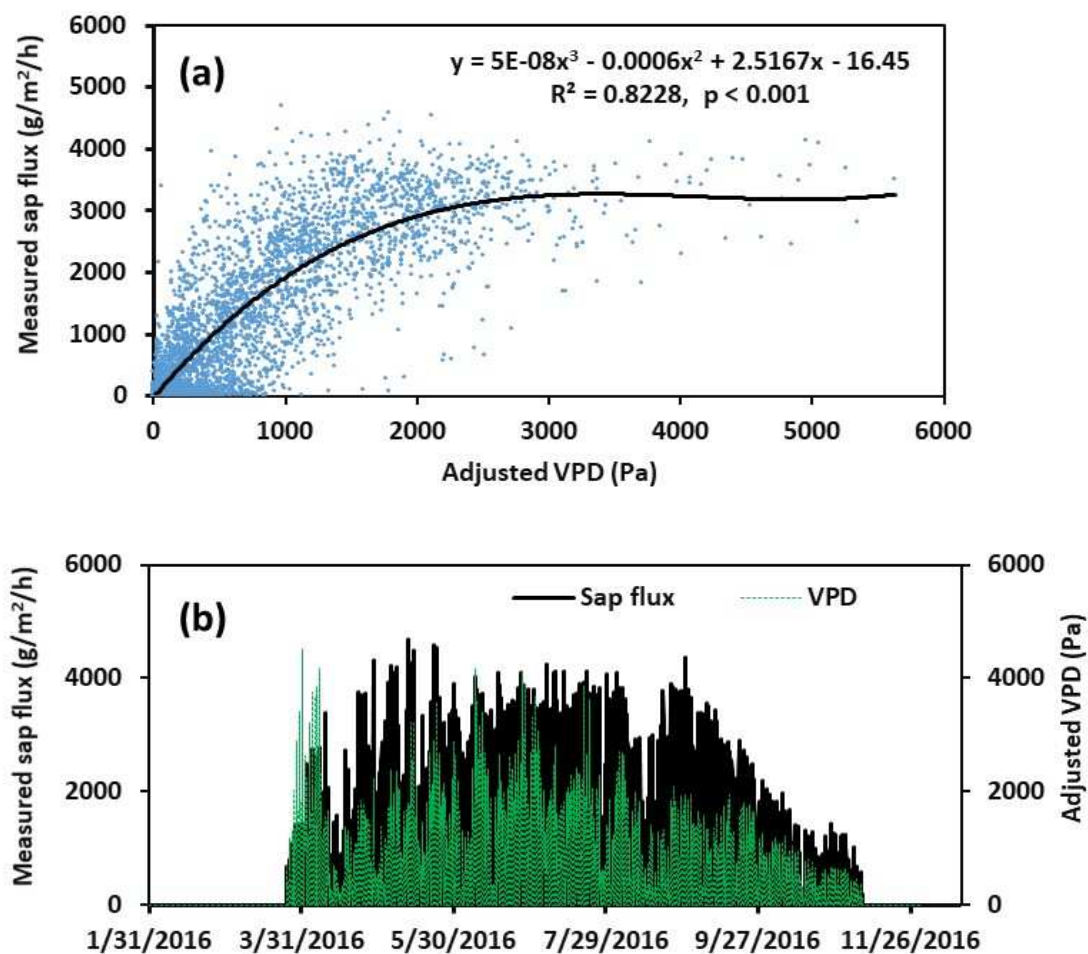
Figure 7. The relationship between measured sap flux and adjusted VPD (**a**) and the time series plots of measured sap flux and the adjusted VPD (**b**) for eastern cottonwood in a biomass production plantation near Hollandale, Mississippi, USA.
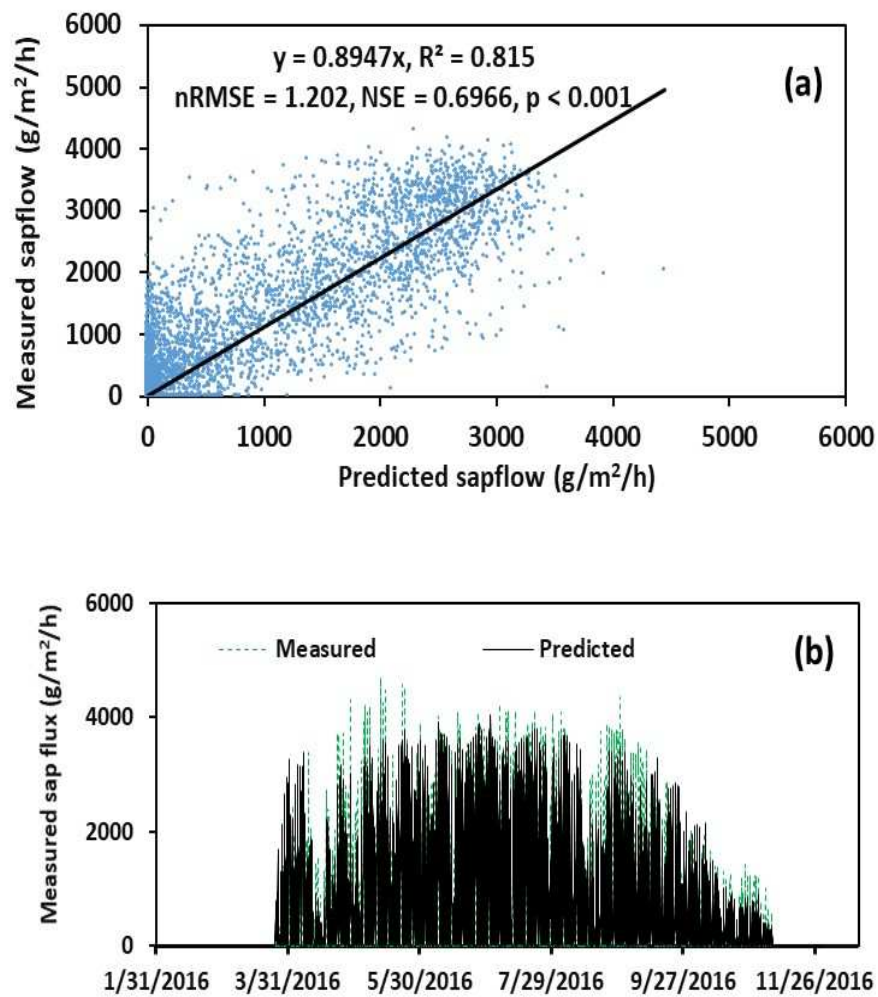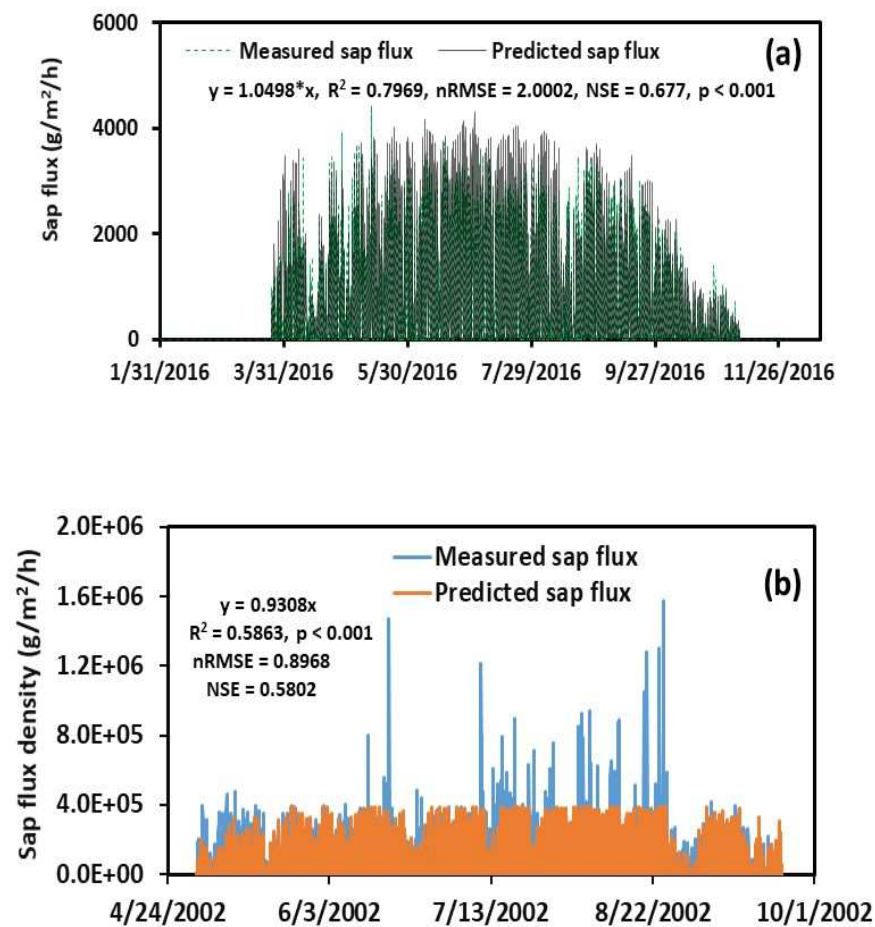
Figure 8. A comparison of the measured and predicted sap flux (**a**) and their time series plots (**b**) during the model validation process for eastern cottonwood in a biomass production plantation near Hollandale, Mississippi, USA.

The NSE is given as [41]

$$\text{NSE} = 1 - \frac{\sum_{i=1}^{n}(O_i - S_i)^2}{\sum_{i=1}^{n}(O_i - \overline{O})^2} \tag{7}$$

The NSE ranges from -∞ to 1, with the values of 1 representing a perfect fit, >0.75 representing a very good fit, between 0.36 and 0.75 representing a reasonable fit, and <0.36 representing an unsatisfied fit to the model. With $R^2 = 0.815$, NSE = 0.697, nRMSE = 1.202 ($g/m^2/h$), and p value < 0.001 (Figure 8a), we suggest that the model developed in this study performed well in predicting eastern cottonwood sap flux. This conclusion was further supported by data presented in Figure 8b, which illustrate diurnal peaks and seasonal trends of predicted sap flux to coincide with those of measured sap flux. For additional validation of the model, we compared predicted sap flux to the measured sap flux from trees in the independent dataset. This second validation confirmed that the developed model predicted sap flux reasonably similar to the measured sap flux based on the relatively high R^2 (0.797) and NSE (0.677) as well as the low nRMSE (2.002) and p value (<0.001) and its conformation to measured sap flux peaks (Figure 9a).

Figure 9. A comparison of the measured and predicted sap flux for eastern cottonwood in a biomass production plantation near Hollandale, MS, USA (**a**) and an experimental plantation near Aiken, SC, USA (**b**).

To develop users' confidence, we further validated the model by comparing the measured sap flux from a different study site to the predicted sap flux from our model. The measured sap flux data were obtained from Samuelson et al. [42]. These authors conducted an experiment to estimate the influence of irrigation and fertilization on transpiration and hydraulic properties of the 3-year-old eastern cottonwood. Their study used marsh clones at a 24.4 ha experimental plantation on the U.S. Department of Energy Savannah River Site located near Aiken, SC. In this validation process, we used the measured sap flux data from Block 2 of their experiment along with the VPD data calculated from local weather variables (i.e., air temperature and relative humidity). A closer look at the measured sap flux data revealed that the maximum sap flux from Samuelson et al. [42] was 5716.8 kg/m^2/s in Aiken, SC but was 586.8 kg/m^2/s in our experiment in Hollandale, MS. The former was about 10 times greater than the latter. Since the sap flux, weather conditions, and eastern cottonwood clones in Aiken, SC are different from those in Hollandale, MS, we have modified Equation (3) for the Aiken study site as follows:

$$Q_{sapflow} = -1E - 06 * VPD^2_{adjusted} + 1.119 * VPD_{adjusted} + 12789 \qquad (8)$$

It should be noted that other input values from Equations (2), (4), and (5) were not changed during this validation process. A comparison of sap flux densities between model prediction and experimental measurement is given in Figure 9b. The model predicted most of sap flux densities very well, except for several unusually high measured sap flux densities. With R^2 = 0.586, NSE = 0.580, nRMSE = 0.897, and $p < 0.01$, we concluded that the model predicted sap flux density reasonably well.

2.2. Model application

The model was applied to predict eastern cottonwood sap flux at the same study site for a simulation period beginning on 30 November 2016 and ending on 30 October 2017. Input data were the same as for model validation except for measured DBH and VPD. Average DBH was changed to 7.2 cm for this simulation period. This number was based on the measured growth in the plantation. Data to calculate VPD for the simulation period were downloaded from the on-site weather station.

The diurnal pattern of predicted sap flux by eastern cottonwood between 22 April and 28 April 2017 is shown in Figure 10a. This projection conforms to the expectations for the diurnal sap flux volume and the pattern of eastern cottonwood. Relatively low sap flux on the first day (0 to 24 h) was a result of low VPD, normally observed on cloudy or rainy days. When higher VPD prevailed, such as a VPD between 72 and 96 h, we observed predicted sap flux in a pattern similar to previous measurements of sap flux. Maximum sap flux during this time period was 3577 $g/m^2/h$, or 16 g/h for the 7.2 cm DBH tree. This rate was within the range reported by Schaeffer et al. (2000), who found that eastern cottonwood sap flux in the spring averaged about 20 g/h. Results indicated that the model provided for reasonable prediction of diurnal sap flux by eastern cottonwood grown in a biomass plantation.
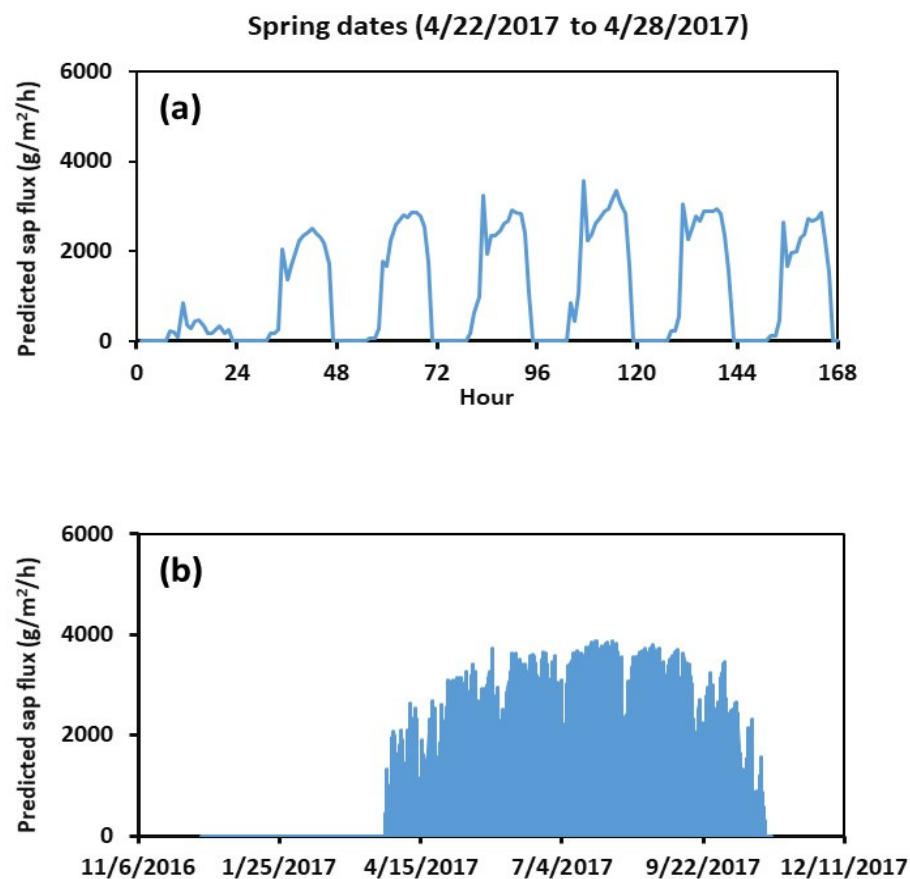
Figure 10. Predicted diurnal (**a**) and annual (**b**) sap flux of eastern cottonwood in a biomass production plantation near Hollandale, Mississippi, USA.

An annual cycle of predicted eastern cottonwood sap flux is presented in Figure 10b. The simulation estimated total annual sap flux at 6,369,309 $g/m^2/y$. Converting this value to be representative of a tree with a DBH of 7.2 cm yields an annual water use of 25,919.52 $g/year$.

We assumed soil water content did not limit eastern cottonwood sap flux in this study. Soil water dynamics and hydrological processes would need to be included in the STELLA

model if this factor were to be considered important. While we developed this model by studying eastern cottonwood sap flux, it could be adapted to estimate the sap flux of other tree species in short-rotation biomass production plantations. This would be done by revising values outlined in the aforementioned eight steps (Section 1.2) to reflect the tree species of interest and the site.

2.3. Impact of Climate Change on Sap Flux

To estimate the impact of climate change on sap flux, a simulation scenario was developed by increasing the VPD by 10% from the original VPD. Up to date, no effort has been devoted to estimating the impact of climate change on VPD and sap flux in our study area. The 10% increase in VPD was considered as an extreme case based on the study reported by Yuan et al. [43]. These authors studied the global VPD and reported that the mean VPD in the growing season from 2011 to 2015 was 11.26% higher than that from 1982 to 1986.

Comparisons of the predicted daily and overall average hourly sap flux of eastern cottonwood between the original VPD and the 10% increased VPD are shown in Figure 11. In general, an increase in VPD resulted in an increase in sap flux (Figure 11a). The results indicate that as the VPD increased due to the air temperature increase and the precipitation decrease under the changing climate, the sap flux of eastern cottonwood increased. Overall, the hourly average sap flux for the simulation period from 6 November 2016 to 1 December 2017 was 793 g/m^2/h with the original VPD but was 838 g/m^2/h with the 10% increased VPD (Figure 11b). The latter was 5.67% greater than the former.
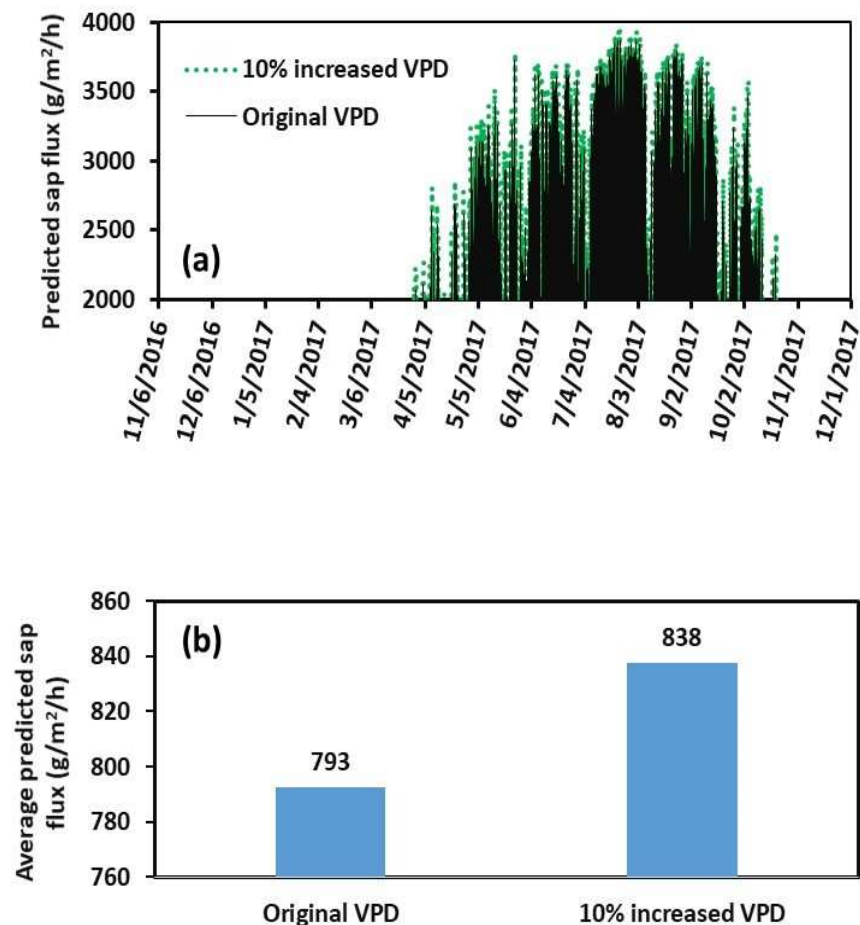
Figure 11. Comparisons of the predicted daily (**a**) and overall average hourly (**b**) sap flux of eastern cottonwood between the original VPD and the 10% increased VPD.

3. Conclusions

This study provides a model to estimate the sap flux of eastern cottonwood grown in short-rotation biomass production plantations. Sap flux was predicted from adjusted VPD, as modeled with STELLA software. The model was validated using two different sap flux datasets collected with sensors between 1 December 2015 and 30 November 2016. Very good agreement was found between predicted and measured sap flux. More specifically, predicted diurnal patterns and annual sap flux cycles matched those of measured sap flux.

The model was then applied to predict eastern cottonwood sap flux for a year-long simulation period (30 November 2016 to 30 October 2017). The model appeared to predict reasonable diurnal patterns and annual cycles of eastern cottonwood sap flux. Overall, a 10% increase in VPD increased the sap flux of eastern cottonwood by about 5%. The model provides a new approach for estimating the sap flux of cottonwood in short-rotation bioenergy plantations in a time-saving and cost-effective manner.

The major limitations of the model were that soil water availability is not a limiting factor for sap flux and the very high sap flux peaks were not easily predicted. Therefore, further study is warranted to include soil water dynamics, hydrological processes, and high sap flux peak accommodations into the STELLA model. Additionally, the response of VPD to sap flux is tree species dependent. Although the model was developed for eastern cottonwood, it can be adapted to estimate the sap flux of other tree species with moderate effort.

Abbreviations

ET	evapotranspiration
PAR	photosynthetically active radiation
VPD	vapor pressure deficit
STELLA	Structural Thinking and Experiential Learning Laboratory with Animation

References

1. McKendry, P. Energy production from biomass (Part 1): Overview of biomass. *Bioresour. Technol.* **2002**, *83*, 37–46. [CrossRef]
2. Gable, M.; Zacchi, G. A review of the production of ethanol from softwood. *Appl. Microbiol. Biotechnol.* **2002**, *59*, 618–628.
3. Berndes, G.; Hoogwijk, M.; van den Broek, R. The contribution of biomass in the future global energy supply: A review of 17 studies. *Biomass Bioenergy* **2003**, *25*, 1–28. [CrossRef]
4. US-DOE (US Department of Energy). *2016 Billion-Ton Report, Advancing Domestic Resources for a Thriving Bioeconomy*; UT-Battelle LLC.: Oak Ridge, TN, USA, 2016; Volume 1.
5. Hall, D.O. Biomass energy in industrialized countries-a view of the future. *For. Ecol. Manag.* **1997**, *91*, 17–45. [CrossRef]
6. Kartha, S.; Larson, E.D. *A Bioenergy Primer: Modernized Biomass Energy for Sustainable development*; United Nations Development Programme: New York, NY, USA, 2000.
7. Gelfand, I.; Sahajpal, R.; Zhang, X.S.; Izaurralde, R.C.; Gross, K.L.; Robertson, G.P. Sustainable bioenergy production from marginal lands in the US Midwest. *Nature* **2013**, *493*, 514–517. [CrossRef]

8. Hauk, S.; Knoke, T.; Wittkopf, S. Economic evaluation of short rotation coppice systems for energy from biomass—A review. *Renew. Sustain. Energy Rev.* **2014**, *29*, 435–448. [CrossRef]

9. Pereira, S.; Costa, M. Short rotation coppice for bioenergy: From biomass characterization to establishment—A review. *Renew. Sustain. Energy Rev.* **2017**, *74*, 1170–1180. [CrossRef]

10. Coleman, M.D.; Stanturf, J.A. Biomass feedstock production systems: Economic and environmental benefits. *Biomass Bioenergy* **2006**, *30*, 693–695. [CrossRef]

11. Zalesny, J.A.; Zalesny, R.S., Jr.; Coyle, D.R.; Hall, R.B. Growth and biomass of Populus irrigated with landfill leachate. *For. Ecol. Manag.* **2007**, *248*, 143–152. [CrossRef]

12. Kline, K.L.; Coleman, M.D. Woody energy crops in the southeastern United States: Two centuries of practitioner experience. *Biomass Bioenergy* **2010**, *34*, 1655–1666. [CrossRef]

13. Gonzalez, R.; Treasure, T.; Wright, J.; Saloni, D.; Phillips, R.; Abtb, R.; Jameel, H. Exploring the potential of eucalyptus for energy production in the Southern United States: Financial analysis of delivered biomass. Part I. *Biomass Bioenergy* **2011**, *35*, 755–766. [CrossRef]

14. Volk, T.A.; Abrahamson, L.P.; White, E.H.; Downing, M. Developing a Willow Biomass Crop Enterprise in the United States. In Proceedings of the IEA Task 17 Short-rotation Woody Crops Meeting, Auburn, GA, USA, 6–9 September 1999.

15. Dye, P.J. Estimating Water Use by Eucalyptus Grandis With the Penman-Monteith Equation. In Proceedings of the Vancouver Symposium of Forest Hydrology and Watershed Management; Swanson, R.H., Bernier, P.Y., Woodard, P.D., Eds.; IAHS Publication: Oxfordshire, UK, 1987; pp. 329–337.

16. Olbrich, B.W.; Le Roux, D.; Poulter, A.G.; Bond, W.J.; Stock, W.D. Variation in water use efficiency and δ 13C levels in Eucalyptus grandis clones. *J. Hydrol.* **1993**, *150*, 615–633. [CrossRef]

17. Soares, J.V.; Almeida, A.C. Modeling the water balance and soil water fluxes in a fast-growing Eucalyptus plantation in Brazil. *J. Hydrol.* **2001**, *253*, 130–147. [CrossRef]

18. Albaugh, J.M.; Dye, P.J.; King, J.S. Eucalyptus and water use in South Africa. *Int. J. Forestry Research.* **2013**, *2013*, 11. [CrossRef]

19. Flanagan, L.B.; Orchard, T.E.; Logieb, G.S.J.; Coburn, C.A.; Rood, S.B. Water use in a riparian cottonwood ecosystem: Eddy covariance measurements and scaling along a river corridor. *Agric. For. Meteorol.* **2017**, *232*, 332–348. [CrossRef]

20. Scott, D.F.; Lesch, W. Streamflow responses to afforestation with Eucalyptus grandis and Pinus patula and to felling in the Mokobulaan experimental catchments, South Africa. *J. Hydrol.* **1997**, *199*, 360–377. [CrossRef]

21. Morris, J.; Zhang, N.N.; Yang, Z.J.; Collopy, J.; Xu, D.P. Water use by fast-growing Eucalyptus urophylla plantations in southern China. *Tree Physiol.* **2004**, *24*, 1035–1044. [CrossRef]

22. Weih, M. Evidence for increased sensitivity to nutrient and water stress in a fast-growing hybrid willow compared with a natural willow clone. *Tree Physiol.* **2001**, *21*, 1141–1148. [CrossRef]

23. Zalesny, R.S., Jr.; Wiese, A.H.; Bauer, E.O.; Riemenschneider, D.E. Sap flux of hybrid poplar (Populus nigra L. P. maximowiczii A. Henry 'NM6') during phytoremediation of landfill leachate. *Biomass Bioenergy* **2006**, *30*, 784–793. [CrossRef]

24. Wieser, G.; Gruber, A.; Oberhuber, W. Sap flow characteristics and whole-tree water use of Pinus cembra across the treeline ecotone of the central Tyrolean. *Alps Eur. J. Forest. Res.* **2013**, *133*, 287–295. [CrossRef]

25. Hogg, E.H.; Hurdle, P.A. Sap flow in trembling aspen: Implications for stomatal responses to vapour pressure deficit. *Tree Physiol.* **1997**, *17*, 501–509. [CrossRef] [PubMed]

26. Nadezhdina, N.; Cermak, J.; Ceulemans, R. Radial patterns of sap flow in woody stems of dominant and understory species: Scaling errors associated with positioning of sensors. *Tree Physiol.* **2002**, *22*, 907–918. [CrossRef] [PubMed]

27. Wilson, K.B.; Hanson, P.J.; Mulholland, K.J.; Baldocchi, D.D.; Wullschleger, S.D. A comparison of methods for determining forest evapotranspiration and its components: Sap-flow, soil water budget, eddy covariance and catchment water balance. *Agric. For. Meteorol.* **2001**, *6*, 153–168. [CrossRef]

28. Deng, J.F.; Ding, G.D.; Gao, G.L.; Wu, B.; Zhang, Y.Q.; Qin, S.G.; Fan, W.H. The sap flow dynamics and response of Hedysarum scoparium to environmental factors in semiarid northwestern China. *PLoS ONE* **2015**, *10*, e0131683. [CrossRef] [PubMed]

29. Liu, X.; Zhang, B.; Zhuang, J.Y.; Han, C.; Zhai, L.; Zhao, W.R.; Zhang, J.C. The relationship between sap flow density and environmental factors in the Yangtze River delta region of China. *Forests* **2017**, *8*, 74. [CrossRef]

30. IPCC. Managing the Risks of Extreme Events and Disasters to Advance Climate Change Adaptation. In *Special Report of Working Groups I and II of the Intergovernmental Panel on Climate Change*; Field, C.B., Barros, V., Stocker, T.F., Qin, D., Eds.; Cambridge University Press: Cambridge, UK, 2012.

31. Lasch, P.; Kollas, C.; Rock, J.; Suckow, F. Potentials and impacts of short-rotation coppice plantation with aspen in Eastern Germany under conditions of climate change. *Reg. Environ. Change* **2010**, *10*, 83–94. [CrossRef]

32. Griffiths, N.A.; Rau, B.M.; Vaché, K.B.; Starr, G.; Bitew, M.M.; Aubrey, D.P.; Martin, J.A.; Benton, E.; Jackson, C.R. Environmental effects of short-rotation woody crops for bioenergy: What is and isn't known. *GCB Bioenergy* **2019**, *11*, 554–572. [CrossRef]

33. Granier, A. Une nouvelle méthode pour la mesure de flux de sève brute dans le tronc des arbres. *Ann. For. Sci.* **1985**, *42*, 193–200. [CrossRef]

34. Murray, F.W. On the computation of saturation vapor pressure. *J. Appl. Meteorol.* **1967**, *6*, 203–204. [CrossRef]

35. Schaeffer, S.M.; Williams, D.G.; Goodrich, D.C. Transpiration of cottonwood/willow forest estimated from sap flux. *Agric. For. Meteorol.* **2000**, *105*, 257–270. [CrossRef]

36. Forrester, J.W. System dynamics—The next fifty years. *Syst. Dyn. Rev.* **2007**, *23*, 359–370. [CrossRef]

37. Ouyang, Y.; Zhang, J.E.; Lin, D.; Liu, G.D. A STELLA model for the estimation of atrazine runoff, leaching, adsorption, and degradation from an agricultural land. *J. Soils Sediments* **2010**, *10*, 263–271. [CrossRef]

38. Ouyang, Y.; Leininger, T.D.; Hatten, J.; Parajuli, P. A STELLA model to estimate soil CO_2 emissions from a short-rotation woody crop. *Water Air Soil Pollut.* **2012**, *224*, 1392. [CrossRef]

39. Ouyang, Y.; Zhang, J.E.; Leininger, T.D.; Frey, B. A STELLA model to estimate water and nitrogen dynamics in a short-rotation woody crop plantation. *J. Environ. Qual.* **2015**, *44*, 200–209. [CrossRef] [PubMed]

40. Taebi, A.; Mansy, H.A. Time-Frequency Distribution of Seismocardiographic Signals: A Comparative Study. *Bioengineering* **2017**, *4*, 32. [CrossRef]

41. Nash, J.E.; Sutcliffe, J.V. River flow forecasting through conceptual models part I—A discussion of principles. *J. Hydrol.* **1970**, *10*, 282–290. [CrossRef]

42. Samuelson, L.J.; Stokes, T.A.; Coleman, M.D. Influence of irrigation and fertilization on transpiration and hydraulic properties of Populus deltoides. *Tree Physiol.* **2007**, *27*, 765–774. [CrossRef]

43. Yuan, W.; Zheng, Y.; Piao, S.; Ciais, P.; Lombardozzi, D.L.; Wang, Y.-P.; Ryu, Y.; Chen, G.; Dong, W.; Hu, Z.; et al. Increased atmospheric vapor pressure deficit reduces global vegetation growth. *Sci. Adv.* **2019**, *5*, eaax1396. [CrossRef]

Climate Drivers and Sources of Sediment and Organic Matter Fluxes in Intermittent Rivers and Ephemeral Streams (IRES) of a Subtropical Watershed, USA

Janet Dewey [1],*, Jeff Hatten [2] , **Byoungkoo Choi [3], Clay Mangum [4] and Ying Ouyang [5]**

[1] Geology and Geophysics Dept. 3006, University of Wyoming, 1000 E. University Ave, Laramie, WY 82071, USA
[2] Forest Engineering, Resources & Management, Oregon State University, 280 Peavy Hall, Corvallis, OR 97333, USA; Jeff.Hatten@oregonstate.edu
[3] Department of Forest Environment Protection, Kangwon National University, Chuncheon 200-701, Korea; bkchoi@kangwon.ac.kr
[4] Weyerhaeuser NR Company, 406 Cole Rd., Hattiesburg, MS 39402, USA; clay.mangum2@weyerhaeuser.com
[5] USDA Forest Service, 775 Stone Blvd., Thompson Hall, MS 39762, USA; ying.ouyang@usda.gov
* Correspondence: jdewey2@uwyo.edu; Tel.: +1-307-223-2265

Abstract: Climate-driven hydrological models rarely incorporate intermittent rivers and ephemeral streams (IRES) due to monitoring difficulties and their perceived minor effect on river networks. Worldwide, IRES represent approximately 50% of river networks and up to 60% of annual flow and are recognized as conduits and processors of organic matter (OM). Climate induced changes in precipitation and discharge (Q) may impact OM fluxes from IRES. We assessed storm-driven source and flux of total suspended solids (TSS) and OM from small IRES in Mississippi, USA. We used linear Pearson correlations to evaluate relationships between water and storm characteristics (e.g., discharge). Stepwise regression was used to predict change in flux. Dissolved OM was derived from saturated flow through soil whereas particulate OM was derived from channel extension during storms. A power log relationship between Q and materials flux indicated that Q was the driver for flux. A 5% increase in Q within IRES may result in flux increase of 2% TSS and 1.7–2.8% OM. Climate change projections of increased storm intensity over a shorter water year will increase channel extension and soil water transfer resulting in higher material flux to downstream reaches. Climate-driven hydrological models of OM flux should incorporate IRES.

Keywords: climate change; IRES; OM; DOC; POC; ephemeral stream; event sampling; headwaters

1. Introduction

Intermittent rivers and ephemeral streams (IRES) have long been perceived as peripheral in their effect on river networks because they only flow in response to rainfall [1,2]. It has been estimated that headwater IRES account for 60% of total mean annual flow (for streams and rivers in the northeastern US) [3] and approximately 50% of the world's total river networks [4]. Intermittent rivers and ephemeral streams drain and connect with much of the Earth's critical zone, so they have considerable potential to release, transport, transform, or sequester organic matter (OM) (e.g., [5,6]); this, in turn, can be released into the atmosphere in the form of CO_2 [7,8]. Approximately 36% of the CO_2 outgassed by river networks can be attributed into headwater streams [8]. Climate change can affect the timing, duration, frequency, and severity of storm events—all of which have the potential to control sediment and OM exports from IRES [9].

Organic matter is a transport vehicle for nutrients, carbon, and pollutants, all of which regulate or impact biological processes [10,11]. Production, transport, degradation, preservation, and sorption of OM are influenced by complex biological, chemical, and hydrological interactions [11–13]. Increases in temperature, precipitation, discharge, and groundwater connectivity associated with climate change may accelerate chemical and physical processes governing OM dynamics [14–19]. Therefore, understanding the source–transport–transform–sink behavior of OM in ephemeral streams (ES) is critical to predicting how OM will affect downstream processes and water quality.

Ephemeral streams function as collection sites for organic inputs and typically flow in response to storm events as infiltration excess [20] or saturated excess [21] overland flow with little or no connectivity to the water table (e.g., Table 1 in Reference [22]). Episodic connectivity during precipitation and flow pulses permits transport of OM, including dissolved and particulate C, to downstream perennial reaches. Storms are important drivers for material flux in headwaters; approximately 90% of dissolved and particulate material in headwater streams is exported during storm events [23]. This flux occurs disproportionately during high flow and is often a power function of the discharge rate [24–26]. Ephemeral streams have been poorly studied in comparison to their intermittent and perennial counterparts with regard to nutrient and energy fluxes due to the fact of their measurement difficulties and rapid discharge (i.e., "flashy behavior").

Recent research suggests that in-channel processing of OC within small inland watersheds is a regionally important source of atmospheric CO_2 [7,8,27]. Frequent wetting and drying cycles that occur in ephemeral streams provide "hot moments" [28] for dissolved organic matter (DOM) production, transformation, and transport. A number of studies have shown that oscillation between wet and dry stream conditions facilitates dissolved organic carbon (DOC) processing (e.g., [29–31]) and CO_2 evasion [32]; therefore, even very small ephemeral streams may be key components of C cycling in riverine systems [33].

Current climate change scenarios predict an increase in the frequency of droughts and high magnitude storm events in the southeastern United States even if mean annual precipitation (MAP) does not change [34]. Predicted changes in frequency [35] and severity of precipitation [36] may increase effective sediment and OC transport processes [37–39]. Equally, the dry component of the wet–dry cycle of ephemeral streams will increase both spatially and temporally as temperatures rise [32] thereby increasing DOM production [40]. Much of the research on streams that exhibit wet–dry cycles has focused on arid and semi-arid regions [41] and neglected ephemeral streams in humid climates. Therefore, understanding the behavior of C in temporary streams of humid ephemeral source areas is important for understanding the contributions of those source areas to C dynamics in general and under accelerated transport efficiency as predicted by some climate change scenarios. Our research was guided by two questions: (1) what are the sources of sediment and OM in IRES and (2) what are the controls on the flux of sediment and OM from very small (<4 ha) IRES to downstream reaches? We used chemical characteristics to determine the source and behavior of OM during storm events within small ephemeral catchments and tracked the behavior of potential exports during storm events. We discuss the implications of our study in the context of climate change.

2. Materials and Methods

2.1. Study Design

We studied a 32 ha watershed (33°30′49.00″ N, 89°25′40.00″ W) within the Upper Gulf Coastal Plain in Webster County, Mississippi. The site has a humid subtropical climate with a mean temperature ranging from 7 °C in winter to 26 °C in summer (US National Weather Service Station #222896, Eupora, MS, USA). The 30 year mean annual precipitation is 1451 mm, much of which falls during winter and spring. Annual discharge is 240×10^3 m^3 year^{-1} [42]. Soils are well- to moderately well-drained Sweatman series: US Department of Agriculture (USDA) taxonomy = fine, mixed, semiactive, thermic Typic Hapludult; World Reference Base (WRB) taxonomy = Profondic Alisol. Soils are high in clay

with A-horizons of either loam or silt loam; pH ranges from 4.5 to 5.5. Slopes are steep, soils are erodible, and dominant land use is woodland [43]. Forest vegetation is characteristic of the southeastern Mixed Forest Province and consists of even-aged loblolly pine (*Pinus taeda* Linnaeus) with a smaller component of mixed hardwoods; a detailed description is provided in Reference [44]. The site has been in pine timber production for 30 years.

Four small ephemeral catchments, nested within a perennial stream watershed (Figure 1), were monitored for dissolved and particulate contributions to downstream water. We used the following field criteria [22] to classify streams: (1) weakly defined channels; (2) interrupted flow, most of which was in response to storms; (3) a water table below the channel surface for most of the year; (4) lacking in aquatic insects; (5) lacking in obvious material transport; (6) scoured beds; and (7) intermittent organic buildup. Ephemeral streams were mapped as depressions by the US Geological survey (1983). We classified the streams as ephemeral based on the aforementioned criteria, recognizing that the boundary between ephemeral and intermittent classification is approximate. Our major focus in this study was on the ephemeral streams (ES) of the IRES.
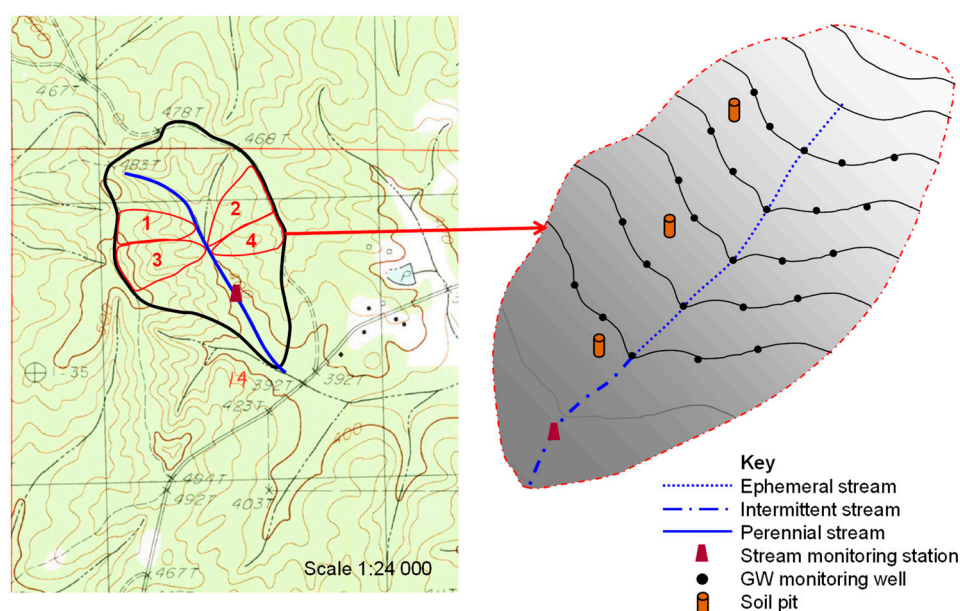
Figure 1. Schematic project layout depicting monitored ephemeral catchments in the study watershed. Numbers 1–4 correspond to the named ephemeral 1–4 watersheds described in this study. Topographic base excerpt are from the Little Sand Creek, Mississippi quadrangle [45].

For monitoring purposes, we defined the upstream limits of the ES segments by the upslope limit of channel development; downstream limits were defined by evidence of a clearly defined channel, over bank deposits, and seasonal streamflow [44]. All monitored ES lacked evidence of a persistent intermittent segment: the ES conducted surface water directly to the perennial stream and flowed in response to storm events. However, storm events in this region occurred frequently enough that steady-state flow (hereafter referred to as base flow) was periodically observed at the downslope limits of the channels. The ES watershed size ranged from 1.8 to 3.8 ha; the remainder (20.6 ha) comprised a mix of uncut and recently cut forest (Table 1) which had recovered for two years prior to monitoring for this study. Soil disturbance and forest cover were not a focus of this paper but are described as a frame of reference for interpreting OM dynamics in the watersheds. Ephemeral channels differed in their forest cover (Table 1 and described in References [44,46]) and were chosen to represent a continuum of soil disturbance and forest cover that may influence OM dynamics.

Table 1. Watershed characteristics and sampling record.

Watershed	Watershed Size (ha)	Stream Length (m)	Harvest Treatment	Length of Q Record (months)	Total Q ($\times 10^3$ m^3 year^{-1})	Storm Flow Samples	Base Flow Samples
Ephemeral 1	2.4	78	* Reference	14.9	27.13	67	14
Ephemeral 2	3.6	83	† BMP2	14.8	5.49	82	21
Ephemeral 3	3.8	92	‡ BMP1	14.0	27.79	14	6
Ephemeral 4	1.8	81	§ CC	15.3	4.99	40	10
Ungaged Ephemeral	20.6	-	-	-	-	-	-
Ephemeral Average					173.51		
Perennial	32.2	-	-		239.91	30	30

Total Q was calculated from all Q measurements across the entire length of the record. * Reference site at which no harvesting has occurred since 1978. † Riparian buffer in which logging debris was not permitted in the ephemeral drainage channel. ‡ Riparian buffer in which logging debris was permitted in the ephemeral drainage channel. § Clearcut with all merchantable timber removed and no riparian buffer.

2.2. Field Sampling

Ephemeral streams (Figure 2) were equipped with stations to monitor stream flow and collect event samples over 17 months (17 February 2010 to 13 July 2011). A 1.8 m long, 254 mm diameter PVC pipe was installed at the outlet of each ephemeral watershed to constrain flow within a measurable cross-sectional area. Water depth, velocity, and discharge within pipes were measured by area velocity sensors controlled by flow loggers (ISCO Inc., Lincoln, NE, USA) programmed to record at 15 min intervals. Discrete water samplers (ISCO Inc., Lincoln, NE, USA) were linked to flow loggers and programmed to start collecting samples on the rising limb of each event. Event sampling was triggered by a 20 mm increase in flow depth in the pipe over a 15 min interval. Discrete samplers were programmed to cease sampling as velocity and/or depth reverted to pre-event levels. Flow was variable among streams and events, so the number and timing of sampled storm events differed among streams. Steady-state base-flow samples were hand-collected from pipe outflow when possible.

Figure 2. Left: Gauged reference stream with a 254 mm diameter pipe, ISCO sampler, and flowmeter. **Right**: Ephemeral stream flowing during storm event.

The perennial stream monitoring station was located 200–300 m downstream from ephemeral monitoring stations. Perennial stream stage was measured with a pressure transducer (In-Situ Level TROLL 300) inside a stilling well (91.8 cm tall, 152 mm diameter). Velocity was measured using a portable flowmeter (Hach Company, Loveland, CO, USA). Discharge was determined using a stage-discharge rating curve, developed from 15 measurements of stream profile, stage, and velocity measurements across a range of flows. The perennial stream was equipped with an area velocity sensor and a discrete sampler which was programmed to initiate sampling in the event of increased depth and/or flow. Base-flow samples were hand-collected during field visits when discharge was at steady state.

Groundwater, precipitation, canopy throughfall, and soil pore-water samples were used to characterize potential source contributions to streamflow. Groundwater was sampled in ephemeral watersheds via a grid of wells arranged in five transects perpendicular to the stream channel; each transect contained five wells spaced at 5 m intervals. Wells were made of 5 cm inner diameter PVC pipe and screened the entire subsurface interval. Wells penetrated to a depth of 2.5 m or until refusal. Well water was sampled monthly using a bailer with a check ball after purging wells. Depth of sampling for the groundwater source varied depending upon well and time period [44,46]. Regional precipitation data (15 min interval) for the period 10 February 2010 to 30 May 2010 were acquired from the Eupora 2E, MS, US (33.56° N, 89.24° W) National Oceanographic and Atmospheric Administration (NOAA) weather station [47]. Onsite precipitation data were collected for the period 30 May 2010 through 13 July 2011 using a tipping bucket rain gauge (ISCO Inc., Lincoln, NE, USA) installed in an open area of the watershed. Precipitation and canopy throughfall were sampled using acid-washed plastic 18.9 L buckets with nylon window screens over the top to prevent contamination by fallen debris. Zero-tension lysimeters collected soil pore water four times during the spring of 2011 at three depths within the soil profile (O, A−10 cm, and A−20 cm). O, A, B, and C soil horizons were sampled from soil pits at representative locations (Figure 1).

2.3. Sample Analysis

We examined the source and flux of water and OM. The flux of OM from IRES is partially controlled by the concentration of the material in the water, which is strongly controlled by source. To understand how climate change will affect the flux of the materials, we must understand the source and mobilization processes of OM.

Water samples were fractionated in the lab into dissolved and particulate components. Samples were filtered to collect particulate matter (PM) through 0.7 μm glass fiber filters (GFFs) that were pre-combusted for 4 h at 350 °C to remove organics. The PM-laden filters were oven-dried overnight at 60 °C and weighed for total suspended solid (TSS) concentration. Filtrate was collected and frozen for analysis of dissolved constituents. Soils and suspended sediment were analyzed for total C and N. Soils were dried overnight at 70 °C, ground to pass a 60 mesh sieve, and dried again prior to analysis. Dried, sediment-laden GFFs were subsampled using a single-hole-punch tool. Samples were analyzed for total organic carbon (OC) and N by flash combustion elemental analyzer (Costech ECS 4010, Valencia, CA, USA). Molar ratios are used where N:C data are presented. Particulate organic carbon (POC) concentration (mg L^{-1}) was calculated as: POC (mg L^{-1}) = g of carbon (from NC analysis)/(area of filter subsampled (cm^2)/area of whole filter (cm^2)). The OC concentration of sediment was calculated as: %OC = POC (mg L^{-1}) / TSS (mg L^{-1}) * 100.

Filtrate was analyzed for chloride (Cl$^-$), nitrite (NO$_2^-$), nitrate (NO$_3^-$), and ammonium (NH$_4^+$) by ion chromatography (Dionex DX−500, Sunnyvale, CA, USA). We measured ultraviolet absorbance at 254 nm (UVA$_{254}$) using a BioMate3 spectrophotometer with a 1 cm cell in order to have a low-cost measurement to correlate with DOC and be able to convert dissolved organic carbon to specific UV absorbance (SUVA$_{254}$) which provides insight into the nature of the organic matter present (e.g., high SUVA$_{254}$ indicates dominance of humic matter and, thus, a soil origin for DOC). Total nitrogen (as TKN) was converted to ammonium cation by sulfuric acid digestion with mercuric oxide catalysis in a microwave digester (MARS X Press, CEM, Matthews, NC, USA). Samples were digested for one hour with a 15 min ramp time and 45 min hold time at 200 °C and analyzed for TKN by salicylate method on a Technicon Autoanalyzer III wet chemistry analyzer (Bran + Luebbe, Norderstedt, Germany). Dissolved inorganic nitrogen (DIN) was determined as sum of nitrite-N (NO$_2$-N), nitrate-N (NO$_3$-N), and ammonium-N (NH$_4$-N). Dissolved organic nitrogen (DON) was calculated as total N minus DIN. We used DON:DOC and PON:POC (rather than the more commonly used DOC:DON and POC:PON) herein because it is statistically more robust due to the higher number (%OC) in the denominator.

Filtered, frozen water, suspended sediment, and soils were sent to the UC Davis Stable Isotope Facility and analyzed within 2 months of sample collection. Dried soils needed no preservation;

water samples were preserved by filtering with a 0.2 micron filter and frozen according to UC Davis standard operating procedures. Water was analyzed for DOC and DOC δ^{13}C PDB using an OI Analytical model 1030 TOC Analyzer (OI analytical, College Station, TX) interfaced to a PDZ Europa 20–20 Isotope Ratio Mass Spectrometer (Sercon Ltd., Cheshire, UK) with a GD−100 gas trap interface (Graden Instruments). Stable isotopic composition of particulate organic carbon (POC; δ^{13}C) and particulate organic nitrogen (PON; δ^{15}N) were determined by flash-combustion elemental analysis coupled with isotope-ratio mass spectrometry (EA-IRMS; Elementar Analysensysteme GmbH, Hanau, Germany) interfaced to a PDZ Europa 20–20 isotope ratio mass spectrometer (Sercon Ltd., Cheshire, UK). Isotopic data for C and N were reported in standard delta notation (‰ per mil) relative to Pee Dee Belemnite (PDB) and air standards, respectively. Standard reference materials covering a range of ^{13}C and ^{15}N signatures were used to evaluate precision and accuracy of mass spectrometer response; analytical precision for δ^{13}C of DOC was 0.4‰; precision for δ^{13}C and δ^{15}N was tighter than 0.3‰.

2.4. Data Analysis

Average concentrations of measured stream water constituents were calculated for each gauged watershed for the length of the study. To determine the effect of storm-specific attributes on composition of dissolved and particulate material, individual flow events were delineated by the change in discharge. The beginning of an event within ES was defined as (1) any discharge >0.002 m^3 s^{-1} or (2) rate of change in discharge >0.0002 m^3 s^{-1} 15 min^{-1} or (3) start of flow. The beginning of an event within perennial streams was defined as any discharge >0.002 m^3 s^{-1}. Where there was a one-hour decline in discharge, followed by an increase in discharge, the event clock was reset, and a new event began. Linear Pearson correlations of log-transformed data were used to evaluate relationships between independent event variables and dependent surface water concentrations and characteristics. We chose event variables that were likely to affect the flux of sediment and OM within our watersheds. Independent event variables tested included: rate change in Q over time; water year date (number of days after 1 October (which was the beginning of the water year); time since flow began in hours; time since event initiation; and time before or after peak flow. Event variables are defined as: Precipitation = the amount of precipitation that fell in the previous 15 min; Q = instantaneous discharge at the time the sample was collected; PeakTime = time before or after peak flow; FlowTime = time since flow began in hours; RateChange = change in Q over time where positive values are on the rising limb and negative values are on the receding limb; EventTime = time since event initiation; WY Day = number of days after 1 October (beginning of water year). Stepwise multiple linear regression was used to explore relationships among event variables and surface water characteristics; data were log-transformed to meet assumptions of normality. The lm function in base R [48] was used to model constituent fluxes from independent event variables; step Akaike Information Criteria (stepAIC function) from the MASS package [49] was used to optimize the size of the model. Herein, we report the standardized coefficients with adjusted R^2 and whole-model *p*-values for purposes of examining the relationships among variables as well as the coefficients and equation used to develop predictive calculations. All estimates of mass fluxes were calculated using instantaneous flow-weighted averages across all storms and streams of within-event measurements.

3. Results and Discussion

3.1. Physical and Chemical Attributes

Over the 17 month study period, 16 events generated discharge in one or more streams (Table 2). Precipitation was monitored for 12 months (May 2010 through May 2011; Figure 2) and ranged from 21–110 mm per event with a mean of 55 mm. The maximum precipitation rate occurred at the onset of an event and ranged from 10–72 mm h^{-1} with a mean of 36 mm h^{-1}. Precipitation between January and May accounted for 53% of the annual total and 94% of the discharge events over 15 months. Event duration ranged from 1.0 h to 22.3 h with a mean of 8.0 h. Precipitation events triggered 233 flow

event samples ranging from a total of 14 to 82 samples per watershed per event (Table 1). Mean event discharge across all recorded events for ephemeral and perennial streams was 749 m^3 event^{-1} and 7324 m^3 event^{-1}, respectively.

Table 2. (A) Average instantaneous flow-weighted within-event values of selected dissolved and particulate stream water constituents across all sampling times. (B) Average values from potential sources.

(A)	Ephemeral 1	Ephemeral 2	Ephemeral 3	Ephemeral 4	Ephemeral Average	Perennial	Pr > Chi-Square
TSS (mg L^{-1})	342.6 ± 74.4	1713.0 ± 708.1	54.1 ± 14.8	154.7 ± 31.3	566.1 ± 386.9	101.1 ± 46.3	<0.0001
POC (mg L^{-1})	21.3 ± 11.0	8.06 ± 1.31	2.27 ± 0.43	5.54 ± 1.79	9.30 ± 4.18	3.46 ± 0.96	0.0004
DOC (mg L^{-1})	11.6 ± 1.9	13.54 ± 0.97	15.15 ± 0.97	17.73 ± 1.42	14.51 ± 1.29	5.83 ± 1.07	<0.0001
Cl (mg L^{-1})	1.89 ± 0.10	1.65 ± 0.07	1.69 ± 0.22	1.26 ± 0.11	1.62 ± 0.13	2.91 ± 0.14	<0.0001
UVA$_{254}$ (cm^{-1})	0.55 ± 0.03	0.47 ± 0.02	0.44 ± 0.05	0.76 ± 0.03	0.56 ± 0.07	0.19 ± 0.02	<0.0001
SUVA$_{254}$ (L mg^{-1} M^{-1})	4.1 ± 0.4	3.56 ± 0.13	3.51 ± 0.18	4.05 ± 0.17	3.79 ± 0.15	4.04 ± 0.49	0.992
DON:DOC	0.17 ± 0.06	0.11 ± 0.03	0.10 ± 0.02	0.04 ± 0.01	0.11 ± 0.03	0.30 ± 0.08	0.0003
DOC-δ^{13}C	−27.20 ± 2.15	−28.50 ± 0.09	−28.90 ± 0.12	−28.80 ± 0.16	−28.30 ± 0.39	−28.60 ± 0.16	0.4865
%OC	4.6 ± 0.5	2.9 ± 0.2	3.8 ± 0.4	4.9 ± 0.7	4.0 ± 0.5	5.3 ± 0.5	0.0012
POC:DOC	1.69 ± 1.24	0.88 ± 0.45	0.15 ± 0.02	0.26 ± 0.09	0.75 ± 0.35	0.67 ± 0.23	0.0470
PON:POC	0.08 ± 0.00	0.08 ± 0.00	0.10 ± 0.01	0.09 ± 0.00	0.09 ± 0.01	0.08 ± 0.00	0.6116
POC-δ^{13}C	−25.10 ± 2.63	−27.47 ± 0.29	−27.58 ± 0.32	−27.31 ± 0.31	−26.86 ± 0.59	−27.66 ± 0.21	0.3550
PON-δ^{15}N	0.91 ± 0.46	0.70 ± 0.25	2.05 ± 0.4	1.83 ± 0.69	1.37 ± 0.33	1.00 ± 0.63	0.7762

(B)	Precipitation	Throughfall	O-horizon	Mineral Soil	Ground Water		
DOC (mg L^{-1})	3.48 ± 1.56	21.82 ± 6.34	26.73 ± 3.43	11.6 ± 1.96	2.8 ± 0.32		
Cl (mg L^{-1})	0.82 ± 0.07	2.05 ± 0.28	1.91 ± 0.57	2.23 ± 0.4	3.52 ± 0.21		
UVA$_{254}$ (cm^{-1})	0.04 ± 0.02	0.44 ± 0.07	1.3 ± 0.04	0.5 ± 0.4	0.13 ± 0.02		
SUVA$_{254}$ (L mg^{-1} M^{-1})	1.39 ± 0.34	2.94 ± 0.30	5.09 ± 0.64	4.78 ± 0.51	8.21 ± 2.25		
DON:DOC	0.36 ± 0.05	0.07 ± 0.01	0.16 ± 0.03	0.04 ± 0.00	0.28 ± 0.03		
DOC-δ^{13}C	−26.60 ± 0.35	−29.40 ± 0.30	−30.3 ± 0.03	−28.7 ± 0.53	−28.2 ± 0.18		

Values are the mean ± standard error. Stream water values are the means of the base flow and event flow. The O-horizon and mineral soil values are from lysimeter solutions. %OC is the % of OC in sediment by mass. The *p*-values are from Mann–Whitney U tests between perennial and ephemeral streams.

Particulate constituent concentrations among ES were highly variable (Table 2-A). The TSS concentration ranged from 54.1 mg L^{-1} to 1713.0 mg L^{-1}, and POC concentrations ranged from 2.27 mg L^{-1} to 21.33 mg L^{-1}. Average ES TSS (566.1 mg L^{-1}; instantaneous flow-weighted average across all streams and storms of within-event measurements; from Table 2) was higher than that of the perennial stream (101.1 mg L^{-1}) by a factor of 5.6; thus, it appears that the perennial stream was a sink for suspended solids. Average ES POC concentration (9.30 mg L^{-1}) was higher than that of the perennial stream (3.46 mg L^{-1}) by a factor of 2.7.

Dissolved constituent values DOC, Cl, UVA$_{254}$, and specific UV absorbance at 254 nm (SUVA$_{254}$) were consistent among ES (Table 2-A). The UVA$_{254}$ of ES was consistently higher than that of the perennial stream, probably due to the average DOC being (14.51 mg L^{-1}) 2.5 times higher than that of the perennial stream (5.83 mg L^{-1}). The SUVA$_{254}$, on the other hand, was similar among perennial and ES. The ES Cl concentration was consistently lower than that of the perennial stream indicating that the perennial stream acquired Cl from another source(s).

We quantified concentrations of five potential source contributors to surface waters: precipitation, canopy throughfall, O-horizon soil leachate, mineral soil leachate, and groundwater (Table 2). The DOC concentration increased from precipitation through the canopy as throughfall and O-horizon leachate then declined through the soil profile reaching a minimum in the groundwater samples suggesting that it was removed or diluted with depth. The Cl concentrations generally increased from the canopy through the soil and into the groundwater. The Cl concentration of ephemeral event water was similar to that of canopy throughfall and O-horizon soil, whereas the Cl concentration in perennial event water was most similar to that of mineral soil leachate and groundwater. There was a strong linear correlation (Pearson's R = 0.923, *p* < 0.001) between UVA$_{254}$ absorbance and DOC concentration, explaining the similar pattern between UVA$_{254}$ and DOC. The UVA$_{254}$ in precipitation was low but increased as

water passed through the forest canopy. Highest UVA$_{254}$ levels were observed in O-horizon leachates; UVA$_{254}$ decreased with depth as water passed through the soil profile. Mean UVA$_{254}$ in ES water (0.56) was nearly three times that of perennial stream water (0.19) suggesting that C was lost or diluted during transport. The ratio of DON:DOC was highest in precipitation and groundwater and reached minimums in throughfall and mineral soil leachate while being relatively high in the O-horizon. Organic horizon water had the most depleted DOC-δ^{13}C, and there was a steady enrichment with soil depth (O, A, to groundwater). The DON:DOC had a relatively small standard error among potential sources and, hence, is probably a good tracer of DOM in stream water. On the other hand, the stable isotopic composition of DOC varied <2‰ among stream water and <4‰ among potential sources; therefore, DOC is indistinguishable from potential sources using stable isotopic signature alone (Table 2). Ephemeral stream DON:DOC and %OC was consistently lower than that of the perennial stream and most closely resembled that of O-horizon leachate, except within the disturbed clear-cut site in which DON:DOC resembled that of mineral soil. Perennial stream DON:DOC was similar to that of groundwater and precipitation. The POC:DOC was similar for ES and perennial stream waters; however, %OC of the perennial stream was significantly higher ($p = 0.002$) than that of ES. Mean ES PON-δ^{15}N was 1.4 (ranged 0.9 to 2.0) as compared to 1.0 in perennial stream water (Table 2). The PON:POC was similar among streams.

We calculated the area-weighted average instantaneous flux for all storms over the water year. Instantaneous flux is the flow-weighted flux at a given time within an event; thus, instantaneous flux could represent a point on the rising limb, peak flow, or the receding limb of an event. Values represent the means for all events in which we were able to collect water samples and quantify Q with rating curves (Table 3). Average Q was higher in the perennial stream than in the ES (Table 1); however, area-weighted discharge (Unit Q) in the ES was more than twice that of the downstream perennial stream (Table 3), even though the overall area was the same for the ES and perennial streams. Event sampling in ES was triggered by a 20 mm increase in flow over 15 min; thus, the Unit Q measurements only represent periods of high flow (storms) in the ES. There was higher Unit Q from the ES than at the downstream perennial stream gauge suggesting that some of the water discharged to the perennial stream was lost to groundwater before exiting the perennial stream gauge.

Table 3. Area-weighted average instantaneous flux of selected surface water constituents.

|		Unit Q		TSS		POC		PN		DOC		DON	
		($\times 10^3$ m^3 s^{-1} ha^{-1})		(g s^{-1} ha^{-1})									
A	Ephemeral	12.6	(26)	3432.1	(7285)	99.6	(307)	7.6	(18)	207.6	(589)	13.5	(41)
	Perennial	5.7	(9)	530.1	(1412)	21.8	(36)	2.1	(4)	96.3	(167)	4.5	(9)
B	Ephemeral	−5.7	(1.7)	−0.6	(2.1)	−4.1	(1.9)	−6.4	(1.8)	−3.5	(2.0)	−6.3	(2.1)
	Perennial	−7.6	(3.3)	−3.8	(3.6)	−6.3	(3.5)	−8.7	(3.4)	−5.0	(3.6)	−7.7	(3.1)

Means of unit Q and constituents were computed from within-event samples collected over an entire water year. Values in parentheses are one standard deviation of the mean. Some data were not normally distributed, so we present un-transformed data (A) and log-transformed data (B).

The ES exports were 2.0–6.5 times that of the perennial stream, depending upon the parameter (Table 3). Unit Q was higher for the ephemeral streams as a result of this value being calculated from the sample set from which the constituents were determined. The ephemeral catchments are very small—from 1.8–3.8 ha; yet during storms, their exports were significant which has implications for changes in storm events due to the climate forcing. Surface water, groundwater, and soil storage water are linked, so we used geochemical signatures from the stream exports and potential source areas in order to understand how the pools and fluxes might interact with changes in climate.

3.2. Source of OM in Surface Waters during Storms: Active and Contributing Areas

In order to get a better understanding of whether ephemeral and perennial stream waters were derived from similar source areas and were therefore connected during storm events, we compared the Cl and UVA_{254} of ephemeral and perennial stream event water to that of groundwater and soil leachate. Cl was used as a conservative tracer of potential contributors to stream water and UVA_{254} was used as a first-order evaluation of DOC inputs. We used UVA_{254} rather than DOC because of the strong linear correlation between the two in our data and because the larger UVA_{254} dataset gave us better control on variability. The UVA_{254} and Cl had a significant negative correlation ($R = -0.595$, $p < 0.001$) such that during an event, UVA_{254} was elevated and Cl concentration was depleted with respect to base flow conditions. The relationship between Cl and UVA_{254} amongst pools suggests that ES Cl and DOC are controlled by water routing through the soil profile, whereas the perennial stream is influenced by groundwater inputs.

We did not attempt to quantify the relative contributions of groundwater versus Horton- and Dunne-type overland flow; however, we used OM characteristics of ES and potential source areas to clarify from which pools ES water may have been derived (Figures 3 and 4). We did not attempt to trace N through the system; however, N and C cycling are coupled therefore we incorporated both components in source-attribution, and the ensuing discussion is framed in terms of OM. Ephemeral storm water DOC-δ^{13}C was intermediate between that of groundwater and soil solution dissolved OM with a DON:DOC composition close to that of soil solution and the *minimum* DON:DOC value (max N:C value) for groundwater (Figure 3).
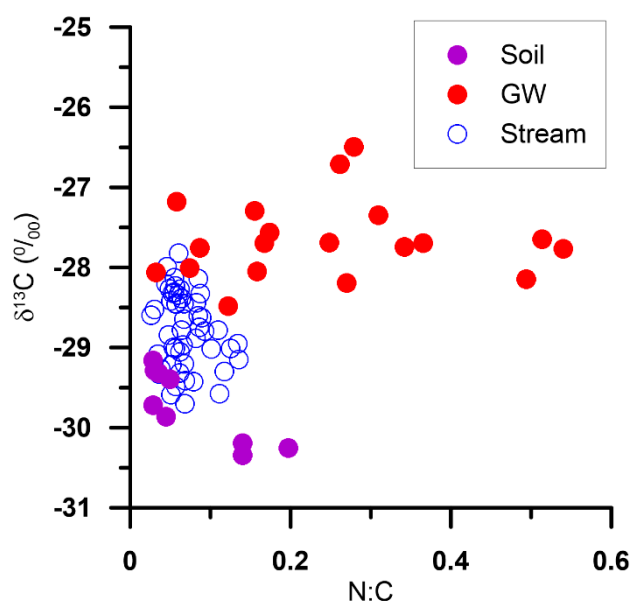

Figure 3. Relationship of N:C and δ^{13}C of DOM from groundwater, soil lysimeter, and ephemeral stream event water. Lysimeter samples were collected from below the litter layer, 10 cm into mineral soil, and 20 cm into mineral soil (undifferentiated in this plot).

A comparison between DOM and suspended sediment particulate organic matter (POM) of ES collected during storm events (Figure 4) illustrates the difference in source attributes for DOM and POM. Ephemeral stream DOM and suspended sediment POM clustered tightly in separate-δ^{13}C versus N:C mixing spaces: storm water plotted in a space that was close to intermediate soil dissolved OM values, whereas suspended sediment particulate DOM plotted closest to values of A- and B-horizon mineral soils (Figure 4a). Soil leachate values plotted close to that of O-horizon POM (and to a lesser extend A-horizon POM) suggesting that O-horizon soils were an accessible source for labile DOM during storm events. Workers have reported that as much as 66% of DOC in stormflow from

headwater streams originated as saturated flow through the uppermost soil horizons within the riparian zone [50]. Estimated contributions from the upper portions of the soil profile (for lowland riparian soils) represent 64–86% of DOC flux in some watersheds (e.g., [51]). High DOC values were attributed to a larger proportion of wetland soils (i.e., larger potential DOC pool) and larger watershed area [51]. Storm-derived ES POM was more closely related to A-horizon and to a lesser extent B-horizon soils (Figure 4a–c), which suggests that these soils are mobilized or reworked enough to release POM during storm events.
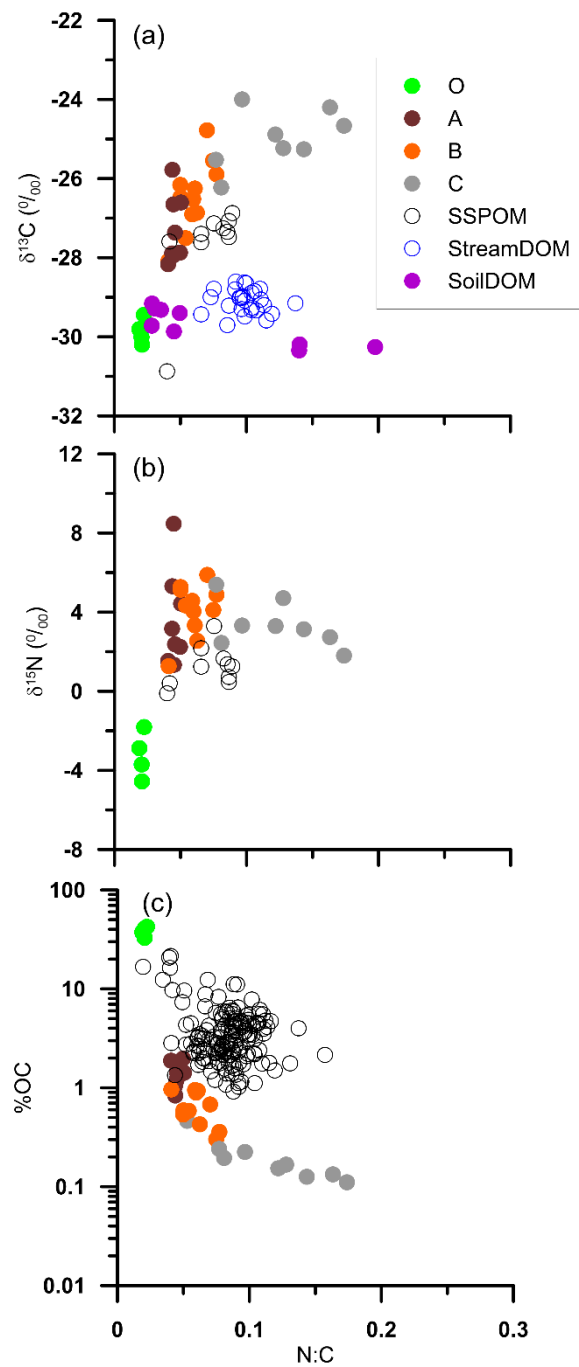
Figure 4. N:C versus (**a**) $\delta^{13}C$ of stream DOM, soil solution DOM, POM from soils (O, A, B, C horizons), suspended sediment (SSPOM); (**b**) $\delta^{15}N$; and (**c**) %OC by mass. Stream DOM and suspended sediment POM values are for ES event samples only. In Figure 5a, purple circles with lower N:C represent DOM from A-horizon lysimeters; purple circles with higher N:C represent DOM from O-horizon lysimeters.

3.3. Storm-Driven C Dynamics

Samples collected during storm events provided evidence that the ES interacted with the soil profile during rainfall events. The next question we wanted to answer was whether the source or proportion of sources changed within a storm event. We selected storm events for which there was sufficient data to construct plots illustrating the behavior of TSS and OM over the course of an event (Figure 5). The TSS concentrations in ES were highest at the start of an event before peak Q and declined as the event progressed (Figure 5a). Peak perennial stream TSS concentration lagged behind ES peak TSS and coincided with an initial increase in Q. The N:C of particulate material remained constant as ES TSS decreased throughout an event (Table 2 and Figure 5b), thus there is a separation of C-poor material and C-rich material as the event progresses. There is a weak trend of enrichment in δ^{13}C with event time (Figure 5c) which suggests a within-event shift in C to progressively deeper sources.
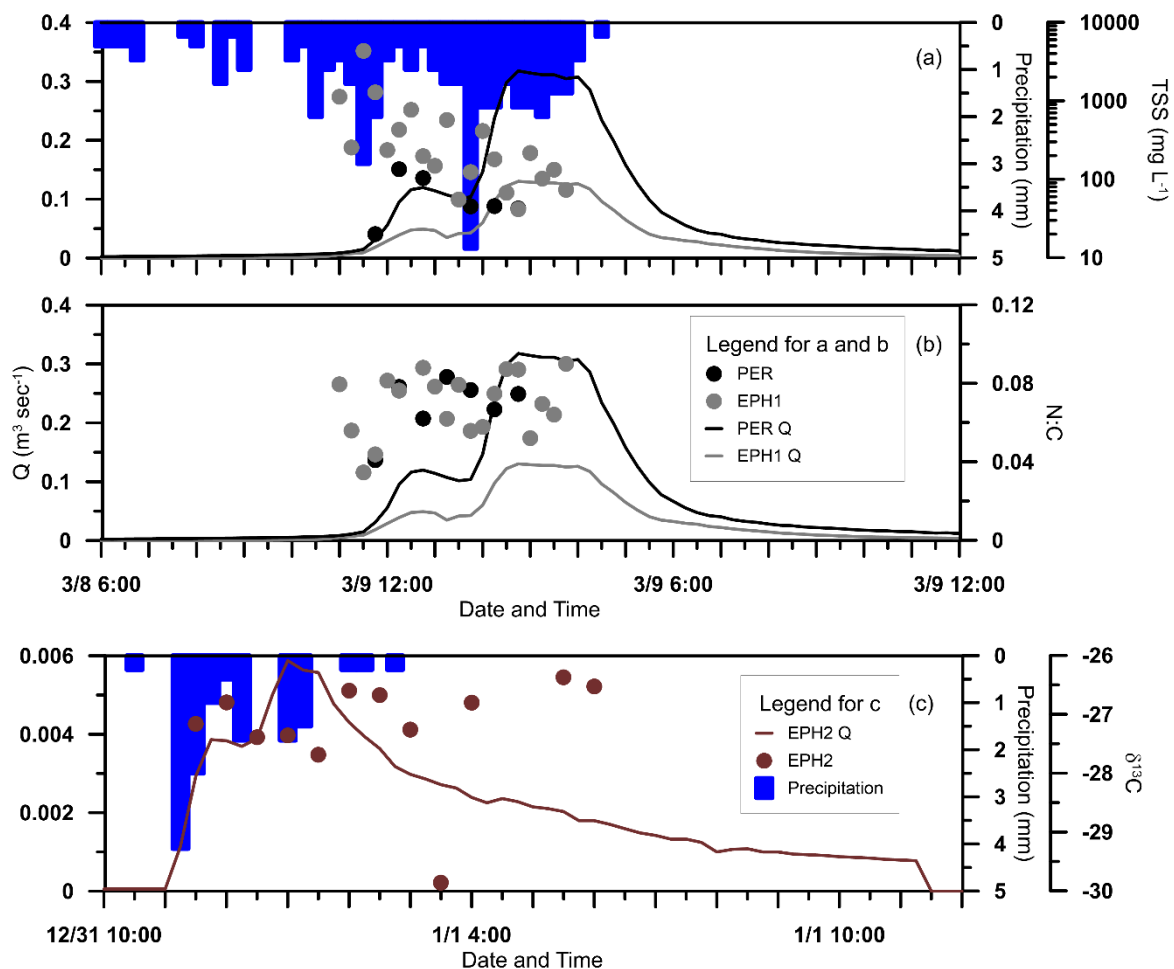
Figure 5. Representative behavior of suspended sediment and POC during selected storm events. Blue bars are precipitation amounts. Solid lines indicate within-storm Q. Circles indicate measured values of discrete samples. PER = perennial stream. EPH = ephemeral stream. (**a**) Suspended Sediment (**b**) N:C of POM in suspended sediment (**c**) Change in δ^{13}C of POM in suspended sediment. Sampling start and stop times were controlled by preset criteria (see methods) and thus do not span the time range from start of precipitation to return to base flow. The single anomalously low δ^{13}C value may be due to entrainment of a piece of fresh leaf litter.

We attempted to track the responses of UVA$_{254}$ (as a proxy for DOC) and Cl to storms in the perennial and ephemeral watersheds by constructing hysteresis plots from each of the 5 potential sources. In general, we found that the ES (31 December 2010, 30 April 2010, and 4 April 2011 storm

panels in Figure 6) had higher UVA$_{254}$ and lower Cl than the perennial stream (23 April 2010 storm panel). However, there were different trends among watersheds and storms.
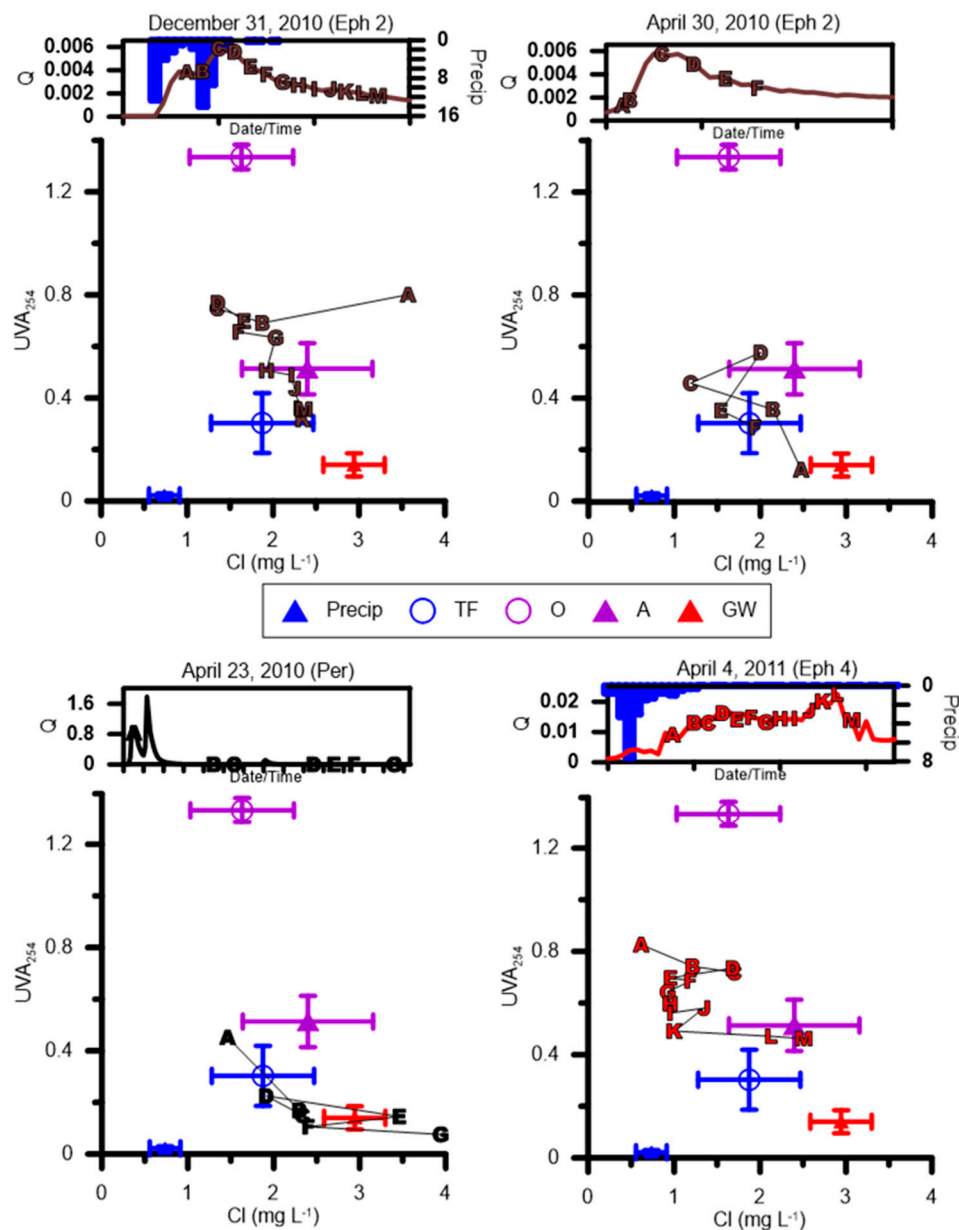
Figure 6. Selected (typical) responses of UVA$_{254}$ versus Cl concentration for several storms. The date of each event is listed above each pair of plots. Major ticks on the date/time axis of storm discharge plots are spaced every 3 h. The top plot of each pair includes a box inset with hydrographs (line representing Q with scale on left) and precipitation where available (bars with scale on right). Hydrographs are color-coded as to the catchment: brown = ephemeral 2; red = ephemeral 4; black = perennial. Precipitation data for April 23 and April 30 do not exist. Below the hydrograph insets, samples for a given event are plotted on a UVA versus Cl plot. Plots of UVA$_{254}$ versus Cl are in alphabetical order by time stamp of sample collection. Letters represent the time point when a sample was collected (in alphabetical order by time stamp of sample collection); corresponding letters on the hydrograph and the UVA–Cl plot are the same sample. Within the plot sample schema: solid blue triangles are precipitation (precip), unfilled blue circles are throughfall (TF), unfilled purples circles are O-horizon leachate (O), solid purple triangles are A horizon leachate (A), and solid red triangles are groundwater samples (GW) (see legend in the center of the figure). Sources are average ± 95% confidence intervals of samples collected throughout the entire study.

An early season storm (31 December 2010) showed what appears to be flushing of a high Cl and UVA$_{254}$ source that could be recently fallen litter. Cl concentration becomes diluted as the source of stream water shifted towards throughfall and then a mixture of O-horizon leachate and precipitation. The source then shifted towards throughfall and A-horizon leachate and eventually towards the groundwater source.

This pattern essentially repeats itself in a later season storm (30 April 2010) in the same watershed (ES2) without the flushing of recently fallen litter. For a late spring storm (4 April 2011) in ES4 (clearcut), there appears to be less influence from throughfall on the earliest storm samples, but the source of water eventually shifts through the soil and towards groundwater. The source of water from the perennial stream (23 April 2010) appears to be from deeper within the soil profile at the onset of a typical storm event relative to the ES. Eventually the source of water appears to be entirely derived from a groundwater source late in the event.

Differences in hysteresis at different times of the year suggest that there may be critical thresholds in some storm parameters that control both the source from which the sediment and OM are derived and the flux of sediment and OM within the system. Due to our sampling protocol, it is possible that the timing of our sampling in relation to the storm hydrograph varied with season; however, our sampling procedure was designed to eliminate as much bias as possible. We compared surface water characteristics to seven event variables related to storms: discharge, peak time, flow time, rate of change, event time, water year day, and precipitation (Table 4) to glean which event variables exerted the greatest control over surface water concentrations and fluxes in ES and perennial streams. Where distributions were not normal, we log-transformed the data. Data presented are those that were significant predictors of constituent flux. The larger the value, the greater the control. The sign determines whether the event variable was negatively or positively associated with the dependent variable.

Table 4. Significance of relationships among event variables and selected surface water characteristics of ephemeral streams (ES) and the perennial stream (PER).

		Precipitation		Q		Peak Time		Flow Time		Rate Change		Event Time		WY Day		R^2
		SC	SE	SC	SE	SC	SE	SC	SE	SC	SE	SC	SE	SC	SE	
TSS	ES	0.300	0.051	1.014	0.115	0.049	0.126	−0.005	0.131	0.065	0.066	−0.209	0.064	0.225	0.057	0.664
	PER	−0.205	0.073	0.468	0.142					0.144	0.065					0.684
POC	ES	0.225	0.044	0.674	0.097			−0.130	0.054			−0.106	0.072	0.111	0.049	0.777
	PER	−0.171	0.052	0.465	0.102					0.117	0.047					0.788
PN	ES	0.248	0.042	0.645	0.080			−0.129	0.047					0.174	0.108	0.805
	PER	−0.329	0.092	0.801	0.179					0.184	0.082					0.796
DOC	ES	0.043	0.032	1.307	0.166	0.324	0.136	−0.291	0.086			−0.179	0.076	−0.117	0.069	0.909
	PER			1.189	0.422											0.581

Standardized coefficients (SCs) and standard error (SE) of predictors that were selected through AIC and stepwise procedures. Dependent variables: Precipitation = amount of precipitation that fell in the previous 15 min; Q = instantaneous discharge at the time the sample was collected; PeakTime = time before or after peak flow; FlowTime = time since flow began in hours; RateChange = change in Q over time where positive values are on the rising limb and negative values are on the receding limb; EventTime = time since event initiation; WY Day = # of days after 1 October (beginning of water year). Q, TSS, POC, PN, and DOC were all log-transformed to meet assumptions of normality.

As expected, Q and precipitation exerted the greatest control on TSS and OM for both streams. Precipitation is interesting in that all of the measured exports of ES increased with increasing precipitation, whereas the reverse was true in the perennial stream either as a result of dilution of exports as they reached the perennial stream or reduced carrying capacity in the perennial stream, or both. An increase in DOC with increasing precipitation and Q has been reported in other headwater studies (e.g., [26]). Rate Change, which is tied to the shape of the hydrograph (i.e., flashy behavior equates to a more rapid rate of change), was a significant predictor for TSS, POC, and PN in the perennial stream, but was weakly correlated to TSS in the ES. The other independent variables, PeakTime, FlowTime, EventTime, and WY DAY, were significant only for ES. Dependent variables decreased with increasing FlowTime and EventTime, which suggests that there was a pool of sediment, DOM, and POM which was accessed early in an event and became depleted over time. The positive

correlation with WY DAY for all dependent variables indicates that the time at which the pools were accessed may be significant in terms of interpreting potential responses to climate change. We recognize that WY DAY likely has a sinusoidal relationship and, thus, may not be a good predictor; however, we explored the use of sin transformation and it did not improve R^2.

3.4. The Water Year

There is a growing body of evidence that the seasonal component to OM pools and fluxes in headwater streams (e.g., [24]) is linked to the wet–dry cycles that are prevalent in IRES and affects the quality and quantity of OM exports from IRES (e.g., [26,30,52,53]). If that is the case, then there should be a relationship between flux and timing within the water year, as the watershed transitions from hot, dry summer conditions to cool, wet winter conditions. We examined correlations between dissolved and particulate constituents and timing within the water year (WY Day; 1 October to 30 September) to see if there were effects associated with wet and/or dry periods (Table 4). There were significant effects between WY Day and flux of TSS, POC, PN, and DOC for ES, whereas these fluxes were not significant for the perennial stream. Flux of TSS, POC, and PN all had positive correlations with WY Day which indicates that flux of these particulates increases over the course of the water year. The most likely mechanism for this would be active downcutting and headward erosion which releases sediment and associated particulate OM into ES with successive storm events.

The negative correlation between water year date versus DOC indicates that ES DOC concentration was highest at the beginning of the "wet" season and gradually decreased over time which is consistent with data from a meta-analysis of 30 forested watersheds in the eastern United States documenting higher DOC exports at the end of a dry period [26]. Flushing of high Cl and UVA$_{254}$ sources (e.g., throughfall and O-horizon material; Table 2) during an early season storm (Figure 6; 31 December 2010 storm panel) is not as evident later in the season. The late season storm (Figure 6; 30 April 2010 storm panel) has a Cl versus UVA$_{254}$ signal which is similar to GW (i.e., wet season base flow) at the event onset, followed by throughfall and A-horizon soil. These relationships suggest that early in the season there was a larger pool of labile DOC available within and leached from the upper soil profile (e.g., O-horizon soil solution) and that over multiple flushing events the labile C pool was depleted. If storm events are "hot moments" for the flushing of stored DOC [28,40], then peak DOC efflux should occur at the onset of the wet season (late fall) and decrease throughout the wetter winter months during successive leaching events. The DOC pool will build during drier months such that events that occur after prolonged dry conditions will have high DOC concentrations [26,54]. Our data support belowground storage of a leachable C pool during the dry season and flushing of the soil C pool during storm events throughout the wet season, such that availability of DOC decreases to minimum at the beginning of the next dry season. In contrast, the flushing signal that is evident within the ES is not detectable within the perennial stream, most likely due to the dilution from groundwater inputs (Figure 6; 23 April 2010) or CO_2 evasion.

3.5. The Climate Connection

Climate projections for the southeastern US indicate a slight increase in warm days and especially warm nights, which will lead to a longer duration of frost-free days, and an increase in drought length [55]. Concurrent with the overall increase in temperature, there is "high confidence" that there will be an increase in the number of annual days for which there are heavy (>75 mm) precipitation events [55] even though MAP is expected to be relatively stable [34]. A comparison of several models from the Mississippi River Basin also predict an increase in temperature which leads to a shift in the seasonality of the precipitation such that precipitation will decrease during summer months and increase during winter months [56]. Regional climate models from the central U.S. postulate a localized summertime warming minimum or "warming hole" [57] such that convective storms will result in precipitation that is greater than evapotranspiration, setting the stage for increases in soil moisture at

the end of the summer season. These models pose a conundrum for how climatic drivers will affect fluxes from IRES to downstream rivers.

If MAP does not change but event precipitation increases, then there must be less frequent events of higher intensity with increased drying time between events. This scenario would result in higher fluxes of Sediment and OM (until it is depleted seasonally) from the ephemeral watersheds with increasing precipitation and Q (Table 4) especially during the first flood pulses as has been reported for both particulate and dissolved OM e.g., [5,26]. The four ephemeral watersheds we gauged had a combined area of 11.6 ha, representing 36% of the source area contributing to the perennial stream at our gauge point, yet as small as they were, they discharged an average of 328 g s^{-1} ha^{-1} of OM (Table 3; POC + PN + DOC + DON) during storm events. The high standard deviations of these measurements indicate that the fluxes could be much higher or much lower. We used the existing relationship between precipitation/Q and the dependent variables within a regression function to provide an indication of how the watershed might respond to increases in precipitation or Q. The equation used was:

$$Ln(X) = B0 + B1 * Ln(unitQ) + B2 * (Peak\ time) + B3 * (Flowtime) + B4 \\ * (Rate\ of\ Change) + B5 * (TimeEvent) + B6 * (WY\ Day) + B7 \\ * (Precip)$$

where *X* is the dependent variable of interest (e.g., TSS, POC, PN, and DOC), B0 is the intercept, and B1–B7 are the coefficients for each of the predictor variables (0 if the predictor variable was not a significant predictor of the dependent). The resultant projected increase or decrease (%) in TSS and OM components given a 5% increase in precipitation or Q is provided in Table 5.

Table 5. Projected increase in TSS and OM components with 5% increase in precipitation or Q and coefficients from which they were derived.

		Q	Precipitation	Peak Time	FlowTime	Rate Change	TimeEvent	WY Day	5% Δ in Precip	5% Δ in Q
TSS	ES	0.408	0.297				−0.211	0.237	2.0	2.0
	PER	0.320	−0.221			4.197			−4.6	1.6
POC	ES	0.388	0.103		−0.012		−0.064	0.003	0.7	1.9
	PER	0.484	−0.268			5.040			−5.4	2.4
PN	ES	0.349	0.131		−0.015			0.007	0.9	1.7
	PER	0.551	−0.349			5.196			−7.0	2.7
DOC	ES	0.563	−0.003	0.018	−0.007		−0.040	−0.003	0.0	2.8
	PER	0.466							0.0	2.3

Projected increase or decrease in each of the dependent variables are in percentage in the two columns to the right. ES = ephemeral streams. PER = perennial stream. Dependent variables: Precipitation = amount of precipitation that fell in the previous 15 min; Q = instantaneous discharge at the time the sample was collected; PeakTime = time before or after peak flow; FlowTime = time since flow began in hours; RateChange = change in Q over time where positive values are on the rising limb and negative values are on the receding limb; EventTime = time since event initiation; WY Day = # of days after October 1 (beginning of water year).

A century-long study of precipitation trends in forest lands of the Lower Mississippi River Alluvial Valley (LMRAV) reported precipitation increases (estimated to be 7%) at the south coastal area of the LMRAV and constant or a slight decrease at the middle area of the LMRAV [58]. Our study site was between the south and middle parts of the LMRAV and, therefore, a 5% increase in precipitation is a reasonable estimate. A 5% increase in stream discharge is considered as the extreme case because not all of the 5% increase precipitation contributes to discharge.

Where there is a 5% increase in precipitation, within ES we would expect increases across all particulate constituents. However, given the perennial stream sensitivity to precipitation there would most likely be a negative effect of on the flux of most constituents. When and how the precipitation occurs can change the outcome insofar as precipitation and Q are coupled. Higher magnitude storms, which may cause an increase in Q, will be the primary drivers for additional materials flux. Given a 5% increase in Q, there was an increase from 1.6% to 2.8% in average instantaneous flux of materials

from both the ES and the perennial stream (Table 5). For example, an increase of 0.63×10^3 m^3 s^{-1} ha^{-1} in Q within ES would result in an increase of 69.0 g s^{-1} ha^{-1} average instantaneous flux of TSS and 7.8 g s^{-1} ha^{-1} of OM (Table 6). While increases appear to be small, it is important to remember these are instantaneous fluxes, so over the course of an event the flux will be much higher depending upon the change in the discharge-rating curve relative to historical data. Changes between ES and the perennial stream are similar, which suggests that materials flux from the ES continues in the perennial stream and that the perennial stream acts as a conduit for materials generated in the ES.

Table 6. Modeled increase in average within-event instantaneous flux of materials given a 5% increase in Q.

	5% Δ Unit Q	Δ TSS	Δ POC	Δ PN	Δ DOC	∑ OM
	(×10³ m³ s⁻¹ ha⁻¹)	(g s⁻¹ ha⁻¹)				
Ephemeral	0.63	69.00	1.90	0.13	5.78	7.82
Perennial	0.28	8.34	0.52	0.06	2.22	2.79

Instantaneous flux is Q × C, where Q is the instantaneous discharge and C is the concentration of the sample at the time of sample collection.

The hydrologic transition from dry to wet in these IRES could result in pulses of DOC release [30,31,59] followed by mineralization and CO_2 release from the perennial stream [60], especially since rates increase with increasing catchment area [61]. Much of the DOC and POC in the ES derived from the soil profile (Figures 2 and 3). If, as a result of climate change, there is an increase in convective storms and greater soil moisture at the end of the summer season, then wetting and drying cycles of soils and streams will be moderated and there may be lower DOC production and flux simultaneously with higher POM due to the increased energy in the system to mobilize particulates and sediment.

If MAP does not change but rainfall shifts to winter months, then presumably the summer drought season would be lengthened. Increased drought during the warmer months followed by short-term high intensity events would result in increased downcutting and headward erosion followed by greater flux of TSS, POC, and PN (Figure 4 and Table 3). A compilation of climate models for an agricultural watershed in Mississippi predicted that an increase in summer temperatures would result in a decrease in runoff, but approximately 12% greater TSS loads, presumably due to the higher intensity precipitation events [62]. Perhaps of greater import is that prolonged drought may increase the areal extent of IRES [1] which means that there would be a greater time and area over which soil OM can accumulate. If Horton infiltration excess is the primary path for DOC to streams, then perhaps there would be no change beyond what is mobilized with sediment due to the erosion. If Dunne saturation excess is the primary source of DOC as is suggested by our data (Figures 2 and 4a), then there will be a greater time over which the pool can build and potentially larger releases to the stream network. Longer-term studies are needed to determine the impact of climate change on the flux of (OM) from IRES in the southeastern US.

4. Conclusions

Our first question was: what are the sources of sediment and OM in ES? DOM was derived from Dunne-type saturated flow through the upper part of the soil profile, particularly during the first flush of storms and after dry periods. Sediment and POM were derived from down cutting and headward erosion during the rising limb of storm events. Changes in processes that affect erosion are going to lengthen stream channel networks and increase the areal extent of ES.

Our second question was: what are the controls on flux of sediment and OM from very small (<4 ha) ES to downstream reaches? Precipitation, WY Day, and variables associated with the shape of the hydrograph all had linear relationships with sediment, DOM, and POM. No matter what happens to the other variables (e.g., precipitation, length of the water year, shape of the hydrograph), discharge will have an overriding effect on the flux of materials because there is a power log relationship between

Q and materials flux. Any changes to Q (i.e., caused by higher-intensity storms) will have a large control over the flux.

The flux of OM in response to climate change is going to be dependent upon how the change affects the source of OM. Projected climate effects are: (1) less frequent, higher-intensity storms and/or (2) shift to heavier precipitation in winter and longer drought in summer. If there is a shorter water year but the same amount of precipitation, there needs to be a longer/larger stream network to accommodate the flow. Precipitation during storms is likely to result in more water transfer through the upper part of the soil profile in conjunction with increased channel incision. Higher intensity storms resulting in higher Q within ES channels will result in greater flux of materials to downstream perennial reaches.

Do small IRES matter in the context of climate change? Given the storm-driven flux of sediment and OM from these small ephemeral watersheds and the potential for that OM to be processed and evolved as CO_2 under projected climate scenarios for the region, the answer is yes—IRES matter. There are three reasons that ES should be incorporated into climate-driven hydrological models: (1) ES are intimately connected to sources of OM; (2) ES are indirectly connected to precipitation through Q; (3) there is likely to be an expansion of the areal extent of ES. For these reasons we need to consider ES when modeling the response of hydrological systems to climate change.

References

1. Datry, T.; Corti, R.; Foulquier, A.; von Schiller, D.; Tockner, K. One for all, all for one: A global river research network. *Eos* **2016**, *97*, 12–15. [CrossRef]

2. Acuña, V.; Datry, T.; Barceló, D.; Dahm, C.N.; Ginebreda, A.; McGregor, G.; Sabater, S.; Tockner, K.; Palmer, M.A. Why should we care about temporary waterways? *Science* **2014**, *33*, 1080–1081. [CrossRef] [PubMed]

3. Alexander, L.C.; Autrey, B.; Demeester, J.; Fritz, K.; Goodrich, D.; Kepner, W.G.; Lane, C.R.; LeDuc, S.; Leibowitz, S.; McManus, M.; et al. Connectivity and Effects of Streams and Wetlands on Downstream Waters: A Review and Synthesis of the Scientific Evidence. EPA/600/R-14/475F. January 2015. Available online: https://nepis.epa.gov (accessed on 7 July 2020).

4. Gutiérrez-Jurado, K.Y.; Partington, D.; Batelaan, O.; Cook, P.; Shanafield, M. What triggers streamflow for intermittent rivers and ephemeral streams in low-gradient catchments in Mediterranean climates. *Water Resour. Res.* **2019**, *55*, 9926–9946. [CrossRef]

5. Brintrup, K.; Amigo, C.; Fernández, J.; Hernández, A.; Pérez, F.; Félez-Bernal, J.; Butturini, A.; Saez-Carillo, K.; Yevenes, M.A.; Figueroa, R. Comparison of organic matter in intermittent and perennial rivers of Mediterranean Chile with the support of citizen science. *Rev. Chil. Hist. Nat.* **2019**, *92*, 3. [CrossRef]

6. Raymond, P.A.; Saiers, J.E.; Sobczak, W.V. Hydrological and biogeochemical controls on watershed dissolved organic matter transport: Pulse—Shunt concept. *Ecology* **2016**, *97*, 5–16. [CrossRef]

7. Raymond, P.A.; Hartmenn, J.; Lauerwald, R.; Sobek, S.; McDonald, C.; Hoover, M.; Butman, D.; Striegl, R.; Mayorga, E.; Humborg, C.; et al. Global carbon dioxide emissions from inland waters. *Nature* **2013**, *503*, 355–359. [CrossRef] [PubMed]

8. Marx, A.; Dusek, J.; Jankovec, J.; Sanda, M.; Vogel, T.; van Geldern, R.; Hartmann, J.; Barth, J.A.C. A review of CO_2 and associated carbon dynamics in headwater streams: A global perspective. *Rev. Geophys.* **2017**, *55*, 560–585. [CrossRef]

9. Fritz, K.M.; Schofield, K.A.; Alexander, L.C.; McManus, M.G.; Golden, H.E.; Lane, C.R.; Kepner, W.G.; LeDuc, S.D.; DeMeester, J.E.; Pollard, A.I. Physical and chemical connectivity of streams and riparian wetlands to downstream waters: A synthesis. *J. Am. Water Res. Assoc.* **2018**, *54*, 323–345. [CrossRef]

10. MacDonald, L.H.; Coe, D. Influence of headwater streams on downstream reaches in forested areas. *For. Sci.* **2007**, *53*, 148–168. [CrossRef]

11. Nadeau, T.; Rains, M. Hydrological connectivity between headwater streams and downstream waters: How science can inform policy. *J. Am. Water Resour. Assoc.* **2007**, *43*, 118–133. [CrossRef]

12. Gomi, T.; Sidle, R.; Richardson, J. Understanding processes and downstream linkages of headwater systems. *Bioscience* **2002**, *52*, 905–916. [CrossRef]

13. Triska, F.; Duff, J.; Sheibley, R.; Jackman, A.; Avanzion, R. DIN retention–transport through four hydrologically connected zones in a headwater catchment of the upper Mississippi River. *J. Am. Water Res. Assoc.* **2007**, *43*, 60–71. [CrossRef]

14. Winterdahl, M.; Bishop, K.; Erlandsson, M. Acidification, dissolved organic carbon (DOC) and climate change. In *Global Environmental Change*; Freedman, B., Ed.; Springer: Dordrecht, The Netherlands, 2014; pp. 281–287.

15. Mengistu, S.D.; Quick, C.G.; Creed, I.F. Nutrient exports from catchments on forested landscapes reveals complex nonstationary and stationary climate signals. *Water Resour. Res.* **2013**, *49*, 3863–3880. [CrossRef]

16. Alveras-Cobelas, M.; Angeler, D.G.; Sanchez-Carillo, S.; Almendros, G. A worldwide view of carbon export from catchments. *Biogeochemistry* **2012**, *107*, 275–293. [CrossRef]

17. Aufdenkampe, A.K.; Mayorga, E.; Raymond, P.A.; Melack, J.m.; Doney, S.C.; Alin, S.R.; Aalto, R.E.; Yoo, K. Riverine coupling of biogeochemical cycles between land, oceans, and atmosphere. *Front. Ecol. Environ.* **2011**, *9*, 53–60. [CrossRef]

18. Tank, J.L.; Rosi-Marshall, E.J.; Griffiths, N.A.; Entrekin, S.A.; Stephen, M.L. A review of allochthonous organic matter dynamics and metabolism in streams. *J. N. Am. Benthol. Soc.* **2010**, *29*, 118–146. [CrossRef]

19. Hejzlar, J.; Dubrovsky, M.; Buchtele, J.; Ruzicka, M. The apparent and potential effects of climate change on the inferred concentration of dissolved organic matter in a temperate stream (the Malse River, South Bohemia). *Sci. Total Environ.* **2003**, *310*, 143–152. [CrossRef]

20. Horton, R.E. Erosional development of streams and their drainiage basins: Hydrophysical approach to quantitative morphology. *Bull. Geol. Soc. Am.* **1945**, *56*, 275–370. [CrossRef]

21. Dunne, T.; Black, R.D. An experimental investigation of runoff production in permeable soils. *Water Resour. Res.* **1970**, *6*, 478–490. [CrossRef]

22. Hansen, W.F. Identifying stream types and management implications. *For. Ecol. Manag.* **2001**, *143*, 39–46. [CrossRef]

23. Wipfli, M.; Richardson, J.; Naiman, R. Ecological linkages between headwaters and downstream ecosystems: Transport of organic matter, invertebrates, and wood down headwater channels. *J. Am. Water Res. Assoc.* **2007**, *43*, 72–85. [CrossRef]

24. Wilson, H.F.; Saiers, J.E.; Raymond, P.A.; Sobczak, W.V. Hydrologic drivers and seasonality of dissolved organic carbon concentration, nitrogen content, bioavailability, and export in a forested New England stream. *Ecosystems* **2013**, *16*, 604–616. [CrossRef]

25. Hatten, J.A.; Goñi, M.A.; Wheatcroft, R.A. Chemical characteristics of particulate organic matter from a small mountainous river system in the Oregon coast Range, USA. *Biogeochemistry* **2012**, *107*, 43–66. [CrossRef]

26. Raymond, P.A.; Saiers, J.E. Event controlled DOC export from forested watersheds. *Biogeochemistry* **2010**, *100*, 197–209. [CrossRef]

27. Moody, C.S.; Worrall, F.; Evans, C.D.; Jones, T.G. The rate of loss of dissolved organic carbon (DOC) through a catchment. *J. Hydrol.* **2013**, *492*, 139–150. [CrossRef]

28. McClain, M.E.; Boyer, E.W.; Dent, C.L.; Gergel, S.E.; Grimm, N.B.; Groffman, P.M.; Hart, S.C.; Harvey, J.W.; Johnston, C.A.; Mayorga, E.; et al. Biogeochemical hot spots and hot moments at the interface of terrestrial and aquatic ecosystems. *Ecosystems* **2003**, *6*, 301–312. [CrossRef]

29. von Schiller, D.; Graeber, D.; Ribot, M.; Timoner, X.; Acuña, V.; Martí, E.; Sabater, S.; Tockner, K. Hydrological transitions drive dissolved organic matter quantity and composition in a temporary Mediterranean stream. *Biogeochemistry* **2015**, *123*, 429–446. [CrossRef]

30. Vázquez, E.; Ejarque, E.; Ylla, I.; Romaní, A.M.; Butturini, A. Impact of drying/rewetting cycles on the bioavailability of dissolved organic matter molecular-weight fractions in a Mediterranean stream. *Freshw. Sci.* **2015**, *34*, 263–275. [CrossRef]

31. Vázquez, E.; Romaní, A.M.; Sabater, F.; Butturini, A. Effects of the dry–wet hydrological shift on dissolved organic carbon dynamics and fate across stream–riparian interface in a Mediterranean catchment. *Ecosystems* **2007**, *10*, 239–251. [CrossRef]

32. Gómez-Gener, L.; Obrador, B.; Marcé, R.; Acuña, V.; Catalán, N.; Casas-Ruiz, J.P.; Sabater, S.; Muñoz, I.; von Schiller, D. When water vanishes: Magnitude and regulation of carbon dioxide emissions from dry temporary streams. *Ecosystems* **2016**, *19*, 710–723. [CrossRef]

33. Benstead, J.P.; Leigh, D.S. An expanded role for river networks. *Nat. Geosci.* **2012**, *5*, 678–679. [CrossRef]

34. Karl, T.R.; Melillo, J.M.; Peterson, T.C. (Eds.) *Global Climate Change Impacts in the United States*; Cambridge University Press: New York, NY, USA, 2009.

35. Haarsma, R.J.; Hazeleger, W.; Severijns, C.; de Vries, H.; Sterl, A.; Bintanja, R.; van Oldenborgh, G.J.; van den Brink, H.W. More hurricanes to hit western Europe due to global warming. *Geophys. Res. Lett.* **2013**, *40*, 1783–1788. [CrossRef]

36. Knutson, T.R.; McBride, J.L.; Chan, J.; Emanuel, K.; Holland, G.; Landsea, C.; Held, I.; Kossin, J.P.; Srivastava, A.K.; Sugi, M. Tropical cyclones and climate change. *Nat. Geosci.* **2010**, *3*, 157–163. [CrossRef]

37. Yoon, B.; Raymond, P.A. Dissolved organic matter export from a forested watershed during hurricane Irene. *Geophys. Res. Lett.* **2012**, *39*, L18402. [CrossRef]

38. Wheatcroft, R.A.; Goñi, M.A.; Hatten, J.A.; Pasternack, G.B.; Warrick, J.A. The role of effective discharge in the ocean delivery of particulate organic carbon by small, mountainous river systems. *Limnol. Oceanogr.* **2010**, *55*, 161–171. [CrossRef]

39. Nash, D.B. Effective Sediment-Transporting Discharge from Magnitude-Frequency Analysis. *J. Geol.* **1994**, *102*, 79–95. [CrossRef]

40. Vidon, P.; Allan, C.; Burns, D.; Duval, T.P.; Gurwick, N.; Inamdar, S.; Lowrance, R.; Okay, J.; Scott, D.; Sebestyen, S. Hot spots and hot moments in riparian zones: Potential for improved water quality management. *J. Am. Water Resour. Assoc.* **2010**, *46*, 278–298. [CrossRef]

41. Leigh, C.; Boulton, A.J.; Courtwright, J.L.; Fritz, K.; May, C.L.; Walker, R.H.; Datry, T. Ecological research and management of intermittent rivers: An historical review and future directions. *Freshw. Biol.* **2015**, *61*, 1181–1199. [CrossRef]

42. Mangum, C. Flux and Source of Dissolved Organic and Inorganic Constituents in Managed Headwaters of the Upper Gulf Coastal Plain, Mississippi. Master's Thesis, Mississippi State University, Starkville, MS, USA, 2012.

43. McMullen, J.W.; Ford, J.G. Soil Survey of Webster County Mississippi. In *Cooperation with the Mississippi Agricultural and Forestry Experiment Station*; Natural Resources Conservation Service, United States Department of Agriculture: Washington, DC, USA, 1978; 99p.

44. Choi, B.; Dewey, J.C.; Hatten, J.A.; Ezell, A.W.; Fan, Z. Changes in vegetative communities and water table dynamics following timber harvesting in small headwater streams. *For. Ecol. Manag.* **2012**, *281*, 1–11. [CrossRef]

45. U.S. Geological Survey. *Little Sand Creek Quadrangle, Mississippi. 1:24,000*; 7.5 Minute Series; United States Department of the Interior: Reston, VA, USA, 1983.

46. Choi, B.; Hatten, J.A.; Dewey, J.C.; Otsuki, K.; Cha, D. Effect of timber harvesting on stormflow characteristics in headwater streams of managed, forested watersheds in the Upper Gulf Coastal Plain of Mississippi. *J. Fac. Agric. Kyushu Univ.* **2013**, *58*, 395–402.

47. National Climatic Data Center. Eupora 2E, MS, US, Precipitation 15 Minute Station Details. NOAA National Centers for Environmental Information. 2013. Available online: http://www.ncdc.noaa.gov/cdo-web/datasets/ PRECIP_15/stations/COOP:222896/detail (accessed on 16 October 2015).

48. R Core Team. *R: A Language and Environment for Statistical Computing*; R Foundation for Statistical Computing: Vienna, Austria, 2017. Available online: https://www.R-project.org/ (accessed on 10 August 2017).

49. Venables, W.N.; Ripley, B.D. *Modern Applied Statistics with S*, 4th ed.; Springer: New York, NY, USA, 2002; ISBN 0-387-95457-0. Available online: http://www.stats.ox.ac.uk/pub/MASS4 (accessed on 10 August 2017).

50. Lambert, T.; Pierson-Wickmann, A.-C.; Gruau, G.; Thibault, J.-N.; Jaffrezic, A. Carbon isotopes as tracers of dissolved organic carbon sources and water pathways in headwater catchments. *J. Hydrol.* **2011**, *402*, 228–238. [CrossRef]

51. Morel, B.; Durand, P.; Jaffrezic, A.; Gruau, G.; Molenat, J. Sources of dissolved organic carbon during stormflow in a headwater agricultural catchment. *Hydrol. Process* **2009**, *23*, 2888–2901. [CrossRef]

52. Shumilova, O.; Zak, D.; Datry, T.; von Schiller, D.; Corti, R.; Foulquier, A.; Obrador, B.; Tocknet, K.; Allan, D.C.; Altermatt, F.; et al. Simulating rewetting events in intermittent rivers and ephemeral streams: A global analysis of leached nutrients and organic matter. *Glob. Chang. Biol.* **2019**, *25*, 1591–1611. [CrossRef] [PubMed]

53. Corti, R.; Datry, T. Invertebrates and sestonic matter in an advancing wetted front travelling down a dry river bed (Albarine, France). *Freshw. Sci.* **2012**, *31*, 1187–1201. [CrossRef]

54. Johnson, M.S.; Lehmann, J.; Selva, E.C.; Abdo, M.; Riha, S.; Couto, E.G. Organic carbon fluxes within and stream exports from headwater catchments in the southern Amazon. *Hydrol. Process* **2006**, *20*, 2599–2614. [CrossRef]

55. Carter, L.; Terando, A.; Dow, K.; Hiers, K.; Kunkel, K.E.; Lascurain, A.; Marcy, D.; Osland, M.; Schramm, P. Southeast. In *Impacts, Risks, and Adaptation in the United States: Fourth National Climate Assessment*; Reidmuller, D.T., Avery, C.W., Easterling, D.R., Kunkel, K.E., Lewis, K.L.M., Maycock, T.K., Stewart, B.C., Eds.; U.S. Global Change Research Program: Washington, DC, USA, 2017; Volume II, pp. 743–808. [CrossRef]

56. Pan, Z.; Zhang, Y.; Liu, X.; Gao, Z. Current and future precipitation extremes over Mississippi and Yangtze River Basins as simulated in CMIP5 models. *J. Earth Sci.* **2016**, *27*, 22–36. [CrossRef]

57. Pan, Z.; Arritt, R.W.; Takle, E.S.; Gutowski, W.J., Jr.; Anderson, C.J.; Segal, M. Altered hydrologic feedback in a warming climate introduces a "warming hole". *Geophys. Res. Let.* **2004**, *31*, L17109. [CrossRef]

58. Ouyang, Y.; Zhang, J.; Feng, G.; Wan, Y.; Leininger, T.D. A century of precipitation trends in forest lands of the Lower Mississippi River Alluvial Valley. *Sci. Rep.* **2020**, *10*, 12802. [CrossRef]

59. Lundquist, E.J.; Jackson, L.E.; Scow, K.M. Wet-dry cycles affect dissolved organic carbon in two California agricultural soils. *Soil Biol. Biochem.* **1999**, *31*, 1031–1038. [CrossRef]

60. Hotchkiss, E.R.; Hall, R.O., Jr.; Sponseller, R.A.; Butman, D.; Klaminder, J.; Laudon, H.; Rosvall, M.; Karlsson, J. Sources of and processes controlling CO_2 emissions change with the size of streams and rivers. *Nat. Geosci.* **2015**, *8*, 696–699. [CrossRef]

61. Datry, T.; Foulquier, A.; Corti, R.; voon Schiller, D.; Tockner, K.; Mendoza-Lera, C.; Clement, J.C.; Gessner, M.O.; Moleón, M.; Stubbington, R.; et al. A global analysis of terrestrial plant litter dynamics in non-perennial waterways. *Nat. Geosci.* **2018**, *11*, 497–503. [CrossRef]

62. Yasarer, L.M.W.; Bingner, R.L.; Garbrecht, J.D.; Locke, M.A.; Lizotte, R.E., Jr.; Momm, H.G.; Busteed, P.R. Climate change impacts on runoff, sediment, and nutrient loads in an agricultural watershed in the Lower Mississippi River Basin. *Appl. Eng. Agric.* **2017**, *33*, 379–392. [CrossRef]

Using AnnAGNPS to Simulate Runoff, Nutrient, and Sediment Loads in an Agricultural Catchment with an On-Farm Water Storage System

Juan D. Pérez-Gutiérrez [1], Joel O. Paz [2],* , Mary Love M. Tagert [2] , Lindsey M. W. Yasarer [3] and Ronald L. Bingner [3]

[1] Northern Colorado Water Conservancy District, Berthoud, CO 80513, USA; jperez@northernwater.org
[2] Department of Agricultural and Biological Engineering, Mississippi State University, J. Charles Lee Building, Starkville, MS 39762, USA; mltagert@abe.msstate.edu
[3] USDA-ARS National Sedimentation Laboratory, Oxford, MS 38655, USA; lindsey.yasarer@ars.usda.gov (L.M.W.Y.); ron.bingner@ars.usda.gov (R.L.B.)
* Correspondence: jpaz@abe.msstate.edu; Tel.: +1-662-325-4798

Abstract: On-farm water storage (OFWS) systems are best management practices that consist of a tailwater recovery (TWR) ditch used with a storage pond to provide irrigation water and improve downstream water quality. These systems have been increasingly implemented in the southeastern US, but the individual and cumulative effects of these systems on a watershed scale are unknown. In this study, the runoff, nutrient, and sediment loads entering a TWR ditch in an agricultural catchment were quantified, and contributing sources were identified using the annualized agricultural non-point source (AnnAGNPS) model. Fields with larger areas and soils with a high runoff potential produced more runoff. The volume of runoff exceeded the TWR ditch storage volume approximately 110 times, mostly during the winter and spring seasons. During years when corn and winter wheat were planted, NO_3–N loads increased because these crops need nitrogen fertilization to grow. Planting winter wheat in priority subwatersheds reduced the total phosphorous (TP) and sediment loads by about 19% and 13%, respectively, at the TWR ditch inlet. Planting winter wheat can reduce runoff, TP, and sediment loads but also result in higher NO_3–N loads. AnnAGNPS simulations quantified the benefits of an OFWS system to advance the understanding of their impact on water availability and quality at a watershed scale.

Keywords: tailwater recovery ditch; AnnAGNPS; BMP

1. Introduction

The global population has been projected to increase between 9.6 billion and 12.3 billion by 2100 [1]. As a result, agriculture will have to double its productivity to feed people [2,3]. Meeting this increasing food demand has led to the intensification of agriculture, which translates into the greater use of chemical inputs and pressure on soil and water resources. Agricultural activities often transfer excess fertilizers through non-point source (NPS) pollution into aquatic ecosystems causing devastating ecological and economical effects [4–8]. Therefore, a balance between increasing yields and mitigating adverse environmental impacts is crucial for the future of agriculture.

The implementation of best management practices (BMPs) has been recognized to significantly reduce NPS pollution from croplands to downstream waterbodies [9–11]. However, much effort is still devoted to quantifying the effectiveness and benefits of such practices, especially newer BMPs. Measuring BMP performance can be a challenge because their benefits vary spatially and temporally due to the heterogeneity of the landscape and seasonality of hydrological factors [12]. The challenge

is even greater when attempting to evaluate the effects of several BMPs combined [13–15], address the shift in BMP performance over time [16], and understand lag times in water quality response [17]. The use of watershed models can be a feasible alternative to quantify the effectiveness of BMPs while accounting for these challenges [16,18–24]. However, due to the diversity of BMPs that can be implemented over agricultural fields, information describing the performance of each BMP and the combined use of different BMPs is limited.

Structural BMPs such as tail-water recovery (TWR) ditches and agricultural ponds (i.e., on-farm water storage systems—OFWS) can improve downstream water quality by significantly reducing nutrient loads from agricultural watersheds [25–27]. The dual benefit of reducing nutrient pollution and supplying water for irrigation is important in areas such as the Lower Mississippi River Valley, where agricultural production strongly depends on irrigation. Farmers and landowners in this region are tasked with (1) reducing off-site movement of nutrients, which contributes to the hypoxic zone in the northern Gulf of Mexico, and (2) conserving water resources to slow the declining groundwater levels in the Mississippi River Valley Alluvial Aquifer (MRVAA), the primary source of water for irrigation. Consequently, OFWS systems have been implemented across the MRVAA, especially in areas with more severe groundwater declines. Although research has highlighted in-ditch and in-pond nutrient reductions, less attention has been placed on estimating the water and nutrient loads entering and exiting OFWS systems [28,29]. Evaluating the OFWS drainage area will quantify the impacts of these systems on a watershed scale, which will advance our understanding of the cumulative effects of these systems on water quality and groundwater decline as more OFWS systems are implemented throughout a watershed.

The annualized agricultural non-point source (AnnAGNPS) model [30,31] is a watershed model that has been designed to measure the impact of agricultural management practices on hydrological and water quality responses in watersheds. Most studies using the AnnAGNPS model demonstrate its performance after model calibration with field-observed data [22,32–39]. However, AnnAGNPS has also been used for similar purposes without conducting calibration with measured data. A study used the model with no calibrated parameters to estimate the runoff and sediment in an agricultural watershed within the Mississippi Delta Region [21]. They concluded that the model had an adequate ability to simulate monthly and annual runoff and sediment yield with no calibration process. This finding is of significant interest because it is difficult and costly to secure sufficient observed data to conduct calibration processes in watershed-scale modeling studies. To date, efforts to assess the benefits of tail-water recovery ditches using watershed scale models has been limited. This is, at least in part, because these ditches have multiple inlets. Therefore, the collection of measured runoff and water quality data (and especially continuous measured runoff and water quality data) is usually impractical and expensive, making it a challenge to collect a sufficient quantity of measured data on even one OFWS system. However, estimating the effects of OFWS systems at various scales is critical to stakeholders and agencies to better identify where these systems can be implemented to improve water quality and relieve pumping pressure on groundwater.

In this study, the AnnAGNPS model was used without calibration with field data to simulate runoff, sediment, and nutrient loads and identify the main contributing areas draining to a TWR ditch established as part of an OFWS system within Porter Bayou Watershed, Mississippi. The quantification of the water, nutrient, and sediment loading is an essential step in understanding the water quality and quantity benefits of OFWS systems when implemented in agricultural watersheds, as well as how the management of these systems might be altered to improve performance. Predictions on the volume of water captured by OFWS systems can also help determine their potential for alleviating local flooding. Finally, this study advances the incorporation of an OFWS system and the associated watershed impacts into the AnnAGNPS model, with the goal of improving the ability of AnnAGNPS to model these systems on a larger scale.

2. Materials and Methods

2.1. Study Site

This investigation was conducted in the Porter Bayou Watershed (PBW; 33°26′39″–33°51′38″ N, 90°48′54″–90°31′34″ W) in the Mississippi Delta Region (MDR), an intensively farmed area located in northwest Mississippi, USA (Figure 1). For the AnnAGNPS simulation, a small 214 ha watershed within the PBW located north of Indianola, MS, in Sunflower county, was selected, and it included Metcalf farm and the surrounding area that drains into the OFWS system outlet at M3 (Figure 1). The major crops grown from 2012 to 2016 were soybeans, corn, and rice (Table 1). Winter wheat was planted during 2013 and 2014 in four and two fields, respectively. The watershed is dominated by the following soil types: Forestdale, Tensas, Dundee, Pearson, and Dowling, which are primarily poorly drained soils and prone to produce high runoff. In addition, the watershed is relatively flat with surface elevations ranging from 130 to 135 m. The average temperature ranged from −8.3 °C in winter 2014 to 32.2 °C in summer 2012 (Figure 2a). The lowest total seasonal precipitation was 99 mm observed in summer 2015, while the highest was 579 mm in spring 2014 (Figure 2b). Average annual precipitation was 1308 mm, and in 2013 and 2014 this average was exceeded by 242 mm and 114 mm, respectively. Meanwhile, 2012 and 2015 were drier years with a total annual rainfall of 1100 and 1133 mm, respectively.
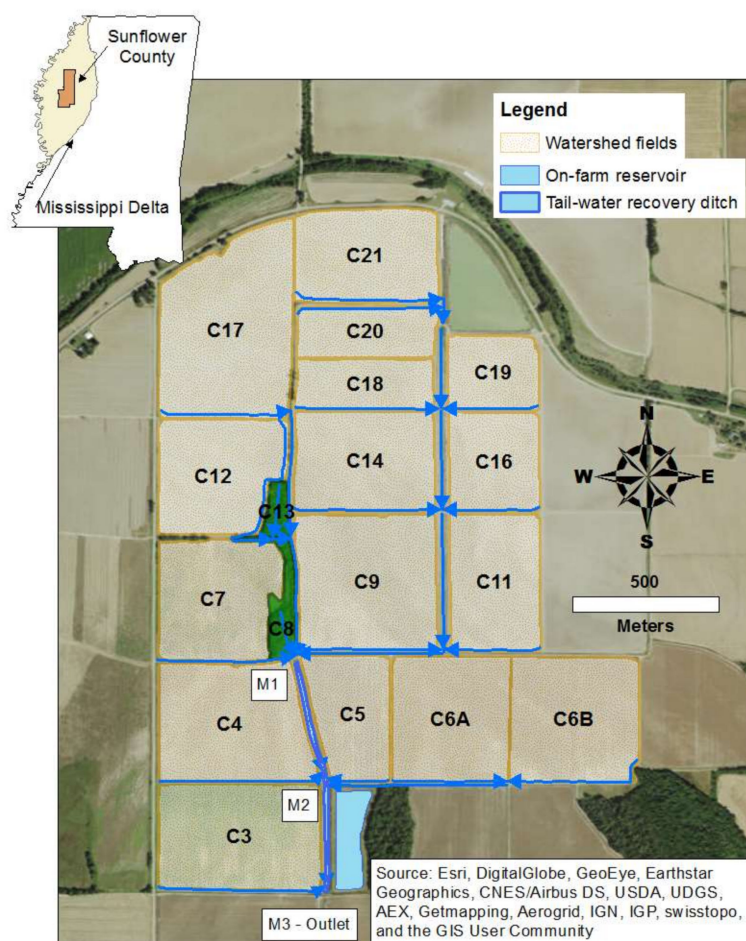

Figure 1. Map of the study area showing the agricultural watershed with the on-farm water storage system investigated in the Mississippi Delta Region. The blue arrows represent the runoff flow direction towards the outlet. (M1: tailwater recovery (TWR) inlet; M2: TWR mid-canal; M3: TWR outlet; labels within fields indicate the subwatershed identification used by the annualized agricultural non-point source (AnnAGNPS) model).

213

Table 1. Basic characteristics and land use including the planting dates of the subwatersheds.

Subwatershed ID	Area (ha)	Average Elevation (ft)	Average Land Slope	Soil Type	Hydrologic Soil Group	Land Use				
						2012	2013	2014	2015	2016
C3	16.85	130	0.0012	Db—Dowling silty clay loam	D	TRNAR	TRNAR	TRNAR	TRNAR	TRNAR
C4	17.00	131	0.0010	Fm—Forestdale silty clay loam	D	Soybean May 11	Soybean March 21	Soybean May 11	Soybean May 4	Soybean May 9
C5	9.40	131	0.0011	Am—Dundee silt loam	C	Soybean May 10	Corn March 21	Soybean May 11	Soybean May 4	Soybean May 9
C6A	14.67	131	0.0018	Am—Dundee silt loam	C	Soybean May 10	Corn March 21	Soybean May 11	Soybean May 4	Soybean May 9
C6B	15.74	131	0.0018	Fb—Forestdale silt loam	D	Soybean May 10	Corn Mar 21	Soybean May 11	Soybean May 4	Soybean May 9
C7	13.63	134	0.0020	Fm—Forestdale silty clay loam	D	Pasture	Pasture	Pasture	Pasture	Pasture
C8	2.34	132	0.0006	Db—Dowling clay	D	Forest	Forest	Forest	Forest	Forest
C9	18.70	132	0.0008	Db—Dowling clay	D	Soybean June 12	Rice May 26	Soybean June 20	Rice May 3	Corn April 25
C11	12.22	132	0.0017	Fb—Forestdale silt loam	D	Soybean April 24	Soybean June 10 WW October 25	Soybean May 20	Soybean April 9	Corn April 25
C12	13.41	133	0.0004	Fb—Forestdale silt loam	D	Rice April 13	Corn April 18	Soybean May 8	Soybean April 30	Rice March 30
C13	1.16	133	0.0016	Fb—Forestdale silt loam	D	Forest	Forest	Forest	Forest	Forest
C14	13.89	133	0.0005	Fb—Forestdale silt loam	D	Soybean April 23	Soybean May 27	Soybean May 6	Soybean April 28	Corn April 25
C16	8.89	134	0.0012	Dk—Silty clay	D	Soybean April 24	Soybean June 10 WW October 25	Soybean May 20	Soybean April 9	Corn April 25
C17	22.54	135	0.0019	Pa—Pearson silt loam	C	Rice April 13	Corn April 18	Soybean May 6 WW October 25	Soybean June 12	Rice March 30
C18	6.95	134	0.0011	Fb—Forestdale silt loam	D	Soybean April 24	Soybean May 18 WW October 25	Soybean May 6	Soybean April 30	Corn April 25
C19	6.66	135	0.0012	Dk—Silty clay	D	Soybean April 24	Soybean June 10	Soybean May 20	Soybean April 9	Corn April 25
C20	7.00	134	0.0004	Dk—Silty clay	D	Soybean April 24	Soybean May 18 WW October 25	Soybean May 7	Soybean April 30	Corn April 25
C21	12.99	134	0.0013	Dk—Silty clay	D	Soybean June 4	Corn April 18	Soybean May 18 WW October 25	Soybean June 12	Rice March 30

TRNAR: turn area; WW: winter wheat.
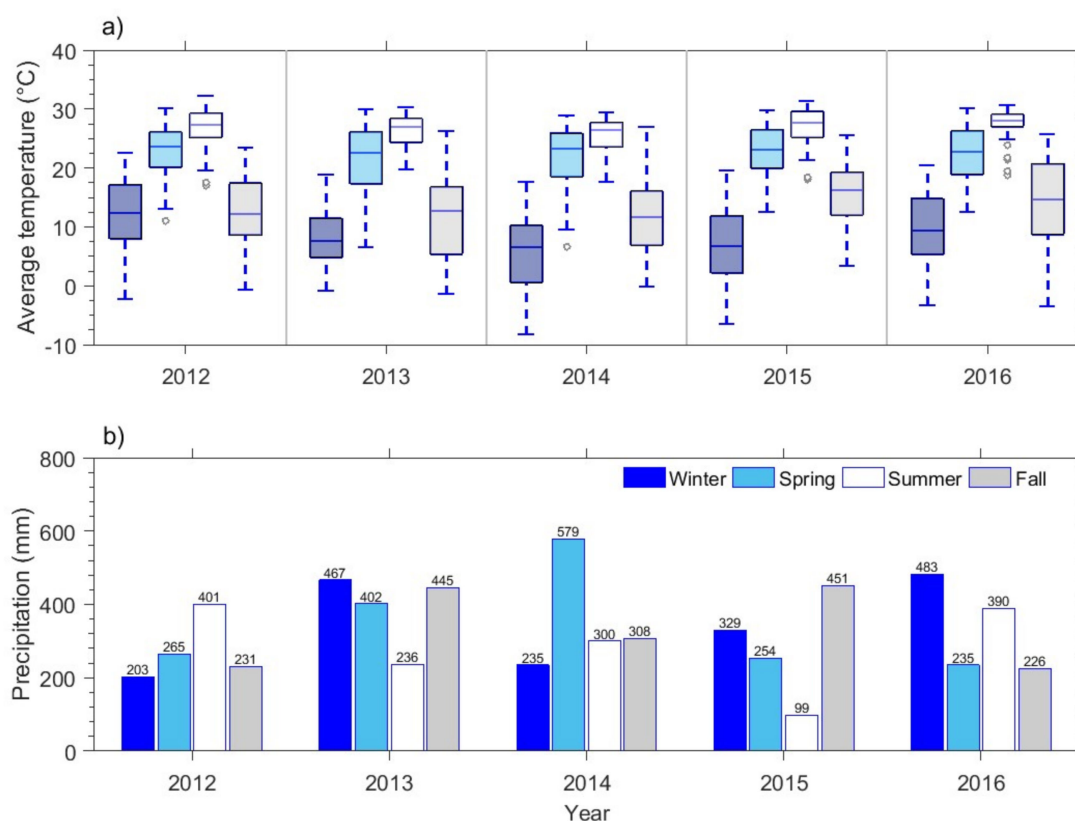
Figure 2. Average temperature and total precipitation by season during the period 2012–2016 at the study site. (**a**) Boxplots of the average temperature. (**b**) Bar chart showing the total precipitation. Winter: January–March; Spring: April–June; Summer: July–September; Fall: October–December. Boxplots were set at 90th (the upper whisker), 75th (the upper quartile), 50th (the median), 25th (the lower quartile), and 10th (the lower whisker) percentiles. Outliers were considered those observations 1.5 times beyond the 25th and 75th percentile and are shown as grey circles.

The OFWS system consists of a trapezoidal-shape TWR ditch and an elongated agricultural pond which have a combined storage volume of 128,020 m^3 (TWR ditch: 13,320 m^3; pond: 114,700 m^3). Water flows from north to south through the ditch, which is 818.8 m long and 1.8 m deep on average; the pond is 2.4 m deep with a surface area of 4.45 ha. Runoff is routed to the single outlet pipe (33°39′35.6″ N, 90°39′11.9″ W) set at 1.2 m above the canal bed (Figure 1). The system was designed according to National Resources Conservation Service (NRCS) [40] guidelines, and more information about its characteristics can be found at Pérez-Gutiérrez, Paz and Tagert [25].

2.2. Model Description

AnnAGNPS is a physical process model developed to simulate the runoff, sediment, nutrient, and pesticide yields at a daily time step in small watersheds. The model divides the watershed into subwatersheds based on homogeneous physical characteristics such as soil type, land use, and land management. AnnAGNPS is a continuous simulation model and has been primarily developed to evaluate the impacts of different agricultural management practices on watersheds. As with other physical process watershed-scale models, the major input data are climate, land characterization, field operations, chemical characteristics, and feedlot operations. A detailed description of the model can be found in Geter and Theurer [30], Bingner, et al. [41], Bosch, et al. [42], Theurer and Cronshey [43], Cronshey and Theurer [44].

2.3. Model Input

A detailed field survey was conducted to identify the field boundaries and collect elevation data required by the model. Eighteen fields were identified as subwatersheds (or cells), and associated reaches were defined for routing runoff to the outlet (M3) in the AnnAGNPS model (Figure 1). Because all fields were precision leveled, they were defined as homogeneous drainage areas or subwatersheds. The delineation of the watershed was done manually with the aid of Google™ Earth and geographic information system (GIS) technologies. Parameters describing the subwatersheds such as area, average elevation, and average land slope were determined from the field survey (Table 1). Parameters representing the time of concentration and travel time were computed from data provided by the field reconnaissance following USDA-SCS [45] methods, modified by Theurer and Cronshey [43]. Soil data and physical properties were obtained from the Soil Survey Geographic (SSURGO) database [46]. Although 15 soil types were identified throughout the watershed, the dominant soil type was determined for each subwatershed as required by the model, using GIS operations (Table 1). Crop planting dates were obtained from the Sunflower county USDA–NRCS office. A crop management schedule was assigned to each field according to the typical management practices conducted in the MDR (Table 2). Irrigation was included in the crop management schedule, starting in late May or June and ending in August. The SCS curve number is an important model parameter used to estimate runoff. Table 3 shows the curve numbers used in the model, based on different land use categories and hydrologic soil types in the watershed. Weather data were recorded automatically at 15-min intervals from March 2012 to December 2016 by a WatchDog 2700 Weather Station (Spectrum® Technologies, Inc., Aurora, IL) located 9.2 km southeast of the outlet (M3). The weather data were subsequently processed to create daily time scale files as required by the AnnAGNPS model. Data from the Parameter-elevation Regressions on Independent Slopes Model (PRISM) Climate Group (http://www.prism.oregonstate.edu/explorer/) were used to fill any gaps in rainfall records. Other missing weather data such as daily maximum and minimum temperature, dew point, wind velocity, and solar radiation were patched using data from the Moorhead, MS climate station, which is located 22 km south of the study site and managed by the National Oceanic and Atmospheric Administration.

Table 2. Typical crop management operation for the crops planted in agricultural watersheds within the Mississippi Delta Region (MDR) used in this study.

Cropland	Activity	Application Rate
Soybean	Bedder	-
	Plant	-
	Harvest	-
	Disk	-
Corn	Bedder	-
	Sprayer (pre)	-
	Plant	-
	Fertilizer	150 kg ha^{-1} (soluble nitrogen)
	Fertilizer	13 kg ha^{-1} (phosphorus)
	Sprayer (post)	-
	Sprayer (insecticide)	-
	Harvest	-
Rice	Sprayer (pre)	-
	Plant	-
	Harvest	-
	Disk	-
Wheat	Plant	-
	Fertilizer	120 kg ha^{-1} (soluble nitrogen)
	Harvest	-
	Burn stubble	-

Table 3. Soil Conservation Service (SCS) curve numbers selected for runoff estimation relative to cropland at the agricultural watershed. Source: USDA-SCS [47].

Cropland		Land Cover Class	Hydrologic Soil Type	
			C	D
Soybean	Plant	Soybean straight row (poor)	88	91
	Harvest	Fallow + crop residue (poor)	90	93
Corn	Plant	Rowcrop with residue	85	89
Rice	Plant	Rowcrop with residue	85	89
Wheat	Plant	Small grain straight row + crop residue (poor)	83	86

AnnAGNPS was used to simulate the runoff, sediment, and nutrient loads entering the TWR ditch. The model was set to run for two initialization years (2010–2011) to establish antecedent conditions before beginning the simulation period over the next five years (2012–2016). As described by Bosch, Theurer, Bingner, Felton and Chaubey [42], AnnAGNPS outputs are predefined by the user for the watershed source of interest (subwatersheds, reaches, among others). The model produces event-based output as well as monthly and annual summaries of hydrologic and water quality parameters. The model partitions nitrogen and phosphorus load into sediment-bound and dissolved fractions. This study used dissolved nitrate nitrogen (NO_3–N) and total phosphorus (TP) to represent NO_3–N and TP, respectively, and employed AnnAGNPS to estimate the runoff, sediment, NO_3–N, and TP loads entering a TWR ditch.

3. Results and Discussion

Table 4 presents the average annual runoff, nutrient and sediment loads entering the TWR ditch per unit area, as well as the contributing fields and total area draining to each point—M1, M2, or main outlet M3—in the TWR ditch. The load values represent the aggregate contributions divided by the area of the fields draining into the TWR ditch at each outlet. These values provide a unique picture of the impact of each source area regardless of size. Annual runoff volume per unit area entering the ditch at mid-point M2 was slightly higher than the runoff entering at the M1 or M3 by about 600 m^3 ha^{-1} yr^{-1}, even though M2 had the smallest drainage area. This difference is attributed to the runoff potential of the fields draining to M2. Subwatershed C4 is the field covering the third largest area of all subwatersheds, and soil in this field has the highest runoff potential (hydrologic soil group D). In addition, reaches transporting runoff flow directly into the ditch from subwatersheds C4 and C5. This direct flow path minimizes the amount of water allowed to infiltrate or evaporate and results in a greater volume of water draining into the ditch.

Table 4. Contributing fields to each channel reach, production of average annual runoff and load of nutrients and sediments entering the TWR ditch.

Category	Unit	TWR Channel Reach		
		M1	M1–M2	M2–M3
Contributing fields		C7, C8, C9, C11, C12, C13, C14, C16, C17, C18, C19, C20, C21	C4, C5	C3, C6A, C6B
Area	ha	140.38	26.40	47.26
Runoff	m^3 ha^{-1} yr^{-1}	6785	7364	6743
NO_3–N	kg ha^{-1} yr^{-1}	4.05	0.96	1.7
TP	kg ha^{-1} yr^{-1}	1.19	0.77	1.56
Sediment	ton ha^{-1} yr^{-1}	1.65	1.54	1.28

The NO_3–N load per unit area was higher at M1 as most of the fields that were planted with corn and winter wheat during the simulation period are located upstream of M1. The TP load entering the ditch at M3 tended to be higher. Subwatershed C3, one of the three fields that drained to M3,

was the only field that was simulated as a turn area. Typically, turn areas have compacted soils and do not have vegetation. This means that the soil in this field is highly susceptible to erosion and the off-site movement of nutrients by rainfall–runoff, which might explain the higher TP load simulated by AnnAGNPS at M3. Sediment loading did not show much variation through the TWR ditch segments, indicating that the sediment load might be equally distributed over the total area contributing to the TWR ditch outlets.

3.1. Spatial Variation

The average annual runoff estimated by the AnnAGNPS model is shown in Figure 3. During the 5-year simulation period (2012–2016), the model estimated an average annual runoff of 1,370,053 m^3 that drained into the main outlet at M3, of which 11% was contributed by irrigation runoff. The five highest runoff-producing subwatersheds were C17 (9.73%), C9 (9.31%), C4 (8.78%), C6B (7.74%), and C3 (7.47%). These five fields cover a large drainage area (a combined 90.83 ha out of the total area of 214.04 ha) when compared to other fields in the watershed, which may explain the high runoff production. NO_3–N load transported throughout the watershed to M3 resulted in 623.2 kg yr^{-1} (Figure 4). Five subwatersheds contributed 56.2% of the average annual NO_3–N load, and the order was: C17 (18.41%) > C21 (16.15%) > C11 (8.29%) > C16 (7.03%) > C6A (6.36%). The average annual TP load from 2012 to 2016 in each subwatershed is shown in Figure 5, and the average annual TP load for the whole watershed resulted in 256 kg yr^{-1}. Five subwatersheds contributed 66.2% of the average annual TP load in the following order: C9 (21.7%) > C3 (18.66%) > C17 (16.16%) > C6A (5.09%) > C21 (4.06%). The average annual sediment load resulted in 312.8 tons yr^{-1}, and five subwatersheds contributed 62% of the average annual sediment load (Figure 6) in the following order: C17 (36.18%) > C6B (7.47%) > C5 (6.45%) > C11 (6.03%) > C21 (5.84%). A list of seven subwatersheds that had the greatest impact on water quantity and quality in the simulated watershed is shown in Table 5. Five subwatersheds (C17, C6B, C21, C9, and C3) were designated as priority subwatersheds because they ranked at least first or second with respect to runoff production, NO_3–N load, TP load, or sediment load. Subwatershed C17, which has the largest area (22.54 ha) and the second highest average slope (0.0019), generated the highest sediment and NO_3–N loads. Soils in this field, classified as a hydrologic soil group C, are shallow and have below-average infiltration, and thus have moderately high runoff potential. Furthermore, crops in this field were more diverse and varied between rice, corn, soybean, and winter wheat with assigned curve numbers ranging from 83 to 90. Higher curve numbers translate into higher runoff, and this effect is magnified over larger fields when rainfall occurs. Runoff transported higher loads of nitrogen when corn and winter wheat were planted because these crops required 150 kg ha^{-1} and 120 kg ha^{-1} of soluble nitrogen fertilizer, respectively. However, winter wheat might have reduced TP load during winter. Therefore, the combined effect of landscape characteristics and fertilizer application played a more influential role in the nutrient load from the C17 subwatershed. Subwatershed C9 has an area of 18.70 ha (ranked second in size) and soils classified as hydrologic soil group D. The C9 subwatershed produced the largest TP load of all subwatersheds and ranked second in terms of runoff volume. This subwatershed was planted in a soybean–rice rotation for four years and then planted with corn, which was fertilized with 150 kg ha^{-1} of soluble nitrogen and 13 kg ha^{-1} of phosphorus in 2016. Thus, the area of the subwatershed seemed to be an important factor for the TP load contribution in the watershed.
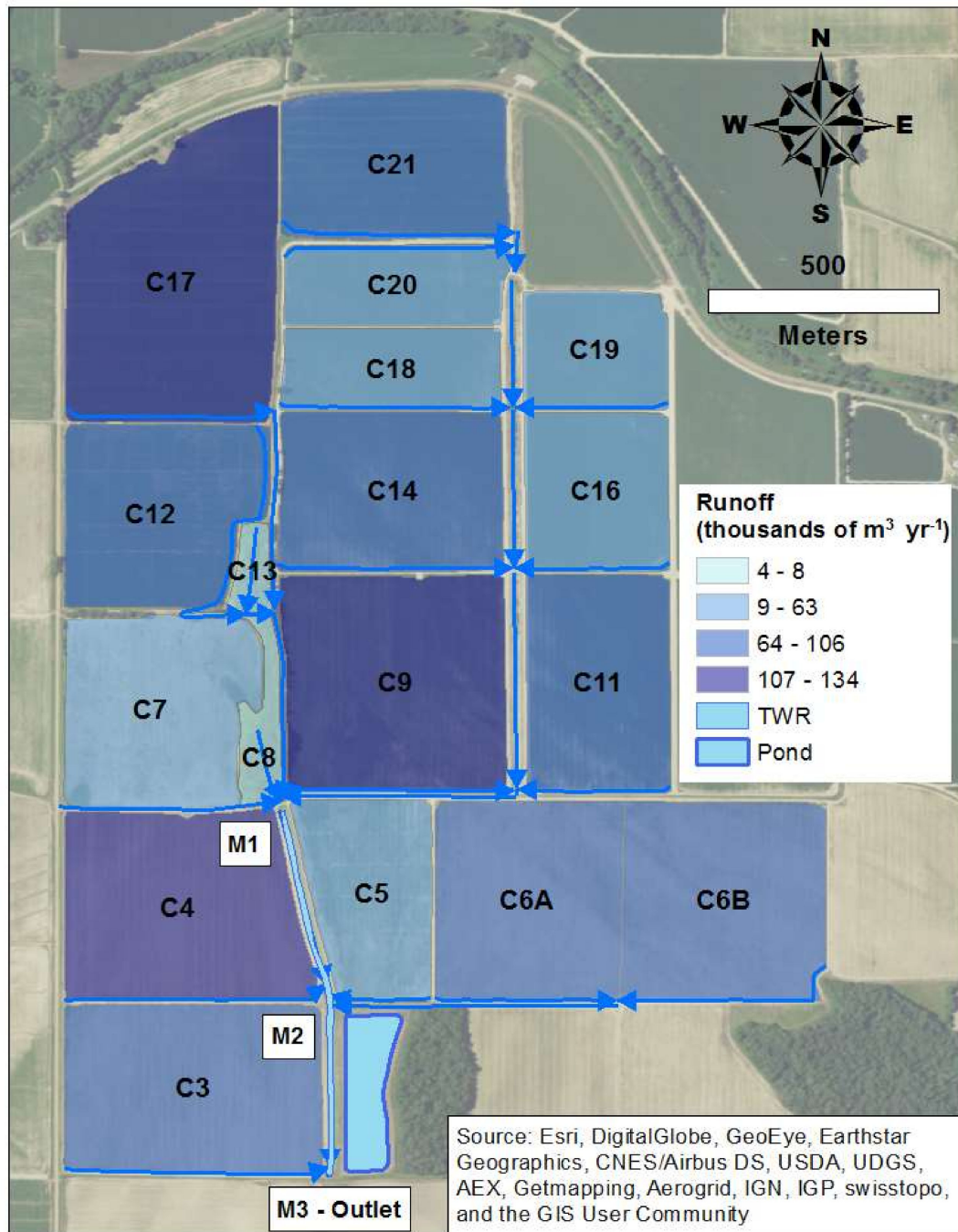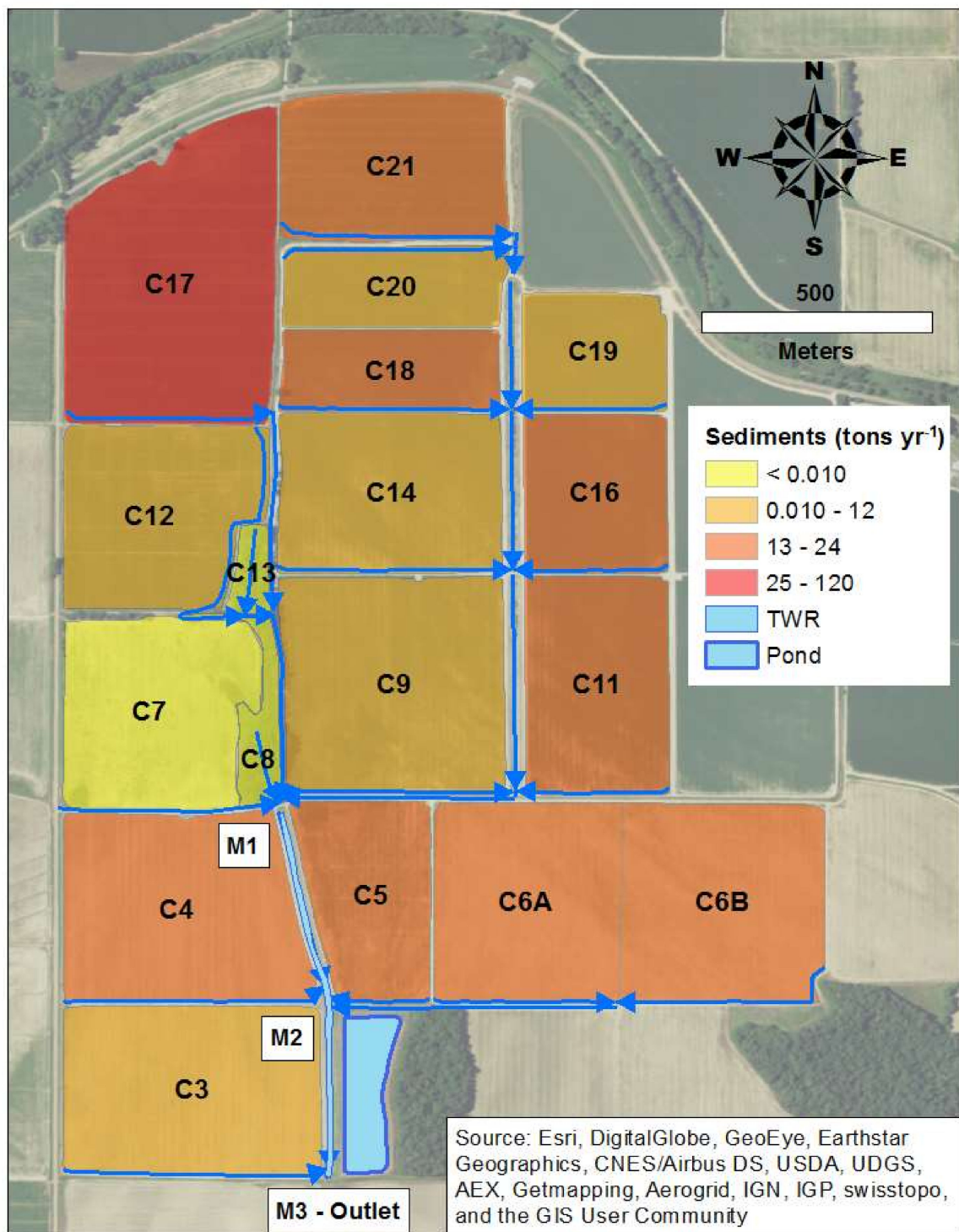
Figure 3. Map of the study area showing the average annual runoff production in the simulated watershed. The blue arrows represent the runoff flow direction towards the outlet. (M1: TWR inlet; M2: TWR mid-canal; M3: TWR outlet; labels within fields indicate the subwatershed identification used by the AnnAGNPS model).
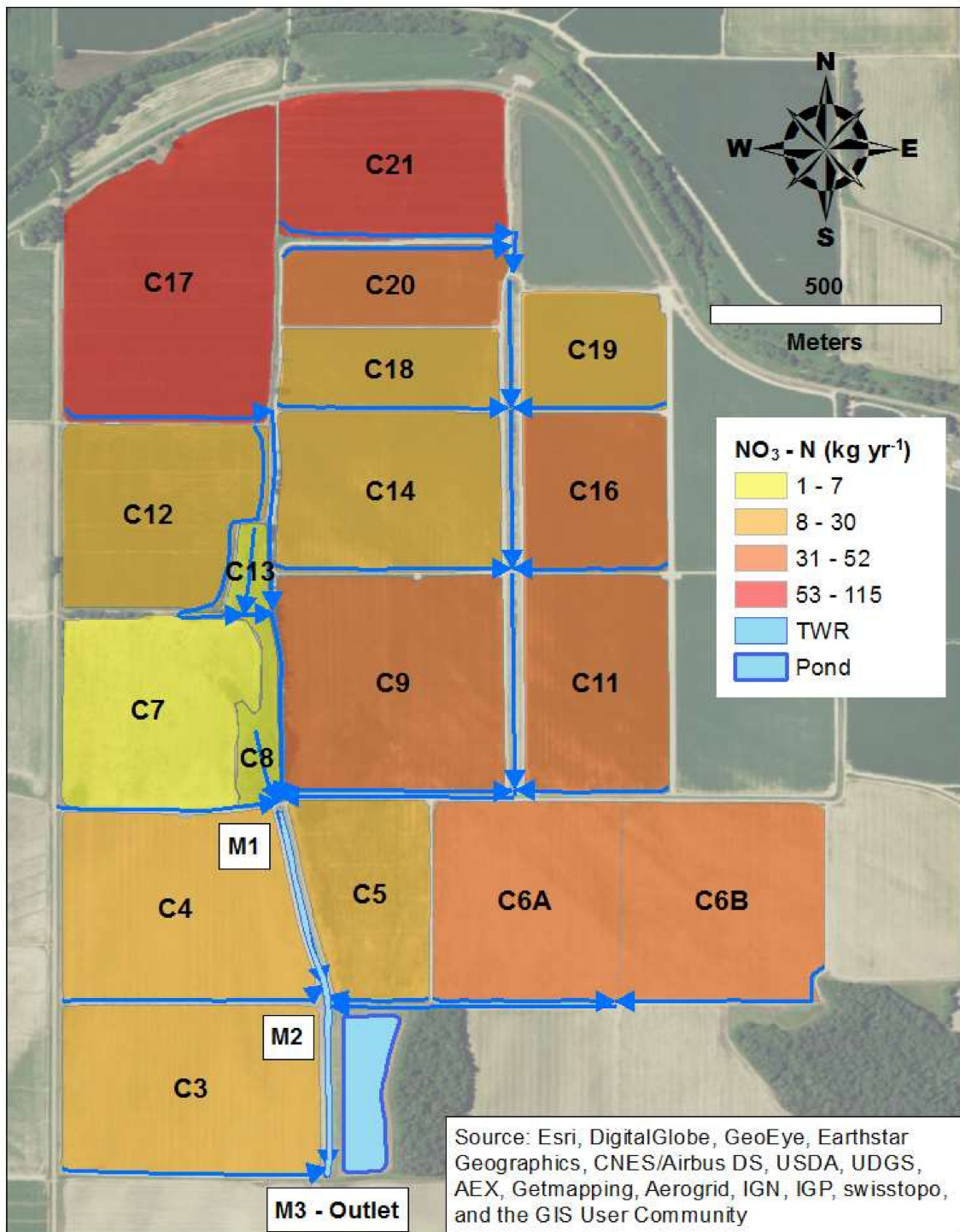
Figure 4. Map of the study area showing the average annual NO$_3$–N load in the simulated watershed. The blue arrows represent the runoff flow direction towards the outlet. (M1: TWR inlet; M2: TWR mid-canal; M3: TWR outlet; labels within fields indicate the subwatershed identification used by the AnnAGNPS model).
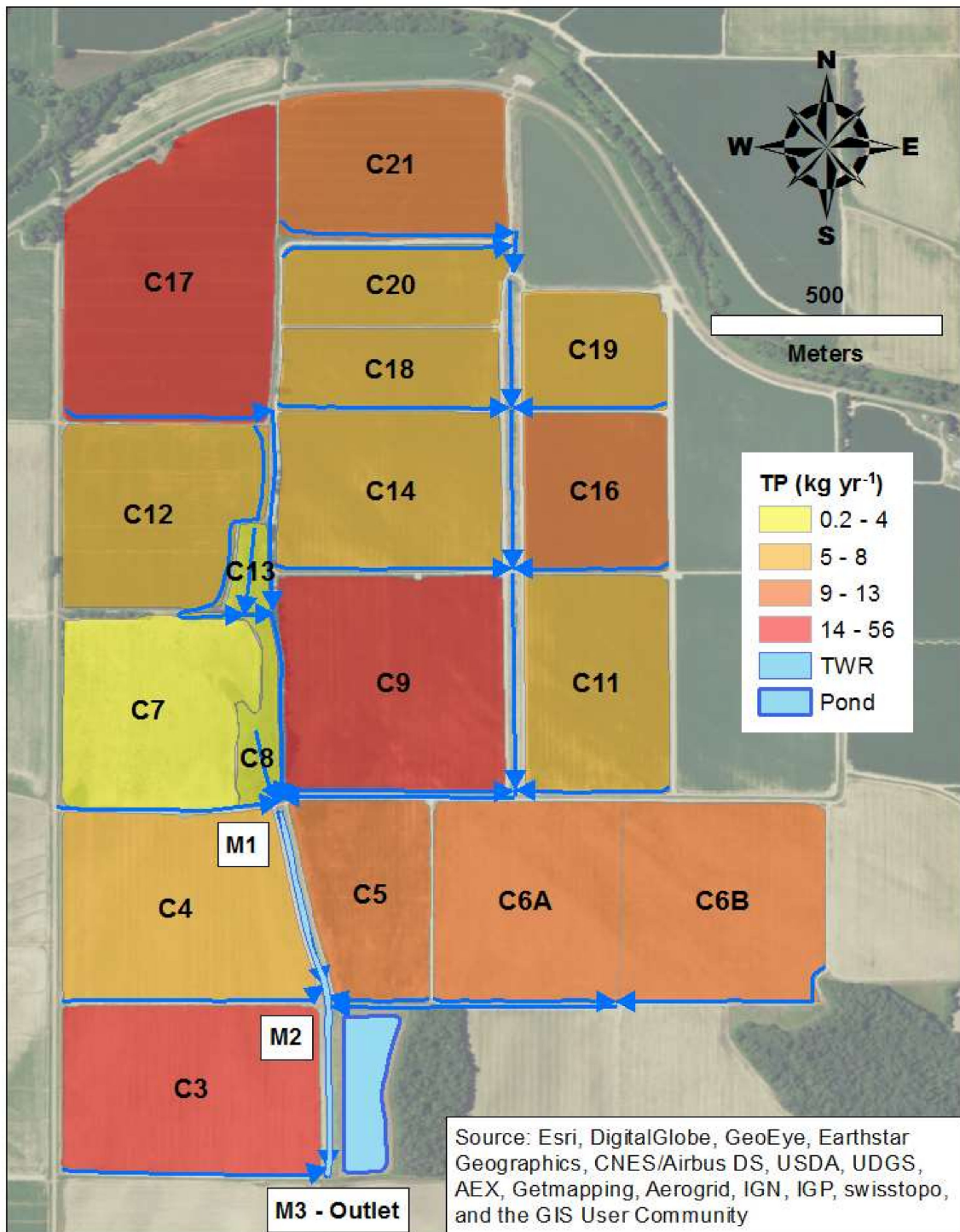
Figure 5. Map of the study area showing the average annual TP load in the simulated watershed. The blue arrows represent the runoff flow direction towards the outlet. (M1: TWR inlet; M2: TWR mid-canal; M3: TWR outlet; labels within fields indicate the subwatershed identification used by the AnnAGNPS model).

Figure 6. Map of the study area showing the average annual sediment load in the simulated watershed. The blue arrows represent the runoff flow direction towards the outlet. (M1: TWR inlet; M2: TWR mid-canal; M3: TWR outlet; labels within fields indicate the subwatershed identification used by the AnnAGNPS model).

Table 5. Rankings of seven subwatersheds based on their impact on water quantity and quality in the simulated watershed.

Subwatershed	Rank				
	Runoff Production	**NO₃–N Load**	**TP Load**	**Sediment Load**	**Total**
C17	1	1	3	1	6
C6B	4	6	7	2	19
C21	9	2	5	5	21
C6A	8	5	4	6	23
C9	2	8	1	13	24
C11	10	3	10	4	27
C3	5	12	2	10	29

Rows with highlighted records indicate that the individual rank resulted in either 1st or 2nd. Subwatersheds with highlighted rows were designated as priority fields.

Subwatershed C6B was ranked fifth and third with respect to the magnitude of the area and average land slope, respectively, and was classified as having soils in hydrologic soil group D. The C6B subwatershed generated the second highest sediment load of all subwatersheds and was planted primarily with soybeans except during 2013, when corn was planted. In addition, the C3 subwatershed ranked fourth in magnitude of area and ninth with respect to the average land slope and generated the second highest TP load of all subwatersheds. The C3 subwatershed had soils classified as hydrologic soil group D and was simulated as a turn area, which explained the high TP load attached to sediments and transported by runoff. Finally, the subwatershed C21 also had soils in hydrologic soil group D and was ranked tenth in areal extent and seventh for average land slope. The C21 subwatershed produced the second highest NO₃–N load of all subwatersheds. Similar to C17, subwatershed C21 was also planted with corn and winter wheat during two consecutive years in 2013 and 2014.

3.2. Temporal Variation

The total annual runoff production and nutrient and sediment load from the simulated watershed, as estimated by the AnnAGNPS model, are shown in Figure 7. During the 5-year simulation period (2012–2016), an average annual total runoff of 1,465,678 m³ drained to the main outlet at M3. This volume exceeds the TWR ditch storage volume by roughly 110 times, which highlights the magnitude of surface water available in the simulated watershed. In terms of runoff produced by year, the order was 2013 > 2014 > 2016 > 2015 > 2012 (Figure 7a), which followed the same pattern for total precipitation by year. Overall, fields draining upstream from the TWR ditch to the inlet at M1 generated the highest volume of runoff at a rate of 952,578 m³ yr⁻¹, which resulted in roughly 65% of the total runoff volume produced annually. Fields draining into the TWR ditch between M1 and M2 contributed 13.3% of the annual runoff production, and fields draining into the ditch between M2 and M3 contributed 21.7% of the average annual runoff.

The changes in total annual NO₃–N load for each TWR ditch segment are shown in Figure 7b. Nitrate nitrogen was highest in 2015, followed in order of magnitude by 2014, 2013, 2016, and 2012. Overall, the area that drained into M1 was responsible for the greatest percentage of the NO₃–N load in the TWR ditch in all years. During the 2013 growing season, 41.4% of the watershed was planted with corn, mainly in five (C17, C6B, C21, C6A, C5) of the highest runoff contributing fields in the simulated watershed (Table 5). Winter wheat covered 12.2% of the watershed after the summer growing season in 2013. Both corn and winter wheat were fertilized with soluble nitrogen, which is reflected by the high NO₃–N load that was simulated by the model in 2013. In 2014, rainfall was highest during spring, roughly equally distributed between summer and fall, and minimal in winter. In fall 2014, the subwatersheds with the highest contributing nitrate loads, C17 and C21, were planted with winter wheat, which was fertilized with soluble nitrogen. Available nitrogen in soil after the fertilizer application was likely transported by runoff from the 2014 winter and 2015 spring rainfall, which might explain the higher NO₃–N load during these years. In addition, soybeans were planted

on 84% of the simulated watershed during 2014. After soybeans were harvested, 33% of the nitrogen that was used by the plant was left over in the soil [48], available for potential transformation mediated by microorganisms and susceptible to movement off fields by runoff.
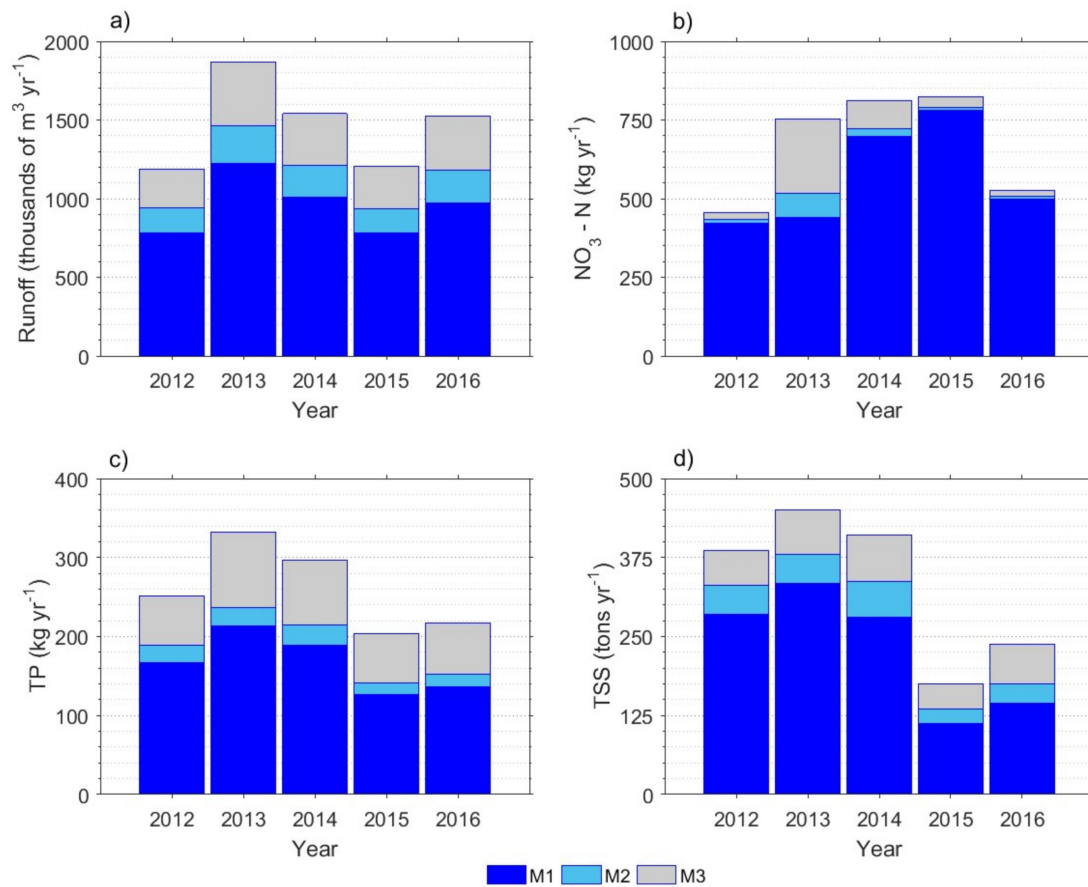
Figure 7. Comparison of (**a**) the total annual runoff production, (**b**) the total annual NO$_3$–N load, (**c**) the total phosphorus (TP) load, (**d**) and the total suspended solids (TSS) in the simulated watershed. M1: TWR inlet; M2: TWR mid-canal; M3: TWR outlet.

Total annual sediment and TP loads were highest in 2013, followed in order of magnitude by 2014, 2012, 2016, and 2015 (Figure 7c,d). The changes in TP and sediment loads were similar and can be attributed to the fact that phosphorus is usually transported as sediment-bound phosphorus. Similar to the pattern observed for NO$_3$–N, the bulk of TP and sediment were from the area that drains into M1. In addition, TP and sediment loads entering the ditch between M2 and M3 were generally higher than the loads entering the system between M1 and M2. In 2013, significant amounts of precipitation were recorded in winter, fall, and spring. These conditions favored the production of runoff from fields with exposed soil, and it is highly likely that erosion due to high runoff resulted in greater loads of TP and sediment in 2013. In contrast, the NO$_3$–N load during 2014 was higher than during 2013. One possible explanation is that most of the fertilizer applied during spring and fall of 2014 was transported off the field as most of the rain fell during these two seasons. In addition, during 2013 and 2014, 41.5% of the simulated watershed was planted with corn and 16.6% with winter wheat. Planting winter wheat after corn seemed to result in larger NO$_3$–N loads transported with runoff. Rainfall was higher during the winter and summer of 2016 and minimal during spring and fall. In 2016, the fields were planted with corn (34.7%), soybean (26.5%), and rice (22.7%). Runoff produced in 2012 and 2015 was the lowest among the 5-year simulation period, which may be attributed to less rainfall observed in 2012 and 2015 as compared to other years. The water savings potential of the TWR ditch was estimated

by combining the simulated runoff and discharge water measured at the ditch outlet available for 2016 (Figure 8). Of the 1,526,105 m^3 of runoff produced, 56.5% (862,581 m^3) was saved by the ditch in 2016.
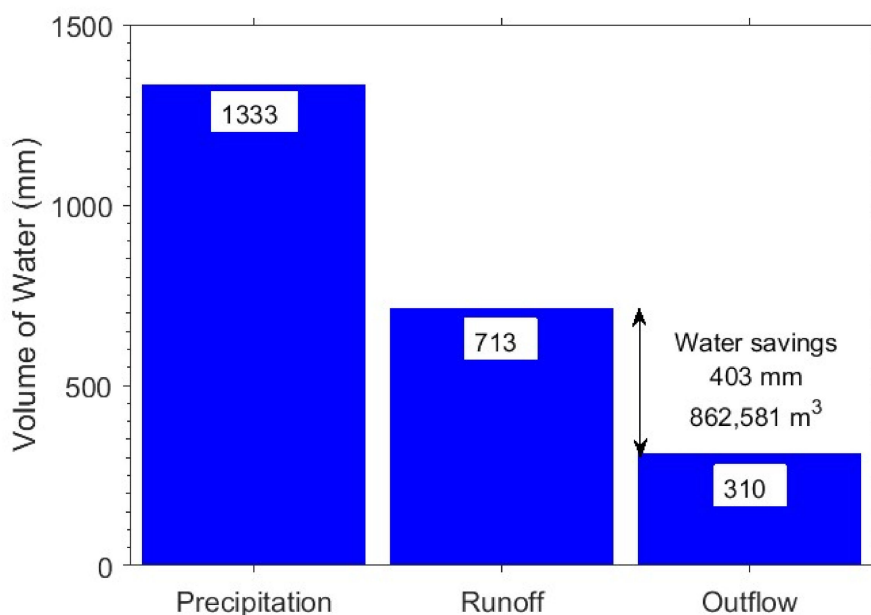

Figure 8. On-farm water storage (OFWS) system water savings potential estimated for 2016. Precipitation: total precipitation; Runoff: AnnAGNPS simulated runoff; Outflow: water discharge measured at the outlet pipe.

3.3. Impact of Additional Agricultural Management Operations

To examine the impacts of management practices on water quality and quantity, two scenarios were implemented in AnnAGNPS. Scenario 1 planted winter wheat in priority subwatersheds (C17, C6B, C21, C9, and C3), and Scenario 2 planted winter wheat in all subwatersheds. With more rainfall occurring outside the summer growing season, winter wheat could be an option for producers unable to irrigate or those trying to use less water for irrigation. The current management practices were set as the baseline scenario. The impacts of Scenarios 1 and 2 on the estimated average annual runoff, sediment, and nutrient loads at different locations within the TWR ditch (M1, M2, and M3) are shown in Figure 9. The targeted implementation of management practices (Scenario 1) reduced the TP and sediment loads at M1 by 19.3% and 12.6%, respectively. However, under Scenario 1, NO$_3$–N loading increased substantially at all locations primarily because winter wheat was fertilized with soluble nitrogen at a rate of 120 kg ha^{-1}. This suggests that some of the nitrogen applied to fields may have been transported off-site by runoff.

Scenario 2 resulted in greater average annual reductions of TP and sediment loads than Scenario 1. If winter wheat is planted in all subwatersheds, TP loads from the areas upstream of M1 are predicted to decrease by approximately 38% from the current conditions. Reductions in TP loads at M2 and M3 were about 63% and 25%, respectively. Reductions in sediment loads followed a similar pattern as those for TP, with a higher percentage reduction at the upstream outlet locations—M1 (24.2%) and M2 (45%)—than at the downstream outlet—M3 (22%). The all winter wheat scenario also showed a reduction in runoff. In total, 188,100 m^3 (97,900 m^3 at M1; 29,700 m^3 at M2; and 60,500 m^3 at M3) of runoff were reduced from the fields draining to the TWR ditch. Despite the positive effects that could result from planting winter wheat in the target watershed, AnnAGNPS simulations showed very high increases in the NO$_3$–N load entering the ditch at M1 due to the nitrogen fertilization necessary to grow winter wheat. Conservationists and policy makers should be mindful that implementing management practices to improve water quality might have positive effects on one variable but associated undesirable tradeoffs on another variable (Smith et al., 2019). Although cover crops may

reduce NO_3–N leaching to groundwater, the NO_3–N load may increase with runoff due to biomass leaching during rainfall events [49]. This effect might be exacerbated if soluble nitrogen is applied over poorly drained soils with a high runoff potential.
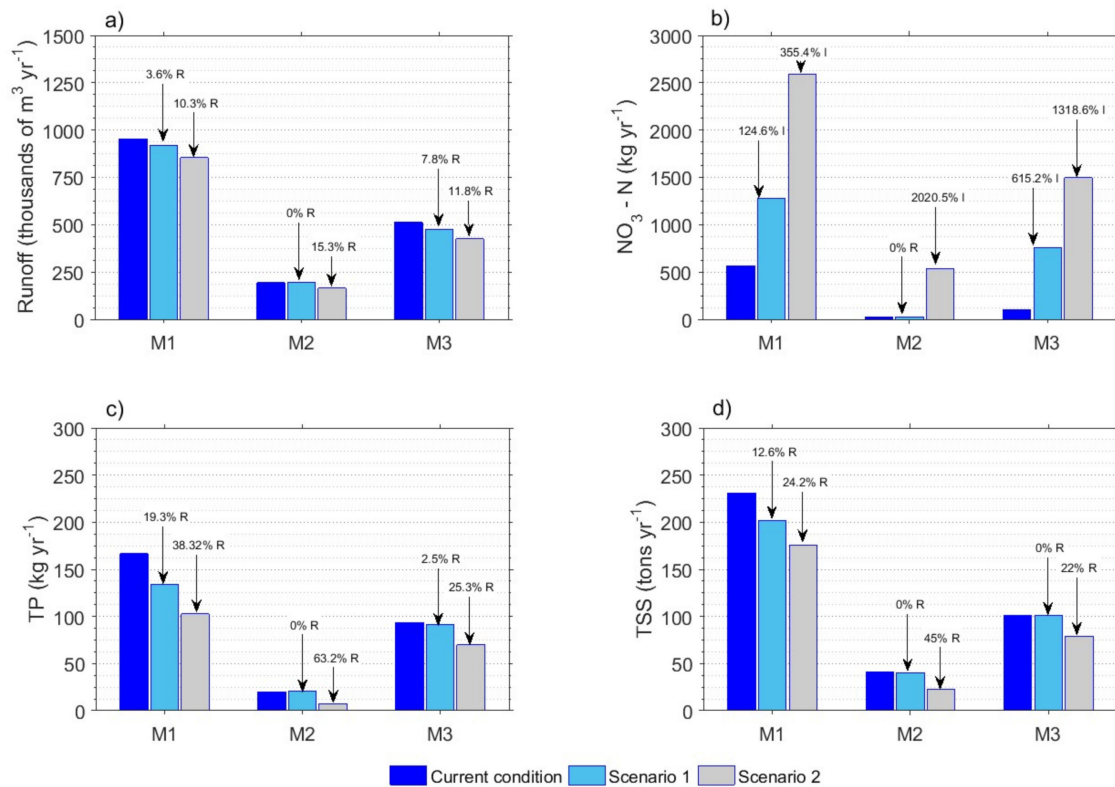
Figure 9. Impacts of two additional agricultural management operations in the simulated watershed on the average of (**a**) total annual runoff production, (**b**) NO_3–N load, (**c**) TP load, and (**d**) sediment load. Text arrows indicate the reduction or increase percentage relative to the current condition scenario; R: reduction; I: increase; WW: winter wheat; M1: TWR inlet; M2: TWR mid-canal; M3: TWR outlet; Scenario 1: planting winter wheat in priority subwatersheds; Scenario 2: planting winter wheat in each subwatershed.

4. Summary and Conclusions

The AnnANGPS model was used to estimate the water, sediment, and nutrient loads entering a TWR ditch implemented as part of an OFWS system in an agricultural watershed within the PBW, Mississippi. Simulations showed that the fields with larger areas that have soils with a high runoff potential (hydrologic soil group C or D) resulted in higher runoff, and this condition mirrored annual rainfall patterns. The volume of runoff exceeded the TWR ditch storage volume by roughly 110 times, mostly during the winter and spring seasons. Therefore, these seasons offer the highest potential for capturing excess water in the OFWS system. Results showed that the fields with larger areas also produced the highest total nutrient and sediment loads. AnnAGNPS simulations showed that NO_3–N loads were sensitive to fertilizer application. Therefore, during years when corn and winter wheat were planted and fertilized, NO_3–N loading increased. The TP and sediment loading patterns were similar and were influenced by the hydrological temporal conditions.

Assessment of different management scenarios indicated that planting winter wheat can benefit water quality by reducing sediment loads and the export of TP. However, winter wheat requires nitrogen fertilizer, which can result in higher NO_3–N loads washed off by runoff. In particular, if winter wheat is planted in the priority subwatersheds (Scenario 1), TP and sediment loads are reduced by about 19% and 13%, respectively, at M1. Although planting winter wheat in all fields (Scenario 2) may

not be feasible, this scenario would substantially reduce TP and sediment loads from the contributing areas draining to M1 (TP: 3%; sediment: 24%) and M2 (TP: 63%; sediment: 45%) in the TWR ditch. Scenario 2 also showed that 188,100 m^3 of runoff can be reduced from fields draining to the TWR ditch.

Results of this study provide both stakeholders and agencies with critical information needed to better identify where these systems can be implemented to improve water quality and relieve pumping pressure on groundwater in the Lower Mississippi River Alluvial Valley. In addition, this study suggests that agricultural watersheds in the MDR might produce substantial amounts of runoff, which could be an important source of water for irrigation if properly managed. While managing the water availability during winter and spring, nutrient reduction benefits of OFWS systems can be maximized.

References

1. Gerland, P.; Raftery, A.E.; Ševčíková, H.; Li, N.; Gu, D.; Spoorenberg, T.; Alkema, L.; Fosdick, B.K.; Chunn, J.; Lalic, N. World population stabilization unlikely this century. *Science* **2014**, *346*, 234–237. [CrossRef]

2. Tilman, D.; Cassman, K.G.; Matson, P.A.; Naylor, R.; Polasky, S. Agricultural sustainability and intensive production practices. *Nature* **2002**, *418*, 671–677. [CrossRef] [PubMed]

3. Tilman, D.; Balzer, C.; Hill, J.; Befort, B.L. Global food demand and the sustainable intensification of agriculture. *Proc. Natl. Acad. Sci. USA* **2011**, *108*, 20260–20264. [CrossRef]

4. Ladapo, H.; Aminu, F. Agriculture and eutrophication of freshwaters: A review of control measures. *J. Res. For. Wildl. Environ.* **2017**, *9*, 67–74.

5. Withers, P.; Neal, C.; Jarvie, H.; Doody, D. Agriculture and eutrophication: Where do we go from here? *Sustainability* **2014**, *6*, 5853. [CrossRef]

6. Rabotyagov, S.; Kling, C.; Gassman, P.; Rabalais, N.; Turner, R. The economics of dead zones: Causes, impacts, policy challenges, and a model of the Gulf of Mexico hypoxic zone. *Rev. Environ. Econ. Policy* **2014**, *8*, ret024. [CrossRef]

7. Rabalais, N.N.; Turner, R.E.; Scavia, D. Beyond science into policy: Gulf of Mexico hypoxia and the Mississippi River nutrient policy development for the Mississippi River watershed reflects the accumulated scientific evidence that the increase in nitrogen loading is the primary factor in the worsening of hypoxia in the northern gulf of mexico. *BioScience* **2002**, *52*, 129–142.

8. Carpenter, S.R.; Stanley, E.H.; Vander Zanden, M.J. State of the world's freshwater ecosystems: Physical, chemical, and biological changes. *Annu. Rev. Environ. Resour.* **2011**, *36*, 75–99. [CrossRef]

9. Osmond, D.L. USDA water quality projects and the National Institute of Food and Agriculture Conservation Effects Assessment Project watershed studies. *J. Soil Water Conserv.* **2010**, *65*, 142A–146A. [CrossRef]

10. Tomer, M.; Sadler, E.; Lizotte, R.; Bryant, R.; Potter, T.; Moore, M.; Veith, T.; Baffaut, C.; Locke, M.; Walbridge, M. A decade of conservation effects assessment research by the USDA Agricultural Research Service: Progress overview and future outlook. *J. Soil Water Conserv.* **2014**, *69*, 365–373. [CrossRef]

11. Tomer, M.; Locke, M. The challenge of documenting water quality benefits of conservation practices: A review of USDA-ARS's Conservation Effects Assessment Project watershed studies. *Water Sci. Technol.* **2011**, *64*, 300–310. [CrossRef] [PubMed]

12. Her, Y.; Chaubey, I.; Frankenberger, J.; Jeong, J. Implications of spatial and temporal variations in effects of conservation practices on water management strategies. *Agric. Water Manag.* **2017**, *180*, 252–266. [CrossRef]

13. Meals, D.W. Detecting changes in water quality in the Laplatte River watershed following implementation of BMPs. *Lake Reserv. Manag.* **1987**, *3*, 185–194. [CrossRef]

14. Arabi, M.; Frankenberger, J.R.; Engel, B.A.; Arnold, J.G. Representation of agricultural conservation practices with SWAT. *Hydrol. Process.* **2008**, *22*, 3042–3055. [CrossRef]

15. Lizotte, R.E.; Yasarer, L.M.W.; Locke, M.A.; Bingner, R.L.; Knight, S.S. Lake nutrient responses to integrated conservation practices in an agricultural watershed. *J. Environ. Qual.* **2017**, *46*, 330–338. [CrossRef]

16. Bracmort, K.S.; Arabi, M.; Frankenberger, J.; Engel, B.A.; Arnold, J.G. Modeling long-term water quality impact of structural BMPs. *Trans. ASAE* **2006**, *49*, 367–374. [CrossRef]

17. Meals, D.W.; Dressing, S.A.; Davenport, T.E. Lag time in water quality response to best management practices: A review. *J. Environ. Qual.* **2010**, *39*, 85–96. [CrossRef]

18. Lam, Q.; Schmalz, B.; Fohrer, N. The impact of agricultural best management practices on water quality in a North German lowland catchment. *Environ. Monit. Assess.* **2011**, *183*, 351–379. [CrossRef]

19. Santhi, C.; Kannan, N.; White, M.; Di Luzio, M.; Arnold, J.; Wang, X.; Williams, J. An integrated modeling approach for estimating the water quality benefits of conservation practices at the river basin scale. *J. Environ. Qual.* **2014**, *43*, 177–198. [CrossRef]

20. Zhang, X.; Zhang, M. Modeling effectiveness of agricultural BMPs to reduce sediment load and organophosphate pesticides in surface runoff. *Sci. Total Environ.* **2011**, *409*, 1949–1958. [CrossRef]

21. Yuan, Y.; Bingner, R.; Rebich, R. Evaluation of AnnAGNPS on Mississippi Delta MSEA watersheds. *Trans. ASAE* **2001**, *44*, 1183–1190. [CrossRef]

22. Parajuli, P.B.; Nelson, N.O.; Frees, L.D.; Mankin, K.R. Comparison of AnnAGNPS and SWAT model simulation results in USDA-CEAP agricultural watersheds in South-Central Kansas. *Hydrol. Process.* **2009**, *23*, 748–763. [CrossRef]

23. Abdelwahab, O.M.M.; Bingner, R.L.; Milillo, F.; Gentile, F. Evaluation of alternative management practices with the AnnAGNPS model in the Carapelle watershed. *Soil Sci.* **2016**, *181*, 293–305. [CrossRef]

24. Lizotte, R.; Locke, M.; Bingner, R.; Steinriede, R.W.; Smith, S. Effectiveness of integrated best management practices on mitigation of atrazine and metolachlor in an agricultural lake watershed. *Bull. Environ. Contam. Toxicol.* **2017**, *98*, 447–453. [CrossRef] [PubMed]

25. Pérez-Gutiérrez, J.D.; Paz, J.O.; Tagert, M.L.M. Seasonal water quality changes in on-farm water storage systems in a south-central U.S. agricultural watershed. *Agric. Water Manag.* **2017**, *187*, 131–139. [CrossRef]

26. Pérez-Gutiérrez, J.D.; Paz, J.O.; Tagert, M.L.; Karki, R. Seasonal variation of water quality in on-farm water storage systems: Case study of a mississippi delta agricultural watershed. In Proceedings of the 2015 ASABE Annual International Meeting, New Orleans, LA, USA, 26–29 July 2015; American Society of Agricultural and Biological Engineers: St. Joseph Charter Township, MI, USA, 2015; p. 7.

27. Moore, M.T.; Pierce, J.R.; Farris, J.L. Water-quality analysis of an intensively used on-farm storage reservoir in the northeast Arkansas Delta. *Arch. Environ. Contam. Toxicol.* **2015**, *69*, 89–94. [CrossRef]

28. Pérez-Gutiérrez, J.D.; Paz, J.O.; Tagert, M.L.M.; Sepehrifar, M. Impact of rainfall characteristics on the NO3—N concentration in a tailwater recovery ditch. *Agric. Water Manag.* **2020**, *233*, 106079. [CrossRef]

29. Karki, R.; Tagert, M.L.M.; Paz, J.O. Evaluating the nutrient reduction and water supply benefits of an on-farm water storage (OFWS) system in east Mississippi. *Agric. Ecosyst. Environ.* **2018**, *265*, 476–487. [CrossRef]

30. Geter, W.F.; Theurer, F.D. AnnAGNPS-RUSLE sheet and rill erosion. In Proceedings of the First Federal Interagency Hydrologic Modeling Conference, Las Vegas, NV, USA, 19–23 April 1998; pp. 10–16.

31. Bingner, R.; Theurer, F. AnnAGNPS: Estimating sediment yield by particle size for sheet and rill erosion. In Proceedings of the 7th Interagency Sedimentation Conference, Reno, NV, USA, 25–29 March 2001.

32. Baginska, B.; Milne-Home, W.; Cornish, P.S. Modelling nutrient transport in Currency creek, NSW with AnnAGNPS and PEST. *Environ. Model. Softw.* **2003**, *18*, 801–808. [CrossRef]

33. Polyakov, V.; Fares, A.; Kubo, D.; Jacobi, J.; Smith, C. Evaluation of a non-point source pollution model, AnnAGNPS, in a tropical watershed. *Environ. Model. Softw.* **2007**, *22*, 1617–1627. [CrossRef]

34. Licciardello, F.; Zema, D.; Zimbone, S.; Bingner, R. Runoff and soil erosion evaluation by the AnnAGNPS model in a small mediterranean watershed. *Trans. ASABE* **2007**, *50*, 1585–1593. [CrossRef]

35. Sarangi, A.; Cox, C.A.; Madramootoo, C.A. Evaluation of the AnnAGNPS model for prediction of runoff and sediment yields in St. Lucia watersheds. *Biosyst. Eng.* **2007**, *97*, 241–256. [CrossRef]

36. Shamshad, A.; Leow, C.S.; Ramlah, A.; Wan Hussin, W.M.A.; Mohd. Sanusi, S.A. Applications of AnnAGNPS model for soil loss estimation and nutrient loading for Malaysian conditions. *Int. J. Appl. Earth Obs. Geoinf.* **2008**, *10*, 239–252. [CrossRef]

37. Kliment, Z.; Kadlec, J.; Langhammer, J. Evaluation of suspended load changes using AnnAGNPS and SWAT semi-empirical erosion models. *CATENA* **2008**, *73*, 286–299. [CrossRef]

38. Zema, D.; Bingner, R.; Denisi, P.; Govers, G.; Licciardello, F.; Zimbone, S. Evaluation of runoff, peak flow and sediment yield for events simulated by the AnnAGNPS model in a Belgian agricultural watershed. *Land Degrad. Dev.* **2012**, *23*, 205–215. [CrossRef]

39. Chahor, Y.; Casalí, J.; Giménez, R.; Bingner, R.L.; Campo, M.A.; Goñi, M. Evaluation of the AnnAGNPS model for predicting runoff and sediment yield in a small mediterranean agricultural watershed in Navarre (Spain). *Agric. Water Manag.* **2014**, *134*, 24–37. [CrossRef]

40. NRCS. Conservation Practice Standard Irrigation System, Tailwater Recovery No. Code 447. Available online: https://www.nrcs.usda.gov/Internet/FSE_DOCUMENTS/stelprdb1045769 (accessed on 10 September 2017).

41. Bingner, R.; Darden, R.; Theurer, F.; Alonso, C.; Smith, P. AnnAGNPS input parameter editor interface. In Proceedings of the First Federal Interagency Hydrologic Modeling Conference, Las Vegas, NV, USA, 19–23 April 1998; pp. 8–15.

42. Bosch, D.; Theurer, F.; Bingner, R.; Felton, G.; Chaubey, I. *Evaluation of the AnnAGNPS Water Quality Model*; ASAE Paper No. 98-2195; ASAE: St. Joseph, MI, USA, 1998; 12p.

43. Theurer, F.D.; Cronshey, R.G. AnnAGNPS-reach routing processes. In Proceedings of the First Federal Interagency Hydrologic Modeling Conference, Las Vegas, NV, USA, 19–23 April 1998; pp. 19–23.

44. Cronshey, R.G.; Theurer, F.D. AnnAGNPS-non point pollutant loading model. In Proceedings of the First Federal Interagency Hydrologic Modeling Conference, Las Vegas, NV, USA, 19–23 April 1998; pp. 1–9.

45. USDA-SCS. Urban hydrology for small watersheds. *US Soil Conserv. Service. Tech. Release* **1986**, *55*, 13.

46. Soil Survey Staff, N.R.C.S.; United States Department of Agriculture. *Soil Survey Geographic (SSURGO) Database for Metcalf Farm, Mississippi. (02/22/2016)*; United States Department of Agriculture: Washington, DC, USA, 2016.

47. USDA-SCS. *National Engineering Handbook. Section 4: Hydrology*; USDA Soil Conservation Service: Washington, DC, USA, 1985.

48. IPNI. IPNI Estimates of Nutrient Uptake and Removal. Available online: http://www.ipni.net/article/IPNI-3296 (accessed on 6 September 2017).

49. Miller, M.H.; Beauchamp, E.G.; Lauzon, J.D. Leaching of nitrogen and phosphorus from the biomass of three cover crop species. *J. Environ. Qual.* **1994**, *23*, 267–272. [CrossRef]